# Magma plumbing beneath the Mid-Atlantic Ridge

Thesis submitted for the degree of
Doctor of Philosophy
at the University of Leicester

by

Laurence Andrew Coogan BSc. (Liverpool)
Department of Geology
University of Leicester

June 1998





ProQuest LLC
789 East Eisenhower Parkway
P.O. Box 1346
Ann Arbor, MI 48106-1346

# Magma plumbing beneath the Mid-Atlantic Ridge


## Laurence Andrew Coogan


## PhD Abstract


A suite of fresh, ~0.75 Ma old, gabbroic samples from ODP Hole 923A on the Mid-Atlantic ridge just south of the Kane Fracture Zone, 23°N, have been studied texturally and by electron probe and ion probe. This hole penetrated ~70 mbsf recovering 40 m of core from the basal 55 m of the hole. The core is dominated by two interlayered lithologies: poikilitic olivine gabbros and brown-pyroxene gabbros, plus volumetrically minor microgabbros, oxide gabbros and leucocratic veins.

Poikilitic olivine gabbros are plagioclase +/- olivine cumulates with relatively primitive mineral composition. Horizons of poikilitic olivine gabbros in the core represent magma chamber replenishment in which the replenishing magma ponded at the base of the chamber and fractionated. Variations in plagioclase trace element compositions (e.g. La/Nd and Ba/K) in part reflect compositional variation in their parental melts derived from the mantle. Calculated equilibrium melt compositions are highly LREE depleted ($La_n/Nd_n$ as low as 0.25).

Brown-pyroxene gabbros are olivine - plagioclase - clinopyroxene cumulates which have more evolved mineral compositions than poikilitic olivine gabbros. A series of major and trace element characteristics of the rocks, and textural phenomena, indicate that post-cumulus processes were important in their formation. In particular, extreme variations in incompatible element abundances, and fractionation of Zr from Y (and REE's), from the core to rim of clinopyroxene crystals occurs. It is proposed that the fractionation of the interstitial melt was caused by reaction between migrating interstitial melt and the crystal assemblage (magmatic metasomatism). This led to the interstitial melt becoming highly evolved in terms of incompatible elements whilst the major elements were efficiently buffered by the crystals.

Broader implications of these data include: (i) magma mixing *within the crust* is important in homogenising magma compositions prior to eruption, (ii) return of interstitial melt to the magma chamber could lead to extensive changes in trace element abundances and ratios in the erupted melts, and (iii) whole-rock gabbro geochemistry may be misleading if the rocks have suffered extensive magmatic metasomatism.

# Acknowledgements

Many people deserve thanking and acknowledging for help and support during the course of my PhD studies. First and foremost Pamela Kempton and Andy Saunders for initiating and supervising the project - thanks. Furthermore, Pamela provided many of the samples used in this study and Andy always had a book on anything I asked about. Illuminating scientific discussions on a whole manner of topics with (Mike) Norry were always enjoyed and are also gratefully acknowledged. Steve Temperley, being one of the few people in Leicester who looks at rocks, was of much assistance in discussing deformation textures. Mike Branney provided informative conversation regarding crystal sedimentation.

Technical support during this study came from a number of sources all of which are thanked. Colin Cunningham made many of the thin sections studied. Rob Wilson provided much help with operation of the electron probe. Rod Branson helped with use of the SEM, photography and, perhaps more importantly, many hours of sanity returning conversations. Andy Smith helped with operation of the XRD. Chris Beckett's assistance with all matters computing was invaluable as was Ceri's help with the NIH image macro (Appendix A.II). Richard Hinton and John Craven (Edinburgh University) provided much assistance with operation of the ion-probe which went beyond the call of duty (especially the beers). Without their help the most interesting parts of this thesis would not have happened.

Pre-prints of papers from the ODP Leg 153 Scientific Results Volume were provided by Kent Ross and Pamela Kempton for which they are thanked. Ed Mathez provided a pre-print of Mathez *et al.*, (1997) which is also gratefully acknowledged. ODP are thanked for provide samples through requests 14930A, B and C, and in particular Walter Hale is thanked for his help and hospitality at the ODP core repository in Bremen. NERC are thanked for funding use of the Edinburgh ion probe facility.

Time spent with friends provided many hours of (generally alcohol accompanied) R and R necessary during the course of a PhD. To list them all would just lead to my forgetfulness missing someone out. However, particular thanks to T for many Skol's, Sarah for broadening my experience of life, Tiff and Roz for taking me in off the streets and Mike and Mary for none geological conversation.

Thanks are also due to Bob Hunter for initiating my interest in magma chambers which lead to my interest in this project and the sound advice to "look at the rocks don't just crush them up". Finally Chris MacLeod is thanked for providing the offer of a job without which the pain of writing this thesis would have dragged on for even longer.

Many other people undoubtedly have helped out at one time or another and for these omissions I apologise for my forgetfulness (early senility).

# Contents

**Chapter VI: Evolution of the crystal mush**



**Chapter VII: Conclusions - a model for magma plumbing beneath the Mid-Atlantic Ridge, and suggestions for future study**

## Appendix A.V: Electron probe data

This is supplied on a Macintosh formatted floppy discs in the attached envelope.



## References

## List of Figures

## List of Tables

# Chapter I: Magma plumbing beneath mid-ocean ridges

## 1.1 Introduction

One of the primary sources of information regarding the processes operating beneath mid-ocean ridge comes from mid-ocean ridge basalt (MORB). In order to be able to use this to interpret mantle dynamics and composition the relationship between the erupted composition and the primary melt produced within the mantle must be known. However, the composition of the melt is likely to be modified extensively within the magma plumbing system. Magma plumbing beneath mid-ocean ridges starts as the mantle crosses its solidus, and involves the extraction of the melt generated within the mantle, mixing of the various melt increments, fractionation of this melt, and its subsequent solidification.

In this thesis a suit of oceanic gabbros sampled by Ocean Drilling Program (ODP) Leg 153 are used to investigate the magma plumbing system. This study has involved extensive standard petrology coupled to electron probe and ion probe analyses. These data are presented in chapters three and four and used to investigate magma plumbing processes in Chapters Five and Six. It is suggested in Chapter Five that the magma chamber which crystallised ODP Hole 923A was regularly replenished by primitive magmas. It is shown that the composition of the added magmas was not identical to MORB and that magma mixing was an important process within this chamber leading to homogenisation of the melt compositions. In Chapter Six the evolution of the crystal mush at the magma chamber margin is investigated. It is suggested that interstitial melt migrated through the crystal mush during its solidification interacting with the crystal assemblage. This lead to both extensive textural and geochemical modification of the crystal assemblage; in particular the interstitial melt became highly fractionated in terms of incompatible trace elements but evolved relatively little in terms of major elements due to the buffering effect of the crystal assemblage.

In this chapter magma plumbing processes are reviewed using diverse data sources and a generalised model developed within which to study these processes. Magma plumbing starts with near-fractional melting and melt extraction. Melt extraction involves interaction between the melt and residual mantle, but not necessarily equilibration between them. Subsequently, melts generated in different parts of the melting regime are efficiently mixed together and extensively fractionated by crystallisation prior to eruption.

## 1.2 Why study mid-ocean ridges ?

Mid-ocean ridge processes are important for diverse reasons. They are central to global tectonics, important for global thermal and chemical budgets, can form ore bodies through hydrothermal activity, and support a unique fauna. Approximately two-thirds of the earth's surface is covered by oceanic crust, which forms mostly at mid-ocean ridges. Subduction of oceanic crust is responsible for continental growth though accretion and arc volcanism. The formation and subduction of oceanic crust must also be fundamentally important to mantle dynamics. Thus understanding mid-ocean ridge processes is a first order aim of the earth sciences.

MORB is interpreted as a partial melt of the sub-ridge upper mantle, thus providing a window into the mantle composition, temperature and dynamics. In order to interpret MORB compositions in terms of these characteristics, it is necessary to know how the melts generated in the mantle relate to those erupted on the seafloor. This requires an understanding of the processes acting to modify melt chemistry between generation and eruption. Part of this modification occurs within magma chambers, the frozen remains of which are sampled as oceanic gabbros. Thus, the study of oceanic gabbros may allow insight into both: (i) the melt compositions added to the magma chambers, and (ii) the compositional modifications produced within magma chambers.

Finally, magma plumbing processes can be modelled better at mid-ocean ridges than in other tectonic environments due to the occurrence of source rocks (oceanic peridotites), fractionation products (oceanic gabbros) and eruptive products (MORB), and the lack of continental crust. Thus understanding of magma plumbing processes gained from detailed study of mid-ocean ridges may provide information about magma plumbing in other environments.

## 1.3 Magma plumbing beneath mid-ocean ridges - a general model

The widely accepted model for mid-ocean ridge volcanism involves generation of melt by pressure-release melting within the mantle as it upwells in response to plate separation, and extraction of this melt to form oceanic crust. Upwelling may be enhanced due to melting leading to mantle buoyancy (active upwelling) or may be simply a response to plate separation (passive upwelling). Melting occurs in the region between where the mantle geotherm intersects its solidus and where either: (i) the mantle stops decompressing (i.e. begins to flow sideways instead of upwards), or (ii) cooling from the surface reduces the mantle temperature to below its solidus (Fig 1.1). Some of the melt is eventually erupted to form MORB and is sampled and used for geochemical investigations. Primary compositional variation within MORB reflects variation in mantle composition,

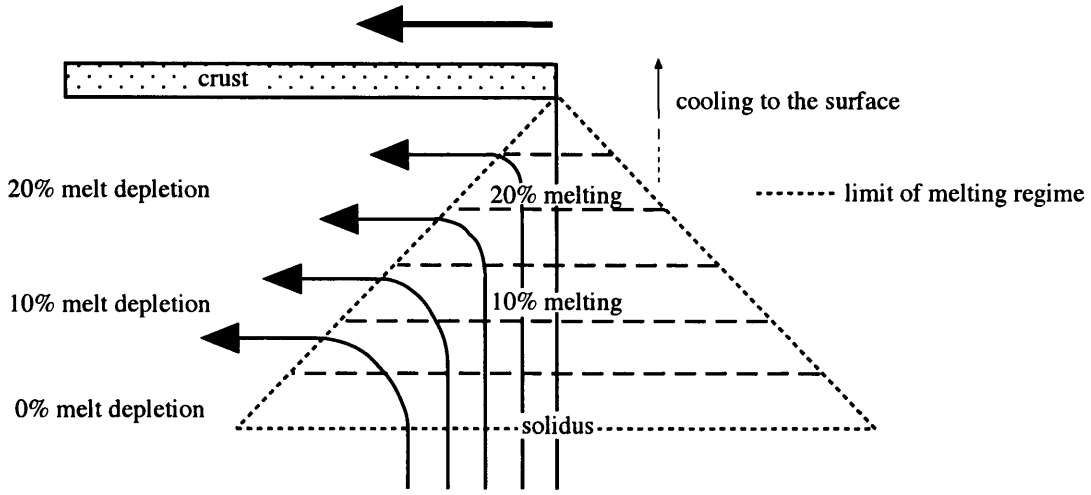


Fig. 1.1a Schematic melting column and mantle flow lines beneath a mid-ocean ridge during passive mantle upwelling modified after Plank and Langmuir (1992). Melting starts where the upwelling mantle crosses its solidus and ceases either when: (i) cooling from the surface (hydrothermal or conductive) reduces the mantle temperature beneath its solidus, or (ii) when decompression ceases due to mantle flow becoming horizontal. This leads to melting in the triangular region defined by the dashed line.

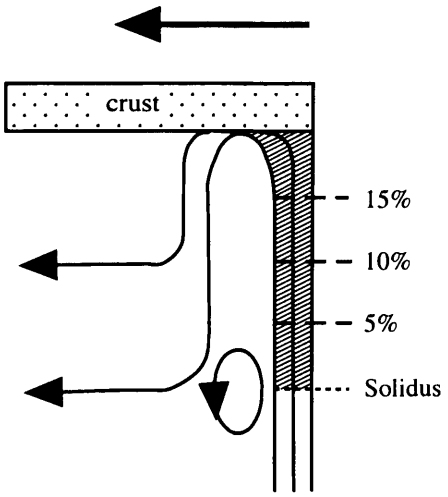


Fig. 1.1b An exaggerated cartoon of active upwelling beneath a mid-ocean ridge modified after Langmuir et al. (1992). Melting is restricted to a narrower zone (hatched) than during passive upwelling. Active upwelling occurs due to buoyancy forces derived from melting.

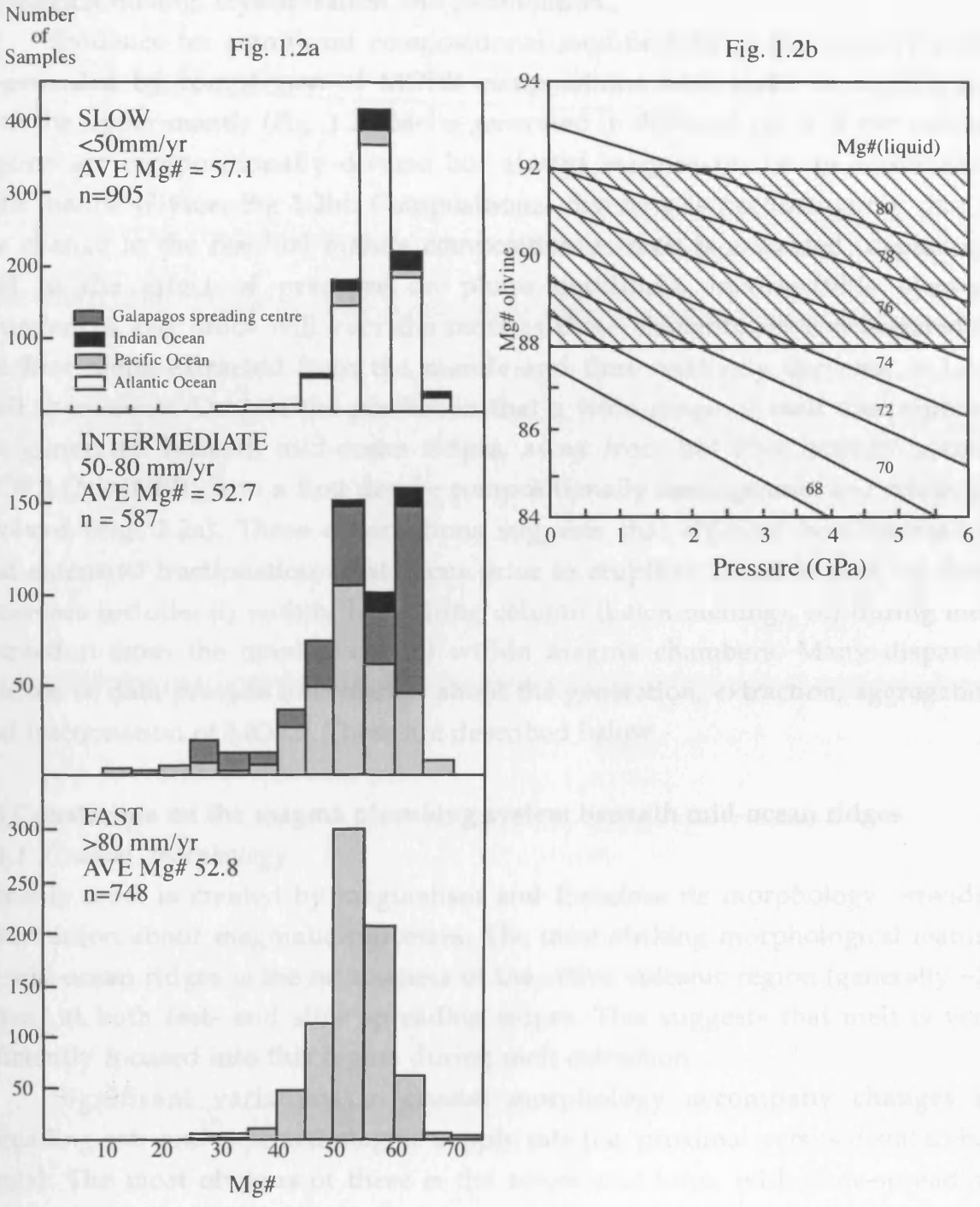


Fig. 1.2a

Fig. 1.2b

Fig. 1.2. (a) Distribution of MORB Mg# (Mg#=100 x Mg/(Mg+Fe)) for different spreading rates from Sinton & Detrick (1992). Note that slow spreading ridges are characterised by more primitive basalt compositions than fast spreading ridges and that the data set is biased so as to basically represent the Atlantic (slow) and Pacific (fast). b) Mg# of melt in equilibrium with different olivine compositions at different pressures (Hess, 1992). Contoured lines represent the composition of melt generated at various pressures (X axis) from olivine of various compositions (Y axis). The field of likely mantle olivine compositions is shaded. As olivine is a ubiquitous mantle phase, melts generated within the mantle must be in Mg-Fe exchange equilibria with mantle olivine.

Note the large difference between the compositions of primary magmas (Fig. b) and those erupted as MORB (Fig. a).

temperature and degree of melting. Further compositional variation is generated by magma mixing, crystallisation and assimilation.

Evidence for significant compositional modification of the primary melts is provided by comparison of MORB compositions with melts in equilibrium with the upper mantle (Fig. 1.2). Melts generated in different parts of the melting regime are compositionally diverse but always magnesian (i.e. in equilibrium with mantle olivine, Fig 1.2b). Compositional diversity is predominantly due to the change in the residual mantle composition as melt is extracted (depletion), and to the effect of pressure on phase equilibria. Incompatible element abundances and ratios will vary the most as these elements are concentrated in the first melts extracted from the mantle and thus relatively depleted in later melt increments. Despite the prediction that a wide range of melt compositions are generated beneath mid-ocean ridges, away from hot spot activity normal MORB (N-MORB) is to a first degree compositionally homogenous and relatively evolved (Fig. 1.2a). These observations suggests that efficient homogenisation and extensive fractionation must occur prior to eruption. Possible sites for these processes include: (i) within the melting column (batch melting), (ii) during melt extraction from the mantle, or (iii) within magma chambers. Many disparate sources of data provide information about the generation, extraction, aggregation and fractionation of MORB. These are described below.

## 1.4 Constraints on the magma plumbing system beneath mid-ocean ridges

### *1.4.1 Crustal morphology*

Oceanic crust is created by magmatism and therefore its morphology provides information about magmatic processes. The most striking morphological feature of mid-ocean ridges is the narrowness of the active volcanic region (generally ~2-5 km) at both fast- and slow-spreading ridges. This suggests that melt is very efficiently focused into this region during melt extraction.

Significant variations in crustal morphology accompany changes in spreading rate and expected magma supply rate (i.e. proximal versus distal to hot spots). The most obvious of these is the across-axis form, with slow-spreading ridges characterised by a deep tectonic axial valley, and fast-spreading ridges by a narrow volcanic axial high, with or without a narrow (100's of m) axial graben. It is common at slow-spreading ridges for the axial valley to be asymmetric and to deepen and widen and become increasingly asymmetric towards transform faults. Volcanic construction within the axial region is dominated by individual seamounts at slow-spreading ridges, but by fissure volcanism at fast-spreading rates (Smith & Cann, 1992). They suggest this reflects variation in the magma chamber with spreading rate. In this model small, transient magma chambers,

feed individual seamounts at slow-spreading ridges, in contrast to permanent magma chambers at fast-spreading ridges.

Both fast- and slow- spreading ridges are segmented along axis in similar ways, although the details of segmentation scale and form differ both with spreading rate and between adjacent areas of a single ridge system (Grindlay *et al.*, 1991). Transform faults provide first-order segmentation of ridges, with transform-bound segments sub-divided by smaller offset and non-offset boundaries. Non-offset boundaries are manifest in thinner crust and a deeper ridge axis. Large-scale segmentation is commonly traceable off axis, indicating that this scale of segmentation is long-lived. The primary question regarding segmentation is whether it represents segmented tectonism, segmented magma supply, segmented magma storage or a combination of these. The likeliest answer is that all these processes have inter-related effects on segmentation and that different processes dominate different scales of segmentation. Large-scale segment centres are commonly underlain by negative mantle Bouguer anomalies, which have been interpreted as upwelling partially molten mantle (Lin *et al.*, 1990). This suggests that large-scale segmentation may be a manifestation of focused (active) melt generation. Petrological variation with proximity to offsets has been found to vary between regions (Bryan *et al.*, 1981; Bender *et al.*, 1984; Langmuir *et al.*, 1986, Reynolds & Langmuir, 1997), suggesting that there is not a unique relationship between segmentation and magma plumbing.

Off-axis oceanic crust has a similar seismic velocity structure and thickness (Fig. 1.3) at spreading rates >10 mm/yr full spreading rate (White *et al.*, 1992). This has been interpreted in terms of similar lithological layering and layer thickness through analogy with ophiolites (e.g. Brown & Mussett, 1981). Lewis (1983) and Detrick *et al.* (1994) have questioned this interpretation and suggest that fracture density and alteration may control the seismic velocity structure not lithology. This is important for models which use seismic crustal thickness to constrain the amount of magma generated beneath mid-ocean ridges. The origin of segmentation and the structure of oceanic crust formed at different spreading rates are two important unresolved questions in marine geoscience.

### *1.4.2 Ophiolite structure*

Ophiolites are inferred to be slices of oceanic crust which have been obducted rather than subducted. This in itself suggests that these are not representative of 'normal' oceanic crust and geochemical studies confirm this (Miyashiro, 1973). Ophiolite chemistry generally suggest arc, not normal mid-ocean ridge, affinities. This leads to many problems in directly relating features of ophiolites to mid-ocean ridges, largely due to the multitude of effects of water on arc related magmatic processes. Further doubt is cast upon the similarities between oceanic

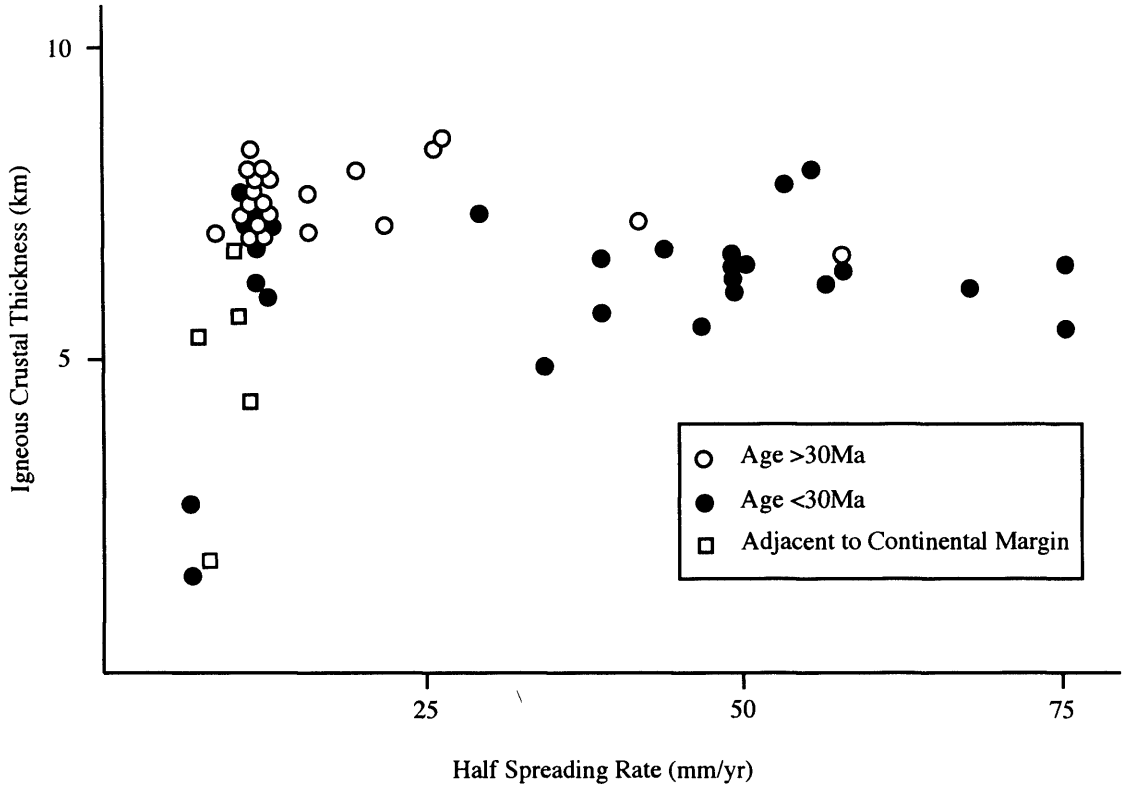


Fig. 1.3 Comparison of seismically determined oceanic crust thickness with half spreading rate. This suggests that crustal thickness is independent of spreading rate at half spreading rates >10mm/year (from White et al., 1992)

crust formed at slow spreading ridges and many ophiolites by the difference between gabbros from Ocean Drilling Program (ODP) Hole 735B and ophiolites (Robinson, Von Herzen, *et al.*, 1989; Dick *et al.*, 1991). Nevertheless, ophiolites may provide an insight into the general structure of crust formed at constructive plate margins.

Fig. 1.4 shows a schematic log through the Oman ophiolite, which is one of the best studied ophiolites in the world. Two critical observations from the mantle section are the diapiric form sometimes defined by the foliations and the occurrence of discordant dunites. Foliations in the form of diapirs are interpreted as frozen mantle diapirs indicating buoyant mantle upwelling (Nicolas, 1989 and references therein). Dunites crossing the foliation are thought to be conduits for rapid melt extraction from the mantle through high porosity channels (Kelemen *et al.*, 1995). The mantle section is overlain by a zone transitional in character between mantle and crust. Boudier and Nicolas (1995) propose that this transition zone is a region of impregnated mantle with high percentages of trapped melt. The gabbroic section which overlies this can be divided into a lower layered gabbro section, and an upper isotropic layer. Layering in the layered gabbros commonly has a concave upward form, but due to problems in locating the ridge axis in ophiolites it is unclear whether it dips towards, or away from the ridge axis.

### *1.4.3 MORB major element compositions*

An early aim of MORB geochemical investigations was to distinguish whether MORB represents primary mantle melt, or a fractionation product of the primary melt which has been significantly compositionally modified since generation within the mantle. The Mg#, where Mg# = 100 x Mg/(Mg+Fe), of primary mantle melt is constrained to be in equilibrium with mantle olivine, as this is a ubiquitous phase. Experimental investigations at various pressure have constrained the equilibrium partitioning of magnesium and iron between melt and olivine (Ulmer, 1989) and abyssal peridotite studies have constrained the range of olivine forsterite contents found in the mantle. Using these data, and the range of Mg# of MORB, Fig. 1.2 shows that most MORB is not in equilibrium with mantle olivine at any pressure. This suggests that melts evolve significantly between extraction from the mantle and eruption on the seafloor. MORB compositions also lie on experimentally determined low-pressure cotectics suggesting that at least some of the compositional modification occurs at low-pressure (O'Hara, 1968). Fig. 1.2a also shows variation in MORB Mg# with spreading rate. Slow-spreading ridges are characterised by higher Mg#s on average than fast-spreading ridges and intermediate spreading rates have a

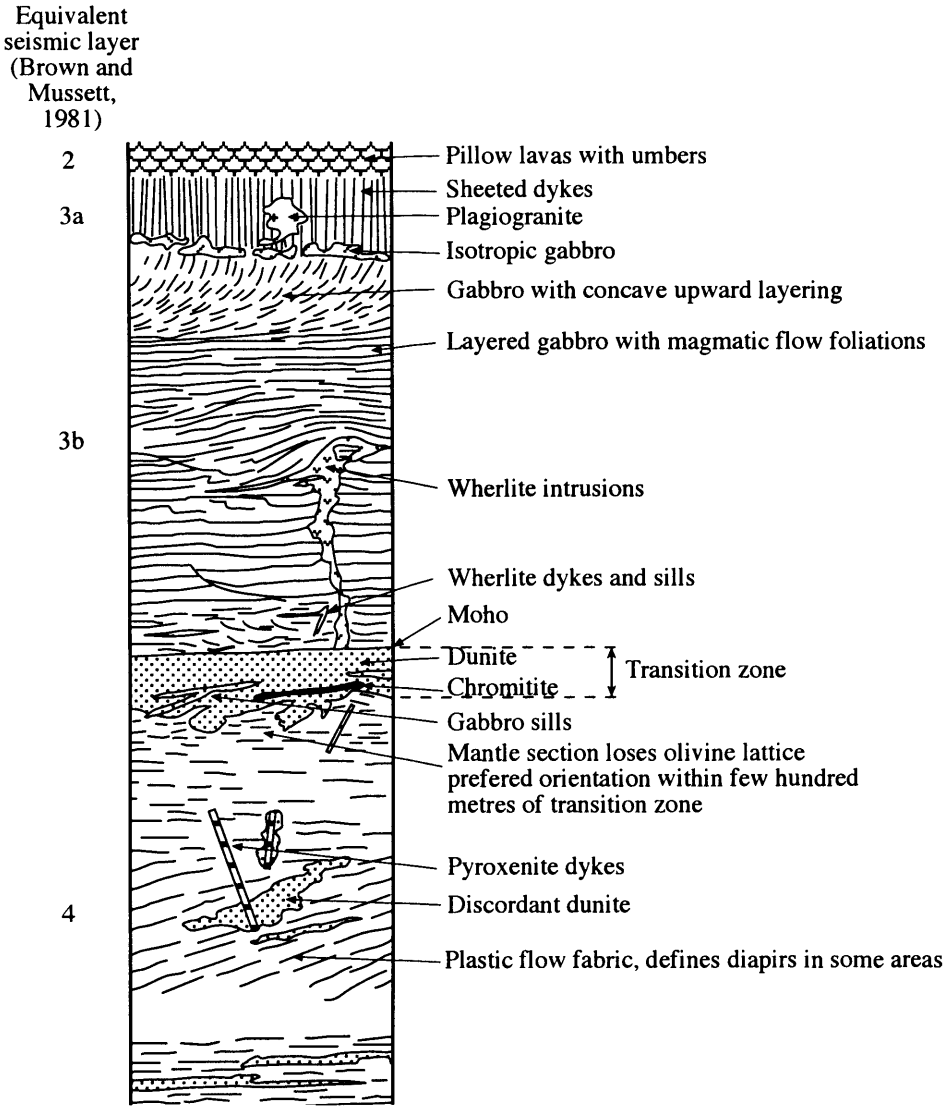


Fig. 1.4 Schematic log through the Oman ophiolite from Nicolas (1989)

bimodal Mg# distribution. This is interpreted as evidence for more extensive fractionation at fast- than slow-spreading ridges (Sinton & Detrick, 1992).

In order to use the major element composition of MORB to interpret melt generation, Klein and Langmuir (1987) propose correction for fractional crystallisation to a MgO content of 8 wt% via the one-atmosphere liquid line of descent model of Weaver and Langmuir (1990). Abundances of elements at a MgO content of 8 wt% are referred to in the form $Na_{8.0}$ and $Fe_{8.0}$ for corrected $Na_2O$ and FeO, respectively. This assumes the liquid line of descent of all MORB suites on MgO variation diagrams is parallel. This correction allows Klein and Langmuir (1987) to identify a negative global (including hot spot influenced ridges) correlation between $Na_{8.0}$ and $Fe_{8.0}$, and a positive global correlation of $Na_{8.0}$ with ridge depth. They interpreted these correlations as signatures of the depth at which melting begins due to variations in mantle potential temperature. Deep initiation of melting (high $Fe_{8.0}$) leads to extensive melting (low $Na_{8.0}$) producing thick (shallow) crust. A key interpretation of this study, assuming that $Fe_{8.0}$ and $Na_{8.0}$ are controlled by the degree and depth of melting, is that melt must be extracted from various depths in the melting column without re-equilibration at shallower levels.

A positive correlation between $Fe_{8.0}$ and $Na_{8.0}$ was later identified for the Mid-Atlantic Ridge (MAR) and named the local trend (Klein & Langmuir, 1989). They interpreted this as mixing of melts from different parts of the melting column. Alternatively, Grove *et al.* (1992) suggest that the positive correlation is due to high pressure fractionation in which clinopyroxene saturation is reached earlier than in the modelled liquid line of descent. Niu and Batiza (1993) show that the so called global and local trends are actually fast- and slow-spreading ridge trends respectively. They propose that reaction between melt and mantle during melt extraction, involving pyroxene dissolution and olivine precipitation, could produce a positive correlation between $Na_{8.0}$ and $Fe_{8.0}$.

Corrected major element abundances have been quantitatively modelled by Niu and Batiza (1991), Langmuir *et al.* (1992), and Kinzler and Grove (1992a, b, c) to predict initial and final pressures of melting, and the melt fraction produced. These models make assumptions about the initial mantle composition, the adiabatic geotherm, and melting thermodynamics and rely on experimental melting equilibria which were obtained at high melt fractions and extrapolated to low melt fractions. Differences exist between the models, but in general they agree that melting begins at depths of around 50-60 km and produce 10-20% melt (McKenzie & Bickle, 1988; Niu & Batiza, 1991; Langmuir *et al.*, 1992; Kinzler & Grove 1992a, b, c). However, Baker *et al.* (1995) find that at low melt fractions partitioning differs considerably from that at high melt fractions raising questions about this modelling.

*1.4.4 MORB trace element compositions*

N-MORB is relatively homogenous, being comprised of light rare earth element (LREE) depleted olivine tholeiites that have low Sr, and high Nd isotope ratios (Engel *et al.*, 1965; Gast, 1965). These observations are interpreted as evidence that the MORB source has undergone previous (ancient) melt extraction (Gast, 1965). Variations in incompatible element abundances and ratios in MORB are generally interpreted either in terms of source heterogeneity or variations in the dynamics or degree of melting. These interpretations assume that fractionation processes have a relatively minor effect on incompatible elements in basalts with relatively high MgO contents.

Assuming secular equilibrium exists in the mantle prior to melting, U-series disequilibria studies provide a powerful tool to study magma plumbing beneath mid-ocean ridges that minimises consideration of source heterogeneity. MORBs commonly have $(^{230}Th/^{238}U) > 1$, where () denotes activity, indicating an excess of $^{230}Th$, with respect to $^{238}U$. This is regarded as evidence that during magma genesis Th is more incompatible than U which is contrary to experimentally determined partition coefficients (D's) for clinopyroxene (Beattie, 1993; Lundstrom *et al.*, 1994). Garnet however can produce the relative partitioning of U and Th to produce Th excess (i.e. $D_{Th}<D_U$). Thus, Th excess is generally interpreted as evidence for initiation of melting within the garnet stability field (Beattie, 1993; Lundstrom *et al.*, 1994). However, theoretical modelling based on lattice site size and elastic strain energy suggest that aluminous clinopyroxene may be capable producing the observed fractionation (Blundy, 1997b). Furthermore, accessory phases, or poorly understood variations in melt structure at low melt fractions, and in the presence of volatiles, may be significant in controlling partitioning. Even if garnet is required to produce the compositional characteristics of MORB, this does not necessarily indicate initiation of melting in the garnet peridotite stability field. If the source contains garnet pyroxenite veins, in which garnet is stable to a lower pressure than in garnet pyroxenite, then partial melts of these may provide the garnet signature (Hirschmann & Stolper, 1996)

To fractionate two very incompatible elements such as Th and U from one another requires extraction of small melt fractions from the source. Once extracted, the melt must be erupted sufficiently rapidly for secular equilibrium not to be regained. To acquire and preserve the observed excess $^{230}Th$ the maximum porosity during melting is thought to have to be <2% (McKenzie, 1985) and possibly <0.1% (Bourdon *et al.*, 1996); the melt must also be erupted within ~75,000 yrs of leaving its source (McKenzie, 1985). Bourdon *et al.* (1996) observe greater $^{230}Th$ excesses at shallow ridges and interpret this as larger

proportions of melting in the garnet stability field due to higher mantle potential temperature leading to melting beginning at greater depth than at deeper ridges. Preserving excess $^{230}Th$ in MORB is also dependent on the U originally left in the source not being added to the aggregated melt prior to eruption. This can be achieved through sideways flow of the mantle at the base of the melting column after Th extraction and/or in-growth of $^{230}Th$ during melting.

Further evidence for initiation of melting in the presence of garnet comes from the Lu-Hf systematics of MORB. Salters and Hart (1989) show that the $^{176}Hf/^{177}Hf$ ratios of MORBs indicate long lived source enrichment of Lu with respect to Hf. In contrast the Lu/Hf ratio of N-MORB (~0.22; Sun & McDonough, 1989) is less than the chondritic ratio (0.24; Sun & McDonough, 1989). They explain this paradox by the fractionation of Lu from Hf during melting, with garnet retaining Lu in the source. These trace element constraints support major element studies in suggesting that melting is near fractional with melt being extracted from throughout the melting column and being transported to the surface without re-equilibration with the mantle. In addition, they suggest initiation of melting in the presence of garnet.

### *1.4.5 Trace element variations interpreted as due to fractionation*

Fractionation trends within MORB suites commonly display two enigmatic characteristics. Firstly, clinopyroxene, a rare phenocryst in MORB, is commonly required by both major and trace element modelling to have been a fractionating phase in order to explain the liquid line of descent of MORB suites (Rhodes *et al.*, 1979; Reynolds & Langmuir, 1997). This phenomenon is commonly referred to as the 'pyroxene paradox'. Secondly, incompatible trace elements are commonly over-enriched compared to major elements (Bryan *et al.*, 1981; Perfit & Fornari, 1983), i.e. in a suite of MORB a smaller degree of fractionation is required to explain the major element variation than the incompatible trace element variation. Two hypotheses have been proposed to explain these phenomenon: (i) mixing between an evolved magma which has fractionated clinopyroxene and become incompatible element enriched, and a more primitive melt (Rhodes *et al.*, 1979; Walker et al., 1979), and (ii) '*in situ*' or 'boundary layer' crystallisation which leads to extraction of phases below the liquidus of the magma and leaves these crystals in the uneruptable crystal mush at the magma chamber margins (Langmuir, 1989).

### *1.4.6 Abyssal peridotites*

Abyssal peridotites are interpreted as mantle residual from decompression melting which has been exposed at the surface through extension during periods of low magma supply. As such they provide information about the melting and

melt extraction processes that may not be possible to acquire from the study of MORB alone. In particular, they provide evidence for the composition of the last melt in equilibrium with the mantle. Since they are found at the surface near the ridge axis, it is assumed that they have undergone the maximum amount of decompressional melting which biases the dataset. Furthermore, most abyssal peridotite samples are from near fracture zones adding further bias to the dataset.

The typical mode for abyssal peridotite is 75% olivine, 21% enstatite, 3.5% diopside and 0.5% spinel, with significant variations within dredges, and a systematic decrease in average diopside abundance with proximity to hot spots (Dick *et al.*, 1984; Michael & Bonatti, 1985). Three key observations from oceanic peridotites constrain magma plumbing beneath mid-ocean ridges. These are: (i) evidence for reaction between residual depleted peridotite and migrating melt, (ii) highly depleted clinopyroxene compositions, and (iii) the occurrence of some samples with textural and compositional evidence for a high proportion of trapped melt.

Evidence for localised reaction between channellised melts and depleted mantle has been observed in Ocean Drilling Program (ODP) drill core (Dick & Natland, 1996) and in the mantle section of ophiolites (Kelemen *et al.*, 1992, 1995). Dick and Natland (1996) observe gabbroic segregations with MORB-like compositions, but with extremely refractory mineral compositions (up to $An_{99}$) within mantle peridotite at ODP Site 895, Hess Deep. These are separated from surrounding harzburgite by dunite. Kelemen *et al.* (1992, 1995) observe discordant dunites within the Trinity and Oman ophiolites which do not displace other forms of mantle layering (e.g. chromite layers). These features are interpreted as evidence for reaction between residual harzburgite and basalt during melt flow through high porosity channels.

Excess olivine (Niu, 1997) and orthopyroxene (Kelemen *et al.*, 1992) within the global oceanic peridotite suite, compared to that which would be expected in residual peridotite have been proposed. It has been suggested that reaction occurs during pervasive porous flow involving high-Ca-pyroxene dissolution and low-Ca-pyroxene precipitation (Kelemen *et al.*, 1992), and high and low Ca-pyroxene dissolution and olivine precipitation (Niu, 1997). Dick (1989) also suggests that porous flow of magma through the upper mantle is an important process in order to explain decoupled major and trace element compositions. He proposes that melt percolation through the mantle is capable of homogenising major elements whilst leaving incompatible elements virtually unaffected. The compositional effects of mantle-melt reaction on MORB depend on: (i) whether the melt involved in reaction is eventually erupted or trapped elsewhere, and (ii) the melt - rock ratio involved in the reaction.

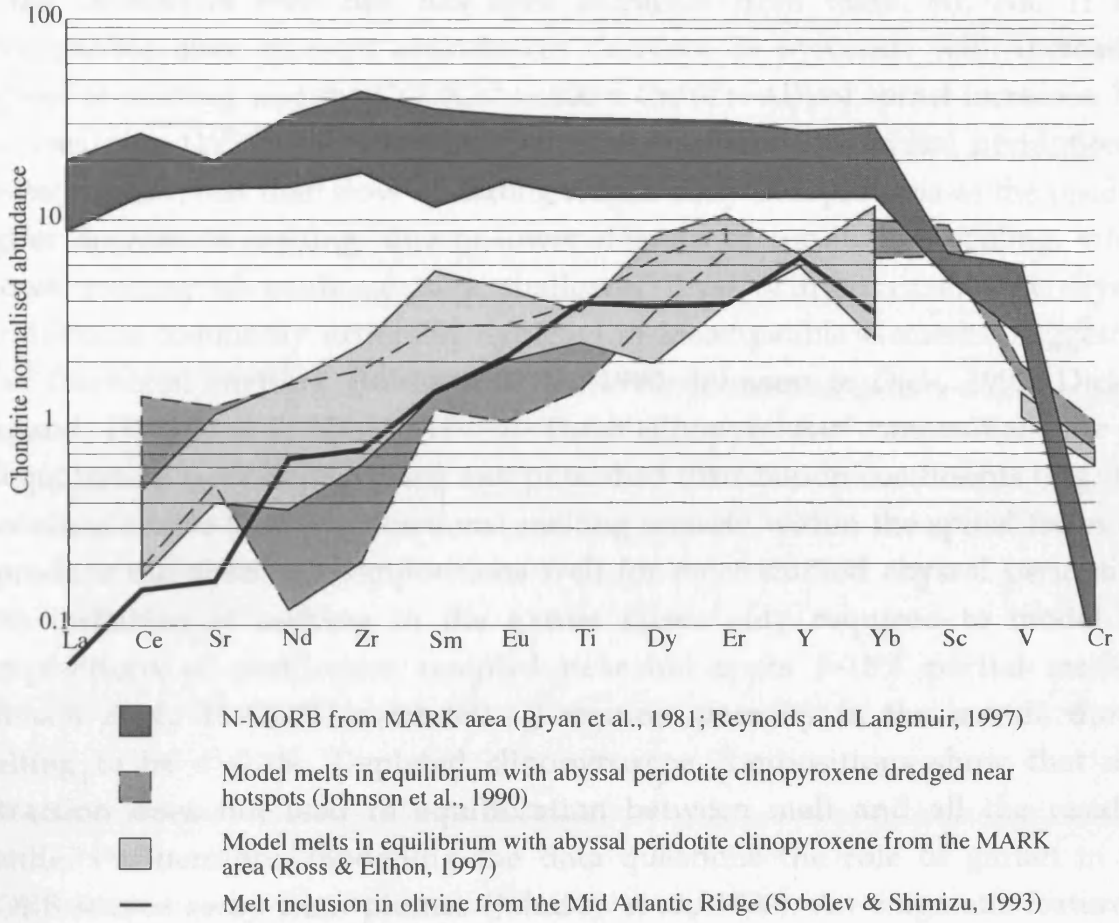


Fig. 1.5 Comparison of depleted melt compositions measured in a melt inclusion and modelled from abyssal peridotite clinopyroxene compositions (using distribution coefficients from Appendix A.I) and MORB from the MARK area (Mid-Atlantic Ridge south of the Kane fracture zone)

Mineral compositions in abyssal peridotites are commonly used as a guide to the amount of melt that has been extracted from them. Al, Na, Ti and incompatible trace element abundances decrease in pyroxene with increasing degrees of melting, and the Cr# [Cr# = 100 x Cr/(Cr+Al)] of spinel increases. Niu and Hekinian (1997) find that the degree of depletion in abyssal peridotites is greater beneath fast than slow spreading ridges. They interpret this as the result of higher degrees of melting, due to lower degrees of conductive cooling, which allows melting to continue to a shallower level. Clinopyroxene in abyssal peridotite is commonly extremely depleted in incompatible elements, suggesting near fractional melting (Johnson *et al.*, 1990; Johnson & Dick, 1992; Dick & Natland, 1996; Ross & Elthon, 1997b). These clinopyroxene compositions are not in equilibrium with MORB using any published distribution coefficients (Fig. 1.5). Modelling shows that near fractional melting entirely within the spinel facies can reproduce the observed compositions well for most studied abyssal peridotites, with initiation of melting in the garnet facies only required to model the compositions of peridotites sampled near hot spots (>15% partial melting; Johnson *et al.*, 1990). This modelling requires porosity in the mantle during melting to be <~0.1%. Depleted clinopyroxene compositions show that melt extraction does not lead to equilibration between melt and all the residual mantle. Furthermore, modelling the data questions the role of garnet in the MORB source away from plumes (Johnson *et al.*, 1990). An enigmatic feature of abyssal peridotite clinopyroxene compositions are negative Zr and Ti anomalies with respect to REEs, which are largest in the most depleted crystals (Salters & Shimizu, 1988; Johnson *et al.*, 1990). Corresponding large HFSE anomalies are not generally observed in MORB, although Casey (1997) finds negative whole rock Ti and Zr anomalies in the most primitive gabbros, and positive anomalies in the most evolved gabbros recovered during ODP Leg 153.

Some abyssal peridotites contain relatively large proportions of plagioclase indicating a large basaltic component. These samples are generally interpreted as being residual mantle that has been impregnated with basalt (Dick *et al.*, 1984; Dick, 1989; Johnson & Dick, 1992). This suggests that porous flow of basalt through the upper mantle is a common process in the upper mantle beneath mid-ocean ridges. Abyssal peridotites thus provide good evidence that melting is near fractional beneath mid-ocean ridges. They also suggest melt extraction is a complex process involving reaction, but not full equilibration, between the primary melt and the residual mantle it is extracted through.

### *1.4.7 Oceanic gabbros*

Like abyssal peridotites, dredged samples of oceanic gabbros have a sampling bias towards fracture zones, and lack spatial relationships. ODP sampling of oceanic

gabbros has suffered from poor recovery with the exceptions of Holes 735B (Leg 118 and 176, Southwest Indian Ridge; SWIR) and 923A (Leg 153, Mid Atlantic Ridge; MAR) from which recovery was >70%. Even in these cores, problems exist with interpreting spatial associations due to the possibility that chilled margins and/or faults (shear zones), which juxtapose genetically unrelated rocks against one another, may not have been recovered. Also the orientation of the core with respect to palaeovertical in the magma chamber is unknown.

Many oceanic gabbros are texturally and compositionally similar to continental tholeiitic gabbros. Two textural characteristics of oceanic gabbros not common in continental intrusions are: (i) grain size layering effecting all phases irrespective of hydraulic properties, and (ii) deformed oxide gabbros (Robinson, Von Herzon *et al.*, 1989; Cannat, Karson, Miller *et al.*, 1995). A compositional enigma exists in clinopyroxene compositions in mid-ocean ridge gabbros. It is normal for oceanic gabbros to contain magnesian ($Mg\#_{82-90}$) clinopyroxene (MAR- 23°N, Ross & Elthon, 1997a; MAR- 37°N, Hodges & Papike, 1976; SWIR - 54°S, Meyer *et al.*, 1989; SWIR - ODP Site 735, Hebert *et al.*, 1991 & Ozawa *et al.*, 1991; SW and Central Indian Ridge, Bloomer *et al.*, 1989; EPR, Constantin *et al.*, 1996; MCR, Elthon, 1987). However, in experiments on magnesian MORB clinopyroxene is not a liquidus phase until ~40-70°C below the temperature of olivine saturation. In these experiments, olivine crystallisation reduces the Mg# of the melt such that the first clinopyroxene has a Mg# of 82-83 (Grove & Bryan, 1983; Tormey *et al.*, 1987; Grove *et al.*, 1992). Experimental data suggest that at higher pressure clinopyroxene saturated is reached at a higher temperature, leading to the idea that oceanic gabbros may generally form at moderate pressure (2-5 kbars; Elthon *et al.*, 1992). However, this is inconsistent with the depth of seismically imaged magma chambers beneath mid-ocean ridges (see section 1.5).

### *1.4.8 MORB Phenocrysts and their melt inclusions*

Plagioclase phenocrysts which are too anorthitic to be in equilibrium with MORB are a common feature of MORB (e.g. Meyer & Shibata, 1990), requiring either a refractory parental melt or unusual crystallisation conditions (e.g. high $H_2O$). These anorthitic crystals are commonly embayed and some show evidence of a complex history of growth and resorption within their zoning profiles. High pressure crystallisation cannot explain these compositions because increasing pressure increases the albite component in plagioclase (Panjasawatwong *et al.*, 1995). However, melts generated near the top of the melting column from depleted mantle are good candidates to be parental to the anorthic plagioclase (Grove *et al.*, 1992).

Melt inclusions within phenocrysts may record the composition of near-primary mantle melts, prior to mixing with melts from different parts of the

melting column. This is suggested by the composition of some melt inclusions found in plagioclase and olivine phenocrysts in MORB which are far more refractory than any MORB. Humler and Whitechurch (1988) and Sinton *et al.* (1993) describe melt inclusions with very refractory major element compositions (1.2-2.1 wt % $Na_2O$; 0.3 wt % $TiO_2$; Mg# 74-77 assuming all Fe as $Fe^{2+}$). An ultra-depleted incompatible trace element signature (Fig. 1.5) has also been found in a melt inclusion from the MAR by Sobolev and Shimizu (1993). These refractory compositions are interpreted in the same way as refractory mineral compositions.

**1.5 Magma chambers beneath mid-ocean ridges**

*Primae facie* evidence for the existence of magma chambers beneath mid-ocean ridges comes from oceanic gabbros, geophysical 'observation' of magma chambers beneath some ridges and the gabbroic section of ophiolites. Oceanic gabbros also provide evidence for the compositional modifications which occur within sub-ridge magma chambers.

At fast spreading ridges magma chambers have been identified by geophysical experiments as sill-like bodies ~1-3 km below the seafloor (Detrick *et al.*, 1987; Collier & Sinha, 1990, Sinton & Detrick, 1992). These are thought to be <3 km wide, 10-200 m thick and continuous along strike for tens of kilometres, even crossing non-offset segment boundaries. This magma lens (or sill) overlies a seismic low velocity zone which is interpreted as a partially molten region. To reconcile these observations with the thick gabbro section in ophiolites (Fig. 1.4), models in which floor cumulates from the magma lens subside as they move off axis have been proposed (Quick & Delinger, 1993; Henstock *et al.*, 1993; Morgan & Chen, 1993). This produces layering which steepens up section, as observed in ophiolites (e.g. Nicolas, 1989).

At slow spreading ridges geophysical experiments have generally been unsuccessful in identifying magma chambers, leading to the suggestion that they are transient features (Detrick *et al.*, 1990; Sinton & Detrick, 1992; Sinha *et al.*, 1997). This is consistent with thermal models which suggest permanent magma chambers cannot exist at slow spreading rates (Sleep, 1975; Kuznir, 1980). Calvert (1995) suppresses high amplitude noise in seismic reflection profiles, which otherwise show no signs of a magma chamber (Detrick *et al.*, 1990), to reveal a reflector that he interprets as a magma chamber beneath the Snake Pit hydrothermal field on the MAR (23°30'N). The reflector is 1-2 km below the seafloor, the same depth as suggested for a heat source by the hydrothermal fluid chemistry (Campbell *et al.*, 1988). Sinha *et al.* (1997) present convincing evidence for a magma body of similar geometry and extent to those found beneath faster spreading ridges from seismic, electromagnetic and magneto-telluric experiments in the volcanically active region of the MAR at 57°N. The similarity in depth of

this body to those at ridges spreading several times faster refutes the suggestion that spreading rate and magma chamber depth correlate (Purdy *et al.*, 1992; Sinha *et al.*, 1997). Preliminary interpretations of this experiment also find magneto-telluric evidence for ~5% partial melt within the mantle between 50 and 100 km depth beneath the ridge in this region (Sinha *et al.*, 1997). A possible problem with this study is its proximity to the Iceland plume, which could fundamentally effect the magma plumbing system, although normal crustal thickness suggest this may be insignificant (Sinha *et al.*, 1997).

### *1.5.1 Magma chamber processes*

Magma compositions are modified within magma chambers through crystallisation, magma mixing and assimilation of wall rock. These process are complex and magma differentiation remains incompletely understood. Fractionation can be split into two main categories: (i) closed system separation of crystals and melt, and (ii) open system processes in which mass is transferred into and/or out of the chamber. Both of these processes probably operate in tandem beneath mid-ocean ridges.

Closed system fractionation has been studied extensively through observations of continental intrusions (Campbell, 1978; McBirney & Noyes, 1979; McBirney, 1995) and lava lakes (Helz, 1987; Barth *et al.*, 1994) as well as through theoretical and experimental modelling (Marsh, 1988a; Sparks *et al.*, 1993). The most important interpretations of these studies have been: (i) that both crystal settling and *in situ* crystallisation at the magma chamber margins are important processes in controlling the compositional evolution of the eruptable melt (Campbell, 1978; McBirney & Noyes, 1979; Langmuir, 1989), and (ii) that compaction and compositional convection within the basal crystal mush leads to migration of evolved interstitial melt within the cumulus pile even at relatively low porosity (Tait *et al.*, 1984; Shirley, 1986, 1987; Mathez *et al.*, 1997).

Crystallisation at the magma chamber margins and in the crystal mush may involve phases below the liquidus of the main body of the magma. Thus, if the fractionated melt is returned to the eruptable magma chamber, then fractionation trends of erupted basalts may record extraction of sub-liquidus phases. The fractionation trends will certainly be different to those produced by homogeneous fractionation (Langmuir, 1989). Furthermore, *in situ* crystallisation has implications for the phenocryst population of the erupted magma.

Open system processes include addition of magma to the chamber (replenishment), removal of magma from the chamber (extrusion / intrusion) and assimilation of wall rock into the magma chamber. The fluid dynamics of replenishment and mixing have a significant control over the compositional effects of open system processes on the erupted magma composition. A major

control on fluid dynamics is variation in melt density with fractionation. Stolper and Walker (1980) and Sparks *et al.* (1980) simultaneously discovered that MORBs have densities close to the density minimum produced during fractionation of a high magnesium basalt. Huppert and Sparks (1980a) suggest that primitive melts pond at the base of a fractionated sub-ridge magma chamber as they are denser than the host magma. They propose the primitive melt fractionates until it reaches a density similar to that of the overlying more fractionated magma, at which point whole sale mixing occurs.

Michael and Schilling (1989) demonstrate that Cl is over-enriched with respect to other similarly incompatible elements in some fresh MORB glasses suggesting assimilation of hydrothermally altered wall rocks.

### 1.6 Summary of magma plumbing system

Passive mantle upwelling leads to the initiation of decompression melting near the garnet - spinel transition, dependent on the temperature and composition of the upwelling mantle. Melt extraction is near fractional throughout melting, although the exact porosity during melting is poorly constrained. Melt is somehow focused towards the ridge axis (e.g. Speigelman & McKenzie, 1987; Sparks & Parmentier, 1991) and aggregated, either within a region of universal porous flow, or within magma chambers or conduits. Melts probably move through the mantle to their aggregation sites in a complex manner which neither leaves the melt composition identical to when it was generated, nor in equilibrium with depleted upper mantle (low-pressure). However, melt batches from at least the upper part of the melting column are kept distinct for sufficient time to form refractory phenocrysts and be trapped within crystals as melt inclusions. This requires that unhomogenised (but not necessarily unmodified) melts survive transit through the melting column into the lithosphere where cooling induces crystallisation. If aggregation occurs primarily in magma chambers, these need not be those observed in the crust by geophysical experiments and may be deeper, e.g. in the mantle (e.g. Fig. 1.6). Multiple magma chambers are suggested by mixed and disequilibrium phenocryst populations.

Many features of this generalised model are poorly understood and may be inaccurate. Some of these problems can be addressed through detailed study of oceanic gabbros which is the aim of this thesis.

### 1.7 Scope of this thesis

Oceanic gabbros record information about both the composition of melt added to their parental magma chamber, and the fractionation processes which operated within the chamber. Their study should thus provide clues as to some of the details of the magma plumbing system beneath mid-ocean ridges. This is the aim

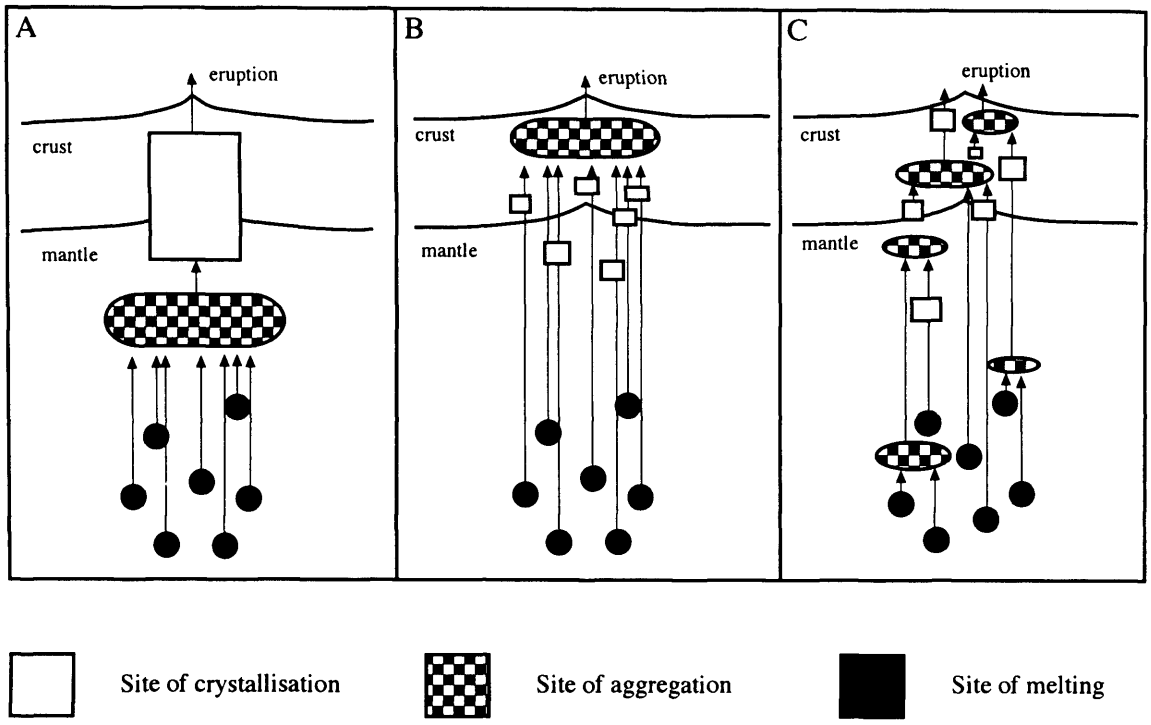


Fig. 1.6 Schematic models of MORB production and evolution from Grove et al. (1992). A) melting followed by aggregation of separate melt batches followed by fractionation then eruption. B) melting followed by fractionation of each melt batch separately followed by aggregation and eruption. C) Melting followed by periodic aggregation and fractionation throughout extraction prior to eruption. Grove et al. (1992) favour model C.

of this thesis. Samples from ODP Hole 923A, an ~50 m section of core from the MARK area of the Mid-Atlantic ridge, have been studied texturally and by electron and ion probe. However, prior to describing and interpreting the gabbros, Chapter Two provides a background to the MARK area. Chapters Three and Four describe the petrology and geochemistry of these rocks respectively with minimal interpretation. Chapter Five discusses open system processes that operated within the magma chamber, and their implications for magma plumbing. Evidence that the magma chamber was open is presented first followed by a discussion of the fluid dynamics of replenishment and mixing. The second half of this chapter discusses the compositions of the melts added to the chamber and their generation. Chapter Six focuses on the development of the crystal mush at the magma chamber margin, and melt differentiation and migration within this region. It is shown that interaction between the crystal assemblage and interstitial melt was very important in the development of the final rock compositions and textures. Chapter Seven summaries the implications of the findings of Chapters Five and Six into a magma plumbing model.

# Chapter II: Geological Setting of ODP Hole 923A

## 2.1 Introduction

Samples studied in this thesis come exclusively from ODP Hole 923A, which was drilled into gabbros exposed on the seafloor in the MARK area (**M**id-**A**tlantic **R**idge south of the **K**ane Fracture Zone, Fig. 2.1) at a latitude of 23°N. This chapter provides the geological background to this area. This is one of the most extensively studied normal (unaffected by a hot spot) portions of the MAR (see Table 1 of Cannat, Karson, Miller, *et al.*, 1995). Owing to this, and the occurrence of known exposures of gabbroic and ultramafic rocks on the seafloor (Karson *et al.*, 1987), it was targeted as a Site for ODP basement drilling (Fig. 2.2), which was undertaken by Leg 153 (Dec. 1993 to Jan. 1994). Below, the structural and tectonic setting of the MARK area are briefly described, and the aims and successes of ODP Leg 153 recounted. An account of petrological studies of the MARK area follows these.

## 2.2 Structure and tectonic setting of the MARK area

The northern boundary of the MARK area is the sinistral Kane transform fault. This is a major offset to the Mid-Atlantic ridge (~150 km) and has been since developing from a small-offset transform ~133 Myrs ago (Tucholke & Schouten, 1988). In this region of the Mid-Atlantic Ridge the axial valley is 10-17 km wide with all volcanism constrained to the central portion. The axial valley becomes wider, deeper and more asymmetric towards the fracture zone as is common on slow-spreading ridges. It has a steep, high western wall and a more subdued eastern wall (Cannat, Karson, Miller, *et al.*, 1995). Spreading rate is also asymmetric with the western plate spreading faster than the eastern (14.1 mm/yr and 11.3 mm/yr, respectively; Schultz *et al.*, 1988). Off-axis the crustal topography is divided into rhombs a few 10's km across, which Gente *et al.* (1995) interpret as the off axis expression of axial segmentation. If this is true, the segmentation scale has not changed significantly over the last 6 Ma, however, the segment locations have.

Immediately south of the Kane transform the MAR is segmented (along-axis) into a northern spreading cell and a southern spreading cell with a complex, small-offset transition zone separating them (Karson *et al.*, 1987; Figs. 2.2 & 2.3). A 600 m high, 40 km long, 4 km wide, <5000 yr old, hydrothermally active neovolcanic ridge runs along the centre of the northern segment (Brown & Karson, 1988). This ridge is the largest volcanic construction identified to date on the Mid-Atlantic ridge. The Snake Pit hydrothermal vent field, which is situated on top of this ridge, emits ~350°C fluids, believed to be derived from a heat source 1-2 km below the seafloor (Campbell *et al.*, 1988). These fluids are similar in

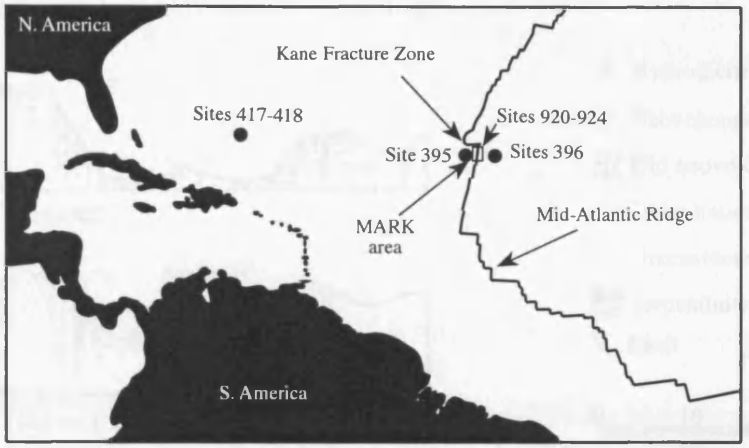


Fig. 2.1 Map showing the location of the MARK area of the Mid-Atlantic Ridge from Cannat, Karson, Miller *et al.* (1995)

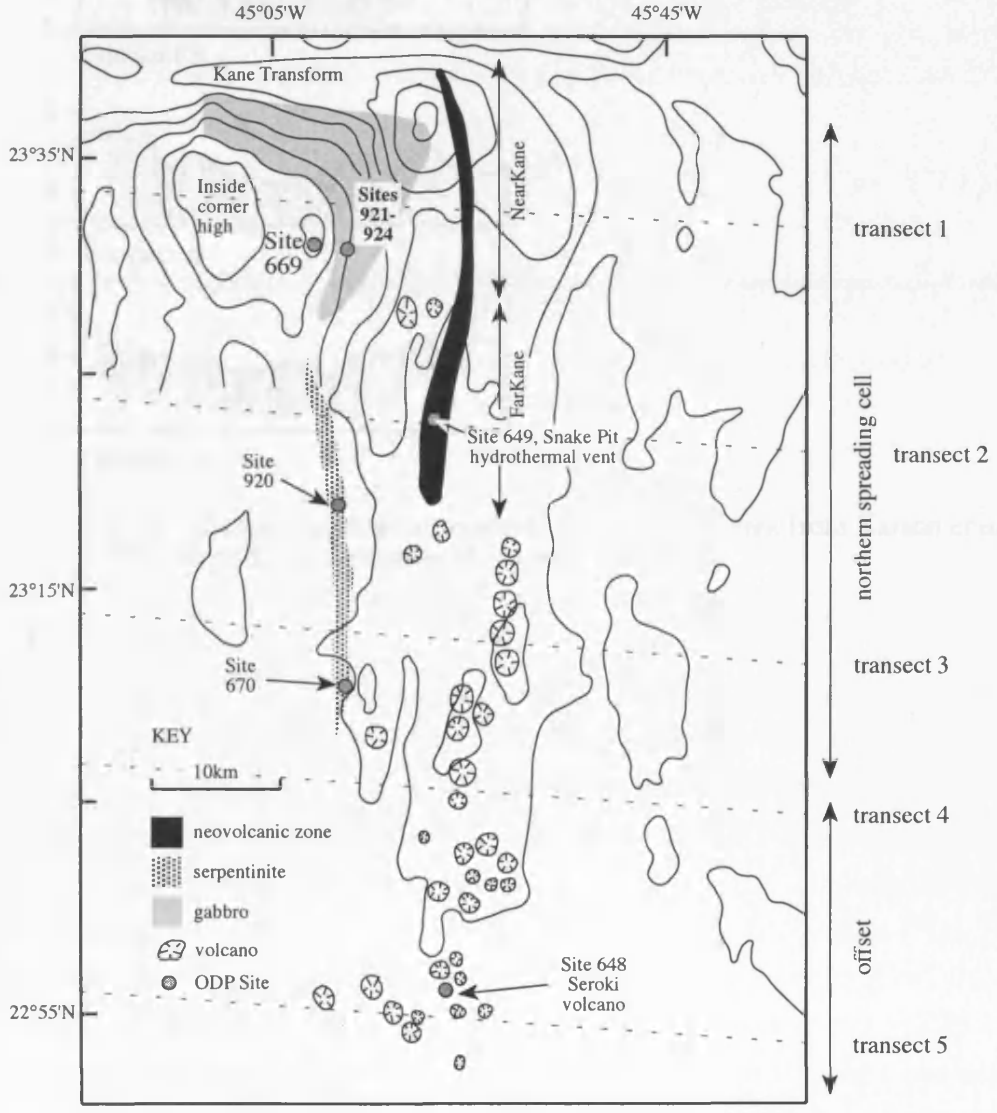


Fig. 2.2 Map of northern part of MARK area. NearKane and FarKane from Reynolds and Langmuir (1997). Location of transects of Fig. 2.3 shown as dashed lines from Karson *et al.* (1987)

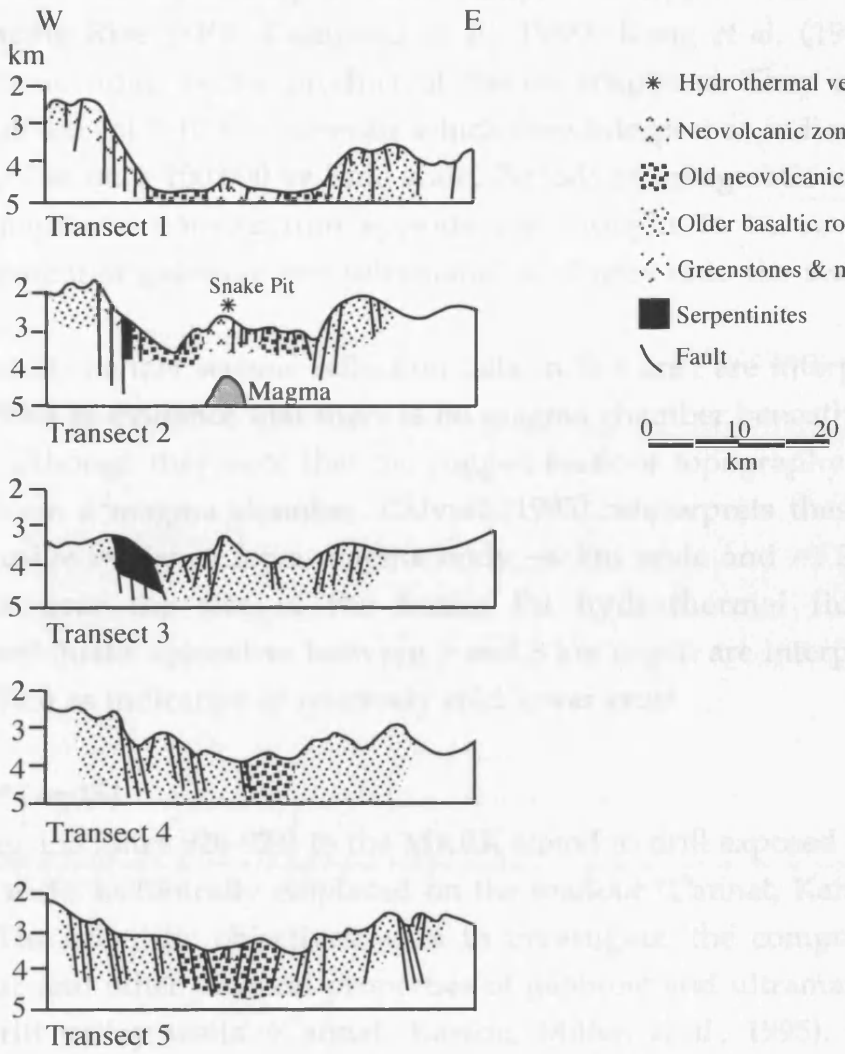


Fig 2.3 Schematic geological transects in the MARK area from Karson *et al.* (1987). See Fig. 2.2 for transect locations

temperature and chemistry to those sampled at hydrothermal vents along the East Pacific Rise (EPR; Campbell *et al.*, 1988). Kong *et al.* (1988) interpret the neovolcanic ridge as the product of fissure eruptions. They also note parallel ridges off-axis at 5-10 km intervals which they interpret as indicative of magmatic construction on a 100,000 yr time scale. Periods of amagmatic extension between these magmatic construction episode are thought to be responsible for the emplacement of gabbroic and ultramafic lithologies onto the seafloor (Figs. 2.2 & 2.3).

Multichannel seismic reflection data in this area are interpreted by Detrick *et al.* (1990) as evidence that there is no magma chamber beneath the MAR in this region, although they note that the rugged seafloor topography could disguise a signal from a magma chamber. Calvert (1995) reinterprets these data and finds inconclusive evidence for a magma body ~4 km wide and ~1.2 km beneath the seafloor near the site of the Snake Pit hydrothermal field. In contrast, microearthquake epicentres between 5 and 8 km depth are interpreted by Toomey *et al.* (1985) as indicative of relatively cold lower crust.

### 2.3 ODP Leg 153

ODP Leg 153 (Sites 920-924) to the MARK aimed to drill exposed lower crustal and mantle rocks tectonically emplaced on the seafloor (Cannat, Karson, Miller, *et al.*, 1995). The scientific objectives were to investigate 'the composition, structure, magnetic and other physical properties of gabbroic and ultramafic rocks exposed in the rift valley walls' (Cannat, Karson, Miller, *et al.*, 1995). One of the main scientific objectives of studies of gabbroic rocks was to 'reveal the igneous evolution of mantle melts' (Cannat, Karson, Miller, *et al.*, 1995). The drilling success, in terms of the recovery and dominant lithology in each Hole is summarised in Table 2.1.

At Site 920 (Fig. 2.2) four holes were drilled into an ultramafic massif identified by Karson *et al.* (1987; Fig. 2.3). Drilling at two of these holes recovered partially serpentinised harzburgite. These contain veins/intrusions of gabbroic rocks, dolerite and gneissic amphibolite. At Sites 921-924 eleven holes were drilled into known gabbroic exposures approximately 6 km south of the Kane Fracture Zone and 10 km west (0.75 Ma) of the neovolcanic ridge (Fig. 2.2). These lie within ~2 km of each other (Cannat, Karson, Miller, *et al.*, 1995). Of these holes in gabbroic exposures, Hole 923A has the highest recovery and yielded the least altered rocks, and has thus been the focus of this study. The good recovery constrains spatial relationships between samples, although as with all studies using incomplete cores the possibility remains that unrecovered sections may include faults or chilled margins. These could invalidate interpretations based on the spatial association of samples within the core.

| Hole | Total recovery (m) | Recovery (%) | Dominant primary lithology |
|---|---|---|---|
| 920B | 47.78 | 39.7 | harzburgite |
| 920D | 95.08 | 47 | harzburgite |
| 921A | 3.10 | 18 | sediment |
| 921B | 10.19 | 29 | gabbro |
| 921C | 6.09 | 11 | gabbro |
| 921D | 6.16 | 12 | gabbro |
| 921E | 17.65 | 21 | gabbro |
| 922A | 9.23 | 63 | gabbro |
| 922B | 11.93 | 31 | gabbro |
| 923A | 40.76 | 74.7 | gabbro |
| 924B | 3.27 | 13.8 | gabbro |
| 924C | 8.22 | 24.3 | gabbro |

Table 2.1 Summary of percent recovery and dominant lithology recovered during ODP Leg 153. Note that recovery both in terms of percentage and volume was considerably better in Hole 923A than in the other gabbroic holes.

Similar lithologies were recovered at all the gabbroic sites, being dominated by interlayered gabbro, olivine-gabbro and troctolite. Small, apparently intrusive, oxide gabbros, leucocratic veins and microgabbros are relatively common but volumetrically minor components of the cores. Ductile deformation in the form of both discrete shear zones and weak pervasive foliations has affected all the cores.

## 2.4 Previous petrological studies in the MARK area

Petrological studies in the MARK area prior to ODP Leg 153 consisted of studies of basalts and peridotites recovered from the seafloor. These are described below, along with the findings of ODP Leg 153.

MORB from the MARK area are typical, relatively homogenous, N-MORB (Fig. 2.4; Bryan *et al.*, 1981; Reynolds & Langmuir, 1997). Isotopically they are at the depleted end of the northern-MAR MORB array in terms of Nd and Sr (Machado *et al.*, 1982; Kempton & Hunter, 1997) with the Kane Fracture Zone marking the limit of the Azores hot spot isotopic signature (Dosso *et al.*, 1993). Major elements show the positive $Na_{8.0}$-$Fe_{8.0}$ correlation ($Na_{8.0}$ and $Fe_{8.0}$ are $Na_2O$ and FeO corrected to an MgO content of 8 wt% via the equations in Klein & Langmuir, 1987) typical of slow spreading ridges (Niu & Batiza, 1993). Only two

detailed studies of MARK area MORB have been published (Bryan *et al.*, 1981; Reynolds & Langmuir, 1997) despite the numerous studies of other aspects of the geology of this region. Both these studies find that clinopyroxene, despite being a rare phenocryst phase, is generally required to have been a fractionating phase to model fractionation trends. Furthermore, Bryan *et al.* (1981) find that clinopyroxene commonly must dominate over olivine in least squares modelling of fractionation trends.

Bryan *et al.* (1981) show that within any sample group most compositional variations can be explained by simple crystal fractionation and crystal accumulation. The exception to this is a common over-enrichment in incompatible elements with respect to that predicted by least squares crystallisation modelling. They also find that some samples contain relatively high abundances of both incompatible and compatible trace elements. They explain these features through mixing between evolved and primitive magmas. Furthermore they show that the $Fe^{3+}/Fe^{2+}$ ratio correlates positively with Ti, an incompatible, relatively immobile, element, suggesting that the magma became more oxidised with increasing fractionation.

Reynolds and Langmuir (1997) use a well located N-MORB data set from along the neovolcanic ridge (see Fig. 2.2) to investigate the effect of the transform fault on basalt compositions (the transform fault effect). They 'correct' all compositions to MgO = 8 wt% (Klein & Langmuir, 1987) prior to interpreting them in an attempt to 'see through' fractionation effects. Samples from near the transform (NearKane on Fig. 2.2 which includes Hole 923A) have lower abundances of highly incompatible trace elements and higher abundances of moderately incompatible elements than samples further from the transform (FarKane on Fig. 2.2; Reynolds & Langmuir, 1997). This observation is partially based on two ICP-MS analyses, one from each section of the ridge. Primary data (not corrected to MgO = 8 wt%) for all samples are plotted in Fig. 2.5, and show that the sites chosen by Reynolds and Langmuir for ICP-MS analysis are the two that show this trend the most clearly. Reynolds and Langmuir (1997) interpret this as indicative that previously partially melted mantle from north of the transform is entrained into the upwelling sub-ridge mantle south of the transform, leading to lower degrees of melting of a more depleted source proximal to the transform.

Ghose *et al.* (1996) investigate the transform fault effect through the study of major and minor element mineral compositions in abyssal peridotite samples. The basis for this study is that melt extraction depletes Al, Na and Ti in pyroxenes and increases the Cr# and decreases the Mg# of spinel. Ghose *et al.* (1996) find that the degree of depletion decreases towards the transform and suggest that this reflects lower degrees of melting due to the thermal edge effect of the transform.

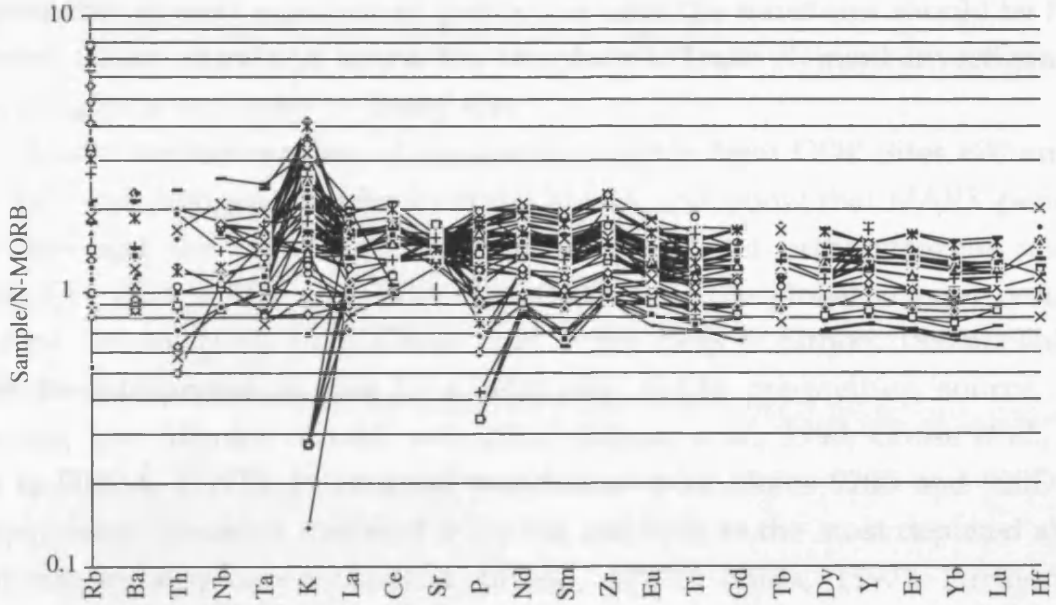


Fig 2.4 N-MORB normalised (Sun & McDonough, 1989) spidergram of MARK area MORB (Data from Dosso et al., 1993; Reynolds and Langmuir, 1997; Bryan et al., 1981). Note positive Sr and Zr anomalies in the lowest abundance samples. Also note that compared to N-MORB these show a slight depletion in HREE with respect to MREE and LREE.

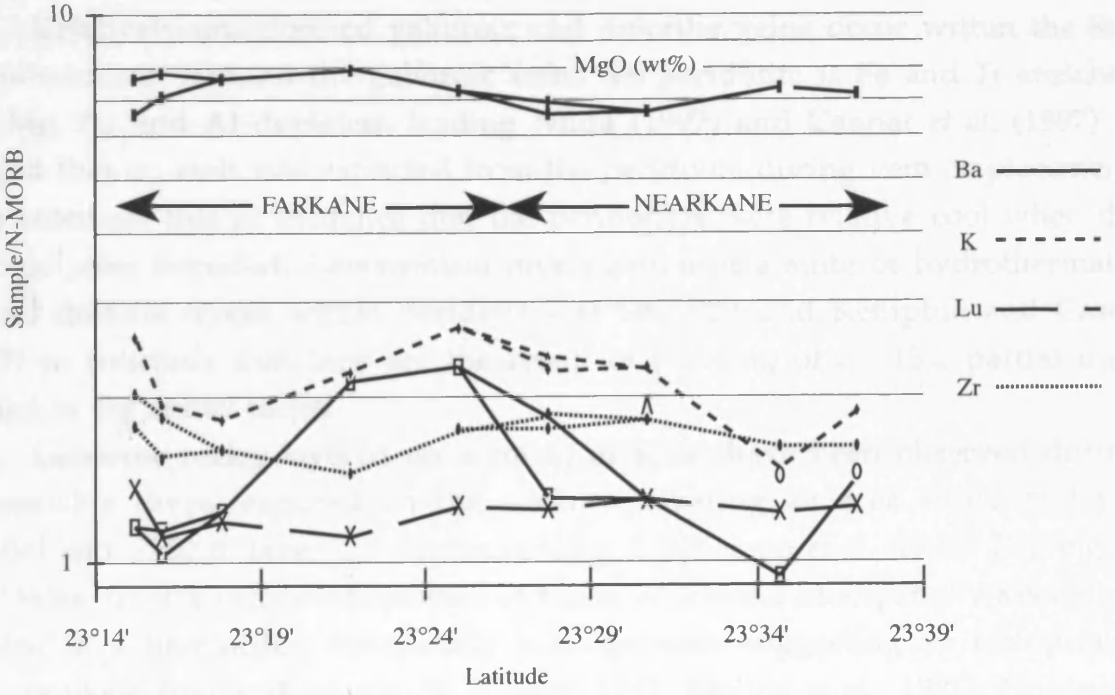


Fig 2.5 Plot of latitude versus abundance for the Reynolds and Langmuir (1997) samples in NEARKANE and FARKANE areas (see Fig. 2.2). Trace elements N-MORB normalised (Sun & McDonough, 1989) plus MgO as wt% as Reynolds and Langmuir corrected the data to 8wt% MgO (Klein & Langmuir, 1987). The two samples analysed by ICP-MS are from ~23°25'N and ~23°35'N (i.e. the highest and lowest abundances from each region).

This appears contrary to the model of Reynolds and Langmuir (1997) which suggests that at least a portion of peridotites near the transform should be highly depleted (those entrained across the transform). Trace element investigation of these samples is necessary to clarify this.

Major element studies of abyssal peridotites from ODP Sites 670 and 920 (Fig. 2.2), and dredged samples from the MARK area show that MARK peridotite have amongst the highest Al contents in clino- and orthopyroxene and the lowest Cr# [Cr# = 100 x Cr/(Cr+Al)] of spinel in the global abyssal peridotite database (Juteau *et al.*, 1990; Ghose *et al.*, 1996, Ross & Elthon, 1997b). This can either be interpreted as due to a relatively fertile pre-melting source, or as reflecting low degrees of melt extraction (Juteau *et al.*, 1990; Ghose *et al.*, 1996; Ross & Elthon, 1997b). In contrast, peridotites from Holes 920B and 920D have clinopyroxene almost as depleted in Ti, Na and REE as the most depleted abyssal peridotite clinopyroxene (Ross & Elthon, 1997b; Niida, 1997). Furthermore, Stephens (1997) and Casey (1997) observe that whole rock analyses of Site 920 peridotites have variable incompatible element patterns, including LREE enrichment, without associated major element variation. These data suggest that the peridotites do not represent the simple residues of partial melting of a depleted source. Open system melt extraction and refertilisation must be invoked to explain the compositional diversity.

Relatively undeformed gabbroic and doleritic veins occur within the Site 920 peridotites. Around the gabbroic veins the peridotite is Fe and Ti enriched and Mg, Ni and Al depleted, leading Niida (1997) and Cannat *et al.* (1997) to suggest that no melt was extracted from the peridotite during vein emplacement. They interpret this as evidence that the peridotites were relative cool when the gabbros were intruded. Geochemical investigation of a suite of hydrothermally altered dolerite dykes within peridotites at Site 920 lead Kempton and Casey (1997) to conclude that they are the result of ponding of a <15% partial melt formed in the spinel facies.

Gabbroic rocks, layered on a cm to m scale, have been observed during submersible dives, exposed on the seafloor covering an area ~1500 m layer parallel and ~750 m layer perpendicular (Fig. 2.3; Karson *et al.*, 1987). Drilling at ODP Sites 921-924 recovered samples of these, which are, like spatially associated basalts, to a first order, isotopically homogeneous suggesting an isotopically homogeneous source (Kempton & Hunter, 1997; Barling *et al.*, 1997). However, they have less radiogenic Pb isotopic ratios and more radiogenic Nd isotopic ratios than present day basalts indicating a slightly more depleted source than the present-day one (Kempton & Hunter, 1997).

Major element compositions show that these gabbros are cumulate (Mg# 74-82; Cannat, Karson, Miller *et al.* 1995). Trace element abundances are highly

variable in whole rock (Barling *et al.*, 1997; Casey, 1997), mineral separate (Ross & Elthon, 1997a), and *in situ* mineral analyses (Ross & Elthon, 1997a). Weak negative correlations exist between Mg# and incompatible trace element abundances. Modelling of whole rock trace element abundances from Sites 921 and 923 by Barling *et al.* (1997) suggest that the compositions can be explained as the product of primitive cumulates plus varying amounts of trapped melt. They propose that these first order variations are modified by magma flow during compaction and adcumulus growth. Ross and Elthon (1997a) use minor and trace element mass balance of whole rock and mineral separate analyses to suggest that gabbros from Sites 921 and 923 contain 0-30% trapped melt.

**2.5 Summary**

ODP Hole 923A is approximately 6 km south of the Kane Fracture Zone, a major tectonic and geochemical boundary on the MAR, and 10 km west of the neovolcanic zone. It lies within the northern-most spreading cell of the MARK area, which is presently characterised by the largest volcanic ridge on the MAR. The Snake Pit hydrothermal field on this ridge emits high temperature hydrothermal fluids, suggesting a shallow heat source, although evidence for the existence of a magma chamber in this area is inconclusive. Large areas of tectonically exposed layered gabbros outcrop on the valley flanks. Drilling into these exposures at ODP Site 923A recovered ~40 m of layered gabbroic rocks with ~75% recovery allowing reasonable interpretation of the spatial relationships between lithologies.

Basalt in this area is relatively homogenous N-MORB. Fractionation trends show two common characteristics of MORB: (i) over-enrichment in incompatible elements with respect to major elements, and (ii) a requirement for clinopyroxene to have been a fractionating phase despite generally not occurring as a phenocryst (Bryan *et al.*, 1981; Reynolds and Langmuir, 1997). Reynolds and Langmuir (1997) suggest that the source for basalts closest to the transform, including the Site of Hole 923A, is a mix of normal upwelling mantle and depleted mantle entrained from north of the Kane Fracture Zone. Abyssal peridotites, thought to be the source for the basalts, are highly depleted in Ti, Na and incompatible trace elements, but not in Al (Ross & Elthon, 1997b), and become less depleted with proximity to the transform (Ghose *et al.*, 1996). Variations in LREE abundances within the peridotite suite suggest open system processes of melt extraction and subsequent metasomatism. Gabbroic lithologies are interpreted as primitive cumulates and varying amounts of trapped melt (Ross & Elthon, 1997a; Barling *et al.*, 1997).

# Chapter III: Stratigraphy and Petrography of ODP Hole 923A

## 3.1 Introduction

In this chapter the distribution of lithologies within ODP Hole 923A is briefly described followed by detailed descriptions of their textures. The observations suggest that the two main lithologies, poikilitic olivine gabbros and brown-pyroxene gabbros, underwent very different crystallisation histories. Poikilitic olivine gabbros formed by plagioclase +/- olivine accumulation, and then cementation by clinopyroxene oikocrysts. The timing of clinopyroxene nucleation, and mechanism of plagioclase and olivine densification (growth versus compaction), probably controlled the textural variation within this lithology. Brown-pyroxene gabbros are characterised by grain size layering which affects cumulus plagioclase, olivine and clinopyroxene, and interstitial ilmenite. This cannot be explained by crystal settling; instead textural characteristics support an important role for secondary texture development in the genesis of this lithology.

This chapter describes the petrography of these lithologies but makes only limited interpretation; most of the interpretation of the processes involved in the genesis of these rocks is made in Chapters Five and Six after the mineral compositions have been describe in Chapter four. This is necessary because many textures do not have a unique method of formation (e.g. McBirney & Hunter, 1995). However some interpretation is made throughout this chapter where knowledge of the mineral compositions does not aid interpretation.

## 3.2 Lithological summary [1]

Shipboard studies (Cannat, Karson, Miller *et al.*, 1995) describe the core in terms of four lithologies. These are: (i) brown-pyroxene gabbros, (ii) poikilitic olivine gabbros, (iii) oxide gabbros, and (iv) leucocratic veins (pgs. 219-226 of Cannat, Karson, Miller *et al.*, 1995). In this thesis this nomenclature is retained but poikilitic olivine gabbros are subdivided into: (i) coarse grained poikilitic olivine gabbros, (ii) fine-grained, plagioclase-rich, clinopyroxene-poor poikilitic olivine gabbros (here termed troctolites), and (iii) heterogeneous poikilitic olivine gabbros (found between 44 and 48 metres below sea floor - mbsf). The mode of the samples studied in detail in this project are summarised in Table 3.1. Samples are referred to in terms of their depth below the sea floor throughout this study in order that spatial relationships are obvious. Reference to their standard ODP sample number can be made in Table 3.1.

Coarse poikilitic olivine gabbros are plagioclase +/- olivine cumulates poikilitically enclosed by clinopyroxene +/- olivine. Troctolites are fine to

[1] More extensive description of the core is available in Cannat, Karson & Miller *et al* (1995)

medium grained, plagioclase-rich, clinopyroxene-poor poikilitic olivine gabbros. The heterogeneous poikilitic olivine gabbros (44 to 48 mbsf) constitute an olivine rich, modally and texturally heterogeneous region of the core. Brown-pyroxene gabbros are plagioclase + clinopyroxene +/- olivine +/- low-Ca pyroxene cumulates with considerable systematic grain size variation. Oxide gabbros are plastically deformed, plagioclase + clinopyroxene + low-Ca pyroxene +/- olivine cumulates. Leucocratic veins have variable modes but are dominated by plagioclase and also contain variable amounts of clinopyroxene, amphibole, apatite and zircon (Cannat, Karson, Miller *et al.*, 1995).

Fig. 3.1 is a summary log of the core from Hole 923A based on shipboard (Cannat, Karson, Miller, *et al.*, 1995) and shore-based observations (this study). The upper 16.4 m of drilling recovered only 0.73 m of wash core, which has been omitted from this study. Below this the core is dominated by brown-pyroxene gabbro and poikilitic olivine gabbro, constituting 56% and 42% of the core respectively (Cannat, Karson, Miller, *et al.*, 1995). Although these lithologies are interlayered, the core is dominated by poikilitic olivine gabbro between 70 mbsf and 44 mbsf and by brown-pyroxene gabbro above this. Leucocratic veins are restricted in occurrence to core recovered below 30 mbsf, where they are commonly adjacent to microgabbros. Oxide gabbros occur in the upper part of the core (above 30 mbsf) within deformed brown-pyroxene gabbro and as a single 'vein' at 66 mbsf within poikilitic olivine gabbro. Lithologies are generally easily distinguished in hand specimen, although some intermediate rock types do occur.

Shipboard studies divided the cored interval into eight 'magmatic cycles' each consistent with upward magmatic evolution (Cannat, Karson, Miller *et al.*, 1995); these are shown in Fig. 3.1. These have sharp bases overlain in sequence by an olivine + plagioclase adcumulate, then an olivine crescumulate that grades into an olivine + plagioclase cumulate enclosed in poikilitic clinopyroxene. The upper portion of each cycle is a grain size layered olivine gabbro. However, not all cycles record the full range of lithologies/textures and are of very different sizes (Cannat, Karson, Miller *et al.*, 1995). In this study extensive reference is not made to these cycles because, due to the lack of sufficient samples, it has not been possible to test the significance of these cycles by detailed petrography and analysis of mineral composition.

### 3.3 Poikilitic olivine gabbros

This name includes a spectrum of gabbroic rocks with large variations in grain size and mode, but which are largely undeformed, plagioclase +/- olivine cumulates enclosed in sub-poikilitic to poikilitic clinopyroxene +/- olivine.

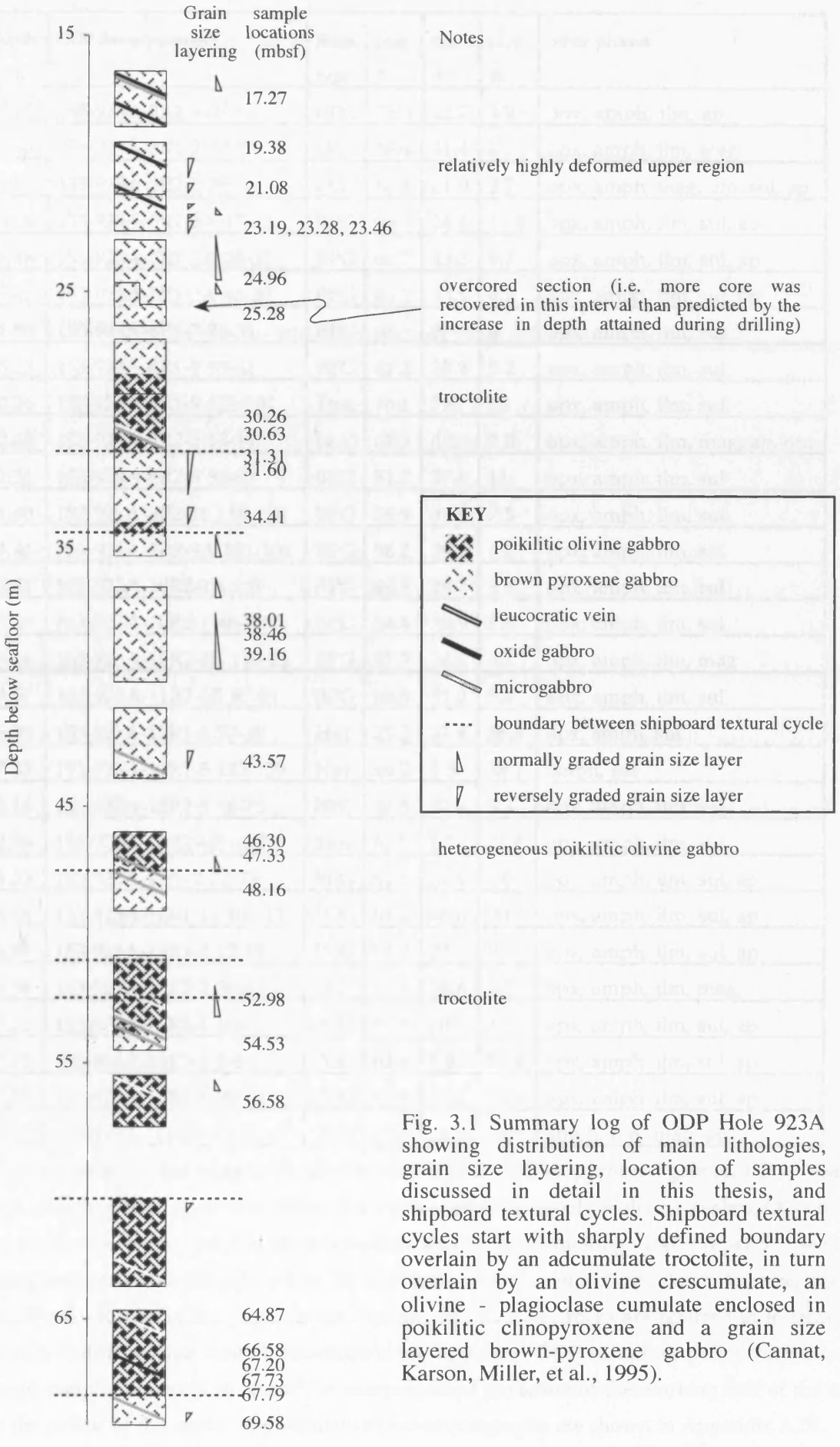


Fig. 3.1 Summary log of ODP Hole 923A showing distribution of main lithologies, grain size layering, location of samples discussed in detail in this thesis, and shipboard textural cycles. Shipboard textural cycles start with sharply defined boundary overlain by an adcumulate troctolite, in turn overlain by an olivine crescumulate, an olivine - plagioclase cumulate enclosed in poikilitic clinopyroxene and a grain size layered brown-pyroxene gabbro (Cannat, Karson, Miller, et al., 1995).

| Depth (mbsf) | ODP Sample number | Rock type | plag % | cpx % | oliv % | other phases |
|---|---|---|---|---|---|---|
| 17.27 | 153-923A-2R1-9 87-94 | BPG | 72.3 | 22.7 | 4.9 | opx, amph, ilm, ap |
| 19.38 | 153-923A-3R1-2 18-22 | OG | 55.4 | 31.4 | 0 | opx, amph, ilm, mag |
| 21.08 | 153-923A-3R2-2 39-45 | OG | 67.4 | 21.9 | 2.7 | opx, amph, mag, ilm, sul, ap |
| 23.19 | 153-923A-5R1-2A 19-22 | BPG | 60.3 | 24.6 | 14.9 | opx. amph, ilm, sul, ap |
| 23.28 | 153-923A-5R1-2A 28-31 | BPG | 66.7 | 23.3 | 9.7 | opx, amph, ilm, sul, ap |
| 23.46 | 153-923A-5R1-2A 46-50 | BPG | 60.2 | 33.5 | 6.2 | opx, amph, ilm, sul, ap |
| 24.96 | 153-923A-6R1-7 26-31 | BPG | 65 | 27 | 8 | opx, amph, ilm, sul |
| 25.28 | 153-923A-6R1-9 58-61 | BPG | 61.2 | 33.5 | 5.2 | opx, amph, ilm, sul |
| 30.26 | 153-923A-8R1-9 126-131 | Troc | 76.1 | 7.8 | 16 | opx, amph, ilm, sul |
| 30.63 | 153-923A-8R2-2 13-19 | Leuc | 87.6 | 0.0 | 0.0 | opx, amph, ilm, mag, ap, qtz, |
| 31.31 | 153-923A-8R2-8 81-88 | BPG | 51.2 | 37.6 | 11 | opx, amph, ilm, sul |
| 31.60 | 153-923A-8R2-10 110-116 | BPG | 56.9 | 34.9 | 7.5 | opx, amph, ilm, sul |
| 34.41 | 153-923A-9R2-9A 101-103 | BPG | 56.2 | 39.5 | 4.2 | opx, amph, ilm, sul |
| 38.01 | 153-923A-10R2-1A 1-4 | BPG | 64.6 | 29.7 | 5.6 | opx, amph, ilm, sul |
| 38.46 | 153-923A-10R2-1 46-52 | BPG | 54.4 | 36.9 | 8.5 | opx, amph, ilm, sul |
| 39.16 | 153-923A-10R2-2B 116-21 | BPG | 57.5 | 34.6 | 5.1 | opx, amph, ilm, mag |
| 43.57 | 153-923A-11R2-6B 87-91 | BPG | 63.3 | 31.2 | 5.4 | opx, amph, ilm, sul |
| 46.30 | 153-923A-12R1-4 30-38 | Het | 25.2 | 37.8 | 36.6 | opx, amph, sul |
| 47.33 | 153-923A-12R1-5 133-139 | Het | 60.2 | 1.5 | 38.1 | amph, sul |
| 48.16 | 153-923A-12R2-5 66-73 | BPG | 47.3 | 47.4 | 5.3 | opx, amph, ilm, sul |
| 52.98 | 153-923A-13R2-6B 68-75 | Troc | 67.5 | 6.7 | 25.4 | opx, amph, ilm, sul |
| 54.53 | 153-923A-13r3-7 73-79 | BPG | 52.6 | 32.9 | 0.0 | opx, amph, ilm, sul, ap |
| 56.58 | 153-923A-14R1-12 100-112 | POG | 63.2 | 36.6 | 0.1 | opx, amph, ilm, sul, ap |
| 64.87 | 153-923A-16R1-2 17-19 | POG | 67.4 | 23.6 | 8.9 | opx, amph, ilm, sul, ap |
| 66.58 | 153-923A-16R2-2 38-41 | OG | 54.8 | 34.6 | 0.0 | opx, amph, ilm, mag, |
| 67.20 | 153-923A-16R2-4 100 | POG | 87.3 | 10.2 | 2.9 | opx, amph, ilm, sul, ap |
| 67.73 | 153-923A-16R3-1 3-6 | POG | 63.4 | 5.8 | 29.4 | opx, amph, ilm, sul, ap |
| 67.79 | 153-923A-16R3-1 09-15 | POG | 69.4 | 13.1 | 17.4 | opx, amph, ilm, sul, ap |
| 69.58 | 153-923A-16R4-7 68-70 | BPG | 55.3 | 44.5 | 0.0 | amph, ilm, mag, ap |

Table 3.1. Summary of the samples studied in detail; BPG - brown-pyroxene gabbro; POG - coarse poikilitic olivine gabbro; Troc - troctolite; Het - heterogeneous poikilitic olivine gabbro; OG - oxide gabbro; Leuc - leucocratic vein. The mode was calculated by point counting ~1000 pts per thin section. Accessory minerals include: opx - low-Ca pyroxene, amph - amphibole, ilm - ilmenite, mag - magnetite, sul - sulphides, ap - apatite, qtz - quartz. In this study rocks are referred to in terms of their depth (mbsf) so that spatial associations are apparent. ODP sampling policy restricts the volume of sample requested to 50 $cm^3/m$ and prevented depletion of the working half of the core during the period of this study. Representative photomicrographs are shown in Appendix A.IV.

Whole rock $Mg^{\#}$s which range from 79 to 82 (with one exception of 73) indicate that these rocks are cumulates (Cannat, Karson, Miller, *et al.* 1995).

*3.3.1 Coarse poikilitic olivine gabbros*

Five samples of coarse poikilitic olivine gabbros have been studied in detail (Table 3.1). Plagioclase is the only universally cumulus phase, generally forming a framework of touching laths which increases in density from oikocryst core to rim (Fig. 3.2). Plagioclase crystals commonly, have optically distinct, irregularly shaped cores, sharply overgrown to various degrees. Olivine occurs as both cumulus crystals and oikocrysts, some of which contain small 'floating' plagioclase crystals. Clinopyroxene occurs as 2 to 6 cm diameter oikocrysts, which only occasionally have cores that are free of plagioclase chadacrysts or contain 'floating' chadacrysts. Plagioclase at the margins of oikocrysts have lower aspect ratios than those in oikocryst cores and can form cm-scale anorthositic patches with little interstitial clinopyroxene. Similar textures are commonly reported in other oceanic gabbros (e.g. Natland & Dick, 1996; Tiezzi & Scott, 1980).

Plagioclase-plagioclase grain boundaries are generally interdigitate on a small scale (~0.5 mm; see Fig. 3.2) and unequilibrated, with the degree of equilibration being higher in plagioclase enclosed in clinopyroxene oikocryst rims than in oikocryst cores. Plagioclase-clinopyroxene grain boundaries range from planar to ragged but are generally relatively smooth on a small scale (Fig 3.2). Olivine grain boundaries are generally the most smoothly curved and are commonly rimmed by approximately 50 μm of ortho- or occasionally clino-pyroxene. Clinopyroxene rims on olivine are generally the continuation of clinopyroxene oikocrysts, as shown in Fig. 3.2b. Olivine-plagioclase grain boundaries are occasionally mutually embayed with no overgrowth of the plagioclase core, but are generally relatively smoothly curved.

Accessory ilmenite, brown amphibole, apatite and composite sulphide grains occur in most coarse grained poikilitic olivine gabbros. Ilmenite is generally found as small crystals associated with brown amphibole +/- apatite at clinopyroxene rims (Fig 3.2b) but also occurs as large (~2 mm diameter) crystals. An opaque phase with a 'fracture filling' form occurs at a plagioclase-plagioclase-clinopyroxene triple junction and within plagioclase at 67.79 mbsf (Fig. 3.3). Brown amphibole occurs as thin discontinuous rims (~10 to 50 μm) on, and as blebs within, clinopyroxene. Apatite crystals are generally very small and occur in association with ilmenite and brown amphibole at clinopyroxene rims, but apatite has also been observed at 67.79 mbsf within an olivine rim. Rounded composite iron sulphides, dominated by pyrrhotite with minor chalcopyrite and pentlandite, occur at silicate phase grain boundaries and within olivine.

Fig. 3.2a

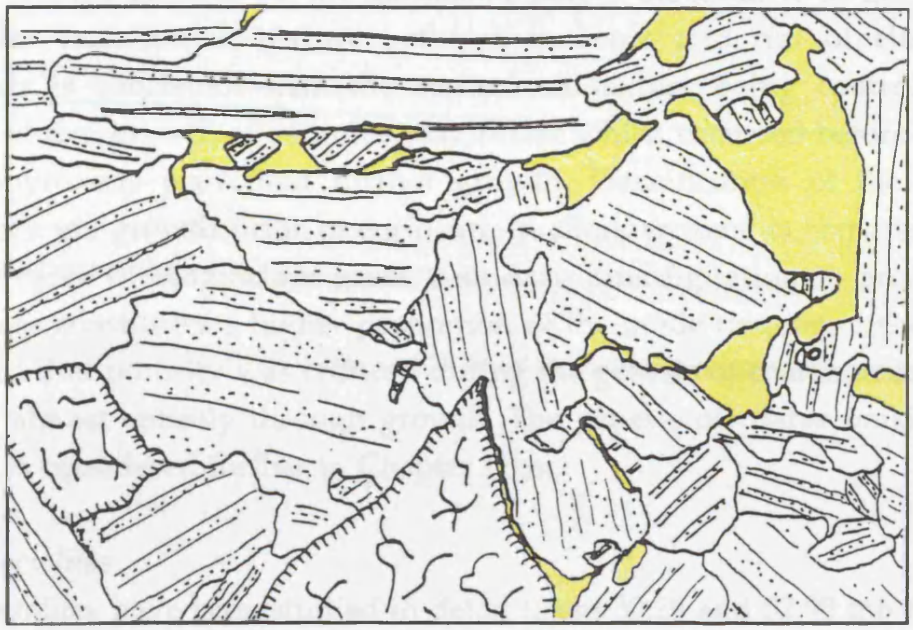

Fig. 3.2b

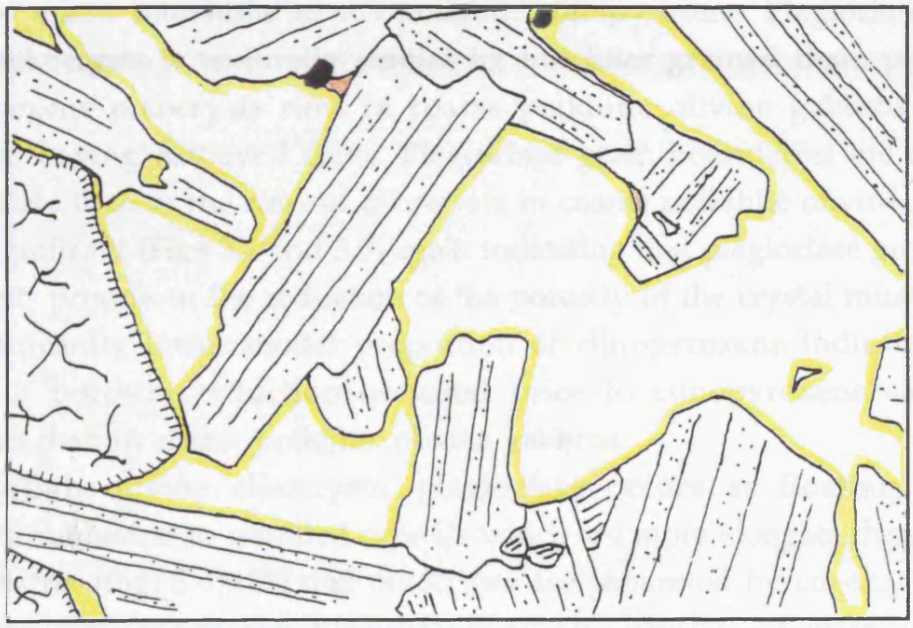


Fig. 3.2 Traced photomicrographs comparing the texture at the rim of a clinopyroxene oikocryst (a), with that at the core of the same oikocryst (b), in a coarse poikilitic olivine gabbro from 67.79 mbsf. Note the interdigitated plagioclase-plagioclase grain boundaries, in particular at the oikocryst margin. Also, note that thin selvages of clinopyroxene occur along plagioclase-olivine grain boundaries.
Legend: Yellow margin and white interior - clinopyroxene; stippled twins in true orientation - plagioclase; hatched margin and schematic cracks - olivine; black - ilmenite; brown - amphibole

Sulphides are generally more abundant in poikilitic olivine gabbros than in brown-pyroxene gabbros but are too small a part of the mode to be quantified.

The variation in texture between the core and rim of clinopyroxene oikocrysts is consistent with the control on texture being controlled by the amount of overgrowth of cumulus plagioclase which occurred before entrapment in clinopyroxene prevented further growth. Densification of the plagioclase framework via growth prior to enclosure in clinopyroxene is consistent with the higher degree of plagioclase grain boundary interdigitation in areas in which plagioclase constitutes a higher proportion of the mode (Hunter, 1996). Thus it is suggested that porosity was reduced during the genesis of coarse poikilitic olivine gabbros almost entirely through growth. The genesis of coarse poikilitic olivine gabbros is considered further in Chapter Five.

### *3.3.2 Troctolites*

Two troctolites have been studied in detail (from 30.26 and 52.98 mbsf; Table 3.1). These are fine to medium-grained plagioclase +/- olivine cumulates with abundant cm-scale olivine oikocrysts, frequently elongate sub-horizontally in the core, and minor interstitial to sub-poikilitic clinopyroxene. Plagioclase outside of olivine oikocrysts is texturally similar to, but finer grained than, plagioclase at clinopyroxene oikocrysts rims in coarse poikilitic olivine gabbros (Fig. 3.2a), including having embayed cores. Plagioclase grain boundaries are slightly less interdigitate than at the rims of oikocrysts in coarse poikilitic olivine gabbros but is still significant (Figs 3.4 and 3.6) again indicating that plagioclase growth was an important process in the reduction of the porosity of the crystal mush. However, the significantly lower modal proportion of clinopyroxene indicates a greater degree of porosity reduction occurred prior to clinopyroxene saturation in troctolites than in coarse poikilitic olivine gabbros.

Within olivine oikocrysts, plagioclase occurs as floating, commonly clustered, subhedral to rounded crystals which are more elongate than plagioclase in the matrix (Fig. 3.4). Olivine oikocrysts are separated by cm-scale patches in which the matrix between plagioclase crystals consists of interstitial to sub-poikilitic clinopyroxene. Clinopyroxene generally occurs as <0.5 mm patches between plagioclase, however, these patches may be in optical continuity over several millimetres. Plagioclase-clinopyroxene grain boundaries are mutually embayed, smoothly curved, generally concave, and are commonly rimmed by brown amphibole, which is more abundant than in other lithologies (Fig. 3.5). Clinopyroxene is not restricted to plagioclase grain boundaries but also occurs within plagioclase and occasionally along plagioclase twin planes (Fig. 3.6).

Low-Ca pyroxene occurs as rare thin rims on olivine. Small, rounded compound sulphides are common along mafic phase margins, but no apatite has

Fig. 3.3

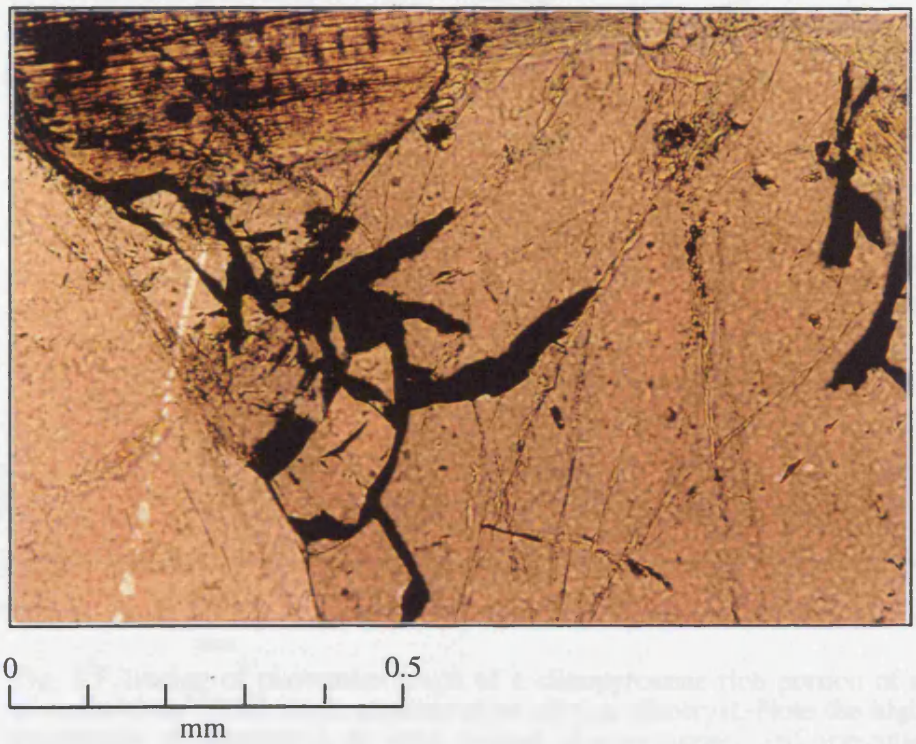


Fig. 3.3 Photomicrograph of oxide within plagioclase in at 67.79 mbsf. The form of the oxide suggests that it is filling a fracture.

Fig. 3.4

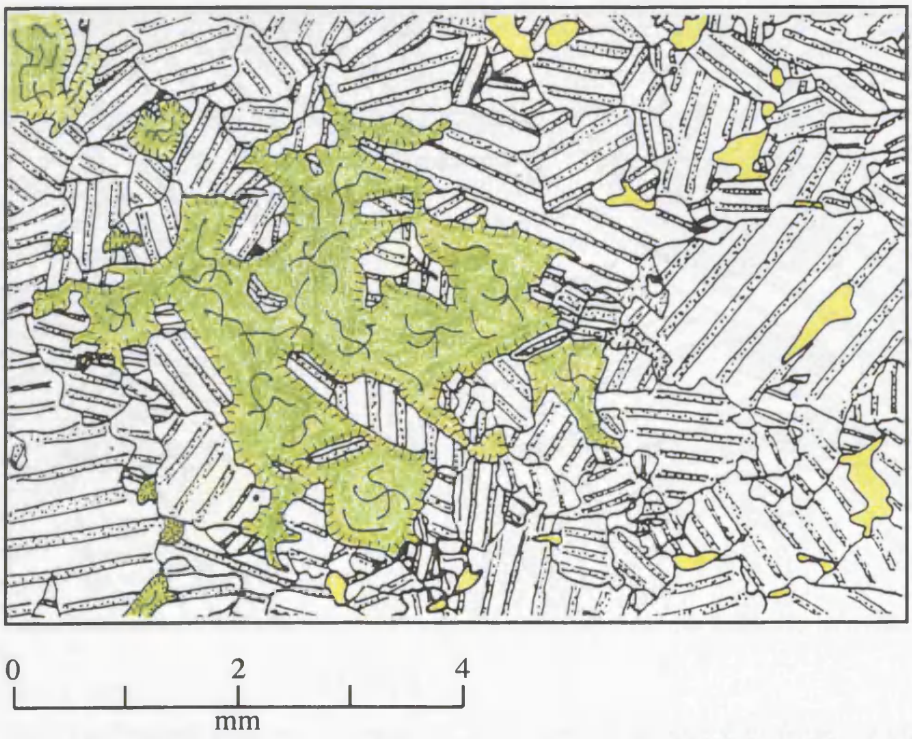


Fig 3.4 Tracing of photomicrograph of an olivine oikocryst in a troctolite at 30.26 mbsf. Note the irregular form of the interstitial clinopyroxene patches
Legend: Stippled twins shown in true orientation - plagioclase; yellow - clinopyroxene; green with hatched margin and crack ornament - olivine.

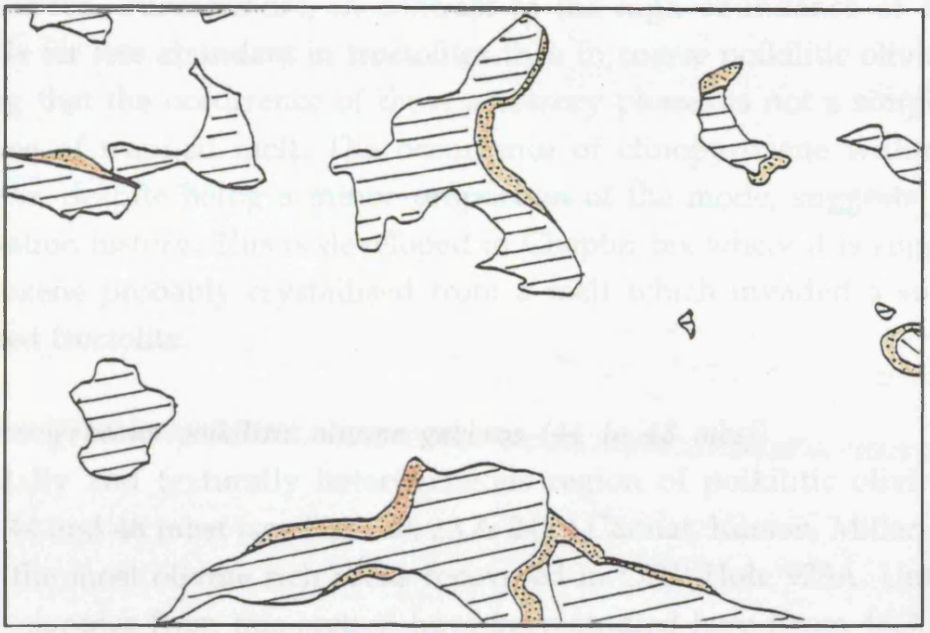


Fig. 3.5 Tracing of photomicrograph of a clinopyroxene rich portion of a troctolite from 30.26 mbsf, adjacent to an olivine oikocryst. Note the high abundance of amphibole as rims around clinopyroxene, and irregular shapes of clinopyroxene patches.
Legend: white - plagioclase, ruled - clinopyroxene; brown and stippled - amphibole.


Fig. 3.6 Traced photomicrograph of a portion of a troctolite from 52.98 mbsf. Note the clinopyroxene within plagioclase, elongate parallel to the plagioclase twin orientation (just below the centre of the figure).
Legend: stippled twins in true orientation - plagioclase; green with hatched margin and crack ornament - olivine; yellow - clinopyroxene

been observed. Furthermore, in contrast to the high abundance of amphibole, ilmenite is far less abundant in troctolites than in coarse poikilitic olivine gabbros indicating that the occurrence of these accessory phases is not a simple function the degree of trapped melt. The occurrence of clinopyroxene within cumulus plagioclase, despite being a minor proportion of the mode, suggests a complex crystallisation history. This is developed in Chapter Six where it is suggested that clinopyroxene probably crystallised from a melt which invaded a substantially crystallised troctolite.

*3.3.3 Heterogeneous poikilitic olivine gabbros (44 to 48 mbsf)*

The modally and texturally heterogeneous region of poikilitic olivine gabbros between 44 and 48 mbsf (see Figs. 20, 23 & 24 of Cannat, Karson, Miller, *et al.* 1995) includes the most olivine rich rocks recovered in ODP Hole 923A. Unfortunately only two samples from this section have been studied here (from 46.30 and 47.33 mbsf; Table 3.1). These are plagioclase + olivine cumulates with very variable proportions of interstitial to poikilitic clinopyroxene on a thin section scale. Proportions of plagioclase and olivine, their texture, morphology, and grain size also all vary within a thin section. Single thin sections of both the samples can be divided into separate lithologies. The sample from 47.33 mbsf has a portion which is medium grained and contains approximately equal proportions of olivine and plagioclase, but only minor interstitial clinopyroxene; the other portion is dominated by coarser plagioclase, with clinopyroxene occurring as a single interstitial crystal. The sample from 46.30 mbsf consists of a clinopyroxene poor portion similar to the medium grained portion of the sample from 47.33 mbsf and an olivine crescumulate enclosed by a single clinopyroxene oikocryst with interstitial plagioclase.

3.3.3.1 The clinopyroxene-poor lithology is a sub-granular plagioclase + olivine cumulate similar in texture to oikocryst rims in coarse poikilitic olivine gabbros, except with a higher modal proportion of olivine and less interdigitated grain boundaries (Fig. 3.7). Olivine and plagioclase are broadly equidimensional but can be irregularly shaped especially at 47.33 mbsf. Minor clinopyroxene occurs as optically continuous thin rims 'wetting' cumulus crystals and filling triple junctions (Fig. 3.7). Plagioclase-plagioclase grain boundaries are broadly straight but locally irregular and interdigitate. Local interdigitation is slightly more angular at 46.30 mbsf than 47.33 mbsf. Olivine-plagioclase grain boundaries are smoothly curved, convex, and are generally only irregular at triple junctions. Clinopyroxene has smooth grain boundaries with both olivine and plagioclase. Low-Ca pyroxene occurs as thin rims on some olivine. Ilmenite, sulphides and brown amphibole occur as accessory phases in lower abundances than in any

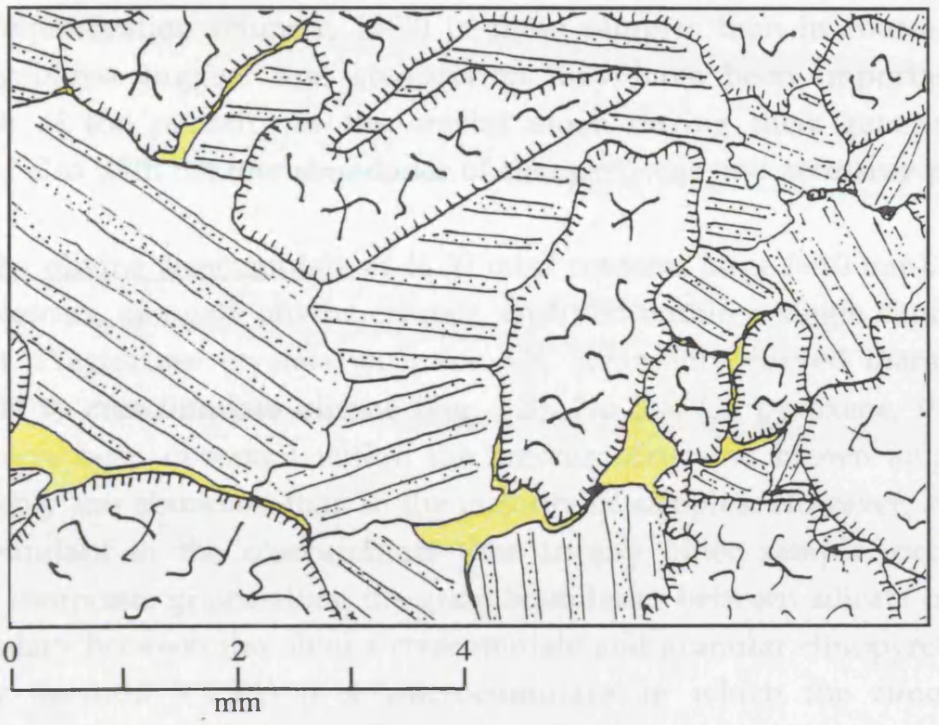


Fig. 3.7 Tracing of a photomicrograph of a granular portion of a heterogeneous poikilitic olivine gabbro from 47.33 mbsf. All the clinopyroxene is in optical continuity and 'wets' other phase boundaries. Legend: stippled twins in true orientation - plagioclase; hatched margin and crack ornament - olivine; yellow - clinopyroxene

other samples studied, and no apatite has been observed. The closer approach to textural equilibration (Hunter, 1987) in these samples than in coarse poikilitic olivine gabbros suggest that compaction may have been important in the reduction of the porosity of the crystal mush during their genesis. This is consistent also with the low abundance of clinopyroxene and accessory phases.

3.3.3.2 The olivine crescumulate at 46.30 mbsf contains large (~10 mm), smoothly curved, convex, elongate olivine crystals, enclosed within a single clinopyroxene oikocryst. Plagioclase crystals with smooth, commonly curved margins occur interstitial to crescumulate olivine (Fig. 3.8). No low-Ca pyroxene, ilmenite or apatite have been observed within the crescumulate and brown amphibole is considerably less abundant than in the majority of samples. However, sulphide is more abundant in the crescumulate than in any other sample, occurring as rounded composite grains along the grain boundaries between silicate crystals. At the boundary between the olivine crescumulate and granular clinopyroxene-poor lithology (Section 3.3.3.1) is a 'microcumulate' in which the clinopyroxene oikocryst contains small (generally <1 mm) floating plagioclase and olivine, as individual crystals and glomerophyric clusters. Plagioclase-plagioclase grain boundaries within glomerophyric clusters are locally equilibrated and in one case four plagioclase crystals form a cluster with their long axes sub-parallel.

The two main interpretations that can be drawn from the textures alone are: (i) densification of the clinopyroxene poor lithologies probably involved significant compaction, and (ii) crescumulate olivine indicates growth into open magma, i.e. this texture formed at the margin of a mainly molten region. Detailed interpretation of the genesis of these rocks is made in Chapter Five.

### 3.4 Crystal size distributions in poikilitic olivine gabbros

To investigate the role of plagioclase accumulation and resorption during the genesis of poikilitic olivine gabbros, crystal size distributions (CSDs; Marsh, 1988b) have been determined in three samples. This is an important exercise if a phase is to be interpreted to have accumulated via a physical mechanism (e.g. crystal settling), as opposed to simply having a cumulus appearance (e.g. Wager & Brown, 1968), because *in situ* crystallisation and secondary textural modification can lead to apparently cumulus textures (McBirney & Hunter, 1995). One coarse poikilitic olivine gabbro (from 67.77 mbsf), and two troctolites (from 52.98 and 30.26 mbsf) were chosen for this study on four criteria: (i) they appear to preserve magmatic textures, (ii) they show petrographic evidence for plagioclase accumulation and resorption, (iii) they are sufficiently fine grained for an adequate number of plagioclase crystals to be measured, and (iv) they are relatively undeformed. Approximately 150 plagioclase crystal lengths per thin

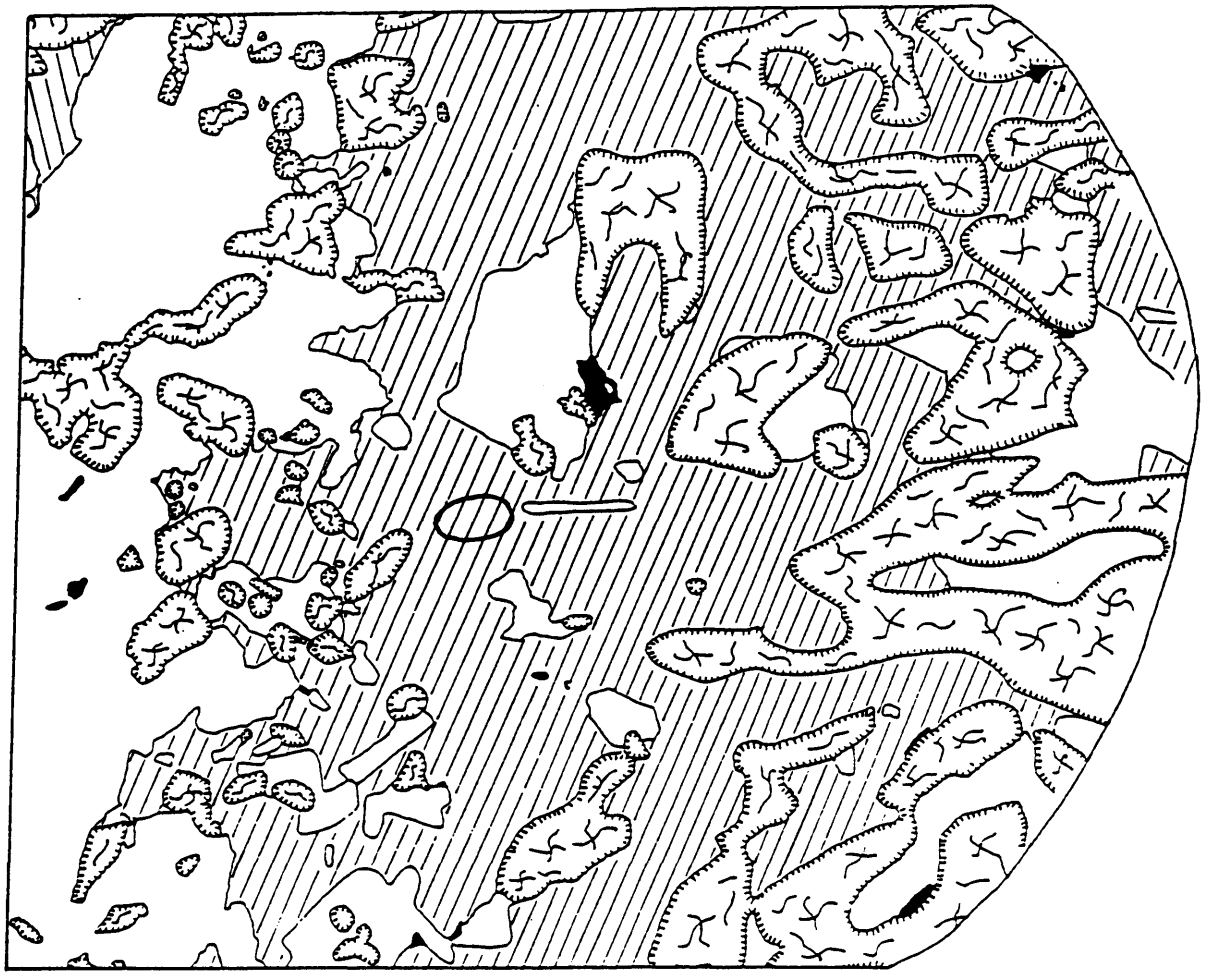


Fig. 3.8 Tracing of a photomicrograph of a heterogeneous poikilitic olivine gabbro from 46.30 mbsf. This sample can be divided into a crescumulate portion enclosed in a single clinopyroxene oikocryst (at the right) and a more granular portion (at the left) with a 'microcumulate' along the margin between the lithologies. Note that some olivine and plagioclase float within the clinopyroxene oikocryst. The analyses of the clinopyroxene core discusses in Chapters Four and Five are enclosed in the circle.
Legend: blank - plagioclase; hatched margin and crack ornament - olivine; ruled - clinopyroxene, black - composite sulphides dominated by pyrrhotite.

section were measured parallel to magmatic twins on enlarged photomicrographs (x14 for the samples from 67.77 and 52.98 mbsf and x56 for the sample from 30.26 mbsf because it is finer grained). The results are presented in Fig. 3.9, in the usual graphical format of ln (population density) versus crystal length (Marsh, 1988b; Cashman & Marsh, 1988).

*3.4.1 Crystal size distribution theory*

The distribution of crystal sizes within crystalline rocks records the processes which occurred during crystal growth, and any subsequent modification such as Ostwald ripening. This simple idea has been developed by Marsh and co-workers into crystal size distribution theory. Population densities for different crystal size intervals are calculated and compared to theoretical size distributions. Population density is the number of crystals per unit area in a given size range, divided by the size range raised to the power 1.5 (Cashman & Marsh, 1988). On plots of ln(population density) versus crystal size linear slopes with negative gradients are predicted for steady state nucleation and growth with kinks and curves being produced in response to variations in the physical and chemical conditions. For example, accumulation of coarse crystals will lead to a concave upward CSDs, whereas loss of coarse crystals (e.g. settling out of an upper boundary layer or floatation from a lower boundary layer) will lead to a convex upwards CSD. In an ideal steady-state system the intercept on the Y axis is the nuclei population density and the gradient is the negative reciprocal of the product of the growth rate and residence time (i.e. all other things being equal, faster growth rates will have shallower gradients; Marsh, 1988b). To ensure that crystal size groupings had not produced artificial kinks in the CSDs, they were checked against plots of cumulative crystal size.

*3.4.2 Crystal size distributions in poikilitic olivine gabbros*

Fig 3.9 shows CSDs for samples from 67.79, 52.98 and 30.26 mbsf. These all have negative ln (population density) versus crystal size correlations, but all CSD curves are non-linear. The sample from 67.79 mbsf, a coarse poikilitic olivine gabbro, has a plateau of constant population density for crystals between 2 and 4 mm in length. The sample from 52.98 mbsf, has a convex upwards CSD at crystal sizes <1.25 mm followed by a sharp kink to a shallower gradient. The CSD for the sample from 30.26 mbsf, is divided into plagioclase within, and outside, olivine oikocrysts. Although few grains were measured within olivine oikocrysts (n=66) they appears to have an approximately log linear CSD, whereas crystals outside of olivine oikocrysts have CSDs similar in form to the sample from 67.79 mbsf, although offset to a finer grain size. The smallest crystals are under-represented

in all samples, as is common in many CSD studies (Higgins, 1991; Waters & Boudreau, 1996) either as an artefact of the difficulty of measuring small crystals, or due to a real depletion. Fines depletion may occur due to reduced nucleation density due to reduced supersaturation, or fines resorption during textural maturation due to the larger surface area/volume ratio of small crystals compared to larger ones which leads to higher surface energy.

The general concave upward form of all the crystal size distributions is consistent with accumulation of a population of coarse plagioclase. The sample from 67.79 mbsf, a coarse poikilitic olivine gabbro, is enriched in crystals > 2 mm long compared to a log-linear CSD defined by the smaller crystals (Fig. 3.9). If the nucleation rate was constant, either grain size dependent growth rates, or a physical process is required to explain this CSD. Growth in this context refers to either positive (growth) or negative (resorption) volume change. Mixing of the coarse portion (higher settling velocity) of a log-linear CSD, with a plagioclase population with a full log-linear CSD, would more simply explain the observed CSD.

The troctolitic poikilitic olivine gabbro from 52.98 mbsf has a log-linear CSD at grain sizes > 1.25 mm as predicted for steady state nucleation and growth (Fig. 3.9). Crystals in the size range 0.5 to 1.25 mm are over-represented which can be explain by: (i) increased nucleation rate, (ii) mixing of two plagioclase populations, or (iii) neoblast production through deformation followed by annealing to produce apparently magmatic textures (e.g. straight, sharp plagioclase twins). The choice of the least deformed samples hopefully minimises the chance of the CSD recording neoblast production from crystal plastic deformation. As with the sample from 67.79 mbsf, the plagioclase CSD in the sample from 52.98 mbsf is consistent with mixing of crystal populations.

The CSD of the sample from 30.26 mbsf, another troctolitic poikilitic olivine gabbro somewhat finer grained than the sample from 52.98 mbsf, is sub-divided into plagioclase floating within olivine oikocrysts, and plagioclase outside of olivine oikocrysts (Fig. 3.9). Plagioclase outside of olivine oikocrysts has a similarly shaped CSD to that observed in the sample from 67.79 mbsf, albeit displace to a finer grain size and with a smaller plateau, and can be interpreted in the same manner. Within olivine oikocrysts plagioclase has a slightly concave upward, but near log-linear CSD for crystals >0.4 mm. Considering the small number of crystals measured, the slight concave up form may well not be real and the near log-linear CSD probably represents simple *in situ* nucleation and growth. Whether the olivine oikocryst grew *in situ* or was a phenocryst is unclear.

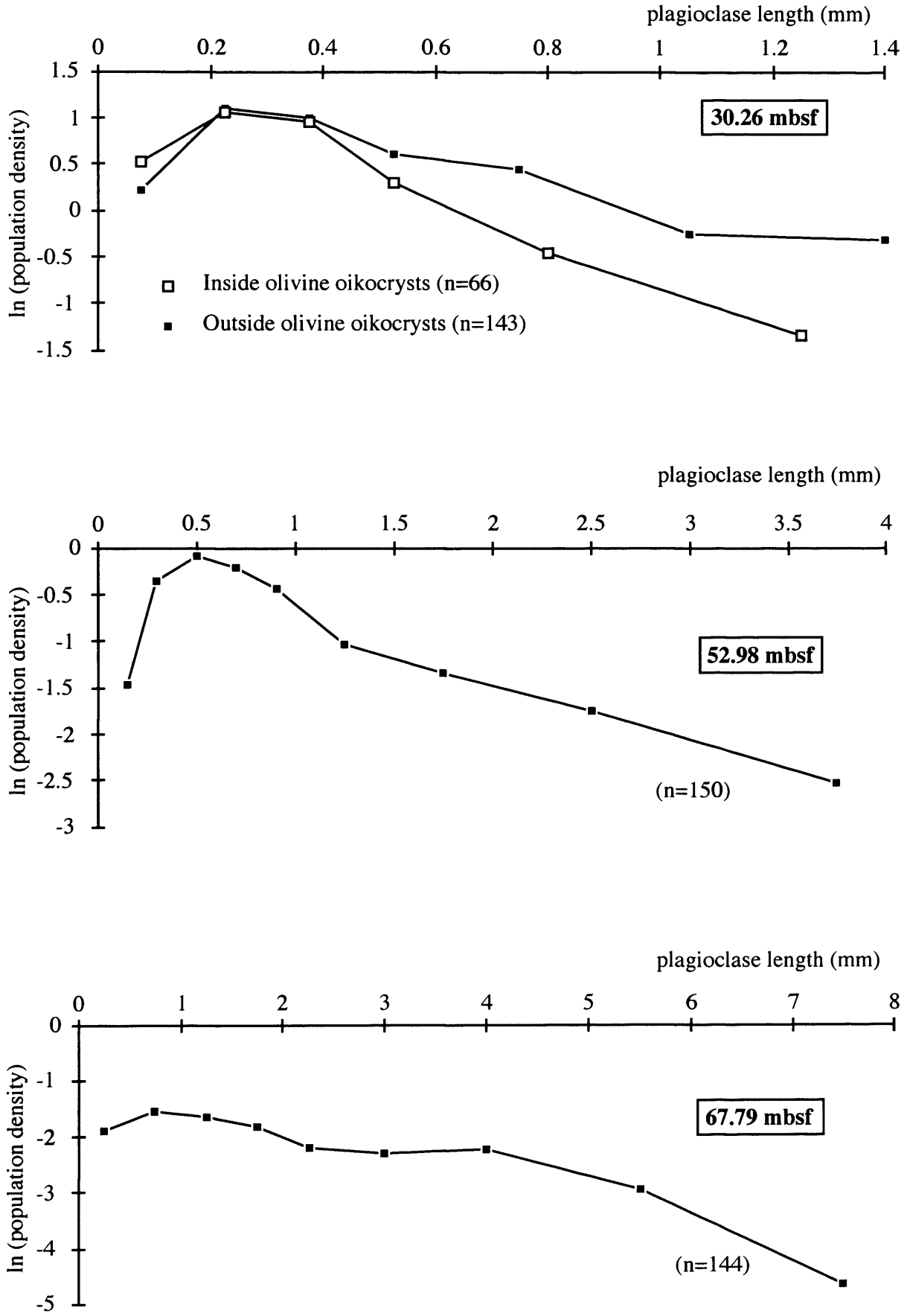


Fig. 3.9 Plagioclase crystal size distributions plots for samples from 30.26, 52.98 and 67.79 mbsf. Note the different scales on each axis for each sample; n = number of crystals

## 3.5 Brown-pyroxene Gabbros

### *3.5.1 Textural variation within brown-pyroxene gabbros*

Brown-pyroxene gabbros are plagioclase + brown clinopyroxene +/- olivine +/- low-Ca pyroxene cumulates, characterised by abundant cm- to dm-scale grain size variation of all cumulus phases. Grain size variation occurs as graded units which both coarsen and fine upwards in the core, and as sharply bound units each with sub-constant grain size (see Figs. 3, 6 & 7 of Cannat, Karson, Miller, *et al.*, 1995). Within this lithology, plagioclase has an approximately constant modal proportion (~60%), whereas the abundances of olivine and clinopyroxene vary inversely; i.e. as the abundance of olivine increases the abundance of clinopyroxene decreases (Cannat, Karson, Miller, *et al.*, 1995). Olivine is cumulus in all of the samples studied in detail, except for those from 54.53 and 69.58 mbsf. Low-Ca pyroxene is cumulus in samples from 39.16 and 54.53 mbsf, and occurs as rims on olivine in all samples which are volumetrically more abundant than in poikilitic olivine gabbros. Crystal plastic deformation has affected brown-pyroxene gabbros to variable degrees, and a consistently higher degree of plastic deformation is observed than in poikilitic olivine gabbros. Grain size variation is accompanied by textural and compositional variations (see Chapter Four), but no consistent modal variation. Fifteen samples have been studied in detail, three from a single normally graded layer (samples from 23.19, 23.28 & 23.46 mbsf), four with sharp grain size boundaries (samples from 31.6, 39.16, 48.66 & 54.53 mbsf), two fine grained (samples from 25.28 & 38.01), four medium grained (samples from 24.96, 34.41, 38.46 & 43.57 mbsf) and two coarse grained (samples from 31.31 & 69.58 mbsf). Apatite occurs in all samples, except between 44 and 32 mbsf where no apatite has been observed either in this study or that of Ross and Elthon (1997a).

Significant textural differences are associated with grain size. Coarse grained samples have cumulus crystals up to ~10 mm in diameter which are sub-equant (granular) and generally show slightly lower degrees of plastic deformation than finer grain samples. Grain boundaries tend to be more smoothly curved (or straight) in coarse grained samples than finer grained ones (compare Figs. 3.10a and b). 1 to 2 mm ilmenite crystals occur interstitially to silicates, often rimmed by brown amphibole but never associated with sulphides. However, small rounded sulphides occur elsewhere throughout coarse grained brown-pyroxene gabbros, possibly in lower abundance than in finer samples but occur in all samples in too low abundance for this to be quantified. Finer grained samples have less equant, more irregularly shaped and interdigitate grains than coarse ones. In fine grained samples clinopyroxene is commonly sub-poikilitic and, despite being interstitial, ilmenite is smaller and slightly less abundant than in coarse samples (Fig. 3.10). Olivine commonly has irregular margins, in contrast

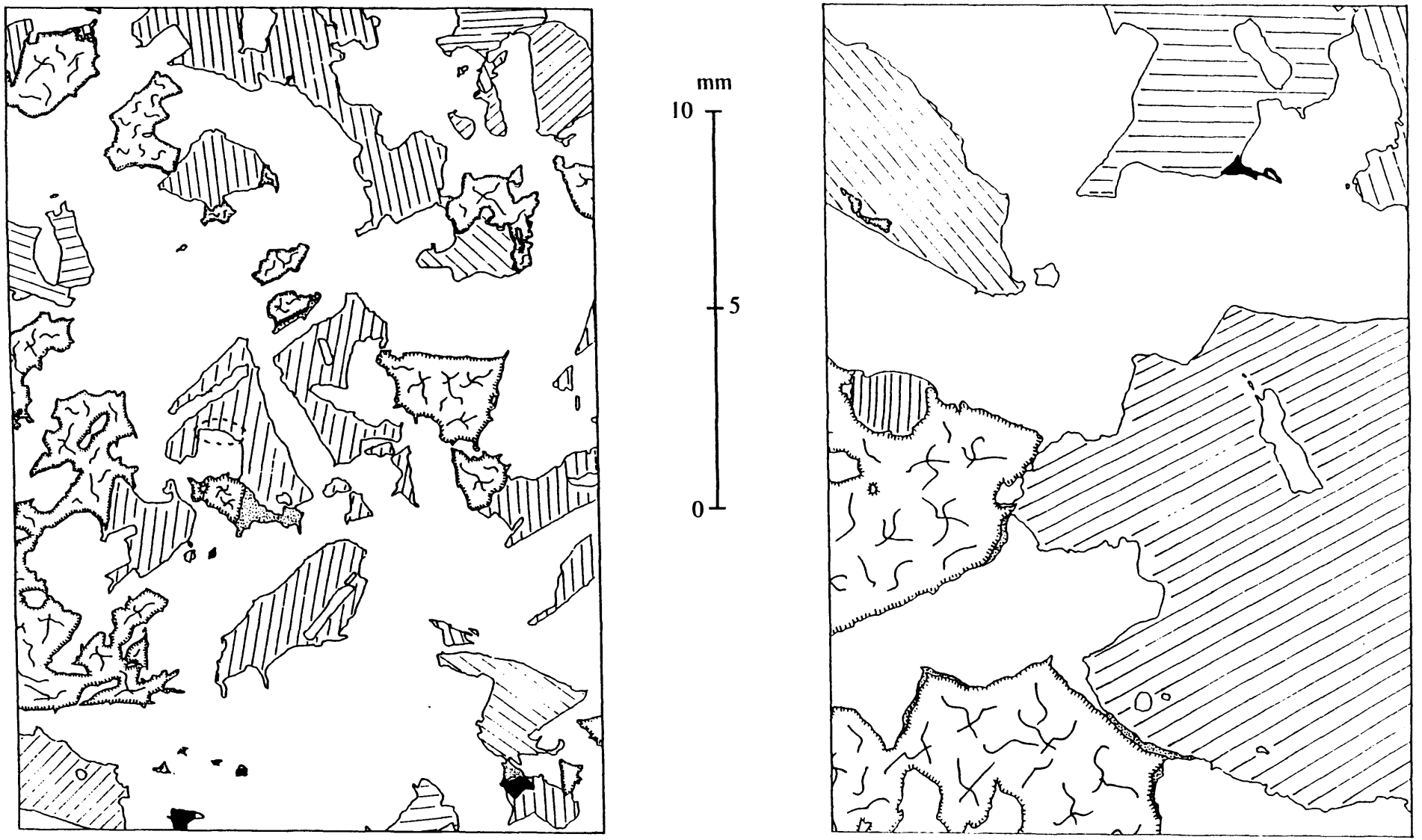


Fig. 3.10 Tracings of montages of photomicrographs of (a) a medium grained brown-pyroxene gabbro (from 23.28 mbsf), and (b) a coarse brown-pyroxene gabbro (from 31.31 mbsf). Note the greater degree of interdigitation of grain boundaries and tendency for clinopyroxene to be sub-poikilitic in the finer grained sample. In the coarser sample note the small olivine enclosed in clinopyroxene in upper left part of the figure. The location of Fig. 3.11 is circled in Fig. 3.10a. Legend: blank - plagioclase; hatched margin and crack ornament - olivine; ruled - clinopyroxene; finely stippled - orthopyroxene; black - ilmenite and compositie sulphides

to the more smoothly curved grain boundaries in coarse grained brown-pyroxene gabbros.

Some characteristics of brown-pyroxene gabbros are independent of grain size. One is the occurrence of small rounded and sometimes embayed plagioclase chadacrysts 'floating' within clinopyroxene. Furthermore, the interface between silicate phases commonly have a ragged appearance on an ~10 to 100 μm scale, especially parallel to plagioclase twins. In one instance the rim of a cumulus clinopyroxene extends ~300 μm into cumulus plagioclase along a twin plane. An extreme grain boundary texture is shown in Fig. 3.11 here, low-Ca pyroxene lamellae extend from a clinopyroxene grain boundary, parallel to orthopyroxene exsolution lamellae in the clinopyroxene, into the adjacent plagioclase parallel to plagioclase deformation twins.

The samples from 54.53 and 48.66 mbsf, do not fit the above description. The sample from 54.53 mbsf includes a boundary between microgabbro and coarse gabbro which is interdigitated on the scale of the grain size of the coarse grains (Fig. 14 of Cannat, Miller, Karson, *et al.*, 1995). The coarse and fine portions are modally (and compositionally) indistinguishable from each other, but texturally very distinct. In the coarse lithology, plagioclase, clinopyroxene, low-Ca pyroxene and apatite are cumulus phases. Ilmenite and amphibole rim clinopyroxene and extend into adjacent plagioclase parallel to plagioclase deformation twins. Large rounded sulphides indent the rim of a cumulus low-Ca pyroxene. The fine lithology consists of a matrix of fine grained, moderately deformed clinopyroxene and plagioclase around abundant small (2 to 5 mm) low-Ca pyroxene oikocrysts. These oikocrysts record a complex crystallisation history with tiny (50 to 100 μm) rounded clinopyroxene crystals enclosed in small plagioclase, in turn enclosed, along with larger clinopyroxene, in the low-Ca pyroxene oikocryst.

The sample from 48.66 mbsf can also be divided on the basis of grain size into two parts separated by a sharp boundary. Both portions are fine grained, and the finer one is the finest brown-pyroxene gabbro studied. This is composed of highly irregularly shaped, but rounded, crystals. A weak plagioclase lattice preferred orientation occurs throughout the sample; however, plagioclase commonly has sharp 'magmatic' twins and coarse crystals do not have margins of neoblasts. Lath-shaped patches of plagioclase composed of multiple grains of similar lattice orientation occur in the coarser portion, as do poorly developed sub-grains in coarse plagioclase of similar size to finer plagioclase grains. These characteristics are consistent with high temperature deformation and annealing.

The coupling of textural variations to grain size variations, and the variation in grain size of all cumulus phases and post-cumulus ilmenite together are inconsistent with simple crystallisation processes. This is discussed in depth in Chapter Six where it is shown that the textures (and mineral compositions) of

(a)

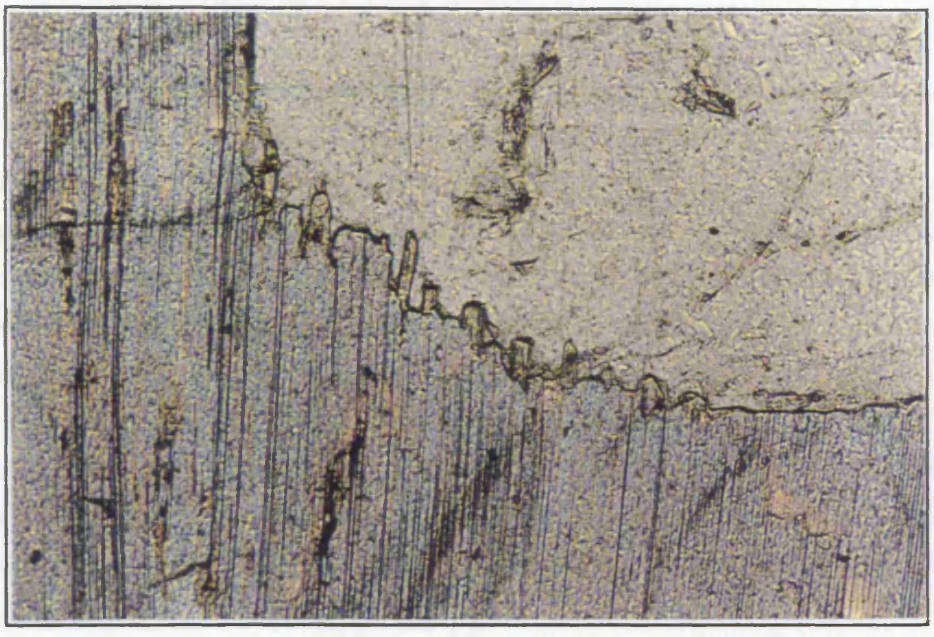

(b)

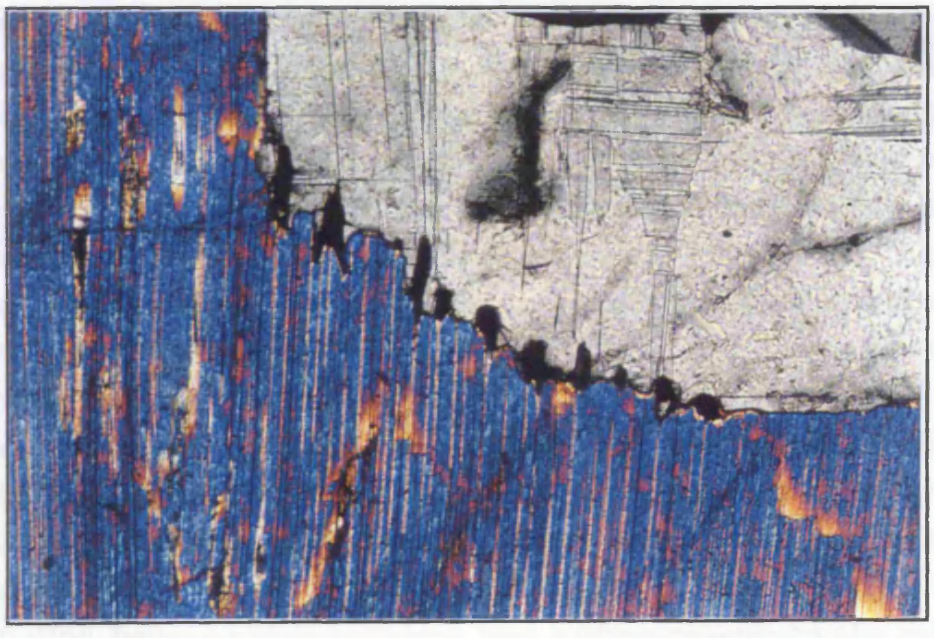

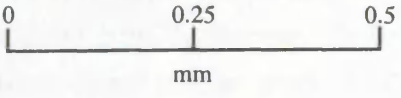


Fig. 3.11 Plane polarised (a) and cross polarised (b) light photomicrographs of a plagioclase-clinopyroxene grain boundary at 23.28 mbsf (see Fig. 3.10 for location). Orthopyroxene lamellae extend from the clinopyroxene grain boundary into the plagioclase in the same general orientation as orthopyroxene exsolution lamellae in clinopyroxene occur.

brown-pyroxene gabbros are most consistent with generation via postcumulus processes operating within the crystal mush.

*3.5.2 Spatial distribution analysis of a brown-pyroxene gabbro*

A spatial association between clinopyroxene and olivine commonly exists in fine and medium grained brown-pyroxene gabbros, with these phases appearing to form composite grains or with olivine enclosed in, or rimmed by, clinopyroxene (Figs. 3.10a & 3.12a). Several origins of a spatial association between these phases, both due to primary and secondary processes, can be envisaged. A primary spatial association between olivine and clinopyroxene may exist if both grew in porosity between cumulus plagioclase, or one phase nucleated on the other. A secondary origin for a spatially association is a reaction relationship between these phases and interstitial melt. The degree of spatial association between these phases, and the distance over which this association occurs, has been tested using the spatial distribution analysis method of Morishita and Obata (1995). This technique involves calculation of the conditional probability (probability as a function of the abundance) of two randomly chosen points lying within a given pair of phases, at a given distance between the two points. A homogeneous texture, at a distance significantly greater than the grain size, will have a conditional probability of any two phases occurring at any given distance of unity. An inhomogeneous texture, for example, with one phase occurring as rims around another phase will have a conditional probability of these phases being found next to each other at distances approximately equal to the radius of the core crystal, greater than one. At distances less than the grain size of the sample the conditional probability will always be greater than one for the two points lying in the same phase and less than one for other combinations of phases.

Analysis was carried out automatically through a macro in NIH image (Appendix A.II) on a digitised image of a thin section, in which each phase has a different greyscale. Images were acquired from montages of backscattered SEM photographs which were scanned and traced within NIH image (Fig. 3.12a). Differentiation between clinopyroxene and orthopyroxene on the SEM images was not possible; however, optical examination showed that orthopyroxene constitutes a very minor part of the mode (< 1%). The macro randomly chooses two points within the image, the greyscale of these locations is recorded and the distance between them calculated. 100,000 measurements were made to give a representative analysis of the image. Using the modal abundances (also calculated by the software from the image), these data were processed in a spreadsheet to calculate the conditional probability of any two phases occurring at any given separation (Morishita & Obata, 1995). Unfortunately, due to the time taken to

acquire an accurate image, only a single thin section of a medium grained brown-pyroxene gabbro from 24.96 mbsf has been analysed.

The area measured was 2000 by 3000 pixels (~14 mm by ~21 mm) and the results are shown in Fig 3.12b. At distances less than 1 to 2 mm, each pair of minerals have conditional probabilities less than one of existing next to each other. This is due to the high probability at these distances of the two points lying within the same grain. At larger distances plagioclase-olivine and plagioclase-clinopyroxene pairs have conditional probabilities of approximately one. This indicates that there is no spatial correlation between these pairs of phases. The scatter about one probably exists because the area analysed is too small, with respect to the grain size of the sample, to be fully representative. Clinopyroxene-olivine pairs have a markedly different spatial distribution, with a high conditional probability of these phases existing close to each over distances up to approximately 6 mm; i.e. greater than the grain size of the sample. It is unclear if the second peak in olivine-clinopyroxene conditional probability, between 8 to 10 mm, is real or reflects scatter. Clearly measurements of many more samples, and preferably larger numbers of crystals, are necessary to quantitatively interpret this. However, this correlation suggests that within medium grained brown-pyroxene gabbros olivine and clinopyroxene have a real spatial association.

The origin of a spatial correlation which exists to distances much greater than the average grain diameter is difficult to reconcile with a model of infilling primary porosity. Furthermore, the texture, approximately cotectic mineral proportions, and relatively evolved mineral compositions (see Chapter four) suggest that all phases co-precipitated. In association with the negative correlation between the modal olivine and clinopyroxene proportions the spatially association between olivine and clinopyroxene is most consistent with the existence of a reaction relationship between these phases and the interstitial melt. This idea is developed further in Chapter Six where it is suggested that extensive reaction between intercumulus melt, and the cumulate assemblage played a fundamental role in the genesis of brown-pyroxene gabbros.

### *3.5.3 Deformation of brown-pyroxene gabbros*

Plastic deformation is evident in all brown-pyroxene gabbros. Plastic deformation textures in olivine include undulose extinction and generally at least some development of subgrains and/or neoblast and/or deformation bands. Olivine deformation bands in coarse grained samples are dominantly sub-vertical with respect to the orientation of the core (Fig. 3.13), although more measurements are required to confirm whether this is representative. This is consistent with uniaxial compression (i.e. compaction; Hunter, 1996). Plagioclase always exhibits deformation twins, and commonly shows some subgrain and neoblast

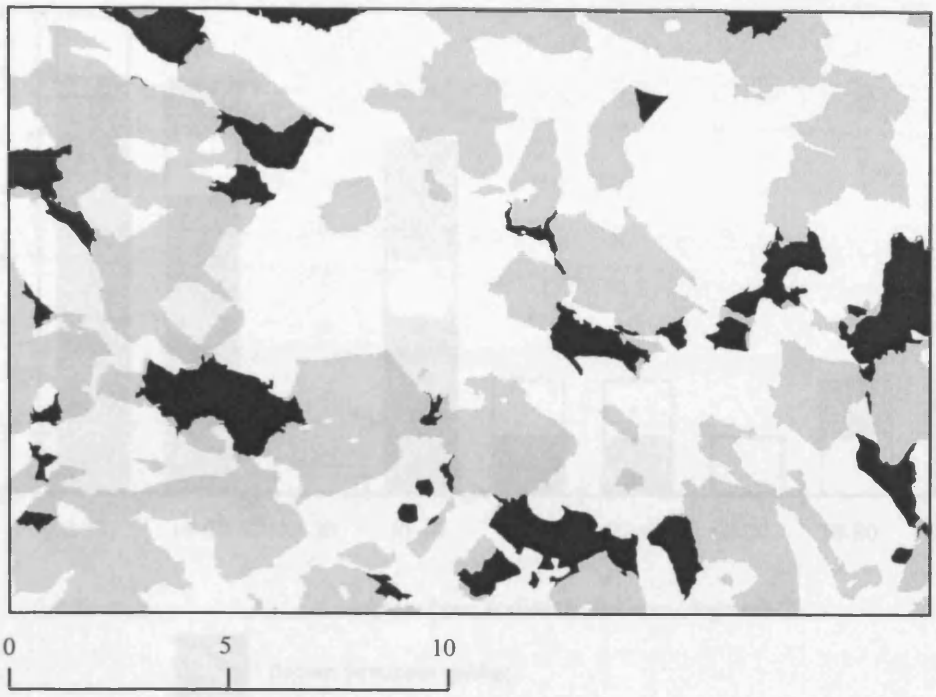


Fig. 3.12a The digitised image of a brown-pyroxene gabbro from 24.96 mbsf used for the spatial distribution analysis.
Legend: white - plagioclase; grey - clinopyroxene; black - olivine.

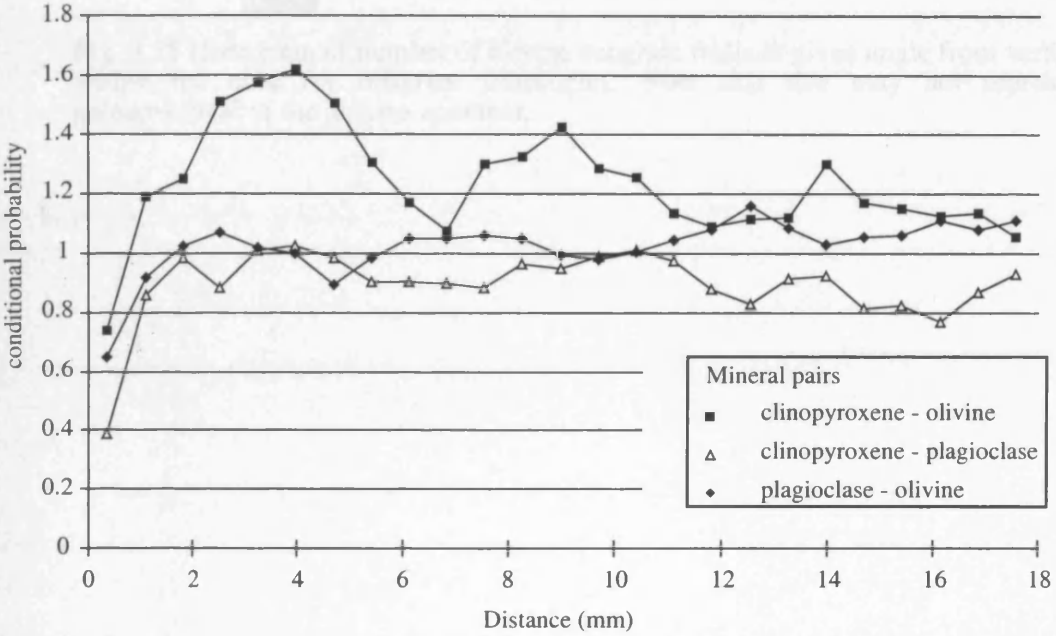


Fig. 3.12b Conditional probability of two phases occurring at a given separation in a medium grain sized brown-pyroxene gabbro (from 24.96 mbsf) shown in Fig. 3.12a, . Clinopyroxene and olivine show a spatial association over a distance of up to 6 mm. At distances greater than this the probabilty of two random points lying in any two phases is proportional to the modal abundances of the phases

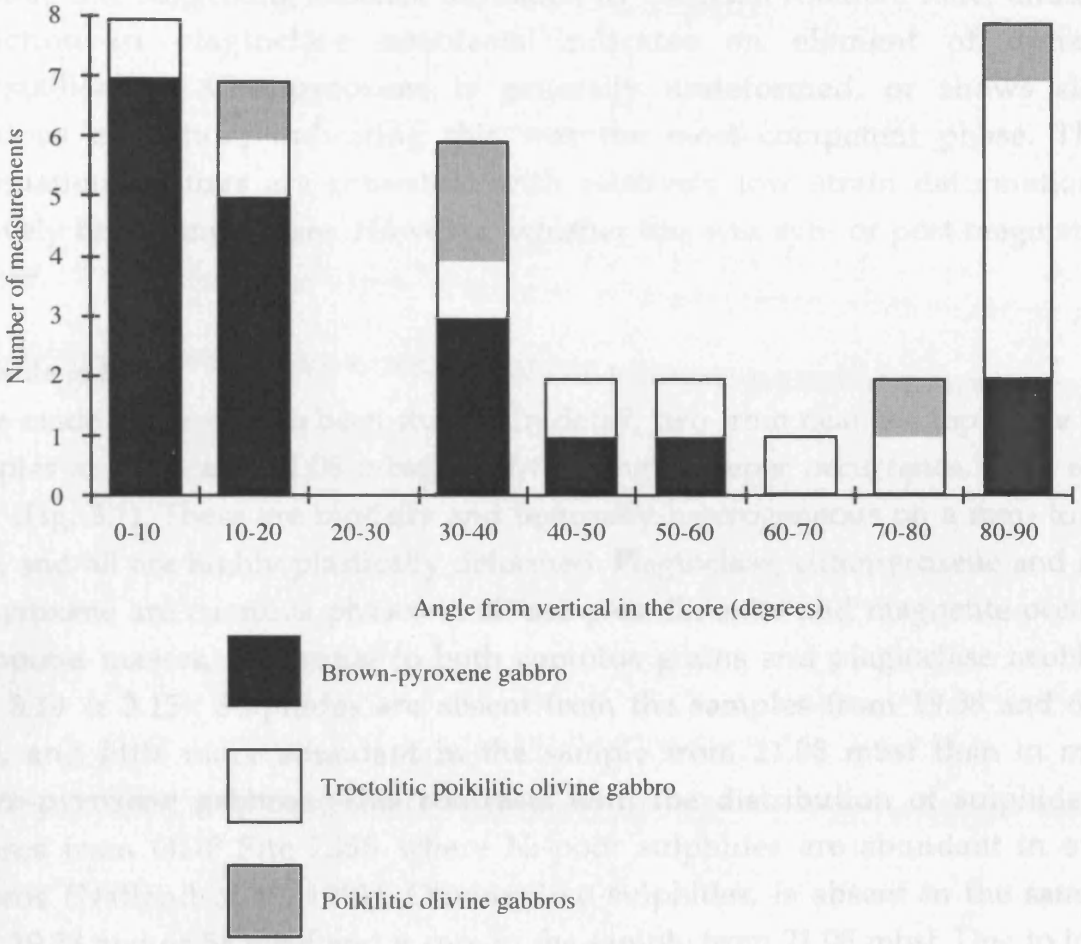


Fig. 3.13 Histogram of number of olivine subgrain walls at given angle from vertical within the core for different lithologies. Note that this may not represent paleaovertical in the magma chamber.

development. Plagioclase neoblasts and subgrains are generally of approximately the same size suggesting neoblast formation by subgrain rotation. Rare, undulose extinction in plagioclase neoblasts indicates an element of dynamic recrystallisation. Clinopyroxene is generally undeformed, or shows slight undulous extinction, indicating this was the most competent phase. These deformation textures are consistent with relatively low strain deformation at relatively high temperature. However, whether this was syn- or post-magmatic is unclear.

### 3.6 Oxide gabbros

Three oxide gabbros have been studied in detail, two from near the top of the core (samples at 19.38 and 21.08 mbsf), and the single deeper occurrence, from 66.58 mbsf (Fig. 3.1). These are modally and texturally heterogeneous on a mm- to cm-scale, and all are highly plastically deformed. Plagioclase, clinopyroxene and low-Ca pyroxene are cumulus phases in all samples. Ilmenite and magnetite occur in compound masses, interstitial to both cumulus grains and plagioclase neoblasts (Fig. 3.14 & 3.15). Sulphides are absent from the samples from 19.38 and 66.38 mbsf, and little more abundant in the sample from 21.08 mbsf than in many brown-pyroxene gabbros. This contrasts with the distribution of sulphides in gabbros from ODP Site 735B where Ni-poor sulphides are abundant in oxide gabbros (Natland *et al.*, 1991). Olivine, like sulphides, is absent in the samples from 19.38 and 66.58 mbsf and is rare in the sample from 21.08 mbsf. Due to intra- and inter-sample heterogeneity the three oxide gabbro samples are described separately below.

The sample from 66.58 mbsf is mylonitic with plagioclase completely recrystallised to fine grained neoblasts (~50 μm) that show a very strong lattice-preferred orientation. Both low- and high-Ca pyroxenes form porphyroblasts, some with recrystallised margins. Ilmenite and magnetite occur dominantly in strain shadows around cumulus pyroxene and interstitial to plagioclase neoblasts. The abundance of brown amphibole is similar to that found in brown-pyroxene gabbros.

The sample from 21.08 mbsf is also strongly deformed with a lattice-preferred orientation throughout the entire sample. The plagioclase neoblast grain size is considerably larger (250 to 500 μm) than in the sample from 66.58 mbsf and plagioclase new-grains commonly have straight, sharply defined twins. Cumulus clinopyroxene, which in some instances encloses olivine or low-Ca pyroxene, is generally almost undeformed internally, although some grains have recrystallised rims. Ilmenite and magnetite occur in a ~10 mm wide band, in which plagioclase neoblasts are the smallest, i.e. oxides are concentrated in the region which records the highest degree of deformation. Oxides occur

(a)

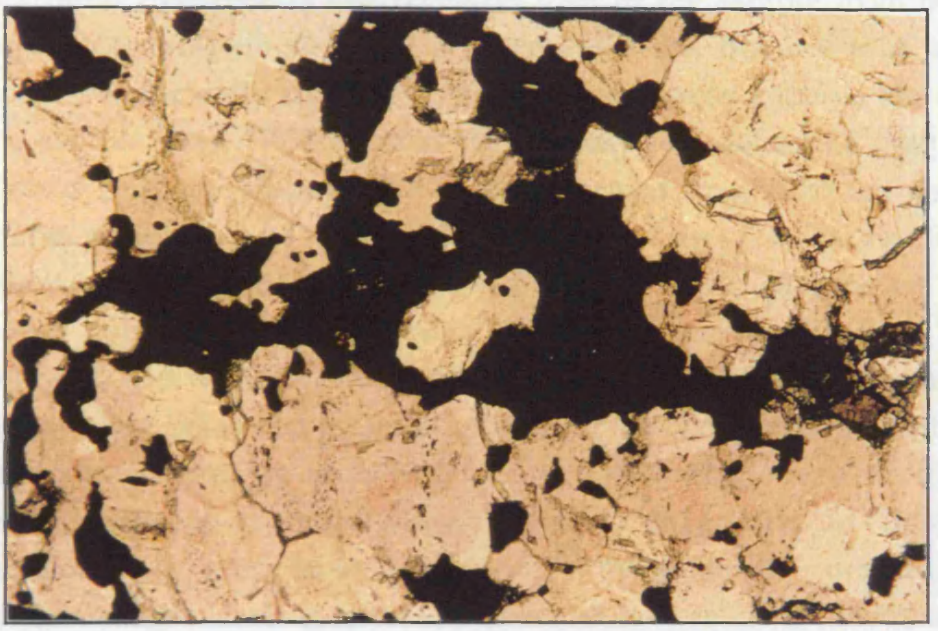

(b)

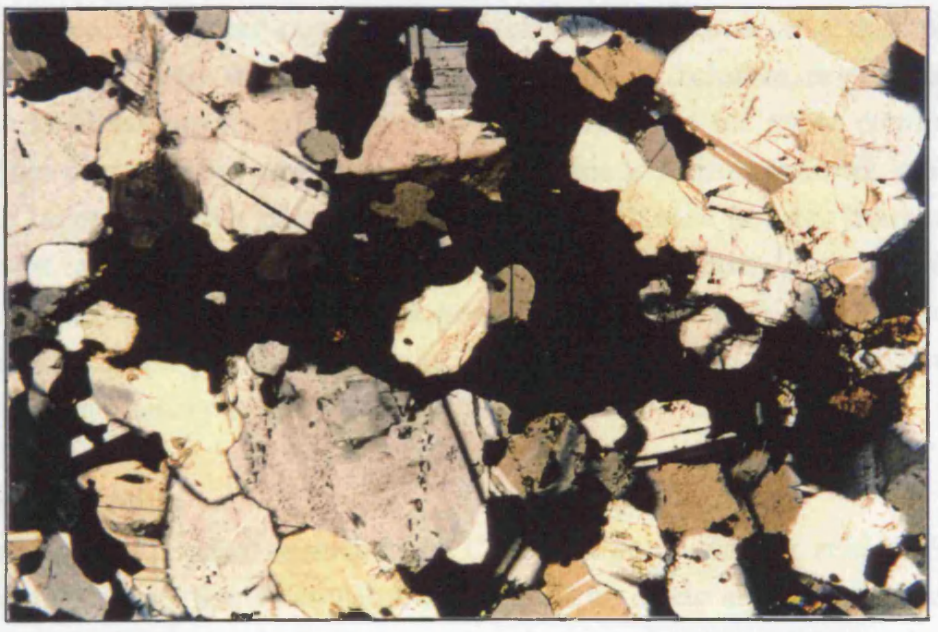

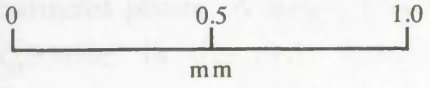


Fig. 3.14 Plane polarised (a) and cross polarised (b) light photomicrographs of oxides (ilmenite and magnetite) in an oxide gabbro (from 21.08 mbsf) which occur interstitially to plagioclase neoblasts. Note the relatively straight and sharp twins, and abundant inclusion trails, in plagioclase.

interstitially to recrystallised plagioclase (Fig. 3.14), and concentration in strain shadows around pyroxene is less common than in the sample from 66.58 mbsf. Brown and green amphibole occur at pyroxene rims, but the total amphibole abundance is insufficiently higher than in brown-pyroxene gabbros too quantify.

The sample from 19.38 mbsf is significantly less deformed than the other oxide gabbros studied, although still more deformed than most brown-pyroxene gabbros. This sample can be sub-divided into three intervals. The first is a coarse oxide gabbro with abundant interstitial oxide in which plagioclase cores are divided into sub-grains and the rims have been recrystallised to neoblasts. Plagioclase enclosed within both clinopyroxene and oxide is almost undeformed. Despite plagioclase being recrystallised, oxides are concentrated as if interstitial to coarse cumulus plagioclase with rims interstitial to plagioclase neoblasts as at 21.08 mbsf. Ilmenite is more abundant than magnetite in this interval. Clinopyroxene-oxide grain boundaries tend to be smoothly curved (Fig. 3.15). Oxides with straight cleavage, where observable (which is uncommon), and straight exsolution form compound masses/aggregates. Some clinopyroxene crystals floating within oxide are in optical continuity with adjacent cumulus crystals, indicating either continuity in three dimensions or a common parent grain which has been dissected without significant relative re-orientation (Fig. 3.15). Bands of secondary inclusions in plagioclase are far more common in this sample than in any other sample. Adjacent to this is a finer grained, oxide-poor, 7 mm wide layer in which plagioclase neoblast grain size is finer than in either of the adjacent layers and low-Ca pyroxene is more abundant. Only a small amount of oxide, dominated by magnetite, is present and is interstitial to plagioclase and pyroxene. The third portion is similar to the first. Green and brown amphibole are abundant accessory phases within this sample.

### 3.7 Leucocratic veins

Only one leucocratic vein, described by Cannat, Karson, Miller, *et al.* (1995) as a 1.5 cm wide plagioclase, brown amphibole, actinolite, oxide and apatite bearing vein, has been studied (30.63 mbsf). Coarse, cloudy and almost undeformed plagioclase is the dominant phase. A single low-Ca pyroxene, approximately 50% replaced by cummingtonite, is the only other cumulus phase. Interstitial ilmenite and magnetite, occur as compound oxide masses generally associated with sub-euhedral apatite. Minor green amphibole, zircon and quartz also occur as interstitial phases.

### 3.8 Intra-crystalline features of clinopyroxene

Amphibole, low-Ca pyroxene and ilmenite occur as lamellae and blebs throughout clinopyroxene in most brown-pyroxene gabbros and oxide gabbros,

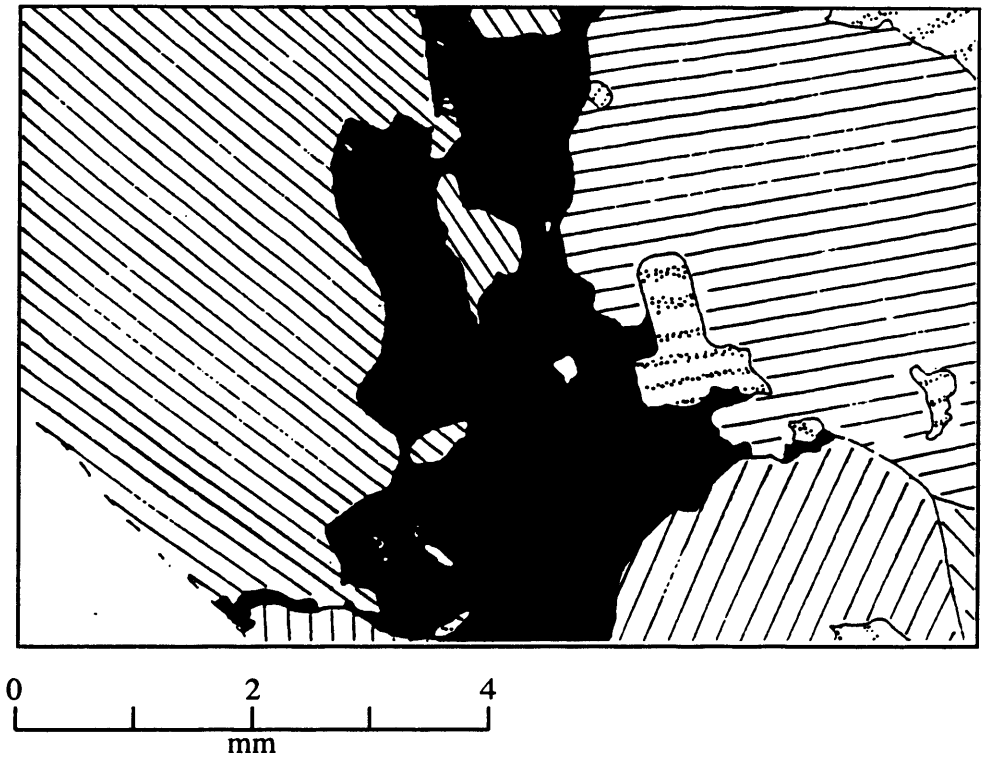


Fig. 3.15 Tracing of a photomicrograph of an oxide gabbro (from 19.38 mbsf), showing oxides (ilmenite and magnetite) interstitial to clinopyroxene. Note the smoothly curved clinopyroxene - oxide grain boundaries and that one of the clinopyroxene enclosed in the oxide is in optical continuity with cumulus clinopyroxene. The other clinopyroxene within the oxide go to extinction with the cumulus clinopyroxene on the left, but have different cleavage orientation. Dashed line in bottom left is the edge of the thin section.
Legend: stippled schematic twins - plagioclase; ruled - clinopyroxene; black - oxides (ilmenite and magnetite)

and to a lesser extent in some poikilitic olivine gabbros. These occur throughout crystals and can be concentrated in crystal cores, suggesting that they are not simple alteration products. In brown-pyroxene gabbros, clinopyroxene cores are commonly recrystallised from a dusty appearance which is due to being full of very fine (~1 μm) lamellae, into a 'clean' clinopyroxene that contains abundant small blebs of low-Ca pyroxene and amphibole (Fig. 3.16). However, in most cases this transformation does not affect the entire crystal. Recrystallised domains commonly have straight sides parallel to the host's cleavage and ragged edges perpendicular to the host's cleavage. Low-Ca pyroxene and brown amphibole, which can occur in composite blebs, are optically continuous throughout the host and amphibole is optically continuous with amphibole rims on clinopyroxene. Sub-rounded 'clean' grains occur at some clinopyroxene rims. A kink in a clinopyroxene in the sample from 21.08 mbsf is 'clean' in contrast to either side of the kink (Fig. 3.17), suggesting that deformation may influence re-crystallisation in some instances. These textures are consistent with fluids playing a role in the late stage development of the crystal mush, an idea that is developed in Chapter Six (Section 6.4).

### 3.9 Discussion and conclusion

The majority of the interpretation of the textures has deliberately been excluded from this chapter. Interpretations are developed in Chapters Five and Six in combination with the variation in mineral compositions described in Chapter Four. The main observations and preliminary interpretations that have been made are:

(i) The textures of coarse poikilitic olivine gabbros, and plagioclase CSDs, suggest these formed via olivine and plagioclase accumulation followed by porosity reduction via overgrowth of these phases and nucleation and growth of clinopyroxene oikocrysts.

(ii) Troctolites can be explained in a similar manner to coarse poikilitic olivine gabbros except with clinopyroxene saturation delayed until after a high degree of densification of the crystal mush. Furthermore, the slightly less interdigitate plagioclase grain boundaries suggests that densification may have involved compaction as well as growth.

(iii) The heterogeneous poikilitic olivine gabbros record a complex history which involves compaction as well as growth.

(iv) The textures of brown-pyroxene gabbros cannot be simply reconciled with either *in situ* crystallisation or crystal settling and a complex post-cumulus history is envisaged.

(a)

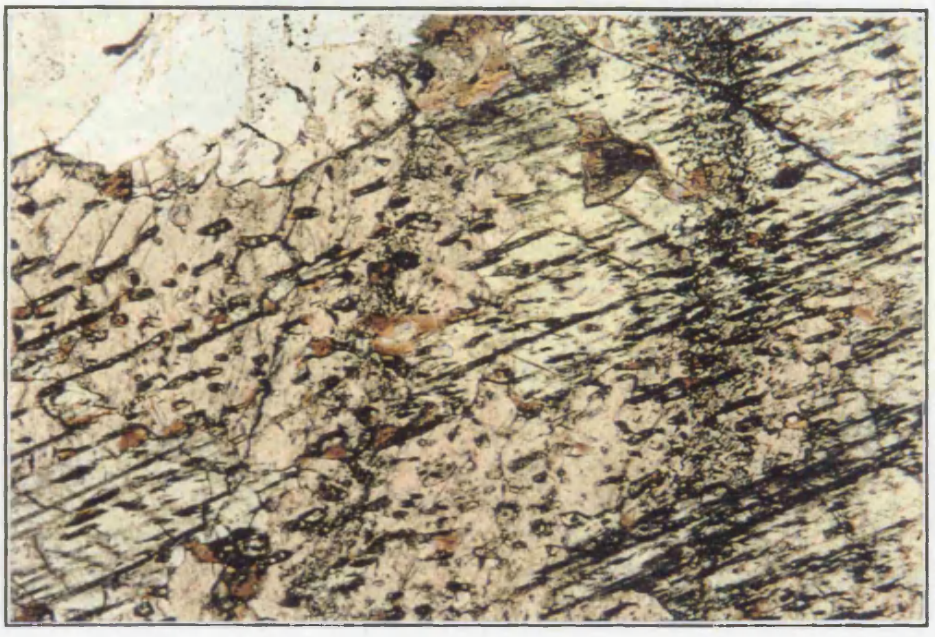

(b)

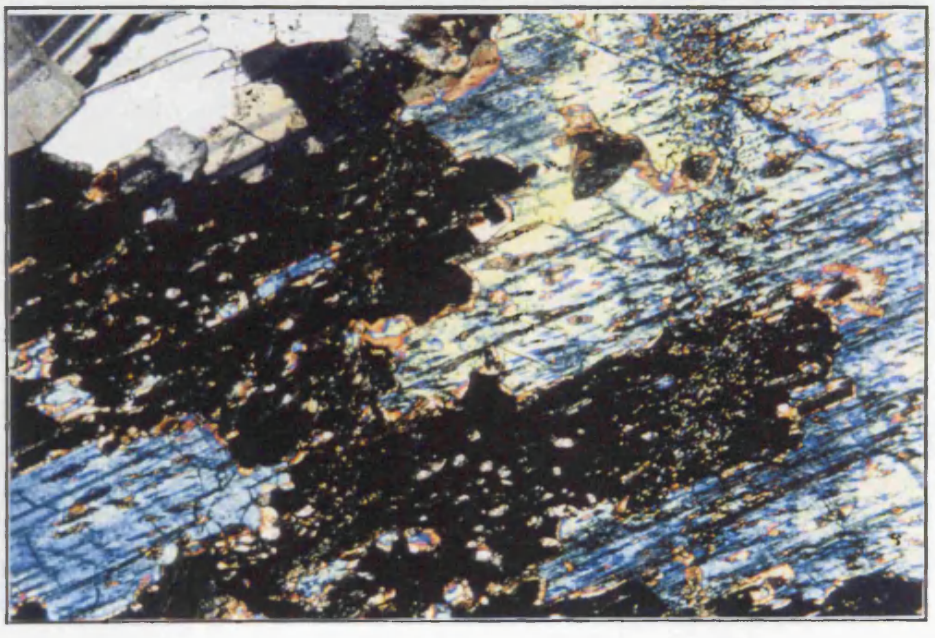

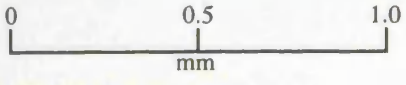


Fig. 3.16 Plane polarised (a) and cross polarised (b) light photomicrographs of a recrystallised clinopyroxene (31.31 mbsf). In the recrystallised region (at extinction in b) clinopyroxene is more transparent, has a sharper extinction and encloses brown amphibole and orthopyroxene blebs.

(a)

(b)

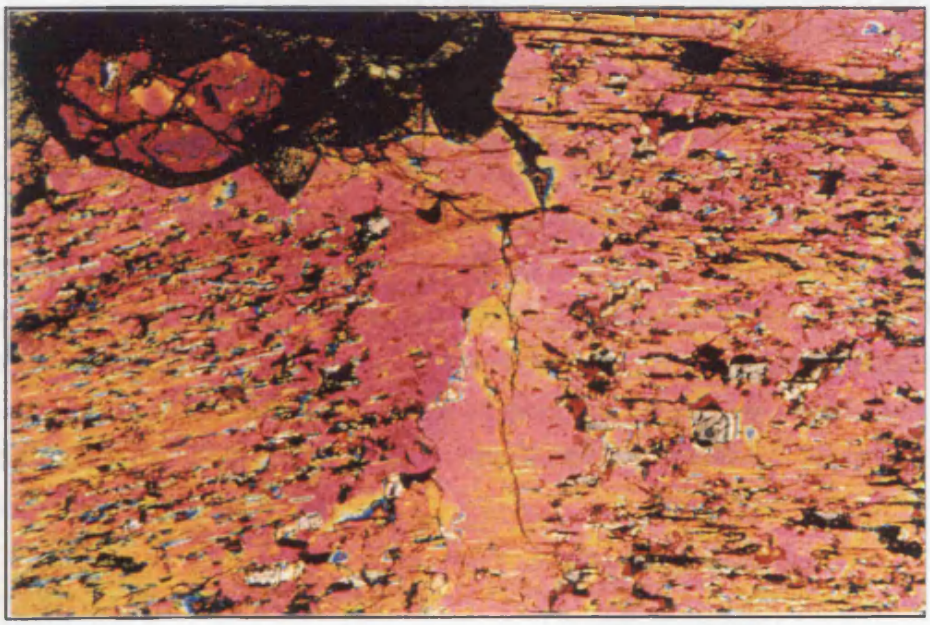

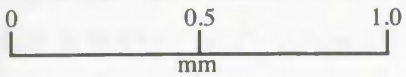


Fig. 3.17 Plane polarised (a) and cross polarised (b) light photomicrographs of a kink in a clinopyroxene in a sample from 21.08 mbsf dividing two portions of the same clinopyroxene crystal with slightly different extinction orientations. Note that in the region of the kink, where strain recovery processes must have operated, there are no inclusions of brown amphibole and orthopyroxene, in contrast to the rest of the crystal.

# Chapter IV: Major, minor and trace element mineral compositions in gabbroic rocks from ODP Hole 923A

## 4.1 Introduction

This chapter describes the compositions observed in *in situ* mineral analyses of samples from ODP Hole 923A. First the analytical techniques used are briefly described. Compositional trends of the average major element composition of co-existing olivine, plagioclase and clinopyroxene are then compared to the co-existing mineral compositions produced in experiments on spatially associated MORB, and subtle differences noted. Significant variation in minor element abundances that correlate to major elements are also shown to occur within the core. However, much larger variations in incompatible trace element abundances occur in clinopyroxene and, to a lesser extent, in plagioclase, that correlate very poorly with major elements. Some correlations exist however between incompatible trace element abundances and ratios.

Major element mineral compositional variation with depth in the core show a general evolution upwards; however, considerable deviations to more primitive compositions occur. Incompatible trace elements do not show this variation with stratigraphic height, being controlled dominantly by lithology and texture. Minor lithologies, i.e. oxide gabbros and leucocratic veins, have the most evolved mineral compositions, irrespective of their location within the core. Finally, melt compositions calculated to be in equilibrium with plagioclase and clinopyroxene are compared to MARK area MORB. To a first approximation these are similar. However, melts modelled to be in equilibrium with the cores of plagioclase in poikilitic olivine gabbros have lower light-REE abundances and La/Nd ratios than MORB. Equilibrium melt compositions modelled from both phases extend to considerably higher incompatible element abundances than are observed in MARK area MORB.

### *4.1.1 Analytical methods*

Major element mineral compositions were acquired on a Jeol Superprobe 8600 using a wavelength dispersive system. A 15 KeV and 30 nA electron beam were used with a 20 second count time on both peak and background. Natural and synthetic standards were used and ZAF matrix corrections applied. A 10 μm electron beam was used to analyse plagioclase and focused (~1 μm), 5 μm or 10 μm beams for other phases. Detection limits (3σ) and standard deviations of counting statistics (2σ) are given in Appendix A.IV. Large variation in the width and spacing of exsolution lamellae/blebs in clinopyroxene means that irrespective of the beam diameter, many analyses do not represent magmatic compositions. All Fe in silicate minerals is reported as FeO because electron probe

analyses are not sufficiently precise or accurate for well constrained determination of $Fe^{3+}$. Throughout the magnesium number of clinopyroxene (Mg#) is calculated assuming all Fe as $Fe^{2+}$ (Mg# = 100 x Mg/(Mg+Fe)). Olivine forsterite content (Fo) is calculated in the same way. The anorthite content of plagioclase (An) is calculated as 100 x Ca/(Ca+Na+K). In these calculations Mg, Fe, Ca, Na and K are cation proportions.

Electron probe data for different phases is of differing quality. Plagioclase analyses with totals between 99 and 101 wt% and cation totals between 19.9 and 20.1 (calculated to 32 oxygens) are considered acceptable. Olivine analyses with totals between 100 and 104 wt% are used, provided the ionic Si abundance is between 0.99 and 1.01, the M site cations sum to between 1.99 and 2.02 and the cation total is between 2.99 and 3.02 (calculated to 4 oxygens). Clinopyroxene analyses are used, provided the analysis total is between 99 and 102 wt% and cation total is between 4 and 4.04 (calculated to 6 oxygens).

Systematic errors exist in plagioclase and olivine electron probe analyses, and probably also in clinopyroxene analyses, but indeterminable $Fe^{3+}$ abundances in clinopyroxene preclude identification of clinopyroxene errors. Plagioclase analyses have good weight percent and cation totals, and are charge balanced, but ionic Si + Al is less than 16, and Ca + Na is greater than 4 (calculated to 32 oxygens) in all analyses. This is due to systematic Ca excess with respect to a 1:1 correlation with Al. Olivine consistently has weight percent totals >100, a common feature of electron probe analyses. Olivine analyses also show a negative correlation between cation Si abundance and both the sum of the M site cations (Mg, Fe, Mn, Ni), and the cation total. Furthermore, the sum of the cations in the M sites correlates positively with the cation sum. No correlations between Si abundance, M site cation total, or cation total and Fe or Mg abundance or Mg# exist. The most likely origin of these errors is in the ZAF correction procedure. However, the scale of these errors is insignificant to the interpretations made in this thesis.

Trace element concentrations in clinopyroxene, plagioclase, ilmenite, amphibole and an olivine were analysed on the Cameca IMS 4F ion probe at Edinburgh University (Appendix A.III). The locations of analyses were chosen after detailed examination of backscattered electron images to avoid altered (and, in clinopyroxene, exsolved) areas. Sputter pits produced during analysis increased in diameter from 10 to 20 μm as the primary current was raised from 5 to 30 nA and the pits are thought to be ~3 μm deep. Thus, to limit the possibility of rim analyses penetrating adjacent crystals, analyses were performed at least twice the pit diameter from grain boundaries. Analyses were performed on gold coated, 1 inch diameter, round thin sections, with analysis locations identified in reflected light. A primary $^{16}O^-$ beam was focused on the specimen and high energy

secondary ions counted in a mass spectrometer. During each analysis, all masses were counted for 10 cycles, with each cycle lasting 5 seconds; consistency between cycles was confirmed before accepting the data. An energy offset of 78 keV was used to reduce molecular interferences, and LREE oxide interferences on HREE were corrected for assuming a NdO/Nd ratio of 0.12. Secondary ion intensities were normalised to $^{30}Si$ (except for ilmenite which was ratioed to $^{51}V$) and electron probe Si and V concentrations were used to calculate absolute abundances. Ion yields were calculated from analysis of standard NBS610 glass for clinopyroxene, amphibole and olivine as their ion yields are thought to be similar to that of glass. Plagioclase analyses were further corrected, by factors given in Appendix A.III.2, because it has slightly higher ion yields than glass (Richard Hinton, pers. com. 1997). These corrections are calculated from Lake County alkali feldspar standard which is thought to have similar ion yields to plagioclase feldspar. The ion yields of ilmenite are unknown and thus absolute abundances are unknown, but ion yields are unlikely to differ from glass by more than a factor of 2 (Richard Hinton, pers. com. 1997). The background was monitored at a mass of 130.5 and was generally zero or one count over the entire 50 second period counted for. The deadtime was $1.7 \times 10^{-8}$ seconds.

Five closely spaced analyses of the core of the clinopyroxene oikocryst from 46.30 mbsf (Fig. 3.8) which has the lowest incompatible element abundance analysed (i.e. likely worst precision), are shown in Fig 4.1a to show instrument precision during analyses. Analyses of Kilbourne Hole clinopyroxene megacryst (KH1) standard were also performed to check precision and accuracy and are shown in Fig. 4.1b. These analyses were performed over the entire period of ion probe analyses (two-sessions, each one week long, four months apart). Electron probe Cr and Ti data form linear arrays with ion probe data. However, electron probe Cr data are displaced to lower abundance by ~ 20 %. The Ti abundance correlation shows significant scatter, probably due to local heterogeneity in Ti abundance caused by small ilmenite inclusions or exsolution.

The chondrite values used throughout this thesis for normalising trace element data are from Anders and Grevasse (1989).

## 4.2 Inter-sample compositional variations

### *4.2.1 Major elements variations*

Fig. 4.2 shows the fields of major element compositions for clinopyroxene, plagioclase and olivine in terms of their end member components. Clinopyroxene shows a relatively limited range of Mg-Fe solid solution but considerable Ca variation towards low-Ca pyroxene. This is at least in part due to varying degrees of overlap with orthopyroxene exsolution lamellae. Fig. 4.3 shows the co-variation of the average plagioclase anorthite content (An), average

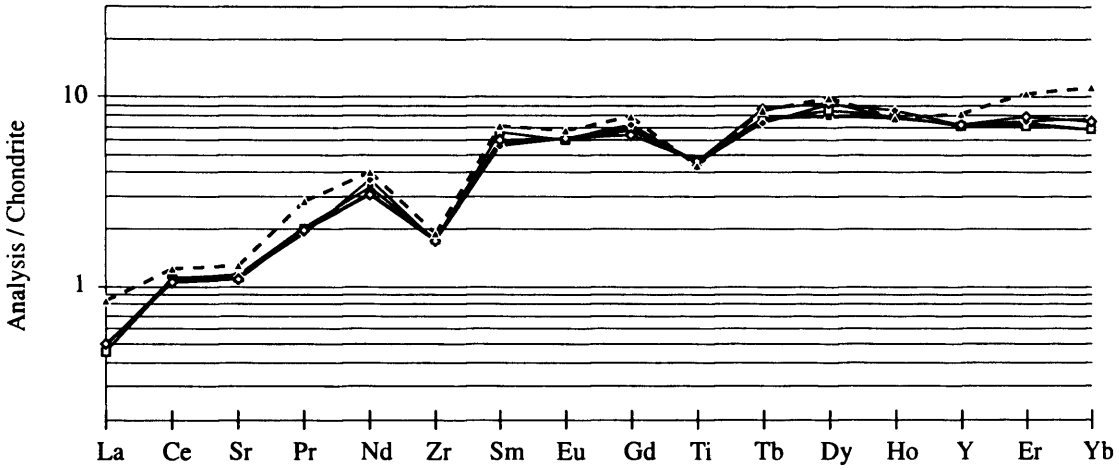


Fig 4.1a Five replicate analyses of the core of the clinopyroxene oikocryst in sample 46.30 to show precision. This clinopyroxene core has incompatible element abundances as low as any clinopyroxene analysed. The dashed analysis was performed four months prior to the other analyses.

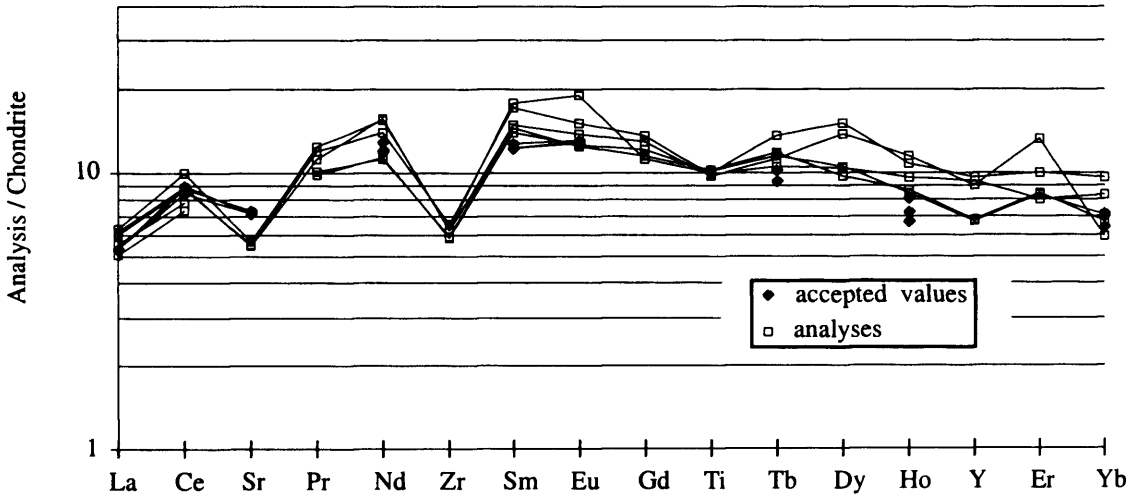


Fig 4.1b Five replicate analyses of Kilbourne Hole clinopyroxene standard (KH1) to show accuracy and precision. These were performed over the entire duration of ion probe analyses (two, one-week sesssions, four months apart).

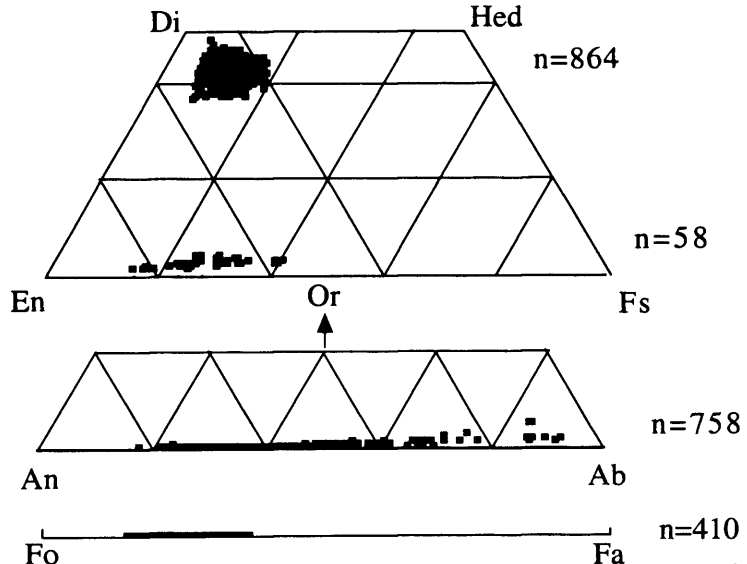


Fig 4.2 Comparison of solid solution components in clinopyroxene, orthopyroxene, plagioclase and olivine. Di = Diopside; Hed = Hedenbergite; En = Enstatite; Fs = Ferrosilite; An = Anorthite; Ab = Albite; Or = Orthoclase; Fo = Forsterite; Fa = Fayalite; n = number of analyses.

clinopyroxene magnesium number (Mg#), and average olivine forsterite content (Fo) within each sample, and those from experimental studies on spatially associated mid-ocean ridge basalt (MORB; Grove & Bryan, 1983; Tormey *et al.*, 1987; Grove *et al.*, 1992). Experimental compositions are from one-atmosphere experiments performed at the quartz-fayalite-magnetite (QFM) oxygen fugacity buffer. Some of the scatter in these plots is due to intra-sample compositional heterogeneity (e.g. zoning). This affects plagioclase the most, followed by clinopyroxene and does not significantly affect olivine. Errors may exist in experimental trends due to sodium volatilisation and kinetic effects. Kinetic effects include disequilibrium growth due to the different crystallisation time scale in experiments and nature, and the possible occurrence of seed crystals of plagioclase and olivine, but not clinopyroxene.

Averaged over entire samples, the co-variation of clinopyroxene Mg#, plagioclase An content and olivine Fo content show different trends for poikilitic olivine gabbros and brown-pyroxene gabbros (Fig. 4.3). The trend defined by poikilitic olivine gabbro is closer to the co-variation observed in crystallisation experiment on MARK area MORB than that defined by brown-pyroxene gabbros, although with considerable scatter. This is seen most clearly in the co-variation of average clinopyroxene Mg# and average olivine Fo content (Fig. 4.3b). Brown-pyroxene gabbros generally have lower average An (~10%) and Fo (~5%) contents for given clinopyroxene Mg# compared to poikilitic olivine gabbros. Oxide gabbros, to a first approximation, lie on an extension of the brown-pyroxene gabbro fields. Notably, the most magnesian clinopyroxene grown in experiments has an Mg# of 83, considerably lower than some clinopyroxene in poikilitic olivine gabbros. The correlation of olivine Fo content and plagioclase An content (Fig. 4.3c) is less easily sub-divided by lithology than their respective correlations with clinopyroxene Mg#s.

### *4.2.2 Minor element variations*

4.2.2.1 Clinopyroxene contains small amounts of Na, Al, Mn, Ti and Cr. Charge balance requires some correlation between these elements (except Mn) as shown in Fig. 4.4. Fig. 4.4 shows that some $Fe^{3+}$ must occur in the clinopyroxene M1 site in all clinopyroxene to achieve charge balance, if perfect analyses are assumed. There is no systematic variation in the $Fe^{3+}$ abundance required to achieve charge balance with lithology. Na, Ti, and Mn behave incompatibly, and Al compatibly, throughout much of the fractionation of MORB (e.g. on MORB Mg# variation diagrams). In clinopyroxene Na, Mn and Al mirror the variation with Mg# observed in MORB (0.23 to 0.64 wt% $Na_2O$; 0.07 to 0.40 wt% MnO; 1.4 to 4.0 wt% $Al_2O_3$). Ti, however, displays a more complex distribution with little overall correlation with Mg# (Fig. 4.5a). However, within individual samples

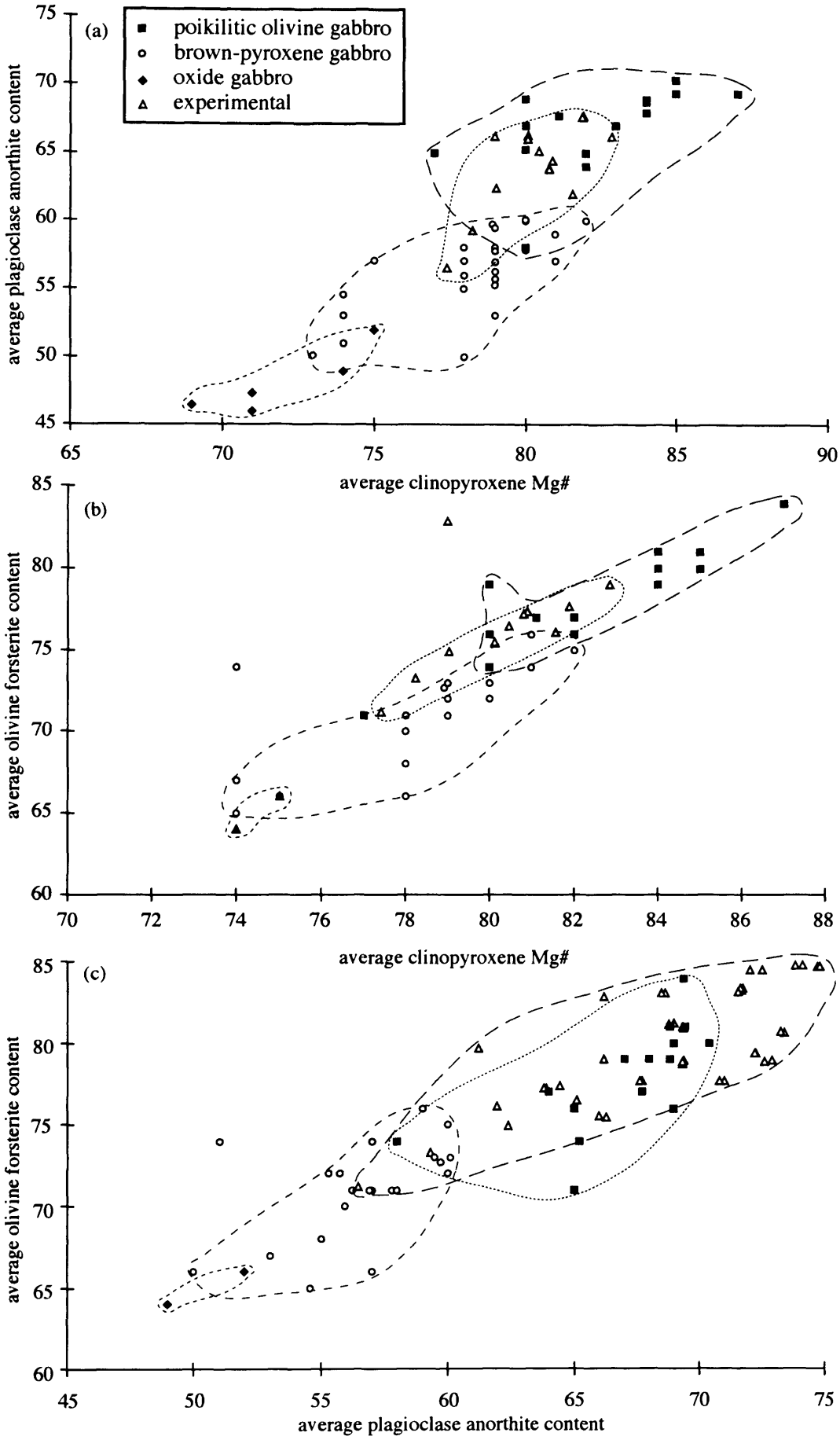


Fig. 4.3 Comparison of the average compositions of clinopyroxene, plagioclase and olivine coexisting in samples, and the compositions produced in one-atmosphere crystallisation experiments on MARK area MORB (Grove & Bryan, 1983; Tormey et al., 1987; Grove et al., 1992). Fields are drawn around the data for clarity, with 'significant outliers' excluded.

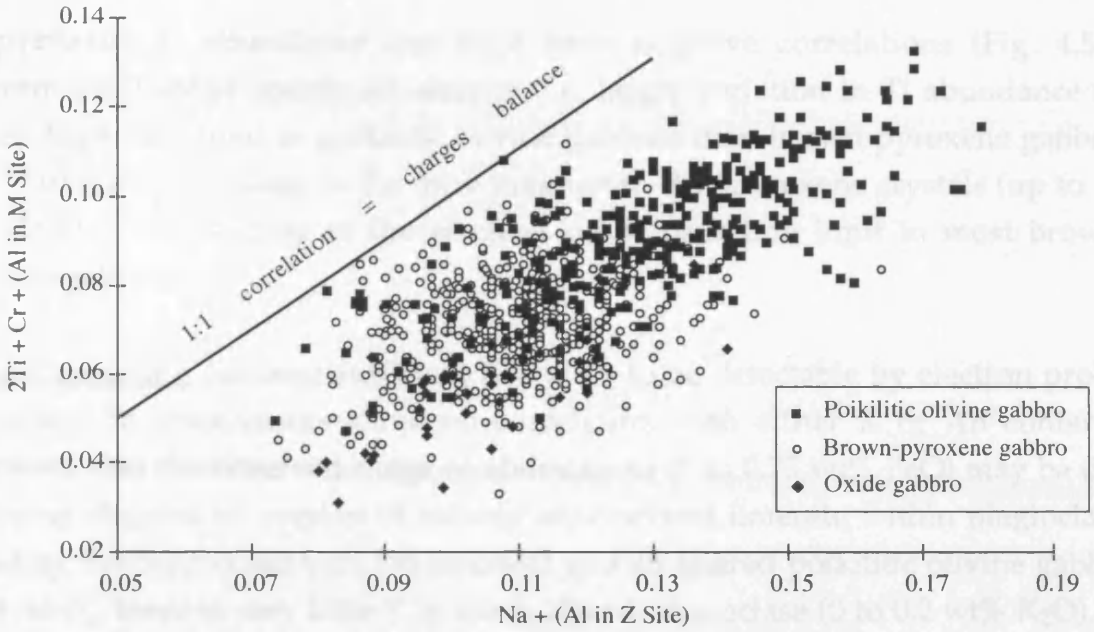


Fig 4.4 Charge balance correlation in clinopyroxene calculated from cation proportions on the basis of 6 oxygens. Al in the Z Site is calculated as 2-Si, and the remaining Al assigned to the M Site. The 1:1 line defines charge balance. The offset of the data from this line could be achieved by some of the Fe in clinopyroxene being $Fe^{3+}$ in the M site in all samples. However there is no systematic variation in the $Fe^{3+}$ abundance required to achieve charge balance either with lithology or analysis location (core or rim). Alternatively, systematic error in electron probe analyses could account for the offset.

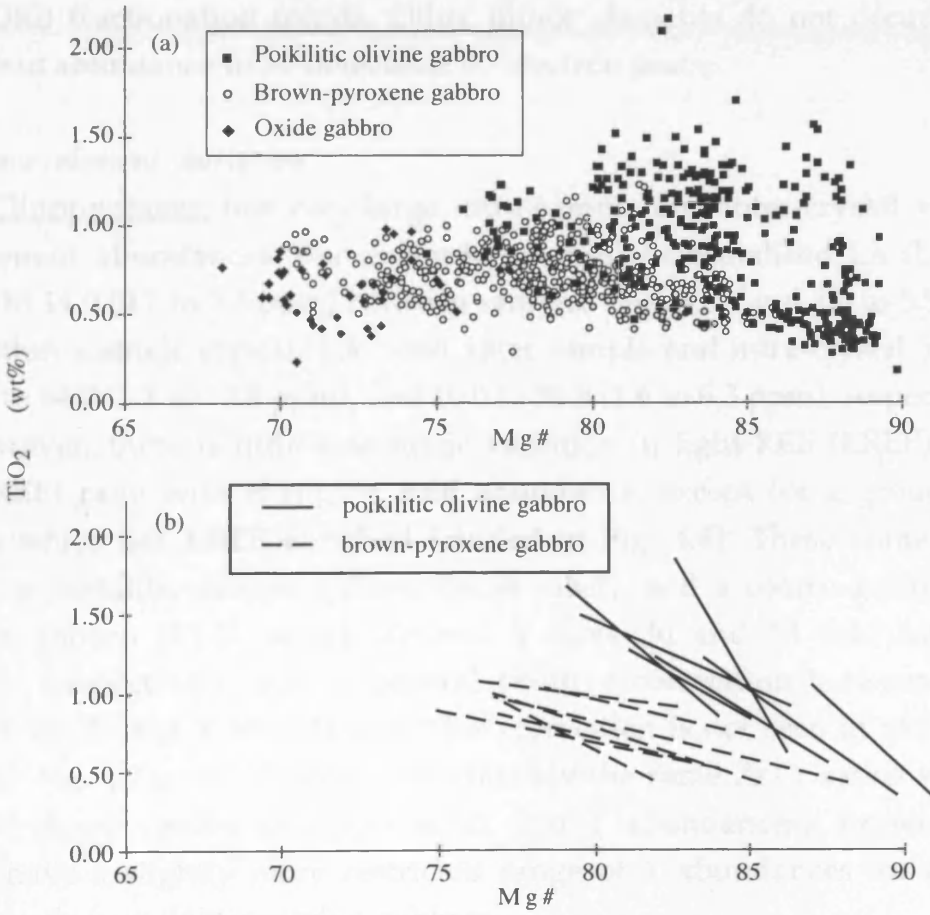


Fig 4.5 Clinopyroxene Mg# (Mg# = 100 x Mg / (Mg + Fe) versus $TiO_2$ content. (a) field of all analyses; (b) trend lines for individual samples which have large variations in both parameters.

clinopyroxene Ti abundance and Mg# have negative correlations (Fig. 4.5b). Furthermore, Ti-Mg# trends are steeper (i.e. larger variation in Ti abundance for a given Mg# variation) in poikilitic olivine gabbros than brown-pyroxene gabbros (Fig. 4.5b). Cr is abundant in the most magnesian clinopyroxene crystals (up to 1.3 wt% $Cr_2O_3$), but is close to the electron probe detection limit in most brown-pyroxene gabbros.

4.2.2.2 Plagioclase contains sufficient K and Fe to be detectable by electron probe. Plagioclase Fe abundances show no correlation with either K or An contents, suggesting that the observed range of abundances (0 to 0.75 wt% FeO) may be due to varying degrees of overlap of inclusions/exsolved ilmenite within plagioclase. Excluding the leucocratic vein (30.63 mbsf) and an altered poikilitic olivine gabbro (64.18 mbsf), there is very little K in the analysed plagioclase (0 to 0.2 wt% $K_2O$). In the leucocratic vein and altered poikilitic olivine gabbro, the $K_2O$ abundance reaches 0.36 and 0.98 wt%, respectively.

4.2.2.3 Olivine Mn (0.19 to 0.55 wt% MnO) and Ni (0 to 0.22 wt% NiO) contents correlate negatively and positively with Fo respectively (Fig. 4.15b), consistent with MORB fractionation trends. Other minor elements do not occur in olivine in sufficient abundance to be detectable by electron probe.

*4.2.3 Trace element variation*

4.2.3.1 Clinopyroxene has very large intra-sample and inter-crystal variation in trace element abundances. For example, chondrite-normalised La ($La_n$) ranges from 0.5 to 14.0 (0.1 to 3.3 ppm) between samples (Fig. 4.6), and 1.0 to 5.5 (0.2 to 1.3 ppm) within a single crystal. Likewise, inter-sample and intra-crystal $Yb_{(n)}$ varies from 6.8 to 84.7 (1.1 to 13.8 ppm), and 10.0 to 38.9 (1.6 to 6.3 ppm), respectively (Fig. 4.6). However, there is little systematic variation in light-REE (LREE) to heavy-REE (HREE) ratio with changing REE abundance, except for a group of seven analyses which are LREE enriched (circled in Fig. 4.6). These come from two samples, a poikilitic olivine gabbro (56.58 mbsf), and a coarse grained brown-pyroxene gabbro (31.31 mbsf). Zr and Y have 30 and 14 fold inter-sample variations, respectively, with a general positive correlation between the Zr/Y ratio and the Zr and Y abundances. This correlation is not seen in oxide gabbros (circled in Fig. 4.7), which have approximately the same Zr/Y ratios as the most primitive clinopyroxene (e.g. lowest Zr and Y abundances). Brown-pyroxene gabbros have a slightly more restricted range of Y abundances for a given Zr abundance than poikilitic olivine gabbros.

Compared to N-MORB (Sun & McDonough, 1989), primitive clinopyroxene analyses are P and, to lesser extents, Zr and Ti depleted with respect

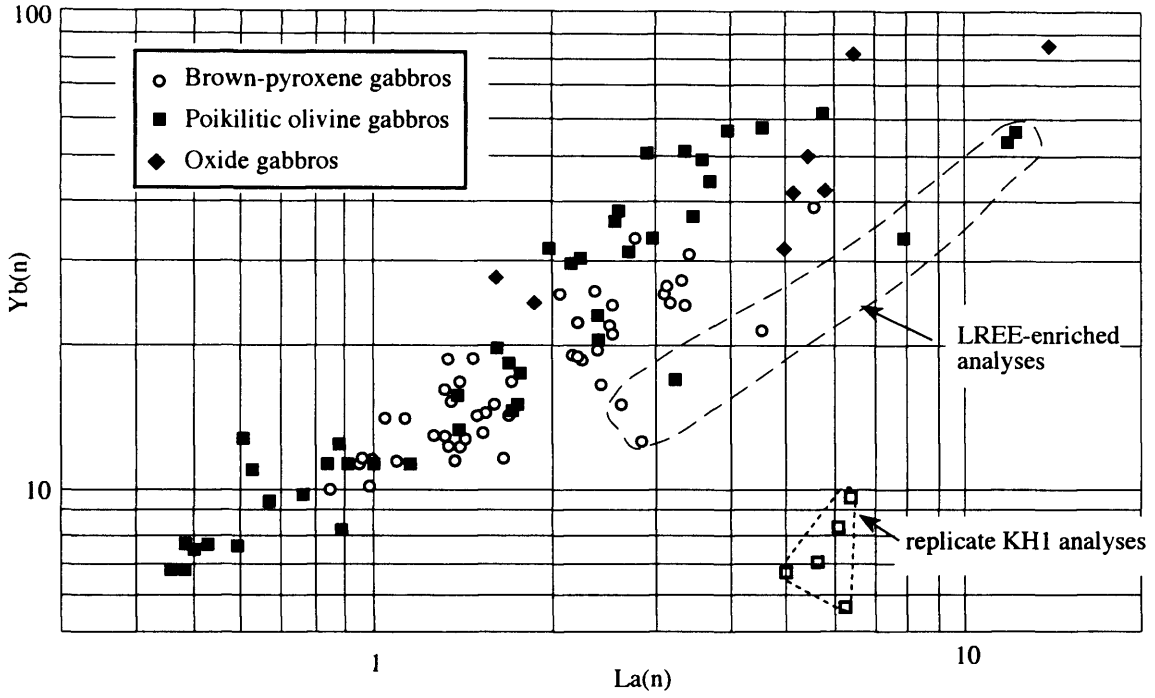


Fig. 4.6 Chondrite-normalised La versus Yb in clinopyroxene (all analyses shown). The dashed line encloses seven LREE-enriched clinopyroxene analyses, three from the rim of a cumulus crystal in a coarse brown-pyroxene gabbro (31.31 mbsf; see Fig. 4.21) and four from a clinopyroxene oikocryst in a poikilitic olivine gabbro (56.58 mbsf). The clinopyroxene in the poikilitic olivine gabbro has the strongest 'dusty' exsolution/alteration (see Section 3.8) of any sample in the core. Note the larger range of REE abundances in poikilitic olivine gabbros than in brown-pyroxene gabbros

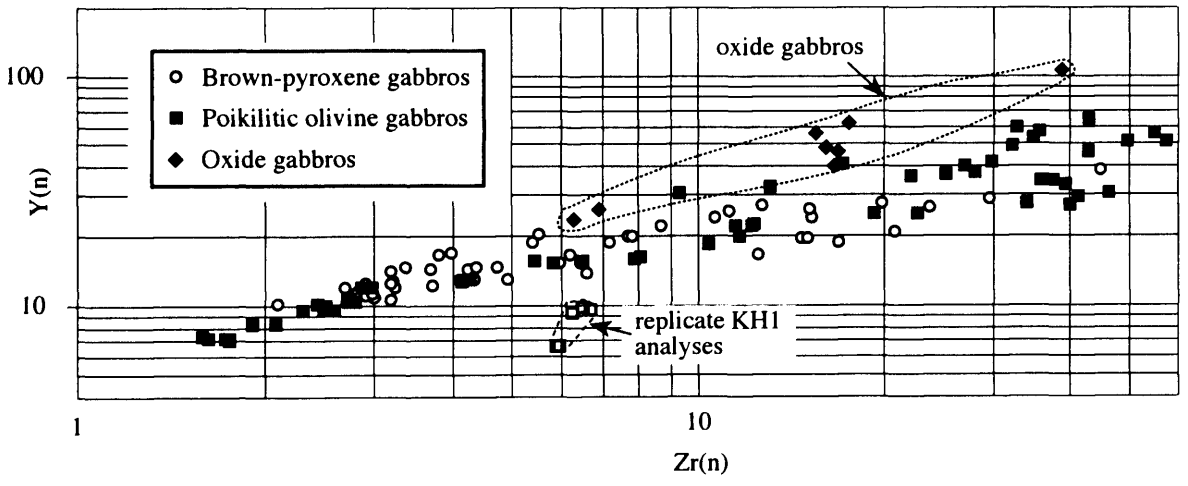


Fig. 4.7 Chondrite-normalised Zr versus Y in clinopyroxene (all analyses shown). Note the divergence from a one to one correlation towards excess Zr with increased Zr abundance in brown-pyroxene gabbros and poikilitic olivine gabbros, but not in oxide gabbros (outlined by dashed line). Also note the narrower range of Y abundances of brown-pyroxene gabbros, for a given Zr abundance, than in poikilitic olivine gabbros. The LREE enriched analyses (in samples from 31.31 and 56.58 mbsf, circled in Fig. 4.6) are indistinguishable from other analyses on this plot (not discriminated).

to REE abundances (Fig. 4.8). In addition, clinopyroxene is depleted in LREE with respect to HREE compared to N-MORB. The observed REE fractionation is qualitatively predicted by all published clinopyroxene distribution coefficients (D's), and is thus not surprising. D's for Zr and Ti are less well constrained and this characteristic is discussed further in Chapter Five (see also Appendix A.I). The P anomaly may reflect either: (i) that clinopyroxene has a much lower $D_P$ than $D_{Nd}$; however, no D's for P have been found in the literature, or (ii) that the melt which crystallised clinopyroxene had a negative P anomaly with respect to N-MORB. In MORB, however, the P/Nd ratio is almost constant (~74, Sun & McDonough, 1989). The chondrite-normalised clinopyroxene $P_{(n)}$ abundance ranges from 0.006 to 0.154 (7 to 187 ppm), a range in abundances similar to that of the LREEs, suggesting that during fractionation P had a similar bulk D to LREEs. Negative Sr and Eu anomalies are observed in most clinopyroxene analyses which are larger the higher the incompatible element abundances as is the Ti anomaly. This suggests that these element behaved less incompatibly than adjacent REEs.

Despite the large ranges in incompatible element abundances in clinopyroxene, there is a poor correlation between incompatible element and major element abundances. The weak correlation that exists between clinopyroxene Mg# and incompatible element abundances (Fig. 4.9) is dominantly controlled by intra-lithology variations.

4.2.3.2 Plagioclase also shows large variations in incompatible element abundances, and ratios, although fewer elements occur in sufficient abundance to be accurately measured by ion probe than in clinopyroxene. Fig. 4.10 shows chondrite-normalised incompatible trace element abundances in plagioclase. The range of incompatible element abundances in plagioclase is considerably smaller than in clinopyroxene. LREE, Zr, Y and Ba show ~10 fold variations in abundance and K, Ti, and Sr progressively smaller variations (Fig. 4.10). Zr and Ti data are not further discussed as they are unsystematic with respect to other incompatible elements, each other, and analysis location. This suggests that magmatic abundances may not have been measured, but, as suggested for FeO abundance in plagioclase (section 4.2.2.2), inclusions or exsolution may control the measured Zr and Ti abundances.

Figure 4.11 shows the variation in chondrite-normalised Sr, Y and La abundances in plagioclase with An content. The Sr abundance in plagioclase is higher at the same anorthite content in plagioclase in brown-pyroxene gabbros than in poikilitic olivine gabbros. However, there is little correlation between the Sr abundance and the An content in any lithology (Fig. 4.11a). In contrast, Y abundances are considerably higher in core analyses of most plagioclase in

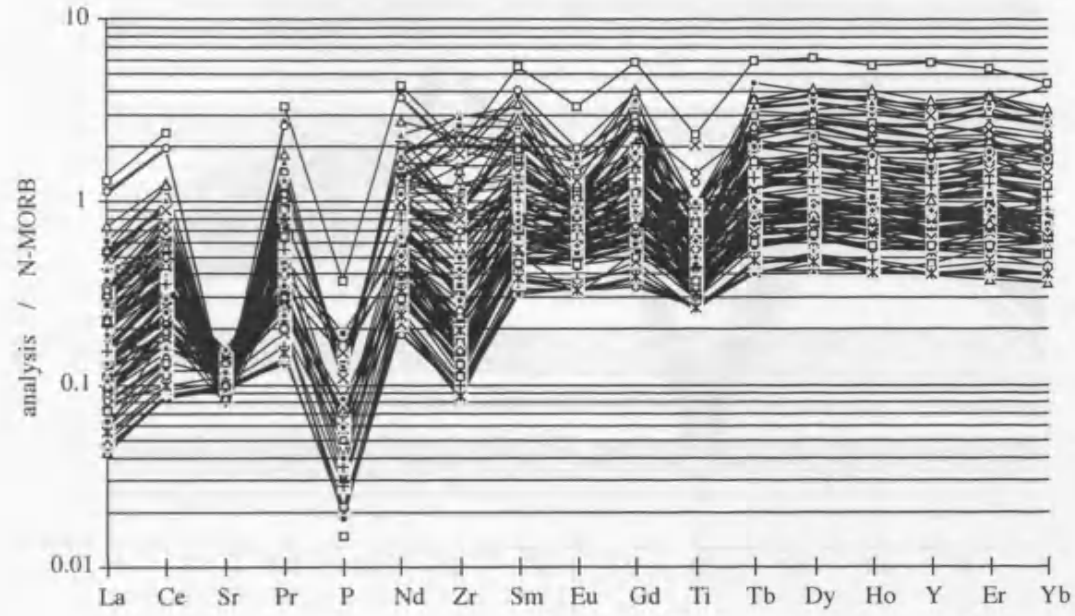


Fig. 4.8 N-MORB normalised incompatible element abundances in clinopyroxene. Note the negative P, Zr and Ti anomalies in the most primitive clinopyroxene, and the development of negative Sr and Eu anomalies with increased incompatible element abundances. N-MORB abundances from Sun and McDonough (1989).

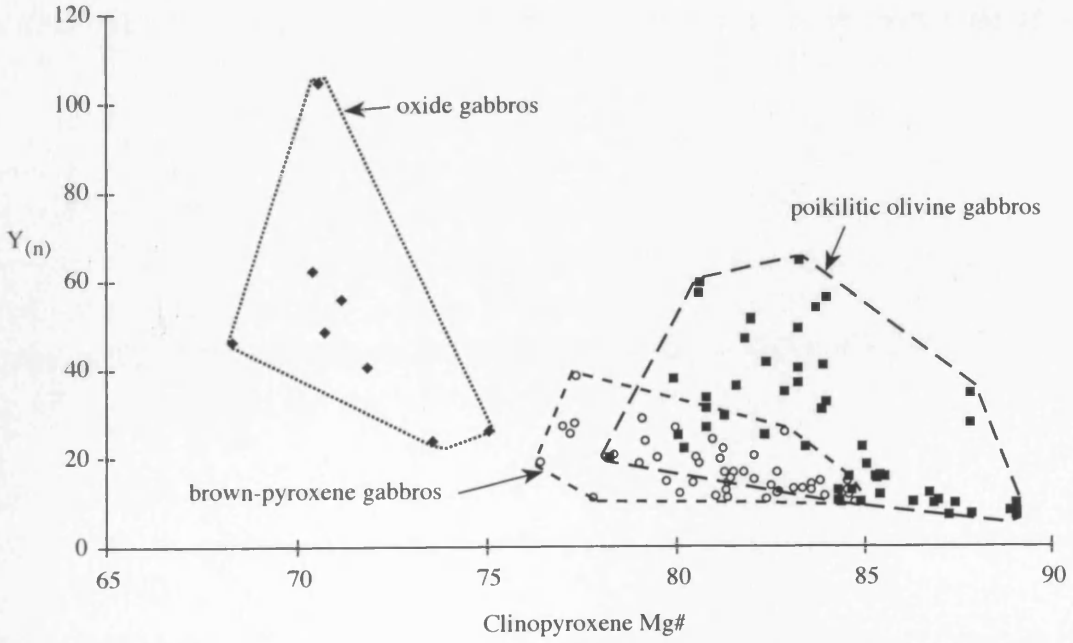


Fig. 4.9 Chondrite normalised Y versus Mg# in clinopyroxene. Within each lithology there is little correlation between Y and Mg#, with the weak overall negative correlation due to inter-lithology variation.

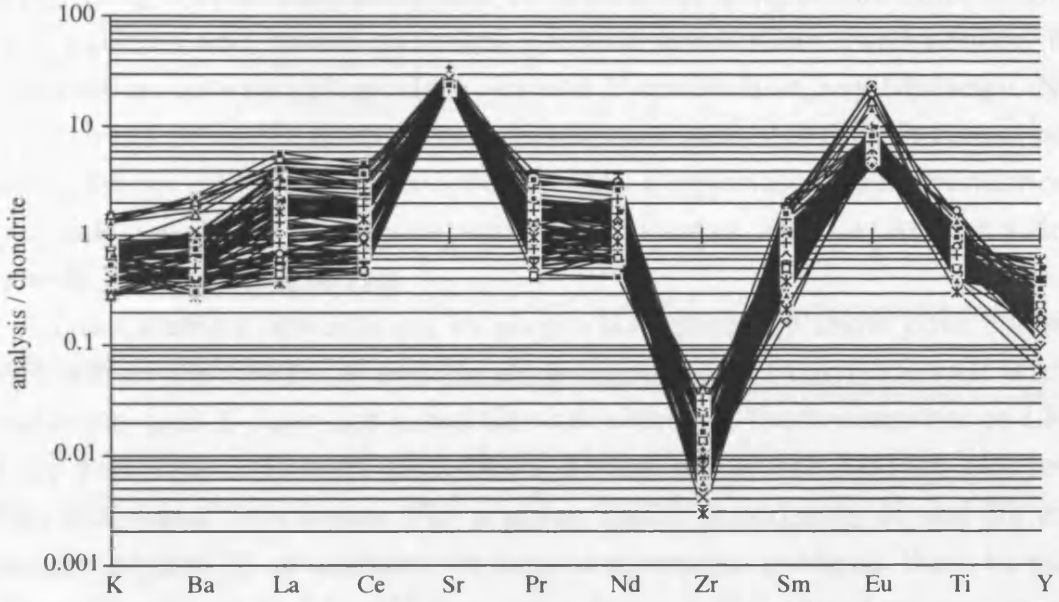


Fig. 4.10 Chondrite normalised plagioclase incompatible element abundances (all analyses shown). The large positive Sr and Eu anomalies are consistent with published distribution coefficients provided some Eu exists as $Eu^{2+}$ as is the large negative Zr anomaly. Note the large ranger of La than Nd abundances unlike in clinopyroxene. The group of analyses with higher Eu abundances than the rest are from oxide gabbros.

poikilitic olivine gabbros than in cores or rims of plagioclase in brown-pyroxene gabbros (Fig. 4.11b). However, the Y contents of plagioclase rims in poikilitic olivine gabbros and brown-pyroxene gabbros are similar. Furthermore, there is no correlation between plagioclase An and Y contents in any lithology. Notably, clinopyroxene Sr and Y abundances do not vary systematically between poikilitic olivine gabbros and brown-pyroxene gabbros. Plagioclase LREE abundances have very weak negative correlations with An; however, the La/An ratio does not vary with lithology (Fig. 4.11c).

Trace element abundances in plagioclase generally show poor correlations, except within the LREEs. K and Ba abundances do not correlate well with LREE abundances, and Y does not correlate with either of these elements or LREEs. K and Ba correlate well with each other across the entire dataset, but less well within individual lithologies. For a given LREE abundance, K and Ba are both generally higher in abundance in brown-pyroxene gabbros than in poikilitic olivine gabbros and higher still in oxide gabbros. LREE abundances in plagioclase correlate positively with the La/Nd ratio, a feature that is not observed in clinopyroxene (Fig. 4.12a). This correlation exists both within the entire data set and within individual crystals, but is most strongly developed in plagioclase cores in brown-pyroxene gabbros. The Ba/K ratio of plagioclase is relatively constant (Fig. 4.12b) except for a small group of core analyses (some analyses from 31.31, 47.33, 56.58, 64.87 mbsf; circled in Fig. 4.12b) which have lower ratios. These analyses all have $La_{(n)}/Nd_{(n)}$ ratios < 1 and show no signs of alteration. The variation in plagioclase incompatible element ratios is suggested to be a result of growth from parental melts unlike N-MORB in Chapter Five.

In summary, plagioclase shows a smaller range of incompatible element abundances than clinopyroxene, but more variation in LREE ratios. Plagioclase incompatible element abundances and ratios differ significantly between lithologies, as well as with analysis location within individual crystals (core versus rim). The low La/Nd ratio of many plagioclase ($La_{(n)}/Nd_{(n)}$ is commonly <1) suggests that their parental melt was strongly LREE-depleted because plagioclase D's are higher for La than Nd (Appendix A.I).

### *4.2.4 Accessory phase compositions*

For the purpose of this study all phases other than plagioclase, clinopyroxene and olivine are termed accessory. This is not strictly true for low-Ca pyroxene in oxide gabbros and a small proportion of the brown-pyroxene gabbros, but is adequate for the purpose of description. Major and minor element abundances in low-Ca pyroxene, amphibole, ilmenite, magnetite, sulphides and apatite were acquired by electron probe. The Mg# of low-Ca pyroxene varies from 65 to 85 (Fig 4.2) and correlates with the Fo content of co-existing olivine. The Mg# of low-Ca pyroxene

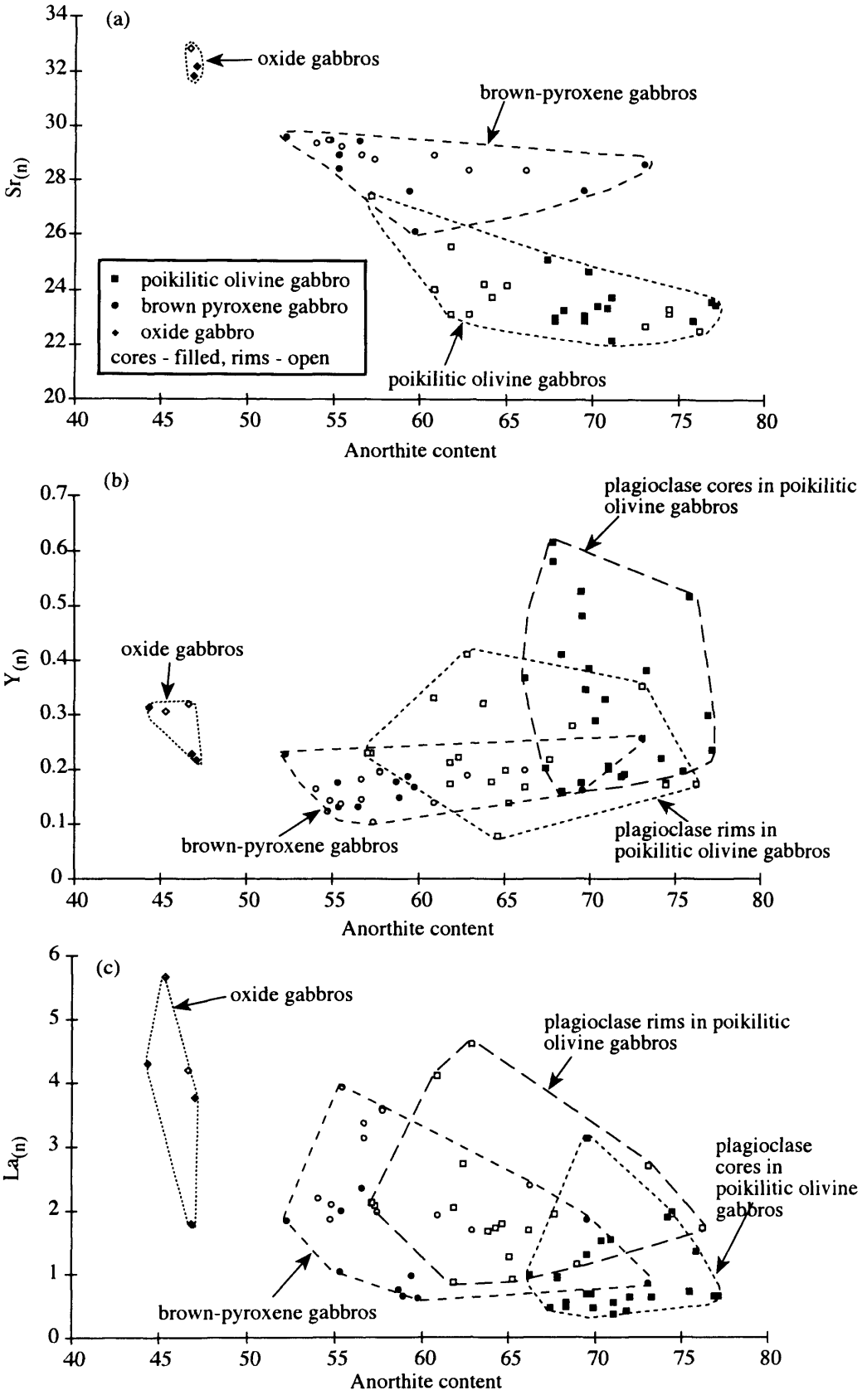


Fig 4.11 Anorthite content versus chondrite-normalised Sr, Y and La in plagioclase. (a) An versus $Sr_{(n)}$ in plagioclase. Note that plagioclase in brown pyroxene gabbros has higher Sr contents for a given An content than plagioclase in poikilitic olivine gabbros; (b) An content versus $Y_{(n)}$. Note plagioclase cores in poikilitic olivine gabbros have both the highest An and Y contents in the core; (c) Plot of plagioclase An content versus $La_{(n)}$. Plagioclase in poikilitic olivine gabbros generally have higher La and lower anorthite content at their rims than in their cores.

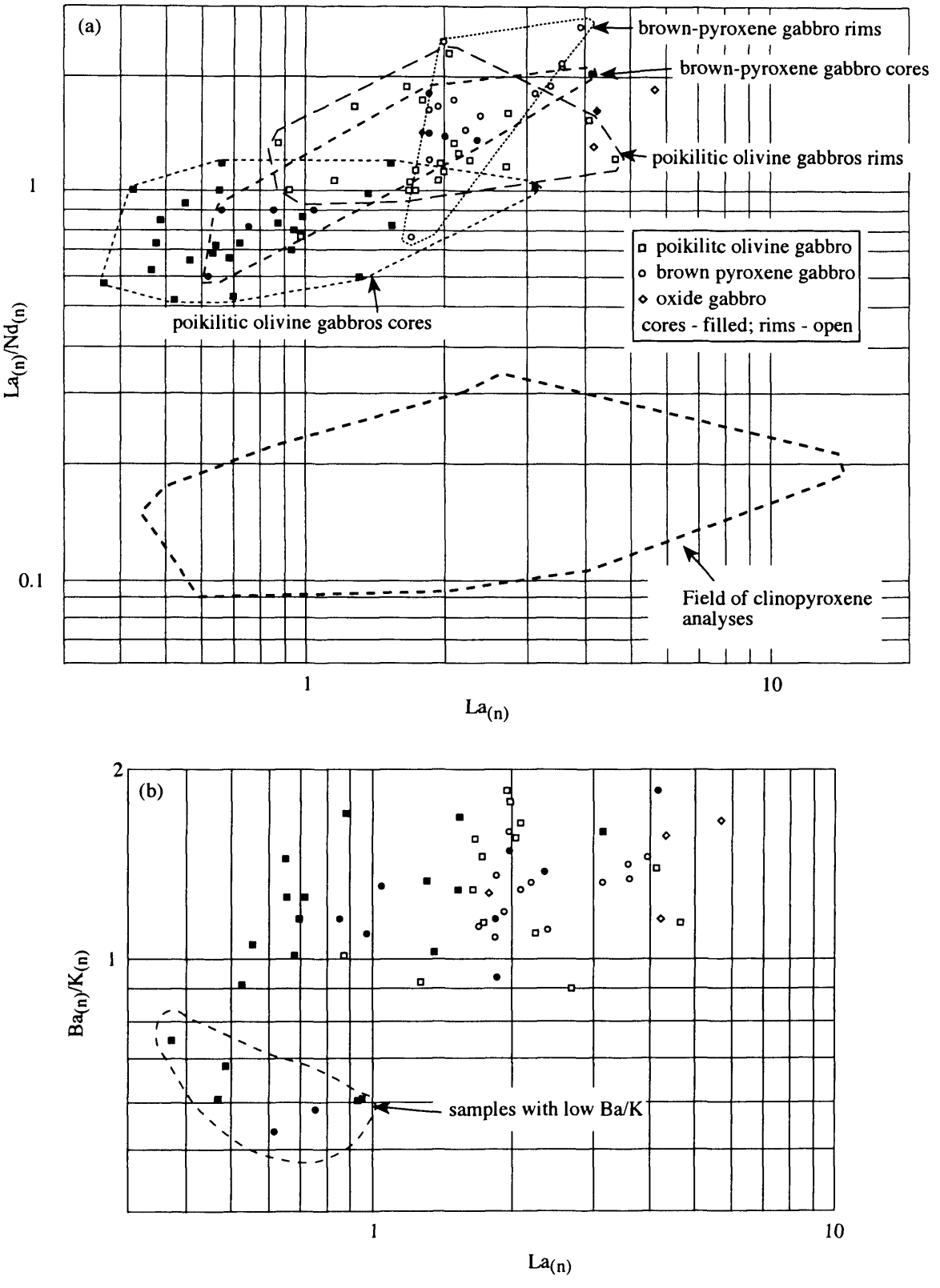


Fig 4.12 Plagioclase trace element compositional variations (all chondrite normalised). (a) comparison of variation in $La_{(n)}/Nd_{(n)}$ with $La_{(n)}$ in plagioclase and clinopyroxene. In plagioclase $La_{(n)}/Nd_{(n)}$ increases with increased $La_{(n)}$, whereas no correlation is seen in clinopyroxene; (b) variation in $Ba_{(n)}/K_{(n)}$ ratio with $La_{(n)}$ in plagioclase. Note that although most plagioclase have similar Ba/K ratios, a small group of plagioclase cores have a distinctly lower $Ba_{(n)}/K_{(n)}$ ratio (circled; some analyses of samples from 31.31, 47.33, 56.58 & 64.87 mbsf). These also have low La abundance and $La_{(n)}/Nd_{(n)} < 1$.

correlates negatively with its Mn abundance, as in olivine and clinopyroxene, but does not correlate with either the Al or Ti abundance.

Brown calcic (CaO >10 wt%) hydroxy-amphibole occurs along some clinopyroxene and ilmenite rims and within some clinopyroxene crystals. Compositionally these are relatively uniform in major components (42 to 46 wt% $SiO_2$, 2.5 to 4.5 wt% $TiO_2$, 10 to 12.5 wt% $Al_2O_3$) and are mainly hornblende to pargasitic-hornblende (nomenclature after Leake, 1978). A small subset of compositionally distinct, commonly green, amphiboles also occur (46 to 52 wt% $SiO_2$, 0 to 3 wt% $TiO_2$, 2 to 9.5 wt% $Al_2O_3$) these are mainly actinolite to actinolitic-hornblende. Hornblende to pargasitic-hornblende encompass a large range of Mg# (60 to 85), but this correlates poorly with Na, Ti and K abundance. However, a moderately good negative correlation exists between Mg# and Mn abundance. Neither Cl nor F occurs in sufficient concentration to be detected by electron probe in any amphibole.

Apatite shows limited compositional variation, except in volatiles. These are dominated by F-OH, but in two brown-pyroxene gabbros (17.10 and 31.31 mbsf) and a leucocratic vein (30.63 mbsf) apatite is Cl-rich (Fig. 4.13). At 31.31 mbsf apatite enclosed within clinopyroxene has a higher Cl content than that at the clinopyroxene rim. The apatite in the leucocratic vein also contains significant REE abundances (Fig. 4.14; see section 4.4.6 also).

Ilmenite is the dominant oxide phase in most of the core, with only minor magnetite. The exceptions to this are the oxide gabbros and leucocratic vein, in which ilmenite and magnetite occur in similar proportions. Up to 8 wt% MgO, 3 wt% MnO and 1 wt% $V_2O_3$ occur in ilmenite, with larger ilmenites containing higher MgO contents irrespective of lithology. The Mg and V concentrations of ilmenite correlate positively but Mn does not correlate with either. Ilmenite in oxide gabbros is consistently MgO-poor (< 1 wt%; this study; Agar & Lloyd, 1997). Magnetite contains <12 wt% $TiO_2$; the $TiO_2$ abundance correlates negatively with Mn (MnO <1 wt%), Al ($Al_2O_3$ 0 to 5 wt%), and $Fe_2O_3$ ($Fe_2O_3$ is calculated from charge balance assuming a perfect electron probe analysis, and that Fe is the only multi-valent element; Droop, 1987).

Composite sulphides, dominated by pyrrhotite with minor chalcopyrite and pentlandite, occur in almost all samples. Pentlandite and chalcopyrite commonly occur as straight sided intergrowths in pyrrhotite, suggesting that they exsolved from an originally homogenous sulphide. Pentlandite contains variable Ni (24 to 38 wt%) and Co (1.2 to 5.7 wt%), with higher Co abundances in pentlandite in brown-pyroxene gabbros than in poikilitic olivine gabbros.

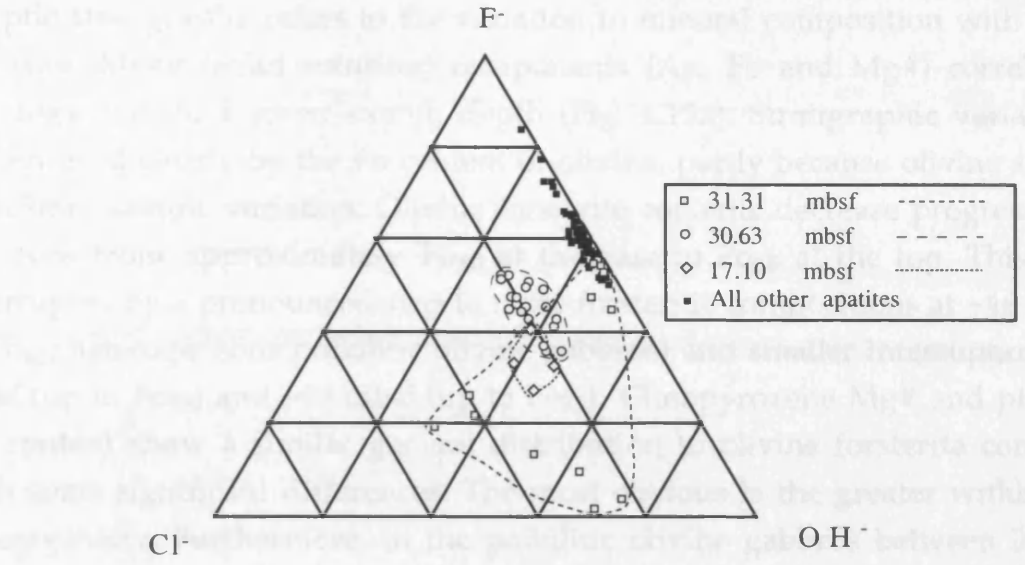


Fig 4.13 Apatite halogen compositions (in cations). Cl and F data are from electron probe analyses. OH calculated as 2-Cl-F in cations.

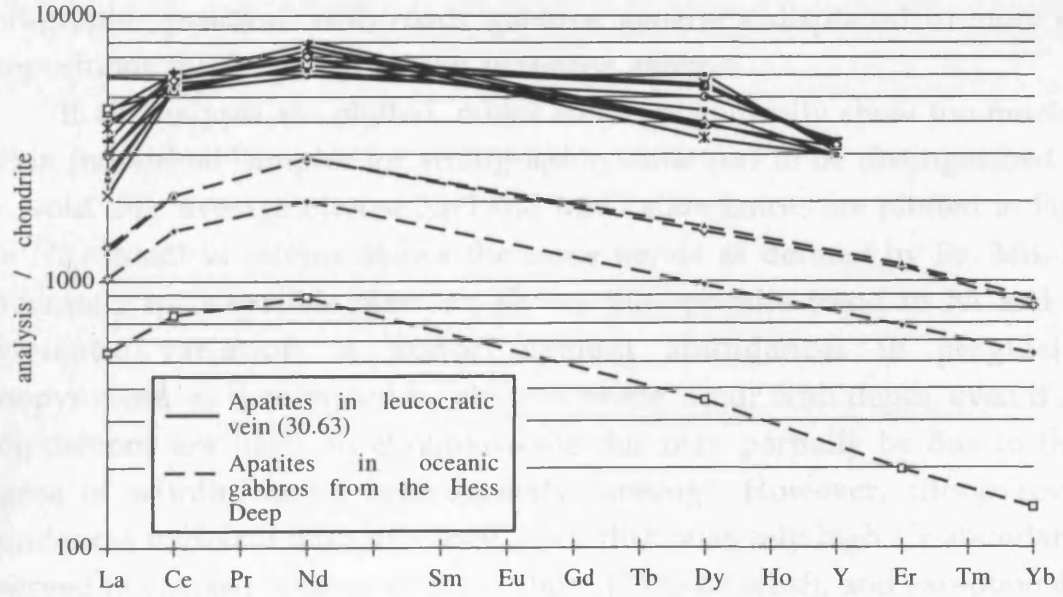


Fig. 4.14 Chondrite normalised REE and Y abundances in apatites in the leucocratic vein (30.63 mbsf) as determined by electron probe. Chondrite-normalised 2σ errors (i.e. on this plot) are La +/- 2000; Ce +/- 700; Nd +/- 950; Dy +/- 1900; Y +/- 190. For comparison ion probe data for Cl-rich apatites (1.3 to 5.8 wt% Cl, < 0.5 wt% F) in oceanic gabbros from ODP Site 894G at Hess Deep (Gillis, 1996) are shown.

## 4.3 Cryptic stratigraphy

### *4.3.1 Major and minor elements*

Cryptic stratigraphy refers to the variation in mineral composition with depth in the core. Major (solid solution) components (An, Fo and Mg#) correlate with lithology and, to a lesser extent, depth (Fig. 4.15a). Stratigraphic variations are shown most clearly by the Fo content of olivine, partly because olivine shows the least intra-sample variation. Olivine forsterite contents decrease progressively up the core from approximately $Fo_{80}$ at the base to $Fo_{65}$ at the top. This trend is interrupted by a pronounced step to more forsteritic compositions at ~46 mbsf (up to $Fo_{85}$; heterogeneous poikilitic olivine gabbros) and smaller interruptions at ~34 mbsf (up to $Fo_{78}$) and ~30 mbsf (up to $Fo_{77}$). Clinopyroxene Mg# and plagioclase An content show a similar general distribution to olivine forsterite content, but with some significant differences. The most obvious is the greater within-sample heterogeneity. Furthermore, in the poikilitic olivine gabbros between 30 and 35 mbsf clinopyroxene does not fit the compositional trend defined by olivine and plagioclase. In this interval plagioclase and olivine have more primitive compositions than the surrounding brown-pyroxene gabbros. However, the Mg# of clinopyroxene in these poikilitic olivine gabbros is not significantly higher than in the adjacent brown-pyroxene gabbros. The upper 5 m of the core is characterised by significant variation in mineral compositions unrelated to stratigraphic position, with oxide gabbros generally displaced to more evolved compositions than adjacent brown-pyroxene gabbros.

If all analyses are plotted, minor elements generally show too much scatter within individual samples for stratigraphic variations to be distinguished clearly. To avoid this, average olivine NiO and MnO abundances are plotted in Fig 4.15b. The Ni content of olivine shows the same trends as defined by Fo. Mn, being a moderately incompatible element, shows the opposite trend to Ni and Fo. No systematic variation in minor element abundances in plagioclase or clinopyroxene, as determined by electron probe, occur with depth, even if average compositions are used. In clinopyroxene this may partially be due to the large degree of within-sample heterogeneity (zoning). However, clinopyroxene Cr abundances correlate with lithology, such that relatively high Cr abundances are observed in coarse poikilitic olivine gabbro (55 to 68 mbsf), and exceptionally high abundances occur in the oikocryst enclosing the crescumulate olivine at 46.30 mbsf (heterogeneous poikilitic olivine gabbro; Fig. 3.8). In contrast, troctolitic poikilitic olivine gabbros (~53 and ~30 mbsf), and the clinopyroxene-poor sample of heterogeneous poikilitic olivine gabbro (47.33 mbsf; Fig. 3.7), are relatively Cr-poor (Fig. 4.15b).

Two samples do not fit the trends in the cryptic stratigraphy described above. These are a leucocratic vein (30.63 mbsf) and an altered poikilitic olivine

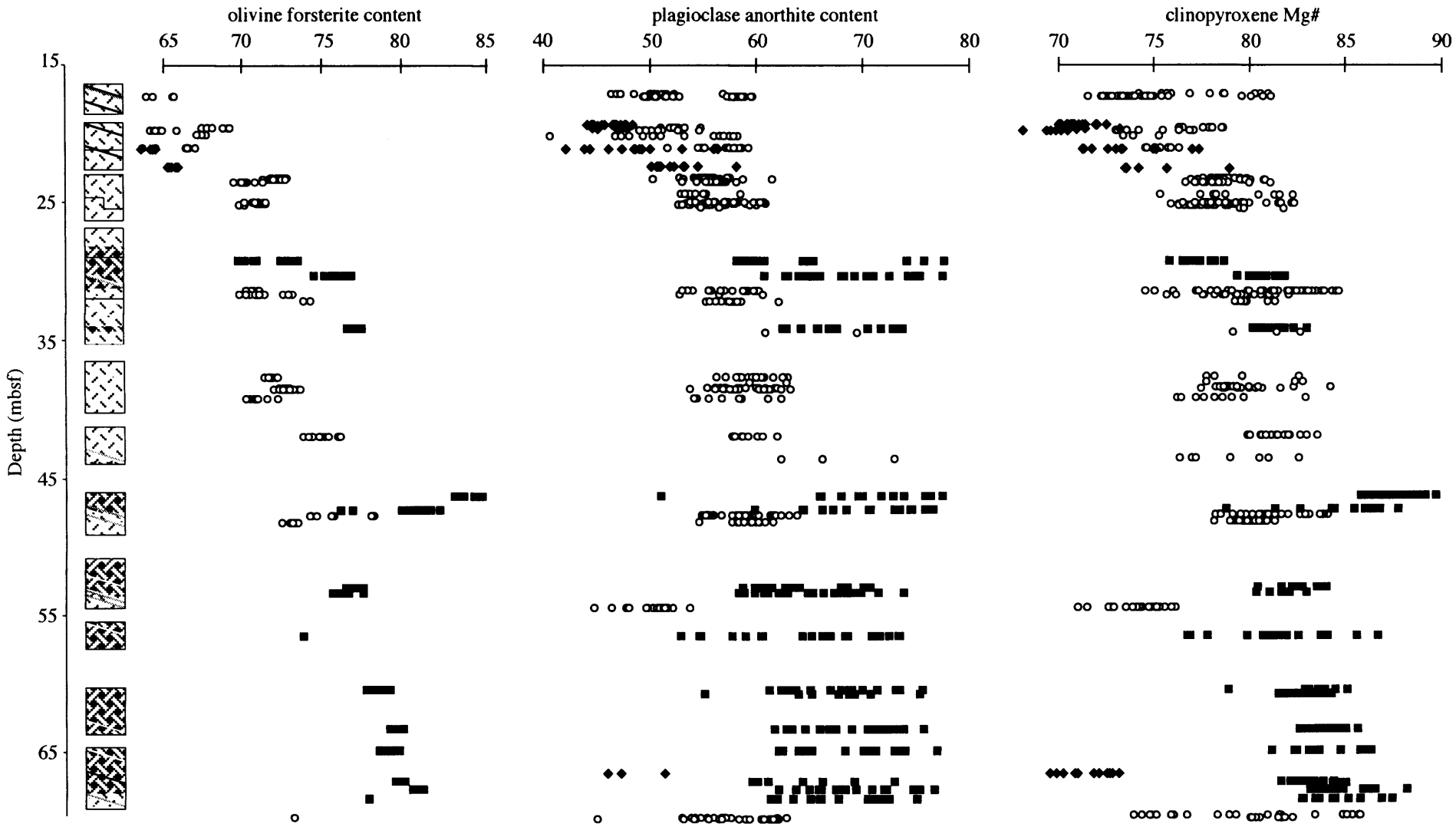


Fig. 4.15a Stratigraphic variations in olivine (Fo), plagioclase (An), and clinopyroxene (Mg#) major element compositions. Olivine composition varies much more smoothly with height than plagioclase and clinopyroxene compositions. Plagioclase compositions appears to be controlled more by lithology than stratigraphy. Note that the upper poikilitic olivine gabbros (30 and 35 mbsf) contain primitive plagioclase and olivine but not clinopyroxene. The leucocratic vein studied (30.63 mbsf) and an altered poikilitic olivine gabbro (64.18 mbsf) are not shown as these would compress the scales. Key as in Fig. 15b.

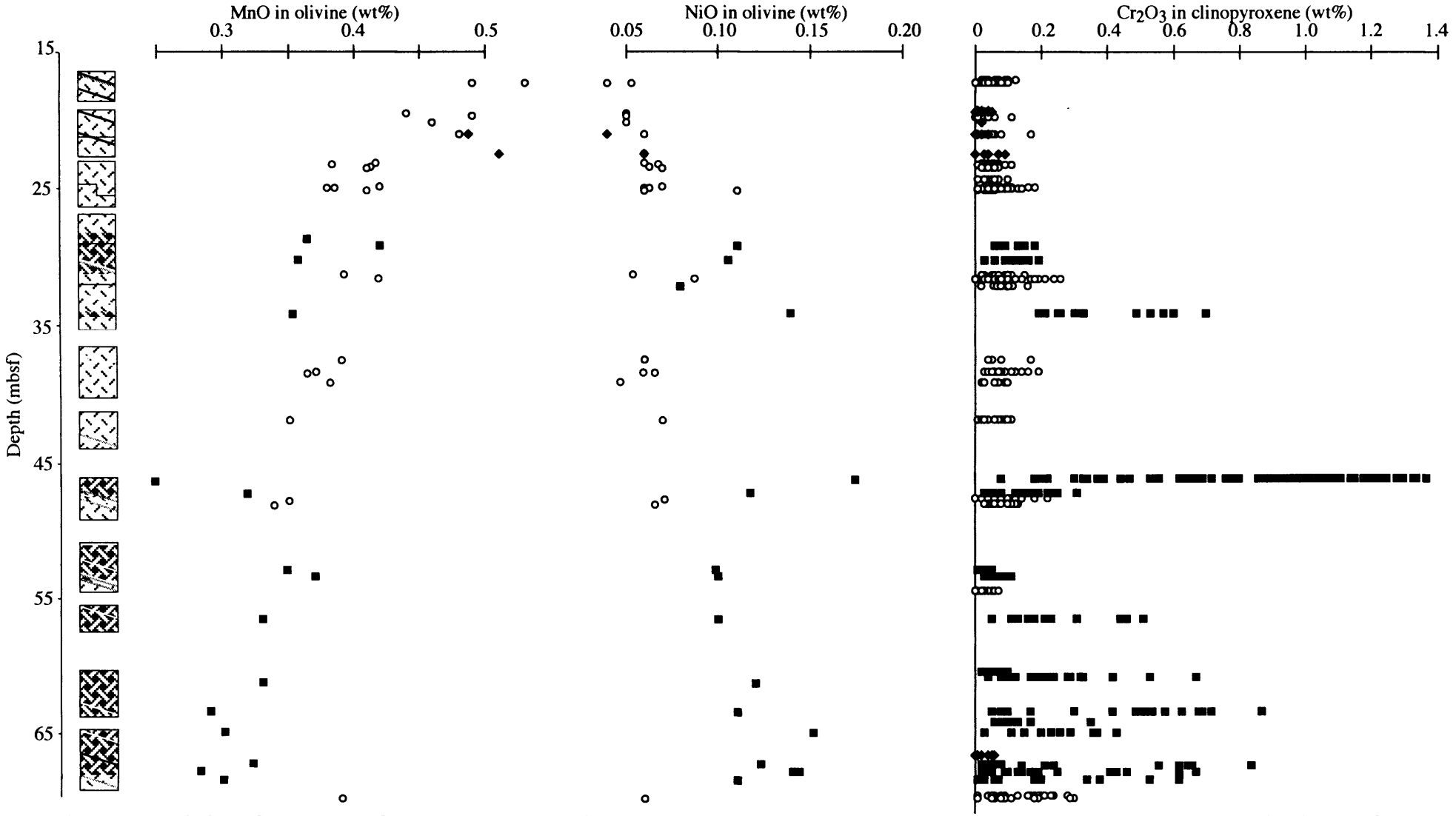


Fig. 4.15b Variation of average MnO and NiO abundance in olivine and all $Cr_2O_3$ analyses in clinopyroxene with depth. MnO and NiO data are from this study and Ross and Elthon (1997a), $Cr_2O_3$ data are from this study. Lithology log as in Fig. 3.1, ■ poikilitic olivine gabbro; ○ brown-pyroxene gabbro; ◆ oxide gabbro.

gabbro (64.18 mbsf). These have been exclude from Fig. 4.15a because to show them would produce unacceptable compression of the other data. These samples both have mineral compositions more evolved than surrounding samples analysed in this study. In Chapter Five the gross variation in mineral compositions is attributed to repeated replenishment of a relatively small magma chamber.

*4.3.2 Trace element stratigraphy*

Neither clinopyroxene nor plagioclase trace element compositions show stratigraphically related compositional variation. Instead, compositional variations are generally controlled by lithology. This may partially be due to insufficient data, but more likely indicates that the processes responsible for controlling trace element abundances were different from those that controlled major element abundances. These processes are discussed in detail in Chapters Five and Six.

## 4.4 Within-lithology compositional variation

*4.4.1 Coarse grained poikilitic olivine gabbros*

In coarse grained poikilitic olivine gabbros, olivine is nearly homogenous within samples. Plagioclase occurs as two populations within poikilitic olivine gabbros. The first population is strongly normally zoned with embayed anorthitic cores ($An_{71}$-$An_{77}$) sharply overgrown by more albitic rims ($An_{60}$-$An_{68}$). Individual crystals sometimes span the entire range of compositions within the sample. It is the cores of this population of plagioclase which have the highest Y abundances of any plagioclase within the cored interval from ODP Hole 923A (Fig. 4.11b). The core to rim transition is apparently equally sharp for trace and major elements, although more extensive trace element analysis would be necessary to confirm this. The second plagioclase population is weakly normally zoned (2 to 3 %An) and have similar compositions to the rims of strongly zoned plagioclase.

Clinopyroxene occurs as oikocrysts which are moderately zoned in major elements (3 to 5 Mg# units), but are very strongly zoned in minor and trace elements. Strong zoning occurs in which incompatible element abundances increase and compatible element abundances decrease towards the margins of oikocrysts. This zoning also occurs at the clinopyroxene grain boundaries with plagioclase and olivine chadacrysts. These incompatible element enriched 'rims' are of similar thickness (~200 to 500 μm), irrespective of whether they are at the margin of an oikocryst, or adjacent to an included crystal. This suggests that late stage porosity existed around chadacrysts as well as between oikocrysts during the final stages of solidification.

Fig. 4.16 shows a zoning profile through part of a clinopyroxene oikocryst and an enclosed plagioclase crystal in the sample from 64.87 mbsf. The clinopyroxene Mg# is normally zoned in each portion of the oikocryst, but this is far more strongly developed in one portion than the other (Fig. 4.16b). Zoning of Ti (Fig. 4.16c) and Al (Fig. 4.16d) in clinopyroxene is also asymmetric between the two portions. The Al content of the clinopyroxene M1 site increases in unison with Ti at the clinopyroxene rim fulfilling charge balance requirements. Incompatible trace element abundances increase from the core to rim of each portion of the clinopyroxene (Fig. 4.16e) with significant fractionation occurring amongst them (Fig. 4.16f). Plagioclase is very strongly, and complexly, zoned in anorthite content ($An_{61}$ to $An_{79}$; Fig. 4.16b). Incompatible trace elements are zoned in the plagioclase (Fig. 4.16g), but these do not correlate with either the An content zonation or the incompatible element zoning in clinopyroxene. Two main difference between trace element zonation in plagioclase and clinopyroxene are: (i) the Y abundance decreases from the core to rim in plagioclase, but increases from the core to rim in clinopyroxene, and (ii) the La/Nd ratio increases from the core to rim in plagioclase, but shows little variation in clinopyroxene, if anything decreasing towards the plagioclase (Fig. 4.16f).

The complexity of plagioclase An zonation, coupled with the difference in style of trace element zonation in clinopyroxene and plagioclase, and reverse zoning of Y in some plagioclase, suggests that plagioclase cores grew from different parental melts than their rims and associated clinopyroxene. These differences cannot be explained by alteration of plagioclase rims as: (i) back scatter electron images show the plagioclase is relatively fresh, (ii) their is no reason to believe that Y but not LREE would be stripped from plagioclase during alteration, (iii) it is unlikely that alteration would change the La/Nd in plagioclase but not adjacent clinopyroxene. Growth of plagioclase cores from different parental melts than their rims is consistent with the suggestion from plagioclase crystal size distributions (Section 3.4) that plagioclase is truly cumulus in poikilitic olivine gabbros. This idea is developed further in Chapter Five.

4.4.1.1 Accessory phase compositions in coarse poikilitic olivine gabbros provide information about the composition of the melt within the crystal mush at late stages of solidification. Calcic hydroxy-amphibole (Fig. 4.17) and adjacent ilmenite (Fig. 4.18) at the rim of a clinopyroxene crystal in a coarse poikilitic olivine gabbro (67.73 mbsf), were analysed by ion probe for trace elements. For comparison, the core and rim of a coarse (1 to 2 mm diameter) ilmenite in the same sample was also analysed. Amphibole has slightly higher REE abundances than an adjacent clinopyroxene rim, but is strongly Zr, Ti, Sr, Nb and Ba enriched compared with the clinopyroxene. This suggests higher D's for these elements for amphibole

**Fig. 4.16 Geochemical traverse through a clinopyroxene oikocryst and enclosed plagioclase crystal in a poikilitic olivine gabbro (64.87 mbsf)**

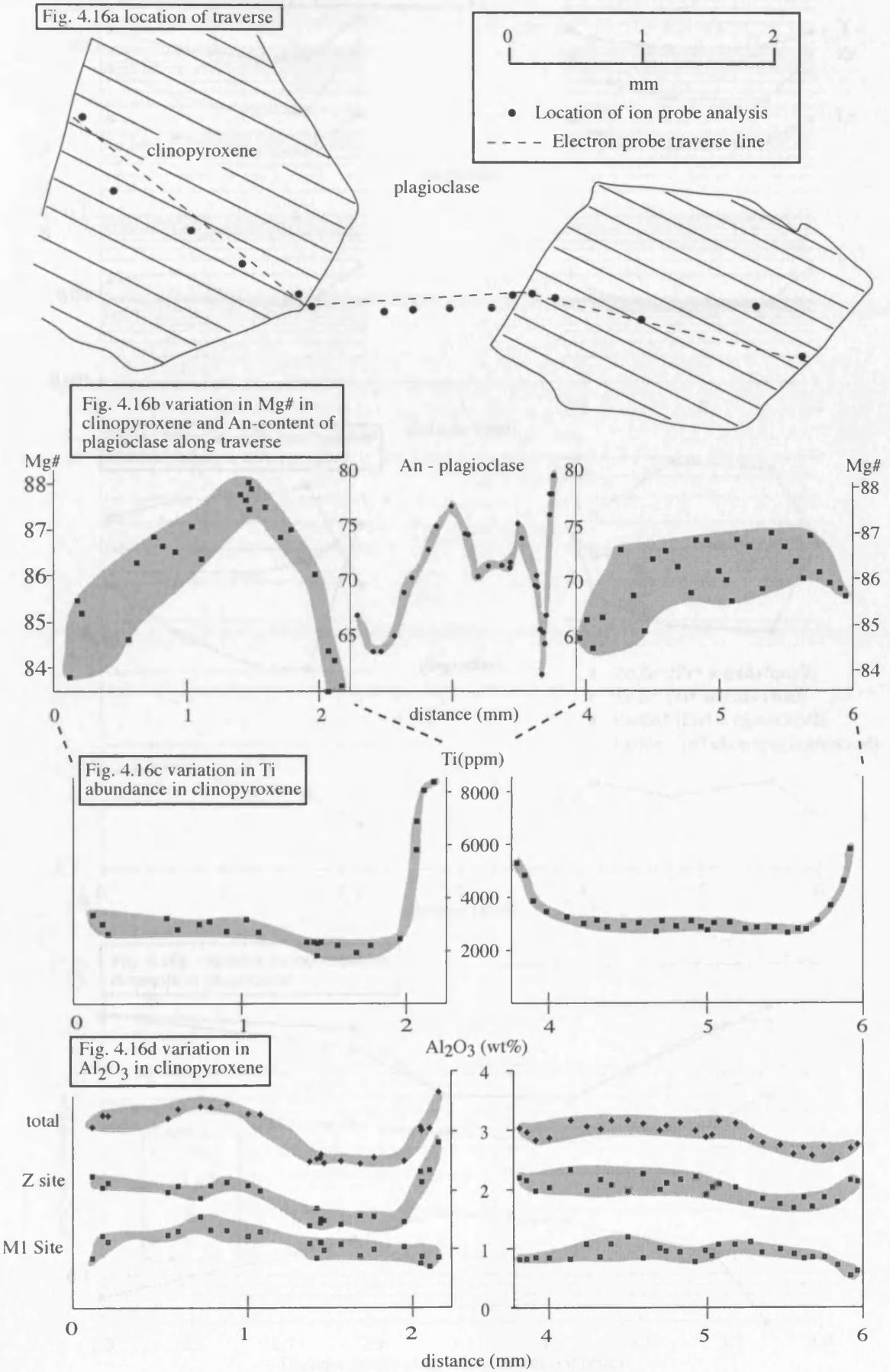

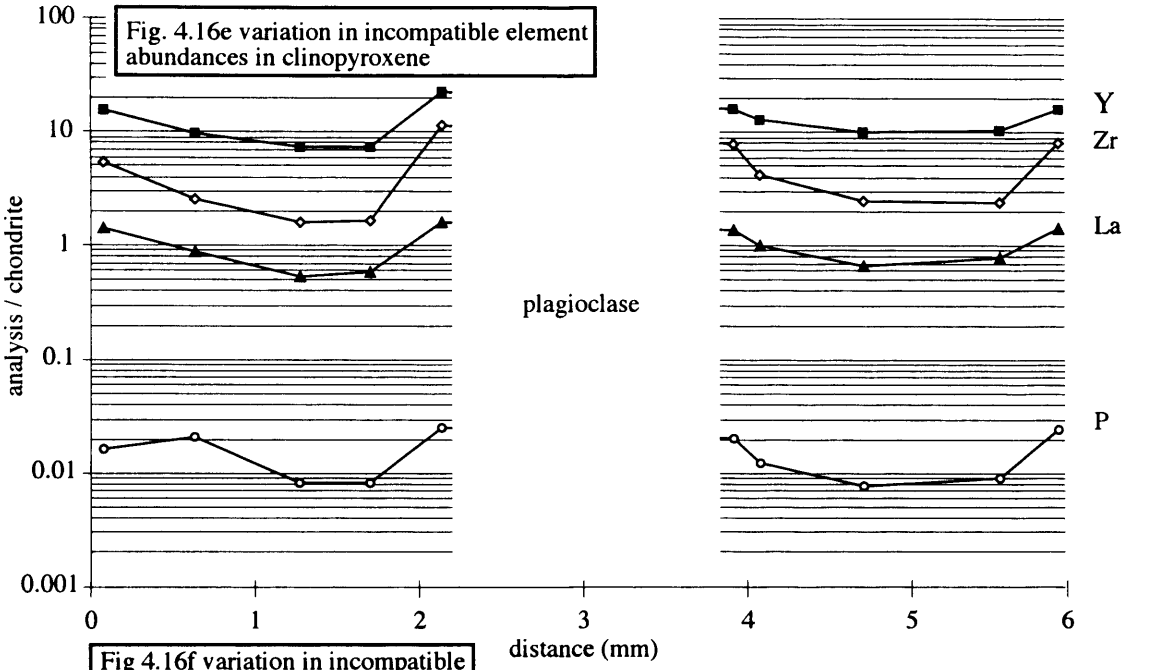
Fig. 4.16e variation in incompatible element abundances in clinopyroxene
100
10
1
0.1
0.01
0.001
analysis / chondrite
Y
Zr
La
P
plagioclase
0
1
2
3
4
5
6
distance (mm)

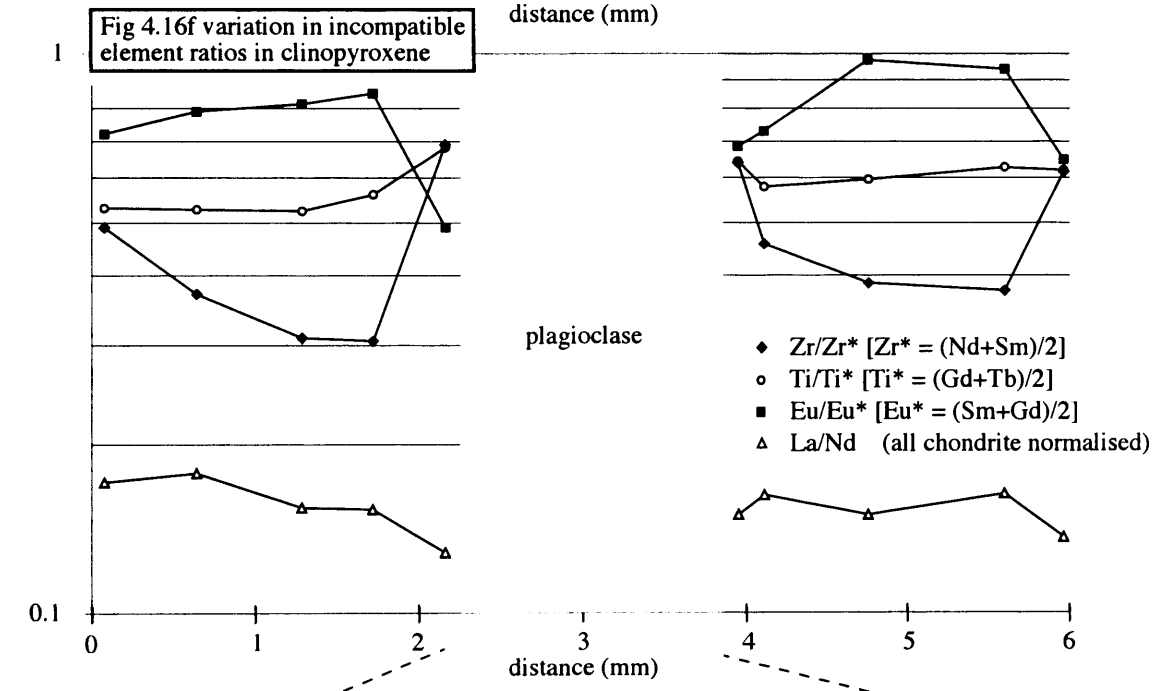
Fig 4.16f variation in incompatible element ratios in clinopyroxene
1
0.1
plagioclase
Zr/Zr* [Zr* = (Nd+Sm)/2]
Ti/Ti* [Ti* = (Gd+Tb)/2]
Eu/Eu* [Eu* = (Sm+Gd)/2]
La/Nd (all chondrite normalised)
0
1
2
3
4
5
6
distance (mm)

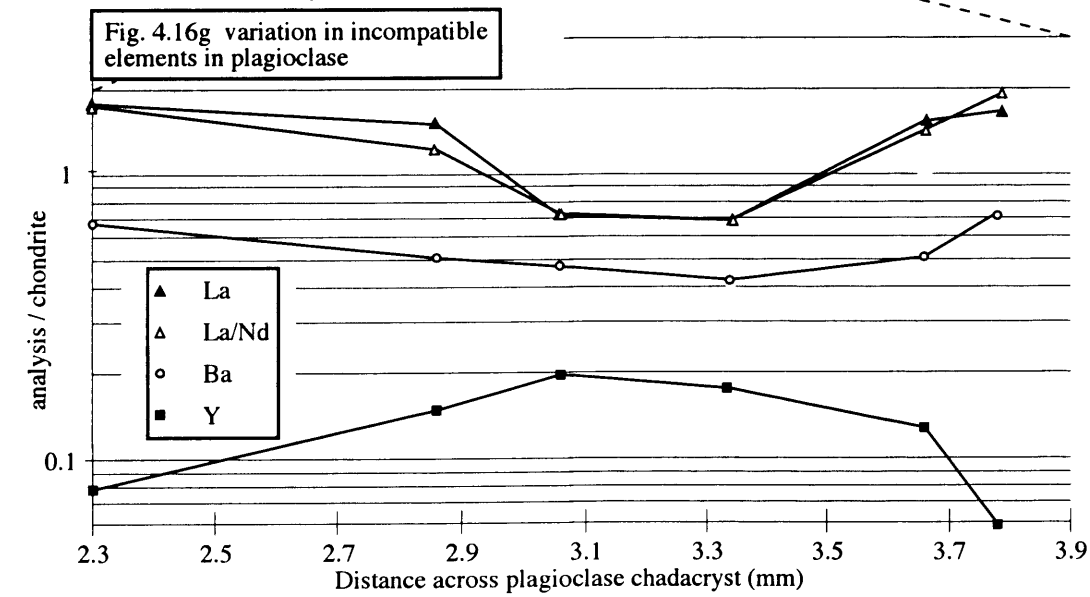
Fig. 4.16g variation in incompatible elements in plagioclase
1
0.1
analysis / chondrite
La
La/Nd
Ba
Y
2.3
2.5
2.7
2.9
3.1
3.3
3.5
3.7
3.9
Distance across plagioclase chadacryst (mm)

Fig 4.16 (a-g) Compositional variation along a 6 mm traverse through part of a clinopyroxene oikocryst in a coarse poikilitic olivine gabbro (64.87 mbsf) including an enclosed plagioclase crystal: (a) tracing of photomicrograph showing traverse line and location of ion probe analyses. The somewhat uneven distribution of ion probe analyses is due to the small field of view available for locating analysis locations; (b) variation in Mg# of clinopyroxene and An content of plagioclase along the traverse. Unlike other plagioclase analyses, for which a 10 μm electron beam was used, for traverses a 5 μm beam was used to make it easier to avoid cracks whilst sticking closely to the traverse line. The assymetry of the plagioclase zonation may represent a "cut effect" through a symetrically zone plagioclase or assymetric zoning. The assymetric clinopyroxene zoning is difficult to interpret as the edge of the oikocryst is off the edge of the thin section; (c) zoning of Ti (ppm) in clinopyroxene, determined by electron probe, showing assymetric on either side of the plagioclase chadacryst; (d) variation in total $Al_2O_3$ in clinopyroxene, and calculated variation in M1 and Z crystal sites. The variations can be explained in part as due to the necessity to charge balance the Ti zoning; (e) variation in chondrite normalised La, Y, Zr and P across the clinopyroxene. Note the increase in incompatible element abundances towards the rim with plagioclase despite this not being the limit of the extent of the clinopyroxene crystal; (f) variation in Zr/Zr*, Ti/Ti*, Eu/Eu*, and La/Nd in clinopyroxene. Note the significant variation in Eu/Eu* and Zr/Zr* suggest that the clinopyroxene grew from melts with significantly different incompatible element ratios; (g) variation in chondrite normalised La, Ba, Y and La/Nd across the plagioclase chadacryst. Note that the Y abundance is higher in the core of the plagioclase than rim despite being the other way around in the clinopyroxene (Fig. 4.16e). Furthermore, La/Nd increases from the core to rim of the plagioclase but shows little variation in clinopyroxene.

than clinopyroxene, consistent with experimentally determined crystal-melt D's (e.g. Brenan *et al.*, 1995).

The large ilmenite is compositionally distinct from the small ilmenite at the rim of a clinopyroxene crystal. The main major element compositional difference is in MgO content, with the large ilmenite having exceptionally high MgO (6 to 8 wt%) and the smaller ilmenite a much lower MgO content (<1 wt%). MgO abundances of 6 to 8 wt%, substituting for FeO, are generally only found in ilmenite in kimberlites (Haggerty, 1976). Trace element ratios also differ between the two ilmenites (Fig. 4.18). The Zr/Hf and Nb/Ta ratios are higher in the big ilmenite ($Zr_{(n)}/Hf_{(n)}$ ~1.25 and $Nb_{(n)}/Ta_{(n)}$ ~1.35, respectively) than the smaller one ($Zr_{(n)}/Hf_{(n)}$ ~0.9 and $Nb_{(n)}/Ta_{(n)}$ ~1.1, respectively). Furthermore, the big ilmenite has higher $Zr_{(n)}/Nb_{(n)}$ and $Hf_{(n)}/Ta_{(n)}$ ratios ($Zr_{(n)}/Nb_{(n)}$ and $Hf_{(n)}/Ta_{(n)}$ both ~0.3) than small ilmenite ($Zr_{(n)}/Nb_{(n)}$ and $Hf_{(n)}/Ta_{(n)}$ both <0.1).

The consistency of element partitioning between amphibole and clinopyroxene with that predicted for co-precipitation from a silicate melt suggests that the amphibole is magmatic and was not formed by alteration of clinopyroxene. Ilmenite compositions suggest that the two sizes of ilmenite grew from melts with significantly different compositions. The high MgO content of the big ilmenite suggests its parental melt had a high Mg activity, a feature not expected when ilmenite reaches the liquidus of a tholeiitic liquid. However, a mechanism to produce a melt with high Mg and Ti activities through buffering of incompatible element enriched interstitial melt by primitive cumulus crystals is developed in Chapter Six. Fractionation of geochemically similar element pairs (Zr/Hf and Nb/Ta) between the two ilmenites was unexpected, and is also discussed in Chapter Six.

### *4.4.2 Troctolites*

In troctolites plagioclase that is not enclosed within olivine oikocrysts can be divided into the same two populations observed in coarse poikilitic olivine gabbros (i.e. strongly normally zoned in anorthite content with high Y cores and weakly normally zoned in anorthite content with low Y cores; Section 4.4.1). Plagioclase enclosed within olivine oikocrysts have anorthitic cores (>$An_{70}$), overgrown by thin rims, that can be either more anorthitic (up to $An_{80}$), or more albitic (~$An_{65}$), than the core. Where clinopyroxene is enclosed within plagioclase (see Section 3.3.2 and Fig. 3.6), the plagioclase surrounding it is markedly less anorthitic (5 to 10 % lower An) than it is away from the clinopyroxene. Clinopyroxene in troctolites has amongst the highest incompatible element abundances and the largest negative Eu anomalies, but amongst the lowest LREE/HREE ratios of any clinopyroxene within the samples studied (Fig. 4.19).

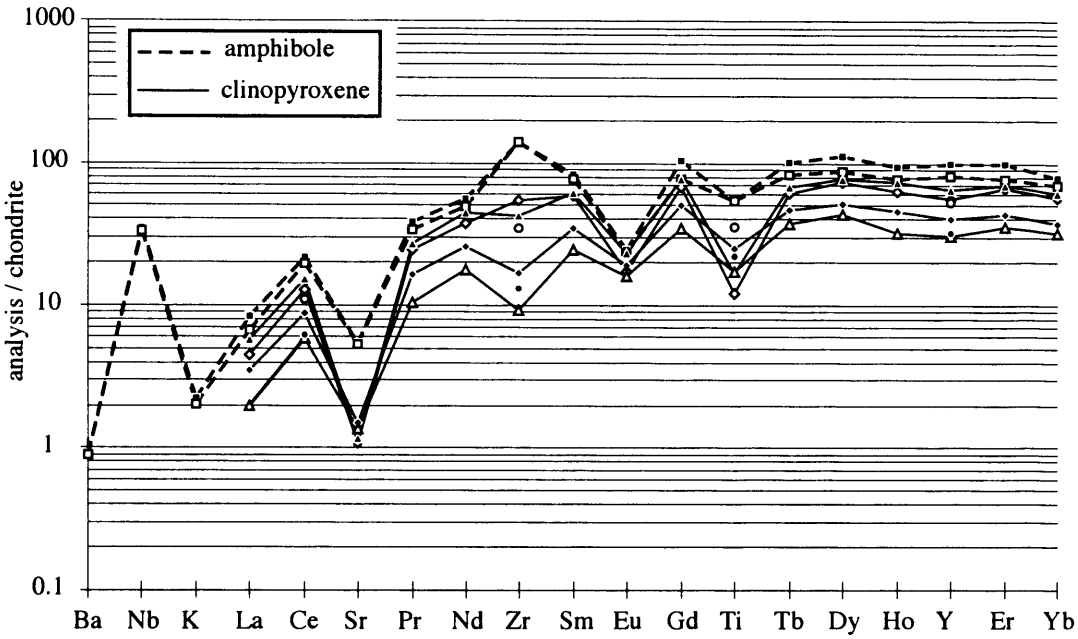


Fig. 4.17 Comparison of amphibole and clinopyroxene compositions in poikilitic olivine gabbro (67.73 mbsf). Amphibole occurs at the clinopyroxene rim adjacent to a small ilmenite the composition of which is shown in Fig. 4.18, and a minute apatite. Note the higher Ba, Nb (both below detection limit in clinopyroxene), Sr, Zr and Ti abundances in amphibole compared to clinopyroxene, but similar REE abundance at the clinopyroxene rim (highest incompatible element abundances in clinopyroxene) as in the amphibole. K was not analysed for in clinopyroxene.

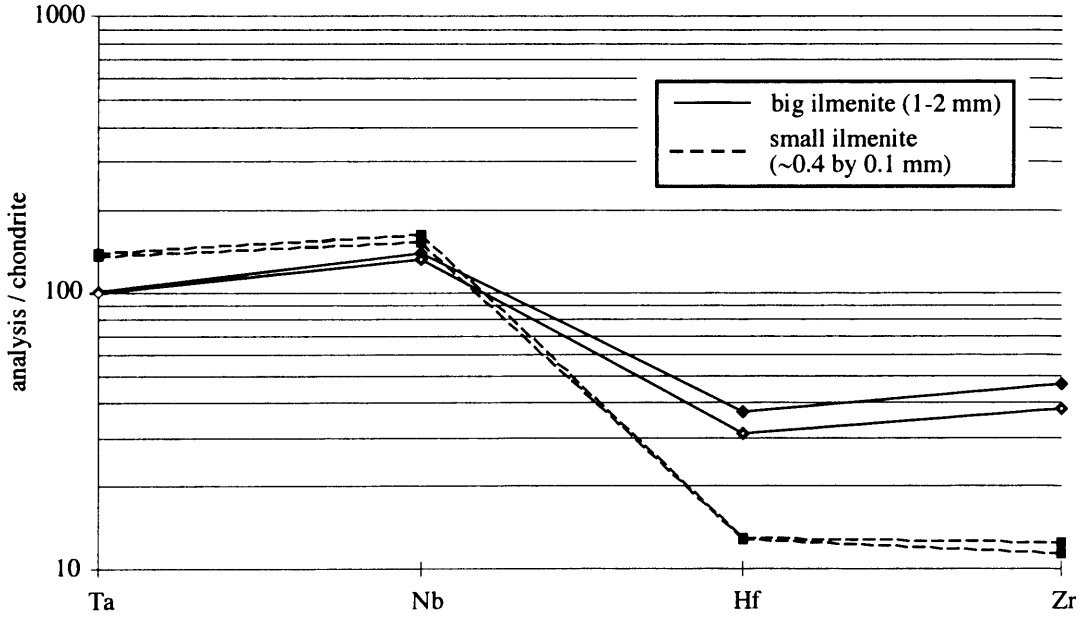


Fig 4.18 Chondrite-normalised plot of ilmenite trace element compositions in poikilitic olivine gabbro (67.73 mbsf). The solid lines are the core (closed diamonds) and rim (open diamonds) of a large ilmenite and the dashed lines two small ilmenites at a clinopyroxene rim, adjacent to the amphibole shown in Fig. 4.17. Note the difference in Zr/Hf and Nb/Ta ratios in the different ilmenites

These characteristics are shared with clinopyroxene in other clinopyroxene-poor poikilitic olivine gabbros (Fig. 4.19).

*4.4.3 Heterogeneous poikilitic olivine gabbros (44 to 48 mbsf)*

Olivine and clinopyroxene compositions vary with texture in both samples of heterogeneous poikilitic olivine gabbro studied (see also Section 3.3.3). Olivine is less forsteritic ($Fo_{76-7}$ versus $Fo_{80-82}$) in the coarse portion of the sample from 47.33 mbsf and more forsteritic in the crescumulate at 46.30 mbsf ($Fo_{85}$ versus $Fo_{83-4}$) than in their respective finer grained portions. Note that the finer grained portions also have lower modal clinopyroxene contents. The Mg# of clinopyroxene shows the same compositional variation as olivine Fo content. The clinopyroxene oikocryst enclosing crescumulate olivine (46.30 mbsf; Fig. 3.8) is the most magnesian ($Mg\#_{86-90}$) and Cr-rich ($Cr_2O_3$ up to 1.3 wt%; Fig. 4.15b) analysed. This clinopyroxene is as Cr-rich as clinopyroxene in spatially associated abyssal peridotite (0.96-1.4 wt% $Cr_2O_3$; Stephens, 1997; Niida, 1997; Ross & Elthon, 1997b; Fig. 4.20). In contrast, clinopyroxene in both portions of the sample from 47.33 mbsf has <0.32 wt% $Cr_2O_3$. Plagioclase in this sample and the clinopyroxene-poor portion of the sample from 46.30 mbsf is similar in composition to the strongly zoned plagioclase in coarse poikilitic olivine gabbros, except with thinner An-poor rims. However, within the olivine crescumulate (46.30 mbsf) plagioclase is smoothly normally zoned ($An_{70-66}$), with neither embayed, nor markedly Y-rich, cores.

Incompatible trace element abundances in the cores of the clinopyroxene oikocryst from 46.30 mbsf (Fig. 3.8) are as low as in any clinopyroxene analysed. The composition of this clinopyroxene, and a clinopyroxene oikocryst from 64.87 mbsf (see Fig. 4.16) are compared to the composition of clinopyroxene in spatially associated abyssal peridotites (ODP Site 920) in Fig. 4.20. Clinopyroxene in the peridotites is only slightly more depleted in HREE than in the oikocrysts, but it is massively more depleted in LREEs (Fig. 4.20). Negative Zr and Ti anomalies exist in both the clinopyroxene in the Site 920 abyssal peridotites and in the primitive clinopyroxene in Hole 923A gabbros. Such depletions are commonly observed in clinopyroxene from abyssal peridotites (Salters & Shimizu, 1989; Johnson *et al.*, 1990; section 1.4.6). The origin of Zr and Ti anomalies is discussed in Chapter Five.

*4.4.4 Brown-pyroxene gabbros*

Brown-pyroxene gabbros consistently have more evolved major element mineral compositions than poikilitic olivine gabbros. In addition, the compositions of mafic phases correlate with the grain size. In spatially associated samples of brown-pyroxene gabbro that have different grain sizes, olivine is 1 to 2% more

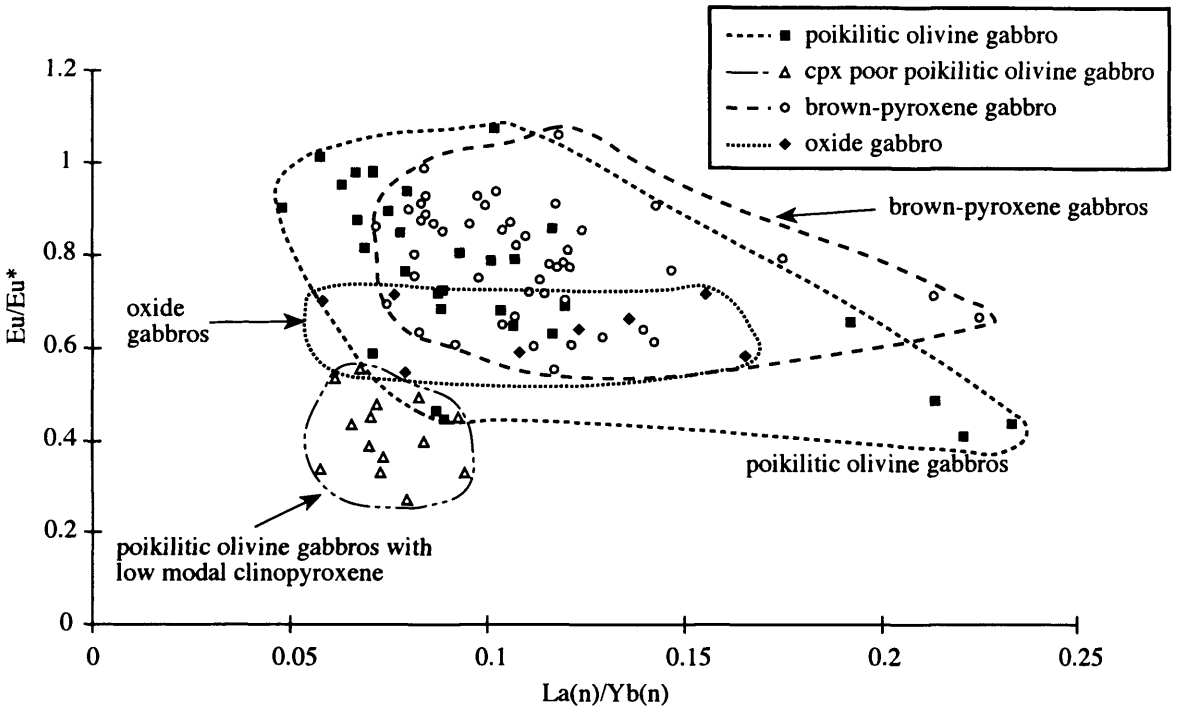


Fig 4.19 Chondrite normalised La/Yb versus Eu/Eu* in clinpyroxene. Eu/Eu* is a measure of the size of Eu anomaly. Note that clinopyroxene-poor poikilitic olivine gabbros ( 67.73 and 47.33 mbsf) and the troctolites (30.26 and 52.98 mbsf) have large negative Eu anomalies but low La/Yb, and are compositionally similar to one another. Note also that oxide gabbros show little variation in Eu anomaly.

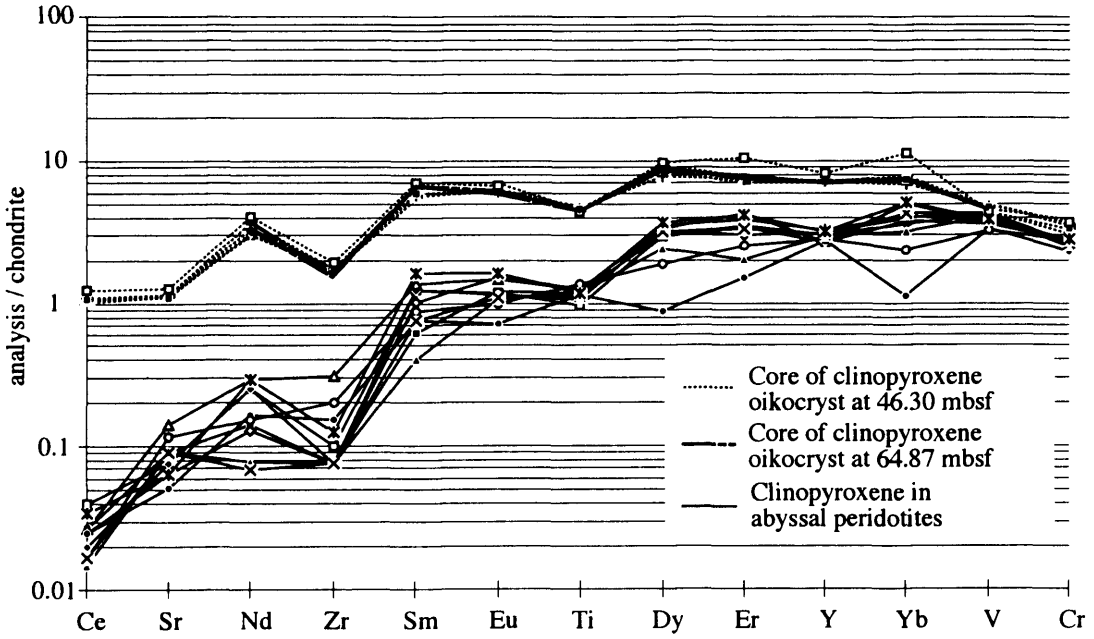


Fig. 4.20 Comparison of the compositions of the most depleted clinopyroxene in gabbros from ODP Site 923A (samples from 46.30 & 64.87 mbsf) and clinopyroxene in spatially associated abyssal peridotites (ODP Site 920; Ross & Elthon, 1997b). Note the divergence towards the LREE with the clinopyroxene in peridotite being far more depleted in these very incompatible elements but only moderately more depleted in moderately incompatible elements (e.g. HREE). Furthermore, clinopyroxene from 46.30 mbsf has a higher Cr abundance than clinopyroxene in spatially associated abyssal peridotites suggesting little or no clinopyroxene or Cr-spinel precipitation occurred between melt generation and precipitation of this clinopyroxene crystal.

forsteritic in fine grained than in coarse grained samples, independent of whether the grain size variation is sharp or gradational. The average $Mg^{\#}$ of clinopyroxene within a sample varies in unison with the forsterite content of olivine. However, this at least in part reflects the fact that coarse clinopyroxene have ~1 mm wide more evolved rims (lower Mg#, higher Ti; e.g. Fig. 4.21b). Plagioclase in brown-pyroxene gabbros shows both weak normal and reverse zoning, with a maximum observed within-crystal variation of 5% An. No variation in plagioclase anorthite content with grain size has been observed, although this may be due to within-sample heterogeneity.

Fig. 4.21a-i shows a detailed traverse through a cumulus clinopyroxene-plagioclase pair in a coarse brown-pyroxene gabbro (31.31 mbsf). Millimetre-scale rims on both phases are normally zoned in major elements and most trace elements. Clinopyroxene Mg# (Fig. 4.21b) increases slightly from the core ($Mg\#_{83}$) to 1.5 mm from the rim ($Mg\#_{85}$) and then decreases smoothly to its rim ($Mg\#_{79}$). The abundance of Al in clinopyroxene varies in a complex manner (Fig. 4.21c) especially when split between crystal sites. Al in the Z site increases towards the rim of the crystal in unison with increased Ti abundance (Fig. 4.21d) as at 64.87 mbsf (Fig. 4.16). Again this suggest that the Al content of the Z site varies in order to achieve charge balance.

Incompatible trace element abundances in clinopyroxene show two important zoning characteristics. Firstly, between ~1 and ~2 mm from the grain boundary with plagioclase, incompatible trace element abundances in the clinopyroxene drop slightly (Figs. 4.21d and 4.21e). Secondly, although all incompatible trace element abundances increase dramatically towards the rim over the outer ~1 mm of the crystal, different elements are enriched to different extents; i.e. incompatible trace elements are fractionated relative to one another (Fig. 4.21f). Furthermore, the P abundance drops in the outer 0.5 mm of the clinopyroxene crystal (Fig. 4.21e), suggesting co-precipitation of apatite. $Eu/Eu^{*}$ and $Ti/Ti^{*}$ drop over the outer 1 mm of the clinopyroxene crystal (Fig. 4.21f), however, Eu and Ti abundances increase consistent with co-precipitation of plagioclase and ilmenite.

Plagioclase and clinopyroxene show contrasting zonation patterns as they do in the sample from 64.87 mbsf (Fig. 4.16). Plagioclase shows little systematic variation in anorthite content, except a small (~0.5 mm) normally zoned rim (Fig. 4.21h). Variation in trace element abundances in this plagioclase are complex. K and Y are homogeneous throughout the crystal, whereas LREE and Ba abundances, and the La/Nd ratio, increase towards the rim (Fig. 4.21i). This contrasts with clinopyroxene in which there is no systematic variation in La/Nd (Fig. 4.21f) and Y is more abundant at the rim than the core (Fig. 4.21e). These differences between plagioclase and clinopyroxene are similar to those observed

in the sample from 64.87 mbsf (Fig. 4.16). Irregularly shaped plagioclase chadacrysts enclosed within clinopyroxene from 31.31 mbsf (Fig. 4.21a) have similar incompatible element abundances and La/Nd ratio as the cumulus plagioclase rim. Clinopyroxene adjacent to these chadacrysts has even higher incompatible element abundances than its rim at the cumulus plagioclase (Fig. 4.21g).

*4.4.5 Oxide gabbros*

Oxide gabbros have generally more evolved mineral compositions than both poikilitic olivine gabbros and brown-pyroxene gabbros (e.g. Figs. 4.3, 4.5, 4.6, 4.9, 4.11, 4.15). Incompatible trace element abundances in plagioclase in oxide gabbros from 19.38 and 21.08 mbsf are similar, except for plagioclase enclosed within cumulus clinopyroxene at 21.08 mbsf. This plagioclase has lower incompatible element abundances than the other plagioclase in oxide gabbros. The concentration of Eu in plagioclase in oxide gabbros increases more for a given increase in the abundance of LREEs than it does in other lithologies, suggesting Eu behaved more incompatibly during the genesis of oxide gabbro than other lithologies. This is also observed, but only weakly, in clinopyroxene from 21.08 mbsf but not in clinopyroxene from 19.38 mbsf. The REE pattern of plagioclase in the oxide gabbro from 19.38 mbsf is enigmatic, having lower HREE abundances than would be predicted by the slope of the LREE (Fig. 4.22). This is not observed in any clinopyroxene analyses, and all other plagioclase have HREE abundances to low to be precisely measured by ion probe. Thus, it is unclear if this is real or an artefact of analytical uncertainty. Clinopyroxene is relatively homogenous in terms of Mg# in the samples from 19.38 and 66.58 mbsf. However, coarse crystals in the sample from 21.08 mbsf have significantly more magnesian cores than rims. Clinopyroxene in the sample from 19.38 mbsf has the highest incompatible element abundance of any clinopyroxene analysed (e.g. HREE abundances of 40 to 100x chondrite), with the highest concentration in a clinopyroxene rim adjacent to oxides. In contrast, the rim of the same clinopyroxene adjacent to plagioclase has incompatible element abundances only slightly higher than the clinopyroxene core. Not surprisingly, clinopyroxene in oxide gabbros have large negative Ti anomalies.

*4.4.6 Leucocratic veins*

Only one leucocratic vein has been studied (30.63 mbsf). This sample contains the most evolved plagioclase ($An_{7-35}$, $Or_{0-2}$) and low-Ca pyroxene (Mg# 58 to 60) in the core. The low-Ca pyroxene is displaced to higher Mn abundance for its Mg# compared to the Mn-Mg# trend defined by low-Ca pyroxene in poikilitic olivine gabbros and brown-pyroxene gabbros. REE-rich, euhedral to anhedral chlorapatite

**Fig. 4.21 Geochemical traverse through cumulus clinopyroxene and plagioclase in a brown-pyroxene gabbro (31.31 mbsf)**

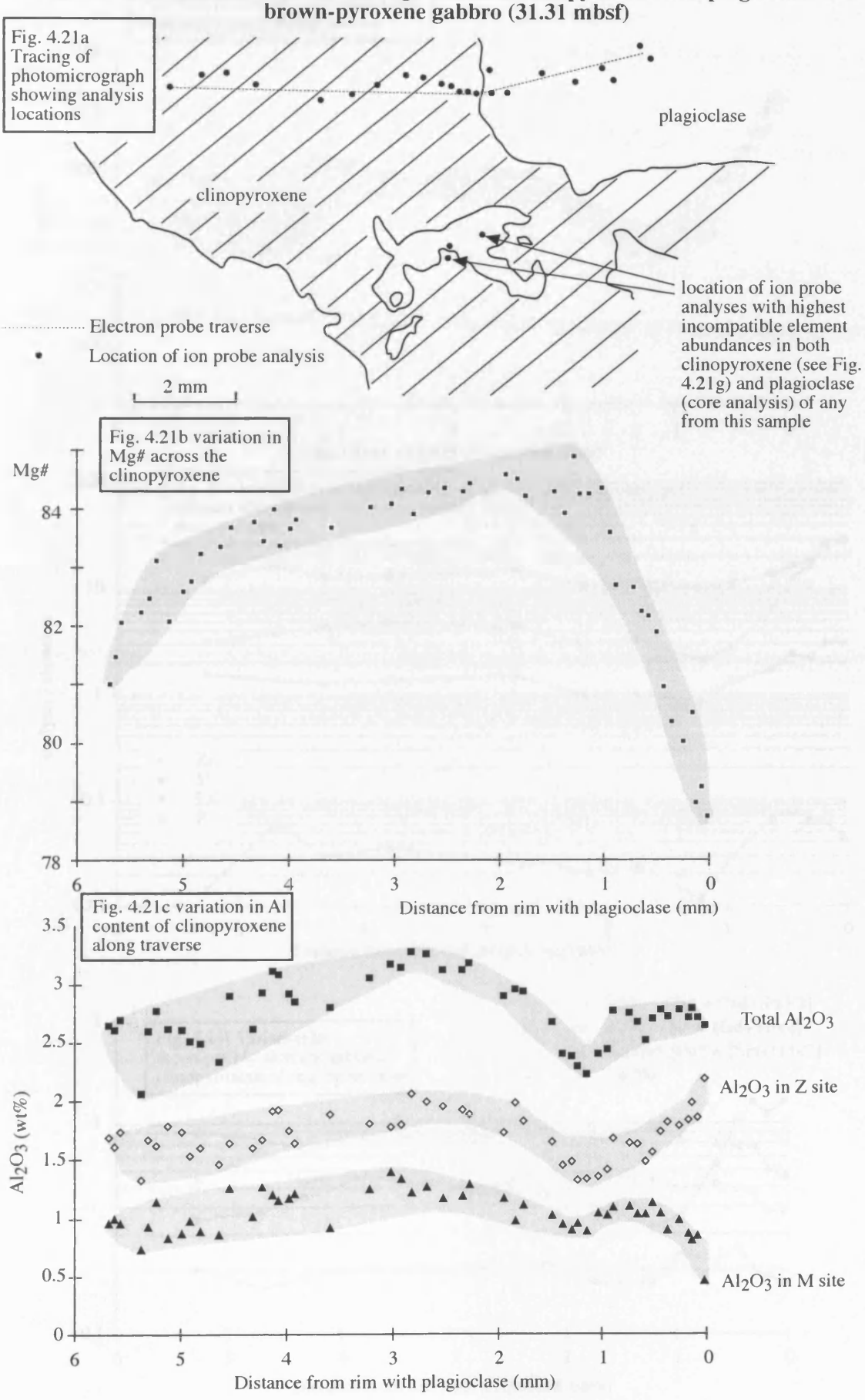

Fig. 4.21d Variation in Ti abundance in clinopyroxene along traverse

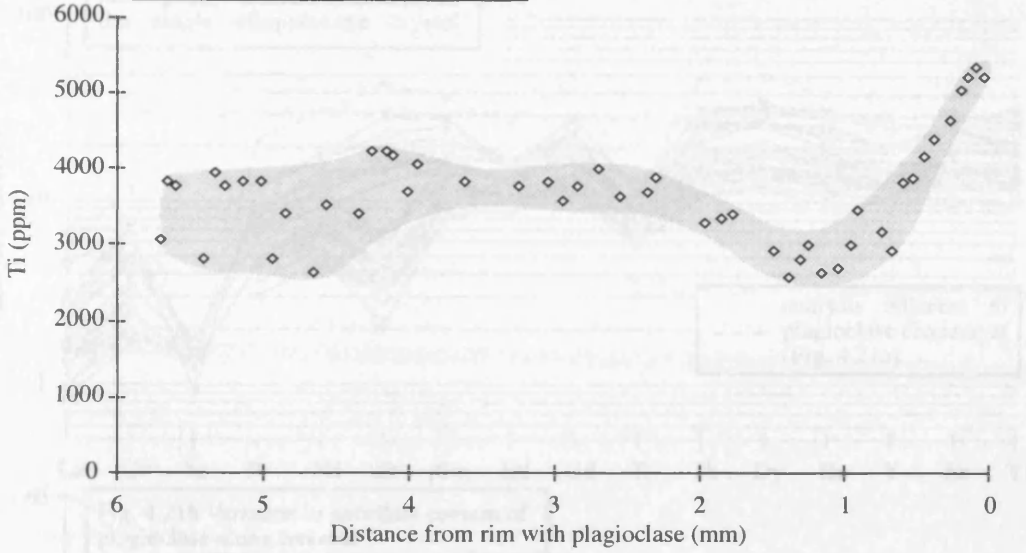


Fig. 4.21e Variation in incompatible element abundances in clinopyroxene along traverse

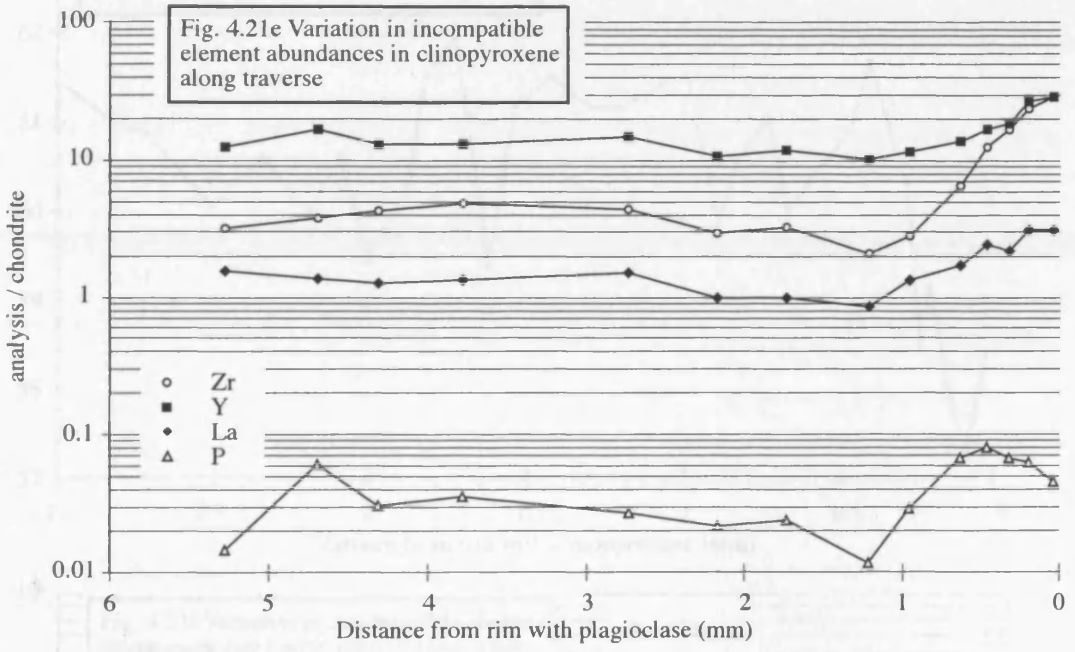


Fig. 4.21f Variation in incompatible element ratios in clinopyroxene along the traverse

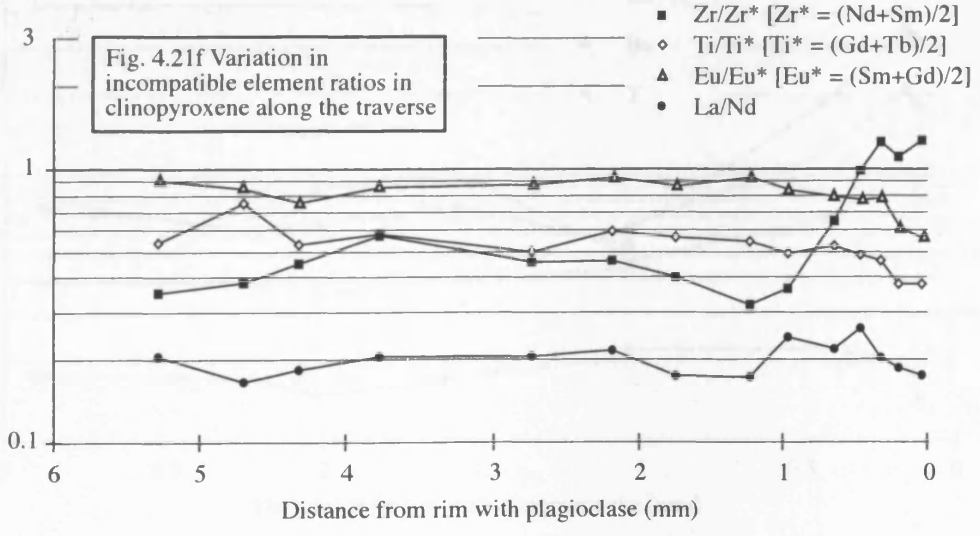

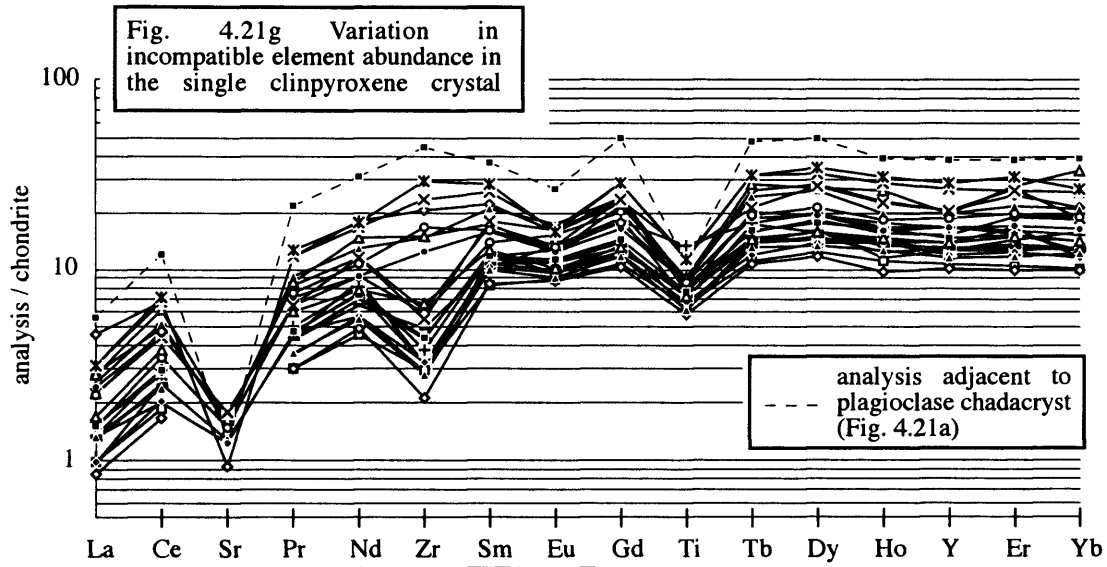
Fig. 4.21g Variation in incompatible element abundance in the single clinpyroxene crystal
100
10
1
analysis / chondrite
analysis adjacent to plagioclase chadacryst (Fig. 4.21a)
La Ce Sr Pr Nd Zr Sm Eu Gd Ti Tb Dy Ho Y Er Yb

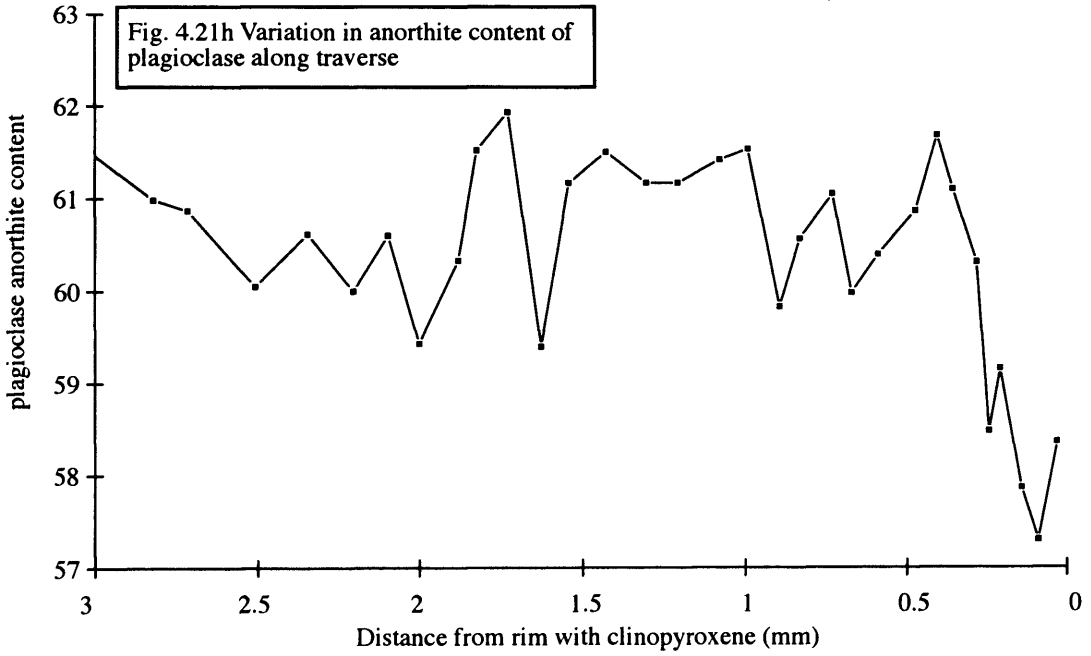
Fig. 4.21h Variation in anorthite content of plagioclase along traverse
63
62
61
60
59
58
57
plagioclase anorthite content
3 2.5 2 1.5 1 0.5 0
Distance from rim with clinopyroxene (mm)

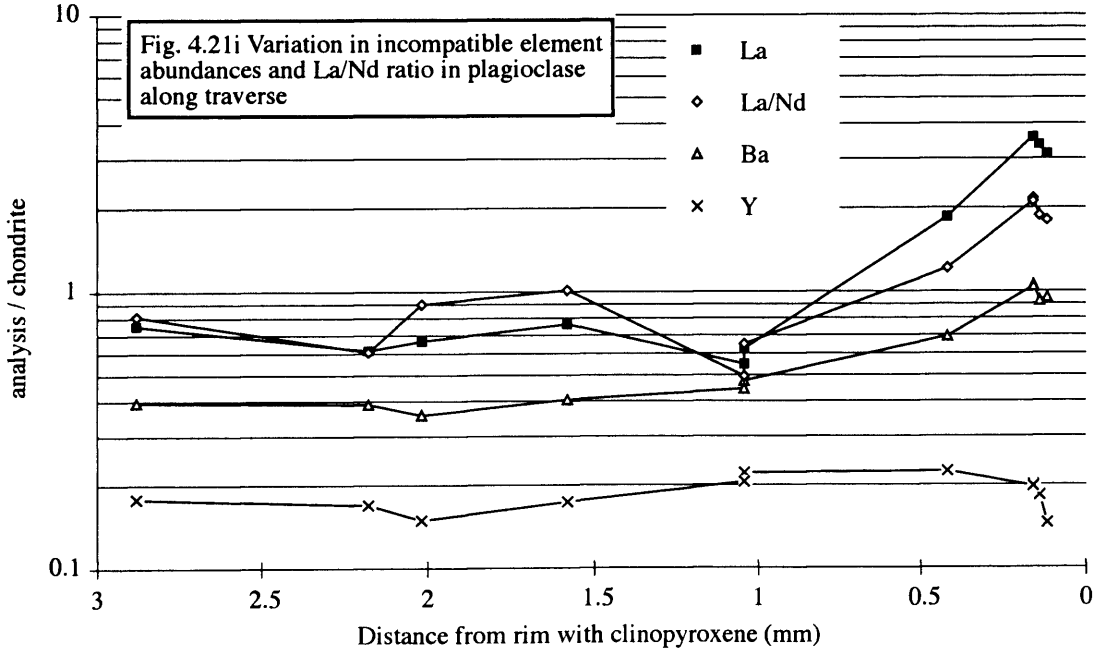
Fig. 4.21i Variation in incompatible element abundances and La/Nd ratio in plagioclase along traverse
La
La/Nd
Ba
Y
10
1
0.1
analysis / chondrite
3 2.5 2 1.5 1 0.5 0
Distance from rim with clinopyroxene (mm)

Fig. 4.21 (a-i) Detailed traverse through a clinopyroxene and adjacent plagioclase in a coarse brown-pyroxene gabbro (31.31 mbsf). (a) tracing of a photomicrograph showing location of electron probe traverse and ion probe analyses; (b) variation in Mg# in clinopyroxene; note the gradual increase in Mg# from the core towards the rim (5 to 1.5 mm) prior to dropping in the outer 1.5 mm before the rim. Millimeter-scale normal zoning occurs in all coarse clinopyroxene in brown-pyroxene gabbros. The drop in Mg# between 5 to 6 mm from the rim is associated with clinopyroxene re-crystallisation and orthopyroxene exsolution (see section 3.8); (c) variation in $Al_2O_3$ in clinopyroxene. If distributed between crystallographic sites (Al in Z = 2-Si, remainder assigned to M1 site), the Al abundance of the Z site correlates with the Ti abundance, suggesting that the variation in Z site abundance is controlled by charge balancing the increasing Ti abundance; (d) variation in Ti abundance in clinopyroxene showing significant zoning; (e) variation in chondrite normalised La, Y, Zr and P, in clinopyroxene. The large increase in incompatible element abundances towards the rim suggest that during solidification of the cumulate the interstitial melt was highly incompatible element enriched. The drop in P abundance in the outer 0.5 mm of the clinopyroxene crystal suggests co-precipitation of apatite. Note also the drop in incompatible element abundances ~1 to 2 mm from the clinopyroxene rim; (f) variations in Ti/Ti*, Zr/Zr*, Eu/Eu* and La/Nd towards the clinopyroxene rim show that incompatible element were fractionated with respect to one another in the interstitial melt. Note the trough in Zr/Zr* between 1 to 2 mm from the rim coincides with a drop in incompatible element abundances (Fig.4.21e); note also the gradual decrease in Ti/Ti* over the outer 1 mm of the crystal. However, the Ti abundance in this crystal increases towards the rim (Fig. 4.21d); (g) spidergram of incompatible element abundances for all analyses of clinopyroxene shown in Fig. 4.21a. The analysis with the highest abundances (dashed) is adjacent to the plagioclase chadacrysts (Fig. 4.21a); (h) anorthite content in plagioclase along the traverse shown in Fig. 4.21a. Unlike other plagioclase analyses a 5 μm electron beam was used for plagioclase analyses in traverses to make it easier to avoid cracks whilst sticking closely to the traverse line; (i) variation in incompatible trace element abundances in plagioclase; note the increasing La/Nd ratio towards the rim which is not observed in clinopyroxene, and little variation in Y abundance despite a significant increase in Y abundance from the core to the rim in clinopyroxene (Fig. 4.21g).

(1 to 1.5 wt% Cl; Fig. 4.13) is an abundant accessory phase. Fig. 4.14 shows that these apatites have similar REE profiles to apatites from ODP Site 894 at the Hess Deep (Gillis, 1996), although offset to higher abundances. Some apatite crystals have slightly altered rims that have lower REE and Cl abundances than their cores, suggesting the high Cl and REE abundances are primary and that alteration leached these elements.

### 4.5 Oxygen fugacity calculated from ilmenite-magnetite pairs

The compositions of co-existing ilmenite-magnetite pairs have been used to calculate equilibrium oxygen fugacities ($fO_2$) and temperatures via the formulations of Powell and Powell (1977). These are plotted in Fig. 4.23 along with equivalent data for ODP Site 735B (Natland *et al.*, 1991). Brown-pyroxene gabbros and oxide gabbros lie on a similar T-$fO_2$ trend to gabbros from Site 735B, however the leucocratic vein (30.63 mbsf), has a different trend. Equilibrium temperatures are all <700°C, indicating that subsolidus, not magmatic, conditions are recorded. Thus, the $fO_2$ conditions during crystallisation are unknown. However, the trend towards more reducing conditions with decreasing temperature in oxide gabbros and brown-pyroxene gabbros (from near the NNO buffer to near the QFM buffer) suggests that oxygenating hydrothermal alteration did not control the trends (Natland *et al.*, 1991).

### 4.6 Model melt compositions

Using the distribution coefficients from Appendix A.I, melt compositions in equilibrium with clinopyroxene and plagioclase have been calculated. These are compared with each other and with spatially associated MORB in Fig. 4.24. Melt compositions modelled from both plagioclase and clinopyroxene span a considerably larger compositional range than MORB. Melts in equilibrium with plagioclase cover a range of abundances from lower to higher than found in MORB. Melts calculated to be in equilibrium with clinopyroxene range from near the lowest abundances found in MORB through to far higher concentrations.

The most primitive melt compositions calculated to be in equilibrium with plagioclase have positive Sr anomalies which develop into negative anomalies with increasing incompatible element abundances. These also have very large negative Zr anomalies, although the distribution coefficient used (0.01; Blundy, 1997a) is poorly constrained and may be too large. $La_{(n)}/Nd_{(n)}$ ratios of melts modelled to be in equilibrium with plagioclase range from 0.25 to 1.3; a much wider range, and extending to more LREE-depleted compositions, than MARK area MORB ($La_{(n)}/Nd_{(n)}$>0.55) In detail the melt compositions modelled from the clinopyroxene that has the lowest incompatible element abundances

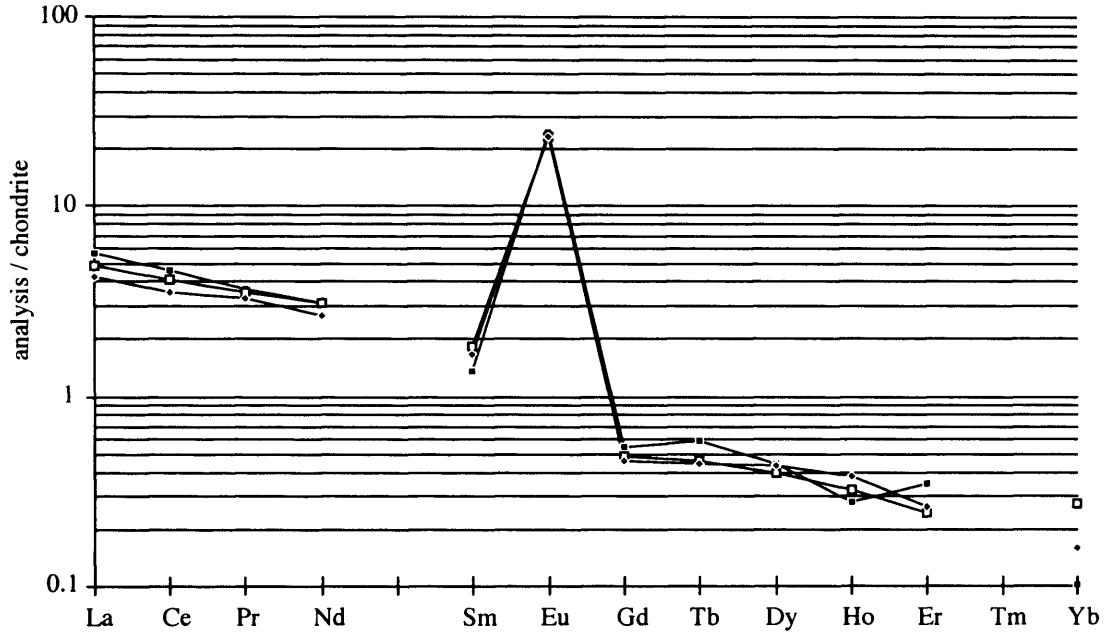


Fig 4.22 Plagioclase REE abundances in an oxide gabbro from 19.38 mbsf. Spidergram shows apparent step at the middle REE to lower HREE abundances than predicted by projection of the LREE trend. It is unclear whether this is real, or an analytical artefact.

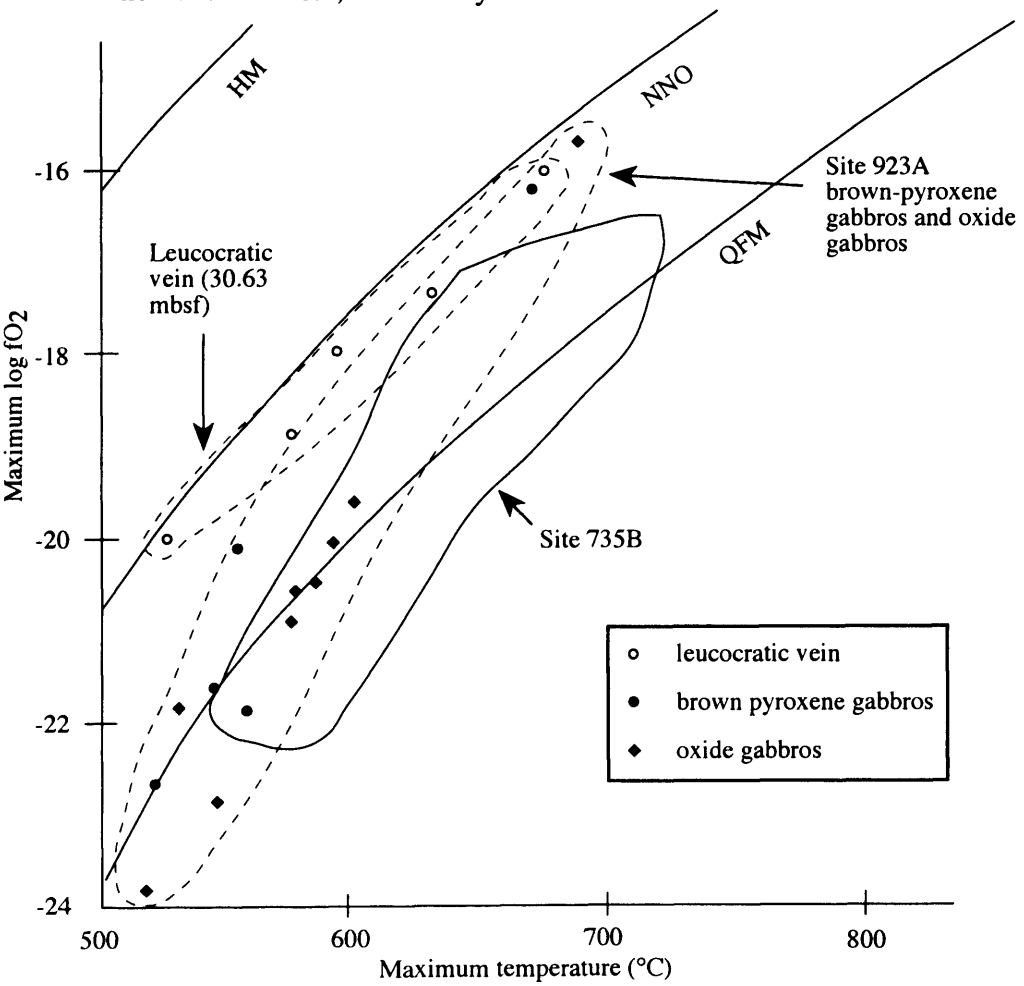


Fig. 4.23 Log $fO_2$ versus temperature calculated from ilmenite - magnetite pairs using the formulations of Powell and Powell (1977). Also shown is the field for gabbroic rocks from ODP Site 735B on the SW Indian Ridge (Natland et al., 1991). HM - heamatite-magnetite buffer; NNO - nickel-nickel oxide buffer; QFM - quartz-fayalite-magnetite buffer

have slightly lower LREE abundances, and higher HREE abundances (i.e. lower La/Yb) than the MARK area basalts with the lowest REE abundances. Melt compositions modelled from clinopyroxene have negative Ti anomalies which are more negative the higher the incompatible element abundances. Equilibrium melt compositions are modelled more extensively in Chapter Five where it is suggested that the anomalous parental melt compositions recorded in plagioclase and clinopyroxene are a fundamental part of the mid-ocean ridge magma plumbing system, even though they may never be erupted.

**4.7 Conclusions**

Several important, and unexpected observations about the geochemistry of the rocks from ODP Hole 923A have been made in this chapter. The most significant of these are:

(i) Very large variations in incompatible element abundances occur within plagioclase and clinopyroxene, both within individual crystals and between samples from different levels in the hole. These do not however correlate well with variations in major elements.

(ii) Fractionation of incompatible elements from each other occurs with increasing incompatible element abundance. For example, with increased incompatible element abundances Zr is enriched with respect to Y and REE in excess of a one to one correlation. This is modelled in Chapter Six where it is suggested that this is due to reaction between the crystals and an evolving migrating interstitial melt.

(iii) Incompatible element abundances and ratios correlate with rock texture. For example, clinopyroxene in troctolites, and other poikilitic olivine gabbros that have low clinopyroxene abundances, have high concentrations of incompatible elements, and large negative Eu anomalies compared to other clinopyroxenes analysed.

(iv) The occurrence of LREE-depleted plagioclase, despite D's for plagioclase increasing from Yb-La, suggests that the parental melt was highly LREE depleted, far more so than MORB. This is discussed in depth in Chapter Five where it is suggested that this records growth of plagioclase from incompletely aggregated MORB.

(v) Zr/Zr* and Ti/Ti* are both less than one in the most primitive clinopyroxene. This is commonly observed in clinopyroxene in abyssal peridotites and suggests that despite Zr and Ti behaving similarly to adjacent REE in erupted MORB (e.g. (Sun & McDonough, 1989) they do not behave similarly throughout the magma plumbing system beneath mid-ocean ridges.

(vi) Trace element zoning patterns are different in coexisting plagioclase and clinopyroxene. In particular, in plagioclase the La/Nd ratio increases with

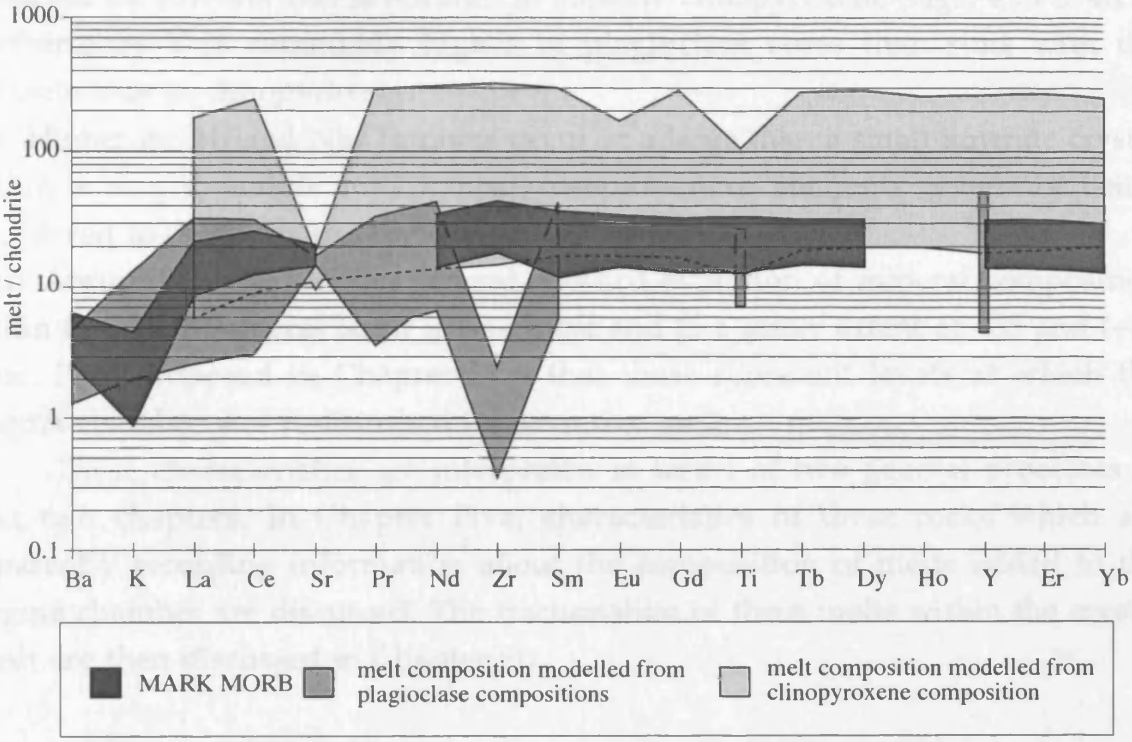


Fig. 4.24 Comparison of model melt compositions calculated from clinopyroxene and plagioclase compositions using the distribution coefficients in Appendix A.I and spatially associated MORB. Note that some model melt compositions calculated to be in equilibrium with plagioclase have much lower LREE abundances than MARK area MORB. MARK area MORB from Bryan et al., 1981; Dosso et al., 1993; Reynolds & Langmuir, 1997)

increased La however this is not seen in adjacent clinopyroxene (Figs. 4.16 & 4.21). Furthermore Y is commonly higher in plagioclase cores than rims with the opposite true in clinopyroxene.

(vii) Higher Zr/Hf and Nb/Ta ratios occur in a large than a small ilmenite crystal within a single sample (67.73 mbsf) despite these elements generally being considered to be geochemically similar.

(viii) Abrupt reversals in the general upward evolution of mineral composition within the cored interval occur at ~44 mbsf and to a lesser extent at ~35 and (~30 mbsf. It is proposed in Chapter Five that these represent levels at which the magma chamber was replenished by primitive melt.

These characteristics are interpreted in terms of two general processes in next two chapters. In Chapter Five, characteristics of these rocks which are apparently recording information about the composition of melts added to the magma chamber are discussed. The fractionation of these melts within the crystal mush are then discussed in Chapter Six.

# Chapter V: Open system magma chamber processes beneath the Mid-Atlantic Ridge, 23°N

## 5.1 Introduction

The openness of a magma chamber refers to the degree of mass transfer into, and out of, the chamber. Addition of mass occurs due to replenishment with magma and assimilation of wall rock. Loss of mass occurs via extrusion and intrusion. The degree of openness of the magma chamber that crystallised to form the gabbroic rocks recovered at ODP Hole 923A (referred to here as "the magma chamber") is of interest in this study for two reasons: (i) open system processes can significantly affect the liquid line of descent of the magma body, and thus the composition of erupted basalts (e.g. O'Hara, 1977, O'Hara & Mathews, 1981), and (ii) mineral compositions should record information about the composition of the melts added to the chamber. This is important in understanding where aggregation and mixing of the diverse melt compositions produced within the mantle occurs. These processes are discussed in turn below after presenting evidence that the magma chamber was open.

## 5.2 Evidence that the magma chamber was open

### *5.2.1 Compositional evidence for an open magma chamber*

The clearest evidence for replenishment are the interruptions of the general upward evolution of mineral compositions by "spikes" to more primitive major element compositions (Fig. 4.15a) in poikilitic olivine gabbros. This suggests two major replenishment events (at ~68 mbsf and ~48 mbsf) and two smaller replenishments (at ~35 mbsf and ~30 mbsf). Redistribution of crystals or melt within a magma chamber, such as crystal bearing plumes descending from the roof or side walls under gravity, is unlikely to be responsible for the scale of compositional variation observed (>10% increases in An and Fo). Redistribution of crystals also cannot easily explain the high Fo content of crescumulate olivine or high Mg# of poikilitic clinopyroxene, both of which grew *in situ*.

Evidence for assimilation is less conclusive, but it is tentatively suggested below that assimilation occurred on the basis of high chlorine contents of some apatite crystals. There is no evidence for loss of magma from the chamber through eruption or intrusion. However, both processes are expected to be common in mid-ocean ridge magma chambers and are unlikely to be recorded in the cumulates.

### *5.2.2 Textural evidence for an open magma chamber*

Plagioclase crystals in poikilitic olivine gabbros with embayed anorthitic cores overgrown by more albitic rims provide evidence for disequilibrium conditions

during plagioclase growth. Embayed crystal forms can record either resorption or growth of skeletal crystals during rapid cooling (Lofgren, 1980). The fact that the cores are more anorthitic than their rims suggests embayments formed during resorption, not growth, because disequilibrium growth leads to precipitation of plagioclase more albitic than the equilibrium composition. Melting of plagioclase crystals during decompression of a plagioclase-phyric magma cannot alone explain these textures because as pressure increases the plagioclase in equilibrium with a given melt composition becomes more albitic (Panjasawatwong *et al.*, 1995) whereas the embayed cores are more anorthitic than their rims.

The best explanation for this texture is mixing between two magmas, the cooler of which was plagioclase-phyric. Upon mixing, the plagioclase phenocrysts in the more evolved magma became out of equilibrium and were partially resorbed prior to plagioclase returning to the liquidus. Preservation of these embayed crystals as cores to cumulus plagioclase in poikilitic olivine gabbros suggests addition of this mixed magma to the magma chamber, and plagioclase accumulation in the crystallising boundary layer. Addition of a plagioclase-phyric magma to the (more evolved) magma chamber, without previously mixing it with a more primitive magma would probably result in overgrowth of anorthitic plagioclase by more albitic rims without an initial period of resorption. Thus, it is necessary to invoke the existence of three magmas simultaneously within the magma plumbing system: (i) a relatively primitive plagioclase phyric magma (parental to the embayed cores of plagioclase crystals in poikilitic olivine gabbros; (ii) a plagioclase supersaturated magma with which magma (i) mixed leading to resorption of its plagioclase phenocrysts; and (iii) the resident magma in the Hole 923A magma chamber into which the hybrid magma intruded.

Evidence that plagioclase in poikilitic olivine gabbros is truly cumulus (i.e. accumulated) comes from plagioclase crystal size distributions in poikilitic olivine gabbros (Section 3.4; Fig. 3.9). Thus it is suggested that post-replenishment of the 923A magma chamber plagioclase within the hybrid magma settled into the crystallising boundary layer where solidification resulted in the formation of poikilitic olivine gabbros.

### *5.2.3 Plagioclase settling ?*

If poikilitic olivine gabbros formed through crystallisation of plagioclase-phyric replenishing magma, plagioclase must have been denser than the magma in order to settle. However, Campbell (1978) and McBirney and Noyes (1979), in questioning cumulate theory (e.g. Wager & Brown, 1968), show that plagioclase is commonly less dense than tholeiitic basalt. Two further lines of evidence suggest plagioclase accumulation is unlikely: (i) if the magma is convecting, the plagioclase settling velocity must overcome the convective velocity in order to

settle; and (ii) basaltic melts are non-newtonian (McBirney & Murase, 1984), requiring the settling force to exceed a yield strength to initiate settling. Thus plagioclase settling seems physically unlikely despite the evidence presented above that it occurred.

Two explanations for plagioclase settling are imagined. Martin and Nokes (1988) show that particles suspended in a convecting fluid will eventually be deposited if they have a positive density contrast with the fluid, even if this is insufficient to overcome the convective velocity. This is because the convective velocity decreases to zero at the margins of the convecting region leading to some particles being carried into, but not back out of, this region. Thus, in a convecting magma, crystals with settling velocities too small to overcome the convective velocity will eventually be deposited. This does, however, require a positive density contrast between the crystals and the magma. This may have been the case if the magma contained significant quantities of volatiles although this seems unlikely. Alternatively, plagioclase may have settled in glomerophyric clusters with denser phases (olivine/sulphide). The occurrence of glomerocrysts floating in a clinopyroxene oikocryst at 46.30 mbsf (Fig. 3.8) suggests that these may have been present in the magma replenishing the chamber. Thus, although plagioclase settling may not be a general phenomenon, it seems theoretically possible, and is the best explanation for the observed textures and compositions.

### 5.3 The effect of open system processes on the composition of erupted magmas

Periodic replenishment and tapping of a fractionating sub-volcanic magma chamber (RTF) can lead to the trace element composition of the erupted lavas being considerably different to that of the parental magma even if the parental melt composition is homogeneous (O'Hara, 1977). In this scenario the composition of the erupted magma is critically dependent on the style of magma plumbing. Below, different models of periodically replenished magma chambers are described and their compositional effects noted. Furthermore, fluid dynamic constraints on magma mixing including the change in magma density during fractionation, have been proposed to have significant effect on the compositions of erupted melts (i.e. MORB; Stolper & Walker, 1980; Huppert & Sparks, 1980a; Sparks *et al.*, 1980). These factors are discussed with respect to the compositions of MARK area MORB, and the fractionation densities (Sparks & Huppert, 1984) of gabbros from ODP Hole 923A, followed by a discussion of the style of replenishment of the magma chamber. Further interpretation of the mechanisms of RTF processes and their geochemical consequences is inhibited through the lack of any control on the timing of eruption (if any occurred).

*5.3.1 Compositional effects of magma mixing*

Many models of the compositional effects of open system fractionation exist (O'Hara, 1977; O'Hara & Mathews, 1981; Albarède, 1985; Cox, 1988; DeFant & Nielsen, 1989; Caroff, 1995; Caroff *et al.*, 1997). O'Hara (1977) was the first to model the geochemical effects of open system fractionation on the composition of the erupted basalts. He showed that for a fixed parental melt composition and volume of melt added to the magma chamber, and a fixed ratio of the mass of magma crystallised to that which is erupted, the extruded lava composition will approach a steady state. This is because the masses of melt crystallised and erupted are defined in proportion to the volume of the chamber at the start of each cycle, whereas the mass added to the chamber is defined relative to the initial size of the chamber (Cox, 1988). Thus, in time the chamber volume approaches a steady state; at this stage, the erupted composition also reaches a steady state (i.e. the volume and composition of magma added by replenishment equal those removed into cumulates and by eruption).

The steady state magma composition may be significantly different from that of the parental magma, and from the expected daughter compositions derived through fractional crystallisation (O'Hara, 1977). Repeated mixing can hold the composition of the steady state magma away from the eutectic, possibly within the field of a single phase. Incompatible trace element abundances (absolute and relative) are dominantly controlled by the ratio of the mass of magma crystallised to that erupted in each cycle. Large differences between the incompatible element abundances and ratios in the parental magma and the steady state magma occur if the ratio of the mass of cumulates formed, to mass of magma erupted, is large. However, significant variation in incompatible element abundances is accompanied by large increases in their abundances. In contrast, it is the absolute mass fractions erupting and crystallising that have the stronger control on compatible element abundances. The lower the absolute mass fractions are the higher the abundance of compatible elements. To achieve significant fractionation of incompatible elements, without large decreases in compatible element abundances, the ratio of the mass of the magma precipitated as cumulates to mass of magma erupted must be large, but their absolute values small.

The dynamics of eruption, with respect to replenishment, are a further factor in controlling the composition of the erupted magma. If replenishment is followed immediately by wholesale mixing between the resident and replenishing magmas, followed by eruption, the composition of the erupted magma will lie on a mixing line between the steady state and replenishing magma compositions (Albarède, 1985; Langmuir, 1989). Incompatible trace elements are dominated by the steady state composition, but compatible trace

elements are controlled by the replenishing magma composition. Thus, the erupted magma can have an incompatible element signature unlike its parent, but be apparently primitive in terms of compatible element abundances (Albarède, 1985). However, fluid dynamic models of a primitive magma replenishing a mid-ocean ridge magma chamber predict that the replenishing magma will pond beneath the resident magma and fractionate until its density approaches that of the resident magma (Huppert & Sparks, 1980, see Section 5.3.2). In this case eruption of the steady state magma composition may occur due to the increased magma volume brought about by replenishment. However, whilst the primitive melt is ponded at the base of the main magma body and fractionating in isolation from the remaining magma, elements compatible in the fractionating assemblage are rapidly stripped from the melt. Consequently, the compatible element abundances in the steady state magma composition are higher in a chamber in which mixing occurs immediate post-replenishment than in one in which the replenishing magma fractionates prior to mixing (O'Hara & Mathews, 1981).

The steady state magma chamber discussed above (O'Hara, 1977; O'Hara & Mathews, 1981) is probably not geologically realistic and various more complex models have been proposed. These include: (i) randomised masses of magma crystallised, erupted and replenished (Cox, 1988), (ii) variation in trace element D's due to variation in the fractionating assemblage (DeFant & Nielsen, 1989), (iii) *in situ* fractionation within the chamber (Caroff, 1995), and (iv) systematic variation in the volume of the chamber (inflating or deflating; Caroff *et al.*, 1997). Other variables are also likely, in particular, variation in the composition of the parental melt. The general conclusion of these more complex models is that considerable compositional variation in the erupted composition can be induced through RTF processes even if the parental magma is homogeneous. Furthermore, identification of parental magma compositions may be impossible, and considerable scatter in the composition of erupted lavas can occur even if the parental composition is homogeneous.

In conclusion, periodic replenishment and tapping of magma chambers has important implications for the interpretation of compositional variation in the erupted basalts. However, these effects are not simple to identify, in part due to the plethora of possible processes controlling the composition of magmas erupted from a magma chamber of this kind. Some constraints on the dynamics of replenishment, and thus their compositional effects, are discussed below.

### *5.3.2 Fluid dynamics of magma mixing*

Sparks *et al.* (1980) and Stolper and Walker (1980) model the variation in magma density during fractionation of a hypothetical picritic parental melt and

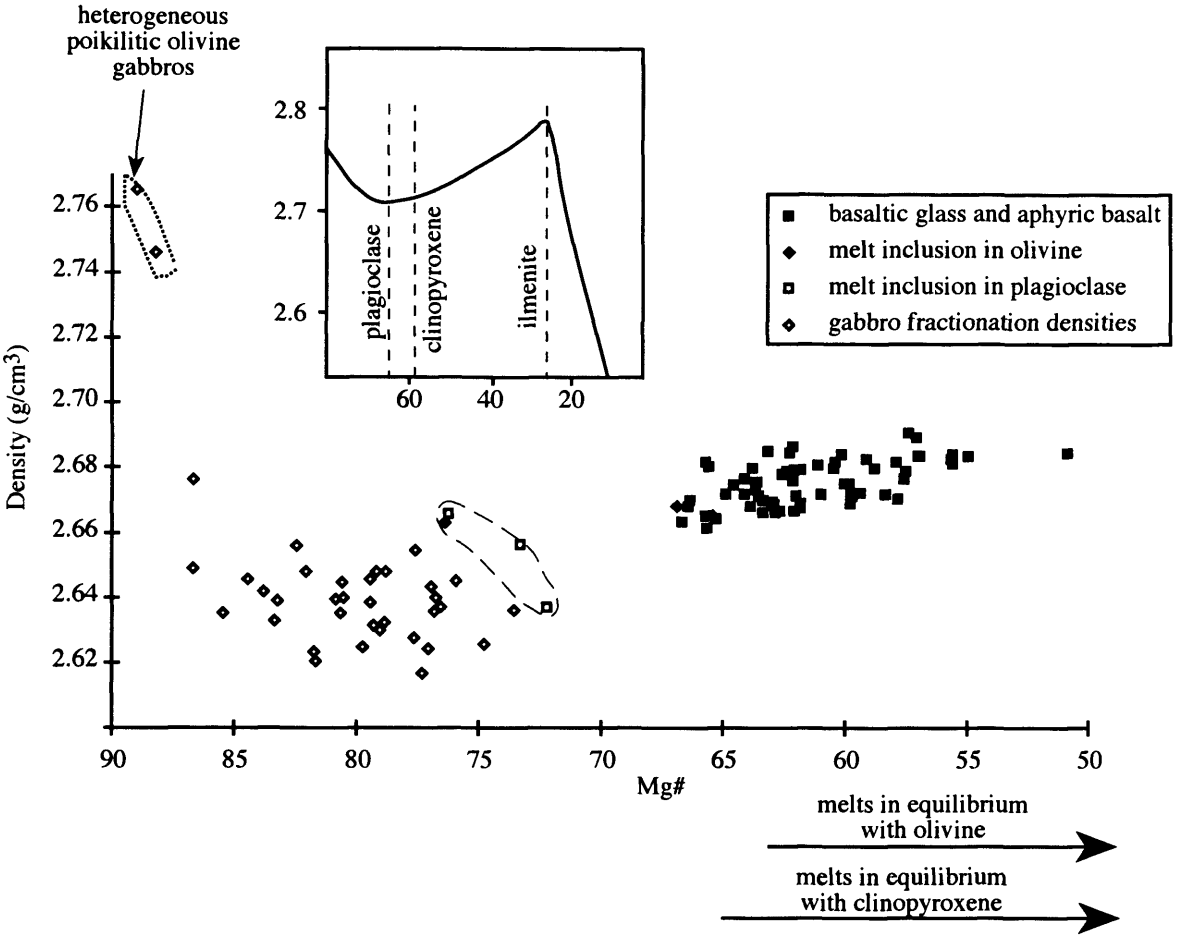


Fig. 5.1 Plot of Mg# versus density (calculated assuming a temperature of 1250°C and 15% Fe as $Fe_2O_3$) for aphyric basalts and MORB glasses from the MARK area (23°10' to 23°40'N; data from Bryan et al., 1981, 1994; Dosso et al., 1993; Reynolds & Langmuir, 1997) showing the common trend in MORB of an increase in density with increased fractionation. Also shown are six reconstructed melt inclusion from phenocrysts from this area (Sullivan, 1991). The most primitive of these (dashed field) show a trend of decreasing density with fractionation. This qualitatively matches the trend shown in the inset for fractionation of picritic basalt (Stolper & Walker, 1980). Fractionation densities for whole rock gabbro from Hole 923A are shown as open diamonds (Cannat, Karson, Miller et al., 1995; Gaggero & Gazzotti, 1996). Fractionation densities (Sparks & Huppert, 1984) are calculated as the density of the components in the melt that go into making the rock. Note that the fractionation densities for samples from the heterogeneous lithology (dotted field) are suitable to force the residual melt density down with fractionation, whereas all other gabbroic samples have fractionation densities suitable to increase the melt density with fractionation. Fractionation densities for the range of mineral compositions within the core are: plagioclase - 2.52 to 2.44; clinopyroxene - 2.74 to 2.8; olivine 3.04 to 3.26; and ilmenite ~4.5 g/cm$^3$ calculated for the most primitive and evolved mineral compositions found in the cored interval respectively (excluding the leucocratic vein). The arrows show the Mg#s of melts calculated to be in equilibrium with olivine and clinopyroxene from Hole 923A. The inset shows the trend for fractionation of a hypothetical picritic basalt (Stolper & Walker, 1980) with the onset of fractionation of plagioclase, clinopyroxene and ilmenite shown. Globally, most MORB plot near the density minimum, and on the increasing density with fractionation limb of this curve.

find that initially the melt density decreases, then with further fractionation it increases (see inset in Fig. 5.1). Melt densities calculated from the composition of sampled MORBs generally increase with decreasing Mg#; i.e. they plot on the increasing density with increased fractionation portion of the hypothetical fractionation versus density curve (Fig. 5.1). They interpreted this as indicating that density variation during fractionation is significant in determining a magmas eruptability. Huppert and Sparks (1980a) propose that this is due to magma chambers beneath mid-ocean ridges acting as density filters with dense primitive melt ponding at the base of a more fractionated magma chamber. In this model fractionation within the primitive magma leads to a drop in melt density prior to mixing into the eruptable portion of the magma chamber.

The densities of the melts parental to MORB glasses and aphyric basalts from the MARK area have been calculated using the method of Bottinga and Weill (1970) assuming a temperature of 1250°C (the lowest temperature for which Bottinga and Weill (1970) provide partial molar volume data), 15% of the total Fe as $Fe_2O_3$, and zero volatile content. The results are shown in Fig. 5.1. Although the absolute magma densities calculated are probably inaccurate, the general trend of increasing density with fractionation is unlikely to be affected. Also shown are primitive melt compositions reconstructed from melt inclusions (Sullivan, 1991) which show a negative Mg# versus density correlation. This fits qualitatively with the trend suggested for fractionation of a picritic parental melt (Stolper & Walker, 1980; Sparks *et al.*, 1980; see inset in Fig. 5.1); i.e. these melt inclusions may record compositions that could not be erupted due to their high density. Potential errors in these calculations come from the assumed temperature and $Fe^{2+}/Fe^{3+}$ ratio used, and ignoring the effect of dissolved volatiles and entrained phenocrysts. The use of a lower temperature would lead to a minor increase in all densities. The effect of decreasing temperature with decrease Mg# (i.e. fractionation) over the temperature and composition range considered will be minor, but will slightly enhance the trend of increasing density with decreasing in Mg#. An increase in the proportion of the Fe as $Fe^{3+}$, as Bryan *et al.* (1981) suggest occurs during fractionation, will reduced the density of the magma counteracting the increase in density due to increased Fe abundance. However, this effect is likely to be small. The effects of entrained phenocrysts and bubbles, and dissolved volatiles, all of which are unaccountable for in this modelling, probably outweigh the variations in temperature and oxidation state of iron.

Basalt Mg#s calculated to be in equilibrium with olivine and clinopyroxene ($Kd_{ol} = 0.30$, $Kd_{cpx} = 0.227$; $Kd = Mg_{melt} \times Fe_{xst} / Mg_{xst} \times Fe_{melt}$; see Section A.I.4) suggest that only the poikilitic olivine gabbros could have crystallised directly from basalt as magnesian as those erupted. However, the measured compositions of minerals may not be the same as their liquidus

compositions due to post-cumulus reaction with interstitial melt probably having decreased the Mg/Fe ratio in all mafic phases to at least a small extent. This is consistent with the cm-scale variation in Mg# (and Fo content) with changes in texture in heterogeneous poikilitic olivine gabbros and brown-pyroxene gabbros. Calculated whole rock fractionation densities (fractionation density = density of the chemical components removed from the melt to produce the solid; Sparks & Huppert, 1984) are also shown in Fig. 5.1. Noticeably, whole rock fractionation densities for the heterogeneous poikilitic olivine gabbros (44 to 48 mbsf) are appropriate as fractionation products prior to the melt reaching the density minimum. In contrast, most Hole 923A gabbros have suitable densities and Mg# as to be the products of crystallisation which would drive MORB to higher density and lower Mg#.

If the major element composition of the melt parental to primitive clinopyroxene and olivine was similar to MORB, Fig. 5.1 predicts that it would have been less dense than more evolved MORB. This suggests that it would rise buoyantly upon replenishing a more evolved magma chamber. However, if the replenishing melt was olivine +/- sulphide phyric, as may be expected given its primitive composition and the cumulus nature of olivine in the heterogeneous lithology, or if the resident magma had a high volatile content, this could outweigh the slightly lower density of the melt to give a bulk density greater than the resident magma. In conclusion, the compositions of the replenishing and resident melts are too poorly constrained to confidently deduce their relative densities.

The fluid dynamics of a mid-ocean ridge magma chamber replenished from below by hot, dense primitive melt has been extensively investigated both theoretically and experimentally (Huppert & Sparks, 1980b; Huppert & Turner, 1981; Campbell & Turner, 1989; Campbell, 1996). Important in controlling the timing of mixing between the replenishing and resident magmas are their densities and the momentum of the replenishing influx. Experimental and theoretical investigations of the passive emplacement of a thin, hot, dense magma layer beneath a thicker, cooler, less dense layer, suggest that the magmas will remain distinct until their densities become similar, at which point wholesale mixing will occur (Huppert & Sparks, 1980a, Huppert & Turner, 1981). During the period of time they remain separate, the large temperature contrast between layers induces vigorous convection in both layers. Crystallisation ceases in the upper, more evolved layer, but is rapid in the hotter, lower layer. Replenishments of this kind have been proposed to explain observations in terrestrial layered intrusions (Weibe & Snyder, 1993; Tegner *et al.*, 1993). Complication is added to this model if the hot dense magma is added to the chamber with excess momentum (Campbell & Turner, 1989). In this scenario a

fountain forms above the input conduit with its height dependent on the excess momentum of the replenishment and the dimensions of the conduit (Campbell & Turner, 1989). Magma already present in the chamber is entrained into the replenishing magma during fountaining. The hybrid magma is still denser than the resident magma and therefore eventually sinks to form a hot, dense, basal layer, which evolves as discussed for the passive emplacement model. If replenishment continues for an extended period, the hybrid layer may become as thick as the fountain is high, at which point further mixing is prevented (Campbell & Turner, 1989; Campbell, 1996).

In the next three sections the fluid dynamics of the magma chamber replenishments which led to crystallisation of the poikilitic olivine gabbro intervals in Hole 923A are discussed. It should be remembered throughout the following discussion however that volatiles dissolved in the melt can play an important role in the fluid dynamics, whilst their presence may not be recorded in the solid rock.

5.3.2.1 The basal poikilitic olivine gabbros form almost the entire cored interval between 68 and 51 mbsf (Fig. 3.1). This suggests either a relatively large-volume replenishment, or repeated small replenishments closely spaced in time. However, the erratic variation in clinopyroxene Cr abundance with height in this section (Fig. 4.15b) cannot be explained simply by a single replenishment. It is more consistent with repeated, or continuous, addition of Cr-rich melt. The systematic decrease in olivine Fo content with stratigraphic height throughout this section can be explained by systematic differences in the degree of compositional modification by reaction with interstitial melt. Alternatively, this may record crystallisation from a hybrid magma that had an increasing proportion of evolved magma in it. The occurrence of relatively evolved brown-pyroxene gabbros with low Cr content at 48 mbsf (Fig. 4.15b), suggests that the crystallising boundary layer was no longer adjacent to primitive magma when these formed. This could be explained by wholesale mixing between the resident and replenishing magmas as their densities became similar due to fractionation of the replenishing magma.

5.3.2.2 Heterogeneous poikilitic olivine gabbros (44 to 48 mbsf) have three important characteristics which suggest that they formed from a replenishment event slightly different to that from which the basal poikilitic olivine gabbros formed. These are: (i) the clinopyroxene Cr abundance at 46.30 mbsf is as high as that in spatially associated peridotites from ODP Site 920; (ii) the difference in olivine Fo content between this interval and the surrounding brown-pyroxene gabbros is 10 to 15%, suggesting a temperature difference between the parental

magmas of 70 to 100°C (see Fig. A.I.3), assuming that the effect of post-cumulus modification on olivine compositions is similar in both lithologies; and (iii) an abrupt return to more evolved compositions at 44 mbsf (Fig. 4.15).

Clinopyroxene Cr abundances in heterogeneous poikilitic olivine gabbros at 46.30 mbsf are as high as in abyssal peridotites from ODP Site 920 suggesting that the replenishing melt cannot have mixed significantly with the evolved (Cr-poor) resident melt prior to clinopyroxene precipitation. This suggests that the replenishment had low momentum and ponded at the base of the chamber. This is consistent with the high calculated whole rock fractionation densities which suggest that heterogeneous poikilitic olivine gabbros precipitated from a melt with a density higher than that of the MORB density minimum (Fig. 5.1). The step to much more evolved compositions at the top of this lithology cannot be explained by fractionation. This is most easily explained by mixing between a primitive melt which precipitated the heterogeneous lithology and a considerably larger volume of more evolved melt. In this model, crystallisation within the hot dense replenished magma led to a decrease in the density of the replenished melt until it approached that in the upper, evolved layer. At this stage wholesale mixing occurred resulting in a sudden return to precipitation of more evolved mineral compositions. Alternatively, the rapid return to more evolved compositions could be explained by the primitive magma draining back into its feeder (Tegner *et al.*, 1993).

5.3.2.3 The upper poikilitic olivine gabbros (~30 and ~35 mbsf), like the heterogeneous lithology, have a very limited vertical extent and do not reset the cryptic stratigraphy (Fig. 4.15). This can best be explained by a process generally similar to that envisaged to explain the heterogeneous lithology (44 to 48 mbsf). However, insufficient sample density does not allow detailed interpretation of fluid dynamics of these replenishments.

### *5.3.3 How should RTF processes beneath slow spreading mid-ocean ridges be modelled?*

The aim of this section has been to investigate the styles of magma mixing that occurred in a sub-ridge magma chamber. Knowledge of the dynamics of mixing provides constraints on the way in which RTF processes should be modelled when investigating compositional variation within MORB suites. However, the above discussion suggests that the style of replenishment is variable. It may be that no simple replenishment model is generally applicable to RTF processes beneath mid-ocean ridges. Good reasons for this to be so include the effects of varying volumes of entrained phenocrysts, magma temperature and magma density (major element composition), and variations in the replenishment

momentum and conduit size. Poikilitic olivine gabbros do, however, provide evidence that the model of Huppert and Sparks (1980a), in which dense melt ponds at the base of the magma chamber, is applicable, at least for some replenishments of mid-ocean ridge magma chambers. A fundamental geochemical characteristic of lavas erupted from a steady state magma chamber fed in this manner is that for a given degree of crystallisation (given increase in incompatible element abundances) the depletion in compatible elements abundances in erupted basalts will be higher than if mixing was immediate upon replenishment. Furthermore, the occurrence of at least three replenishments with 50 m of core suggests that the timescale of replenishments is small.

## 5.4 Evidence for assimilation and it effects

### *5.4.1 Introduction*

Assimilation is widely regarded as an important process in controlling the modification of magma compositions (e.g. O'Hara, 1977). *En masse* assimilation of fresh, basaltic, wall rock will have little effect on the composition of the magma within a mid-ocean ridge magma chamber. However, if assimilation is not *en masse*, or the wall rock has been altered, the effects of assimilation may be significant. Both of these scenarios are more likely than bulk assimilation due to the thermal constraints on the mass of cold fresh basalt which can be assimilated, and the likelihood of hydrothermal alteration of magma chamber walls at mid-ocean ridges. Evidence for preferential ingestion of a Cl-rich assimilate in some mid-ocean ridge magma chambers comes from enrichment of Cl over similarly incompatible elements in some fresh MORB glasses (Michael & Schilling, 1989). They propose that bulk assimilation of altered basalt is unlikely to increase the Cl content in the chamber sufficiently to explain their observations due to thermal constraints on the volume of cold basalt that can be assimilated. They therefore suggest selective assimilation of Cl-rich brines and/or amphibole breakdown as the most likely mechanism to produce Cl-enrichment. The same model has been proposed to explain high $Cl/H_2O$ in basalts from the MARK area (Jambon *et al.*, 1995).

Cl-rich apatite in some samples from ODP Hole 923A suggests the possibility that a similar process may have operated during their genesis. Three sources for the Cl in these apatites are envisaged: (i) Cl derived from the mantle during melting, (ii) Cl derived from assimilation of Cl-rich wall rock, and (iii) Cl addition post-crystallisation during interaction with seawater derived fluids. Below, the crystal chemistry of apatite, with respect to its halogen and REE compositions, is briefly reviewed. It is suggested from this that both the high Cl content of some apatite crystals, and the high REE and Cl abundances in the leucocratic vein (30.63 mbsf), are primary features. This is followed by a

discussion of the behaviour of Cl in magmatic systems. Finally, it is suggested that the most probable origin of the Cl was through assimilation of Cl-rich wall rock, and the implications of this are discussed.

*5.4.2 Apatite crystal chemistry*

In order to determine whether Cl-rich apatite formed due to equilibration between pre-existing apatite and a Cl-rich fluid (i.e. alteration of magmatic apatite), it is necessary to understand the rate and style of halogen re-equilibration in apatite. The general consensus is that halogen diffusion in apatite is slow, with Cl diffusing slower than F or OH (Tacker & Stormer, 1989; Leitfink *et al.*, 1994; Boudreau & McCallum, 1990). Under conditions of both high temperature hydrothermal alteration (Tacker & Stormer, 1989; Leitfink *et al.*, 1994), and greenschist facies alteration (Boudreau & McCallum, 1990) apatite is relatively immune to halogen re-equilibration with a hydrothermal fluid. These authors all find that apatite-halogen re-equilibration, when it occurs, is facilitated by whole-scale recrystallisation, not diffusion. Furthermore, during recrystallisation all REEs are leached into hydrothermal fluids, but LREE are leached preferentially to HREE (Leitfink *et al.*, 1994; Boudreau & McCallum, 1990). It should be noted however that in contrast to these studies, Brenan (1994) has experimentally shown that Cl diffusion into fluorapatite can be relatively rapid. Brenan's (1994) experiments predict that if diffusive exchange begins at 800°C, and the cooling rate is 1°C/yr, apatites larger than 100 μm will not completely re-equilibrate with a hydrothermal fluid by diffusion. Since high cooling rates are expected beneath slow spreading mid-ocean ridges (Sleep, 1975; Kuznir, 1980), it seem unlikely that sufficient time was available for this to occur. Furthermore, fresh olivine occurs adjacent to Cl-rich apatite at 31.31 mbsf suggesting that it is unlikely that a sufficient volume of hydrothermal fluids passed through these rocks to add Cl to apatite.

The origin of the REE concentration in apatite in the leucocratic vein (30.63 mbsf), which also has a high-Cl content, is of interest in determining the origin of these apatite crystals. The apatite REE profile is humped in the MREE, as is predicted for growth from a parent with a flat REE pattern, whether the parent was a silicate melt (Watson & Green, 1981) or an aqueous fluid (Ayers & Watson, 1993). Seawater has very low REE abundances (Elderfield & Greaves, 1982) and thus cannot be responsible for addition of REE to apatite. Hydrothermal vent fluids have higher REE abundances than seawater, but have very high LREE/HREE ratios (Campbell *et al.*, 1988) and thus also are an unlikely source of REE in apatite. However, the composition of hydrothermal fluids at depth in the oceanic crust may not be the same as those emitted from hydrothermal vents (Gillis, 1996). Nevertheless, if their REE profile is controlled by reaction with

plagioclase (Campbell *et al.*, 1988) then they will also have high LREE/HREE ratios and the above argument holds.

*5.4.3 The behaviour of Cl in magmas*

Apatite crystals in terrestrial intrusions are generally Cl-poor (Boudreau, 1995). Very Cl-rich apatite (approaching end-member chlorapatite) is only found within and below the major PGE-bearing zones in the Stillwater and Bushveld intrusion (Boudreau *et al.*, 1986; Boudreau, 1995). Moderately Cl-rich apatite occurs in other terrestrial intrusions (e.g. the Great Dyke, Duluth), but is only found in the more primitive cumulates (Boudreau, 1995). In more evolved lithologies the Cl/F ratio consistently decreases with increasing fractionation, even in intrusions in which apatite is the only halogen-bearing phase (Boudreau, 1995). The observation that:

$$\text{Cl/F apatite} < \text{Cl/F melt} < \text{Cl/F vapour} \qquad \text{(Mathez, 1989)}$$

leads to the interpretation that the decreasing Cl/F ratio in apatite in terrestrial intrusions with increasing degree of whole rock evolution indicates degassing of a high Cl/F vapour phase. Pristine MORB generally has a Cl/F <1 (Boudreau *et al.*, 1997), and apatite partitioning is such that it favours F over OH, and OH over Cl (Boudreau *et al.*, 1986). This is consistent with most apatite in ODP Hole 923A growing from a MORB-like magma. In contrast, a mechanism must be envisaged to increase the Cl/F ratio of the parent for chlorapatite. The Cl/F ratio of the melt is unlikely to increase significantly through the crystallisation of amphibole, the only other halogen bearing phase present, because amphibole has both F and Cl abundances below electron probe detection. Furthermore, amphibole and apatite occur in insufficient abundance to be likely to be responsible for significant increases in the Cl/F ratio unless the volume of melt was very small. However, even if the volume of melt was small, a fractionation trend from Cl-poor to Cl-rich apatite should be seen. Contrary to this, Fig. 4.13 shows that there is no fractionation trend of increased Cl abundance. Two mechanisms to produce the high Cl/F parent for apatite can be envisaged: (i) apatite growth from an exsolved vapour phase with a high Cl/F ratio, and/or (ii) episodic addition of Cl via assimilation of a Cl-rich assimilate.

The primary origin of this Cl cannot be definitively resolved with the present data, although the absence of Cl-rich apatite in evolved lithologies in terrestrial intrusions suggests a process specific to the mid-ocean ridge environment. This strongly implies assimilation of Cl-rich wall rock. Possible solution to the origin of the Cl would be found by analysis of apatite Cl-isotopes or Cl/Br ratios, as these both differ significantly between seawater and the mantle (Boudreau *et al.*, 1997; Jambon *et al.*, 1995).

## 5.5 Compositions of magmas added to the chamber

As discussed in Chapter One, a wide variety of melt compositions are thought to be generated in the mantle beneath mid-ocean ridges, whereas the basalts sampled on the seafloor are relatively homogeneous. A possible site for mixing of these diverse magmas to produce N-MORB is within magma chambers. This hypothesis can be tested using the trace element composition of cumulus minerals to calculate the composition of the melt from which they grew. Furthermore, the major element composition of the parental melts can be investigated by comparison of the major element compositions of phases within Hole 923A gabbros, with those produced in low-pressure experimental studies of crystallisation of primitive MARK area MORB (Grove & Bryan, 1983; Tormey *et al.*, 1987; Grove *et al.*, 1992). These approaches have been taken here.

The trace element compositions of the replenishing melts have been calculated using the compositions of the most primitive plagioclase and clinopyroxene and the D's given in Appendix A.I. The most primitive plagioclase compositions are the embayed, anorthitic cores in poikilitic olivine gabbros. The most primitive clinopyroxene compositions are those of the cores of clinopyroxene oikocrysts from 46.30 and 64.87 mbsf. The parental melt compositions for plagioclase and clinopyroxene are discussed separately, as the constraints discussed in Section 5.2 suggest that they were different. As plagioclase cores grew prior to clinopyroxene oikocrysts, their compositions may record melt compositions that existed deeper in the magma plumbing system than those recorded by clinopyroxene, thus plagioclase compositions will be discussed first.

### *5.5.1 Trace element compositions of primitive plagioclase*

In Section 5.2.2 it was suggested that the embayed anorthitic plagioclase cores in poikilitic olivine gabbros were entrained in a magma replenishing the magma chamber. Thus, they probably crystallised at a deeper level in the MORB plumbing system than was sampled by ODP Hole 923A. Consequently, these potentially provide information about the composition of melts at a relatively deep level within the plumbing system. In comparison to other plagioclase crystals within Hole 923A, including their rims, the anorthitic core have lower LREE abundances, lower La/Nd and Nd/Y ratios, and higher Y abundances.

### *5.5.2 Melt compositions modelled from embayed plagioclase cores in poikilitic olivine gabbros*

Fig. 5.2 compares melt compositions calculated to be in equilibrium with plagioclase cores in poikilitic olivine gabbros (plagioclase model melts) with MARK area MORB (Bryan *et al.*, 1981; Dosso *et al.*, 1993; Reynolds & Langmuir,

1997). Also shown in Fig. 5.2 (Fig. 5.2b) is a calculated equilibrium melt for the core of a cumulus plagioclase in a brown-pyroxene gabbro (31.31 mbsf), as this has similar incompatible trace element characteristics to the embayed plagioclase core population in poikilitic olivine gabbros. Model melt compositions were calculated using the D's in Appendix A.I, which are approximately constant for most elements; however, variation in the anorthite content of the plagioclase causes considerable variation in D's for Y, Sr and Ba (Blundy & Wood, 1991, 1994; Appendix A.I). This has been accounted for in the D's used, assuming that the measured anorthite content represents the magmatic composition. This is probably a valid assumption as coupled CaAl-NaSi diffusion is slow in plagioclase (Morse, 1984; Grove *et al.*, 1984), and because sharp steps in anorthite-zonation are preserved (e.g. Fig. 4.16). Increasing anorthite content causes $D_Y$ to increase and $D_{Sr}$ and $D_{Ba}$ to decrease (Appendix A.I). The large negative Zr anomaly in melts modelled from plagioclase compositions may well be due to use of an inapplicable distribution coefficient (0.01 is used; Appendix A.I) as this feature is present in all melt compositions modelled from plagioclase (Fig. 4.24). Variations in the size of the Zr anomaly may be significant; however, due to analytical uncertainty in $D_{Zr}$, this will not be considered further.

There are three main differences between the primitive model melt compositions and MARK area MORB: (i) Positive Sr anomalies exist in some hypothetical melt compositions which decrease in size with increased LREE abundances as the Sr abundance is relatively constant (173 to 195 ppm in these plagioclase cores). This cannot be accounted for by variation in $D_{Sr}$ with anorthite content of the plagioclase because there is no correlation between plagioclase An content and Sr/Sr* (where Sr* = [Ce + Pr] / 2). Thus, if the use of inappropriately low $D_{Sr}$ is invoked to explain the positive Sr anomalies, then no plagioclase analysed is in equilibrium with MARK area MORB which seems unlikely; (ii) Primitive model melts have much lower LREE concentrations than MARK area MORB, but similar Y abundances, suggesting the melt parental to these plagioclase crystals was LREE-depleted; (iii) The Ba and K abundances, and Ba/K ratio of the modelled melts, generally do not resemble MARK area MORB. This may be due to the use of inappropriate Ds, lack of preservation of magmatic compositions, or different Ba and K systematics in the parental melts than in MORB. The relatively high mobility of K limits the confidence with which K data can be interpreted, and thus this is not pursued here. Ba and LREE abundances correlate well within most of these plagioclase cores. However, some analyses of plagioclase cores in samples from 47.33, 52.98 and 56.58 mbsf, which have low LREE abundances and low La/Nd ratios, are displaced from the LREE-Ba correlation to lower Ba abundances. These observations suggest that the melt

parental to the most primitive plagioclase was LREE and Ba depleted with respect to MARK area MORB, but had a positive Sr anomaly.

The lower LREE, but higher Y abundances in plagioclase cores in poikilitic olivine gabbros, relative to both their rims and plagioclase in other lithologies, rules out a single parental melt for all plagioclase. Furthermore, this compositional difference suggests either: (i) a role for garnet in the source, or (ii) source heterogeneity. This is because during progressive melting of a homogeneous source without residual garnet, the LREE and Y abundances in the melts produced will correlate positively. However, if garnet is present in the source, or the source is heterogeneous, this may not be the case. A role for garnet in the generation of MARK area MORB is suggested by the higher Sm/Yb ratio of most MARK basalts than N-MORB. The $Sm_{(n)}/Yb_{(n)}$ ratio of MARK area MORB ranges from 0.97 to 1.39, averaging 1.13 in contrast with 0.95 in N-MORB (Sun & McDonough, 1989). An alternative explanation for variations in the partitioning of MREE to HREE during melting is that this relates to the variation in clinopyroxene distribution coefficients with the change in clinopyroxene composition during decompression and melting (Blundy, 1997b). In this scenario, shallow melting involves a relatively Ca-rich, Al-poor, clinopyroxene which has a larger M2 Site and thus has lower $D_{Sm}$ and $D_{Yb}$ than higher pressure clinopyroxene, but also a higher ratio $D_{Sm}/D_{Yb}$ (see Appendix A.I); i.e. this would produce a melt with a lower Sm/Yb ratio than a deeper melt. Thus, to invoke clinopyroxene as the control over the high Sm/Yb in MARK area MORB instead of garnet requires a greater proportion of melting to occur at depth in the MARK area than for N-MORB. This could be the case if the cooling edge effect of the transform is significant in controlling the degree of melting. However, there is no systematic variation in Sm/Yb ratio with proximity to the transform.

The model melts from primitive plagioclase have lower LREE abundances and La/Nd ratios than MARK area MORB, suggesting that they grew from a melt more depleted than sampled MORB. This can be explained by the parental melt to these plagioclase being incompletely aggregated MORB; i.e. lacking some highly incompatible element rich melt component compared to MORB. The positive Sr anomaly in the most primitive plagioclase model melts may either be a mantle-derived phenomenon, or due to resorption of exotic plagioclase. Resorption of plagioclase could occur within a plagioclase-bearing crust-mantle transition zone, or within a magma chamber.

In conclusion, embayed, anorthitic plagioclase cores in poikilitic olivine gabbros have incompatible element abundances and ratios which distinguish them from other plagioclase in the cored interval. These plagioclase cores cannot have grown from the same parental melt as other plagioclases including their rims. Possible origins of the compositional diversity are: (i) melting of a

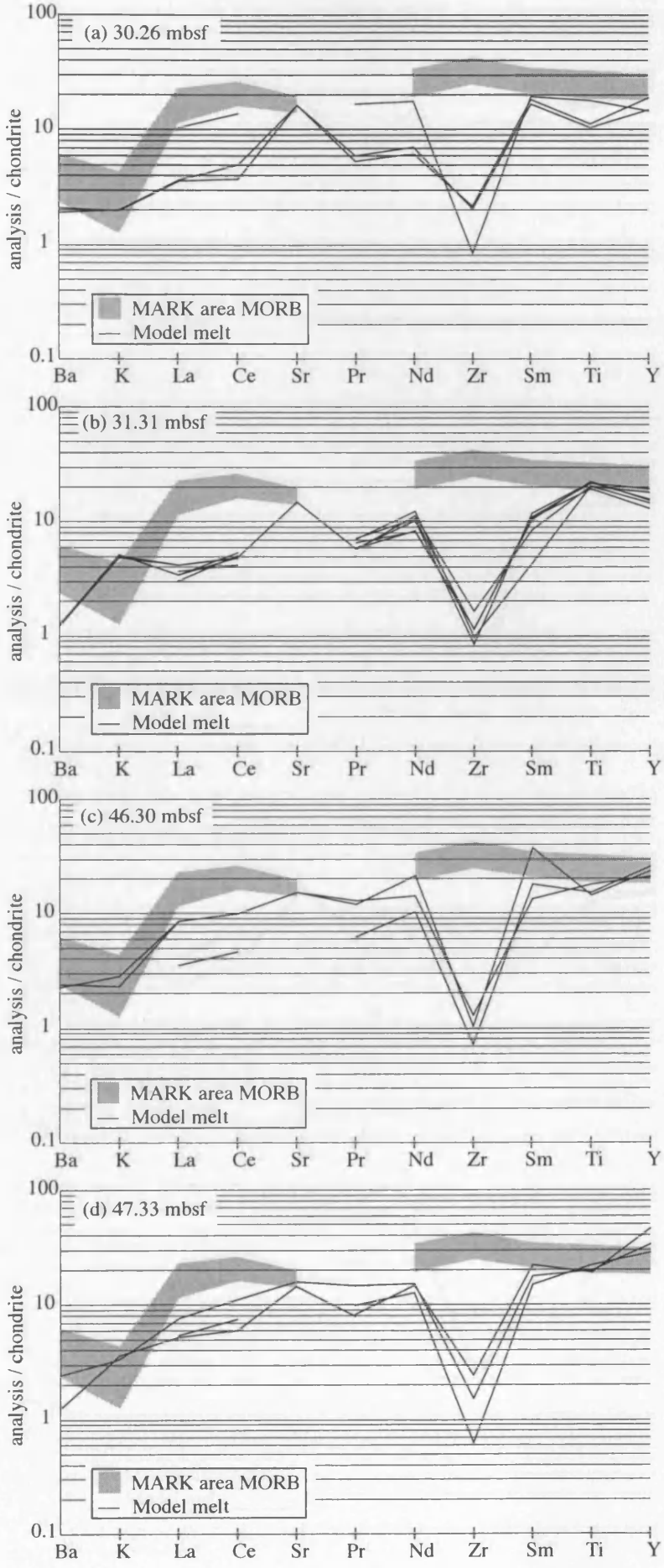


Fig. 5.2 Comparison of melt compositions calculated to be in equilibrium with plagioclase cores in poikilitic olivine gabbros, and a single cumulus plagioclase core in a brown-pyroxene gabbro (31.31 mbsf), with MARK area MORB (grey field; Bryan et al., 1981; Dosso et al., 1993; Reynolds & Langmuir, 1997). All plagioclase core analyses for each sample are shown (a) a troctolitic poikilitic olivine gabbro (30.26 mbsf). The modelled melt has similar Y abundances in all analyses, despite the significant variation in LREE abundances. Also note the large positive Sr anomalies in the analyses with the lower LREE abundances. (b) a brown-pyroxene gabbro (31.31 mbsf). The modelled melt has very low Ba/K and La/Nd ratios. (c) a poikilitic olivine gabbro (46.30 mbsf) from the heterogeneous lithology. This sample contains the most primitive clinopyroxene in the core, however the melt compositions modelled from plagioclase cores are not the most incompatible element depleted. Again, note the little variation in Y abundance considering the range in LREE abundances. (d) a poikilitic olivine gabbro (47.33 mbsf) from the heterogeneous lithology. The modelled melt compositions are little more incompatible element depleted than MORB.

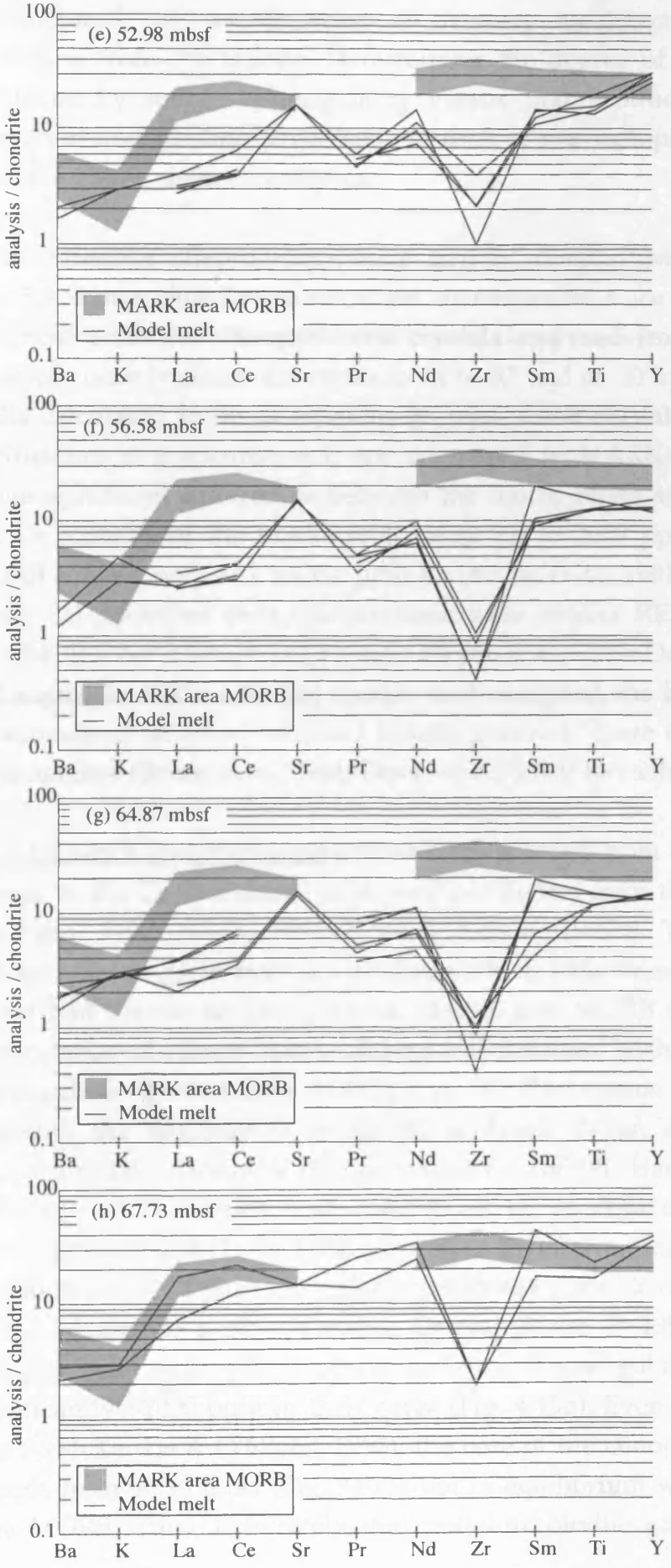


Fig. 5.2 cont. (e) a troctolitic poikilitic olivine gabbro (52.98 mbsf). These model melt compositions have positive Sr anomalies, and high Y abundance but low LREE abundances. (f) a coarse poikilitic olivine gabbro (56.58 mbsf). These model melts have large positive Sr anomalies and low Ba/K ratios. (g) a coarse poikilitic olivine gabbro (64.87 mbsf). Again, the modelled melt compositions have large positive Sr anomalies and low LREE abundances. (h) a coarse poikilitic olivine gabbro (67.73 mbsf). The modelled melt patterns from plagioclase cores in this sample are similar to MARK area MORB.

heterogeneous source, (ii) extraction of melt from diverse parts of the melting regime, and (iii) modification of primary melt compositions during melt extraction from the mantle. Determining the degree of compositional variation produced by source heterogeneity versus that produced by melt generation, extraction and pooling processes requires *in situ* isotopic analysis and/or more extensive trace element analyses.

*5.5.3. Primitive clinopyroxene trace element compositions*

Fig. 5.3 shows chondrite-normalised incompatible trace elements abundances in the most primitive clinopyroxene crystals analysed from ODP Hole 923A (the cores of clinopyroxene oikocrysts from 64.87 and 46.30 mbsf). The composition of melts calculated to be in equilibrium with these crystals, using the distribution coefficients in Appendix A.I, are compared to MARK area MORB in Fig. 5.4. Three significant differences between the model melts and MARK MORB are: (i) the Cr contents of the model melt range up to 2600 ppm, whereas MARK area MORB contain only 161 to 351 ppm Cr (Bryan *et al.*, 1981; Reynolds & Langmuir, 1997), (ii) modelled melt compositions have similar REE abundances to MARK area MORB, but a lower La/Yb ratio (Bryan *et al.*, 1981; Dosso *et al.*, 1993; Reynolds & Langmuir, 1997), and (iii) model melt compositions have significant negative Ti anomalies, whereas analysed basalts generally have only very small negative Ti anomalies (Bryan *et al.*, 1981; Dosso *et al.*, 1993; Reynolds & Langmuir, 1997).

5.5.3.1 Cr-rich clinopyroxene contains up to 10,000 ppm Cr (46.30 mbsf), which is similar to the Cr abundance in abyssal peridotites from the MARK area (Fig. 4.20; Stephens, 1997; Niida, 1997; Ross & Elthon, 1997b). This suggests that these clinopyroxenes grew from a melt from which little or no clinopyroxene and Cr-spinel had previously precipitated. MARK area MORB shows clear evidence for precipitation of clinopyroxene during fractionation, such as decreasing CaO with fractionation. Furthermore, MARK area MORB contains only 161 to 351 ppm Cr, although the database is small (30 analyses; Bryan *et al.*, 1981; Reynolds & Langmuir, 1997). Using a clinopyroxene $D_{Cr}$ of 3.8 (Hart & Dunn, 1993; see also Appendix A.I), MARK area MORB is in equilibrium with clinopyroxene containing only 612 to 1334 ppm Cr. Primitive dolerite intrusions within peridotites at ODP Site 920 contain up to 489 ppm Cr (Kempton & Casey, 1997) which equates to a clinopyroxene Cr abundance of 1859 ppm. However, most clinopyroxene oikocrysts in coarse poikilitic olivine gabbros have Cr abundances significantly >2000 ppm in their cores (Fig. 4.15b). Even if $D_{Cr}$ for clinopyroxene was 9 (McKenzie & O'Nions, 1995), the core of the clinopyroxene oikocryst in the sample from 46.30 mbsf (Fig. 3.8) is not in equilibrium with any analysed MARK area MORB. Thus, it is likely that poikilitic olivine gabbros were precipitated

from melts with higher Cr abundances than MORB; i.e. they had previously precipitated little or no clinopyroxene or Cr-spinel since melt generation.

5.5.3.2 Lower $La_{(n)}/Yb_{(n)}$ and $La_{(n)}/Sm_{(n)}$ ratios as well as lower Sr and Zr abundances are observed in modelled melt composition than analysed MARK area MORB (Fig. 5.4). If the difference between the model melt composition and MARK area MORB is due to use of inappropriate D's, $D_{La}$ would have to be ~40% lower (i.e. 0.05 not 0.08), and D's for the HREE would have to be ~50% higher (i.e. $D_{Dy}$ = 0.6 not 0.41). This range of variation in D's does not seem likely (see Appendix A.I), suggesting that the melt that crystallised these clinopyroxene was probably compositionally distinct from sampled MORB (i.e. had a lower $La_{(n)}/Yb_{(n)}$). Furthermore, D's for Zr and Sr would have to be similarly incorrect for the model melts to show smooth incompatible element abundance profiles (Fig. 5.4). However, it is possible that the D's used may be sufficiently inaccurate to explain this difference.

The similarity in the trace element compositions of clinopyroxene from 64.87 and 46.30 mbsf suggest that the composition of the magma added to the chamber in these separate replenishment events was similar (Fig. 5.3). Furthermore, despite the subtle difference between the model parental compositions for clinopyroxene in these samples and MARK area MORB, they are generally similar. This suggests a nearly fully aggregated parental melt, with a slightly greater proportion of depleted melt than fully aggregated MORB replenished the chamber. This is consistent with the depleted melt composition calculated from plagioclase composition.

5.5.3.3 Negative Zr and Ti anomalies occur in abyssal peridotite whole rock and clinopyroxene analyses (Salters & Shimizu, 1988; Johnson *et al.*, 1990), and thus it is interesting to record their occurrence in primitive clinopyroxene in oceanic gabbros. Model melt compositions calculated from clinopyroxene compositions do not have significant negative Zr anomalies, but do have significant negative Ti anomalies. If the linear relationship between $D_{Ti}$ and $D_{Zr}$ found by Forsythe *et al.* (1994; see Fig. 5.5 and Section A.I.3.3.2.1) is applicable, then changing $D_{Ti}$ so as to remove the Ti anomaly in the model melts would create a positive Zr anomaly. This suggests that HFSE anomalies exist in melts at relatively shallow levels within the MORB plumbing system, making it interesting to speculate on their origin.

5.5.3.4 Zr and Ti in N-MORB show slight relative enrichment ($Zr/Zr^* = 1.1$), and depletion ($Ti/Ti^* = 0.94$) with respect to the adjacent REE (Sun & McDonough, 1989). Basalts from the MARK area consistently have positive Zr anomalies

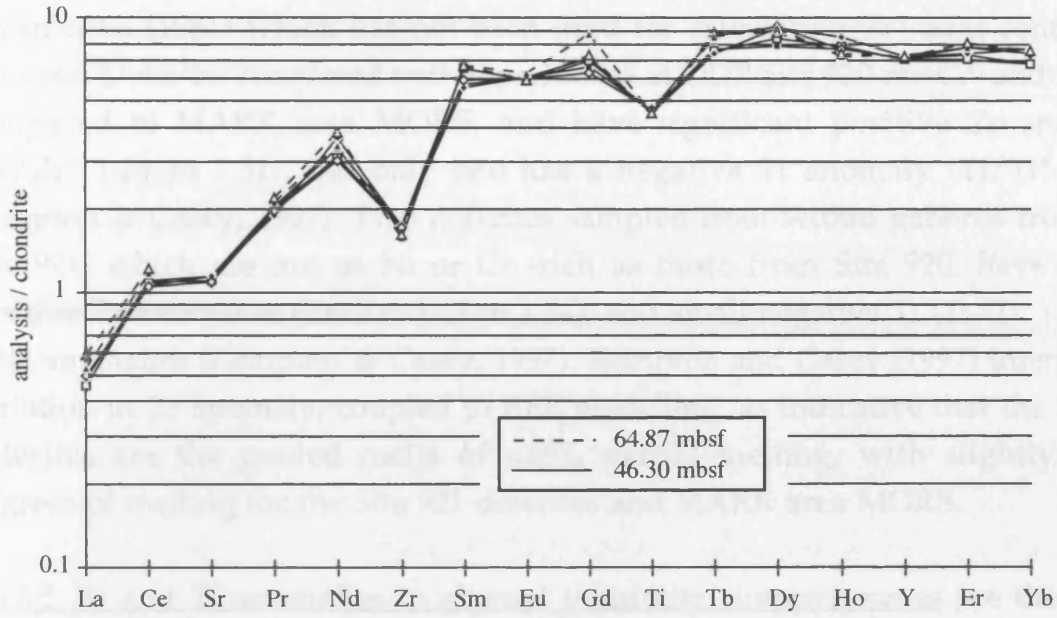


Fig. 5.3 Chondrite-normalised incompatible element abundances in the most primitive clinopyroxene analyses from samples in the cored interval. The plots show negative Zr and Ti anomalies typical of clinopyroxene in abyssal peridotites. Six analyses are shown, four from the core of a clinopyroxene oikocryst at 46.30 mbsf (see Fig. 3.8), and two from the core of a clinopyroxene oikocryst at 64.87 mbsf (see Fig. 4.21). Note the small negative Sr anomaly. The smaller variation in Y abundance than HREE presuambly represents greater precision for Y due to higher abundance.

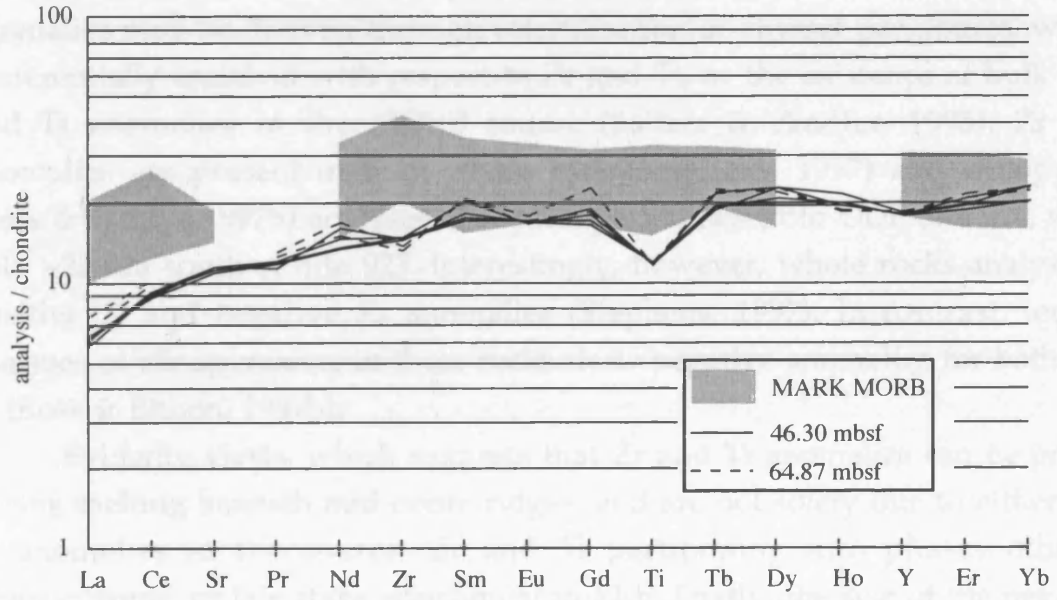


Fig. 5.4 Comparison of melt composition calculated to be parental to the clinopyroxene analyses shown in Fig. 5.3, and MARK area MORB (23°10' to 23°40'N; shaded field; Bryan et al., 1981; Dosso et al., 1993; Reynolds and Langmuir, 1997)). Note that the Zr and Sr anomalies seen in the clinopyroxene analysis are not seen in the model melt due to the lower distribution coefficients used in calculating the melt composition for these elements than adjacent REEs. However, the Ti anomaly remains. The distribution coefficients used to calculate melt compositions from clinopyroxene compositions are from Appendix A.I.

(Zr/Zr* 1.07 to 1.35; av. 1.23), and generally have slight negative Ti anomalies (Ti/Ti* 0.82 to 1.08; av. 0.93). Most of the scatter in Ti/Ti* comes from the data of Bryan *et al.* (1981) which has not been used for calculating Zr* as it contains no Nd data. Dolerites recovered within peridotite at ODP Site 920 are Cr- and Ni- rich compared to MARK area MORB, and have significant positive Zr anomalies (Zr/Zr* 1.24 to 1.31), but only one has a negative Ti anomaly (Ti/Ti* = 0.89; Kempton & Casey, 1997). Two dolerites sampled from within gabbros from ODP Site 921, which are not as Ni or Cr -rich as those from Site 920, have smaller positive Zr anomalies (Zr/Zr* 1.12 to 1.14), and small negative Ti (Ti/Ti* = 0.91 to 0.94) anomalies (Kempton & Casey, 1997). Kempton and Casey (1997) interpret the variation in Zr anomaly, coupled to REE modelling, as indicative that the Site 920 dolerites are the pooled melts of <15% partial melting, with slightly higher degrees of melting for the Site 921 dolerites and MARK area MORB.

5.5.3.5 Zr and Ti anomalies in abyssal peridotite clinopyroxenes are thought to represent bulk rock Zr and Ti depletions (Salters & Shimizu, 1988), even though D's for Zr and Ti are higher than for the adjacent REE in spinel, olivine and orthopyroxene (Kelemen *et al.*, 1990; Salters & Zindler, 1995). These phases provide a possible complementary reservoir for Zr and Ti in the source which is not available for REEs suggesting that Zr and Ti anomalies in abyssal peridotite clinopyroxene should be interpreted with caution. Furthermore, Zr and Ti anomalies may be derived through refertilisation of abyssal peridotites, with REE preferentially enriched with respect to Zr and Ti, or the existence of bulk rock Zr and Ti anomalies in the MORB source (Salters & Zindler, 1995). Zr and Ti anomalies are present in both whole rock (Stephens, 1997) and clinopyroxene (Ross & Elthon, 1997b) analyses of abyssal peridotites from ODP Site 920, which is only ~25 km south of Site 923. Interestingly, however, whole rocks analyses have positive Ti and negative Zr anomalies (Stephens, 1997). In contrast, ion probe analyses of clinopyroxene in these rocks show negative anomalies for both Zr and Ti (Ross & Elthon, 1997b).

Evidence exists, which suggests that Zr and Ti anomalies can be produced during melting beneath mid-ocean ridges, and are not solely due to either Zr and Ti anomalies in the source, Zr and Ti partitioning into phases other than clinopyroxene, or late stage enrichment in REE. Firstly, the size of the negative Zr and Ti anomalies in some abyssal peridotite clinopyroxenes increases with increased incompatible element depletion (Johnson *et al.*, 1990). This is inconsistent with either a model of Zr and Ti anomalies being a source characteristic, or being due to REE refertilisation. Rather, it implies that increased degrees of melt extraction are, in some circumstances, coupled to preferential extraction of Zr and Ti. Secondly, melt inclusions in an olivine phenocryst from

the Mid-Atlantic ridge show both positive and negative Zr and Ti anomalies (Sobolev & Shimizu, 1993; Sobolev, 1996). Thirdly, the existence of Zr and Ti anomalies in clinopyroxene in oceanic gabbros, which cannot both be explained by variations or uncertainties in D's, indicates that melts with HFSE anomalies were delivered to the upper parts of the plumbing system. Thus, it appears that Zr and Ti, despite behaving similarly to adjacent REE in erupted MORB, behave differently to them during melt generation (and it is shown in Chapter Six, that this is also true during differentiation). This conclusion holds irrespective of whether HFSE anomalies are present in the source prior to the initiation of melting.

5.5.3.6 Derivation of Zr and Ti anomalies in both abyssal peridotite clinopyroxene and oceanic gabbro clinopyroxene can be explained by variations in bulk distribution coefficient for these elements, with respect to adjacent REEs, within the MORB plumbing system. However, the lack of significant anomalies within erupted MORB suggest that the anomalies in primary melts must be eradicated by mixing between melts with equal but opposite anomalies. Three mechanisms to explain the generation of both positive and negative Zr and Ti anomalies in primary mantle melts are:

(i) Variation in distribution coefficients for clinopyroxene. These occur mainly due to variation in the major element composition of clinopyroxene which leads to variation in the size and elasticity of the crystal lattice sites into which trace elements substitute (Wood & Blundy, 1997; see Appendix A.I). Clinopyroxene composition in the mantle will change during melting due to changes in pressure and bulk rock chemistry. However, the effects on the M1 and M2 sites of clinopyroxene will not be identical. Therefore, since REE's substitute into the clinopyroxene M2 site, and Zr and Ti substitute into the M1 site (Cameron & Papike, 1980; Wood & Blundy, 1997; Blundy, 1997b) variation in the composition of clinopyroxene will affect the relative partitioning of Zr/Zr* and Ti/Ti*. Furthermore, the effect on Ti* will differ from the effect on Zr*. This is because at the onset of melting clinopyroxene is expected to have high Al and low Ca contents, leading to higher D's for all REE than at low pressures where the Al content of clinopyroxene is lower and Ca abundance higher (Wood & Blundy, 1997). However, the change in D's with clinopyroxene composition is considerably greater for $D_{Gd}$ and $D_{Tb}$ than $D_{Sm}$ and $D_{Nd}$. Thus, if the change in D's for clinopyroxene with composition control the development of Zr and Ti anomalies within the MORB plumbing system, consistency between Zr and Ti anomalies should not be expected. Forsythe *et al.* (1994) show experimentally how the clinopyroxene $D_{Zr}$ and $D_{Ti}$ change with clinopyroxene composition. Fig. 5.5 shows their experimentally determined D's for Ti and Zr plotted as a function of

the Al content of the clinopyroxene. As with the REEs, the distribution coefficients for Zr and Ti do not correlate perfectly, with $D_{Zr}$ increasing more rapidly with increased Al content than $D_{Ti}$. This is consistent with the radius of Ti being closer to the size of the clinopyroxene M1 site than that of Zr (Appendix A.I).

A further variation in clinopyroxene D's during melting is suggested by Baker *et al.* (1995) who show experimentally and thermodynamically that at very low melt fractions, $D_{Ti}$ for clinopyroxene is relatively large. They suggest that this is due to the high abundance of incompatible minor elements (Na, Al) in clinopyroxene during the early stages of melting which provide charge balance for Ti. However, as these elements are lost from the clinopyroxene during progressive melt extraction, so too must Ti be lost to maintain charge balance. This suggests that Ti and Zr, as $4^+$ cations, will undergo larger variation in D during the early stages of melting than $REE^{3+}$ cations. The combination of the factors discussed above suggest that Zr and Ti anomalies are likely to develop during melting purely as a function of variation in clinopyroxene distribution coefficients.

(ii) Variation in bulk distribution coefficients due to changes in mode will occur in the mantle during melting due to the higher distribution coefficients for Zr and Ti in olivine, orthopyroxene and spinel than their adjacent REE (Kelemen *et al.*, 1990; Green, 1994; McKenzie & O'Nions, 1991, 1995). This will have two effects. Firstly, the bulk distribution coefficients for Zr and Ti will be greater relative to Zr* and Ti* than if clinopyroxene alone controlled them. Secondly, as bulk D's for the REE decrease with decreased modal clinopyroxene content during melting, Ti and Zr bulk D's will decrease more slowly. Thus, as the modal proportion of clinopyroxene decreases, the ratio $D_{REE}/D_{HFSE}$ will decrease.

(iii) Variations in distribution coefficients due to variation in melt structure may occur due to the significant compositional variation expected in small degree partial melts (Baker *et al.*, 1995). This is due to the large effect on melt structure caused by alkali and volatile elements which are concentrated in the first melts. For example, increased alkali concentrations lead to a decrease in the activity coefficient of silica, and thus increased silica abundance to maintain the same silica activity. Whether changes in melt structure will effect HFSE and REE partitioning in similar or differing manners is unclear, although having different charge/size ratios this seem quite possible.

The above discussion shows that it is inevitable that the behaviour of Zr and Ti will differ from that of REEs during partial melting of the mantle. Thus,

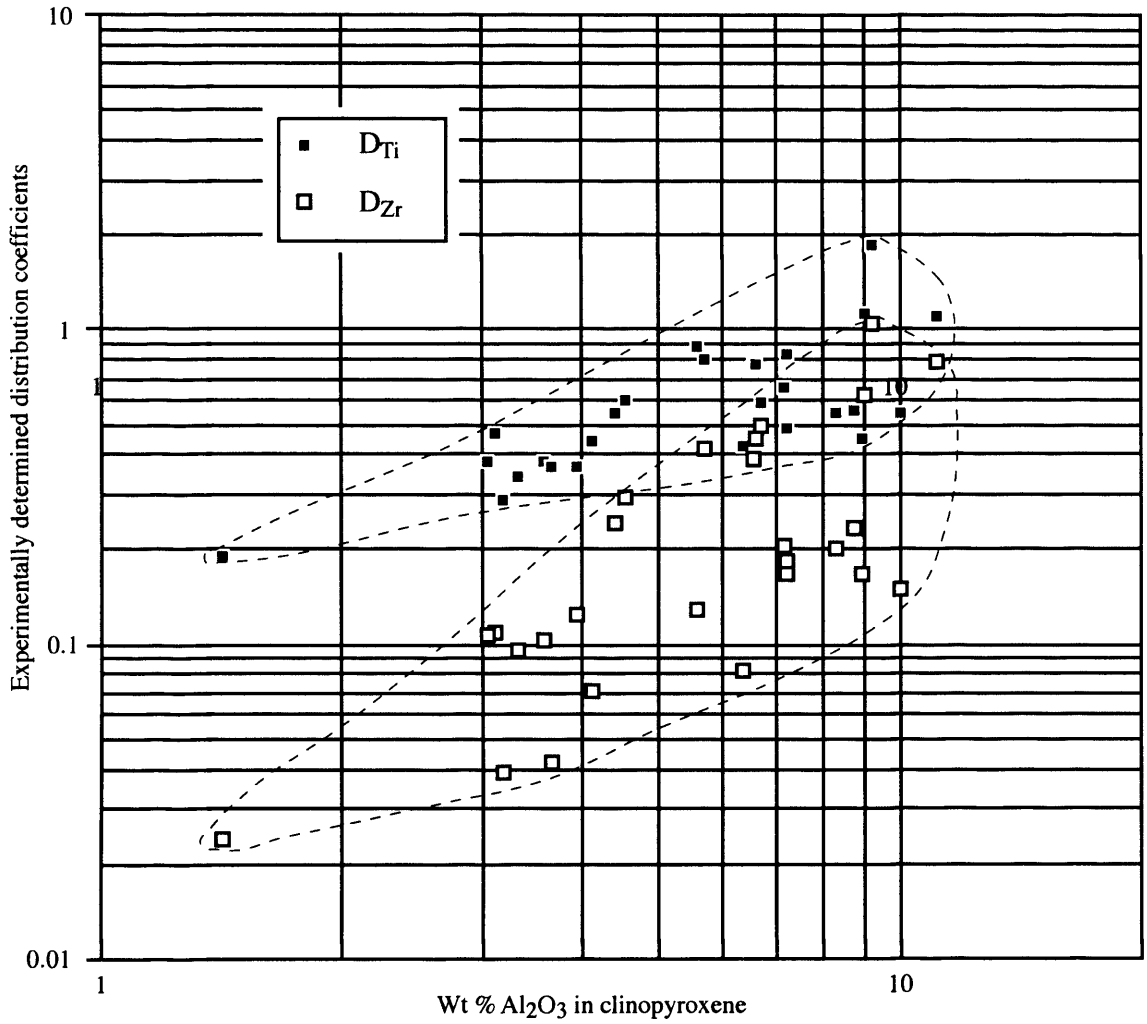


Fig. 5.5 Plot of experimentally determined clinopyroxene distribution coefficients for Ti and Zr versus the $Al_2O_3$ content of the clinopyroxene (data from Forsythe et al., 1994). The distribution coefficient for Zr increases more than that for Ti for a given increase in clinopyroxene $Al_2O_3$ content. At high pressure clinopyroxene contains more $Al_2O_3$ and thus is expected to have high $D_{Zr}$ and $D_{Ti}$ than at low pressure. However, the decrease in D with pressure is expected to be greater for Zr than Ti. This is consistent with Ti having a radius closer to the size of the clinopyroxene M1 site than Zr (Appendix A.I). The data cannot be explained by disequilibrium growth leading to D's converging on one, as this process leads to enrichment as a function of of the charge/radius$^2$ of the element in question (Shimizu, 1981). This would lead to greater enrichment in Ti than Zr, the opposite of the trend observed.

the observation that Zr and Ti behave generally coherently with REE in MORB implies that the magma plumbing system efficiently wipes out primary variations in Zr/Zr* and Ti/Ti*. The interpretation that melts with Ti anomalies fed a magma chamber beneath the Mid-Atlantic ridge suggests that the removal of these anomalies occurs, at least in part, at relatively shallow levels.

It is also interesting in this context that clinopyroxene trace element compositions show negative P anomalies with respect to MORB. Three explanations for this are proposed: (i) $D_P$ may be less than $D_{Nd}$ for clinopyroxene, with partitioning of P into other phases maintaining the bulk $D_P$ ~ bulk $D_{Nd}$ to explain their relatively constant ratio in MORB (73 +/- 14, Sun & McDonough, 1989); (ii) P may partition into apatite, implying apatite fractionation played a role throughout crystallisation; or (iii) P anomalies may have existed in the parental melts. The first model, that clinopyroxene $D_P < D_{Nd}$ but that P is partitioned into phases other than clinopyroxene in significant proportions, for example into all silicate phases in place of Si, is supported by the occurrence of 30 ppm phosphorous in the single olivine analysis performed by ion probe (Appendix A.III.3). Furthermore, there is no correlation between the sum of the normative modal proportions of diopside and hypersthene (as an approximation of the modal clinopyroxene abundance) in gabbros from Hole 923A and P abundance, but there is with HREE abundances. Also, the range of Nd/P ratios in whole rock analyses ranges from 16 to 311 (Barling *et al.*, 1997; Casey, 1997). P/Nd ratios greater than in MORB are consistent with apatite 'accumulation' whereas those less than in MORB prove the existence of either: (i) melts with negative phosphorous anomalies, or (ii) crystal assemblages with bulk $D_P < D_{Nd}$. Negative P anomalies in the melts could be generated by apatite fractionation or if apatite exists in the MORB source. These hypotheses are untestable with the present data but again show that mixing of diverse melt compositions must be important within the MORB plumbing system to produce both the incompatible element abundances and ratios observed in MORB.

*5.5.4 Major elements*

The major element composition of the parental melt is more difficult to calculate from the composition of the minerals than the trace element composition. However, by comparing the average major element compositions of coexisting olivine, plagioclase and clinopyroxene in the gabbros with compositions produced in one-atmosphere experiments on MARK area MORB (Fig. 4.3), this can be attempted in a qualitative way. The main difference between these is the lower clinopyroxene Mg#s observed in experiments than in Hole 923A gabbros. This is a common characteristic of oceanic gabbros and it has been suggested that

this is due to crystallisation of oceanic gabbros at moderate-pressure (Elthon *et al.*, 1992). Below, this model is discussed and alternative explanations suggested.

5.5.4.1 The Mg#s of clinopyroxene in many poikilitic olivine gabbros is higher than in any clinopyroxene grown in one-atmosphere crystallisation experiments on MORB (Grove & Bryan, 1983; Tormey *et al.*, 1987). The idea that this may be due to crystallisation of gabbros under moderate pressure (Elthon *et al.*, 1992) comes from the observation that clinopyroxene is a liquidus phase at a higher temperature (higher melt Mg#) in high pressure experiments than in lower pressure experiments (e.g. Grove *et al.*, 1990, 1992). High-pressure fractionation has also been invoked to explain the pyroxene paradox (Rhodes *et al.*, 1979) in which MORB suites free of clinopyroxene phenocrysts follow fractionation trends that require clinopyroxene fractionation (Sullivan, 1991). In this scenario clinopyroxene crystallisation occurs at depth, producing the clinopyroxene fractionation fingerprint in the composition of the basalts erupted, but phenocrysts are resorbed upon decompression prior to eruption and thus not found in MORB. Prior to discussing alternative explanations for the occurrence of high Mg# clinopyroxene in oceanic gabbros other evidence that has been cited for high pressure crystallisation of oceanic gabbros is presented.

5.5.4.2 Evidence for crystallisation of oceanic gabbros at moderate-pressure comes from five common characteristics of oceanic gabbros (Elthon *et al.*, 1992). These are: (i) The Mg# of clinopyroxene is commonly higher than found in one-atmosphere experiments on primitive MORB, (ii) The Mg# of orthopyroxene is commonly higher than found in one-atmosphere experiments on primitive MORB, (iii) the low-Ca pyroxene in oceanic gabbros is commonly orthopyroxene not (inverted) pigeonite, whereas pigeonite is the common low-Ca pyroxene in MORB, (iv) the $Na_2O$ content of clinopyroxene in oceanic gabbros is commonly higher than in clinopyroxene grown in one-atmosphere crystallisation experiments or MORB phenocrysts, and (v) the $TiO_2$ content of clinopyroxene in oceanic gabbros is commonly higher than in clinopyroxene grown in one-atmosphere crystallisation experiments.

5.5.4.3 Physical arguments against high pressure crystallisation of oceanic gabbro include the following. (i) Geophysically imaged magma chambers beneath mid-ocean ridges are shallow (1-3 km; Detrick *et al.*, 1987; Calvert, 1995; Sinha *et al.*, 1997), as are gabbros in ophiolites. (ii) Many oceanic gabbros drilled and dredge from the seafloor are relatively undeformed, however, if they formed at or below the base of the crust significant plastic deformation might be expected during unroofing. (iii) Seafloor topography and detachment fault dips (Cann *et al.*, 1997)

are inconsistent with exhuming rocks from significant depths (5 to 15 km) near axis without significant ductile deformation. (iv) Fluid inclusions in gabbros from Hole 923A suggest an entrapment depth of ~2.5 km, and rule out entrapment at >7 km depth (Kelley, 1997).

5.5.4.4 Alternative explanations for apparently high-pressure signatures in oceanic gabbros include:

(i) high Mg# clinopyroxene - Firstly, the absence of clinopyroxene with high Mg#s in low-pressure experiments may be due to sluggish clinopyroxene nucleation kinetics. This is supported by the overgrowth of a seed crystal in a one atmosphere experiment (Grove & Bryan, 1983) with magnesian clinopyroxene (Mg# = 87). Secondly, a sector-zoned clinopyroxene microphenocryst (i.e. that crystallised at low pressure) in basalt dredged on the Kane fracture zone has sector Mg#s of 87.4 and 86.6 (Bryan *et al.*, 1981), indicating that high Mg# clinopyroxene is not necessarily indicative of high pressure fractionation. Thirdly, thermodynamic modelling of low-pressure MORB fractionation (Ghiorso, 1997) predicts clinopyroxene saturation at a temperature ~18°C lower than olivine saturation. This is a considerably smaller temperature interval than observed in one atmosphere experiments (generally 40 to 50°C, Tormey *et al.*, 1987; Grove *et al.*, 1992).

(ii) high Mg# orthopyroxene - The only high Mg# orthopyroxene found in Hole 923A gabbros occurs as rims on olivine, presumably formed by reaction between interstitial melt and olivine. Extensive reaction of this kind could result in the formation of significant amounts of high Mg# orthopyroxene. Alternatively the same arguments can be made for the origin of magnesian orthopyroxene as magnesian clinopyroxene. Soret fractionation can lead to crystallisation of magnesian orthopyroxene (Walker & DeLong, 1982). However, there is no evidence for the sustained temperature gradient necessary for this process.

(iii) the structure of low-Ca pyroxene in oceanic gabbros - In experimental studies, pigeonite is the first low-Ca pyroxene to crystallise from MORB at low-pressure, and with increased pressure it is replaced by orthopyroxene (Elthon *et al.*, 1992). Elthon *et al.* (1992) propose that this is not directly related to the pressure of crystallisation, but that at high pressure low-Ca pyroxene is a liquidus phase at higher temperature, and thus higher magnesian content of the melt. This favours orthopyroxene stability, whereas the lower magnesium content of the melt at the onset of low-Ca pyroxene crystallisation at low-pressure favours pigeonite stability (Elthon *et al.*, 1992). However, the details of the effects of minor components in controlling the relative stability of pigeonite and orthopyroxene, and the possibility of the breakdown of pigeonite to orthopyroxene during post-cumulus modification, prevent detailed discussion of this.

(iv) and (v) high $Na_2O$ and $TiO_2$ contents of oceanic gabbro clinopyroxene - $Na_2O$ and $TiO_2$ are incompatible during MORB fractionation; thus they will be concentrated in evolved interstitial melts. Reaction of these evolved interstitial melts, either as trapped melts (Meyer *et al.*, 1989) or as migrating interstitial melts (see Chapter Six), with the cumulus clinopyroxene will increase the abundance of these elements in the clinopyroxene. Thus, higher Na and Ti abundances of clinopyroxene in oceanic gabbros than in equilibrium with MORB may be simply a function of the composition of the melt with which they last equilibrated.

Thus, it does not appear necessary to invoke high-pressure crystallisation to explain the mineral compositions in oceanic gabbros. Another way to explain the higher Mg# of clinopyroxene in oceanic gabbros than in one-atmosphere experiments is for the melt compositions parental to the gabbros to be different from those used in experiments. This possibility is explored next.

5.5.4.5 A different major element composition of the melt parental to high Mg# clinopyroxene than those melts used in experiments could explain the high Mg# of the clinopyroxene. As the Ca/Al ratio of a basalt increases, the temperature at which clinopyroxene reaches the liquidus increases because the stability field of clinopyroxene increases at the expense of that of plagioclase. The Ca/Al ratio of melts produced during decompressional mantle melting is at a minimum at the initiation of melting and increases with increasing degree of melting, provided clinopyroxene is not exhausted (Klein & Langmuir, 1987; Baker & Stolper, 1994). Consequently, melts generated from a relatively depleted source, near the top of the melting column, have the highest Ca/Al ratio. Thus, the high Mg#s of clinopyroxene in many oceanic gabbros could be explained by invoking a parental melt with a high Ca/Al ratio; i.e. containing a high proportion of melt derived from a shallow, depleted source. If this is the correct explanation for high Mg#s of clinopyroxene in oceanic gabbros, then it implies that a depleted (high Ca/Al) melt component is an integral and widespread part of the shallow level magma plumbing system beneath mid-ocean ridges. This is consistent with the occurrence of high $CaO/Al_2O_3$ melt inclusion in phenocrysts in MORB (Dungan & Rhodes, 1978; Humler & Whitechurch, 1988; Sobolev & Shimizu, 1993). Interestingly, increasing the Ca/Al ratio of a melt increases its density (Bottinga & Weill, 1970), which may explain why these melt compositions are not common in erupted MORB.

To summarise, clinopyroxene more magnesian than that produced in one atmosphere experiments can be explained in a number of ways. Moderate- to high-pressure crystallisation is one mechanism, but it is not unique. Others

include differences between experimental and natural crystallisation processes, and different parental melt compositions.

### 5.6 Open system magma chamber processes beneath the Mid-Atlantic ridge

In this chapter it has been argued that Hole 923A represents a section through a frozen open system magma chamber. The main conclusions that have been reached are:

i) Replenishment was a common occurrence, with at least three replenishments occurring during the crystallisation of 50 m of core. Furthermore, all the replenishments contained resorbed anorthitic plagioclase crystals indicating that the replenishing magma was a hybrid between a plagioclase-phyric and a more primitive magma.

ii) Replenishments ponded at the base of the magma chamber with varying degrees of mixing with the resident, more evolved, magma. Fractionation within the ponded magma led to compatible elements being efficiently removed from the replenishing magma. The composition of the homogenised magma chamber, after mixing between the replenishing and resident magma had occurred, will thus have been depleted in compatible elements compared to if mixing between the replenishing magma and resident magma was instantaneous upon replenishment. This is consistent with the low abundances of compatible elements in MORB.

iii) Assimilation of Cl-rich wall rock probably occurred, although this is poorly constrained.

iv) The trace element compositions of magmas in equilibrium with embayed plagioclase cores in poikilitic olivine gabbros were depleted in LREEs and Ba with respect to MORB. However, they were variably enriched and depleted in Y with respect to MORB suggesting either a heterogeneous or garnet bearing source or complex melt extraction processes.

v) The hybrid magma that carried embayed plagioclase cores into the magma chamber was primitive, having previously crystallised little or no clinopyroxene or Cr-spinel. Furthermore, it was slightly LREE-depleted with respect to MARK area MORB and had a negative Ti anomaly.

vi) The common occurrence of clinopyroxene in oceanic gabbros with high Mg#s may be due to crystallisation from a melt more depleted than MORB; i.e. with a higher Ca/Al ratio than MORB. This is consistent with the depleted trace element compositions of these clinopyroxene crystals.

Taken collectively, conclusions (iv) to (vi) suggest that melts exist within the upper part of the magma plumbing system beneath mid-ocean ridges which are not fully aggregated MORB; i.e. some of the mixing of the distinct magma

compositions which are produced beneath mid-ocean ridges occurs at a relatively shallow level.

# Chapter VI: Evolution of the crystal mush

## 6.1 Introduction

The processes by which crystals separate from magma is imperfectly understood. One of the most fundamental unanswered question is whether crystallisation in magma chambers occurs dominantly *in situ* at the chamber margins (after heterogeneous nucleation; Campbell, 1978; McBirney & Noyes, 1979), or throughout the body of the magma chamber followed by crystal settling (after homogenous nucleation; Wager & Brown, 1968; Martin & Nokes, 1988). This question has important implications for the compositional evolution of the melt in the chamber, and thus interpretation of the composition of erupted lava suites (Langmuir, 1989; Nielsen & DeLong, 1992). Even if homogeneous crystallisation is an important process in magma chambers, the maximum packing of crystal sediments is likely to be <60% and thus at least 40% porosity must be lost post-accumulation (Campbell *et al.*, 1978). The effectiveness of *in situ* crystallisation in differentiating the eruptable magma is, however, dependent on a process for returning melt from the crystal mush to the overlying magma chamber. Thus, to understand the evolution of the eruptable magma chamber it is essential to understand how the crystal mush develops both compositionally and physically. Furthermore, if melt migrates through the developing crystal mush, both the compositions and texture of the resulting rocks will be modified by interaction between the interstitial melt and crystals (magmatic metasomatism). In this chapter it is shown that post-cumulus processes controlled the composition and texture of brown-pyroxene gabbros and oxide gabbros, and affected the genesis of poikilitic olivine gabbros. These processes fundamentally affected the compositions and textures of these rocks.

### *6.1.1 In situ and post-cumulus processes*

Whether a crystal mush at the margin of a magma chamber develops through *in situ* nucleation and growth or via crystal sedimentation post-cumulus processes can modify the primary textures and compositions. At one extreme the interstitial melt can solidify in place, with no interaction with the surrounding melt (orthocumulate crystallisation of Wager & Brown, 1968). This results in zoned crystals and maybe interpretable from whole rock geochemistry as a mixture between cumulus crystals and interstitial melt. Furthermore, this has no effect on the composition of the magma reservoir. However, it is more likely, as discussed below, that melt will migrate through the crystal mush during solidification. In this scenario the migrating melt will interact with the crystals it passes, modifying them compositionally and texturally (e.g. Boudreau &

McBirney, 1997). Furthermore, some of this evolved melt may be returned to the eruptable magma reservoir leading to its fractionation.

Return of melt which crystallised within the crystal mush to the magma reservoir is commonly termed *in situ* crystallisation (Langmuir, 1989) or boundary layer fractionation (Nielsen & DeLong, 1992). One end member process of *in situ* crystallisation is the progressive crystallisation of a solid interface between the (convecting) magma reservoir and the cumulate mush (Morse, 1986). The compositional effect of this on the magma reservoir is that of perfect fractional crystallisation. At the other extreme, crystallisation occurs in a perfectly closed system at the magma chamber margin until almost complete solidification has occurred. After crystallisation, some (or all) of the interstitial melt is then mixed back into the main magma body, resulting in its compositional evolution. This has the effect of fractionating incompatible elements more effectively than homogeneous crystallisation, whilst the major element composition of the melt is modified less (Langmuir, 1989). Return of interstitial melt to the magma reservoir can occur via compositional convection (Tait *et al.*, 1984; Tait & Jaupart, 1992), compaction (McKenzie, 1984; Shirley, 1986) and possibly through tectonic deformation of the crystal mush (Dick *et al.*, 1991). Understanding the relative roles of these processes in a mid-ocean ridge magma chamber requires understanding the evolution of the partial molten crystal mush. Further reasons for studying the evolution of crystal mushes in magma chambers are: (i) the similarities between melt migration and compositional modification in this scenario and during mantle melting, and (ii) the role that post-cumulus processes play in the genesis of economic ore deposits within layered intrusion (Boudreau, 1995; Mathez, 1995; Mathez *et al.*, 1997).

In the next two sections it is shown that many compositional and textural characteristics of rocks from ODP Hole 923A, in particular brown-pyroxene gabbros, are best explained by post-cumulus processes. Trace element modelling (Section 6.2) suggests that both within-crystal and between-sample variations can be best explain as the result of magmatic metasomatism (Mathez, 1995). Textural features (Section 6.3) cannot be explained as primary characteristics and are most simply explained by extensive post-cumulus textural modification.

### 6.2. Compositional characteristics indicative of post-cumulus processes

Clinopyroxene crystals show two main compositional characteristics indicative of the importance of postcumulus processes. Firstly, the significant enrichment in more incompatible elements (i.e. Zr) over less incompatible elements (e.g. Y) with increased abundance (fractionation). This can only occur during fractional crystallisation in association with much larger increases in incompatible element abundances than are observed (Section 6.2.1.2). Secondly, the lack of good

correlations between the abundances of incompatible trace elements and compatible major elements suggesting that simple fractionation processes did not control the mineral compositions. Furthermore, ubiquitous enrichment in incompatible elements at cumulus crystal rims, compared to their cores, suggests that during the growth of each crystal the melt from which it grew became incompatible element rich with decreased porosity. Various explanations for these observations are now considered.

*6.2.1 Crystallisation of trapped melt*

The simplest explanation for large trace element enrichments at crystal rims is through *in situ* crystallisation of trapped melt (e.g. Cawthorn, 1996a & 1996b). This can either occur by equilibrium crystallisation or fractional crystallisation.

6.2.1.1 Equilibrium crystallisation of trapped melt occurs through continual equilibration between the entire crystal assemblage and the interstitial melt that it is crystallising from. This can be discounted as a general mechanism to explain the incompatible element abundances in clinopyroxene as it produces unzoned crystals. However, as trapped melt has been strongly advocated as a mechanism to explain incompatible element abundances in mafic plutonic rocks (Cawthorn, 1996a & 1996b), it seems appropriate to test this hypothesis for the two samples in which clinopyroxene is almost unzoned (from 30.26 and 47.33 mbsf). This has been done using the model proposed by Cawthorn (1996a). Plagioclase in these samples is zoned; thus, this approach is not strictly valid, but it provides a first order test for equilibrium crystallisation of trapped melt. This model calculates the final compositions of each of the minerals present after equilibrium crystallisation of a given proportion of trapped melt via mass balance. The input parameters are the phase proportions (including melt fraction), the composition of the trapped melt, and the mineral D's. The relative proportions of the mineral phases were assumed to equal those observed in the solid rock (Table 3.1) for want of a better approximation. The D's and melt composition used are give in Table 6.1 and discussed in the caption and the results of the modelling are shown in Fig. 6.1.

Using these input parameters, the composition of clinopyroxene is not satisfactorily modelled by equilibrium crystallisation of trapped melt for either sample. This is shown by the greater amount of trapped melt required to model the LREE than HREE abundances in both samples (Fig. 6.1); i.e. to explain the clinopyroxene compositions by equilibrium crystallisation of trapped melt, the melt would need to have had a higher LREE/HREE ratio than that used in the modelling. The significant difference between the modelled and real Eu anomaly may be a function of the use of an inappropriately large plagioclase $D_{Eu}$. Two

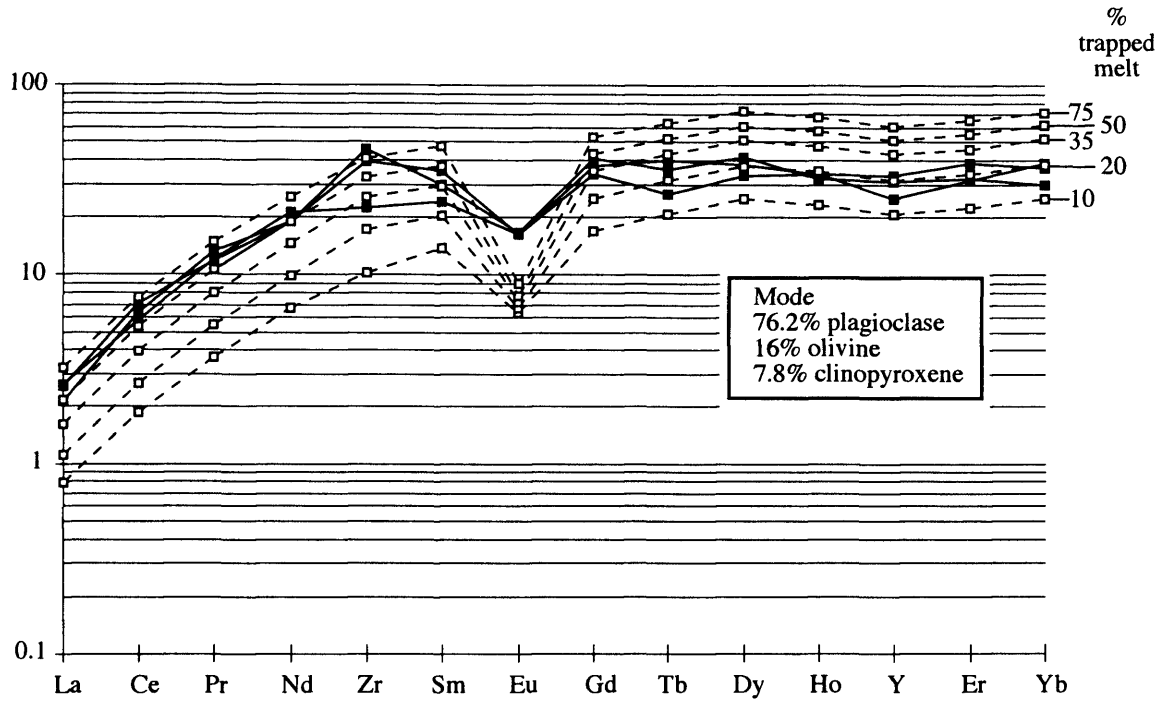


Fig. 6.1a Chondrite-normalised incompatible element abundances in clinopyroxene in the sample from 30.26 mbsf (filled squares and solid lines) and model concentrations (open squares and dashed lines) for different degrees of trapped melt (10, 20, 35, 50 & 75 %) calculated using the equations of Cawthorn (1996a). Note the different degrees of trapped melt required to model the LREE and HREE abundance. See text for discussion of modelling procedure and Table 6.1 for the input parameters.

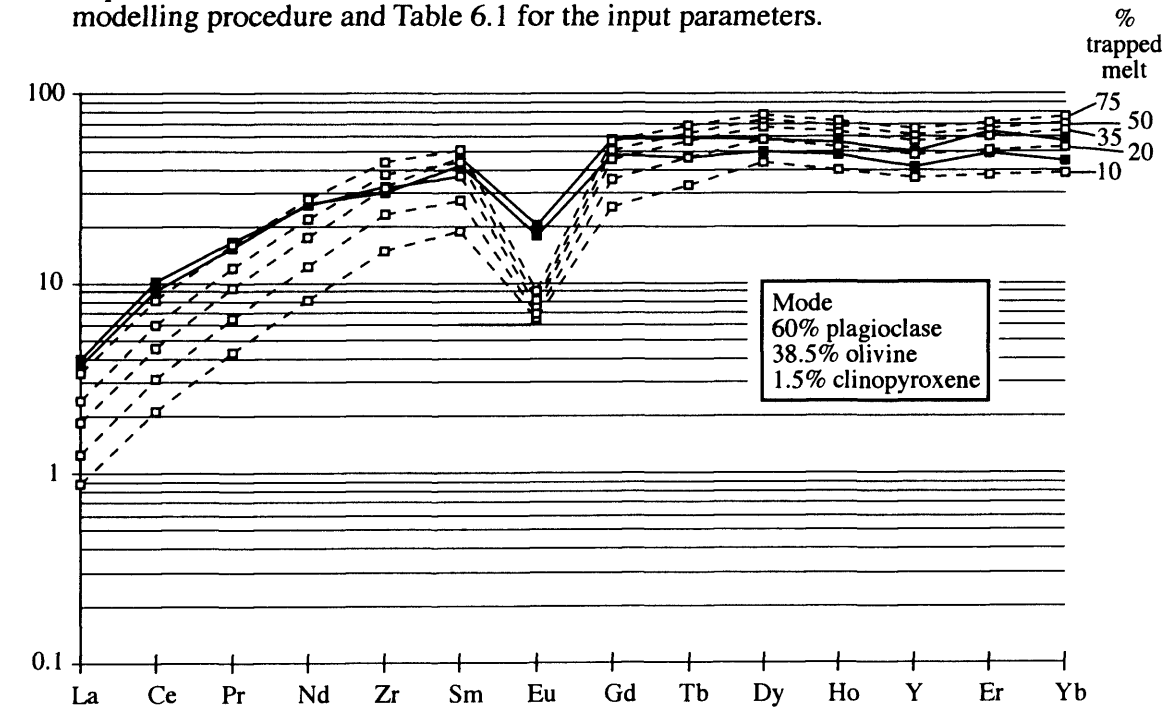


Fig. 6.1b Chondrite-normalised incompatible element abundances in clinopyroxene in the sample from 47.33 mbsf (filled squares and solid lines) and model concentrations (open squares and dashed lines) for different degrees of trapped melt (10, 20, 35, 50 & 75 %) calculated using the equations of Cawthorn (1996a). Note the different degrees of trapped melt required to model the LREE and HREE abundance. See text for discussion of modelling procedure and Table 6.1 for input parameters.

further lines of evidence suggest that the composition of clinopyroxene in these samples is not controlled by trapped melt: (i) their relatively low Cr abundances, and (ii) the high Fo content of olivine adjacent to clinopyroxene at 47.33 mbsf. Firstly, the primitive olivine and plagioclase compositions in both of these samples (see Fig. 4.15) suggest that trapped melt would have been Cr-rich. During plagioclase and olivine precipitation the Cr abundance in the melt would increase; thus, if clinopyroxene grew from trapped melt it would be expected to be Cr-rich. However, in both of these samples clinopyroxene is Cr-poor. Secondly, the effect of trapping >50% trapped melt needed to explain the clinopyroxene compositions (Fig. 6.1) at 47.33 mbsf would have been to massively reduce the Fo content of the olivine. The primary Fo content of olivine in this sample would have had to be $Fo_{90-94}$ (Barnes, 1986; his Fig. 2). This is more magnesian than olivine in abyssal peridotite samples from the MARK area ($Fo_{90-91}$, Ross & Elthon. 1997b; Stephens, 1997). Thus, the uniformly high incompatible element abundances in clinopyroxene in samples from 30.26 and 47.33 mbsf almost certainly did not form by equilibrium crystallisation of trapped melt. However, this conclusion is clearly dependent on the composition of the melt trapped, for which there is no external control.

| | La | Ce | Pr | Nd | Zr | Sm | Eu | Gd | Tb | Dy | Ho | Y | Er | Yb |
|---|---|---|---|---|---|---|---|---|---|---|---|---|---|---|
| Plag. | .18 | .15 | .12 | .09 | .01 | .05 | 1.0 | .03 | .02 | .01 | .01 | .01 | .01 | .001 |
| Cpx | .08 | .12 | .17 | .23 | .12 | .33 | .36 | .39 | .40 | .41 | .40 | .40 | .38 | .34 |
| Oliv. | $4E^{-6}$ | $1E^{-5}$ | $4E^{-5}$ | $5E^{-5}$ | $7E^{-3}$ | $2E^{-4}$ | $4E^{-4}$ | $6E^{-4}$ | $2E^{-3}$ | $2E^{-3}$ | $3E^{-3}$ | $3E^{-3}$ | $5E^{-3}$ | .01 |
| Bulk D | .13 | .13 | .12 | .12 | .04 | .13 | .71 | .14 | .13 | .13 | .13 | .13 | .12 | .10 |
| $Melt_{(n)}$ | 6.0 | 9.0 | 11.7 | 14.3 | 14.6 | 18.1 | 16.8 | 17.4 | 19.6 | 21.2 | 19.9 | 17.9 | 19.5 | 21.2 |

Table 6.1. The distribution coefficients (D's) and melt composition used in modelling. Sources of D's: all clinopyroxene (cpx) D's and plagioclase (plag) $D_{LREEs}$ & $D_{Zr}$ from Table A.I.1 in Appendix A.I; plagioclase $D_{HREE's}$ calculated for same An ($An_{60}$) and temperature (1150°C) as for LREE using model of Blundy & Wood (1994; Appendix A.I.1); plagioclase $D_{Eu}$ from Drake & Weill (1975) for $fO_2$ near QFM; Olivine $D_{REE}$ and $D_Y$ from experiment L2 of Beattie (1994), olivine $D_{Zr}$ from Kelemen *et al.* (1990). The bulk D is calculated assuming crystallisation of 60% plagioclase, 30% clinopyroxene and 10% olivine. The melt composition is calculated to be in equilibrium with the average of four analyses of core of the clinopyroxene oikocryst in the sample from 46.30 mbsf, and is chondrite-normalised. Ti is not considered because the modal proportion of ilmenite is to small to quantify accurately, but will have a significant influence on the behaviour of Ti.

6.2.1.2 Fractional crystallisation of trapped melt occurs when crystallisation proceeds without equilibration between the melt and previously formed crystals. In this process the melt is in equilibrium with the growing surface of the crystal, but not previously formed parts of the crystal. This provides a possible

explanation for incompatible element rich rims on clinopyroxene crystals in all lithologies. Fractional crystallisation can be tested using the samples from 31.31 mbsf, a brown-pyroxene gabbro, and from 64.87 mbsf, a poikilitic olivine gabbro, for which detailed zoning profiles are available (Figs. 4.16 & 4.21). This can most simply be shown to be incapable of producing the observed compositional variation in X-Y plots of Zr versus Y (Fig. 6.2). Modelling of this, and all further modelling in this chapter, assumes modal proportions of 60% plagioclase, 30% clinopyroxene, and 10% olivine (i.e. the bulk D's in Table 6.1 are used). Lowering the bulk $D_{Zr}$ used in modelling cannot lead to the Rayleigh fractionation trends fitting the data, and to fit the data by increasing the bulk $D_Y$ requires excessively large D's (bulk $D_Y$ ~0.65 at 31.31 mbsf, and ~0.45 at 64.87 mbsf). These are well outside the likely errors in the D's used.

An alternative way to test this *in situ* Rayleigh fractionation is to calculate the volume of melt which remained during crystallisation of the rim of the cumulus clinopyroxene from 31.31 mbsf and use this to model the Rayleigh fractionation trend. Assuming that crystallisation from trapped melt started 1.2 mm from the rim where incompatible element abundances begin to increase, the volume of melt remaining is calculated assuming that the clinopyroxene is a cube and constituted 30% of the crystallising mode. Fig. 6.3 shows that the model fractional crystallisation trends do not fit the data. Two important characteristics of the model trends compared to the observed trends are: (i) a significantly higher Y abundance at the crystal rim in the model than is observed, and (ii) tightly curved model trends compared to the sub-linear trends observed. These difference suggest that the incompatible element zoning of this samples cannot be explained by fractional crystallisation of trapped melt.

Finally, the entire clinopyroxene Zr - Y dataset is modelled in Fig. 6.4. This shows that clinopyroxene analyses with the lowest Zr/Y ratios, mainly oxide gabbros, can be derived from the most primitive analyses by fractional crystallisation. However, the majority of the dataset, in particular brown-pyroxene gabbros, cannot. As with modelling for individual samples, varying the bulk $D_{Zr}$ cannot account for the observed trend, and the bulk $D_Y$ has to be increased to ~0.6 to model the highest Zr/Y ratio. This is unrealistically high.

In conclusion, Rayleigh fractionation of trapped melt cannot explain the within-crystal or between-sample trace element distributions in clinopyroxene. This is not surprising considering the convincing arguments that melt will not be stationary within the crystal mush, but will migrate due to compaction and convection (Sparks *et al.*, 1985; Kerr & Tait, 1986; Shirley, 1986, 1987). However, despite discounting trapped melt as a mechanism to explain the observed compositional variation within clinopyroxene, a small volume of melt is always likely to be trapped, as permeability decreases with the cube of porosity.

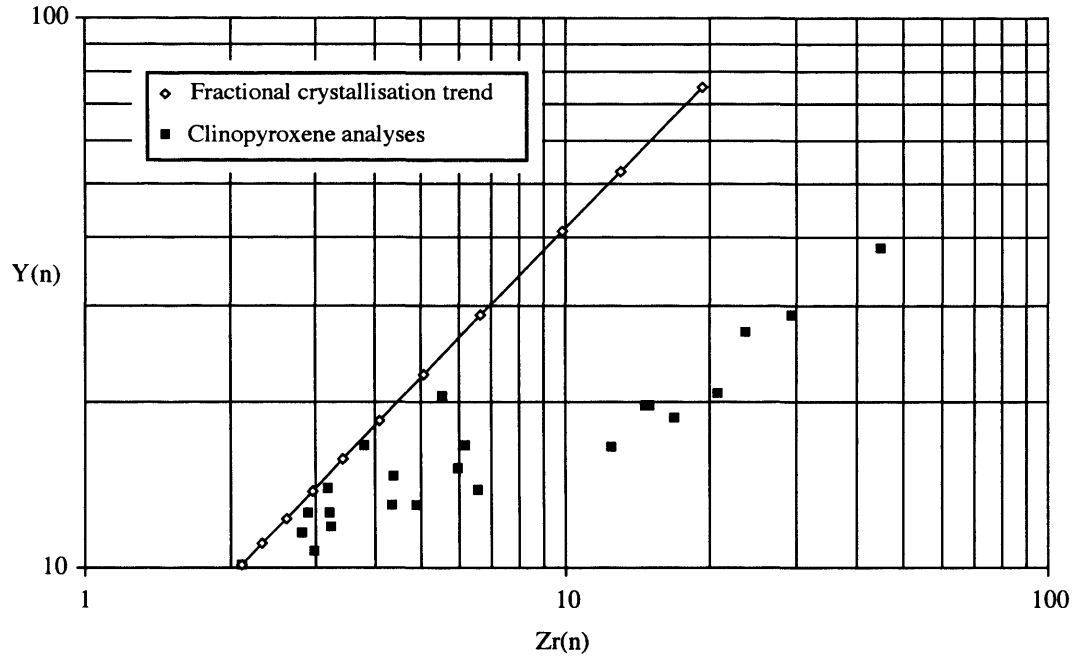


Fig. 6.2a Chondrite-normalised Zr versus Y in clinopyroxene in the sample from 31.31 mbsf, a brown-pyroxene gabbro (filled squares), and a model trend for Rayleigh fractionation (open diamonds). Clearly, Rayleigh fractionation cannot explain the data.

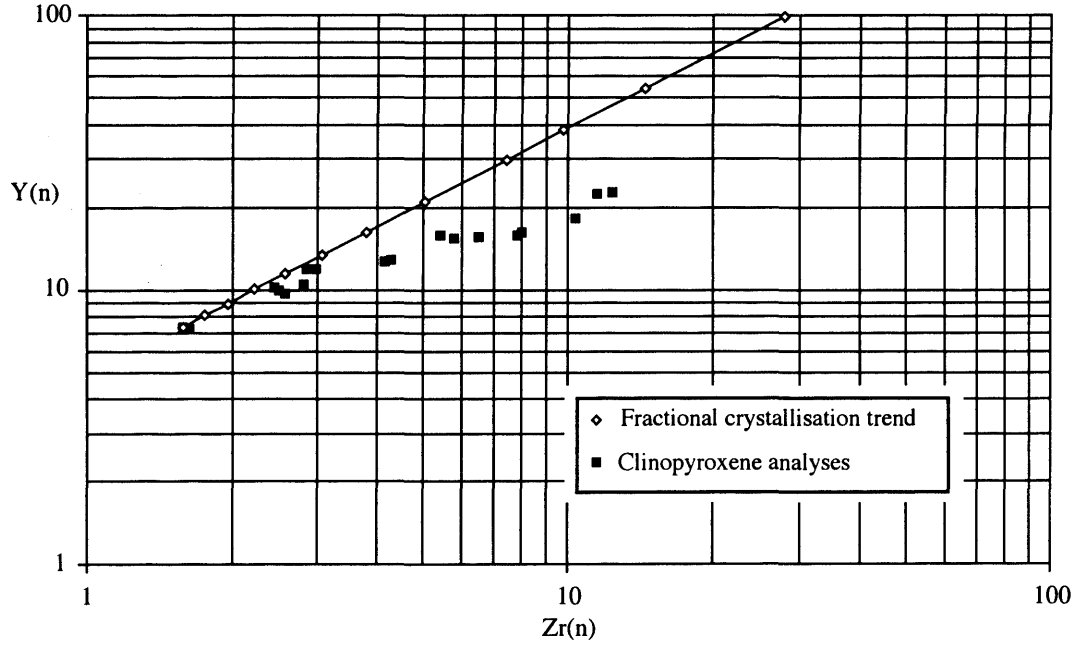


Fig. 6.2b Chondrite-normalised Zr versus Y in clinopyroxene in the sample from 64.87 mbsf, a poikilitc olivine gabbro (filled squares) and a model trend for Rayleigh fractionation (open diamonds). As with the brown-pyroxene gabbro, Rayleigh fractionation cannot explain the data.

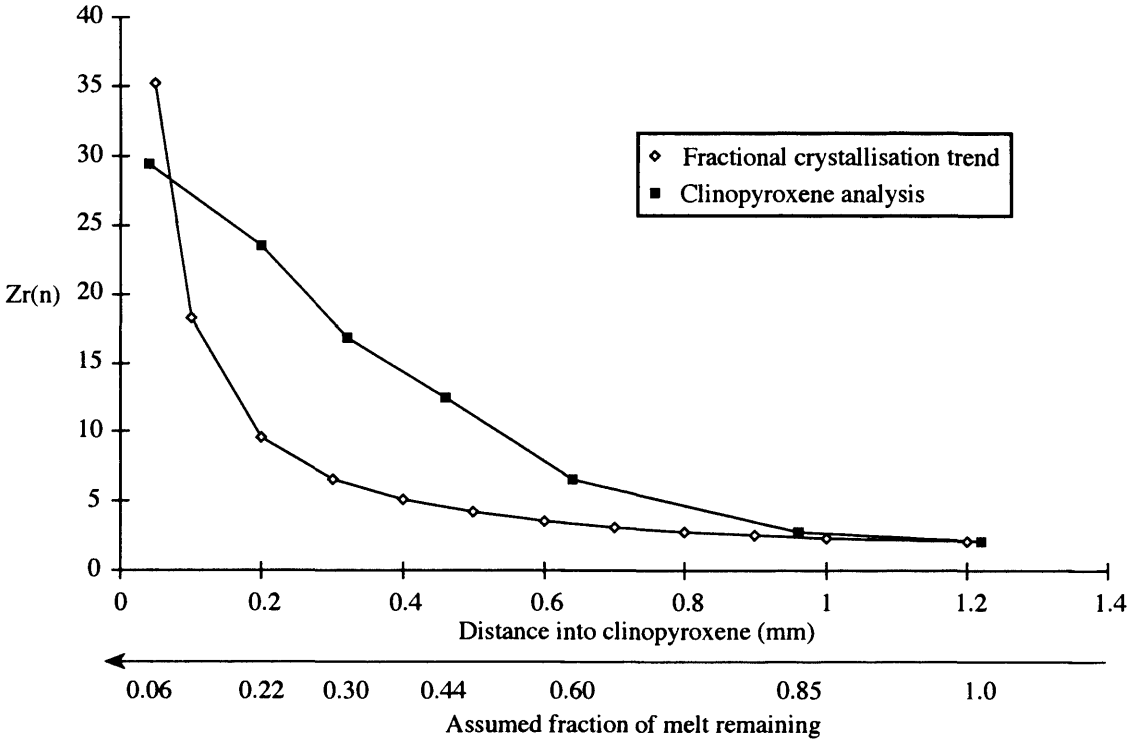


Fig. 6.3a Chondrite-normalised Zr plotted as a function of distance into a clinopyroxene crystal (filled squares) in the sample from 31.31 mbsf (see Fig. 4.21), and a Rayleigh fractionation trend (open diamonds) calculated by making assumptions about the relationship between the radius of the clinopyroxene crystal and the volume of melt remaining (see text for details). Clearly the Rayleigh fractionation trend does not fit the data.

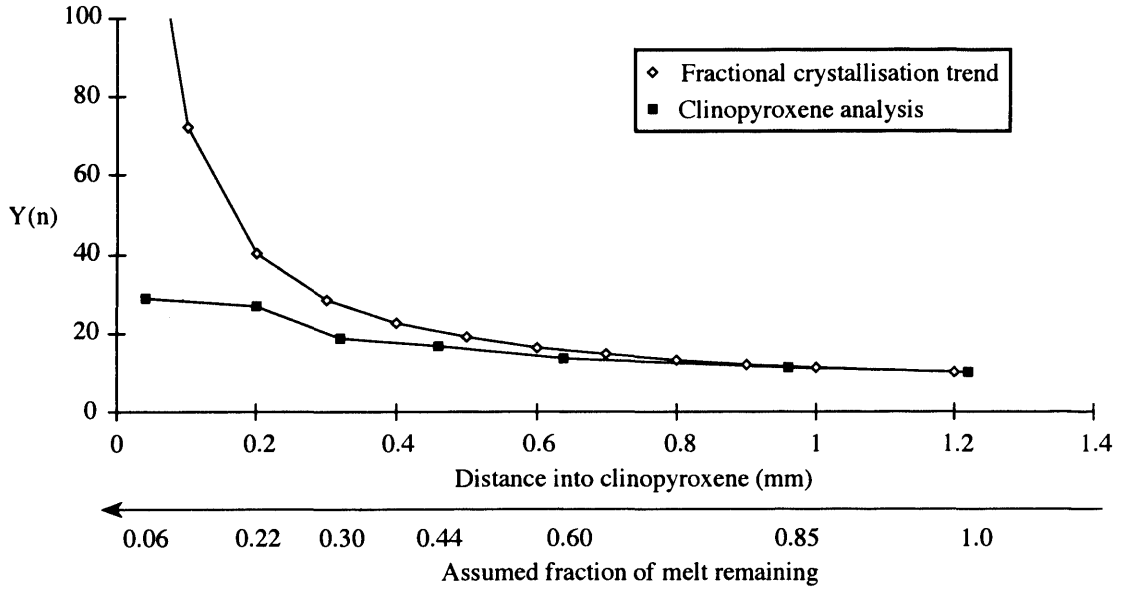


Fig. 6.3b Chondrite-normalised Y plotted as a function of distance into a clinopyroxene crystal (filled squares) in the sample from 31.31 mbsf, and a Rayleigh fractionation trend (open diamonds) calculated by making assumptions about the relationship between the radius of the clinopyroxene crystal and the volume of melt remaining (see text for details). Clearly the Rayleigh fractionation trend does not fit the data. Furthermore, comparing the Rayleigh fractionation trends for Zr (Fig 6.3a) and Y shows that the Zr/Y ratio does not increase in Rayleigh fractionation as much as it does in the crystal.

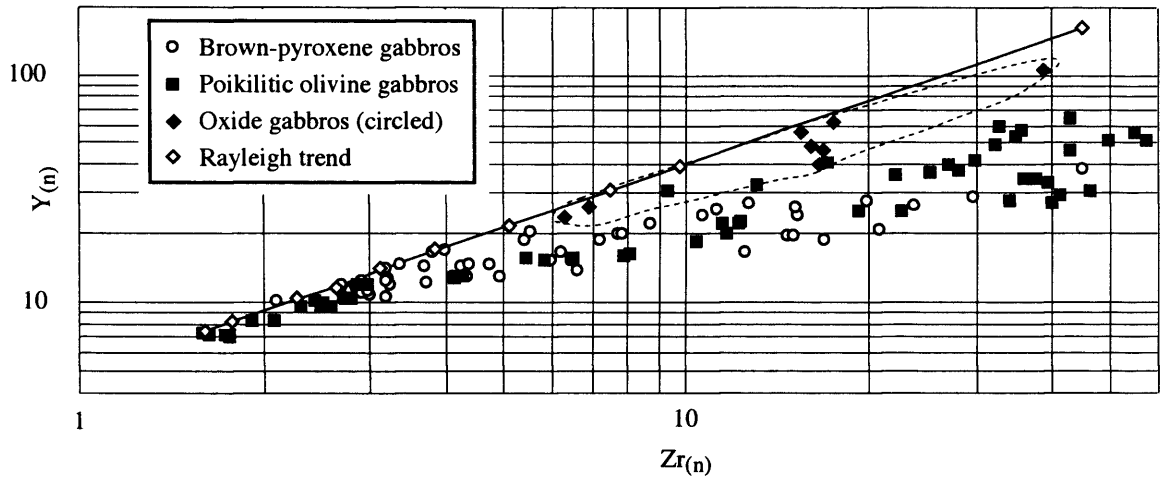


Fig. 6.4 Chondrite-normalised Zr versus Y in clinopyroxene (all analyses shown) and a model trend for Rayleigh fractionation (open diamonds). The Rayleigh fractionation trend fits the trend shown by analyses with the lowest Zr/Y ratios but does not approach the higher Zr/Y ratios. Note that the oxide gabbros lie close to the trend defined by Rayleigh fractionation.

The above discussion has only considered clinopyroxene compositions for three reasons. Firstly, more extensive and better quality trace element data are available for clinopyroxene than plagioclase. Secondly, the incompatible trace elements for which good data are available for plagioclase all have similar bulk D's (LREE, Y; Table 6.1). Thirdly, it is believed that some plagioclase crystals record a more complex genesis than clinopyroxene crystals (see Chapter Five).

*6.2.2 Diffusive modification of magmatic zoning profiles*

Post-crystallisation redistribution of trace elements may occur through diffusion, thus modifying the primary crystallisation zoning profiles. This is not believed to have been significant for several reasons. Firstly, Mg# zoning is preserved in clinopyroxene (e.g. Figs. 4.16 and 4.21), despite Fe and Mg diffusing faster than trivalent trace elements in clinopyroxene (Brady & McAllister, 1983; Sneeringer *et al.*, 1984). Secondly, $Sr^{2+}$ and $Sm^{3+}$ diffuse at similar rates in clinopyroxene (Sneeringer *et al.*, 1984), suggesting that Y and Zr, trivalent and quadrivalent cations, may diffuse at similar rates also. Thus, variations in the Zr/Y ratio are unlikely to be due to differential diffusion rates. Thirdly, for a Rayleigh fractionation zoning profile to be turned into the observed zoning profile, net loss of Y from the crystal is required (e.g. Fig. 6.3b). This is unlikely given the lack of an obvious sink for Y. Finally, calculation of the characteristic diffusion length for $Sm^{3+}$ (and $Sr^{2+}$) in clinopyroxene suggest that in a rapidly cooling environment, such as a mid-ocean ridge magma chamber, diffusion will only be important over short distances. For example, the characteristic diffusion length (eqn. 6.i) for Sm in clinopyroxene over 100,000 yrs decreases from 0.5 mm at 1200°C to 0.02 mm at 1000°C and to 0.002 mm at 900°C (Sneeringer *et al.*, 1984).

$$\text{characteristic diffusion length} = [D \times t]^{1/2} \qquad \text{(equ. 6.i)}$$

in which:

D = diffusion coefficient for given temperature

t = time over which diffusion occurs

*6.2.3 Different parental melts*

Growth of clinopyroxene cores and rims from melts derived from different parental compositions provides another possible mechanism to explain the compositional variation within clinopyroxene. However, the compositional variation within clinopyroxene is dominated by variation between elements of different compatibility in a plagioclase-clinopyroxene dominated system; i.e. little fractionation between REEs occurs, but Zr is significantly fractionated from REE and Y, and little Sr and Eu fractionation. Furthermore, the fractionation trends

are relatively smooth, not stepped as might be expected for growth from different parental melt compositions. It is therefore considered unlikely that the main compositional variation within clinopyroxenes is due to different parental melt compositions.

### *6.2.4 Magmatic metasomatism*

Magmatic metasomatism provides another possible explanation for the trace element distributions in clinopyroxene (Mathez, 1995). This is the processes of reaction and (partial) re-equilibration between a migrating interstitial melt and the crystal assemblage and occurs due to disequilibrium between the interstitial melt and the cumulate assemblage which it invades. Disequilibrium between the interstitial melt and the crystal assemblage will be common as melt migrates through a crystal mush due to stratigraphic variations in mineral and melt compositions and modal proportions. The magmatic metasomatism process can be modelled in two ways: (i) as a chromatographic column (Navon & Stolper, 1987), and (ii) as combined assimilation and fractional crystallisation (AFC, DePaolo, 1981; Kelemen, 1986). The advantages and disadvantages of these approaches are discussed next.

The chromatographic column approach to modelling magmatic metasomatism assumes a column of partially molten, constant porosity crystals into which a constant melt composition is added at the base (Navon & Stolper, 1987). If the melt and matrix are not in equilibrium, then chemical exchange between them will occur. For example, consider an initially homogeneous cumulate pile that has an increment of incompatible element rich melt added to it from below which percolates upwards through the system. Given sufficient time, the incompatible element rich melt will equilibrate with the crystals it passes, enriching them in incompatible elements. If the column of crystals is sufficiently large, the incompatible element abundances in the added melt will eventually be reduced to the levels in the initial interstitial melt (i.e. in equilibrium with the primary crystal assemblage). However, the more incompatible an element is the greater the mass of crystals it will be able to equilibrate with before being stripped from the evolved melt batch. This is because it requires a smaller mass of highly incompatible elements to equilibrate with a crystal assemblage than it does for less incompatible elements. Accentuation of this effect will occur if the initial enrichment of incompatible elements in the added melt is proportional to their incompatibility. This will be the case if the incompatible element rich melt is produced by crystallisation at the base of the crystal column. Notably, compatible elements will be stripped from

the matrix during this process, buffering their abundance in the interstitial melt, because the overall budget of these elements in the system is dominated by the crystals.

Modelling magmatic metasomatism using the AFC equations of DePaolo (1981) has been extensively utilised by Kelemen and co-workers in the context of reactive melt migration within the mantle (Kelemen, 1986, 1990; Kelemen *et al.*, 1992, 1993). This formulation can be used to calculate the composition of the melt as it progressively fractionates and equilibrates with the crystal mush. For example, melt migrating through the crystal mush may resorb (assimilate) part of the cumulate assemblage, whilst precipitating either the same or different phases with modified compositions. The input parameters for modelling are the bulk D's of the assimilated and fractionated assemblages, the fraction of melt remaining (F), and the ratio of the mass assimilated to mass crystallised ($M_a/M_c$). Both the bulk D's and the $M_a/M_c$ ratio are likely to be variable during magmatic metasomatism. F is likely to generally decrease due to cooling, although if the concentration of volatiles in the interstitial melt may under some circumstances lead to hydration melting, and thus increased F (McBirney, 1987). The ratio of the mass assimilated to that precipitated depends on the thermodynamics of the system and cannot be simply predicted. However, Ghiorso and Kelemen (1987) show that in general isothermal assimilation of phase(s) more refractory than those precipitated will lead to $M_a/M_c$ being less than one and that cooling will enhance this effect. Likewise, if the phase(s) assimilated are less refractory than those precipitated, then $M_a/M_c$ will generally be greater than one under isothermal conditions. The special case of the assimilation and reprecipitation of the entire crystal assemblage, i.e. $M_a/M_c$ equal to one, is zone refining. Because of the high number of variables, modelling using the AFC equation is more useful in determining whether magmatic metasomatism is capable of producing a given composition than it is in determining the details of how a given composition was produced.

The AFC modelling approach is used here, because the assumptions of the chromatographic column model (constant melt composition added to the crystal mush and constant melt volume) are inapplicable in a cumulate mush. Prior to showing that this process can explain the compositional variation observed, the physical model envisaged is expanded.

Consider a crystal mush of either constant or varying porosity, but varying mode and/or phase compositions (although these are not strictly required), as is likely to exist at the floor of a magma body. Cooling from below induces crystallisation throughout the cumulate pile, but dominantly at the base of the mush zone. This modifies the composition of the interstitial melt, in particular, increasing its concentration of incompatible elements, including volatiles. This

melt then moves upwards due to buoyancy forces into a new crystal assemblage with which it is not in equilibrium. The local phase relations will control the process of (partial) equilibration between the phases present. For instance, if the melt is highly enriched in volatiles, phase relations may shift such that one or more phase is resorbed. Alternatively, if the bulk composition of the melt is little modified, chemical exchange between the crystals and melt may simply enrich the cumulus crystals in incompatible elements and deplete them in compatible elements via diffusion. The effect of this process is to produce an incompatible element rich melt, which is not markedly evolved in major (or compatible trace) elements due to the buffering effect of the crystals.

6.2.4.1 Modelling magmatic metasomatism requires knowledge of the bulk D's, the fraction of melt remaining (F), the ratio of the mass assimilated to mass crystallised, and the composition of the assimilated material (assimilate). For simplicity, in the modelling that follows the bulk D's are assumed to be the same for assimilate and precipitate. Furthermore, the composition of the assimilated cumulates is assumed to be in trace element equilibrium with the initial melt composition. As the purpose of the modelling is to test whether magmatic metasomatism provides a possible explanation for the observations, not to attempt to determine the details of the process, these are reasonable assumptions. The modelling was carried out using the bulk D's in Table 6.1, and the $M_a/M_c$ ratio was varied to achieve the best fit to the data. Fig. 6.5 reproduces Figs. 6.2 with model trends for magmatic metasomatism added. Clearly both the individual sample trends can be modelled better by magmatic metasomatism than by fractional crystallisation. Fig. 6.6 reproduces Fig. 6.3, but with a fractionation trend for magmatic metasomatism added. The magmatic metasomatism curve does not fit the data well, but unlike the fractional crystallisation modelling it does reproduce the Zr and Y abundances and Zr/Y ratio of the clinopyroxene rim. Furthermore, the melt fraction remaining at this Zr/Y ratio would potentially be mobile (~3% in contrast to ~0.00001% in the Rayleigh fractionation trend). Furthermore, the entire Zr-Y dataset for clinopyroxene fits between a trend defined by fractional crystallisation and a metasomatic trend with Ma/Mc = 0.89 (Fig. 6.7). Magmatic metasomatism can also explain the decoupling of major and trace elements, i.e. the large variation in incompatible element abundances with little correlation to major elements seen in clinopyroxene. Fig. 6.8 shows $Zr_{(n)}$ versus the MgO/FeO ratio for all clinopyroxene analyses and model AFC trends for Ma/Mc ratios of 0.4 and 0.85. D's for Mg and Fe for clinopyroxene, olivine and plagioclase were calculated from the experiments of Tormey *et al.* (1987) on MORB from the MARK area (clinopyroxene $D_{Mg}$ - 2.61, $D_{Fe}$ - 0.57; olivine $D_{Mg}$ - 5.77, $D_{Fe}$ - 1.64; plagioclase $D_{Mg}$ - 0.05, $D_{Fe}$ - 0.08). All analyses plot between the

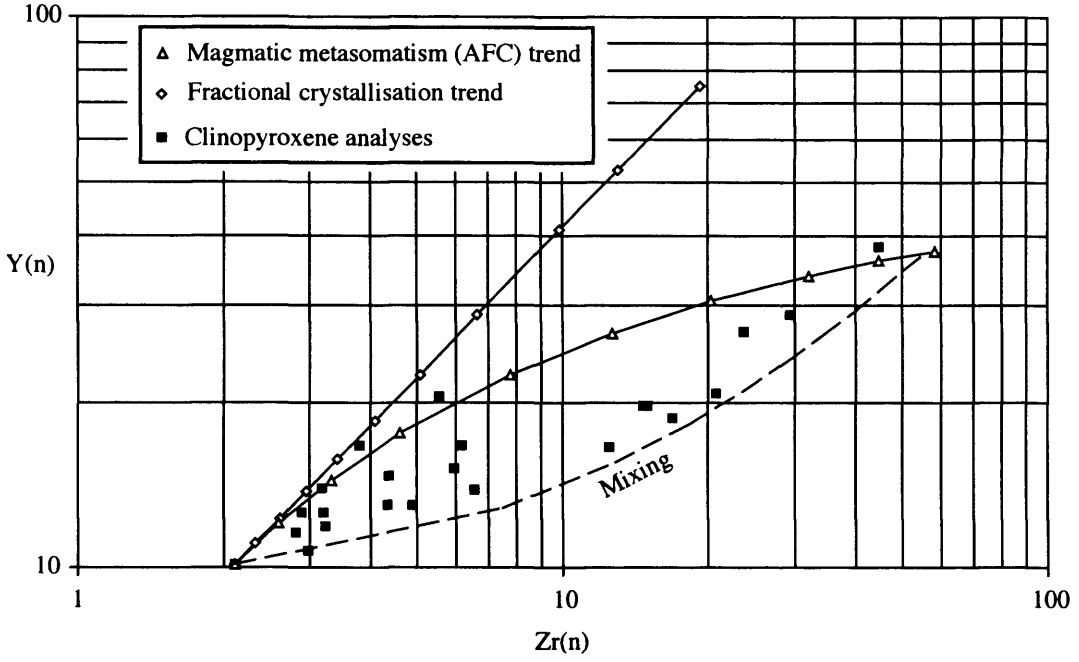


Fig. 6.5a Chondrite-normalised Zr versus Y in clinopyroxene in a sample from 31.31 mbsf (filled squares), a model trend for Rayleigh fractionation (open diamonds) as in Fig. 6.2, and a model trend for magmatic metasomatism (open triangles). The magmatic metasomatism trend (Ma/Mc = 0.89) fits the data far better than the rayleigh fractionation trend, and mixing between the end members produced by magmatic metasomatism (dashed line) brackets the data with the pure metasomatism trend.

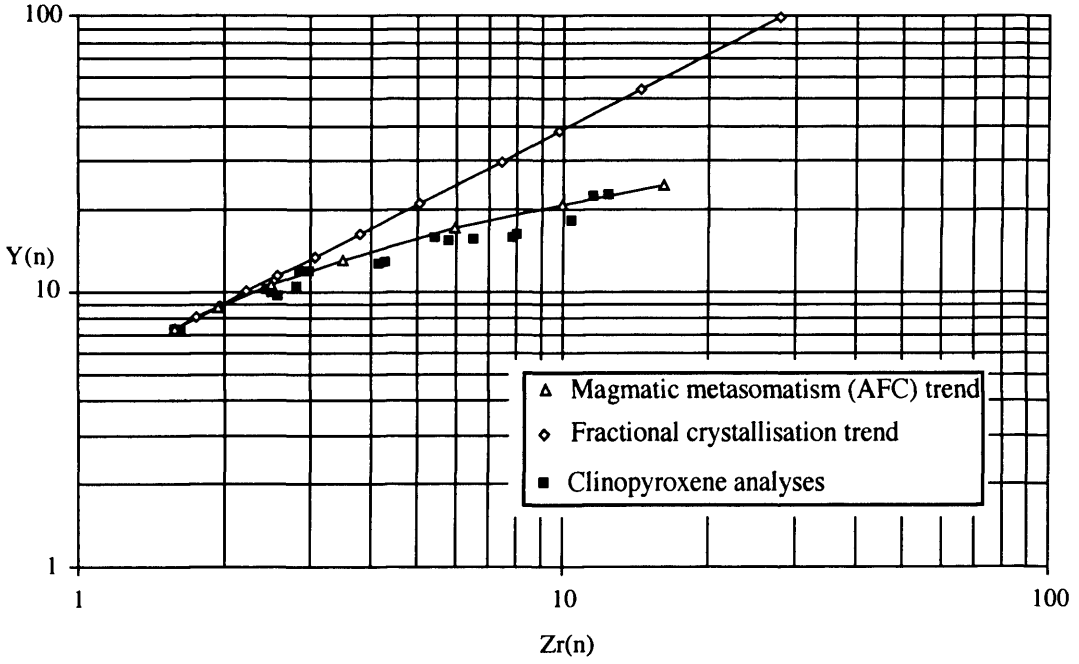


Fig. 6.5b Chondrite-normalised Zr versus Y in clinopyroxene in a sample from 64.87 mbsf (filled squares), a model trend for Rayleigh fractionation (open diamonds) as in Fig. 6.2b, and a model trend for magmatic metasomatism (open triangles). The magmatic metasomatism trend (Ma/Mc = 0.88) fits the data far better than the Rayleigh fractionation trend.

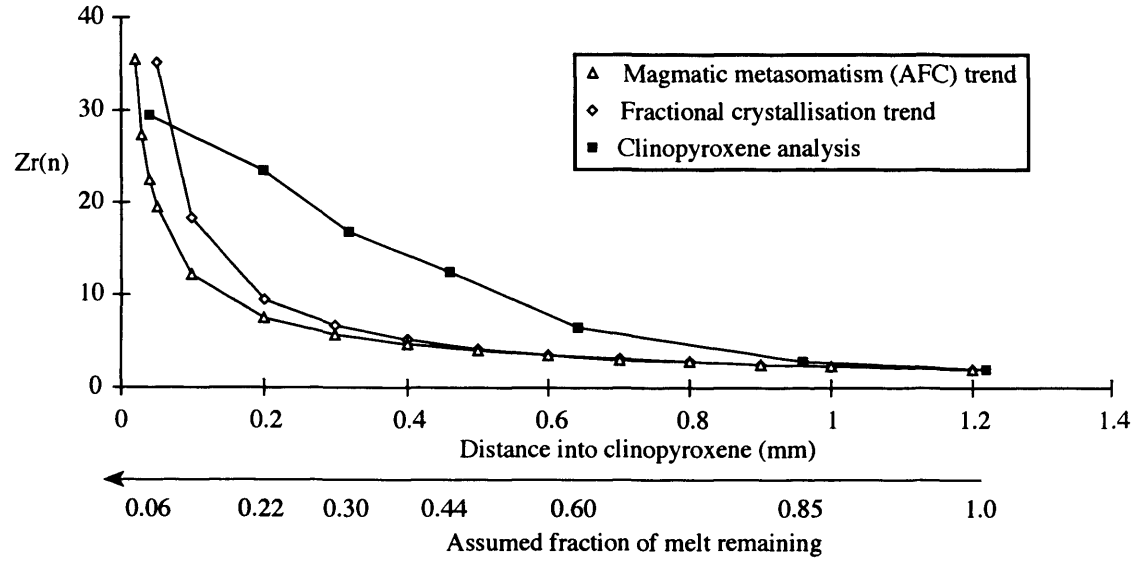


Fi.g 6.6a Chondrite-normalised Zr plotted as a function of the distance into a clinopyroxene crystal (filled squares) in the brown-pyroxene gabbro from 31.31 mbsf, as in Fig. 6.3a. A Rayleigh fractionation trend (open diamonds) and magmatic metasomatism trend (open triangles; Ma/Mc = 0.89) are also shown. These were calculated by making assumptions about the relationship between the radius of the clinopyroxene crystal and the volume of melt remaining (see text for details).

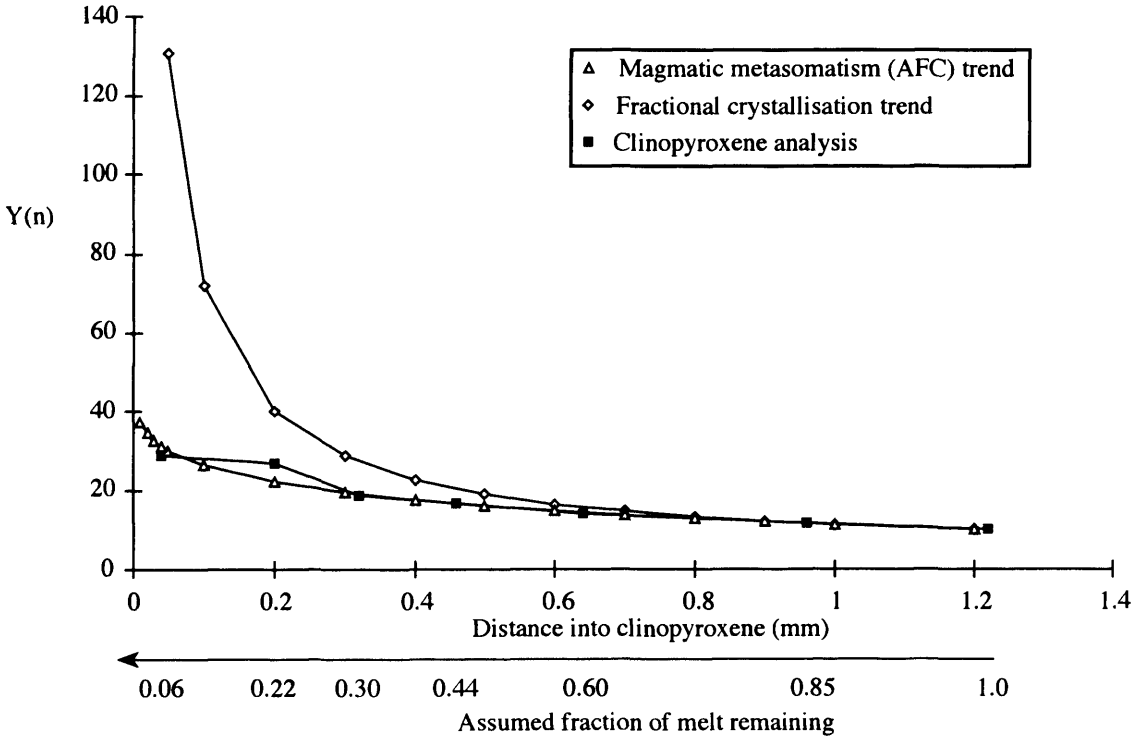


Fig. 6.6b Chondrite-normalised Y abundance plotted as a function of distance into a clinopyroxene crystal (filled squares) in the sample from 31.31 mbsf, as in Fig. 6.3b. A Rayleigh fractionation trend (open diamonds) and magmatic metasomatism trend (open triangles; Ma/Mc = 0.89) are also shown. These were calculated by making assumptions about the relationship between the radius of the clinopyroxene crystal and the volume of melt remaining (see text for details). Clearly the magmatic metasomatism Y trend fits the data much more closely than the fractional crystallisation trend.

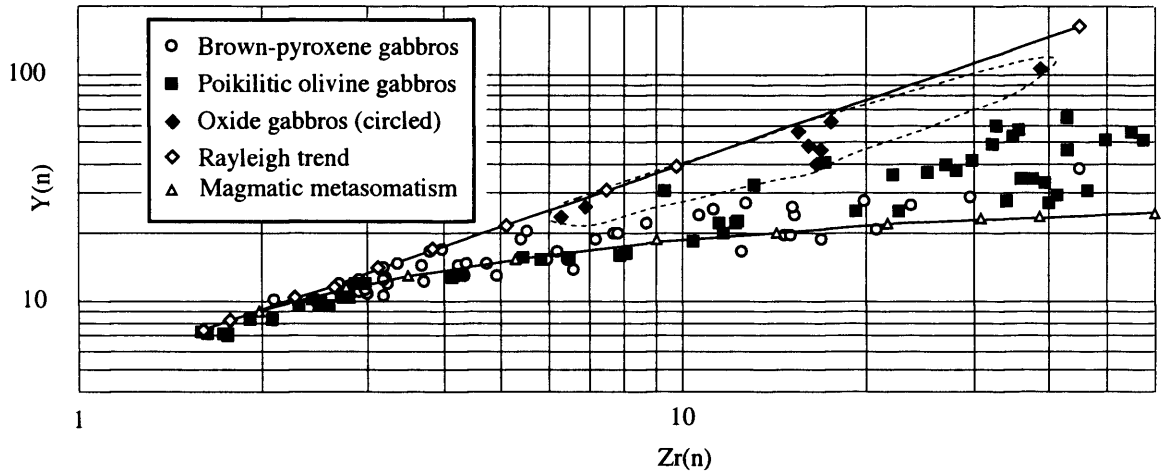


Fig. 6.7 Chondrite-normalised Zr versus Y in clinopyroxene (all analyses shown) and a model trend for Rayleigh fractionation (open diamonds) as in Fig. 6.4. Also shown is a model trend for magmatic metasomatism (Ma/Mc = 0.89) which along with the Rayleigh fractionation trend brackets almost all the data; i.e. a combination of fractional crystallisation and magmatic metasomatism can explain the data.

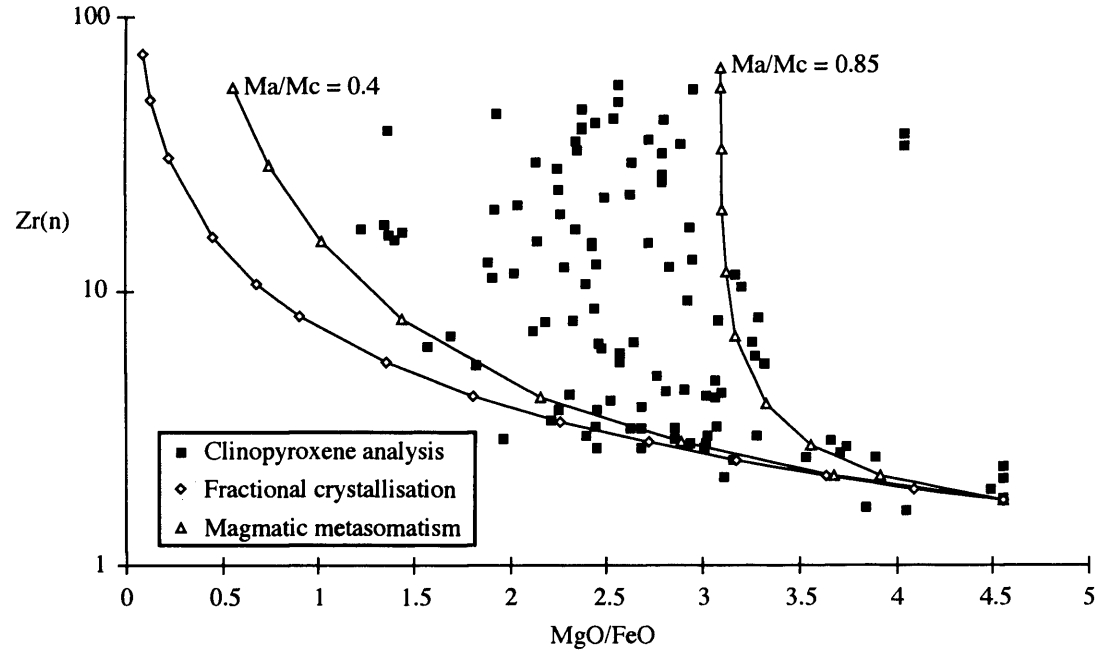


Fig. 6.8 Clinopyroxene MgO/FeO ratio plotted versus chondrite-normalised Zr (filled squares) for all analyses. Model fractionation trends are shown for Rayleigh fractionation (open diamonds) and magmatic metasomatism (AFC) with two different ratios of the mass assimilated to mass fractionated (open triangles). The Rayleigh fractionation trend does not fit most of the data. However, the magmatic metasomatism trends bracket almost all the data points.

trends defined by Ma/Mc ratios of 0.4 and 0.85, whereas the fractional crystallisation trend cannot explain the majority of the data.

6.2.4.2 Mixing between a primitive melt and an evolved melt produced by magmatic metasomatism can explain the clinopyroxene zoning at 31.31 mbsf very well (Fig. 6.9). In this modelling increasing proportions of the evolved end member melt are mixed into the interstitial melt to produce the compositions observed with approach to the crystal rim. This assumes that as the metasomatic melt migrates through the crystal mush it does not completely displace the overlying interstitial melt, but mixes with it. The good fit of the data to the mixing trends for both incompatible and compatible elements (Fig. 6.9) suggests that this may have been an important process in generating the rim compositions. However, it is unlikely that the composition of the evolved end member would be constant, and thus the calculated proportions of evolved and primitive melt are probably meaningless.

**6.3 Textural characteristics indicative of postcumulus processes**

Six textural characteristics imply that secondary textural development (Hunter, 1996) within the crystal mush was important in the genesis of the observed textures. These are:

(i) grain-size layering in brown-pyroxene gabbros, which includes cumulus plagioclase, clinopyroxene, and olivine *and interstitial ilmenite*, and is systematically associated with compositional variations and a general decrease in degree of interdigitation of crystals, with increased grain size (Fig. 3.10).

(ii) the correlation between lithology and the degrees of plastic deformation, i.e. oxide gabbros record the highest degree of crystal plastic deformation and poikilitic olivine gabbros the least.

(iii) the spatial correlation between olivine and clinopyroxene (Fig. 3.12), the occurrence of both clinopyroxene and orthopyroxene rims on olivine, and the inverse correlation between olivine and clinopyroxene modal proportions in brown-pyroxene gabbros (i.e. as the modal proportion of olivine increases, that of clinopyroxene decreases).

(iv) orthopyroxene exsolution lamellae extending out of clinopyroxene into adjacent plagioclase (Fig. 3.11).

(v) the distribution of oxides in oxide gabbros (Figs. 3.14 and 3.15).

(vi) the distribution of clinopyroxene in troctolites, and its spatial association with brown amphibole.

The characteristics are discussed in turn below.

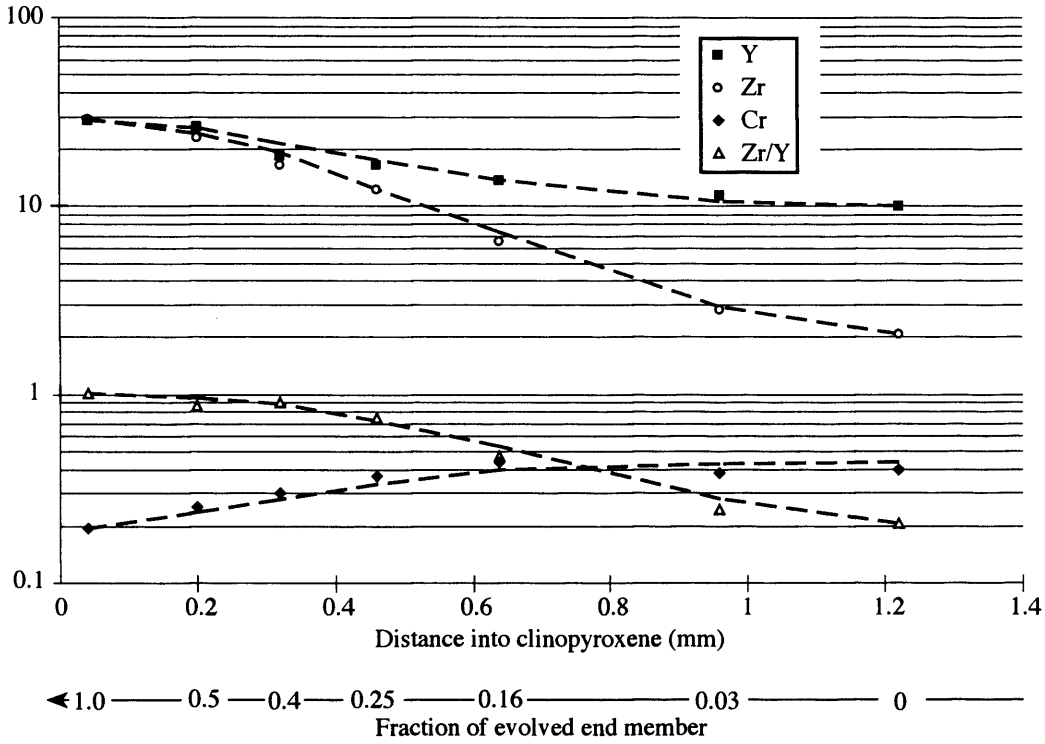





Fig. 6.9 Chondrite-normalised Zr, Y and Cr abundances and Zr/Y ratio (data points) plotted as a function of distance into a cumulus clinopyroxene in the sample from 31.31 mbsf (see Fig. 4.21). Also shown are model mixing curves (dashed lines). The mixing lines are calculated by adding varying proportions of the evolved end member composition (closest to the rim) to the previous composition. The proportion of the evolved end member added in each increment of mixing is given along the arrow at the bottom of the figure. The good fit of the curves for both incompatible (Zr and Y) and compatible (Cr) elements and the Zr/Y ratio suggest that mixing may well have been an important process in generating the observed compositions.

*6.3.1 Grain-size layering in brown-pyroxene gabbros*

Grain size layering in brown-pyroxene gabbros affects cumulus plagioclase, olivine and clinopyroxene and post-cumulus ilmenite. Layering of this kind is also common in core from ODP Hole 735B (Robinson, Von Herzen *et al.*, 1989), but is not common in terrestrial intrusions. The critical observations required to interpret this grain size layering are: (i) its coupling to compositional variations (Section 4.4.4), (ii) the decrease in grain boundary interdigitation with increased grain size (Fig. 3.10), and (iii) the lack of a correlation between grain size and mode.

Many origins of igneous layering have been proposed (e.g. Naslund & McBirney, 1996). Primary origins fall into two basic categories: (i) layering formed by variations of *in situ* nucleation and growth rates (e.g. Parsons, 1979), and (ii) layering formed by sedimentation of crystals (e.g. Irvine, 1980). *In situ* nucleation and growth cannot simply explain the observations. Variations in *in situ* nucleation and growth rate are not expected to affect all phases equally due to the different degrees of supersaturation required for nucleation; in which case this process should lead to a correlation between grain size and mode, and is unlikely to explain the compositional variation with grain size or the larger post-cumulus ilmenite in coarser brown-pyroxene gabbros.

Vast differences in the hydraulic properties of the cumulus phases preclude an origin of grain size layering via crystal settling. Sedimentation from high concentration density currents in which grain interactions control grain distributions could explain the co-variation in grain size of the cumulus phases (Hunter & Kokelaar, 1994; Naslund & McBirney, 1996). However, there is no apparent reason to expect abundant high density gravity flows to occur within mid-ocean ridge magma chambers, but not in terrestrial intrusions. Furthermore, this cannot simply explain the occurrence of coarser post-cumulus ilmenite in the coarser lithologies, or the compositional and grain shape variations with grain size. Thus, irrespective of the primary textures of the coarse and fine lithologies, secondary (post-cumulus) processes must be responsible for much of the variation with grain size. It is likely, however, that some primary difference in texture must have existed for post-cumulus modification to affect different regions of the crystal mush in different manners.

Reaction between interstitial melt and cumulus crystals is proposed above to explain the trace element compositional variations in clinopyroxene. This process can also explain the grain size layering and associated characteristics in brown-pyroxene gabbros. This model requires greater interaction between interstitial melt and cumulus crystals in coarse grained brown-pyroxene gabbros than in fine grained ones. This will lead to greater extents of Ostwald ripening, and thus, coarser grain sizes in all phases and less interdigitated grain boundaries.

Furthermore, this will lead to lower Mg#s of olivine and clinopyroxene due to reaction with the melt (Barnes, 1986). However, the primary cumulus mode will exert a strong influence on the final mode, and thus this will not necessarily correlate with grain size.

For secondary processes to affect different portions of the crystal mush in different manners, it is likely that there were primary textural variations within the crystal mush. Systematic compositional variation would probably have led to modal variations with grain size. For example, variation in volatile content in the interstitial melt could lead to the development of grain size variations, but the effect of volatiles on phase relations should be reflected in modal variations. Thus, it is likely that primary texture variations existed which control the primary porosity and permeability of the crystal mush and therefore controlled the flux of interstitial melt.

*6.3.2 Variation in the degrees of plastic deformation with lithology*

The higher degree of plastic deformation in more evolved lithologies can be explained in two ways. Firstly, more evolved lithologies may be weaker, and thus, may deform plastically under lower stresses than more primitive lithologies. Alternatively, deformation of the crystal mush may focus evolved interstitial melt into deforming regions (Dick *et al.*, 1991), leading to a correlation between degree of deformation and composition.

There are three reasons why more primitive lithologies are likely to be stronger than more evolved lithologies. Firstly, the constituent minerals in the more primitive lithologies are stronger than those in the more evolved compositions. For example, plagioclase, which is the dominant phase in all lithologies, is stronger the more calcic it is (Tullis, 1983), whereas oxide minerals, which are more abundant in the most evolved lithologies, are weaker than silicate phases (Agar & Lloyd, 1997). Secondly, clinopyroxene oikocrysts in poikilitic olivine gabbros will act as a cement, strengthening these rocks, because clinopyroxene is the most competent of the main mineral phases. Thirdly, more primitive lithologies have higher solidus temperatures and thus deformation at a given temperature is at a higher homologous temperature for more evolved lithologies.

Deformation of the crystal mush while it is partially molten may lead to evolved interstitial melt migrating into regions of increased deformation (Dick *et al.*, 1991). In this scenario the differing degrees of syn-magmatic deformation in the different lithologies is fundamental to their different compositions. Furthermore, this is a possible mechanism to explain variations in the primary porosity and grain size within the crystal mush. The high degree of deformation in all oxide gabbros, and the distribution of oxides in this lithology (discussed

below, Section 6.3.5) is consistent with syn-magmatic tectonic deformation being important in the generation of, oxide gabbros at least.

*6.3.3 The spatial correlation between olivine and clinopyroxene*

The spatial correlation between olivine and clinopyroxene, and the inverse correlation of their modal proportions, can be explained by reaction between cumulate crystals and an interstitial magma that is a mixture between evolved and primitive interstitial melt. This is because the olivine-clinopyroxene phase field boundary in MORB is strongly concave towards clinopyroxene (Walker *et al.*, 1979). Thus, mixing between a primitive and evolved melt produces a melt within the clinopyroxene (+ plagioclase) field. Reaction between this and an olivine-rich (or just olivine-bearing) cumulate assemblage will have the effect of resorbing olivine and precipitating of clinopyroxene, and thus can explain the spatial association between these phases, and their complimentary modal abundance variations.

*6.3.4 Orthopyroxene lamellae extending out of clinopyroxene*

Orthopyroxene lamellae extending from the rim of clinopyroxene into adjacent plagioclase (Fig. 3.11), parallel to exsolution lamellae in the clinopyroxene, are most easily explained by grain boundary migration after exsolution in the clinopyroxene. In this scenario clinopyroxene exsolves orthopyroxene upon cooling, then, due to either melt or fluid infiltration the clinopyroxene dissolves and plagioclase is precipitated, without significantly effecting the orthopyroxene. Zingg (1996) explains similar textures involving dissolution of orthopyroxene and precipitation of plagioclase as due to variation in $H_2O$ activity. Whether this provides an appropriate mechanism to explain these textures is unclear because clinopyroxene, but not orthopyroxene, was dissolved.

*6.3.5 The distribution of oxides in oxide gabbros*

Similar textures to that shown in Fig. 3.15, i.e. where clinopyroxene is enclosed in oxide masses but in optical continuity with cumulus clinopyroxene and clinopyroxene-oxide grain boundaries are rounded and embayed, have been observed in the Skaergaard intrusion (McBirney, 1995). These are interpreted to be the result of reaction between an invading FeTi-rich melt and a partially molten cumulate (McBirney, 1995) an interpretation that may also be applicable in this instance. This is consistent with the higher incompatible element abundances in clinopyroxene adjacent to oxides than adjacent to plagioclase at 19.38 mbsf (see Section 4.4.5), presuming the invading FeTi-rich melt was incompatible element rich. The high density of an FeTi-rich melt requires that it either percolated downwards through the crystal mush, or that the driving force

for interstitial melt migration was large. The only likely driving force large enough to drive FeTi-rich melts upwards is tectonic deformation of the crystal mush. Evidence that this may have played a role in the distribution of FeTi-rich melt in the genesis of oxide gabbros comes from the occurrence of oxides interstitial to plagioclase neoblasts (Fig. 3.14), and the consistently highly deformed nature of oxide gabbros. Furthermore, the apparently fracture filling form of an oxide at 67.79 mbsf (Fig. 3.3) further supports the driving force behind FeTi-rich melt being large. However, a detailed analysis of the deformation of oxide gabbros is beyond the scope of this study.

*6.3.6 The distribution of clinopyroxene in troctolites*

The low modal abundance of clinopyroxene in troctolites (< 10%), coupled with the occurrence of clinopyroxene inside cumulus plagioclase and indenting plagioclase grain boundaries (Figs. 3.4 and 3.6), suggest a complex crystallisation history. Furthermore, the abundance of brown amphibole rims on this clinopyroxene (Fig. 3.5) suggests that water played an important role in the genesis of these rocks. Clinopyroxene must have been a late crystallising phase in troctolites, otherwise it would occur in higher modal proportions. However, the occurrence of clinopyroxene within cumulus plagioclase is inconsistent with its crystallisation from interstitial melt. The most reasonable interpretation is that the clinopyroxene was precipitated from a melt which invaded, and partially melted, a plagioclase-olivine cumulate. The high abundance of brown amphibole suggests that hydration melting may have occurred. This is consistent with the rounded form of the clinopyroxene crystals, their distribution, and their distinct compositions. The low La/Yb and Eu/Eu* of these clinopyroxene crystals (Fig. 4.19) is consistent with extensive equilibration with plagioclase as would be expected in this model. Furthermore, this is consistent with the tendency for clinopyroxene to be elongate along plagioclase twin planes which are more easily dissolved than normal crystal faces. Thus, the initial plagioclase-olivine cumulate may have acted as a permeability barrier into which upward migrating melt flowed.

In conclusion, the combination of the textural characteristics discussed above are best explained by extensive cumulate maturation within a partially molten crystal mush. Cumulate maturation involves crystal coarsening, modification of mafic phase $Mg^{\#}$, and increasing textural equilibration, all of which are characteristics of coarser lithologies. Higher mafic phase $Mg^{\#}$s in the finer lithologies indicate higher solidus temperatures and consequently imply shorter periods of maturation. Deformed oxide gabbros suggest that FeTi-rich melt was associated with tectonic deformation although the ultimate origin of

this melt is unclear. This model is consistent with the model of magmatic metasomatism proposed to explain the incompatible trace element distributions in clinopyroxenes. Two outstanding questions will be addressed in the next two sections. Firstly, what is the role of volatile species, either dissolved in the melt, or as a separate fluid phase within the crystal mush, including, how did the oxygen fugacity vary ? Secondly, what effect did accessory phases have on the evolution of the interstitial melt ?

## 6.4 Further consideration of the development of the crystal mush

In this section it is proposed that fluids exsolved from within the crystal mush may have played an important role in the development of textures and the distribution of trace elements. Furthermore, the occurrence of sulphide globules within the mush may have buffered the oxygen fugacity in the interstitial melt, inhibiting magnetite precipitation. However, accessory phases, with the exception of ilmenite, were probably relatively unimportant to the compositional evolution of the interstitial melt in the crystal mush.

### *6.4.1 The role of volatiles*

Enrichment of incompatible trace elements in the interstitial melt suggests that it will also have been relatively enriched in volatiles, a suggestion supported by the occurrence of hydrous accessory phases in some samples. The role played by volatiles in this scenario may be very important in a number of ways. Whilst dissolved in the melt, volatiles can shift phase relations and change distribution coefficients. However, saturation of volatile species in the interstitial melt will lead to exsolution of a vapour phase, providing a buffer to the maximum concentration attained. Migration of an exsolved vapour phase through the crystal mush may also modify phase relations through interaction with the interstitial melt it moves through, and/or may chemically modify the crystal assemblage it passes (e.g. Mathez, 1989). Due to the low viscosity, and high buoyancy, of a vapour phase this may continue into the subsolidus (Zingg, 1996). Both textures and mineral compositions suggest that fluid migration within the cumulate pile was an important process. This is also supported by the occurrence of $CO_2$-rich fluid inclusions with >700°C entrapment temperatures (Kelley, 1997).

Textural evidence that fluids played an important role in the evolution of the crystal mush comes from the occurrence of amphibole within and around clinopyroxene. The association of amphibole within clinopyroxene with exsolved orthopyroxene (Fig. 3.16) suggests that amphibole may have been "exsolved" from clinopyroxene during recrystallisation. The amphibole and orthopyroxene free kink in a clinopyroxene at 21.08 mbsf (Fig. 3.17) suggests the components required for orthopyroxene and amphibole formation were removed during

strain recovery. These observations suggest that the components which went into amphibole during recrystallisation, in particular OH, were present in the clinopyroxene at temperatures above that at which exsolution and recovery occurred. Two possible explanations for this texture have been proposed by Buseck *et al.* (1980): (i) exsolution from a clinopyroxene having a minor solid solution towards amphibole, or (ii) hydration of an originally stoichiometric pyroxene. It is unlikely that the magma was constantly OH-saturated leading to crystallisation of non-stoichiometric clinopyroxene. It is far more likely that an exsolved fluid phase hydrated already crystallised clinopyroxene as it migrated through the near-solidus crystal mush. In this scenario exsolution of orthopyroxene from the hydrated clinopyroxenes would have been accompanied by exsolution of amphibole. The more common occurrence of amphibole enclosed within clinopyroxene, and associated with clinopyroxene recrystallisation (Fig. 3.16) in brown-pyroxene gabbros than other lithologies suggests that fluid infiltration may have been more significant in their genesis than in other lithologies.

The main compositional evidence for the role of fluids within the crystal mush comes from the occurrence of Cl-rich apatite. The constraints discussed in Chapter Five (section 5.4) suggest that a Cl-rich fluid phase may have been involved in the genesis of the Cl-rich apatite. Importantly, at 31.31 mbsf Cl-rich apatite occurs both at the margin of a coarse clinopyroxene, and within it adjacent to a recrystallised portion of the clinopyroxene crystal. The higher Cl-abundance of apatite within this clinopyroxene than apatite at the margin of the clinopyroxene further implicates the role of fluids in the recrystallisation of clinopyroxene. A further compositional characteristic of clinopyroxene which could be explained through interaction between an exsolved fluid and the crystal mush is the high La/Yb of clinopyroxene in the samples from 31.31 mbsf and 56.58 mbsf (Fig. 4.6). This can be explained by LREEs being redistributed within the crystal mush by a Cl-rich vapour phase because LREEs complex with Cl in high temperature fluids (Valsami-Jones *et al.*, 1994). Re-solution of this vapour phase into the magma that crystallised clinopyroxene, or perhaps more likely, interaction of the fluid directly with clinopyroxene, could lead to LREE-enrichment in the clinopyroxene. However, for this process to effectively transport LREEs requires that exsolution occurred from a small volume of evolved melt, otherwise major element cations (e.g. Fe, Mg, Al, Ca) within the melt will dominate the halogen complexes due to their much higher abundances (Adam *et al.*, 1993). The observation that apatite in gabbros from Site 922 contains high-Cl apatite (Ross & Elthon, 1997a) and have higher whole rock REE abundances and La/Yb ratios than samples from the other Sites drilled on Leg 153 (Barling *et al.*, 1997) is consistent with the idea that Cl-rich fluids transported REE.

However, gabbros from Site 922 are more altered than those from the other Sites (Cannat, Karson, Miller *et al.*, 1995) and thus this requires a detailed study to test this hypothesis.

6.4.1.1 Oxygen fugacity, which has an important control on phase relations, and is thus important to the differentiation of the melts, is partially controlled by volatile species within the melt (Carmichael & Ghiorso, 1986; Mathez, 1984, 1989). Observations pertinent to interpretation of the variation in, and controls on, oxygen fugacity are recapped next, and a model proposed in which immiscible sulphide globules buffer the oxygen fugacity in the interstitial melt.

Equilibrium $fO_2$ and temperature conditions calculated from ilmenite-magnetite pairs give sub-magmatic temperatures (Fig. 4.23) and extrapolation to magmatic temperatures may be unjustified. However, the different trend in $fO_2$ versus temperature for the leucocratic vein (parallel to NNO) than other samples (trending from NNO to QFM with decreasing temperature) is noteworthy. This indicates that the oxygen fugacity varied on a small scale, consistent with local buffering. The behaviour of Eu with respect to adjacent REEs also provides information about the $fO_2$ conditions during crystallisation. In both clinopyroxene and plagioclase Eu shows less variation in abundance than adjacent REE, indicating a higher bulk D. Thus, some Eu must have existed as $Eu^{2+}$. The correlation between Eu and Sm in clinopyroxene is similar for individual samples to the overall trend in the data, suggesting that the compatibility of Eu was similar throughout the crystallisation history; thus, the oxygen fugacity was similar. However, in oxide gabbros the correlation between Eu and Nd in plagioclase is closer to one to one than in other lithologies. This can be explained by Eu behaving more incompatibly during the genesis of oxide gabbro than of other lithologies, implying a higher $Eu^{3+}/Eu^{2+}$ ratio. This is consistent with magnetite occurring in these samples, implying a higher $Fe^{3+}/Fe^{2+}$ ratio than in other lithologies; i.e. oxide gabbros crystallised under more oxidised conditions than other lithologies. However, the $fO_2$ was similar during crystallisation of other lithologies.

Ilmenite and sulphides are common interstitial phases in all brown-pyroxene gabbros and poikilitic olivine gabbros. However, magnetite is rare, and where present is associated with ilmenite and/or sulphides. This is unexpected because since the crystal mush probably behaved as a closed system with respect to oxygen, $Fe^{3+}$ should have become concentrated in the melt prior to magnetite saturation. This implies that the oxygen fugacity in the interstitial melt was buffered, preventing the activity of $Fe^{3+}$ increasing sufficiently to induce magnetite precipitation. The most likely buffer is the almost ubiquitous

interstitial sulphide because of the large amount of oxygen consumed in the reaction:

$$S^{2-} + 2O_2 \rightarrow SO_4^{2-} \qquad \text{(i)} \qquad \text{Mathez (1989)}$$

or in terms of Fe speciation:

$$FeS + 5\ Fe_2O_3 \rightarrow SO_4^{2-} + 11\ FeO \qquad \text{(ii)}$$

As sulphides occur in all samples except two oxide gabbros (samples from 19.38 and 66.58 mbsf) and the leucocratic vein studied (30.63 mbsf), this reaction would have been capable of buffering the oxygen fugacity of the interstitial melt through much of the evolution of the crystal mush. Furthermore, as sulphides probably resided in the crystal mush as molten droplets throughout most of the crystallisation due to their low solidus temperature (~1000°C, Naldrett, 1989), they will have been able to react rapidly with the silicate melt. The $SO_4^{2-}$ produced by reaction (ii) may have been lost from the interstitial melt in an exsolved fluid phase, thereby removing oxygen from the system. The absence of sulphides, but occurrence of magnetite, in two of the oxide gabbros (19.38 and 66.58 mbsf) and the leucocratic vein is consistent with more oxidising conditions existing where sulphides are not present to buffer the oxygen fugacity. If the $SO_4$ was returned to the melt dominated portion of the magma chamber it may have been re-dissolved and lead to oxidation of the eruptable melt.

In contrast to gabbros from ODP Hole 923A, those from ODP Hole 735B near the S.W. Indian Ridge have a positive correlation between oxide (ilmenite and magnetite) and sulphide abundance (Robinson, Von Herzen, *et al.*, 1989). This is interpreted as due to sulphide precipitation in response to a decrease in the solubility of S in the melt as Fe is removed from the melt by oxide precipitation (Natland *et al.*, 1991). The difference between these areas can be explained by the generally S-poorer nature of the parental magma on the S.W. Indian Ridge compared to that at the Mid-Atlantic Ridge, leading to initial undersaturation in sulphides in S.W. Indian ridge MORB (Natland *et al.*, 1991).

*6.4.2 Accessory phases*

Ilmenite, apatite, amphibole, low-Ca pyroxene and compound sulphide globules are common interstitial phases within the core and magnetite occurs in oxide gabbros, the leucocratic vein and occasionally in brown-pyroxene gabbros. These phases provide information about the conditions within the crystal mush during its solidification, and may have played an important role in the compositional evolution of the interstitial melt. Thus, the occurrence and composition of these

phases is discussed next. It is concluded that ilmenite was an important phase throughout much of the evolution of the crystal mush, whereas apatite and amphibole saturation occurred later and thus were less important to the compositional evolution of the interstitial melt. Furthermore, different Zr/Hf and Nb/Ta ratios in two generations of ilmenite at 67.73 mbsf suggest fractionation of even these geochemically similar elements within the interstitial melt. The main effect of sulphides within the interstitial melt, other than buffering the oxygen fugacity, was in incorporating transition metals. The compositional variation observed in magnetite is that expected for simple solid solution between magnetite and ulvospinel, dominated by the magnetite end-member, and thus is not discussed in detail. The compositional variation in low-Ca-pyroxene also does not provide any information about the evolution of the crystal mush. However, its distribution along the rims of olivine suggests that the activity of Si in the interstitial melt increased during crystallisation.

6.4.2.1 Sulphides are common in the Hole 923A gabbros and potentially provide information on the transition metal abundances within the interstitial melt. The generally rounded form and compound nature of the sulphides suggest that they formed by immiscible separation from the silicate melt. Pentlandite (and chalcopyrite) lamellae, thus, probably formed by exsolution. Pentlandite absorbed almost all of the Ni and Co during exsolution; thus, the higher Co abundances in pentlandite in brown-pyroxene gabbros than poikilitic olivine gabbros simply reflects a higher initial Co/Ni ratio in the parental immiscible sulphides.

6.4.2.2 Ilmenite shows three compositional characteristics which require explanation. These are: (i) the very high MgO content of some ilmenites, and the higher MgO contents in coarser grained ilmenites, irrespective of lithology, (ii) higher Zr/Hf and Nb/Ta ratios in the coarser grained ilmenite than in the finer grained ilmenite at 67.73 mbsf, and (iii) higher Zr/Nb and Hf/Ta ratios in the larger ilmenite than in the smaller ilmenite at 67.73 mbsf. These features will be addressed in turn.

The very high MgO contents of ilmenite (up to 8 wt% at 67.73 mbsf) suggest crystallisation from a melt with both high Mg activity and high Ti activity. An explanation for this that fits well with the model of interstitial melt migration developed above is the mixing of an incompatible element (including Ti) rich melt with a partially solidified primitive cumulate. In this model cumulus olivine (+ clinopyroxene) buffers the MgO activity of the interstitial melt, keeping it high, whilst fractionation within the underlying crystal mush leads to a high Ti abundance in the migrating melt. Lower MgO contents in small (late) ilmenite

suggest that the buffering effect of the cumulate assemblage decreased with decreasing melt fraction.

Higher Zr/Hf and Nb/Ta ratios in the coarse grained than fine grained ilmenite at 67.73 mbsf was unexpected, given the geochemical similarity of these pairs of elements. In this regard it is notable that Hf is slightly smaller than Zr, but Nb and Ta are the same size to 0.01 of an angstrom (Shannon, 1976). It is likely that all ilmenite crystallised in the crystal mush, and thus, that fractionation not different parental melt compositions, caused this variation. Two mechanisms of fractionating these geochemically similar elements from each other are envisaged. These are: (i) diffusion controlled fractionation in which heavier elements (Hf and Ta) diffuse more slowly than lighter (Zr and Nb) elements (Niu & Hekinian, 1997a), and (ii) fractionation of a phase(s) with $D_{Nb}>D_{Ta}$ and $D_{Zr}>D_{Hf}$. The only phases likely to significantly fractionate these elements are ilmenite, amphibole and apatite all of which have $D_{Hf} > D_{Zr}$ (LaTourette *et al.*, 1995; Brenan *et al.*, 1995; Chazot *et al.*, 1996). Clinopyroxene also has $D_{Hf} > D_{Zr}$ (Hart & Dunn, 1993; Chazot *et al.*, 1996). Amphibole has similar D's for Nb and Ta and ilmenite has $D_{Ta} > D_{Nb}$ (Green, 1994). These D's are all opposite to those required for the compositional variations observed. The only other possible phase is zircon (or baddeleyite, Ross & Elthon, 1997a), for which D's are unavailable. Zircons exist that have both sub- and super-chondritic Zr/Hf ratios (Hinton & Upton, 1991) suggesting that $D_{Hf}$ is probably similar to $D_{Zr}$ for zircon.

Fractionation controlled by diffusion could explain the observed variations in the following way. If incompatible-element-rich melt migrating through the crystal mush achieved partial equilibration with the crystal mush via diffusion, then faster diffusing incompatible elements would have been less enriched in the residual melt than slower diffusing ones. Thus, the Zr/Hf and Nb/Ta ratios in the interstitial melt would drop during fractionation. However, if the abundance data are correct, this cannot readily explain the data, because significant fractionation of these elements would require large enrichments in their abundances which are not seen. A final possible explanation for the variations in Zr/Hf and Nb/Ta ratio is through variations in the activities of volatiles within the melt. For example, carbonatitic melts commonly have high Zr/Hf ratios (Dupuy, 1992).

Fractionation of Zr and Hf from Nb and Ta can be explained in three ways: (i) that the bulk D's for the $4^+$ cations is larger than for the $5^+$ cations, (ii) equilibration with (unobserved) zircon or baddeleyite, and (iii) equilibration between the small ilmenite and the surrounding amphibole. Fractionation of Zr from Y occurred during magmatic metasomatism due to a relatively small difference in their D's, and thus it is reasonable that Nb and Ta may have been enriched with respect to Zr and Hf by the same process. However, the lack of

significant increase in abundances, if real, raises doubts about this model. Secondly, baddeleyite has been observed at 67.75 mbsf by Ross and Elthon (1997a) providing a simple explanation for depletion in Zr and Hf in the interstitial melt and thus lower Zr/Nb and Hf/Ta ratios in the later ilmenite. Thirdly, equilibration with amphibole could also produce the same relative fractionation as amphibole has higher $D_{Zr}$ (and Hf ?) and lower $D_{Nb}$ (and Ta ?) than ilmenite (Table 6.4). Distinguishing between these models is not possible with the present data.

An important implication of ilmenite occurring as an interstitial phase within the crystal mush, even in the most primitive lithologies, is that Ti should behave more compatibly than it would if only silicate phases were precipitating. This is consistent with the general increase in the size of the negative Ti anomaly with increasing incompatible element abundances observed in clinopyroxene (Fig. 4.8).

6.3.2.3 Apatite is important to the evolution of the crystal mush in two ways. Firstly, dissolved phosphorous in the melt has a significant effect on phase relations in basalt because of its effect on the melt structure (Toplis *et al.*, 1994). Secondly, many elements which are incompatible prior to apatite saturation are highly compatible in apatite; thus, their enrichments in the interstitial melt through crystallisation may be slowed or even stopped by apatite precipitation. Toplis *et al.* (1994) suggest that phosphorous dissolves in basalt by replacing Si in Si-O-NM bonds (NM - Network Modifying Cation), thus increasing Si activity in the melt. Furthermore, phosphorous has a preference for trivalent NM cations in silicate melts (Ryerson & Hess, 1978; Toplis *et al.*, 1994) leading to increased solubility of REEs and $Fe^{3+}$ in the melt with increased phosphorous abundance. This effect, coupled with the increase in Si activity, has the effect of destabilising olivine, clinopyroxene and magnetite with increased $P_2O_5$, and stabilising pigeonite (Toplis *et al.*, 1994).

The approximately ten fold variation in clinopyroxene phosphorous abundance within the core suggests that the $P_2O_5$ abundance in the interstitial melt may have reached ~1 wt%, assuming a parental melt with ~0.1 wt% $P_2O_5$. This is similar to the estimated $P_2O_5$ concentration required for apatite saturation in MORB (DeLong & Chatelain, 1990). In the experiments of Tolpis *et al.* (1994) 1 wt% $P_2O_5$ was sufficiently high to have a noticeable effect on phase relations. That this effect was relatively unimportant is suggested by the lack of abundant pigeonite, and the small volume of apatite, in all lithologies. However, the trough in the Al content in the Z site of clinopyroxene approaching the rim of the clinopyroxene crystal at 31.31 mbsf (Fig. 4.21c) coincides with an increase in the phosphorous content, consistent with an increase in Si activity in the melt.

However, this is not a unique explanation for this observation. A high phosphorous abundance in the interstitial melt could also help explain the absence of interstitial magnetite.

The high distribution coefficients for apatite for a number of trace elements (such as P, REE, Y and Sr) means that equilibration with apatite can have a significant effect on the composition of the interstitial melt. This has been tested for using the rim of the clinopyroxene crystal analysed in the sample from 31.31 mbsf in which the phosphorous abundance drops over the outer ~0.5 mm of the crystal (Fig. 4.21e). However, there is no discernible effect on the rate of increase in abundance of elements compatible in apatite (e.g. REE; Watson & Green, 1976) compared to those which are not (e.g. Zr; Chazot *et al.*, 1996) in this portion of the crystal. Neither is there any relative fractionation between the MREE (most compatible in apatite; Watson & Green, 1981) and the LREE or HREE (less compatible in apatite; Watson & Green, 1981). This suggests that apatite crystallisation did not significantly effect the bulk D's for REEs.

6.4.2.4 Amphibole is an ever present accessory phase in Hole 923A gabbros, but is never very abundant. Due to the close proximity of the amphibole and ilmenite analysed by ion probe in the sample from 67.73 mbsf, distribution coefficients for Zr and Nb between these phase have been calculated, assuming equilibrium. These are shown in Table 6.2. Published amphibole-melt and ilmenite-melt distribution coefficient are consistent with the estimated for $D_{Nb}$ (i.e. are ~10 time greater for amphibole than ilmenite) but suggest that Zr should be approximately evenly distributed between these phases (Green, 1994). The explanation for the apparent preferential partitioning of Zr into amphibole than ilmenite may be incomplete equilibration between these phases and a Zr-rich phase (zircon or baddeleyite), perhaps exsolved from the ilmenite.

| | $D_{amph/ilm}$ |
|---|---|
| Zr | 11.2-12.4 |
| Nb | 0.20-0.23 |

Table 6.2 Computed Nernst distribution coefficients between coexisting amphibole (amph) and ilmenite (ilm) in the sample from 67.73 mbsf.

## 6.5 Discussion

### *6.5.1 Introduction*

Many compositional and textural characteristics of brown-pyroxene gabbros and some characteristics of poikilitic olivine gabbros and oxide gabbros have been shown above to be consistent with a genesis involving extensive post-cumulus modification during interaction between the crystal assemblage and the

interstitial melt. In this section this model is developed further. The driving force behind melt migration is discussed, and it is concluded that a combination of compaction (McKenzie, 1984) and syn-magmatic, tectonic deformation (Dick *et al.*, 1991) were probably important. The generation of the most evolved lithologies, oxide gabbros and leucocratic veins, is then investigated and immiscible separation of an evolved melt into an Fe-rich melt and a Si-rich melt ruled out.

*6.5.2 A driving force for melt migration*

The magmatic metasomatism model proposed above requires migration of melt through the crystal mush. A driving force for melt migration is thus required if this model is to be considered applicable. Compositional convection (Tait *et al.*, 1984), compaction (McKenzie, 1984; Shirley, 1986) and syn-magmatic tectonic deformation (Dick *et al.*, 1991) have been proposed as driving forces for melt percolation in crystal mushes. These processes are discussed in turn below. Firstly however, the thermal regime within the crystal mush is considered as all these processes require that porosity is maintained within the mush for an extended period.

The temperature interval, and thus time period, over which the crystal mush remains partially molten can be estimated either from geophysical constraints, through thermal modelling (e.g. Irvine, 1970) or by calculating the difference between the liquidus and solidus of the crystalline assemblage. Geophysical experiments at slow spreading mid-ocean ridges shows that magma chambers must be transient phenomenon. Furthermore, thermal modelling (Sleep, 1975; Kuznir, 1980) shows that these bodies must cool relatively rapidly compared to terrestrial intrusions. However, the size of these bodies, when they exist, is poorly constrained, and may be relatively large. For example, Meyer *et al.* (1989) suggest that gabbros from the S.W. Indian Ridge crystallised in magma chambers at least 2.5 km wide and 5.5 km deep, and Sinha *et al.* (1997) suggest that a geophysically imaged magma body beneath the Mid-Atlantic Ridge is of similar dimensions to those observed beneath fast spreading ridges. However, lack of detailed constraints on the size of these bodies prevents detailed thermal modelling.

By analogy with crystallisation experiments on basalts from the MARK area, a drop in clinopyroxene Mg# of 6 from core to rim, as at 31.31 mbsf (Fig. 4.21b; $Mg\#_{85\text{-}79}$), requires a temperature drop of ~40°C (Grove & Bryan, 1983; Tormey *et al.*, 1987; Grove *et al.*, 1992). However, the composition of the interstitial melt may have significantly differed from the melt in the experiments (e.g. higher volatile content) making this estimate dubious. An alternative approach to estimating the temperature interval over which the cumulate solidified is from the liquidus temperatures of interstitial accessory phases. For

MORB, experimental and geochemical investigations suggest that ilmenite saturation is reached at ~1100°C and apatite saturation at ~985°C (DeLong & Chatelain, 1990). The common occurrence of interstitial ilmenite and interstitial apatite within all lithologies thus suggest that porosity existed over a considerable temperature interval (> 100°C). However, concentration of incompatible elements in the interstitial melt, whilst the major element composition was buffered, as in the magmatic metasomatism model proposed, invalidates this estimate. It is therefore difficult to accurately estimate the temperature interval over which porosity existed in the mush, because of both the lack of external and internal constraints. Furthermore, replenishments at the magma-mush interface may have kept the crystal mush hot, and thus helped maintained porosity. Next the three potential driving forces for interstitial melt migration, compositional convection, compaction, and syn-magmatic deformation are considered.

*6.5.3 Compositional convection*

If the fractionated interstitial melt in the crystal mush is less dense than the less evolved melt in the overlying chamber it will rise buoyantly, if it overcomes the viscous drag forces (exceeds a given porous medium Rayleigh number; Worster, 1991). Three arguments suggest that compositional convection was not important for driving melt migration through the crystal mush at Site 923A, although it may have been important at the magma-mush interface. Firstly, the driving force for compositional convection must have been very small. The driving force (density difference) is conveniently assessed through consideration of the fractionation density (Sparks & Huppert, 1984) of the precipitating assemblage. This is defined as the density of the components in the melt that go into the crystals. Thus, if the bulk fractionation density of the crystal assemblage is greater than the density of the melt, fractionation will lead to a decrease in melt density. Appropriate fractionation densities for phases from Hole 923A are given in Table 6.3. Using these the bulk fractionation density of the crystallising assemblage is estimated to be generally similar to the density of MORB; i.e. there can never have been a large driving force for compositional convection. This is also shown in Fig. 5.1 in which bulk rock fractionation densities are shown to be generally lower than the density of erupted MORB. Furthermore, buffering of the major element composition of the interstitial melt by the crystal assemblage, as proposed above, will have inhibited major element evolution of this melt, which controls the density of the melt. The exception to this is if volatiles are concentrated in the fractionated magma, causing its density to decrease (Bottinga & Weill, 1970).

Secondly, compositional convection in a mushy layer operates by upward flow of the evolved melt through chimneys, and downward flow of less evolved,

denser melt everywhere else in the mush (Worster, 1991; Tait & Jaupart, 1992). This suggests that the effects of the migration of evolved interstitial melt through the crystal mush should be concentrated in isolated chimneys, and the cumulates in all other areas should record the migration of primitive melt into the mush. This is in contrast with the observations at Site 923A.

Thirdly, porosity estimates suggest that melt migration must have occurred down to low porosities to explain the extreme incompatible element enrichments and the zoning of clinopyroxene crystals. However, compositional convection becomes rapidly less efficient as the permeability, which is strongly controlled by the porosity, decreases (Fig. 6.10).

| | Primitive composition | Evolved composition |
|---|---|---|
| Olivine | 3.04 ($Fo_{85}$) | 3.26 ($Fo_{65}$) |
| Clinopyroxene | 2.74 ($Mg\#_{90}$) | 2.80 ($Mg\#_{70}$) |
| Plagioclase | 2.52 ($An_{75}$) | 2.44 ($An_{45}$) |
| Ilmenite | 4.44 (8 wt% MgO) | 4.70 (0 wt% MgO) |
| Typical MORB | 2.67 ($Mg\#_{65}$) | 2.71 ($Mg\#_{55}$) |

Table 6.3 Fractionation densities of the dominant phases in gabbros from Hole 923A calculated for a temperature of 1250°C and all Fe as FeO. Also shown is the typical density of MARK area MORB from Fig. 5.1. The fractionation density is the density of the components in the melt that go into making the crystal (Sparks & Huppert, 1984). Thus, if the bulk fractionation density of the crystallising assemblage is greater than that of the melt, fractionated melt will be less dense than unfractionated melt.

### *6.5.4 Compaction*

Compaction of a crystal mush can occur under three different driving forces: deviatoric stress, surface energy and thermal/chemical potential (Hunter, 1996). Compaction due to the density difference between the melt and crystal mush (matrix) has been modelled extensively (Shirley, 1986, 1987; McKenzie, 1987; Meurer & Boudreau, 1996; Mathez *et al.*, 1997) and is considered first. This process is consistent with the dominance of sub-vertical deformation bands in coarse grained olivine in brown-pyroxene gabbros (Fig. 3.13) that suggest uniaxial compression (Hunter, 1996). The random orientation of deformation bands in finer grained olivine may reflect larger local effects. However, it is difficult to distinguish between magmatic and solid-state deformation textures.

Compaction at high porosities can occur through mechanical re-organisation of the crystal mush. However, even while the porosity is still high (~40 to 50%), the crystal mush becomes rigid and further compaction requires viscous deformation of the matrix (crystals). McKenzie's (1984) equations show that compaction of an infinitely thick crystal-melt mixture overlying an

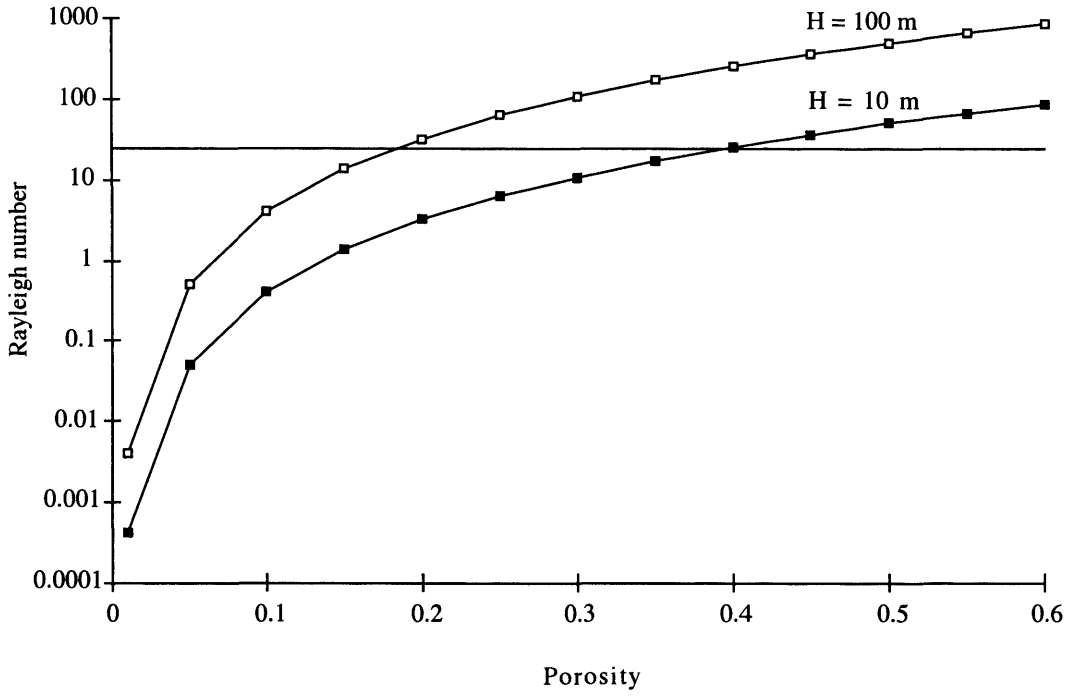


Fig. 6.10 Comparison of the Rayleigh number for convection in a porous medium with porosity for mush layer thicknesses of 10 m and 100 m. Convection occurs if the Rayleigh number is greater than ~25 (Tait & Jaupart, 1992). The rayleigh number (Ra) is calculated as $Ra = [(g.D.k.H)/K.\mu]$, where g is the acceleration due to gravity, D is the density difference between the interstitial and overlying melts, k is the permeability, H is the thickness of the mush, K is the thermal diffusivity, and $\mu$ is the viscosity of the melt (Worster, 1991). The values used in the calculation of these curves are: $g = 9.81$ m/s$^2$, $D = 50$ kg/m$^3$, $k = [(d^2.\emptyset^3)/300]$ from Cheadle (1989), where d is the grain diameter (5 mm used here) and $\emptyset$ is the porosity, $K = 1 \times 10^{-7}$ m$^2$/s (Tait & Jaupart, 1992), and $\mu = 10$ PaS. These values should maximise the possibilty of convection. The horizontal line at Ra = 25 is the approximate lower limited of the rayleigh number for compositional convection. Even for a 100 m thick mush zone convection in the mush will cease when the porosity is reduced to < 20%.

impermeable layer only occurs at the base of the crystal mush. The remainder of the crystal pile does not compact as the upward velocity of the melt driven out of the basal compacting layer supports the weight of the matrix. For magmatic metasomatism to be effective at enriching the cumulate assemblage in incompatible elements during compaction, certain conditions must be met. Firstly, the melt being driven through the crystal mush must be incompatible element enriched through overgrowth of the cumulate crystals. Secondly, a substantial flux of this evolved melt should migrate through the crystal mush, and preferably densification of the crystal mush should occur via crystal growth not compaction; i.e. compaction should not reduce the porosity of the crystal mush rapidly. These criteria will be best fulfilled if the compacting region is confined to the basal part of the crystal mush, with the upper part of the crystal mush interacting with, and growing from, the melt that is forced upward from the compacting region. Thus, prior to investigating the rate of melt flux through the cumulates, the likely size of the compacting region must be estimated.

6.5.4.1 Modelling parameters for calculation of compaction rates and lengths are given in Table 6.4. Most parameters can be assumed to be at least of the correct order of magnitude. In contrast, the range of estimates of the matrix viscosity are considerable ($10^{12}$ to $10^{18}$ PaS). Recent estimates have been at the lower end of this scale (Jin *et al.*, 1994; Nicolas & Ildefonse, 1996). Jin *et al.*, (1994) show experimentally that deformation of a partially molten peridotite under low differential stress leads to melt being distributed along the grain edges as well as along triple grain boundary tubes. This has the effect of decreasing the matrix viscosity through increased grain boundary sliding and solution-reprecipitation. This effect of grain boundary wetting under differential stress has also been observed in feldspar aggregates (Tullis *et al.*, 1993), suggesting that gabbroic rocks may also have reduced effective viscosity during compaction under differential stress. However, as the reason for this phenomenon is unclear (Jin *et al.*, 1994) the effect of grain size cannot be accounted for. The effective viscosity of these

| Parameter | Best estimate |
|---|---|
| grain size | 5 mm |
| matrix - melt density difference | 250 Kg/m$^3$ |
| melt viscosity | 10 PaS |
| matrix viscosity | $10^{12}$ - $10^{18}$ PaS |

Table 6.4 Input parameters for compaction calculations

partially molten aggregates is ~$10^{12}$ PaS (Stevenson, 1994). Nicolas and Ildefonse (1996) show that pressure solution can also lead to lowering of the matrix

viscosity for plagioclase dominated crystal mushes to around $10^{14-16}$ PaS. Furthermore, in the presence of water the matrix viscosities may be still lower (Hirth & Kohlstedt, 1996), and reaction between the interstitial melt and matrix is likely to further lower the effective viscosity.

6.5.4.2 The size of the compacting region is controlled by the compaction length, which is dependent on the porosity (melt fraction), permeability and the matrix and melt viscosities, but not the density difference between the melt and matrix (McKenzie, 1984). Fig. 6.11 shows the variation in compaction length as a function of porosity for different matrix viscosities. If compaction is to be restricted to the basal region of the crystal mush, and not occur throughout it, the matrix viscosity must be low, the thickness of crystal mush large, or the porosity low.

The relative velocity between the melt and matrix above the compacting region is controlled by the porosity, permeability, density difference between the melt and matrix, and the melt viscosity, but it is independent of the matrix viscosity (McKenzie, 1984). Fig. 6.12 shows the rate of separation of the melt and matrix during compaction for various input parameters. Whilst the porosity is relatively high (> ~10%), considerable melt will flux through the region above the compacting basal layer. Even at lower porosities (<5%) melt will still move within the crystal mush considerably quicker than it diffuses, or than solidification is likely to occur through growth. Thus, simply under buoyancy forces the melt will move upward through the crystal mush even at low porosities, provided the mush is thicker than the compaction length. In reality, however, compaction will be far more complex than modelled here due to spatial variations in all input parameters within the crystal mush, in particular the porosity and permeability.

6.5.4.3 Surface energy and thermal/chemical potential variations provide further driving forces for compaction of the crystal mush. The lack of general well equilibrated textures suggests that surface energy minimisation was not an important process in driving melt migration. However, the less interdigitated grain boundaries in coarse grained brown-pyroxene gabbros than finer grained ones, and moderately well equilibrated texture at 47.33 mbsf (Fig. 3.7) suggest that surface energy minimisation may have played a minor role in compaction (Hunter, 1987). Chemical potential gradients (Lesher & Walker, 1988) are unlikely to have been important in driving compaction in brown-pyroxene gabbros as these show relatively minor compositional variation. However, this process may have been more important in the genesis of the small poikilitic olivine gabbros horizons that have significantly more evolved intervals of brown-pyroxene

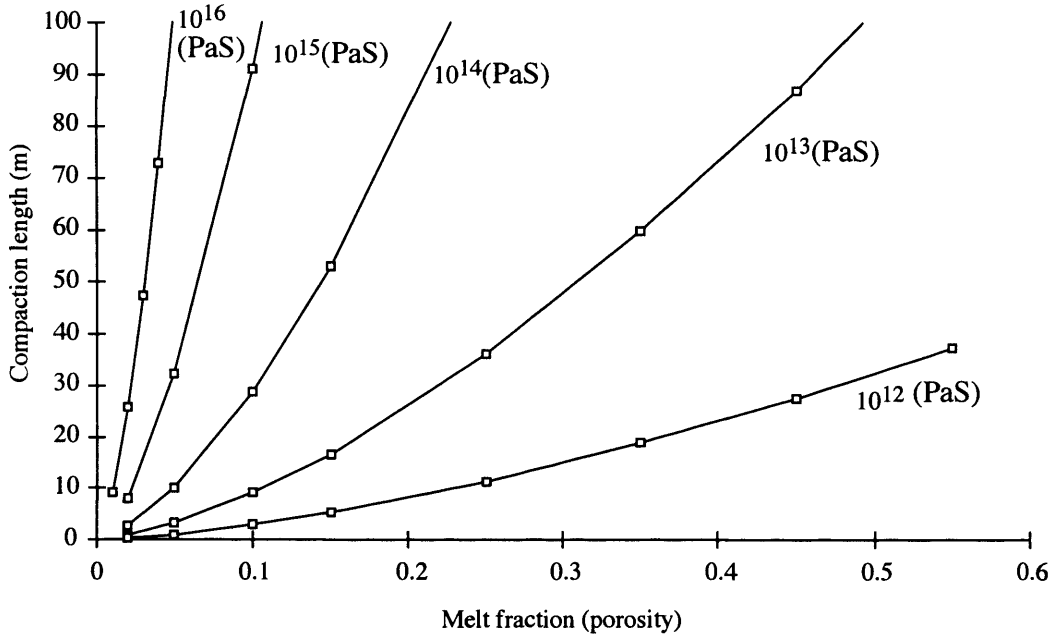


Fig. 6.11 Variation in compaction length with cumulate porosity for different matrix viscosities (McKenzie, 1984). The compaction length controls the height of the mush which is compacting, whilst above this region the matrix is supported by the upward flux of melt. This is calculated as: $(M.k)/\mu)^{0.5}$, where M is the matrix viscosity (PaS) and other parameters are as in 6.10.

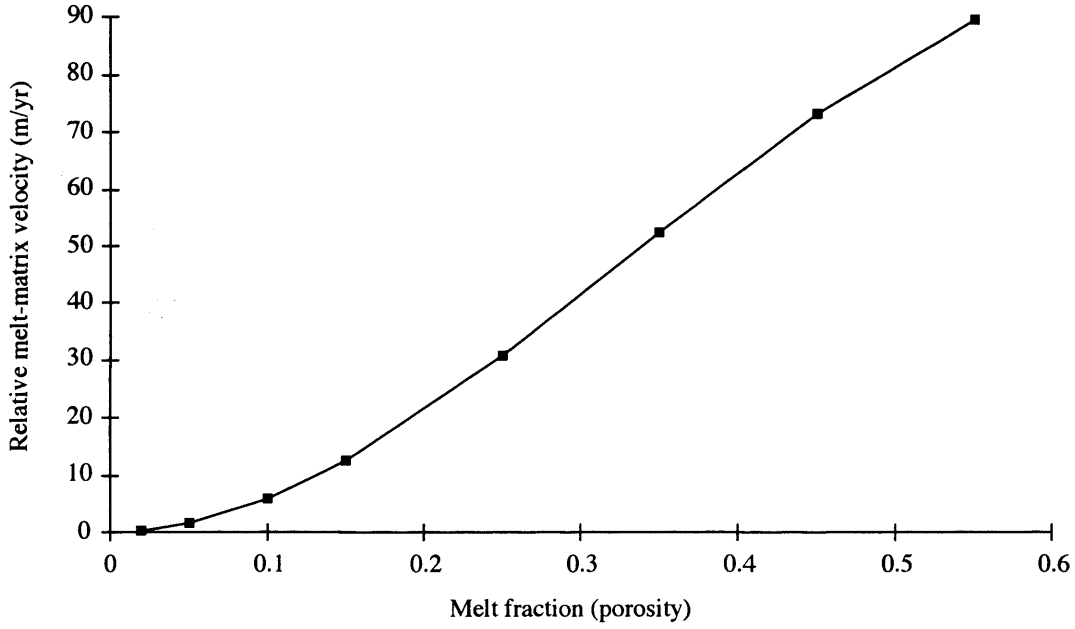


Fig. 6.12 Rate of separation of melt from the matrix during compaction in the non-compacting region calculated as $(k.(1-Ø).D.g)/(\mu.Ø)$ with symbols as in Fig. 6.11 (McKenzie, 1984). D is the density difference between the melt and matrix; 250 $Kg/m^3$ is used in this modelling. This shows that even at low porosities the relative velocity between the melt and matrix will be large in this region relative to diffusion and growth rates.

gabbros on either side of them (Fig. 4.15). If these layers formed by emplacement of a primitive plagioclase-phyric magma at the mush-magma interface at the base of the magma chamber followed by plagioclase accumulation, plagioclase at the top (i.e. hot end) of the newly deposited mush may then have dissolved and been reprecipitated at the base of the layer (i.e. cold end). This process could account for the plagioclase-rich nature of the troctolitic poikilitic olivine gabbros.

*6.5.5 Syn-magmatic tectonic deformation*

Dick *et al.* (1991) propose interstitial melt migration can occur due to variations in pore pressure induced by tectonic deformation of the crystal mush. However, the effect of this process at different strain rates and porosities, and during the operation of different deformation mechanism, is unclear. The correlation between degree of plastic deformation and lithology is consistent with this process and the highly strained nature of oxide gabbros requires that tectonic deformation was involved in their genesis. It is uncertain, however, whether deformation was concentrated into regions in which there was a high proportion of evolved interstitial melt or evolved melt migrated into shear zones.

A final, speculative, mechanism for driving interstitial melt migration within the crystal mush is exsolution of volatiles. Whether exsolved bubbles will escape leaving the interstitial melt in place, or drive melt migration is unclear. Melt expulsion could be induced by the increased volume of interstitial fluid (melt plus bubbles) or due to the decreased density of the melt due to its bubble content. However, a high concentration of bubbles in the melt would increase its viscosity, inhibiting motion.

The final constraint on melt flow for magmatic metasomatism to be effective is that melt must flow relatively uniformly through the crystal mush, not in isolated channels. This is predicted by experiments in which crystallisation occurs during flow, but not if dissolution occurs during flow, in which case flow becomes focused in channels (Aharanov *et al.*, 1997).

*6.5.6 Genesis of oxide gabbros and leucocratic veins*

Oxide gabbros and leucocratic veins record important information about the final stages of differentiation and the generation and mobility of evolved melts. Immiscible separation of an evolved melt into a Si-rich and an Fe-rich melt has been proposed to explain the co-existence of similar lithologies in core from ODP Site 735 (Natland *et al.*, 1991), as well as the formation of oceanic plagiogranites (Dixon & Rutherford, 1979). This model can be tested for the Site 923A gabbros using the trace element abundances in these lithologies because data from experimental (Watson, 1976; Ryerson & Hess, 1978; Ellison & Hess, 1989)

and natural systems (Philpotts & Doyle, 1983) suggest significant partitioning of elements other than Fe and Si between immiscible melts. Ti, Mg, Mn, Ca, phosphorous and REE's partition preferentially into the Fe-rich melt, whereas K, Na and Al partition into the silicic melts during immiscible separation (Watson, 1976; Ryerson & Hess, 1978; Ellison & Hess, 1989). Phosphorous is especially strongly partitioned into the Fe-rich melt (by a factor of about ten; Watson, 1976). Modal proportions, and, assuming approximately constant mineral-melt distribution coefficients, mineral compositions are inconsistent in many ways with oxide gabbros and leucocratic veins being the crystallisation products of immiscible melts.

Apatite is more abundant in the leucocratic vein than any other lithology, and only slightly more abundant in oxide gabbros than in brown-pyroxene gabbros. This is inconsistent with the oxide gabbros crystallising from a melt with a phosphorous abundance ten times that of the parental melt for the leucocratic vein. Also, the P/Nd ratio of clinopyroxene in oxide gabbros is lower than in other lithologies (Fig. 6.13), not higher as predicted for crystallisation from an Fe-rich immiscible melt. High ilmenite abundances, and the presence of zircon in the leucocratic vein are also inconsistent with crystallisation from a silicic immiscible melt because Fe, Ti and Zr are depleted in a Si-rich immiscible melt. Furthermore, the displacement of the low-Ca-pyroxene in the leucocratic vein to a higher Mn/Mg# ratio than other low-Ca pyroxene is inconsistent with growth from a melt depleted in Mn. It is unclear, however, whether the melts which formed these evolved lithologies had evolved through magmatic metasomatism of the crystal mush. Particularly important in this regard is the low Zr/Y ratio of clinopyroxene in oxide gabbros, even with high incompatible element abundances. This is consistent with an origin through simple fractional crystallisation of a primitive composition (Fig. 6.4). For example, if the melt dominated portion of the magma chamber fractionated to high FeTi basalt which was sufficiently dense to settle into the crystal mush this could explain the observed compositions. However, the high abundance of ilmenite in these samples will have affected the partitioning of Zr, and thus it is difficult to interpret the origin of the Zr-Y trend.

The pervasive plastically deformed nature of the oxide gabbros but not the leucocratic veins (Cannat, Karson, Miller, *et al.*, 1995) suggest that Fe-rich melts were produced earlier in the differentiation history than silicic ones, i.e. oxide gabbros formed during ductile deformation, whereas leucocratic veins formed when the crystal pile had begun to deform brittlely. This is consistent with oxide gabbro precipitation leading to the last melt fractions becoming Si-enriched.

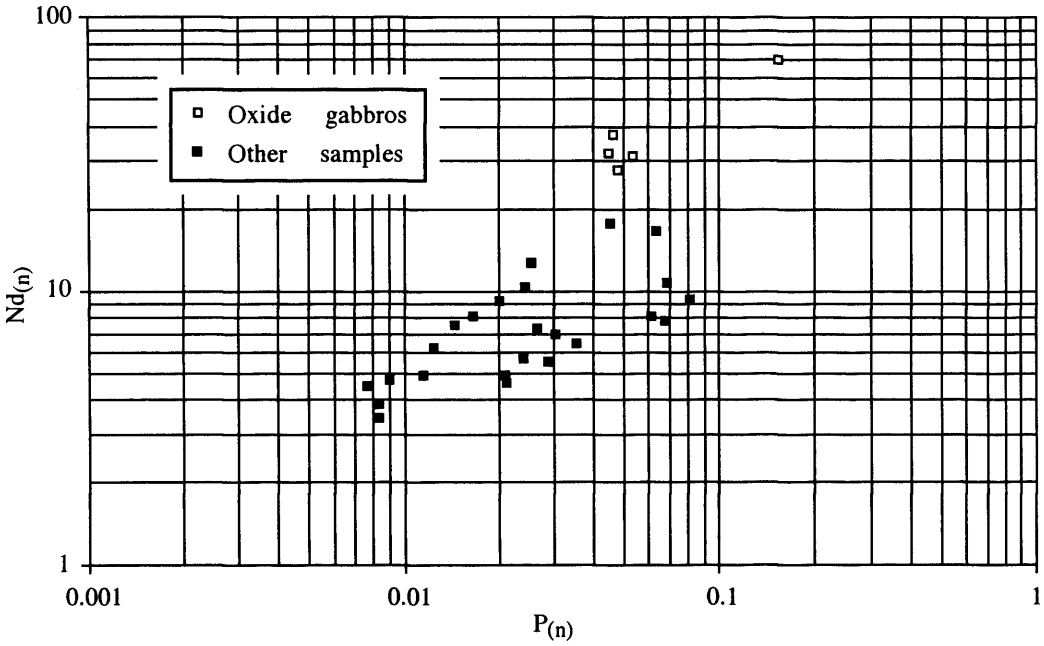


Fig. 6.13 Chondrite-normalised P versus Nd in clinopyroxene. Clinopyroxene in oxide gabbros, shown as open symbols, is slightly P-poor with respect other clinopyroxene for a given Nd content. This is the opposite of what would be expected if oxide gabbros formed by immiscible separation of an Fe-rich melt from a basaltic melt (Watson, 1976; Ryerson & Hess, 1978).

*6.5.7 The process of metasomatism*

A final point of interest about magmatic metasomatism is how partial equilibration between the interstitial melt and crystals occurs. Is it by dissolution and reprecipitation or diffusion ? The lack of significant anorthite zoning in plagioclase at 31.31 mbsf (Fig. 4.21h) and relatively minor An-zoning in plagioclase in most brown-pyroxene gabbros, despite very slow coupled CaAl-NaSi diffusion in plagioclase (Morse, 1984; Grove *et al.*, 1984), suggests that equilibration of plagioclase must have been via dissolution-reprecipitation. Furthermore, the variations in grain size and shape in brown-pyroxene gabbros suggest dissolution-reprecipitation was an important processes within the crystal mush. Alternatively, the fractionation of Zr from Hf and Nb from Ta suggests a role for diffusive equilibration. These speculations are consistent with, but poor evidence for, equilibration by different processes for different phases.

**6.6 Conclusions**

Compositional and textural characteristics of brown-pyroxene gabbros suggest that post-cumulus processes were crucial in their genesis. Incompatible element zonation and fractionation of incompatible elements from one another suggest extensive chemical interaction between migrating interstitial melt and the crystal mush. Less significant major element zonation suggests that this interaction effectively buffered these elements. The role of accessory phases within the crystal mush may have been important, as might volatile species, both dissolved in the melt and as an exsolved vapour phase. However, more extensive analysis of trace element abundances in accessory phases, coupled with better constraints on their distribution coefficients, are necessary to use the information stored in these phases to gain a better understanding of the evolution of the interstitial melt in crystal mushes. Melt migration within the crystal mush was probably driven by a combination of compaction and tectonic deformation. To understand this process in more detail requires further detailed trace element traverses in brown-pyroxene gabbros of different grain sizes and at different levels in a brown-pyroxene gabbro sequence, and in oxide gabbros. Furthermore, modelling of compatible elements in unison with incompatible elements would provide a greater understanding of the buffering effect of the crystal mush.

A final point of note is that if considerable portions of melt extraction from the mantle is via porous flow (e.g. Niu, 1997) extensive compositional modification is to be expected due to reaction between the melt and matrix during extraction (e.g. Navon & Stolper, 1987). In the next chapter the models developed in this chapter and Chapter Five are combined to produce a model of the

evolution of melts within magma chambers beneath slow-spreading mid-ocean ridges.

# Chapter VII: Conclusions - a model for magma plumbing beneath the Mid-Atlantic Ridge, and suggestions for future study

## 7.1 Introduction

This chapter draws together the ideas and interpretations presented in Chapters Five and Six, and models of magma plumbing beneath mid-ocean ridges from the literature, into a model of magma plumbing beneath the Mid-Atlantic Ridge (Section 7.2). This model involves multiple small melt lenses within the crust which act as filters for melts transecting the crust, and in which mixing is a common phenomenon. Crystallisation, and thus chemical fractionation, occurs dominantly in episodic bursts when cooling is rapid such as during periods of magma transport, but is slower and more complex when melts pond and cool more slowly. The implications of this model for the generation of compositional diversity within MORB suites are discussed in Section 7.3. A less specific conclusion of this study - that understanding magma chamber processes requires the combination of detailed textural studies and *in situ* mineral analyses - is discussed in Section 7.4. It is shown that whole-rock compositions of gabbroic rocks can be misleading if interpreted without *in situ* mineral analyses. In Section 7.5 ideas for future research and tests for the models proposed in this thesis are suggested (Section 7.5). Finally, the main conclusions of this thesis are reiterated in Section 7.6.

## 7.2 A model for magma plumbing beneath slow-spreading mid-ocean ridges

### *7.2.1 Introduction*

In this section a model for magma plumbing beneath slow-spreading mid-ocean ridges is developed. It is assumed for the purpose of this discussion that the magma chamber which formed the Hole 923A gabbros was part of a sub-volcanic magma plumbing system. This cannot be tested with the present data. However, gabbros have generally suitable whole-rock compositions such that extraction of them from primitive MORB would generate more evolved MORB.

The size of magma chambers beneath mid-ocean ridges has received much attention in recent years and is an important control on the nature of the magma plumbing system and the mechanism of crustal accretion. At first sight, the significant compositional evolution with height in the cored interval from ODP Hole 923A (e.g. the decrease in average olivine Fo content from ~80 to ~65 over 50 m, Fig. 4.15) suggests that the height of the chamber must have been small. However, the variation in composition with depth also reflects the difference in compositions between the host and replenishing magma and the effects of post-cumulus compositional modification. It is therefore not possible to constrain the height of the magma chamber from these data. Similar lithologies to those

recovered at ODP Site 923 were recovered at Sites 921, 922 and 924, which span an area of several square kilometres (Cannat, Karson, Miller *et al.*, 1995). This suggests that either: (i) the magma chamber covered an area of several kilometres, (ii) the exposure of gabbroic rocks is tectonically controlled and does not represent the size of the intrusion, or (iii) similar processes operated in several magma chambers leading to similar lithologies forming in different intrusions. Distinguishing between these hypotheses will require considerable detailed study of both the samples recovered from the different sites and of the exposure of gabbros on the seafloor by submersible.

### *7.2.2 A model for magma plumbing*

In this section some of the main interpretations from Chapters Five and Six are briefly reiterated and these are used, along with models from the literature, to develop a model of the magma plumbing system beneath the Mid-Atlantic ridge.

The occurrence of resorbed anorthitic cores in many plagioclase crystals in poikilitic olivine gabbros which have trace element characteristics distinct from their rims provides evidence for multiple melt compositions existing and crystallising within the magma plumbing system (Section 5.2). It was argued in Section 5.2 that the characteristics of these rocks are best explained by the simultaneous occurrence of at least three melt compositions within the crustal magma plumbing system: (i) the melt parental to anorthitic plagioclase cores, (ii) the plagioclase undersaturated melt which resorbed these crystals, and (iii) the melt in the Hole 923A magma chamber into which the hybrid of magmas (i) and (ii) was intruded. The variation in trace element abundances and ratios in these plagioclase populations indicates that the melt compositions crossing the Moho were also compositionally diverse as their compositional characteristics are unlikely to have been produced by crystallisation within the crustal plumbing system. Thus, mixing of distinct melt batches and fractionation (e.g. plagioclase precipitation) were penecontemporaneous. These interpretations also suggest the existence of at least two melt reservoirs within the plumbing system.

The very high Cr content of the clinopyroxene in poikilitic olivine gabbros (Fig. 4.15b), especially at 46.30 mbsf, shows that melts which had not precipitated significant amounts of Cr-spinel or clinopyroxene were delivered to the Hole 923A magma chamber. The Zr and Ti anomalies in the incompatible element abundance patterns of these clinopyroxene (Fig. 5.3) show that the well know Zr and Ti anomalies in abyssal peridotite clinopyroxene (Salters & Shimizu, 1988) are preserved into the crustal magma plumbing system. The limited compositional range in sampled MORB in the MARK area (e.g. Bryan *et al.*, 1981) shows that this compositional diversity recorded in these plagioclase and

clinopyroxene compositions is usually efficiently eradicated within the crustal plumbing system through magma mixing.

The importance of magma mixing is thus a central feature of the model shown in Fig. 7.1 in which discrete batches of magma from the mantle proceed through the crust in a series of steps. Melts pond where they reach their level of neutral buoyancy (Ryan, 1993) or where they intersect a pre-existing melt reservoir. The evidence from poikilitic olivine gabbros suggests that the replenishing melts commonly pond at the base of the melt reservoirs which they feed (Section 5.3.2) indicating they are denser than the host magma. The high density may be due to the melt composition or a high suspended crystal load as discussed in Section 7.2.3. Fractionation within these ponded layers, and/or deposition of suspended crystals, leads to a drop in density until wholesale mixing occurs within the magma chamber. As the melt density decreases further upon fractionation it becomes buoyant and given the opportunity - for example the opening of a fracture or fault by tectonic extension - the melt will move upwards until it intersects another melt reservoir. This stepwise upwards progress, in which the crust acts as a density filter, leads to both fractionation and magma mixing being almost ubiquitous prior to eruption.

### *7.2.3 Fractionation related to magma transport and replenishment*

In the model proposed above fractionation occurs as a series of rapid steps, separated by slower more complex fractionation (i.e. punctuated fractionation, Marsh, 1996). As melt moves between reservoirs the rate of heat loss is high leading to rapid crystallisation (Marsh *et al.*, 1991; Marsh, 1996). After replenishing a higher level magma chamber the compositional effects of fractionation are partially dependent on the degree of mixing between the host and replenishing magmas. If the replenishing magma is denser than the resident magma then it ponds at the floor of the chamber and cools rapidly (e.g. Huppert & Sparks, 1980a). However, if the replenishing magma is less dense than the resident magma, upon replenishment it will tend to rise buoyantly and mix with the resident magma.

Clinopyroxene occurs as oikocrysts within poikilitic olivine gabbros which are interpreted to have crystallised when primitive magmas ponded at the base of the more evolved chamber. This suggests that clinopyroxene was probably not a phenocryst phase in the primitive magma. However, the primitive compositions of these clinopyroxene crystals (e.g. Fig. 4.15) show that they did not grow from trapped interstitial melt, but rather in a system open to the overlying melt. Thus, their crystallisation will have imparted a clinopyroxene fractionation signature on the melt within the eruptable reservoir. Crystallisation of clinopyroxene in

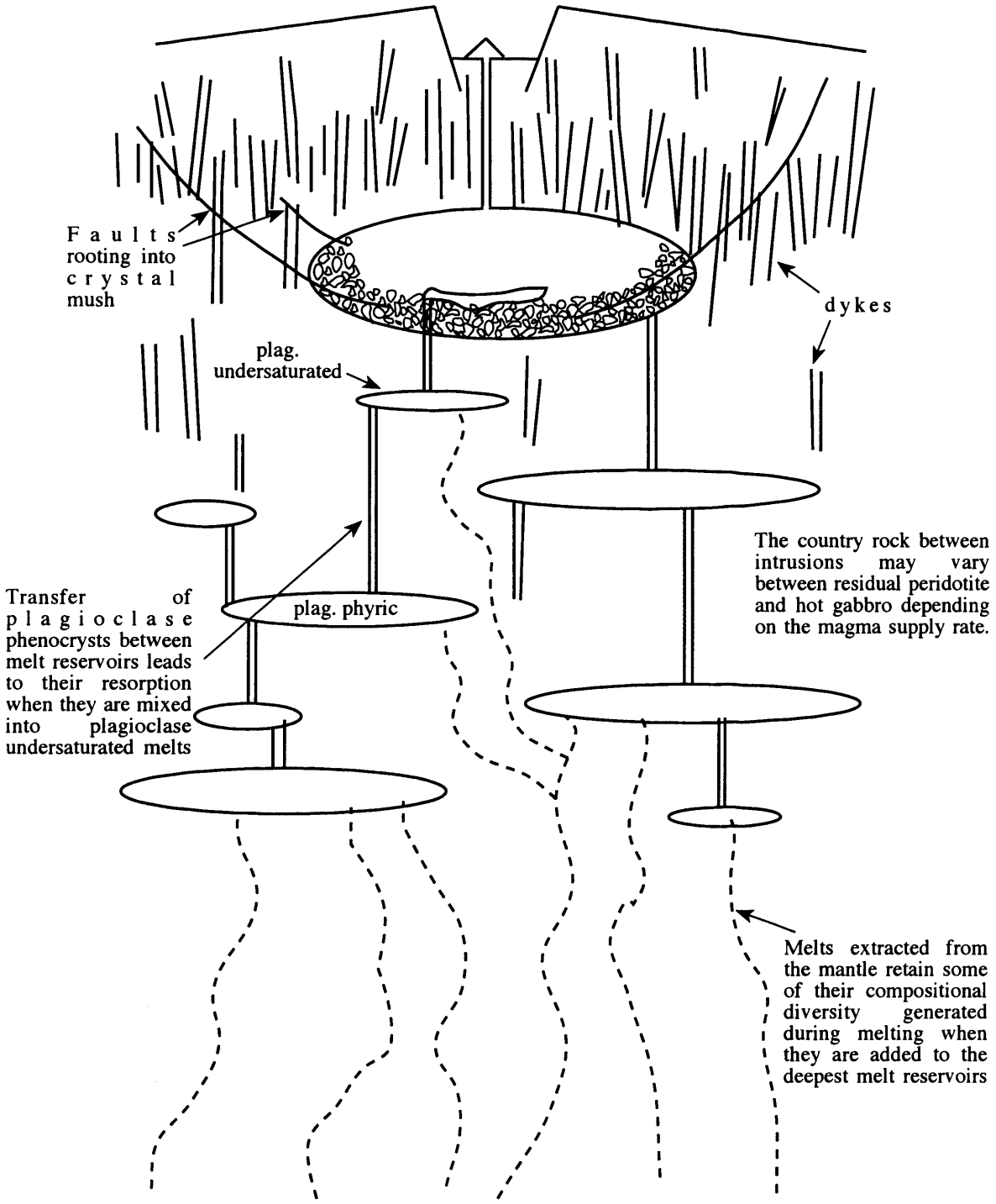


Fig. 7.1 Schematic illustration of magma plumbing system beneath a mid-ocean ridge (not to scale). Melt is extracted from the mantle (dashed lines) and ponds in small magma reservoirs in which magma mixing and fractionation occur. As the melt density drops due to fractionation the melt in the deeper bodies may move upward and feed higher level reservoirs. Fractionation probably occurs as episodic bursts during magma transport immediately after a replenishment prior to full mixing between the resident and replenishing magma, followed by slower fractionation dominated by boundary layer processes.

this way can explain the pyroxene paradox (Section 1.4.5; Dungan & Rhodes, 1978; Langmuir, 1989).

Assimilation of altered wall rock, either during transport between melt reservoirs or from the margins of the reservoir, may occur. This could explain the occurrence of Cl-rich apatite in some of the Hole 923A gabbros.

*7.2.4 Fractionation within the crystal mush*

In the intervals between replenishments differentiation within the melt lenses may be concentrated at their margins due to slow cooling. Crystallisation and melt-rock reaction as interstitial melts migrate through the crystal mush produces highly evolved melts (Section 6.2.4), which, if returned to the magma reservoir, may be important in controlling the trace element characteristics of the erupted magmas. However, the buffering effect of the crystal assemblage prevents the melt becoming highly evolved in terms of compatible (major) elements.

The effectiveness of fractionation via return of the interstitial melt to the main magma reservoir is limited by physical constraints on the return of highly evolved interstitial melt to the eruptable magma chamber. This is due to the continual accumulation of crystals, along with interstitial melt, at the magma-mush interface. Thus, as evolved melt moves upward through the crystal mush it is the most recently trapped (i.e. least fractionated) melt which is returned to the magma chamber. Scenarios in which evolved interstitial melt may be returned to the eruptable magma reservoir include: (i) if the rate of crystal accumulation slows sufficiently for interstitial melt to be compacted out of the mush (Shirley, 1986), (ii) if the interstitial melt rises due to having a lower density than the overlying melt (i.e. compositional convection), (iii) if the crystal mush is physically disrupted.

The rate of crystal accumulation at the magma-mush interface is expected to slow with time due to a decrease in the rate of cooling as a magma chamber becomes established and heats up the surrounding rocks. This may be accentuated during the waning stages of a magma chamber's life as the percentage of crystallisation per unit drop in temperature decreases (Marsh, 1981; Sinton & Detrick, 1992). However, unless accumulation almost stops, or compaction of the crystal mush is very rapid, it is unlikely that highly evolved melt will ever be returned to the magma reservoir. Furthermore, during the final stages of a magma chambers life span it is unlikely to erupt.

As discussed in Section 6.5.3, crystallisation of a gabbroic assemblage does not lead to a substantial change in the density of the parental melt and thus there is little driving force for compositional convection. The one scenario in which compositional convection may be efficient within a gabbroic crystal mush is if volatiles are involved, either dissolved in the melt, or as a separate phase.

Disruption of the crystal mush may occur through tectonic deformation (e.g. shaking), or gravitational instability within a boundary layer. However, neither of these processes are likely to occur after the porosity has been reduced significantly. Marsh (1988a) suggests that a crystal mush becomes rigid at ~25% crystals and at higher crystallinities it is unlikely to become unstable under gravity.

It is thus unlikely that significant volumes of highly evolved interstitial melt will be returned from the crystal mush to the eruptable magma reservoir under normal circumstances. Despite these physical arguments, the effect on the composition of the eruptable melt induced by mixing interstitial melt into the eruptable magma are investigated below (Section 7.3) as a presently unknown process may make extraction of the interstitial melt possible.

### *7.2.5 Consistency with other models*

The model proposed is consistent in many respects with recent models of magmatic construction at slow spreading ridges (Sinton & Detrick, 1992; Smith & Cann, 1992; Cannat, 1993, 1996). The lack of detection of magma bodies by geophysical experiments (e.g. see Sinton & Detrick, 1992) at slow spreading ridges does not contradict the proposed model as this is only applicable during times of high magma supply (i.e. periods of magmatic construction). Furthermore, in the model each magma body within the crust is small and may not be within the resolution of seismic experiments. Sinton and Detrick (1992) propose that much of the fractionation within mid-ocean ridge magma chambers occurs within crystal mush zones and that melt-dominated regions occur as transient sills at slow-spreading ridges. This is very similar to the model shown in Fig. 7.1. The proposed model is also consistent with that of Smith and Cann (1992). They show that the median valley of the Mid-Atlantic Ridge is constructed out of overlapping seamounts and suggest each is fed by an individual magma chamber. Cannat (1993, 1996) suggests that the lithosphere at slow spreading ridges is made up of individual gabbroic bodies which do not overlap if the spreading rate is sufficiently slow. This is also consistent with Fig. 7.1 with the degree of overlap of gabbro bodies controlled by the relative rates of magma supply and extension.

## 7.3 Implications of the plumbing model for the interpretation of MORB suites

The model proposed above suggests that the crustal magma plumbing system beneath mid-ocean ridges is important in determining the composition of melts erupted at the surface. This occurs through the homogenisation and fractionation of the melt compositions which enter the crust. However, it has traditionally been the compositions of erupted melts (sampled as MORB), due to their ease of sampling, which have been used to interpret the sub-surface magmatic processes

and to infer the mantle composition. In this section the compositional evolution of a melt within the proposed crustal plumbing system is discussed.

The main differences between the evolution of a melt in the model crustal plumbing system and a simple fractionation model calibrated from one-atmosphere crystallisation experiments can be attributed to four things: (i) the variation in the parental melt compositions, (ii) the higher temperature of clinopyroxene saturation than in one-atmosphere crystallisation experiments, (iii) the mixing of diverse melt compositions together prior to eruption, and (iv) the variation in the differentiation process operating (e.g. homogeneous versus boundary layer crystallisation). These are discussed in turn below.

*7.3.1 Variation in the parental melt compositions*

Without an extensive melt inclusion database, or extensive trace element analyses of minerals from throughout the crustal section, it is difficult to determine the extent of the variation in parental composition within the crustal plumbing system. However, the limited melt inclusion data, combined with the highly depleted compositions of abyssal peridotites and the composition of plagioclase cores in poikilitic olivine gabbros, show that there are significant variations in the compositions of melts within the crust. Thus, fractionation will not follow a single trend, but will depend on the composition of the parental melt.

*7.3.2 High temperature clinopyroxene fractionation*

Higher temperature clinopyroxene saturation within the MORB plumbing system than in one-atmosphere experiments is indicated by the much higher Mg#'s of clinopyroxene crystals in the Hole 923A gabbros than of clinopyroxene formed in one-atmosphere crystallisation experiments on primitive MARK area MORB (Sections 4.2.1 & 5.5.4). This has two main effects on the compositional evolution of melts within the plumbing system. Firstly, elements which are compatible in clinopyroxene but not plagioclase and olivine (+/- spinel) will be compatible from an earlier stage of MORB fractionation than predicted in the experiments. For example, Ca becomes compatible when clinopyroxene becomes a liquidus phase whereas Al is compatible from the onset of plagioclase fractionation. Thus, the Ca/Al ratio of a basalt, assuming a single stage fractionation process (i.e. no mixing), is partially dependent on the timing of clinopyroxene saturation. However, the Ca/Al ratio of MORB is used to determine the extent of melting, because it is though to increase with increased extent of melting (Klein & Langmuir, 1987). Thus, variations in the timing of clinopyroxene saturation which led to variations in the Ca/Al ratio of the melt could be mis-interpreted as indicative of different degrees of melting. Clearly, the

timing of clinopyroxene saturation will be strongly influenced by the major element composition of the melt and thus these factors will be interlinked; i.e. a high degree partial melt will have a high Ca/Al ratio which in turn will, all other things being equal, lead to earlier clinopyroxene saturation than a lower degree, lower Ca/Al, partial melt. Evidence that clinopyroxene fractionation affected the composition of almost all MARK area MORB is provided by the good negative correlation between incompatible element and CaO abundances in these basalts (Bryan *et al.*, 1981; Dosso *et al.*, 1993; Reynolds & Langmuir, 1997).

*7.3.3 Magma mixing*

Magma mixing can have numerous effects on the melt composition as discussed in Section 5.3. Two of the more important of these are: (i) replenishments which pond at the base of a magma chamber have the incompatible elements rapidly removed from them (Albarède, 1985), (ii) mixing magmas at different stages of evolution can produce hybrid melts which apparently require a different parental composition. For example, incompatible elements can be over-enriched with respect to the degree of fractionation predicted by compatible elements. This is shown in Fig. 7.2 which shows Zr versus Ni for MARK area MORB and a model Rayleigh fractionation curve. The data cannot be explained by simple fractionation of a single parental composition. However, mixing between an evolved and a more primitive melt derived from the same parental composition can explain the data

The fluid dynamics of mixing, which are controlled to a large degree by the melt density, have a considerable influence on the composition of melt produced by mixing and their eruptability. Melts which have relatively high densities, either due to the composition of their parent or due to their degree of fractionation (very primitive or highly fractionated; Fig. 5.1; Stolper & Walker, 1980; Sparks *et al.*, 1980) have lower eruptability than less dense melts. For example, high-pressure partial melts have higher FeO contents for a given degree of fractionation (high $Fe_{8.0}$) than melts derived from melting at lower pressure (Klein & Langmuir, 1987). Because the FeO content has a major influence on the density of a basalt, melts with high $Fe_{8.0}$ will be denser than melts at a similar degree of fractionation with a lower $Fe_{8.0}$ and will thus have a lower probability of being erupted. Fig. 7.3 shows the calculated densities of melts produced in partial melting experiments on peridotite versus the percentage melt (data from Baker & Stolper, 1994). The low degree melts have considerably lower densities than the higher degree melts. Thus, if these melts are incompletely mixed when they reach the crust their eruptabilities will vary.

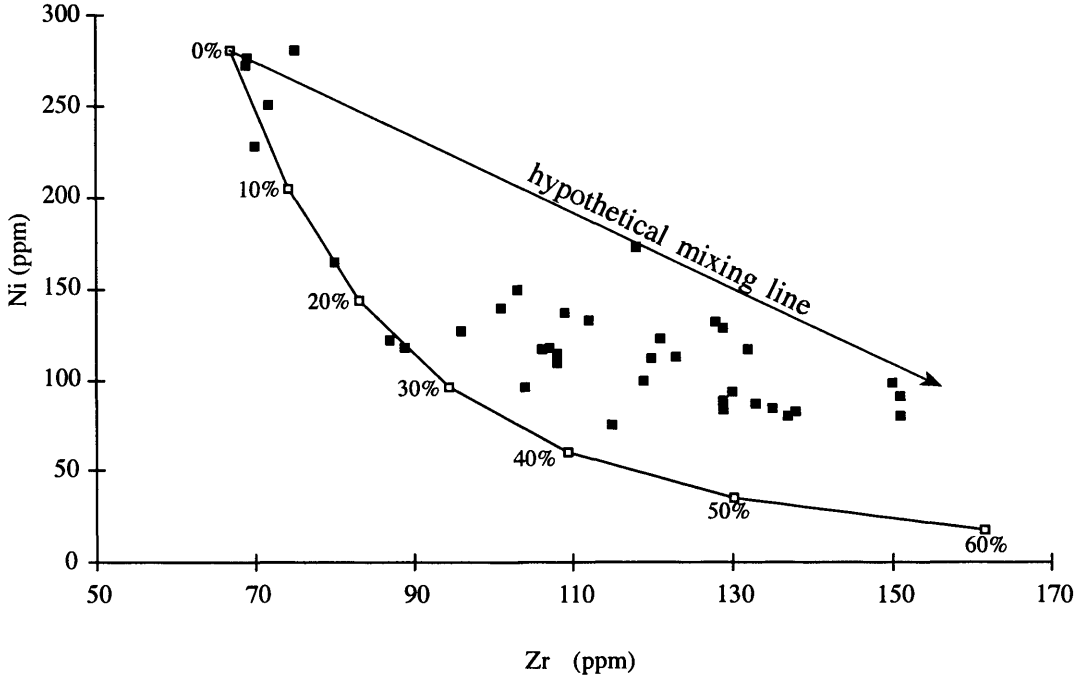


Fig. 7.2 Zr versus Ni abundance in MARK area MORB (Bryan et al., 1981; Dosso et al., 1993; Reynolds & Langmuir, 1997) and dolerite dykes from ODP Site 920 (Kempton & Casey, 1997). Also shown is a Rayleigh fractionation trend assuming the most primitve composition as a parental composition and $D_{Zr} = 0.04$ and $D_{Ni} = 4$ for (squares at 10% crystallisation intervals). Clearly most of the samples can be explained better by mixing between a primitive and an evolved melt than simple fractionation.

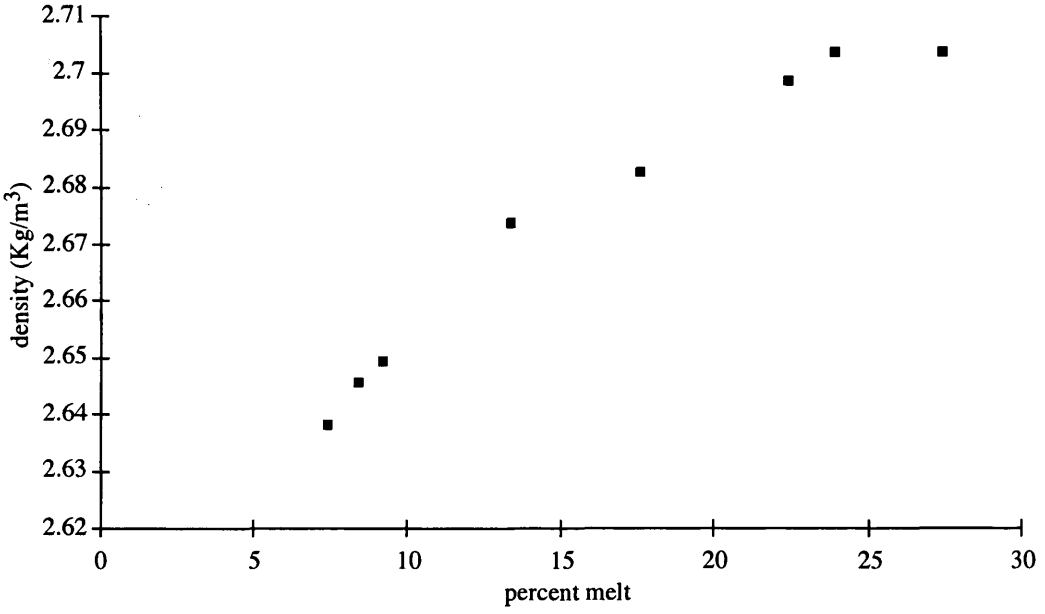


Fig. 7.3 Variation in melt density with percentage melt produced in partial melting experiments performed on peridotite (Baker & Stolper, 1994). This shows that small degree partial melts of the mantle will be less dense than more depleted higher degree melts.

*7.3.4 Variations in fractionation processes within the crust*

The variation in the fractionation mechanisms within the magma plumbing system proposed above suggests that, even without different parent melt compositions, high-T clinopyroxene saturation and magma mixing, the melt composition will not follow a simple liquid line of descent. During periods of rapid cooling differentiation probably follows a liquid line of descent close to that predicted for Rayleigh fractionation. However, if the dominant mechanism of fractionation during periods of stasis is via crystallisation at the margins of the magma reservoir and within the crystal mush, the fractionation effects will be different; compatible element abundances will be buffered by the crystals, and incompatible elements may be fractionated from one another (Section 6.2.4). This could provide another mechanism of explaining the Zr - Ni systematics shown in Fig. 7.2. A diagnostic characteristic of a fractionation trend controlled by return of evolved interstitial melt to the eruptable magma chamber is an enrichment in Zr over Nd and Sm with little variation in REE pattern (Section 6.2.4). Fig. 7.4 shows the composition derived by mixing small amounts of melt in equilibrium with the interstitial clinopyroxene in a troctolitic poikilitic olivine gabbro from 30.26 mbsf with a melt with a smooth MORB-like incompatible element profile. The addition of only one percent of the evolved melt to the MORB-like magma results in the generation of a significant positive Zr anomaly ($Zr/Zr^* = 1.17$, addition of 2.5 vol. % leads to $Zr/Zr^* = 1.39$). Furthermore, negative Ti anomalies develop. Both these are characteristics of N-MORB (Section 5.5.3.4).

The efficiency of return of interstitial melt to the main body of the magma chamber in generating compositional variation within the eruptable melt reservoir has also been modelled in Fig. 7.5. The premise behind this modelling is to investigate whether extraction of interstitial melt when the porosity is high or low has the greater effect on the composition of the magma reservoir to which the interstitial melt is added upon extraction from the crystal mush. This is not obvious as the effects of decreasing melt volume and increasing degree of fractionation operate to counteract each other. This modelling assumes that the melts in equilibrium with the different portions of the clinopyroxene crystal analysed by ion probe from 31.31 mbsf were returned to the eruptable magma reservoir, and the volume of melt returned is assumed to be proportional to the porosity. The same assumptions of the relationship between the porosity and the distance of the analysis from the rim of the crystal were used as in modelling in Section 6.2.1.2, and the equilibrium melt composition was calculated using the D's from Appendix A.I. Fig. 7.5 shows the relationship between the product of the calculated equilibrium melt composition and the volume of melt remaining. This product reflects the relative effect of mixing the interstitial melt into the eruptable melt reservoir; i.e. assuming all the interstitial melt is extracted from

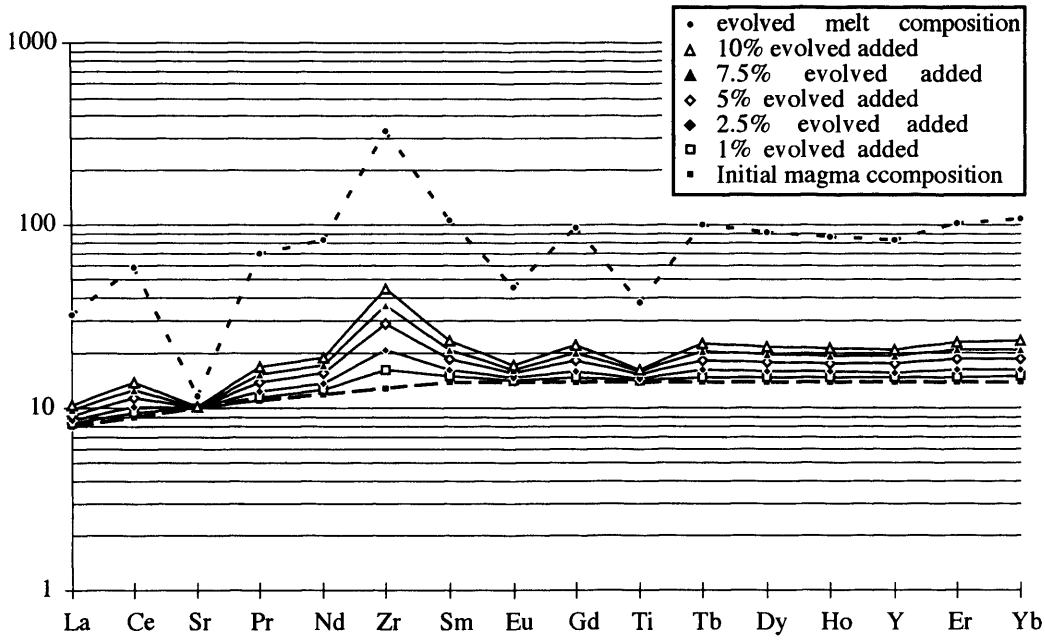


Fig. 7.4 Incompatible element abundances in modelled hybrid magmas derived from mixing evolved interstitial melt (dotted line) with a magma reservoir which has a smooth incompatible element abundance profile (dashed line). The evolved melt composition was calculated to be in equilibrium with interstitial clinopyroxene in the troctolitic poikilitic olivine gabbro from 30.26 mbsf (using the distribution coefficients from Appendix A.I). The composition of the magma reservoir was set so as to have a smooth, slightly LREE-depleted profile. Note that even with only 2.5% interstitial melt added to the magma chamber a significant positive Zr anomaly develops.

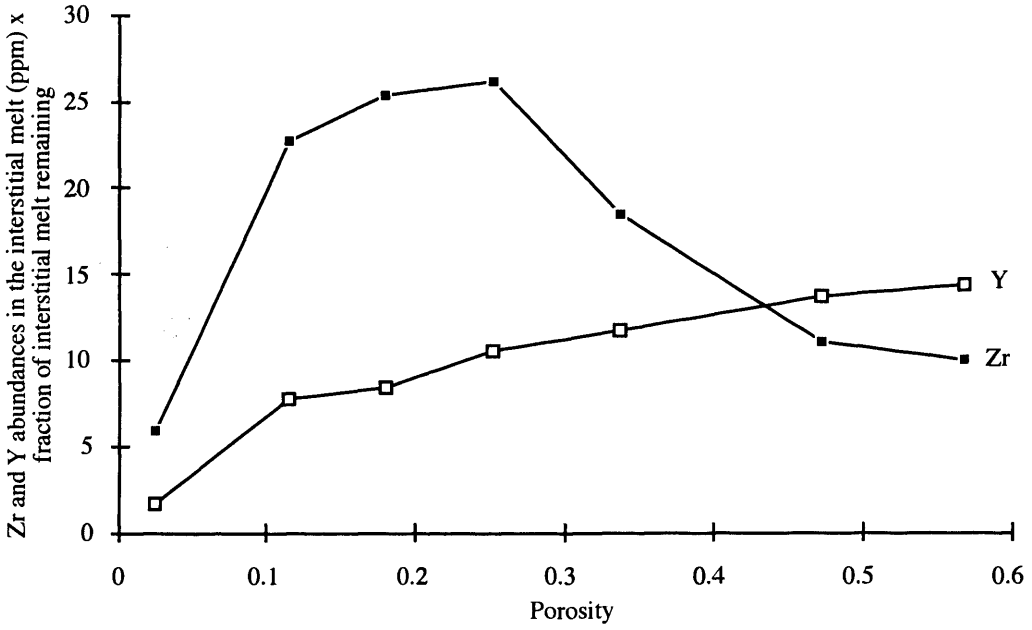


Fig. 7.5 Plot of estimated porosity versus the product of element abundances in the melt and porosity during crystallisation of the clinopyroxene crystal analysed from 31.31 mbsf (see text for details). The product of the abundance of an element in the interstitial melt and the porosity of the crystal mush shows what the relative effects on the composition of the eruptable magma reservoir would be if the interstitial melt was mixed back into it. Clearly the effects differ between the elements with the maximum increase in the Zr abundance being caused by mixing back interstitial melt when the porosity was 15-25%. However, the maximum increase in the Y abundance would be through mixing the interstitial melt back into the magma reservoir while the porosity was much higher (>50%). The composition of the melt was calculated from the crystal composition using the distribution coefficients from Appendix A.I and the porosity is as in section 6.2.1.2.

the crystal mush instantaneously and mixed into the eruptable melt the higher the product of the volume and abundance, the larger the increase in the abundance in the eruptable melt reservoir will be. Fig. 7.5 shows that extraction of the interstitial melt at a porosity of ~25% would have the maximum effect on the Zr abundance of the eruptable melt. However, the maximum effect on the Y abundance would be through extraction of the melt at a porosity of ~55%.

### 7.4 Implications of magmatic metasomatism for interpretation of whole-rock gabbro geochemistry

An important finding of this study has been the extreme variation in incompatible element abundances and ratios within single crystals of both clinopyroxene and plagioclase which do not reflect *in situ* crystallisation of trapped melt (Section 6.2.1). This observation shows that both whole-rock and mineral separate analysis of minerals from gabbros record mixed compositional signatures which may be very difficult to interpret correctly. Furthermore, since post-cumulus crystallisation did not occur from trapped melt, whole-rock compositions do not lie on mixing lines between the composition of the cumulus crystal assemblage and a melt composition.

Because the Zr/Y ratio of the interstitial melt varied throughout solidification (Sections 4.2.3.1 & 6.2.4), and the bulk rock inventory of these elements generally resides in clinopyroxene in these rocks, the timing of clinopyroxene growth will substantially control the whole-rock Zr/Y ratio. However, if clinopyroxene is a cumulus phase, the Zr/Y ratio of the whole-rock will be controlled by the degree of reaction between evolved interstitial melt and clinopyroxene. This is borne out for samples from Hole 923A by the negative correlation between whole-rock Hf/Yb (using Hf as a proxy for Zr) and modal proportion of clinopyroxene in the data of Ross and Elthon (1997a; Fig. 7.6). Furthermore, a negative correlation exists between the Zr/Y ratio and the sum of the normative diopside and hypersthene (used as a proxy for the modal proportion of clinopyroxene as this is not given in the data sources) in other whole-rock data for Hole 923A gabbros (Fig. 7.7; Casey, 1997; Gaggero & Gazzotti, 1996). However, most incompatible element abundances increase with increasing clinopyroxene abundance as shown in Fig. 7.8. Thus, a lack of correlation between trace element abundances and ratios cannot be considered to be indicative of variations in the parental melt composition. Considerable scatter exists in Figs. 7.6, 7.7 and Fig. 7.8 for several reasons. Firstly, the correlation only exists in samples in which the timing of clinopyroxene saturation within the crystal mush varied. Secondly, significant variation in the Zr/Y ratio was imparted to samples by melt fluxing, however, this did not significantly effect the modal proportion of clinopyroxene. Thirdly, the abundance of accessory phases which concentrate

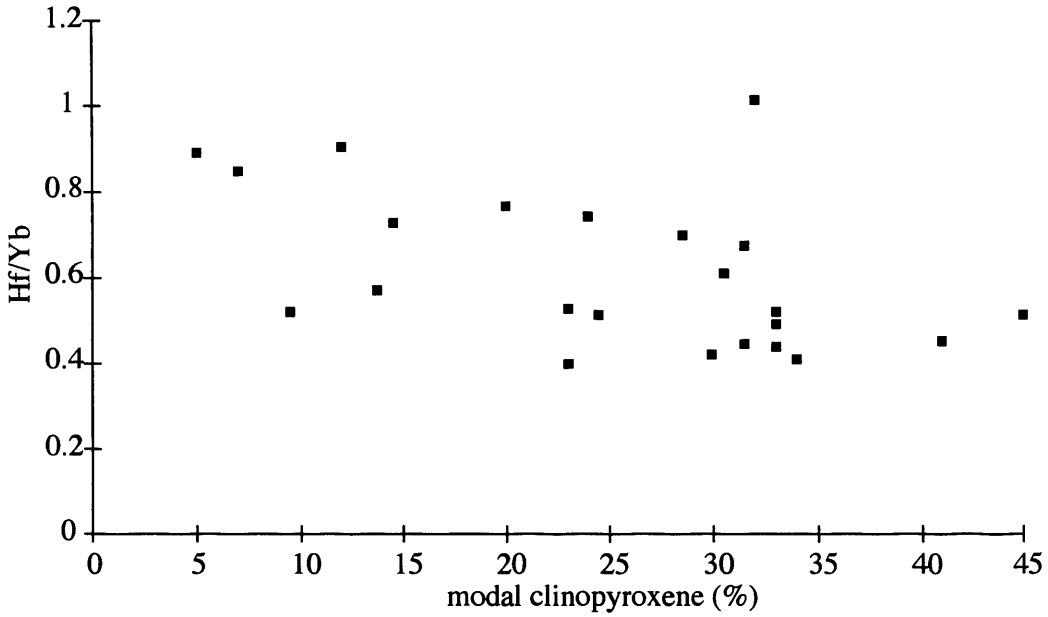


Fig. 7.6 Variation in the Hf/Yb ratio in whole-rock INAA analyses with modal proportion clinopyroxene (Data from Ross & Elthon, 1997a). The weak negative trend is consistent with magmatic metasomatism being important in the genesis of these rocks.

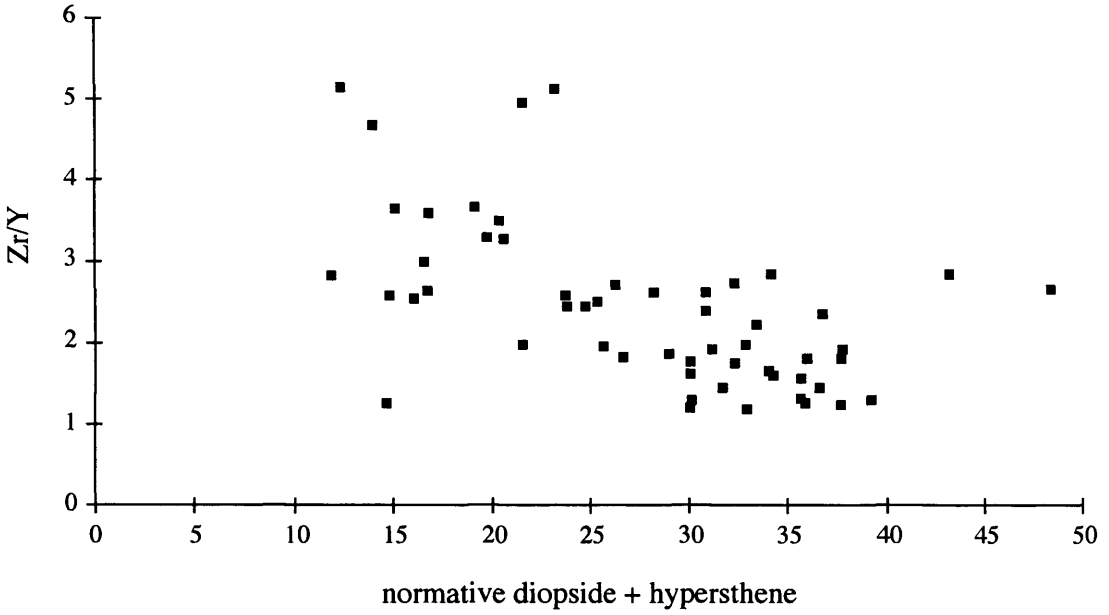


Fig. 7.7 Whole-rock Zr/Y versus normative (diopside + hypersthene); data from Casey (1997) and Gaggero & Gazzotti (1996) for samples from ODP Hole 923A. Because modal data are not available for most whole rock analyses, normative diopside + hypersthene is used as a proxy for the modal clinopyroxene abundance. The overall negative correlation shows that low modal proportions of clinopyroxene are associated with high Zr/Y ratios as predicted for crystallisation from evolved migrating melt. However, if it was assumed that fractionation of a gabbroic assemblage would not significantly fractionate Zr from Y the variation in Zr/Y ratio may incorrectly be ascribed to variations in the Zr/Y ratio of the parental melt.

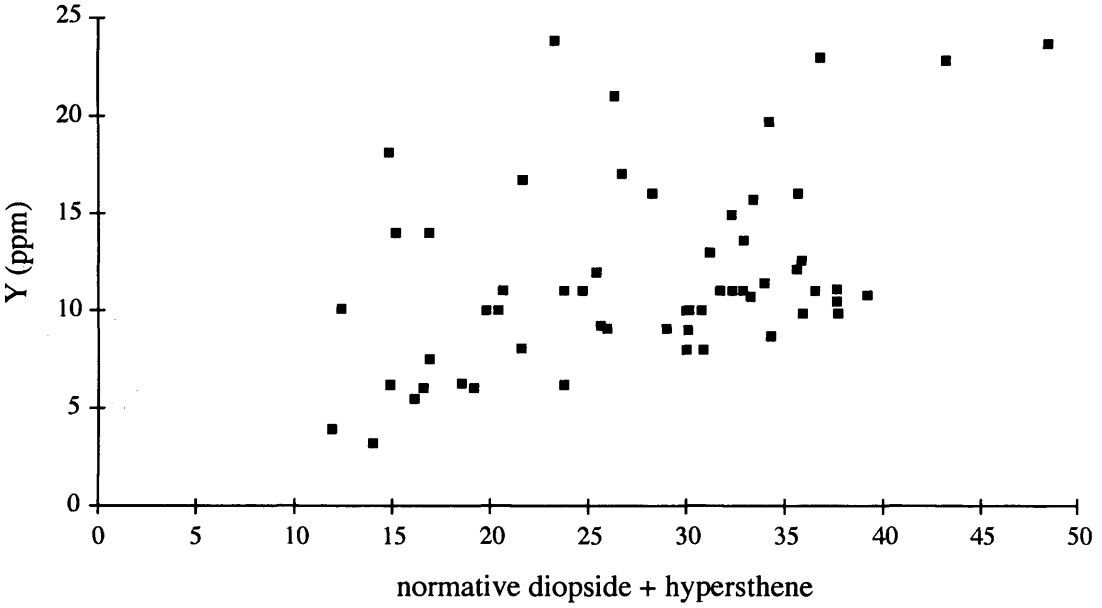


Fig. 7.8 Whole-rock Y abundance versus normative diopside + hypersthene) showing a positive correlation for samples from ODP Hole 923A; data from Casey (1997) and Gaggero & Gazzotti (1996). Assuming diopside plus hypersthene is an adequate proxy for the modal proportion of clinopyroxene, this suggests that the modal proportion of clinopyroxene has a control on the Y abundance, as expected from clinopyroxene having the highest $D_Y$ of the main phases.

these incompatible elements (e.g. zircon, apatite) will affect the incompatible element abundances and ratios. Furthermore, normative diopside plus hypersthene is not a perfect proxy for the modal proportion of clinopyroxene.

The effect of post-cumulus modification also complicates interpretation of textures. For example, the coarsening and increased granularity of crystals during interaction between interstitial melt and the primary crystal assemblage may lead to post-cumulus phases becoming apparently cumulus. Thus, understanding the relationships between samples and lithologies both compositionally and texturally is essential as the study of individual samples may be misleading.

A major conclusion of this study is, thus, that full interpretation of the genesis if gabbroic rocks is dependent on *in situ* analysis of trace element abundances (e.g. ion probe or laser ICP-MS), performed in conjunction with other studies (field relations, textures, electron microprobe analyses and elemental mapping). Without these data interpretation of both textural and geochemical characteristics are likely to be non-unique.

### 7.5 Future work

Much more work is necessary before we have a good understanding of the full magma plumbing system beneath mid-ocean ridges. Ideas for some future work are presented below.

(i) Investigating mantle derived compositional diversity within the magma plumbing system requires understanding the processes involved in melt generation, extraction and fractionation. This needs an extensive integrated study of mineral compositions (in association to textures) in spatially-associated abyssal peridotites, oceanic gabbros and MORB phenocrysts *and* whole-rock MORB and melt inclusion compositions. A suite of elements is required with as broad a range of geochemical properties as possible. This should include elements with significantly different compatibility in different phases (both incompatible and compatible) which vary with pressure and phase compositions, and behave differently in the presence of fluids. By combining these data for one area, the possibility of large scale mantle heterogeneity being an important parameter is minimised.

(ii) Mixing in the magma plumbing system. The hypothesis that mixing plays a fundamental role in the MORB plumbing system could be tested through a combined study of plagioclase microphenocryst crystal size distributions and their trace element compositions in MORB. The CSD data would show whether mixing occurred, and if so the timing of mixing prior to eruption (e.g. Higgins, 1996). The compositional diversity between the melts which mixed together

should be recorded in the trace element composition of plagioclase (micro)phenocrysts. This may show how far through the plumbing system very diverse melt compositions exist. For example, if plagioclase CSD distributions show that mixing occurred immediately prior to eruption was important, but plagioclase trace element compositions are identical, the compositions of the melts mixed together were similar. However, if the plagioclase compositions fall into two very diverse groups, mixing prior to eruption was important in determining the bulk composition of erupted magma.

(iii) The role of assimilation could be tested through the analysis of the abundances of volatile elements, +/- their isotopic ratios, in interstitial apatite and amphibole. For example, the Cl/Br ratio of MORB (~430) is higher than that of seawater (~290; Jambon *et al.*, 1995). Thus, given appropriate partitioning data for these phases, their Cl/Br ratios could be used as a signature of the source of these elements (all other things being equal). Better still, the Cl isotopic ratio of these phases might distinguish between these source as pristine MORB have $\delta^{37}Cl$ of 3 to 7‰ defined relative to seawater (Boudreau *et al.*, 1997).

(iv) The origin of the compositional diversity in the melts parental to plagioclase would be best investigated through *in situ* isotopic analysis of plagioclase crystals with different incompatible trace element signatures. This would determine whether the compositional diversity is due to source heterogeneity or melting dynamics. For example, if the decoupling of Y and LREE abundances in plagioclase is due to melting of a homogeneous source in the presence of garnet (i.e. initial melting at high-pressure) no isotopic variation would exist between plagioclase crystals. However, if the compositional diversity is due to melting of a heterogeneous source (e.g. a source containing garnet pyroxenite veins; Hirschmann & Stolper, 1996) isotopic ratios should correlate with trace element chemistry.

(v) Testing the speculations about the origins of Zr and Ti anomalies (with respect to adjacent REE's) in the MORB plumbing system requires extensive experimental and theoretical determination of partition coefficients for these elements under variable conditions (P, T, mineral and melt compositions and volatile species activities). Furthermore, more extensive trace element analysis of minerals in oceanic peridotite and gabbros are required to investigate alternative sinks for these elements (e.g. orthopyroxene). However, a recent study (Yang *et al.*, 1998) provides support for the hypothesis that increasing melt extraction generates Zr and Ti anomalies in oceanic peridotites (Section 5.5.3). They determined the trace element composition of clinopyroxene crystals in xenoliths

thought to be representative of different depths in the residual melt column from the East Pacific Rise. Clinopyroxene crystals with the lowest incompatible element abundances also have the lowest Zr/Zr* and Ti/Ti* (Fig. 7.9). Furthermore, there is an overall correlation between Zr/Zr* and Ti/Ti* but the different samples define different fields which are not co-linear. Unfortunately modal abundances are not given in this paper, and neither are co-existing orthopyroxene analyses, thus the origin of these variations cannot be modelled.

(vi) The suggestion that magnesian clinopyroxenes in oceanic gabbros may have crystallised from melts unlike MORB (higher Ca/Al) could be partially tested by determining the incompatible trace element abundances in a wide spectrum of magnesian clinopyroxene. If they all record depleted parental melt compositions then this provides a simpler explanation for these compositions than high-pressure crystallisation. The opposite is not true, however, because the addition of a small amount of highly enriched melt to a depleted melt could have a significant effect on its incompatible trace element composition, but little effect on the major elements. Extensive analysis of melt inclusions would also provide information about the abundance of high Ca/Al melts within the magma plumbing system beneath mid-ocean ridges.

(vii) The model of magmatic metasomatism proposed to have been important during the genesis of brown-pyroxene gabbros could be tested via the analysis of more clinopyroxene zoning profiles. This should be done in samples of different grain size, and in samples from different stratigraphic levels. The model predicts that the size of the incompatible element enriched rims on clinopyroxene is proportional to the grain size, and for a given grain size there should be a general up-hole increase in the degree of fractionation (although whether this would be observed in a 50 m core depends on the length scale over which migration occurred). Furthermore, analysis of a more extensive suite of elements would provide better constraints for modelling. In particular analysis of: (i) transition metals would provide a greater constraint on the buffering effect of the cumulate assemblage (although the occurrence of sulphides may complicate this), (ii) volatile elements (e.g. Cl and F) may provide a clue as to the role of volatiles in the development of the crystal mush, and (iii) Hf may show whether the variation in Zr/Hf in ilmenite was produced through diffusion controlled fractionation. Furthermore, whether exsolution of volatile species from the interstitial melt occurred could be tested by extensive analysis of the volatile abundances, in conjunction with other incompatible elements, of interstitial apatite and amphibole. If volatile and incompatible element abundances do not co-vary in the manner expected for fractionation of the crystal assemblage,

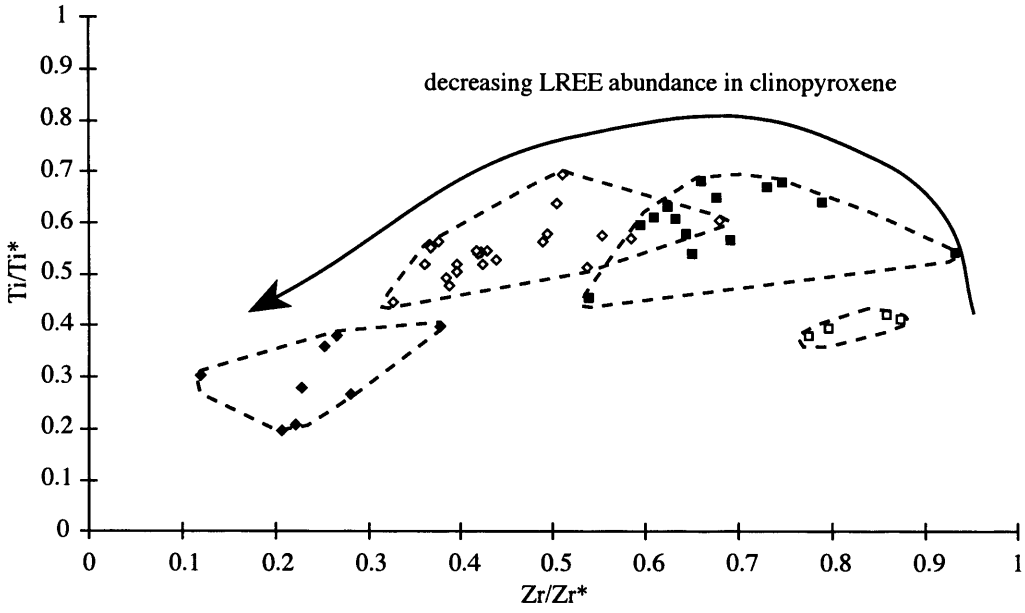


Fig. 7.9 Zr/Zr* versus Ti/Ti* in clinopyroxene in xenoliths of oceanic lithosphere from Hawaii (Yang et al., 1998). The curve shows the order of decrease in LREE abundances between the samples, which is thought to record the degree of melt extraction (i.e. open squares - highest LREE abundances, filled diamonds - lowest LREE abundances). Zr* = (Sm + Nd) / 2 and Ti* = (Gd + Tb) / 2.

exsolution is likely to have occurred. Furthermore, the ratios of volatile elements will vary in different manners for fractionation and exsolution. For example, during crystallisation of amphibole and apatite (plus plagioclase, olivine and clinopyroxene) the Cl/F ratio in the melt will increase; however, if exsolution occurs this ratio will drop.

The widespread applicability of the percolation model can be tested to a first approximation for other suites of gabbroic rocks by comparing the whole-rock Zr/Y ratio to the modal abundance of clinopyroxene (or if only whole-rock data are available the normative diopside + hypersthene abundance). However, this is dependent on the modal clinopyroxene proportion being controlled mainly by the relative timing of clinopyroxene saturation with respect to evolved melt percolation, and the bulk D's for these elements being different (i.e. a clinopyroxene-plagioclase dominated system). If the modal proportion of clinopyroxene is fixed, a better test may be to determine the correlation between grain size (and shape) or degree of textural equilibration and very incompatible element / moderately incompatible element ratio. Furthermore, in lithologies with different mineralogy different element ratios would be more appropriate (e.g. Yb/La in plagioclase dominated systems).

### 7.6 Main conclusions of this thesis

- The gabbroic rocks recovered from ODP Hole 923A on the Mid-Atlantic ridge record textural and compositional evidence for primitive magma chamber replenishments. These magma batches contained resorbed plagioclase phenocrysts which grew from melts compositionally distinct from MARK area MORB. These replenishments ponded at the base of the Hole 923A magma chamber where they fractionated prior to wholesale mixing with the host magma. Fractionation within the ponded primitive layer lead to the rapid removal of compatible elements from the replenishing melt. These replenishment horizons show that at times magma bodies exist beneath mid-ocean ridges which are predominantly molten.

- The compositions of melts within the crustal magma plumbing system, as recorded in clinopyroxene and plagioclase trace element compositions, are more diverse than those erupted as MORB in the MARK area. For example, significant variations in trace element ratios such as La/Nd, La/Y and Nd/Y occur in plagioclase crystals. Thus, some of the mixing that occurs between the diverse melt compositions generated in the MORB plumbing system happens in the crust. i.e. melts crossing the petrological Moho retain compositional diversity generated during melting/melt extraction.

- The crystal mush zones around the margin of the magma chamber underwent a complex textural and chemical evolution (diagenesis). This involved extensive chemical interaction between the migrating interstitial melt and the crystal assemblage (melt-rock reaction) which modified the compositions of the crystals and melt are effected the resulting rock texture. One effect of this was to increase the abundance of incompatible trace elements in the interstitial melt, whilst the abundance of compatible elements was buffered by the crystal assemblage. Concentration of volatile elements within the interstitial melt occurred, and may have been important in controlling phase relations. The oxygen fugacity of the interstitial melt was buffered, however, by the occurrence of sulphide globules. Return of interstitial melt to the eruptable portion of the magma chamber, although physically unlikely, may lead to significant fractionation of incompatible trace elements without significant major or compatible element fractionation. These findings prove that interstitial melts are mobile and question the concept of trapped melt.

  Texturally, increase melt-rock reaction increased the degree of textural equilibrium and increased the grain size (i.e. lowered the surface energy of the system) with crystals becoming more granular and less interdigitated with increased melt flux.

- Chemical exchange between evolved interstitial melt and the crystal assemblage led to whole-rock compositions that could easily be misinterpreted as indicative of different parental melt compositions.

- The best way to gain a better understanding of magma chamber processes, in particular the evolution of crystal mushes, is by combined textural and *in situ* mineral composition analyses (ideally elemental mapping). The application of these techniques to thick olivine-pyroxene cumulates may increase our understanding of the physical and chemical processes involved in mantle melting and melt extraction.

# Appendix A.I

# Discussion of the distribution coefficients used in this thesis

# Appendix A.I: Distribution coefficients

## A.I.1 Introduction

To maximise the interpretation of mineral compositions it is necessary to back-calculate the composition of the melt from which the crystal grew. This requires knowledge of appropriate distribution (or partition) coefficients (D's), and the assumptions of: (i) equilibrium between the crystal and melt during growth, and (ii) preservation of magmatic compositions. This Appendix discusses the controls on D's and suggests appropriate values which have been used in this study.

### *A.I.1.1 Distribution coefficients*

Distribution coefficients can be divided into two categories: Nernst distribution coefficients and equilibrium constants of reactions. Nernst distribution coefficients are defined as the ratio of the concentration of an element in the mineral to that in the melt at equilibrium (Equation A.I.i). These are specific for a certain mineral-melt pair (i.e. single mineral and melt composition) under a given set of conditions (i.e. P and T), and are only appropriate if Henry's Law is obeyed (i.e. at low concentrations; Navrotsky, 1978).

$$D = C_x / C_m \qquad \text{(A.I.i)}$$

where:

D = Nernst distribution coefficient
$C_x$ = concentration of the element in the crystal
$C_m$ = concentration of the element in the melt

An equilibrium constant (Kd) for an exchange reaction between a mineral and melt is defined from the activity ratio. For example, the distribution of $Mg^{2+}$ and $Fe^{2+}$ between a crystal and melt can be defined by the appropriate Kd in the equation:

$$Kd = Mg_m.Fe_x / Fe_m.Mg_x \qquad \text{(A.I.ii)}$$

where:

Kd = equilibrium constant of the exchange reaction of Fe and Mg between the mineral and melt
$Mg_x$ = mole fraction Mg in the crystal
$Fe_m$ = mole fraction Fe in the melt
$Mg_m$ = mole fraction Mg in the melt
$Fe_x$ = mole fraction Fe in the crystal

Both types of distribution coefficient are dependent on the crystal and melt compositions and the pressure and temperature of crystallisation. Nernst distribution coefficients and equilibrium constants are discussed separately below.

## A.I.2 Nernst distribution coefficients

### *A.I.2.1 Internal controls on Nernst distribution coefficients*

Crystal and melt compositions (structures) provide the two internal sources of variation in D's. Recent studies (Blundy & Wood, 1991, 1994; Gaetani & Grove, 1995; Wood & Blundy, 1997) have proposed that crystal chemistry is the dominant control on D's, while the degree of polymerisation in the melt remains constant. The rationale for this is that the strain energy associated with distribution of a trace element between a crystal and melt is dominated by the crystal (Wood & Blundy, 1997). This is due to the melt deforming more easily than the crystal.

### *A.I.2.2 Crystal chemical controls on distribution coefficients*

Trace elements generally substitute into the sites normally occupied by major elements in minerals. The ease with which they can do this is controlled by their size in comparison to the crystal lattice site, and the ease with which the crystal lattice can deform to allow elements which are not of exactly the same size as the lattice site to substitute into the site. For a mineral that forms part of a solid solution series the dominant control on the crystal lattice site and elasticity is its composition. Charge balance for the substituting trace element, if it has a different valency to the major element it is replacing, is probably not important in controlling the distribution coefficient in minerals in which Al can substitute for Si, and in which defects occur. However, this will not be the case for elements which occur in minor abundances, such as Ti and Na in clinopyroxene.

For a given crystal site and substituting cation valency, plots of D (abscissa) versus cation radius (ordinate; an Onuma plot) form parabolae (Fig. A.I.1; Onuma *et al.*, 1968; Jensen, 1973). The form of the parabola is dependent on the site size ($r_o$) and the strain energy associated with substitution as well as the temperature and pressure (Beattie, 1994; Blundy & Wood, 1994). The strain energy is controlled by the site elasticity, or Young's Modulus, and the peak position equals the crystal lattice site size. The elasticity of the site controls the curvature of the parabola, with inelastic sites having tightly curved parabola which indicate that the distribution coefficient is very sensitive to the size of a cation. The Young's Modulus is controlled both by the mineral composition and the charge of the substituting cation. With increasing cation charge, the Young's Modulus of the site increases (Fig. A.I.1b; Blundy & Wood, 1994) and thus the Onuma parabola

becomes more tightly curved. The variation in distribution coefficient with changes in the crystal composition depend on the location of a cation on the Onuma plot. Cations which have radii similar to the size of the site will have relatively constant D's across a range of mineral compositions (A on Fig. A.I.1a) compared to those which have sizes which plot on the limbs of the Onuma plot (B on Fig. A.I.1a).

A thermodynamic formulation of this model has been developed by Blundy and Wood (Blundy & Wood, 1994; Wood & Blundy, 1997). This uses the Brice equation (Brice, 1975) to calculate the energetics of substitution of a trace element into a crystal in place of a major element. This model assumes that this is the major control on partitioning, and assumes that the strain energy associated with substitution into the melt is negligible. It requires knowledge of the crystal site(s) into which substitution occurs, the site size, and the site Young's Modulus. Furthermore, the Brice equation also assumes that the sites and cations are spherical, which is not true for distorted lattice sites or cations with lone pairs of electrons (e.g. $Pb^{2+}$).

*A.I.2.3 Mineral specific considerations of distribution coefficients*

In this section the controls on substitution of trace elements into clinopyroxene and plagioclase are discussed, as these are the two minerals for which trace element data are available. Olivine also occurs in Hole 923A gabbros, and thus understanding the partitioning of trace elements into olivine is important for modelling the trace element evolution of these rocks. However, $D_{olivine}$ for most incompatible trace elements are so small as to be negligible.

A.I.2.3.1 Clinopyroxene D's for $3^+$ cations have been modelled by Wood and Blundy (1997) under varying conditions. They suggest that the Young's Modulus (E) of the M2 site in clinopyroxene into which many trace elements are thought to substitute, varies such that $E^{1+} \sim 1/2\ E^{2+} \sim 1/3\ E^{3+}$, and that $E^{2+} \sim E_{clinopyroxene}$. Thus, given $E_{clinopyroxene}$, the Young's Modulus for the M2 site for different valency substituting cations can be calculated. They show also that the composition of the clinopyroxene has little effect on the Young's Modulus; however, the pressure and temperature do (their Equation 14). They also propose that the only significant controls on the radius of the M2 site are the abundance of Ca (in the M2 site) and of Al (in the M1 site), such that higher Ca and lower Al contents lead to a larger M2 site (their Equation 15).

A.I.2.3.2 Plagioclase D's correlate well with major element composition. The higher the albite component of the plagioclase the larger the M site and the lower the $E^{1+}$ and $E^{2+}$. However, increasing the albite component leads to an increase in

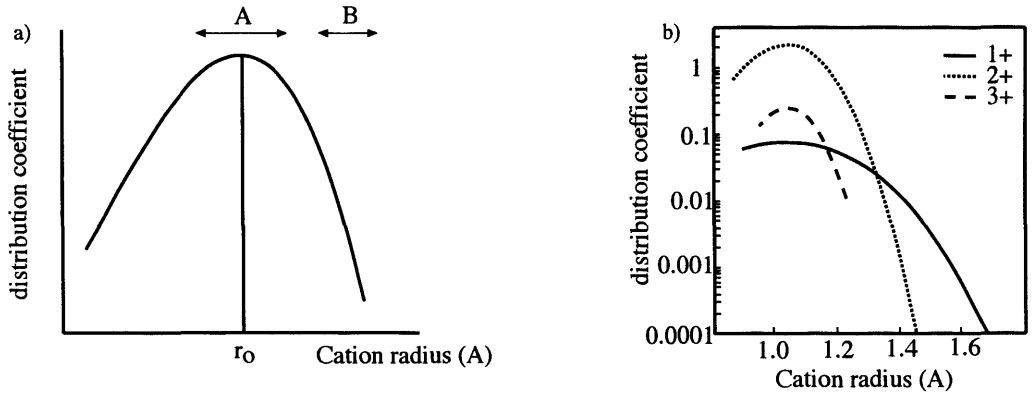


Fig. AI.1 (a) General form of Onuma plot modified from Wood and Blundy (1997) $r_o$ - size of site. In region A small differences in radii between cations has little effect on their distribution coefficients relative to in region B due to the gradient of the parabala. (b) Onuma plot for different valency ions in clinopyroxene from Blundy and Wood (1994). Note the tightening of the parabolae with increased charge due to increasing effective Young's Modulus of the lattice site. Decreasing temperature has the same relative effect. This means that small differences in ionic radius of highly charged ions will lead to large differences in distribution coefficient relative to less highly charged ions.

$E^{3+}$ (Blundy & Wood, 1994). The effect of temperature and pressure on the size and Young's Modulus of the plagioclase M site have not been investigated; however, it seems likely that, as with clinopyroxene, the lattice becomes less flexible with increased pressure and decreased temperature. Eu partitioning into plagioclase is dependent on the oxygen fugacity (Sun *et al.*, 1974). Reducing conditions favour the formation of $Eu^{2+}$, which partitions more strongly than $Eu^{3+}$ into plagioclase.

*A.I.2.4 Variation in melt composition/structure*

Equilibrium distribution of an element between a crystal and melt requires the activity of the element to be equal in the two phases. Thus, the solubility of an element in the melt is important in determining D's. The solubility of an element in a melt varies as the melt composition/structure varies. Silicate melt structures are complex and imperfectly understood (e.g. Mysen, 1990). However, experimental studies of diffusion in a temperature gradient (Soret diffusion; Lesher, 1986) and element partitioning between immiscible liquids (Watson, 1976; Ellison & Hess, 1989) have lead to a partial understanding of the influence of melt structure on element partitioning. The main control over the solubility of elements in a silicate melt depends on the degree of polymerisation of the melt. $2^+$ and $3^+$ cations become less soluble in the melt as it becomes more polymerised leading to higher D's for these elements. The opposite is true for singly-charged cations as these act as charge balancers for $3^+$ network forming cations (Lesher, 1986). Lesher (1986) also shows that changes in the degree of polymerisation of the melt affects cation activities in relation to their charge/radius ratio, with significant variation occurring within the range of polymerisation observed in basalts.

*A.I.2.5 External control on distribution coefficients*

Pressure and temperature are the external controls on D's. There are two main effects of temperature on D's. Firstly, the temperature influences the Young's Modulus of crystal sites and thus the strain energy of substitution. Decreased temperature leads to decreased site elasticity, and thus a more tightly curved Onuma parabola. Secondly, temperature affects the activity of components / cations. In the thermodynamic model of Blundy and Wood (1994) this manifests itself as a divisor in the exponential relating a known to an unknown D. Increasing pressure leads to a decrease in the elasticity of the lattice site leading to a tightening of the Onuma parabola (e.g. Equation 14 of Wood & Blundy, 1997). Temperature and pressure are also intimately related to crystal and melt compositions and thus are not truly separate variables.

**A.I.3 Distribution coefficients for use in this study**

The above discussion suggests that in the absence of suitable experimentally determined D's (i.e. internal and external conditions), good estimates of appropriate D's can be made from predictive equations. Furthermore, this approach allows the D's to be varied with variation in mineral compositions. This is the approach taken here. However, before discussing the calculation of D's appropriate for use in this study, it is necessary to show that surface equilibrium was attained during growth.

*A.I.3.1. Equilibrium partitioning ?*

Disequilibrium partitioning can be tested for by comparing the behaviour of elements which have similar equilibrium distribution coefficients but which achieve equilibrium at very different rates. Shimizu (1981) shows that during crystal growth the rate at which equilibrium is achieved is dependent on the ratio of the ionic charge to ionic radius squared ($Z/r^2$). This is due to an increase in the activation energy of desorption of ions in protosites on the surface of the growing crystal with an increase in $Z/r^2$. If this process significantly influenced trace element distributions in clinopyroxene, elements with similar bulk D's would show fractionation trends dependent on their $Z/r^2$ ratios.

Zr and Nd, and Ti and Gd, are thought to have similar bulk distribution coefficients but have very different $Z/r^2$ ($Z/r^2$: Zr - 5.7; Nd - 2.4; Ti - 7.3; Gd - 2.7; ionic radii from Shannon, 1976). In detail it is likely that bulk $D_{Zr}$ was slightly lower than bulk $D_{Nd}$ due to the greater partitioning of Nd than Zr into plagioclase (Blundy, 1997a). In contrast, it is likely that bulk $D_{Ti}$ was slightly higher than bulk $D_{Gd}$ due to the partitioning of Ti into ilmenite. Thus, if equilibrium was achieved, Zr-Nd and Ti-Gd are expected to have approximately one to one correlation with possibly slight excess enrichments in Zr and Gd with increased abundance compared to Nd and Ti. However, if disequilibrium partitioning was important, excess enrichment in both the REEs is expected because of the increased apparent D's for Ti and Zr due to their high $Z/r^2$. Figure A.I.2 shows that Zr is enriched with respect to Nd and Gd enriched with respect to Ti as expected for equilibrium partitioning. This is consistent with Watson's (1996) conclusion that equilibrium growth is expected in basaltic systems at natural growth rates.

A similar test cannot be applied to plagioclase because of the restricted range of elements for which trace element data are available and its apparently more complex crystallisation history (see Chapter Five). However, it seems unlikely that disequilibrium growth effected plagioclase and not coexisting clinopyroxene.

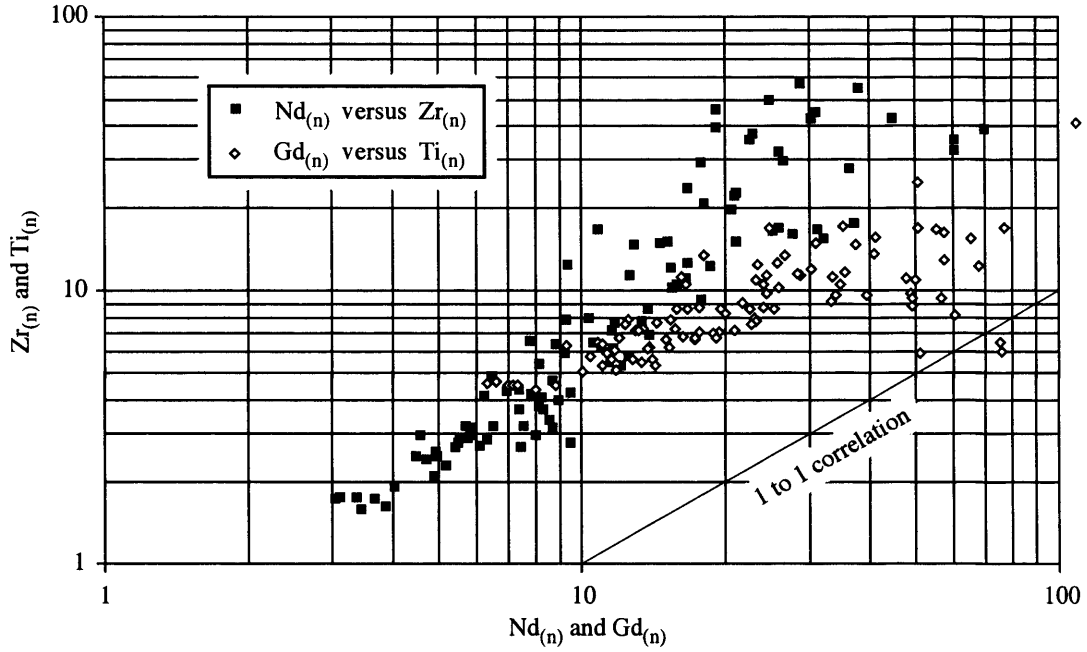


Fig. AI.2 Zr versus Nd and Ti versus Gd for all clinopyroxene ion probe analyses. The slight over-enrichments in Zr and Gd with respect to one to one correlations are consistent with equilibrium partitioning. These trends cannot be explained by significant disequilibrium partitioning as this would lead to apparent distribution coefficients for Ti and Zr being greater than for REE due to their higher charge/radius$^2$ ratio (Shimizu, 1981).

*A.I.3.2 External controls*

A.I.3.2.1 Pressure was probably approximately constant throughout the crystallisation of the Hole 923A gabbros and thus not a variable influencing distribution coefficients. Plagioclase interpreted to have been phenocrysts entrained in magma replenishing the magma chamber (see Chapter Five) may have formed at higher pressure. However, because there is no control on this it cannot be accounted for in the distribution coefficients.

A.I.3.2.2 Temperature must have varied considerably during the crystallisation of the Hole 923A gabbros to produce the range of mineral compositions; for example the forsterite content of olivine ranges from $Fo_{64}$ to $Fo_{85}$ within the core (Fig. 4.15a). By analogy with experiments on spatially associated MORB, this probably represents a temperature interval of ~140°C (Fig A.I.3). The effect of temperature on site elasticity in clinopyroxene has been quantified by Wood and Blundy (1997) for $3^+$ cations (their Equation 14). At low pressure, a drop in temperature from 1220°C to 1080°C is equivalent to an increase in apparent site Young's Modulus from 265 GPa to 270 GPa. The combined effect of activity variation and site elasticity variation are shown in Fig. A.I.4. This shows that the relative change in D as the temperature drops is dependent on whether the cation is larger or smaller than Ca (the dominant major element in the M2 site into which REEs substitute). For REEs larger than Ca (i.e. LREE) D's drop with decreased temperature and increase with increased temperature (Fig. A.I.4). For elements larger than Ca the opposite is true. Over the temperature interval 1220°C to 1080°C the largest change in $D^{3+}$ is for an element of equal size to the crystal site. Y has the closest radius to the clinopyroxene M2 site; however, the increase in $D_Y$ with increased temperature is only from 0.46 to 0.50. The temperature dependency of D's for plagioclase becomes less important with increasing cation charge (Fig. A.I.5).

*A.I.3.3 Internal controls*

The internal controls on partitioning are the melt and crystal compositions provided there is no separate fluid phase.

A.I.3.3.1 Variation in the melt composition can play an important role in determining distribution coefficients. Phase proportions and compositions within Hole 923A suggest that the melt was generally basaltic throughout crystallisation. This suggests that melt polymerisation was probably nearly constant throughout crystallisation. In addition, increased $SiO_2$ activity, which would increase the degree of polymerisation, will have been inhibited by reaction with olivine to produce the commonly observed orthopyroxene rims on olivine (i.e. the activity of silica was buffered). The likely exception to this is the

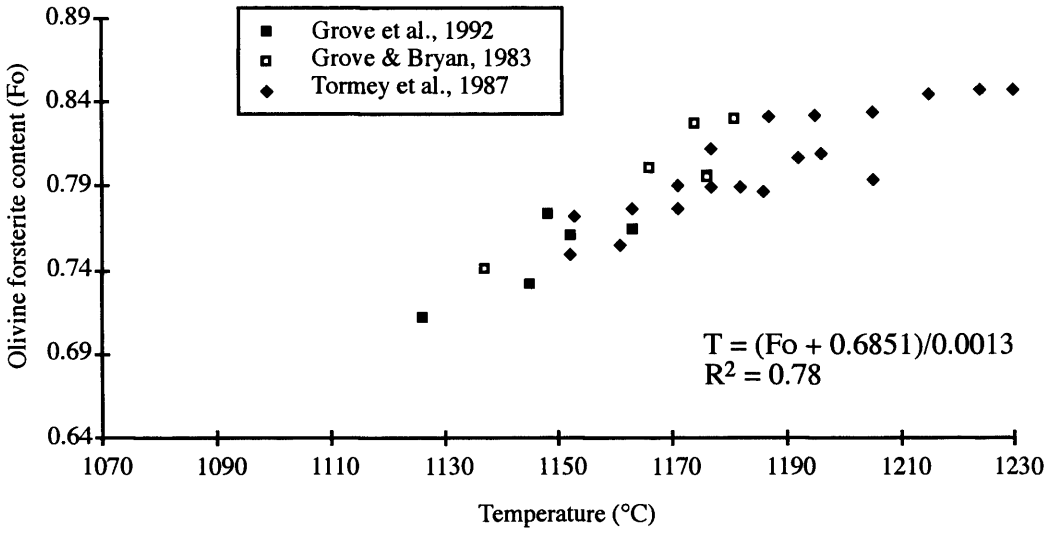


Fig. AI.3 Olivine forsterite contents (Fo) versus temperatures (°C) from experiments on MORB from the MARK area. Projection of the trend over the range of forsterite contents in ODP Hole 923A (85-64) suggests crystallisation over a ~140°C temperature interval (1220-1080°C).

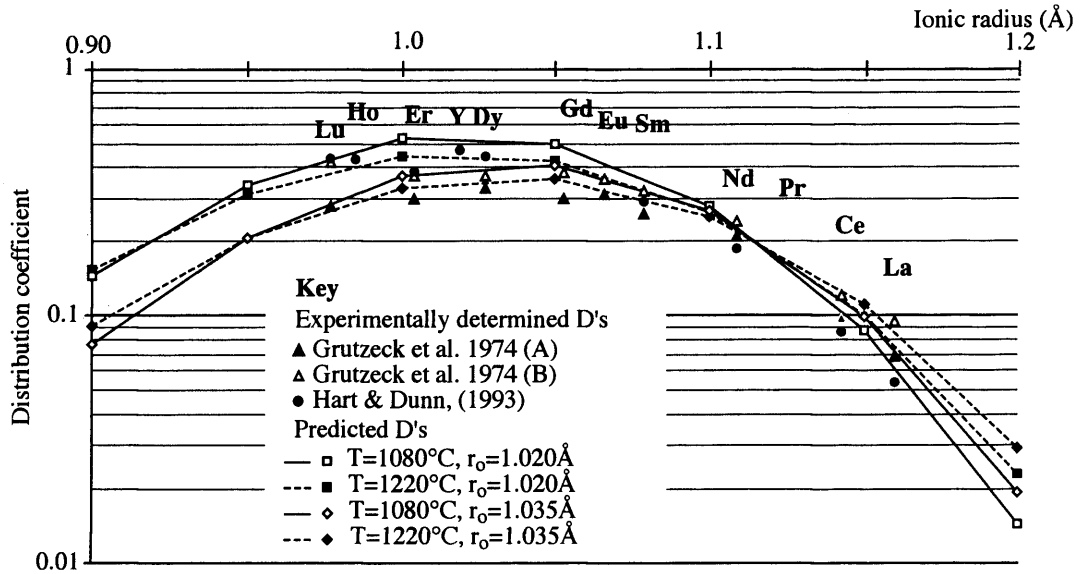


Fig. AI.4 Onuma plot of distribution coefficients for $3^+$ cations in clinopyroxene. Four model curves are shown which are calculated using the model of Wood and Blundy (1997) for the range of crystallisation conditions predicted for gabbros from ODP Hole 923. The two sets of data from Grutzeck et al. (1974) refer to their experiments A and B.

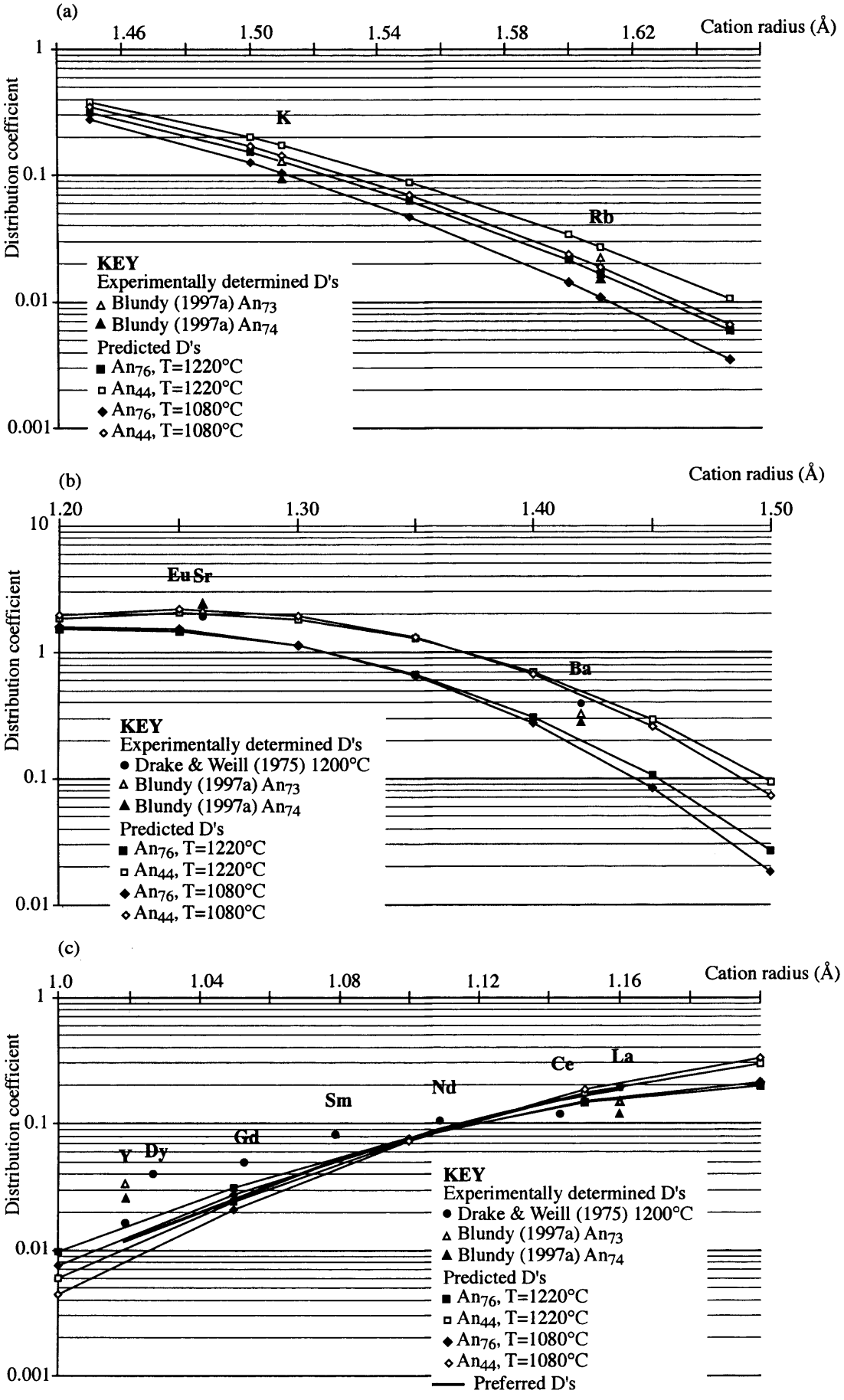


Fig. AI.5 Comparison of measured and predicted distribution coefficients for $1^+$, $2^+$ and $3^+$ cations in plagioclase. Note the different scales on each figure.

concentration of volatiles in interstitial melt as indicated by the occurrence of late amphibole (OH) and apatite (OH-F-Cl) in many samples. The effects of this are twofold. Firstly, volatiles can lead to de-polymerisation of the melt and, secondly, volatiles can potentially form complexes with trace elements increasing their solubility in the melt. De-polymerisation of the melt will decrease D's except in the case of singly charged ions (e.g. alkalis; Lesher, 1986) as will the formation of complexes in the melt. The details of the effects of volatiles dissolved in silicate melts are poorly understood, and the concentrations in the melt during late stage crystallisation are also poorly known. Therefore their effect on D's cannot quantitatively be accounted for.

Exsolution of a fluid phase is capable of affecting mineral compositions. This could occur either through concentration, and subsequent loss, of trace elements in the fluid phase, or through changes in melt structure due to loss of volatiles from the melt. Fluid inclusion studies suggest the first phase exsolved during crystallisation of gabbroic rocks recovered on ODP Leg 153 was a $CO_2$-rich fluid which became more $H_2O$-rich over time (Kelley, 1997).

In summary, it is probable that the main effect of melt composition on D's is due to the concentration of volatiles at a late stage in the interstitial melt. Both the effects of volatiles, their concentration in the melt, and the composition of the melt are insufficiently well known for it to be appropriate to make allowances for these in calculating D's.

A.I.3.3.2 Mineral compositional variations can be accounted for in determining distribution coefficients as discussed above. An assumption in using major element compositions to predict trace element D's is that the major and trace element compositions were produced at the same time. i.e. that diffusive re-equilibration has not occurred. The preservation of solid solution component zoning in both plagioclase and clinopyroxene, and commonly extremely narrow exsolution lamellae in clinopyroxene, suggest relative little diffusive equilibration. This is consistent with an estimated age of ~0.75 Ma for these rocks (Cannat, Karson, Miller *et al.*, 1995). Also plagioclase major (Morse, 1984) and trace (Giletti & Casserley, 1994) element diffusion is thought to be sufficiently slow as to be unimportant in relatively rapidly cooled rocks.

A.I.3.3.2.1 Clinopyroxene contains two different sites into which trace elements are thought to commonly substitute, the M1 and M2 (Deer *et al.*, 1966; Cameron & Papike, 1980; Wood & Blundy, 1997). Of the trace elements analysed in clinopyroxene, REE, Y and Sr probably substitute into the M2, site for which site size and Young's Modulus data are available. Equation 15 of Wood and Blundy (1997), which relates the M2 site size to the Ca and Al content of the

clinopyroxene, has been used to calculate the M2 site sizes for clinopyroxenes in Hole 923A. These lie in the range $r_o$ = 1.02 - 1.035 Å. Fig A.I.4 compares the Onuma plots for $3^+$ cations calculated for this site size range, over the temperature interval 1080 to 1220°C with experimentally determined D's. In this figure $D_{\text{trace element}}$ has been scaled to 1/5 of $D_{Ca}$ to match the relative D values at the Ca site size (1.12Å, Shannon, 1976) as closely to the experimental data as possible. The spread of experimental D's is similar to the spread of calculated D's. Due to the relatively minor effect of crystal composition, and unaccountable for variation in other factors (T, melt composition), it is not considered realistic to calculate different D's for each spot analysed dependent on its composition. Thus D's for $3^+$ cations calculated for the average temperature (1130°C, from average $Fo_{71}$) and average site size of 1.031Å are used throughout (Table A.I.1). Relative errors due to D variation during crystallisation are minimum near Nd and increase with both increased and decreased ionic radius. Maximum relative D variation is unlikely to exceed a factor of 1.25.

$D_{Sr}$ can also be calculated from the thermodynamically-derived equations of Wood and Blundy (1997) over the conditions of interest. Being considerably larger than the REE's, Sr lies on the limb of the Onuma parabola, and thus D varies more with site size and temperature variation than for the REE's. There is a factor of two difference in $D_{Sr}$ between that calculated for 1220°C and a 1.035Å M2 site and that calculated for 1080°C and a 1.02Å M2 site. Conversion of relative D's into absolute D's is more difficult than for $3^+$ cations, because Sr is the only $2^+$ cation which is commonly measured in experiments. In experimental studies, Grutzeck *et al.*, (1974) and Hart and Dunn (1993) found $D_{Sr}$ = 0.078 and 0.12 respectively. An average value of 0.1 will be used, but this is open to significant error.

The remaining trace and minor elements for which data are available are Zr, Ti, Cr, V and Sc. Ti, Zr and Cr substitute into the M1 site (Cameron & Papike, 1980; Blundy, 1997b) and on size considerations it is likely that V and Sc do also. Young's Modulus and site size data are unavailable for the clinopyroxene M1 site and thus published D's from experimental studies will be used. It is generally assumed that $D_{Ti}$ is similar to $D_{Gd}$ (e.g. Hart & Dunn, 1993) although since they occupy different sites this must be a function of major element composition, however, this will be assumed in this study. Notably $D_{Ti}$ calculated from experiments on MORB from the MARK area are somewhat lower ranging from 0.25-0.37 (average 0.31; Grove & Bryan, 1983; Tormey *et al.*, 1987; Grove *et al.*, 1992). $D_{Zr}$ is calculated from $D_{Ti}$ using the formula of Forsythe *et al.* (1994; $D_{Zr}$ = $0.64D_{Ti}$ - 0.13 = 0.12). This is in agreement with the experimentally determine $D_{Zr}$ of Hart and Dunn (1993). Since Ti is more compatible than Zr it must be nearer the peak of the $4^+$ M1 Onuma parabola (i.e. closer in size to the site), and thus will

be subject to less variation in D with varying crystal composition and / or temperature. This cannot be quantified without M1 site size and Young's Modulus data. It should be noted that this leads to $D_{Zr}$ being considerably lower than $D_{Nd}$ and $D_{Sm}$ the REE's with which Zr is generally compared. D's for Sc, V and Cr decrease in the order $D_{Cr} > D_V > D_{Sc}$ (Hart and Dunn, 1993) forming a smooth curve on an Onuma plot. Thus, variation in D's during crystallisation probably increases in the order Sc > V > Cr. This assumes that V occurs predominantly as $V^{3+}$, however $V^{4+}$ and $V^{5+}$ may also occur under natural conditions (Shervais, 1982).

A.I.3.3.2.2 Plagioclase shows large inter-sample ($An_{44-76}$) and intra-crystal ($An_{\leq 14}$) variation in anorthite content in samples analysed by ion probe suggesting that crystal chemistry may have a significant control on D's. Fig. A.I.5 shows the difference in D's between $An_{76}$ and $An_{44}$ for differently charged ions at 1080°C and 1220°C. Fig A.I.5c shows a range of Onuma plots for $3^+$ cations over the range of conditions discussed above. An average curve for $An_{60}$ and 1150°C is also shown. Errors induced by using the average value are minor for the LREE. $D_Y$ spans a factor of 2 variation (0.008 to 0.016, with the average conditions value at 0.011) which is significant. This has been accounted for in modelling by fitting a polynomial regression (R = 1.0) to an An versus $D_Y$ curve calculated using the model $E^{3+}$ and $r_o$ values of Blundy and Wood (1994). In this temperature is assumed to vary linearly with An content. Due to the substantial effect of oxidation state on $D_{Eu}$ suitable partition coefficients cannot be predicted without knowledge of the oxygen fugacity.

Figure A.I.5b shows D's for $2^+$ cations for different temperatures and plagioclase compositions. The dominant control is the plagioclase composition with a factor of ~ 1.33 variation in D's for Sr and $Eu^{2+}$ and a factor of 2.5 variation in $D_{Ba}$. The variation in $D_{Ba}$ is greater than $D_{Sr}$ and $D_{Eu}{}^{2+}$ as it is on the limb of the Onuma plot. These variations have been accounted for in the same way as for Y ($R_{Ba}$ = 0.9999; $R_{Sr}$ = 1.0). Fig A.I.5a shows that although there is a reasonably large spread in the D's for singly charged cations there is little difference in D's for $An_{76}$ at 1220°C and $An_{44}$ at 1080°C. D's used are thus an average between these.

It is thought that in plagioclase Ti and Zr replace Al (Deer *et al.*, 1966) which is smaller than either Ti or Zr. This is consistent with the experimental determination of that $D_{Ti} > D_{Zr}$ (Blundy, 1997a). As these are the only published D's which have been found, they will be used whilst bearing in mind that $D_{Zr}$ is likely to vary more than $D_{Ti}$. Both are likely to be subject to significant variation due to the tightness of Onuma parabola of highly charged cations.

### *A.I.4 Major element partitioning - equilibrium constants*

The equilibrium constant of an exchange reaction is given by the activity ratio of the elements being exchanged. For Mg and Fe exchange between olivine and basalt, Roeder and Emslie (1970) show that this is independent of temperature. They find that the equilibrium constant for the exchange in equation A.I.ii is ~0.30. Ulmer (1989) shows that this is pressure-dependent, rising to ~0.37 at 3 GPa (see Fig. 1.2b). An equilibrium constant of 0.30 is used for calculating melt Mg# from olivine Mg#, based on the assumption that crystallisation occurred at low-pressure. It should be noted that olivine compositions are subject to re-equilibration with trapped and / or migrating melt within a crystal mush due to rapid diffusion. This means that olivine compositions probably do not record the composition of the melt in which they initially grew.

The average equilibrium constant for clinopyroxene-melt Mg-Fe exchange calculated from the experiments of Grove and Bryan (1983), Tormey *et al.*, (1987), and Grove *et al.*, (1992), is 0.227 (ranging from 0.194-0.237). This is used in calculation of melt Mg# from clinopyroxene compositions. This is consistent the partitioning of Mg and Fe between coexisting olivine and clinopyroxene in MARK area peridotites (ODP Site 920), which, using a Kd of 0.30 for olivine predict $Kd_{cpx} = 0.24$ (using the data of Stephens, 1997)

Equilibrium constants for Ca-Na exchange between plagioclase and melt (e.g. Grove *et al.*, 1992) have not been used in this study as they are dependent on more variables (P and melt composition; Grove *et al*, 1992).

| Element | Ti | Zr | La | Ce | Pr | Nd | Sm | Eu | Gd | Tb | Dy |
|---|---|---|---|---|---|---|---|---|---|---|---|
| Dcpx | 0.39 | 0.12 | 0.08 | 0.12 | 0.17 | 0.23 | 0.33 | 0.36 | 0.39 | 0.40 | 0.41 |
| Dplag | 0.04 | 0.01 | 0.18 | 0.15 | 0.12 | 0.09 | 0.05 | | | | |

| Element | Y | Ho | Er | Tm | Yb | Cr | V | Sc | Sr | Ba | K |
|---|---|---|---|---|---|---|---|---|---|---|---|
| Dcpx | 0.40 | 0.40 | 0.38 | 0.36 | 0.34 | 3.8 | 3.1 | 1.31 | 0.10 | | |
| Dplag | var[1] | | | | | | | | var[2] | var[3] | 0.14 |

Table A.I.1 Distribution coefficients used in this study. var. - variable with major element composition. Notably the bulk distribution coefficients for REE during crystallisation of a gabbroic assemblage are approximately equal (~0.15).

var[1] $D_Y = 1.52 \times 10^{-6}\ An^2 + 4.7 \times 10^{-5}\ An + 0.0032$ ($R^2 = 1.0$)

var[2] $D_{Sr} = 9.297 \times 10^{-5}\ An^2 - 3.1511 \times 10^{-2}\ An + 3.3075$ ($R^2 = 1.0$)

var[3] $D_{Ba} = 1.25 \times 10^{-4}\ An^2 - 2.4444 \times 10^{-2}\ An + 1.3277$ ($R^2 = 0.9999$)

# Appendix A.II

# Macro for use in 'NIH image' to analyse the spatial distribution of minerals using the method of Morishita and Obata (1995)

## Appendix A.II - NIH Image macro for spatial distribution analysis

This macro analyses 8000 pairs of points and displays the distance between the points (Users 1) and the sum of their greyscales (Users 2).

```
macro 'Pixel Query ... [P]'
var
 x,y,a,b,i,p1,p2,d:integer;
begin
 { NewTextWindow('Data',1,1);}
 for i:=1 to 8000 do
 begin
  {SelectWindow('untitled1');}
  x:=trunc(random*2000);
  y:=trunc(random*3000);
 p1:=GetPixel(x,y);
  a:=trunc(random*1000);
  b:=trunc(random*1000);
 p2:=GetPixel(a,b);
 d:=sqrt(sqr(x-a)+sqr(y-b));
  {SelectWindow('Data');}
rUser1[i]:=d;
rUser2[i]:=p1+p2;
 {Writeln(x:10,'  ',y:10,'  ',a:10,'  ',b:10,'  ',p1:10,'  ',p2:10,'
      ',d:10,'  ',rUser1[i]:10,'  'rUser2[i]);}
 end;
 SetCounter(8000);
end;
```

# Appendix A.III

# Ion probe data

## (1) Clinopyroxene data

Abbreviations

core - analysis of the core of the crystal
intermed - analysis of a point between the core and rim of the crystal
rim - analysis of the rim of the crystal
chada - analysis of chadacryst enclosed in clinopyroxene

| Sample | 153-923A-3R1-2 18-22 | 153-923A-3R1-2 18-22 | 153-923A-3R1-2 18-22 | 153-923A-3R1-2 18-22 | 153-923A-3R1-2 18-22 | 153-923A-3R2-2 39-45 | 153-923A-3R2-2 39-45 | 153-923A-3R2-2 39-45 | 153-923A-5R1-2A 46-50 | 153-923A-5R1-2A 46-50 | 153-923A-5R1-2A 46-50 | 153-923A-6R1-9 58-61 | 153-923A-6R1-9 58-61 | 153-923A-6R1-9 58-61 | 153-923A-6R1-9 58-61 | 153-923A-8R1-9 126-131 | 153-923A-8R1-9 126-131 |
|---|---|---|---|---|---|---|---|---|---|---|---|---|---|---|---|---|---|
| **Analysis** | P3R1150 | P3R1151 | P3R1152 | P3R1153 | P3R1154 | 3R2LAC8 | 3R2LAC9 | 3R2LC10 | 5R1LC18 | 5R1LC19 | 5R1LC20 | 6R1LC27 | 6R1LC28 | 6R1LC29 | 6R1LC30 | 8R1LC37 | 8R1LC38 |
| **Location** | core | rim | intermed | intermed | rim | rim | intermed | core | rim | intermed | core | rim | intermed | core | core | interstit | interstit |
| **Depth (m)** | 19.38 | 19.38 | 19.38 | 19.38 | 19.38 | 21.08 | 21.08 | 21.08 | 23.46 | 23.46 | 23.46 | 25.28 | 25.28 | 25.28 | 25.28 | 30.26 | 30.26 |
| **wt %** | | | | | | | | | | | | | | | | | |
| **SiO2** | 52.02 | 51.57 | 51.58 | 52.05 | 51.84 | 52.13 | 52.09 | 52.68 | 52.49 | 52.78 | 52.75 | 53.08 | 52.38 | 52.78 | 52.76 | 52.28 | 52.12 |
| **TiO2** | 0.65 | 0.69 | 0.66 | 0.73 | 0.67 | 0.87 | 0.95 | 0.87 | 0.96 | 0.60 | 0.69 | 0.78 | 0.58 | 0.55 | 0.63 | 1.25 | 1.20 |
| **Al2O3** | 1.87 | 2.02 | 1.99 | 2.26 | 1.90 | 2.64 | 2.55 | 2.24 | 2.72 | 2.71 | 2.80 | 2.72 | 2.51 | 2.10 | 2.27 | 2.85 | 3.33 |
| **Cr2O3** | 0.02 | 0.00 | 0.03 | 0.04 | 0.02 | 0.03 | 0.04 | 0.02 | 0.03 | 0.08 | 0.09 | 0.05 | 0.12 | 0.08 | 0.12 | 0.07 | 0.11 |
| **FeO** | 10.26 | 10.19 | 11.92 | 10.27 | 9.96 | 9.88 | 8.92 | 10.82 | 7.80 | 6.40 | 6.53 | 7.20 | 6.91 | 7.76 | 6.55 | 5.98 | 6.44 |
| **MnO** | 0.33 | 0.35 | 0.32 | 0.35 | 0.29 | 0.32 | 0.26 | 0.31 | 0.23 | 0.21 | 0.21 | 0.22 | 0.26 | 0.21 | 0.20 | 0.18 | 0.17 |
| **MgO** | 13.70 | 13.71 | 14.43 | 13.93 | 13.80 | 14.15 | 15.05 | 16.90 | 14.90 | 15.64 | 16.45 | 15.66 | 15.25 | 17.91 | 16.05 | 15.63 | 15.21 |
| **CaO** | 20.49 | 21.21 | 18.31 | 20.09 | 20.81 | 20.39 | 19.94 | 17.02 | 21.43 | 21.54 | 20.62 | 21.68 | 21.69 | 18.61 | 21.30 | 22.48 | 22.14 |
| **NaO2** | 0.44 | 0.48 | 0.42 | 0.47 | 0.39 | 0.51 | 0.48 | 0.43 | 0.42 | 0.38 | 0.38 | 0.45 | 0.40 | 0.34 | 0.47 | 0.39 | 0.41 |
| **Total** | 99.81 | 100.26 | 99.68 | 100.21 | 99.70 | 100.96 | 100.31 | 101.31 | 100.72 | 100.35 | 100.54 | 101.87 | 100.17 | 100.43 | 100.43 | 100.89 | 101.16 |
| **Cations** | | | | | | | | | | | | | | | | | |
| **Si** | 1.95 | 1.93 | 1.94 | 1.94 | 1.95 | 1.93 | 1.93 | 1.93 | 1.93 | 1.94 | 1.93 | 1.93 | 1.93 | 1.93 | 1.94 | 1.91 | 1.90 |
| **Ti** | 0.02 | 0.02 | 0.02 | 0.02 | 0.02 | 0.02 | 0.03 | 0.02 | 0.03 | 0.02 | 0.02 | 0.02 | 0.02 | 0.02 | 0.02 | 0.03 | 0.03 |
| **Al** | 0.08 | 0.09 | 0.09 | 0.10 | 0.08 | 0.11 | 0.11 | 0.10 | 0.12 | 0.12 | 0.12 | 0.12 | 0.11 | 0.09 | 0.10 | 0.12 | 0.14 |
| **Cr** | 0.00 | 0.00 | 0.00 | 0.00 | 0.00 | 0.00 | 0.00 | 0.00 | 0.00 | 0.00 | 0.00 | 0.00 | 0.00 | 0.00 | 0.00 | 0.00 | 0.00 |
| **Fe** | 0.32 | 0.32 | 0.38 | 0.32 | 0.31 | 0.31 | 0.28 | 0.33 | 0.24 | 0.20 | 0.20 | 0.22 | 0.21 | 0.24 | 0.20 | 0.18 | 0.20 |
| **Mn** | 0.01 | 0.01 | 0.01 | 0.01 | 0.01 | 0.01 | 0.01 | 0.01 | 0.01 | 0.01 | 0.01 | 0.01 | 0.01 | 0.01 | 0.01 | 0.01 | 0.01 |
| **Mg** | 0.77 | 0.77 | 0.81 | 0.77 | 0.77 | 0.78 | 0.83 | 0.92 | 0.81 | 0.85 | 0.90 | 0.85 | 0.84 | 0.98 | 0.88 | 0.85 | 0.83 |
| **Ca** | 0.82 | 0.85 | 0.74 | 0.80 | 0.84 | 0.81 | 0.79 | 0.67 | 0.84 | 0.85 | 0.81 | 0.84 | 0.86 | 0.73 | 0.84 | 0.88 | 0.87 |
| **Na** | 0.03 | 0.03 | 0.03 | 0.03 | 0.03 | 0.04 | 0.03 | 0.03 | 0.03 | 0.03 | 0.03 | 0.03 | 0.03 | 0.02 | 0.03 | 0.03 | 0.03 |
| **Total** | 4.01 | 4.02 | 4.01 | 4.01 | 4.01 | 4.01 | 4.01 | 4.01 | 4.00 | 4.00 | 4.01 | 4.01 | 4.01 | 3.96 | 3.96 | 4.01 | 4.01 |
| **Mg#** | 70.4 | 70.6 | 68.3 | 70.7 | 71.2 | 71.8 | 75.0 | 73.6 | 77.3 | 81.3 | 81.8 | 79.5 | 79.7 | 80.4 | 81.4 | 82.3 | 80.8 |

| Sample | 153-923A-3R1-2 18-22 | 153-923A-3R1-2 18-22 | 153-923A-3R1-2 18-22 | 153-923A-3R1-2 18-22 | 153-923A-3R1-2 18-22 | 153-923A-3R2-2 39-45 | 153-923A-3R2-2 39-45 | 153-923A-3R2-2 39-45 | 153-923A-5R1-2A 46-50 | 153-923A-5R1-2A 46-50 | 153-923A-5R1-2A 46-50 | 153-923A-6R1-9 58-61 | 153-923A-6R1-9 58-61 | 153-923A-6R1-9 58-61 | 153-923A-6R1-9 58-61 | 153-923A-8R1-9 126-131 | 153-923A-8R1-9 126-131 |
|---|---|---|---|---|---|---|---|---|---|---|---|---|---|---|---|---|---|
| **Analysis** | P3R1150 | P3R1151 | P3R1152 | P3R1153 | P3R1154 | 3R2LAC8 | 3R2LAC9 | 3R2LC10 | 5R1LC18 | 5R1LC19 | 5R1LC20 | 6R1LC27 | 6R1LC28 | 6R1LC29 | 6R1LC30 | 8R1LC37 | 8R1LC38 |
| **Location** | core | rim | intermed | intermed | rim | rim | intermed | core | rim | intermed | core | rim | intermed | core | core | interstit | interstit |
| **Depth (m)** | 19.38 | 19.38 | 19.38 | 19.38 | 19.38 | 21.08 | 21.08 | 21.08 | 23.46 | 23.46 | 23.46 | 25.28 | 25.28 | 25.28 | 25.28 | 30.26 | 30.26 |
| **Traces (ppm)** | | | | | | | | | | | | | | | | | |
| **F** | n.d. | n.d. | n.d. | n.d. | n.d. | n.d. | n.d. | n.d. | n.d. | n.d. | n.d. | n.d. | n.d. | n.d. | n.d. | n.d. | n.d. |
| **P** | 56 | 187 | 65 | 59 | 55 | n.d. | n.d. | n.d. | n.d. | n.d. | n.d. | n.d. | n.d. | n.d. | n.d. | n.d. | n.d. |
| **Cl** | n.d. | n.d. | n.d. | n.d. | n.d. | n.d. | n.d. | n.d. | n.d. | n.d. | n.d. | n.d. | n.d. | n.d. | n.d. | n.d. | n.d. |
| **Sc** | 143 | 156 | 142 | 142 | 140 | n.d. | n.d. | n.d. | n.d. | n.d. | n.d. | n.d. | n.d. | n.d. | n.d. | n.d. | n.d. |
| **Ti** | 3581 | 17799 | 3848 | 4273 | 4113 | 4097 | 5219 | 4947 | 5106 | 3103 | 3487 | 4586 | 2975 | 3177 | 2406 | 4238 | 6454 |
| **V** | 787 | 661 | 397 | 402 | 387 | 438 | 507 | 475 | 499 | 364 | 402 | 436 | 340 | 320 | 273 | 389 | 547 |
| **Cr** | 124 | 140 | 127 | 142 | 138 | 337 | 368 | 373 | 428 | 435 | 535 | 635 | 851 | 1055 | 1058 | 1867 | 1335 |
| **Sr** | n.d. | n.d. | n.d. | n.d. | n.d. | 10.80 | 8.75 | 8.59 | 10.06 | 9.38 | 9.87 | 9.70 | 10.09 | 8.12 | 7.02 | 8.56 | 9.14 |
| **Zr** | 69.15 | 152.80 | 66.22 | 63.50 | 60.83 | 65.13 | 27.18 | 24.69 | 78.28 | 14.53 | 15.73 | 30.30 | 13.28 | 16.54 | 10.58 | 89.21 | 155.35 |
| **Y** | 97.35 | 163.37 | 72.13 | 75.53 | 87.15 | 63.18 | 41.05 | 36.90 | 43.64 | 22.68 | 26.29 | 31.20 | 22.88 | 22.39 | 17.13 | 39.15 | 52.05 |
| **Ba** | 0.44 | 8.71 | 0.02 | 0.04 | 0.13 | 0.07 | 0.06 | 0.08 | 0.78 | 0.07 | 0.13 | 0.64 | 0.37 | 0.12 | 0.25 | 0.97 | 0.08 |
| **La** | 1.53 | 3.29 | 1.21 | 1.36 | 1.27 | 1.17 | 0.44 | 0.38 | 0.81 | 0.34 | 0.33 | 0.52 | 0.32 | 0.32 | 0.31 | 0.61 | 0.60 |
| **Ce** | 8.88 | 17.93 | 7.21 | 6.72 | 7.28 | 6.13 | 2.75 | 2.43 | 4.88 | 2.06 | 1.77 | 2.36 | 1.65 | 1.77 | 1.41 | 3.49 | 4.22 |
| **Pr** | 2.27 | 4.40 | 1.80 | 1.62 | 1.92 | 1.61 | 0.65 | 0.73 | 1.22 | 0.48 | 0.46 | 0.55 | 0.35 | 0.54 | 0.43 | 1.09 | 1.06 |
| **Nd** | 16.80 | 31.70 | 14.06 | 12.55 | 14.55 | 11.38 | 6.28 | 4.97 | 9.36 | 3.75 | 4.06 | 5.30 | 3.88 | 3.54 | 3.37 | 9.55 | 8.65 |
| **Sm** | 8.65 | 14.55 | 6.61 | 6.43 | 7.90 | 5.16 | 3.55 | 2.70 | 4.47 | 1.80 | 1.38 | 2.86 | 1.70 | 2.57 | 1.80 | 3.60 | 5.16 |
| **Eu** | 1.84 | 3.42 | 1.69 | 1.73 | 1.82 | 1.70 | 1.09 | 0.84 | 1.34 | 0.54 | 0.90 | 1.11 | 0.83 | 0.70 | 0.62 | 0.91 | 0.92 |
| **Gd** | 12.29 | 21.59 | 8.39 | 9.17 | 10.85 | 9.33 | 5.70 | 4.55 | 6.52 | 2.92 | 3.78 | 4.85 | 3.52 | 2.71 | 2.63 | 4.67 | 7.95 |
| **Tb** | 2.34 | 3.98 | 1.77 | 1.85 | 2.21 | 1.56 | 1.03 | 1.07 | 1.36 | 0.63 | 0.73 | 0.81 | 0.59 | 0.62 | 0.55 | 0.96 | 1.46 |
| **Dy** | 17.28 | 27.99 | 12.91 | 13.13 | 15.66 | 12.77 | 8.14 | 6.62 | 8.34 | 4.54 | 4.60 | 5.85 | 4.54 | 4.40 | 3.92 | 8.11 | 9.14 |
| **Ho** | 3.61 | 5.65 | 2.63 | 2.63 | 3.15 | 2.47 | 1.57 | 1.37 | 1.67 | 1.04 | 1.09 | 1.22 | 0.96 | 0.88 | 0.76 | 1.90 | 1.90 |
| **Er** | 10.38 | 16.15 | 7.41 | 7.08 | 8.76 | 6.55 | 4.42 | 4.24 | 5.33 | 3.12 | 2.78 | 3.37 | 2.53 | 2.70 | 2.66 | 4.97 | 6.21 |
| **Yb** | 13.32 | 13.76 | 6.79 | 6.91 | 8.14 | 5.21 | 3.97 | 4.54 | 5.07 | 2.08 | 2.71 | 3.61 | 1.88 | 1.98 | 2.99 | 6.28 | 5.95 |

| Sample | 153-923A-8R1-9 126-131 | 153-923A-8R1-9 126-131 | 153-923A-8R1-9 126-131 | 153-923A-8R2-8 81-88 | 153-923A-8R2-8 81-88 | 153-923A-8R2-8 81-88 | 153-923A-8R2-8 81-88 | 153-923A-8R2-8 81-88 | 153-923A-8R2-8 81-88 | 153-923A-8R2-8 81-88 | 153-923A-8R2-8 81-88 | 153-923A-8R2-8 81-88 | 153-923A-8R2-8 81-88 | 153-923A-8R2-8 81-88 | 153-923A-8R2-8 81-88 | 153-923A-8R2-8 81-88 | 153-923A-8R2-8 81-88 |
|---|---|---|---|---|---|---|---|---|---|---|---|---|---|---|---|---|---|
| Analysis | 8R1LC39 | P8R2084 | P8R1084 | 8R2LC5 | 8R2LC6 | 8R2LC7 | 8R2LC66 | 8R2LC67 | 8R2LC68 | 8R2LC69 | 8R2LC70 | 8R2LC71 | P8R2102 | P8R2103 | P8R2104 | P82R105 | P8R2106 |
| Location | interstit | interstit | interstit | rim | intermed | core | rim | rim | intermed | intermed | intermed | core | traverse 5.28 | distance 4.7 | from 4.32 | rim 3.78 | (mm) 2.74 |
| Depth (m) | 30.26 | 30.26 | 30.26 | 31.31 | 31.31 | 31.31 | 31.31 | 31.31 | 31.31 | 31.31 | 31.31 | 31.31 | 31.31 | 31.31 | 31.31 | 31.31 | 31.31 |
| wt % | | | | | | | | | | | | | | | | | |
| SiO2 | 52.12 | 52.40 | 51.89 | 51.78 | 52.66 | 53.46 | 52.92 | 52.64 | 52.64 | 53.46 | 52.83 | 52.83 | 52.98 | 52.51 | 52.99 | 52.39 | 52.78 |
| TiO2 | 1.20 | 1.01 | 1.11 | 0.91 | 0.70 | 0.55 | 0.69 | 0.70 | 0.70 | 0.55 | 0.66 | 0.66 | 0.59 | 0.62 | 0.45 | 0.79 | 0.64 |
| Al2O3 | 3.33 | 2.72 | 2.89 | 2.67 | 2.82 | 2.59 | 2.54 | 2.73 | 2.73 | 2.59 | 2.64 | 2.64 | 2.62 | 2.59 | 2.47 | 3.13 | 3.03 |
| Cr2O3 | 0.11 | 0.13 | 0.11 | 0.07 | 0.08 | 0.11 | 0.05 | 0.07 | 0.07 | 0.11 | 0.09 | 0.09 | 0.13 | 0.10 | 0.09 | 0.14 | 0.14 |
| FeO | 6.44 | 6.36 | 6.54 | 7.80 | 6.19 | 6.01 | 7.45 | 6.47 | 6.47 | 6.01 | 6.17 | 6.17 | 6.60 | 5.92 | 5.77 | 5.66 | 5.44 |
| MnO | 0.17 | 0.22 | 0.17 | 0.25 | 0.21 | 0.19 | 0.22 | 0.23 | 0.23 | 0.19 | 0.22 | 0.22 | 0.20 | 0.19 | 0.14 | 0.15 | 0.15 |
| MgO | 15.21 | 15.48 | 15.43 | 14.94 | 15.31 | 17.15 | 15.10 | 15.61 | 15.61 | 17.15 | 15.85 | 15.85 | 16.12 | 15.86 | 16.20 | 15.62 | 15.79 |
| CaO | 22.14 | 21.96 | 21.79 | 21.61 | 22.31 | 20.55 | 21.11 | 22.06 | 22.06 | 20.55 | 21.86 | 21.86 | 21.46 | 21.84 | 21.61 | 21.76 | 21.87 |
| NaO2 | 0.41 | 0.39 | 0.40 | 0.40 | 0.44 | 0.33 | 0.40 | 0.36 | 0.36 | 0.33 | 0.39 | 0.39 | 0.41 | 0.40 | 0.65 | 0.44 | 0.46 |
| Total | 101.16 | 100.70 | 100.35 | 100.56 | 100.75 | 101.00 | 100.53 | 100.90 | 100.90 | 101.00 | 100.72 | 100.72 | 101.15 | 100.06 | 100.44 | 100.11 | 100.34 |
| Cations | | | | | | | | | | | | | | | | | |
| Si | 1.90 | 1.92 | 1.91 | 1.91 | 1.93 | 1.94 | 1.94 | 1.92 | 1.92 | 1.94 | 1.93 | 1.93 | 1.93 | 1.93 | 1.94 | 1.92 | 1.93 |
| Ti | 0.03 | 0.03 | 0.03 | 0.03 | 0.02 | 0.02 | 0.02 | 0.02 | 0.02 | 0.02 | 0.02 | 0.02 | 0.02 | 0.02 | 0.01 | 0.02 | 0.02 |
| Al | 0.14 | 0.12 | 0.13 | 0.12 | 0.12 | 0.11 | 0.11 | 0.12 | 0.12 | 0.11 | 0.11 | 0.11 | 0.11 | 0.11 | 0.11 | 0.14 | 0.13 |
| Cr | 0.00 | 0.00 | 0.00 | 0.00 | 0.00 | 0.00 | 0.00 | 0.00 | 0.00 | 0.00 | 0.00 | 0.00 | 0.00 | 0.00 | 0.00 | 0.00 | 0.00 |
| Fe | 0.20 | 0.19 | 0.20 | 0.24 | 0.19 | 0.18 | 0.23 | 0.20 | 0.20 | 0.18 | 0.19 | 0.19 | 0.20 | 0.18 | 0.18 | 0.17 | 0.17 |
| Mn | 0.01 | 0.01 | 0.01 | 0.01 | 0.01 | 0.01 | 0.01 | 0.01 | 0.01 | 0.01 | 0.01 | 0.01 | 0.01 | 0.01 | 0.00 | 0.00 | 0.00 |
| Mg | 0.83 | 0.84 | 0.85 | 0.82 | 0.83 | 0.93 | 0.83 | 0.85 | 0.85 | 0.93 | 0.86 | 0.86 | 0.87 | 0.87 | 0.88 | 0.85 | 0.86 |
| Ca | 0.87 | 0.86 | 0.86 | 0.86 | 0.87 | 0.80 | 0.83 | 0.86 | 0.86 | 0.80 | 0.86 | 0.86 | 0.84 | 0.86 | 0.85 | 0.86 | 0.86 |
| Na | 0.03 | 0.03 | 0.03 | 0.03 | 0.03 | 0.02 | 0.03 | 0.03 | 0.03 | 0.02 | 0.03 | 0.03 | 0.03 | 0.03 | 0.05 | 0.03 | 0.03 |
| Total | 4.01 | 4.01 | 4.01 | 4.02 | 4.01 | 4.00 | 4.00 | 4.01 | 4.01 | 4.00 | 4.01 | 4.01 | 4.01 | 4.01 | 4.02 | 4.00 | 4.00 |
| Mg# | 80.8 | 81.3 | 80.8 | 77.3 | 81.5 | 83.6 | 78.3 | 81.1 | 81.1 | 83.6 | 82.1 | 82.1 | 81.3 | 82.7 | 83.3 | 83.1 | 83.8 |

| Sample | 153-923A-8R1-9 126-131 | 153-923A-8R1-9 126-131 | 153-923A-8R1-9 126-131 | 153-923A-8R2-8 81-88 | 153-923A-8R2-8 81-88 | 153-923A-8R2-8 81-88 | 153-923A-8R2-8 81-88 | 153-923A-8R2-8 81-88 | 153-923A-8R2-8 81-88 | 153-923A-8R2-8 81-88 | 153-923A-8R2-8 81-88 | 153-923A-8R2-8 81-88 | 153-923A-8R2-8 81-88 | 153-923A-8R2-8 81-88 | 153-923A-8R2-8 81-88 | 153-923A-8R2-8 81-88 | 153-923A-8R2-8 81-88 |
|---|---|---|---|---|---|---|---|---|---|---|---|---|---|---|---|---|---|
| **Analysis** | 8R1LC39 | P8R2084 | P8R1084 | 8R2LC5 | 8R2LC6 | 8R2LC7 | 8R2LC66 | 8R2LC67 | 8R2LC68 | 8R2LC69 | 8R2LC70 | 8R2LC71 | P8R2102 | P8R2103 | P8R2104 | P82R105 | P8R2106 |
| **Location** | interstit | interstit | interstit | rim | intermed | core | rim | rim | intermed | intermed | intermed | core | traverse 5.28 | distance 4.7 | from 4.32 | rim 3.78 | (mm) 2.74 |
| **Depth (m)** | 30.26 | 30.26 | 30.26 | 31.31 | 31.31 | 31.31 | 31.31 | 31.31 | 31.31 | 31.31 | 31.31 | 31.31 | 31.31 | 31.31 | 31.31 | 31.31 | 31.31 |
| **Traces (ppm)** | | | | | | | | | | | | | | | | | |
| **F** | n.d. | 360 | 230 | n.d. | n.d. | n.d. | n.d. | n.d. | n.d. | n.d. | n.d. | n.d. | n.d. | n.d. | n.d. | n.d. | n.d. |
| **P** | n.d. | 44 | 38 | n.d. | n.d. | n.d. | n.d. | n.d. | n.d. | n.d. | n.d. | n.d. | 18 | 74 | 37 | 43 | 32 |
| **Cl** | n.d. | 30.11 | 8.49 | n.d. | n.d. | n.d. | n.d. | n.d. | n.d. | n.d. | n.d. | n.d. | n.d. | n.d. | n.d. | n.d. | n.d. |
| **Sc** | n.d. | 135 | 131 | n.d. | n.d. | n.d. | n.d. | n.d. | n.d. | n.d. | n.d. | n.d. | 126 | 127 | 125 | 120 | 125 |
| **Ti** | 5920 | 6595 | 5997 | 4799 | 3371 | 3051 | 3737 | 3783 | 3976 | 2727 | 3620 | 5440 | 3156 | 5897 | 3158 | 3426 | 3343 |
| **V** | 527 | n.d. | n.d. | 479 | 354 | 354 | 348 | 399 | 428 | 329 | 366 | 457 | 399 | 501 | 377 | 373 | 390 |
| **Cr** | 840 | n.d. | n.d. | 546 | 1262 | 899 | 674 | 915 | 960 | 1182 | 1148 | 986 | 869 | 1051 | 1312 | 976 | 1138 |
| **Sr** | 9.49 | n.d. | n.d. | 9.45 | 12.75 | 10.04 | 7.30 | 11.84 | 12.79 | 9.70 | 11.61 | 14.07 | n.d. | n.d. | n.d. | n.d. | n.d. |
| **Zr** | 182.03 | 162.25 | 157.16 | 176.32 | 24.28 | 12.56 | 81.58 | 57.72 | 59.02 | 11.43 | 23.44 | 21.78 | 12.64 | 14.99 | 17.04 | 19.27 | 17.21 |
| **Y** | 48.58 | 45.90 | 42.09 | 59.85 | 26.13 | 21.87 | 32.41 | 30.88 | 30.79 | 19.68 | 23.74 | 32.02 | 19.73 | 26.09 | 20.32 | 20.38 | 23.01 |
| **Ba** | 0.39 | 0.03 | 0.01 | 0.17 | 0.20 | 0.10 | 0.55 | 0.30 | 0.07 | 0.13 | 0.21 | 0.40 | 0.01 | 0.42 | 0.99 | 0.05 | 0.03 |
| **La** | 0.50 | n.d. | n.d. | 1.30 | 0.67 | 0.23 | 1.07 | 0.60 | 0.65 | 0.31 | 0.35 | 0.52 | 0.36 | 0.32 | 0.30 | 0.31 | 0.35 |
| **Ce** | 3.78 | 3.27 | 3.02 | 7.24 | 2.97 | 1.52 | 4.07 | 3.12 | 3.67 | 1.21 | 2.07 | 2.62 | 1.70 | 1.79 | 1.52 | 1.49 | 1.80 |
| **Pr** | 1.19 | n.d. | n.d. | 1.94 | 0.74 | 0.40 | 1.05 | 0.83 | 0.77 | 0.42 | 0.58 | 0.57 | 0.41 | 0.44 | 0.38 | 0.38 | 0.42 |
| **Nd** | 8.66 | n.d. | n.d. | 13.97 | 5.27 | 3.93 | 8.21 | 5.84 | 6.62 | 2.60 | 4.17 | 5.19 | 3.40 | 3.69 | 3.16 | 2.93 | 3.33 |
| **Sm** | 4.35 | n.d. | n.d. | 5.44 | 2.52 | 1.52 | 3.25 | 3.12 | 2.57 | 1.67 | 2.05 | 2.64 | 1.58 | 1.72 | 1.80 | 1.58 | 1.72 |
| **Eu** | 0.94 | n.d. | n.d. | 1.50 | 0.76 | 0.75 | 0.89 | 0.99 | 0.70 | 0.62 | 0.86 | 0.90 | 0.61 | 0.71 | 0.54 | 0.56 | 0.64 |
| **Gd** | 7.45 | n.d. | n.d. | 8.21 | 3.94 | 3.20 | 5.68 | 4.27 | 4.55 | 2.95 | 4.27 | 4.48 | 2.64 | 3.49 | 2.66 | 2.77 | 2.68 |
| **Tb** | 1.30 | n.d. | n.d. | 1.73 | 0.74 | 0.63 | 0.95 | 0.88 | 1.03 | 0.51 | 0.57 | 0.77 | 0.50 | 0.65 | 0.51 | 0.53 | 0.59 |
| **Dy** | 10.20 | n.d. | n.d. | 12.03 | 4.72 | 3.83 | 6.83 | 6.35 | 6.58 | 3.93 | 4.46 | 6.73 | 3.53 | 4.83 | 3.65 | 3.87 | 4.31 |
| **Ho** | 1.78 | n.d. | n.d. | 2.17 | 0.99 | 0.79 | 1.27 | 1.12 | 1.46 | 0.64 | 0.87 | 1.27 | 0.79 | 0.93 | 0.70 | 0.74 | 0.92 |
| **Er** | 5.11 | n.d. | n.d. | 6.01 | 2.47 | 2.67 | 3.92 | 3.47 | 4.42 | 2.30 | 3.07 | 4.24 | 2.04 | 2.57 | 2.18 | 2.09 | 2.43 |
| **Yb** | 4.85 | n.d. | n.d. | 6.33 | 2.06 | 1.87 | 3.46 | 3.41 | 5.47 | 2.60 | 3.02 | 3.07 | 2.13 | 2.48 | 2.11 | 2.08 | 2.31 |

| Sample | 153-923A-8R2-8 81-88 | 153-923A-8R2-8 81-88 | 153-923A-8R2-8 81-88 | 153-923A-8R2-8 81-88 | 153-923A-8R2-8 81-88 | 153-923A-8R2-8 81-88 | 153-923A-8R2-8 81-88 | 153-923A-8R2-8 81-88 | 153-923A-8R2-8 81-88 | 153-923A-9R2-9A 101-103 | 153-923A-9R2-9A 101-103 | 153-923A-9R2-9A 101-103 | 153-923A-10R2-1A 1-4 | 153-923A-10R2-1A 1-4 | 153-923A-10R2-1A 1-4 | 153-923A-11R2-6B 87-91 | 153-923A-11R2-6B 87-91 |
|---|---|---|---|---|---|---|---|---|---|---|---|---|---|---|---|---|---|
| Analysis | P8R2123 traverse | P8R2119 cont. | P8R2107 | P8R2120 | P8R2108 | P8R2121 | P8R2122 | P8R2109 | P8R2110 | 9R2LC24 | 9R2LC25 | 9R2LC26 | 10RLC58 | 10RLC59 | 10RLC60 | 11RLC34 | 11RLC35 |
| Location | 2.18 | 1.74 | 1.22 | 0.96 | 0.64 | 0.46 | 0.32 | 0.20 | 0.04 | core | intermed | rim | core | rim | intermed | rim | core |
| Depth (m) | 31.31 | 31.31 | 31.31 | 31.31 | 31.31 | 31.31 | 31.31 | 31.31 | 31.31 | 34.41 | 34.41 | 34.41 | 38.01 | 38.01 | 38.01 | 43.57 | 43.57 |
| wt % | | | | | | | | | | | | | | | | | |
| SiO2 | 52.88 | 52.68 | 54.03 | 53.06 | 53.45 | 52.70 | 52.42 | 52.46 | 52.43 | 53.44 | 52.92 | 52.11 | 53.27 | 53.04 | 52.28 | 52.16 | 52.60 |
| TiO2 | 0.59 | 0.51 | 0.48 | 0.45 | 0.57 | 0.57 | 0.63 | 0.75 | 0.94 | 0.47 | 0.59 | 1.02 | 0.40 | 0.48 | 0.89 | 0.70 | 0.49 |
| Al2O3 | 3.12 | 3.12 | 2.43 | 2.31 | 2.64 | 2.65 | 2.64 | 2.65 | 2.75 | 2.46 | 2.28 | 2.86 | 2.76 | 2.82 | 2.57 | 2.50 | 2.52 |
| Cr2O3 | 0.15 | 0.15 | 0.09 | 0.10 | 0.12 | 0.11 | 0.04 | 0.05 | 0.06 | 0.14 | 0.08 | 0.02 | 0.24 | 0.16 | 0.04 | 0.10 | 0.13 |
| FeO | 5.30 | 5.19 | 5.34 | 5.60 | 6.06 | 6.41 | 6.60 | 6.84 | 7.14 | 6.56 | 6.45 | 7.12 | 6.34 | 5.93 | 7.94 | 7.59 | 6.54 |
| MnO | 0.13 | 0.15 | 0.16 | 0.24 | 0.19 | 0.15 | 0.18 | 0.18 | 0.19 | 0.21 | 0.18 | 0.21 | 0.17 | 0.17 | 0.21 | 0.18 | 0.22 |
| MgO | 16.03 | 15.95 | 16.63 | 16.44 | 16.02 | 15.63 | 15.39 | 15.33 | 15.16 | 17.59 | 15.87 | 15.18 | 16.66 | 16.09 | 15.60 | 16.01 | 15.66 |
| CaO | 21.94 | 21.88 | 22.19 | 21.32 | 21.83 | 21.47 | 21.18 | 21.19 | 21.11 | 19.57 | 21.63 | 21.58 | 21.22 | 22.08 | 20.92 | 19.55 | 21.43 |
| NaO2 | 0.43 | 0.44 | 0.39 | 0.40 | 0.41 | 0.42 | 0.42 | 0.41 | 0.42 | 0.32 | 0.42 | 0.40 | 0.35 | 0.41 | 0.37 | 0.38 | 0.40 |
| Total | 100.59 | 100.09 | 101.80 | 99.95 | 101.33 | 100.15 | 99.53 | 99.87 | 100.23 | 100.77 | 100.47 | 100.54 | 101.34 | 101.20 | 100.87 | 99.17 | 100.00 |
| Cations | | | | | | | | | | | | | | | | | |
| Si | 1.93 | 1.93 | 1.94 | 1.95 | 1.94 | 1.94 | 1.94 | 1.94 | 1.93 | 1.94 | 1.94 | 1.92 | 1.93 | 1.93 | 1.92 | 1.94 | 1.94 |
| Ti | 0.02 | 0.01 | 0.01 | 0.01 | 0.02 | 0.02 | 0.02 | 0.02 | 0.03 | 0.01 | 0.02 | 0.03 | 0.01 | 0.01 | 0.02 | 0.02 | 0.01 |
| Al | 0.13 | 0.13 | 0.10 | 0.10 | 0.11 | 0.11 | 0.12 | 0.12 | 0.12 | 0.11 | 0.10 | 0.12 | 0.12 | 0.12 | 0.11 | 0.11 | 0.11 |
| Cr | 0.00 | 0.00 | 0.00 | 0.00 | 0.00 | 0.00 | 0.00 | 0.00 | 0.00 | 0.00 | 0.00 | 0.00 | 0.01 | 0.00 | 0.00 | 0.00 | 0.00 |
| Fe | 0.16 | 0.16 | 0.16 | 0.17 | 0.18 | 0.20 | 0.20 | 0.21 | 0.22 | 0.20 | 0.20 | 0.22 | 0.19 | 0.18 | 0.24 | 0.24 | 0.20 |
| Mn | 0.00 | 0.00 | 0.00 | 0.01 | 0.01 | 0.00 | 0.01 | 0.01 | 0.01 | 0.01 | 0.01 | 0.01 | 0.01 | 0.01 | 0.01 | 0.01 | 0.01 |
| Mg | 0.87 | 0.87 | 0.89 | 0.90 | 0.87 | 0.86 | 0.85 | 0.84 | 0.83 | 0.95 | 0.87 | 0.83 | 0.90 | 0.87 | 0.85 | 0.89 | 0.86 |
| Ca | 0.86 | 0.86 | 0.86 | 0.84 | 0.85 | 0.85 | 0.84 | 0.84 | 0.83 | 0.76 | 0.85 | 0.85 | 0.82 | 0.86 | 0.82 | 0.78 | 0.85 |
| Na | 0.03 | 0.03 | 0.03 | 0.03 | 0.03 | 0.03 | 0.03 | 0.03 | 0.03 | 0.02 | 0.03 | 0.03 | 0.02 | 0.03 | 0.03 | 0.03 | 0.03 |
| Total | 4.00 | 4.00 | 4.00 | 4.01 | 4.00 | 4.00 | 4.00 | 4.00 | 4.00 | 4.00 | 4.01 | 4.01 | 4.01 | 4.01 | 4.01 | 4.00 | 4.01 |
| Mg# | 84.3 | 84.6 | 84.7 | 84.0 | 82.5 | 81.3 | 80.6 | 80.0 | 79.1 | 82.7 | 81.4 | 79.2 | 82.4 | 82.9 | 77.8 | 79.0 | 81.0 |

| Sample | 153-923A-8R2-8 81-88 | 153-923A-8R2-8 81-88 | 153-923A-8R2-8 81-88 | 153-923A-8R2-8 81-88 | 153-923A-8R2-8 81-88 | 153-923A-8R2-8 81-88 | 153-923A-8R2-8 81-88 | 153-923A-8R2-8 81-88 | 153-923A-8R2-8 81-88 | 153-923A-9R2-9A 101-103 | 153-923A-9R2-9A 101-103 | 153-923A-9R2-9A 101-103 | 153-923A-10R2-1A 1-4 | 153-923A-10R2-1A 1-4 | 153-923A-10R2-1A 1-4 | 153-923A-11R2-6B 87-91 | 153-923A-11R2-6B 87-91 |
|---|---|---|---|---|---|---|---|---|---|---|---|---|---|---|---|---|---|
| **Analysis** | P8R2123 traverse | P8R2119 cont. | P8R2107 | P8R2120 | P8R2108 | P8R2121 | P8R2122 | P8R2109 | P8R2110 | 9R2LC24 | 9R2LC25 | 9R2LC26 | 10RLC58 | 10RLC59 | 10RLC60 | 11RLC34 | 11RLC35 |
| **Location** | 2.18 | 1.74 | 1.22 | 0.96 | 0.64 | 0.46 | 0.32 | 0.20 | 0.04 | core | intermed | rim | core | rim | intermed | rim | core |
| **Depth (m)** | 31.31 | 31.31 | 31.31 | 31.31 | 31.31 | 31.31 | 31.31 | 31.31 | 31.31 | 34.41 | 34.41 | 34.41 | 38.01 | 38.01 | 38.01 | 43.57 | 43.57 |
| **Traces (ppm)** | | | | | | | | | | | | | | | | | |
| **F** | n.d. | n.d. | n.d. | n.d. | n.d. | n.d. | n.d. | n.d. | n.d. | n.d. | n.d. | n.d. | n.d. | n.d. | n.d. | n.d. | n.d. |
| **P** | 26 | 29 | 14 | 35 | 83 | 98 | 83 | 77 | 55 | n.d. | n.d. | n.d. | n.d. | n.d. | n.d. | n.d. | n.d. |
| **Cl** | n.d. | n.d. | n.d. | n.d. | n.d. | n.d. | n.d. | n.d. | n.d. | n.d. | n.d. | n.d. | n.d. | n.d. | n.d. | n.d. | n.d. |
| **Sc** | 115 | 119 | 107 | 114 | 122 | 131 | 131 | 140 | 135 | n.d. | n.d. | n.d. | n.d. | n.d. | n.d. | n.d. | n.d. |
| **Ti** | 2838 | 2926 | 2511 | 2665 | 3152 | 3753 | 3778 | 5006 | 4960 | 2910 | 2906 | 4790 | 2356 | 4472 | 2451 | 3756 | 2339 |
| **V** | 341 | 363 | 314 | 331 | 385 | 416 | 425 | 517 | 523 | 318 | 318 | 439 | 298 | 409 | 303 | 375 | 283 |
| **Cr** | 1185 | 1177 | 1046 | 1009 | 1162 | 988 | 804 | 677 | 515 | 1277 | 1083 | 670 | 2015 | 607 | 1663 | 1078 | 1237 |
| **Sr** | n.d. | n.d. | n.d. | n.d. | n.d. | n.d. | n.d. | n.d. | n.d. | 9.50 | 7.80 | 8.28 | 10.47 | 8.69 | 10.83 | 8.75 | 9.41 |
| **Zr** | 11.77 | 12.73 | 8.28 | 11.07 | 25.88 | 49.19 | 66.41 | 92.89 | 116.14 | 12.57 | 25.37 | 59.84 | 12.59 | 59.50 | 11.47 | 28.29 | 11.73 |
| **Y** | 16.75 | 18.59 | 15.83 | 18.07 | 21.70 | 25.99 | 29.21 | 41.89 | 45.11 | 19.55 | 24.15 | 37.25 | 16.57 | 40.45 | 17.25 | 29.27 | 17.60 |
| **Ba** | 0.04 | 0.07 | 0.01 | 0.01 | 0.01 | 0.08 | 0.02 | 0.01 | 0.02 | 1.15 | 0.16 | 0.32 | 0.09 | 0.22 | 0.21 | 0.18 | 0.19 |
| **La** | 0.23 | 0.23 | 0.20 | 0.31 | 0.40 | 0.57 | 0.52 | 0.73 | 0.73 | 0.36 | 0.40 | 0.49 | 0.39 | 0.78 | 0.26 | 0.52 | 0.27 |
| **Ce** | 1.13 | 1.23 | 1.00 | 1.44 | 2.29 | 2.76 | 2.86 | 4.07 | 4.27 | 1.33 | 2.67 | 3.46 | 1.75 | 4.56 | 1.34 | 2.94 | 1.54 |
| **Pr** | 0.27 | 0.32 | 0.27 | 0.33 | 0.54 | 0.63 | 0.67 | 1.04 | 1.13 | 0.36 | 0.60 | 0.87 | 0.37 | 1.15 | 0.44 | 0.59 | 0.38 |
| **Nd** | 2.08 | 2.58 | 2.22 | 2.49 | 3.52 | 4.21 | 4.90 | 7.55 | 8.08 | 2.64 | 3.98 | 6.87 | 2.96 | 9.57 | 2.51 | 5.23 | 2.64 |
| **Sm** | 1.22 | 1.51 | 1.24 | 1.47 | 1.86 | 2.34 | 2.37 | 3.81 | 4.19 | 1.53 | 1.97 | 3.21 | 1.38 | 3.69 | 1.44 | 2.61 | 1.83 |
| **Eu** | 0.50 | 0.54 | 0.49 | 0.51 | 0.57 | 0.70 | 0.74 | 0.93 | 0.89 | 0.64 | 0.75 | 0.95 | 0.54 | 1.16 | 0.52 | 0.85 | 0.60 |
| **Gd** | 2.17 | 2.61 | 2.13 | 2.38 | 2.71 | 3.19 | 3.69 | 5.95 | 6.09 | 2.98 | 2.41 | 5.34 | 3.28 | 6.51 | 2.76 | 4.20 | 2.72 |
| **Tb** | 0.40 | 0.44 | 0.39 | 0.48 | 0.53 | 0.68 | 0.71 | 1.15 | 1.14 | 0.60 | 0.50 | 0.97 | 0.40 | 0.98 | 0.51 | 0.75 | 0.55 |
| **Dy** | 3.03 | 3.39 | 2.87 | 3.27 | 3.88 | 4.70 | 5.23 | 7.90 | 8.47 | 3.87 | 4.19 | 8.27 | 2.89 | 7.21 | 2.78 | 5.51 | 4.08 |
| **Ho** | 0.63 | 0.77 | 0.55 | 0.70 | 0.81 | 0.91 | 1.03 | 1.60 | 1.73 | 0.86 | 0.94 | 1.41 | 0.69 | 1.52 | 0.59 | 1.18 | 0.77 |
| **Er** | 1.67 | 1.99 | 1.57 | 1.89 | 2.40 | 2.70 | 3.19 | 4.18 | 4.94 | 2.26 | 2.65 | 4.41 | 1.77 | 4.54 | 2.47 | 3.45 | 2.12 |
| **Yb** | 1.64 | 1.87 | 1.62 | 1.98 | 2.32 | 2.68 | 3.10 | 4.17 | 4.33 | 2.35 | 2.71 | 4.13 | 1.89 | 4.47 | 1.86 | 3.03 | 2.27 |

| Sample | 153-923A-11R2-6B 87-91 | 153-923A-11R2-6B 87-91 | 153-923A-11R2-6B 87-91 | 153-923A-11R2-6B 87-91 | 153-923A-11R2-6B 87-91 | 153-923A-12R1-4 30-38 | 153-923A-12R1-4 30-38 | 153-923A-12R1-4 30-38 | 153-923A-12R1-4 30-38 | 153-923A-12R1-4 30-38 | 153-923A-12R1-4 30-38 | 153-923A-12R1-4 30-38 | 153-923A-12R1-4 30-38 | 153-923A-12R1-4 30-38 | 153-923A-12R1-4 30-38 | 153-923A-12R1-5 133-139 | 153-923A-12R1-5 133-139 |
|---|---|---|---|---|---|---|---|---|---|---|---|---|---|---|---|---|---|
| **Analysis** | 11RLC36 | 11RLC74 | 11RLC75 | 11RLC76 | 11RLC77 | P12R098 | P12R099 | P12R100 | P12R101 | 12RLC43 | 12RLC44 | 12RLC45 | 12RLC46 | P12R079 | P12R080 | 133LC41 | 133LC42 |
| **Location** | rim | core | rim | rim | core | core | core | core | core | core | core | intermed | rim | rim | core | interstit | interstit |
| **Depth (m)** | 43.57 | 43.57 | 43.57 | 43.57 | 43.57 | 46.30 | 46.30 | 46.30 | 46.30 | 46.30 | 46.30 | 46.30 | 46.30 | 46.30 | 46.30 | 47.33 | 47.33 |
| **wt %** | | | | | | | | | | | | | | | | | |
| **SiO2** | 52.23 | 51.97 | 51.85 | 51.68 | 52.72 | 53.32 | 53.32 | 53.32 | 53.32 | 52.49 | 53.32 | 52.13 | 52.15 | 52.15 | 53.32 | 52.94 | 52.67 |
| **TiO2** | 0.50 | 0.81 | 0.92 | 0.83 | 0.43 | 0.41 | 0.41 | 0.41 | 0.41 | 0.36 | 0.41 | 0.41 | 1.32 | 1.32 | 0.41 | 0.73 | 0.93 |
| **Al2O3** | 2.60 | 2.70 | 2.61 | 2.47 | 2.40 | 3.65 | 3.65 | 3.65 | 3.65 | 3.51 | 3.65 | 3.69 | 3.26 | 3.26 | 3.65 | 2.38 | 2.09 |
| **Cr2O3** | 0.11 | 0.07 | 0.05 | 0.01 | 0.17 | 1.20 | 1.20 | 1.20 | 1.20 | 1.16 | 1.20 | 1.02 | 0.29 | 0.29 | 1.20 | 0.13 | 0.10 |
| **FeO** | 6.67 | 8.20 | 7.93 | 7.72 | 6.17 | 3.55 | 3.55 | 3.55 | 3.55 | 3.74 | 3.55 | 4.13 | 4.03 | 4.03 | 3.55 | 5.71 | 6.10 |
| **MnO** | 0.22 | 0.25 | 0.22 | 0.19 | 0.20 | 0.12 | 0.12 | 0.12 | 0.12 | 0.08 | 0.12 | 0.13 | 0.11 | 0.11 | 0.12 | 0.21 | 0.21 |
| **MgO** | 15.47 | 14.90 | 14.87 | 14.65 | 16.52 | 16.14 | 16.14 | 16.14 | 16.14 | 16.80 | 16.14 | 16.08 | 16.26 | 16.26 | 16.14 | 15.87 | 16.03 |
| **CaO** | 21.63 | 20.84 | 21.15 | 21.13 | 21.37 | 22.42 | 22.42 | 22.42 | 22.42 | 21.94 | 22.42 | 22.36 | 22.60 | 22.60 | 22.42 | 22.44 | 21.70 |
| **NaO2** | 0.58 | 0.45 | 0.43 | 0.43 | 0.37 | 0.44 | 0.44 | 0.44 | 0.44 | 0.38 | 0.44 | 0.41 | 0.38 | 0.38 | 0.44 | 0.30 | 0.38 |
| **Total** | 100.07 | 100.24 | 100.03 | 99.16 | 100.37 | 100.28 | 100.28 | 100.28 | 100.28 | 100.51 | 100.28 | 100.39 | 100.43 | 100.43 | 100.28 | 100.74 | 100.84 |
| **Cations** | | | | | | | | | | | | | | | | | |
| **Si** | 1.93 | 1.92 | 1.92 | 1.93 | 1.93 | 1.92 | 1.92 | 1.92 | 1.92 | 1.91 | 1.92 | 1.90 | 1.90 | 1.90 | 1.92 | 1.93 | 1.93 |
| **Ti** | 0.01 | 0.02 | 0.03 | 0.02 | 0.01 | 0.01 | 0.01 | 0.01 | 0.01 | 0.01 | 0.01 | 0.01 | 0.04 | 0.04 | 0.01 | 0.02 | 0.03 |
| **Al** | 0.11 | 0.12 | 0.11 | 0.11 | 0.10 | 0.15 | 0.15 | 0.15 | 0.15 | 0.15 | 0.15 | 0.16 | 0.14 | 0.14 | 0.15 | 0.10 | 0.09 |
| **Cr** | 0.00 | 0.00 | 0.00 | 0.00 | 0.00 | 0.03 | 0.03 | 0.03 | 0.03 | 0.03 | 0.03 | 0.03 | 0.01 | 0.01 | 0.03 | 0.00 | 0.00 |
| **Fe** | 0.21 | 0.25 | 0.25 | 0.24 | 0.19 | 0.11 | 0.11 | 0.11 | 0.11 | 0.11 | 0.11 | 0.13 | 0.12 | 0.12 | 0.11 | 0.17 | 0.19 |
| **Mn** | 0.01 | 0.01 | 0.01 | 0.01 | 0.01 | 0.00 | 0.00 | 0.00 | 0.00 | 0.00 | 0.00 | 0.00 | 0.00 | 0.00 | 0.00 | 0.01 | 0.01 |
| **Mg** | 0.85 | 0.82 | 0.82 | 0.82 | 0.90 | 0.87 | 0.87 | 0.87 | 0.87 | 0.91 | 0.87 | 0.87 | 0.88 | 0.88 | 0.87 | 0.86 | 0.88 |
| **Ca** | 0.86 | 0.83 | 0.84 | 0.85 | 0.84 | 0.86 | 0.86 | 0.86 | 0.86 | 0.85 | 0.86 | 0.87 | 0.88 | 0.88 | 0.86 | 0.88 | 0.85 |
| **Na** | 0.04 | 0.03 | 0.03 | 0.03 | 0.03 | 0.03 | 0.03 | 0.03 | 0.03 | 0.03 | 0.03 | 0.03 | 0.03 | 0.03 | 0.03 | 0.02 | 0.03 |
| **Total** | 4.02 | 4.01 | 4.01 | 4.01 | 4.02 | 3.99 | 3.99 | 3.99 | 3.99 | 4.01 | 3.99 | 4.01 | 3.99 | 3.99 | 3.99 | 4.00 | 4.01 |
| **Mg#** | 80.5 | 76.4 | 77.0 | 77.2 | 82.7 | 89.0 | 89.0 | 89.0 | 89.0 | 88.9 | 89.0 | 87.4 | 87.8 | 87.8 | 89.0 | 83.2 | 82.4 |

| Sample | 153-923A-11R2-6B 87-91 | 153-923A-11R2-6B 87-91 | 153-923A-11R2-6B 87-91 | 153-923A-11R2-6B 87-91 | 153-923A-11R2-6B 87-91 | 153-923A-12R1-4 30-38 | 153-923A-12R1-4 30-38 | 153-923A-12R1-4 30-38 | 153-923A-12R1-4 30-38 | 153-923A-12R1-4 30-38 | 153-923A-12R1-4 30-38 | 153-923A-12R1-4 30-38 | 153-923A-12R1-4 30-38 | 153-923A-12R1-4 30-38 | 153-923A-12R1-4 30-38 | 153-923A-12R1-5 133-139 | 153-923A-12R1-5 133-139 |
|---|---|---|---|---|---|---|---|---|---|---|---|---|---|---|---|---|---|
| **Analysis** | 11RLC36 | 11RLC74 | 11RLC75 | 11RLC76 | 11RLC77 | P12R098 | P12R099 | P12R100 | P12R101 | 12RLC43 | 12RLC44 | 12RLC45 | 12RLC46 | P12R079 | P12R080 | 133LC41 | 133LC42 |
| **Location** | rim | core | rim | rim | core | core | core | core | core | core | core | intermed | rim | rim | core | interstit | interstit |
| **Depth (m)** | 43.57 | 43.57 | 43.57 | 43.57 | 43.57 | 46.30 | 46.30 | 46.30 | 46.30 | 46.30 | 46.30 | 46.30 | 46.30 | 46.30 | 46.30 | 47.33 | 47.33 |
| **Traces (ppm)** | | | | | | | | | | | | | | | | | |
| **F** | n.d. | n.d. | n.d. | n.d. | n.d. | n.d. | n.d. | n.d. | n.d. | n.d. | n.d. | n.d. | n.d. | 300 | 185 | n.d. | n.d. |
| **P** | n.d. | n.d. | n.d. | n.d. | n.d. | n.d. | n.d. | n.d. | n.d. | n.d. | n.d. | n.d. | n.d. | 69 | 7 | n.d. | n.d. |
| **Cl** | n.d. | n.d. | n.d. | n.d. | n.d. | n.d. | n.d. | n.d. | n.d. | n.d. | n.d. | n.d. | n.d. | 11.10 | 5.83 | n.d. | n.d. |
| **Sc** | n.d. | n.d. | n.d. | n.d. | n.d. | n.d. | n.d. | n.d. | n.d. | n.d. | n.d. | n.d. | n.d. | 135 | 98 | n.d. | n.d. |
| **Ti** | 4021 | 3762 | 4924 | 4583 | 2474 | 2019 | 1989 | 1983 | 2016 | 1906 | 2244 | 2230 | 7415 | 7552 | 2323 | 5620 | 4846 |
| **V** | 426 | 377 | 445 | 410 | 304 | 271 | 265 | 266 | 267 | 249 | 285 | 284 | 592 | n.d | n.d | 635 | 644 |
| **Cr** | 1169 | 996 | 677 | 634 | 1484 | 9815 | 9469 | 9005 | 9039 | 10083 | 10250 | 9853 | 2789 | n.d | n.d | 1211 | 1137 |
| **Sr** | 9.39 | 9.72 | 9.06 | 8.87 | 9.55 | 8.90 | 8.67 | 8.90 | 8.47 | 9.96 | 10.77 | 10.03 | 10.33 | n.d | n.d | 9.88 | 9.16 |
| **Zr** | 30.61 | 21.14 | 49.82 | 44.01 | 10.57 | 6.94 | 6.93 | 6.87 | 6.83 | 7.55 | 9.05 | 9.82 | 148.32 | 134.24 | 8.20 | 126.68 | 117.05 |
| **Y** | 31.54 | 29.59 | 42.60 | 39.68 | 18.72 | 11.21 | 11.02 | 11.27 | 11.15 | 12.82 | 15.06 | 15.01 | 53.86 | 43.53 | 12.88 | 76.94 | 64.77 |
| **Ba** | 0.28 | 0.41 | 0.19 | 0.27 | 0.08 | 0.01 | 0.02 | 0.01 | 0.02 | 0.13 | 0.07 | 0.05 | 0.14 | 0.11 | 0.01 | 0.13 | 0.25 |
| **La** | 0.56 | 0.56 | 0.75 | 0.79 | 0.22 | 0.11 | 0.11 | 0.11 | 0.12 | 0.20 | 0.15 | 0.20 | 0.64 | n.d. | n.d. | 0.93 | 0.88 |
| **Ce** | 2.59 | 2.66 | 4.50 | 3.99 | 1.38 | 0.66 | 0.66 | 0.64 | 0.64 | 0.75 | 0.90 | 1.01 | 3.96 | 3.03 | 0.86 | 6.15 | 5.52 |
| **Pr** | 0.89 | 0.77 | 1.20 | 1.11 | 0.38 | 0.18 | 0.18 | 0.17 | 0.18 | 0.25 | 0.31 | 0.34 | 1.07 | n.d. | n.d. | 1.47 | 1.37 |
| **Nd** | 6.04 | 5.46 | 7.56 | 7.47 | 2.46 | 1.52 | 1.40 | 1.66 | 1.38 | 1.83 | 2.35 | 2.25 | 10.33 | n.d. | n.d. | 11.72 | 12.01 |
| **Sm** | 3.67 | 2.25 | 4.36 | 3.72 | 1.18 | 0.85 | 0.97 | 0.82 | 0.88 | 1.04 | 1.17 | 1.35 | 4.98 | n.d. | n.d. | 6.76 | 6.17 |
| **Eu** | 0.99 | 0.84 | 1.11 | 1.08 | 0.52 | 0.34 | 0.33 | 0.34 | 0.34 | 0.38 | 0.56 | 0.32 | 1.10 | n.d. | n.d. | 1.13 | 1.00 |
| **Gd** | 4.68 | 3.56 | 5.88 | 6.89 | 2.72 | 1.63 | 1.58 | 1.60 | 1.35 | 2.05 | 1.96 | 2.26 | 8.07 | n.d. | n.d. | 12.27 | 10.06 |
| **Tb** | 1.08 | 0.85 | 1.12 | 0.97 | 0.58 | 0.28 | 0.28 | 0.27 | 0.31 | 0.31 | 0.37 | 0.45 | 1.47 | n.d. | n.d. | 2.12 | 1.66 |
| **Dy** | 8.00 | 5.64 | 7.35 | 7.60 | 3.99 | 1.91 | 2.05 | 2.23 | 2.25 | 2.39 | 3.20 | 3.31 | 11.63 | n.d. | n.d. | 13.91 | 12.13 |
| **Ho** | 1.30 | 1.07 | 1.69 | 1.56 | 0.73 | 0.43 | 0.44 | 0.48 | 0.43 | 0.43 | 0.68 | 0.72 | 2.19 | n.d. | n.d. | 3.09 | 2.64 |
| **Er** | 4.22 | 3.31 | 5.49 | 5.17 | 2.39 | 1.17 | 1.12 | 1.18 | 1.25 | 1.67 | 1.99 | 1.74 | 6.60 | n.d. | n.d. | 10.08 | 7.78 |
| **Yb** | 4.19 | 3.15 | 4.01 | 3.93 | 1.84 | 1.11 | 1.11 | 1.26 | 1.22 | 1.83 | 1.78 | 2.00 | 5.08 | n.d. | n.d. | 9.22 | 7.23 |

| Sample | 153-923A-12R1-5 133-139 | 153-923A-12R1-5 133-139 | 153-923A-12R2-5 66-73 | 153-923A-12R2-5 66-73 | 153-923A-12R2-5 66-73 | 153-923A-12R2-5 66-73 | 153-923A-12R2-5 66-75 | 153-923A-13R2-6B 68-75 | 153-923A-13R2-6B 68-75 | 153-923A-13R2-6B 68-75 | 153-923A-13R2-6B 68-75 | 153-923A-13R2-6B 68-75 | 153-923A-14R1-12 100-112 | 153-923A-14R1-12 100-112 | 153-923A-14R1-12 100-112 | 153-923A-14R1-12 100-112 | 153-923A-14R1-12 100-112 |
|---|---|---|---|---|---|---|---|---|---|---|---|---|---|---|---|---|---|
| Analysis | P133092 | P133093 | 12R2L53 | 12R2L54 | 12R2L55 | 12R2L56 | 12R2L57 | 13RLC21 | 13RLC22 | 13RLC23 | 13RLC72 | 13RLC73 | 14RLC11 | 14RLC12 | 14RLC13 | 14RLC14 | 14RLC15 |
| Location | interstit | interstit | core | core | rim | core | intermed | core | interstit | interstit | core | interstit | rim | core | intermed | intermed | intermed |
| Depth (m) | 47.33 | 47.33 | 48.16 | 48.16 | 48.16 | 48.16 | 48.16 | 52.98 | 52.98 | 52.98 | 52.98 | 52.98 | 56.58 | 56.58 | 56.58 | 56.58 | 56.58 |
| wt % | | | | | | | | | | | | | | | | | |
| SiO2 | 52.94 | 52.94 | 53.59 | 53.59 | 52.10 | 52.82 | 53.18 | 52.23 | 52.38 | 52.31 | 52.23 | 52.55 | 52.06 | 52.88 | 53.26 | 53.55 | 53.69 |
| TiO2 | 0.73 | 0.73 | 0.58 | 0.58 | 1.22 | 0.97 | 0.56 | 1.32 | 1.01 | 1.31 | 1.28 | 1.22 | 0.86 | 0.49 | 0.53 | 0.56 | 0.51 |
| Al2O3 | 2.38 | 2.38 | 2.21 | 2.21 | 3.01 | 2.64 | 2.74 | 2.84 | 2.96 | 3.43 | 3.35 | 3.15 | 2.52 | 3.45 | 2.16 | 2.02 | 1.85 |
| Cr2O3 | 0.13 | 0.13 | 0.09 | 0.09 | 0.06 | 0.06 | 0.08 | 0.06 | 0.05 | 0.06 | 0.05 | 0.03 | 0.16 | 0.43 | 0.18 | 0.17 | 0.11 |
| FeO | 5.71 | 5.71 | 5.45 | 5.45 | 6.49 | 7.55 | 6.81 | 6.72 | 5.76 | 6.18 | 6.40 | 6.32 | 6.88 | 4.40 | 6.97 | 6.71 | 6.73 |
| MnO | 0.21 | 0.21 | 0.16 | 0.16 | 0.21 | 0.12 | 0.18 | 0.28 | 0.21 | 0.21 | 0.23 | 0.19 | 0.17 | 0.12 | 0.20 | 0.25 | 0.24 |
| MgO | 15.87 | 15.87 | 16.70 | 16.70 | 15.48 | 17.02 | 16.54 | 16.69 | 15.62 | 15.78 | 16.19 | 16.12 | 15.66 | 16.45 | 15.58 | 15.69 | 15.68 |
| CaO | 22.44 | 22.44 | 21.85 | 21.85 | 21.68 | 19.41 | 20.66 | 20.41 | 22.45 | 21.73 | 21.06 | 21.96 | 21.34 | 22.57 | 22.05 | 21.96 | 21.98 |
| NaO2 | 0.30 | 0.30 | 0.40 | 0.40 | 0.42 | 0.35 | 0.38 | 0.43 | 0.36 | 0.44 | 0.40 | 0.43 | 0.37 | 0.46 | 0.35 | 0.44 | 0.41 |
| Total | 100.74 | 100.74 | 101.07 | 101.07 | 100.71 | 100.95 | 101.18 | 101.01 | 100.81 | 101.50 | 101.22 | 102.01 | 100.07 | 101.29 | 101.31 | 101.40 | 101.25 |
| Cations | | | | | | | | | | | | | | | | | |
| Si | 1.93 | 1.93 | 1.94 | 1.94 | 1.91 | 1.92 | 1.93 | 1.90 | 1.91 | 1.90 | 1.90 | 1.90 | 1.92 | 1.91 | 1.94 | 1.95 | 1.96 |
| Ti | 0.02 | 0.02 | 0.02 | 0.02 | 0.03 | 0.03 | 0.02 | 0.04 | 0.03 | 0.04 | 0.04 | 0.03 | 0.02 | 0.01 | 0.01 | 0.02 | 0.01 |
| Al | 0.10 | 0.10 | 0.09 | 0.09 | 0.13 | 0.11 | 0.12 | 0.12 | 0.13 | 0.15 | 0.14 | 0.13 | 0.11 | 0.15 | 0.09 | 0.09 | 0.08 |
| Cr | 0.00 | 0.00 | 0.00 | 0.00 | 0.00 | 0.00 | 0.00 | 0.00 | 0.00 | 0.00 | 0.00 | 0.00 | 0.00 | 0.01 | 0.01 | 0.00 | 0.00 |
| Fe | 0.17 | 0.17 | 0.17 | 0.17 | 0.20 | 0.23 | 0.21 | 0.20 | 0.18 | 0.19 | 0.19 | 0.19 | 0.21 | 0.13 | 0.21 | 0.20 | 0.21 |
| Mn | 0.01 | 0.01 | 0.00 | 0.00 | 0.01 | 0.00 | 0.01 | 0.01 | 0.01 | 0.01 | 0.01 | 0.01 | 0.01 | 0.00 | 0.01 | 0.01 | 0.01 |
| Mg | 0.86 | 0.86 | 0.90 | 0.90 | 0.85 | 0.92 | 0.90 | 0.91 | 0.85 | 0.85 | 0.88 | 0.87 | 0.86 | 0.89 | 0.85 | 0.85 | 0.85 |
| Ca | 0.88 | 0.88 | 0.85 | 0.85 | 0.85 | 0.76 | 0.80 | 0.80 | 0.88 | 0.84 | 0.82 | 0.85 | 0.84 | 0.87 | 0.86 | 0.86 | 0.86 |
| Na | 0.02 | 0.02 | 0.03 | 0.03 | 0.03 | 0.02 | 0.03 | 0.03 | 0.03 | 0.03 | 0.03 | 0.03 | 0.03 | 0.03 | 0.03 | 0.03 | 0.03 |
| Total | 4.00 | 4.00 | 4.01 | 4.01 | 4.01 | 4.01 | 4.01 | 4.01 | 4.01 | 4.01 | 4.01 | 4.02 | 4.01 | 4.01 | 4.01 | 4.01 | 4.00 |
| Mg# | 83.2 | 83.2 | 84.5 | 84.5 | 81.0 | 80.1 | 81.2 | 81.6 | 82.9 | 82.0 | 81.8 | 82.0 | 80.2 | 86.9 | 79.9 | 80.6 | 80.6 |

| Sample | 153-923A-12R1-5 133-139 | 153-923A-12R1-5 133-139 | 153-923A-12R2-5 66-73 | 153-923A-12R2-5 66-73 | 153-923A-12R2-5 66-73 | 153-923A-12R2-5 66-73 | 153-923A-12R2-5 66-73 | 153-923A-13R2-6B 68-75 | 153-923A-13R2-6B 68-75 | 153-923A-13R2-6B 68-75 | 153-923A-13R2-6B 68-75 | 153-923A-13R2-6B 68-75 | 153-923A-14R1-12 100-112 | 153-923A-14R1-12 100-112 | 153-923A-14R1-12 100-112 | 153-923A-14R1-12 100-112 | 153-923A-14R1-12 100-112 |
|---|---|---|---|---|---|---|---|---|---|---|---|---|---|---|---|---|---|
| Analysis | P133092 | P133093 | 12R2L53 | 12R2L54 | 12R2L55 | 12R2L56 | 12R2L57 | 13RLC21 | 13RLC22 | 13RLC23 | 13RLC72 | 13RLC73 | 14RLC11 | 14RLC12 | 14RLC13 | 14RLC14 | 14RLC15 |
| Location | interstit | interstit | core | core | rim | core | intermed | core | interstit | interstit | core | interstit | rim | core | intermed | intermed | intermed |
| Depth (m) | 47.33 | 47.33 | 48.16 | 48.16 | 48.16 | 48.16 | 48.16 | 52.98 | 52.98 | 52.98 | 52.98 | 52.98 | 56.58 | 56.58 | 56.58 | 56.58 | 56.58 |
| Traces (ppm) | | | | | | | | | | | | | | | | | |
| F | 182 | 126 | n.d. | n.d. | n.d. | n.d. | n.d. | n.d. | n.d. | n.d. | n.d. | n.d. | n.d. | n.d. | n.d. | n.d. | n.d. |
| P | 22 | 19 | n.d. | n.d. | n.d. | n.d. | n.d. | n.d. | n.d. | n.d. | n.d. | n.d. | n.d. | n.d. | n.d. | n.d. | n.d. |
| Cl | 9.71 | 7.82 | n.d. | n.d. | n.d. | n.d. | n.d. | n.d. | n.d. | n.d. | n.d. | n.d. | n.d. | n.d. | n.d. | n.d. | n.d. |
| Sc | 164 | 170 | n.d. | n.d. | n.d. | n.d. | n.d. | n.d. | n.d. | n.d. | n.d. | n.d. | n.d. | n.d. | n.d. | n.d. | n.d. |
| Ti | 5170 | 4757 | 3096 | 3150 | 6534 | 2953 | 5528 | 6861 | 4213 | 7118 | 7316 | 6758 | 4249 | 2456 | 2599 | 2618 | 2840 |
| V | n.d. | n.d. | 367 | 375 | 478 | 336 | 441 | 561 | 536 | 602 | 648 | 681 | 399 | 307 | 319 | 334 | 340 |
| Cr | n.d. | n.d. | 1051 | 943 | 671 | 806 | 738 | 400 | 426 | 427 | 489 | 478 | 1338 | 3852 | 1728 | 1334 | 1431 |
| Sr | n.d. | n.d. | 11.52 | 10.40 | 9.80 | 10.08 | 10.43 | 8.94 | 8.05 | 8.83 | 10.07 | 10.19 | 9.14 | 10.52 | 7.87 | 8.37 | 8.79 |
| Zr | 105.98 | 99.43 | 16.13 | 18.67 | 41.84 | 14.66 | 34.10 | 87.28 | 140.86 | 194.90 | 168.90 | 226.32 | 48.17 | 10.77 | 110.75 | 128.77 | 139.99 |
| Y | 62.58 | 57.42 | 20.15 | 23.13 | 37.49 | 19.13 | 34.74 | 56.58 | 54.35 | 79.75 | 73.04 | 80.41 | 34.72 | 16.11 | 58.90 | 92.92 | 89.22 |
| Ba | 0.02 | 0.01 | 1.64 | 0.24 | 0.04 | 0.06 | 0.05 | 0.40 | 0.58 | 0.43 | 0.58 | 0.48 | 0.91 | 0.40 | 0.08 | 0.22 | 0.49 |
| La | n.d. | n.d. | 0.62 | 0.25 | 0.60 | 0.38 | 0.59 | 0.69 | 0.53 | 0.68 | 0.79 | 0.84 | 0.76 | 0.27 | 1.84 | 2.77 | 2.85 |
| Ce | 4.28 | 4.23 | 2.28 | 2.21 | 3.27 | 2.02 | 3.11 | 4.61 | 3.58 | 5.40 | 6.02 | 5.39 | 3.29 | 1.21 | 9.54 | 14.56 | 14.89 |
| Pr | n.d. | n.d. | 0.52 | 0.53 | 0.83 | 0.42 | 0.81 | 1.25 | 1.06 | 1.75 | 1.62 | 1.73 | 0.98 | 0.34 | 2.42 | 3.66 | 3.45 |
| Nd | n.d. | n.d. | 3.72 | 3.92 | 7.19 | 3.34 | 6.24 | 9.51 | 10.19 | 11.26 | 13.66 | 12.97 | 6.97 | 2.76 | 16.45 | 27.38 | 27.39 |
| Sm | n.d. | n.d. | 2.02 | 1.97 | 3.87 | 1.70 | 3.12 | 4.98 | 4.32 | 6.80 | 5.73 | 7.11 | 3.01 | 1.29 | 7.41 | 9.98 | 10.76 |
| Eu | n.d. | n.d. | 0.70 | 0.67 | 1.05 | 0.54 | 0.95 | 0.94 | 0.70 | 0.99 | 1.15 | 1.06 | 0.83 | 0.69 | 1.25 | 1.65 | 2.03 |
| Gd | n.d. | n.d. | 2.81 | 2.77 | 4.91 | 2.88 | 4.91 | 7.30 | 7.73 | 12.89 | 10.97 | 12.02 | 4.71 | 2.31 | 10.89 | 15.42 | 14.46 |
| Tb | n.d. | n.d. | 0.64 | 0.67 | 0.93 | 0.45 | 0.93 | 1.63 | 1.34 | 1.80 | 2.00 | 2.25 | 0.85 | 0.44 | 1.66 | 3.00 | 2.44 |
| Dy | n.d. | n.d. | 4.44 | 4.45 | 7.44 | 4.09 | 6.19 | 10.80 | 10.48 | 14.62 | 13.63 | 16.13 | 6.35 | 3.22 | 12.21 | 18.27 | 17.22 |
| Ho | n.d. | n.d. | 0.85 | 0.89 | 1.53 | 0.85 | 1.25 | 2.15 | 1.90 | 3.49 | 2.72 | 3.34 | 1.33 | 0.56 | 2.23 | 3.70 | 3.84 |
| Er | n.d. | n.d. | 2.37 | 2.85 | 4.23 | 2.04 | 3.93 | 5.95 | 5.58 | 9.05 | 9.14 | 9.81 | 3.51 | 1.80 | 6.44 | 11.13 | 11.47 |
| Yb | n.d. | n.d. | 2.45 | 2.27 | 3.96 | 2.44 | 3.56 | 5.43 | 4.96 | 8.19 | 8.32 | 7.98 | 2.75 | 1.83 | 5.48 | 8.69 | 9.22 |

| Sample | 153-923A-14R1-12 100-112 | 153-923A-14R1-12 100-112 | 153-923A-14R1-12 100-112 | 153-923A-16R1-2 17-19 | 153-923A-16R1-2 17-19 | 153-923A-16R1-2 17-19 | 153-923A-16R1-2 17-19 | 153-923A-16R1-2 17-19 | 153-923A-16R1-2 17-19 | 153-923A-16R1-2 17-19 | 153-923A-16R1-2 17-19 | 153-923A-16R1-2 17-19 | 153-923A-16R1-2 17-19 | 153-923A-16R1-2 17-19 | 153-923A-16R1-2 17-19 | 153-923A-16R1-2 17-19 | 153-923A-16R1-2 17-19 |
|---|---|---|---|---|---|---|---|---|---|---|---|---|---|---|---|---|---|
| Analysis | P14R085 | P14R086 | P14R087 | 16RLC31 | 16RLC32 | 16RLC33 | 16RLC61 | 16RLC62 | 16RLC63 | 16RLC64 | 16RLC65 | P16R124 | P16R125 | P16R126 | P16R127 | P16R128 | P16R135 |
| Location | rim | intermed | core | rim | intermed | core | core | rim | core | rim | rim | traverse 0.08 | distance 0.64 | from 1.28 | rim 1.72 | 2.16 | 3.96 |
| Depth (m) | 56.58 | 56.58 | 56.58 | 64.87 | 64.87 | 64.87 | 64.87 | 64.87 | 64.87 | 64.87 | 64.87 | 64.87 | 64.87 | 64.87 | 64.87 | 64.87 | 64.87 |
| wt % | | | | | | | | | | | | | | | | | |
| SiO2 | 50.90 | 52.65 | 52.85 | 53.18 | 53.25 | 52.79 | 52.07 | 53.02 | 52.82 | 52.86 | 52.82 | 52.93 | 52.63 | 53.75 | 53.27 | 52.88 | 52.38 |
| TiO2 | 0.69 | 0.67 | 0.57 | 0.70 | 0.53 | 0.62 | 1.14 | 0.53 | 0.49 | 0.56 | 0.95 | 0.64 | 0.51 | 0.38 | 0.44 | 1.19 | 0.82 |
| Al2O3 | 3.07 | 2.27 | 3.58 | 2.50 | 2.97 | 3.16 | 3.01 | 3.11 | 3.07 | 2.97 | 2.63 | 3.36 | 3.33 | 2.35 | 2.51 | 3.08 | 2.87 |
| Cr2O3 | 0.11 | 0.19 | 0.47 | 0.30 | 0.34 | 0.40 | 0.22 | 0.28 | 0.34 | 0.32 | 0.33 | 0.52 | 0.53 | 0.43 | 0.38 | 0.19 | 0.23 |
| FeO | 7.59 | 6.82 | 5.47 | 5.02 | 5.59 | 5.04 | 5.56 | 4.99 | 4.79 | 5.34 | 5.07 | 4.93 | 4.39 | 4.59 | 4.49 | 5.12 | 5.45 |
| MnO | 0.23 | 0.20 | 0.19 | 0.18 | 0.11 | 0.14 | 0.18 | 0.13 | 0.18 | 0.15 | 0.20 | 0.12 | 0.13 | 0.15 | 0.13 | 0.17 | 0.16 |
| MgO | 15.26 | 15.37 | 16.47 | 16.40 | 16.86 | 16.39 | 15.68 | 16.38 | 17.55 | 16.53 | 16.22 | 16.37 | 16.27 | 18.58 | 17.25 | 16.20 | 16.79 |
| CaO | 20.53 | 22.18 | 20.27 | 22.42 | 21.30 | 22.24 | 22.56 | 22.61 | 21.01 | 21.57 | 22.70 | 21.86 | 22.26 | 20.70 | 21.20 | 22.59 | 20.71 |
| NaO2 | 0.33 | 0.34 | 0.39 | 0.41 | 0.39 | 0.41 | 0.38 | 0.36 | 0.36 | 0.39 | 0.35 | 0.40 | 0.43 | 0.35 | 0.37 | 0.41 | 0.36 |
| Total | 98.75 | 100.69 | 100.31 | 101.11 | 101.37 | 101.24 | 100.87 | 101.43 | 100.62 | 100.70 | 101.33 | 101.19 | 100.52 | 101.31 | 100.09 | 101.86 | 99.83 |
| Cations | | | | | | | | | | | | | | | | | |
| Si | 1.91 | 1.93 | 1.92 | 1.93 | 1.92 | 1.91 | 1.90 | 1.92 | 1.92 | 1.92 | 1.92 | 1.91 | 1.92 | 1.93 | 1.94 | 1.91 | 1.92 |
| Ti | 0.02 | 0.02 | 0.02 | 0.02 | 0.01 | 0.02 | 0.03 | 0.01 | 0.01 | 0.02 | 0.03 | 0.02 | 0.01 | 0.01 | 0.01 | 0.03 | 0.02 |
| Al | 0.14 | 0.10 | 0.15 | 0.11 | 0.13 | 0.14 | 0.13 | 0.13 | 0.13 | 0.13 | 0.11 | 0.14 | 0.14 | 0.10 | 0.11 | 0.13 | 0.12 |
| Cr | 0.00 | 0.01 | 0.01 | 0.01 | 0.01 | 0.01 | 0.01 | 0.01 | 0.01 | 0.01 | 0.01 | 0.01 | 0.02 | 0.01 | 0.01 | 0.01 | 0.01 |
| Fe | 0.24 | 0.21 | 0.17 | 0.15 | 0.17 | 0.15 | 0.17 | 0.15 | 0.15 | 0.16 | 0.15 | 0.15 | 0.13 | 0.14 | 0.14 | 0.15 | 0.17 |
| Mn | 0.01 | 0.01 | 0.01 | 0.01 | 0.00 | 0.00 | 0.01 | 0.00 | 0.01 | 0.00 | 0.01 | 0.00 | 0.00 | 0.00 | 0.00 | 0.01 | 0.00 |
| Mg | 0.85 | 0.84 | 0.89 | 0.89 | 0.91 | 0.89 | 0.85 | 0.88 | 0.95 | 0.90 | 0.88 | 0.88 | 0.88 | 1.00 | 0.94 | 0.87 | 0.92 |
| Ca | 0.82 | 0.87 | 0.79 | 0.87 | 0.82 | 0.86 | 0.88 | 0.88 | 0.82 | 0.84 | 0.88 | 0.85 | 0.87 | 0.80 | 0.83 | 0.87 | 0.81 |
| Na | 0.02 | 0.02 | 0.03 | 0.03 | 0.03 | 0.03 | 0.03 | 0.03 | 0.02 | 0.03 | 0.02 | 0.03 | 0.03 | 0.02 | 0.03 | 0.03 | 0.03 |
| Total | 4.02 | 4.01 | 3.99 | 4.01 | 4.01 | 4.01 | 4.01 | 4.01 | 4.01 | 4.01 | 4.01 | 4.00 | 4.01 | 4.01 | 4.00 | 4.01 | 4.00 |
| Mg# | 78.2 | 80.1 | 84.3 | 85.3 | 84.3 | 85.3 | 83.4 | 85.4 | 86.7 | 84.7 | 85.1 | 85.5 | 86.8 | 87.8 | 87.3 | 84.9 | 84.6 |

| Sample | 153-923A-14R1-12 100-112 | 153-923A-14R1-12 100-112 | 153-923A-14R1-12 100-112 | 153-923A-16R1-2 17-19 | 153-923A-16R1-2 17-19 | 153-923A-16R1-2 17-19 | 153-923A-16R1-2 17-19 | 153-923A-16R1-2 17-19 | 153-923A-16R1-2 17-19 | 153-923A-16R1-2 17-19 | 153-923A-16R1-2 17-19 | 153-923A-16R1-2 17-19 | 153-923A-16R1-2 17-19 | 153-923A-16R1-2 17-19 | 153-923A-16R1-2 17-19 | 153-923A-16R1-2 17-19 | 153-923A-16R1-2 17-19 |
|---|---|---|---|---|---|---|---|---|---|---|---|---|---|---|---|---|---|
| **Analysis** | P14R085 | P14R086 | P14R087 | 16RLC31 | 16RLC32 | 16RLC33 | 16RLC61 | 16RLC62 | 16RLC63 | 16RLC64 | 16RLC65 | P16R124 | P16R125 | P16R126 | P16R127 | P16R128 | P16R135 |
| **Location** | rim | intermed | core | rim | intermed | core | core | rim | core | rim | rim | traverse 0.08 | distance 0.64 | from 1.28 | rim 1.72 | 2.16 | 3.96 |
| **Depth (m)** | 56.58 | 56.58 | 56.58 | 64.87 | 64.87 | 64.87 | 64.87 | 64.87 | 64.87 | 64.87 | 64.87 | 64.87 | 64.87 | 64.87 | 64.87 | 64.87 | 64.87 |
| **Traces (ppm)** | | | | | | | | | | | | | | | | | |
| **F** | 128 | 142 | 340 | n.d. | n.d. | n.d. | n.d. | n.d. | n.d. | n.d. | n.d. | n.d. | n.d. | n.d. | n.d. | n.d. | n.d. |
| **P** | 56 | 33 | 18 | n.d. | n.d. | n.d. | n.d. | n.d. | n.d. | n.d. | n.d. | 20 | 26 | 10 | 10 | 31 | 25 |
| **Cl** | 31.53 | 6.41 | 16.48 | n.d. | n.d. | n.d. | n.d. | n.d. | n.d. | n.d. | n.d. | n.d. | n.d. | n.d. | n.d. | n.d. | n.d. |
| **Sc** | 118 | 118 | 125 | n.d. | n.d. | n.d. | n.d. | n.d. | n.d. | n.d. | n.d. | 120 | 117 | 95 | 94 | 125 | 121 |
| **Ti** | 3874 | 3040 | 2845 | 3318 | 2323 | 3453 | 5838 | 2723 | 2704 | 2937 | 5065 | 3753 | 2597 | 1972 | 1977 | 7350 | 4907 |
| **V** | n.d. | n.d. | n.d. | 305 | 289 | 329 | 441 | 326 | 323 | 317 | 396 | 380 | 338 | 264 | 265 | 559 | 439 |
| **Cr** | n.d. | n.d. | n.d. | 2743 | 3243 | 3435 | 2332 | 2830 | 2765 | 2842 | 2317 | 4224 | 4792 | 3591 | 3568 | 1577 | 1797 |
| **Sr** | n.d. | n.d. | n.d. | 8.02 | 7.70 | 9.01 | 8.12 | 10.07 | 9.06 | 7.56 | 7.71 | n.d. | n.d. | n.d. | n.d. | n.d. | n.d. |
| **Zr** | 45.82 | 75.74 | 10.66 | 22.86 | 11.04 | 25.58 | 48.51 | 11.70 | 11.26 | 16.83 | 40.78 | 21.38 | 10.16 | 6.24 | 6.43 | 45.09 | 30.86 |
| **Y** | 31.39 | 39.01 | 16.46 | 24.02 | 16.28 | 24.38 | 35.19 | 18.53 | 18.66 | 20.16 | 28.55 | 24.64 | 15.09 | 11.49 | 11.31 | 34.93 | 24.76 |
| **Ba** | 0.31 | 0.03 | 0.43 | 0.56 | 0.16 | 0.11 | 0.17 | 0.01 | 0.02 | 0.12 | 0.50 | 0.05 | 0.34 | 0.00 | 0.01 | 0.06 | 0.02 |
| **La** | n.d. | n.d. | n.d. | 0.41 | 0.40 | 0.40 | 0.56 | 0.21 | 0.14 | 0.41 | 0.56 | 0.33 | 0.21 | 0.12 | 0.14 | 0.38 | 0.33 |
| **Ce** | 3.31 | 5.45 | 1.03 | 2.42 | 1.59 | 2.53 | 3.51 | 1.55 | 1.46 | 2.22 | 3.41 | 1.88 | 1.04 | 0.71 | 0.74 | 2.63 | 2.10 |
| **Pr** | n.d. | n.d. | n.d. | 0.71 | 0.60 | 0.61 | 0.85 | 0.31 | 0.40 | 0.49 | 0.75 | 0.46 | 0.27 | 0.19 | 0.20 | 0.71 | 0.58 |
| **Nd** | n.d. | n.d. | n.d. | 5.66 | 4.30 | 4.78 | 8.40 | 3.62 | 2.87 | 4.28 | 7.01 | 3.67 | 2.24 | 1.56 | 1.75 | 5.72 | 4.18 |
| **Sm** | n.d. | n.d. | n.d. | 3.10 | 2.87 | 2.72 | 3.17 | 1.89 | 1.22 | 1.69 | 2.97 | 2.07 | 1.31 | 1.00 | 0.99 | 3.03 | 2.25 |
| **Eu** | n.d. | n.d. | n.d. | 1.05 | 0.69 | 0.66 | 0.92 | 0.60 | 0.56 | 0.68 | 0.86 | 0.60 | 0.45 | 0.36 | 0.33 | 0.62 | 0.61 |
| **Gd** | n.d. | n.d. | n.d. | 3.60 | 2.83 | 3.85 | 5.82 | 3.03 | 2.95 | 3.55 | 4.07 | 3.24 | 2.15 | 1.57 | 1.59 | 4.90 | 3.36 |
| **Tb** | n.d. | n.d. | n.d. | 0.95 | 0.52 | 0.78 | 0.88 | 0.50 | 0.44 | 0.56 | 0.84 | 0.61 | 0.41 | 0.31 | 0.32 | 0.90 | 0.68 |
| **Dy** | n.d. | n.d. | n.d. | 5.94 | 3.76 | 4.60 | 7.85 | 3.58 | 3.13 | 3.71 | 6.00 | 4.56 | 2.94 | 2.23 | 2.15 | 6.15 | 4.54 |
| **Ho** | n.d. | n.d. | n.d. | 1.19 | 0.68 | 0.88 | 1.47 | 0.76 | 0.80 | 0.89 | 1.25 | 0.91 | 0.56 | 0.41 | 0.41 | 1.32 | 0.94 |
| **Er** | n.d. | n.d. | n.d. | 2.89 | 2.00 | 2.59 | 3.99 | 2.34 | 2.22 | 2.09 | 3.89 | 2.56 | 1.53 | 1.24 | 1.30 | 3.78 | 2.47 |
| **Yb** | n.d. | n.d. | n.d. | 2.45 | 3.00 | 2.33 | 3.77 | 1.84 | 2.06 | 2.84 | 3.33 | 2.59 | 1.34 | 1.25 | 1.24 | 3.22 | 2.54 |

| 153-923A-16R1-2 17-19 | 153-923A-16R1-2 17-19 | 153-923A-16R1-2 17-19 | 153-923A-16R1-2 17-19 | 153-923A-16R3-1 3-6 | 153-923A-16R3-1 3-6 | 153-923A-16R3-1 3-6 | 153-923A-16R3-1 3-6 | 153-923A-16R3-1 3-6 | 153-923A-16R3-1 3-6 | KH1 standard | KH1 accepted values | KH1LAC 3 | KH1LAC 4 | KH1LAC 48 | KH1 0117 | kh1PL16 2 |
|---|---|---|---|---|---|---|---|---|---|---|---|---|---|---|---|---|
| P16R136 | P16R137 | P16R138 | P16R139 | 17RLC49 | 17RLC50 | 17RLC51 | 17RLC52 | P17R090 | P17R091 | | | | | | | |
| 4.12 | 4.76 | 5.60 | 5.96 | core | rim | intermed | core | core | rim | | | | | | | |
| 64.87 | 64.87 | 64.87 | 64.87 | 67.73 | 67.73 | 67.73 | 67.73 | 67.73 | 67.73 | | | | | | | |
| 53.67 | 53.03 | 54.58 | 52.99 | 51.98 | 52.43 | 51.75 | 52.41 | 51.60 | 51.58 | | | | | | | |
| 0.63 | 0.52 | 0.42 | 0.78 | 1.20 | 1.09 | 1.35 | 0.92 | 1.44 | 1.30 | | | | | | | |
| 2.98 | 3.11 | 2.71 | 2.75 | 3.66 | 2.93 | 3.14 | 2.57 | 3.91 | 4.02 | | | | | | | |
| 0.32 | 0.30 | 0.22 | 0.29 | 0.08 | 0.05 | 0.09 | 0.05 | 0.05 | 0.06 | | | | | | | |
| 5.97 | 4.98 | 6.78 | 4.96 | 5.39 | 5.38 | 5.59 | 5.54 | 5.37 | 5.44 | | | | | | | |
| 0.15 | 0.13 | 0.17 | 0.18 | 0.21 | 0.20 | 0.27 | 0.18 | 0.19 | 0.17 | | | | | | | |
| 18.00 | 17.58 | 21.39 | 16.30 | 15.77 | 15.81 | 15.62 | 16.17 | 15.81 | 15.66 | | | | | | | |
| 19.37 | 20.56 | 16.05 | 21.83 | 22.51 | 22.61 | 22.20 | 22.09 | 22.01 | 22.48 | | | | | | | |
| 0.39 | 0.32 | 0.28 | 0.40 | 0.34 | 0.38 | 0.37 | 0.25 | 0.44 | 0.43 | | | | | | | |
| 101.50 | 100.56 | 102.65 | 100.48 | 101.15 | 100.91 | 100.40 | 100.41 | 100.89 | 101.17 | | | | | | | |
| 1.93 | 1.92 | 1.93 | 1.93 | 1.89 | 1.91 | 1.90 | 1.92 | 1.88 | 1.88 | | | | | | | |
| 0.02 | 0.01 | 0.01 | 0.02 | 0.03 | 0.03 | 0.04 | 0.03 | 0.04 | 0.04 | | | | | | | |
| 0.13 | 0.13 | 0.11 | 0.12 | 0.16 | 0.13 | 0.14 | 0.11 | 0.17 | 0.17 | | | | | | | |
| 0.01 | 0.01 | 0.01 | 0.01 | 0.00 | 0.00 | 0.00 | 0.00 | 0.00 | 0.00 | | | | | | | |
| 0.18 | 0.15 | 0.20 | 0.15 | 0.16 | 0.16 | 0.17 | 0.17 | 0.16 | 0.17 | | | | | | | |
| 0.00 | 0.00 | 0.01 | 0.01 | 0.01 | 0.01 | 0.01 | 0.01 | 0.01 | 0.01 | | | | | | | |
| 0.96 | 0.95 | 1.12 | 0.88 | 0.85 | 0.86 | 0.85 | 0.88 | 0.86 | 0.85 | | | | | | | |
| 0.75 | 0.80 | 0.61 | 0.85 | 0.88 | 0.88 | 0.87 | 0.87 | 0.86 | 0.88 | | | | | | | |
| 0.03 | 0.02 | 0.02 | 0.03 | 0.02 | 0.03 | 0.03 | 0.02 | 0.03 | 0.03 | | | | | | | |
| 4.00 | 4.00 | 4.01 | 4.00 | 4.01 | 4.01 | 4.01 | 4.01 | 4.01 | 4.02 | | | | | | | |
| 84.3 | 86.3 | 84.9 | 85.4 | 83.9 | 84.0 | 83.3 | 83.9 | 84.0 | 83.7 | | | | | | | |

| 153-923A-16R1-2 17-19 | 153-923A-16R1-2 17-19 | 153-923A-16R1-2 17-19 | 153-923A-16R1-2 17-19 | 153-923A-16R3-1 3-6 | 153-923A-16R3-1 3-6 | 153-923A-16R3-1 3-6 | 153-923A-16R3-1 3-6 | 153-923A-16R3-1 3-6 | 153-923A-16R3-1 3-6 | KH1 standard | KH1 accepted values | KH1LAC 3 | KH1LAC 4 | KH1LAC 48 | KH1 0117 | kh1PL16 2 |
|---|---|---|---|---|---|---|---|---|---|---|---|---|---|---|---|---|
| P16R136 | P16R137 | P16R138 | P16R139 | 17RLC49 | 17RLC50 | 17RLC51 | 17RLC52 | P17R090 | P17R091 | | | | | | | |
| 4.12 | 4.76 | 5.60 | 5.96 | core | rim | intermed | core | core | rim | | | | | | | |
| 64.87 | 64.87 | 64.87 | 64.87 | 67.73 | 67.73 | 67.73 | 67.73 | 67.73 | 67.73 | | | | | | | |
| n.d. | n.d. | n.d. | n.d. | n.d. | n.d. | n.d. | n.d. | 392 | 923 | | | | | | | |
| 15 | 9 | 11 | 30 | n.d. | n.d. | n.d. | n.d. | n.d. | 77 | | | | | | 29 | 30 |
| n.d. | n.d. | n.d. | n.d. | n.d. | n.d. | n.d. | n.d. | 17.06 | 34.94 | | | | | | | |
| 111 | 111 | 114 | 111 | n.d. | n.d. | n.d. | n.d. | 144 | 146 | | | | | | 54 | 59 |
| 3305 | 2801 | 2773 | 4592 | 10927 | 5384 | 7392 | 7501 | 9712 | 15488 | | | 4255 | 4305 | 4339 | 4470 | 4430 |
| 352 | 340 | 334 | 388 | 718 | 611 | 647 | 582 | n.d. | n.d. | | | 320 | 325 | 331 | 347 | 342 |
| 2729 | 2721 | 2763 | 2327 | 939 | 676 | 732 | 917 | n.d. | n.d. | | 305+/-10 | 494 | 507 | 513 | 495 | 487 |
| n.d. | n.d. | n.d. | n.d. | 11.74 | 8.56 | 9.08 | 10.56 | n.d. | n.d. | | 56.5+/-5 | 42.47 | 43.31 | 44.40 | | |
| 16.36 | 9.86 | 9.59 | 31.55 | 67.18 | 216.70 | 168.27 | 36.53 | 51.54 | 136.99 | | | 24.54 | 25.66 | 24.70 | 23.10 | 22.90 |
| 19.91 | 15.64 | 15.97 | 25.30 | 63.70 | 87.93 | 100.68 | 47.87 | 50.69 | 83.93 | | | 14.1 | 14.54 | 14.98 | 10.60 | 10.50 |
| 0.02 | 0.00 | 0.02 | 0.13 | 0.61 | 0.25 | 0.42 | 0.48 | 0.30 | 0.37 | | | | | | | |
| 0.24 | 0.16 | 0.18 | 0.33 | 0.82 | 1.07 | 1.35 | 0.46 | n.d. | n.d. | | 1.25 | 1.44 | 1.41 | 1.47 | 1.18 | 1.29 |
| 1.58 | 0.93 | 0.98 | 2.19 | 5.31 | 7.72 | 9.22 | 3.61 | 3.75 | 6.72 | | 5.25+/-0.15 | 5.32 | 5.29 | 6.04 | 4.44 | 4.69 |
| 0.42 | 0.29 | 0.27 | 0.56 | 1.46 | 2.19 | 2.43 | 0.95 | n.d. | n.d. | | | 1.00 | 1.07 | 1.10 | 0.89 | 0.88 |
| 2.81 | 2.03 | 2.13 | 4.69 | 11.77 | 17.17 | 20.16 | 8.07 | n.d. | n.d. | | 5.6+/-0.2 | 7.08 | 6.33 | 6.97 | 5.09 | 5.14 |
| 1.77 | 1.24 | 1.21 | 2.29 | 5.08 | 8.71 | 9.13 | 3.62 | n.d. | n.d. | | 1.84+/-0.04 | 2.19 | 2.51 | 2.61 | 2.14 | 2.05 |
| 0.50 | 0.53 | 0.46 | 0.58 | 1.08 | 0.96 | 1.29 | 0.89 | n.d. | n.d. | | 0.72+/-0.01 | 0.77 | 0.84 | 1.07 | 0.69 | 0.70 |
| 2.46 | 2.09 | 2.15 | 3.31 | 8.45 | 12.90 | 14.10 | 6.05 | n.d. | n.d. | | | 2.84 | 3.01 | 2.76 | 2.35 | 2.05 |
| 0.51 | 0.38 | 0.40 | 0.63 | 1.71 | 2.22 | 2.47 | 1.35 | n.d. | n.d. | | 0.38+/-0.04 | 0.40 | 0.38 | 0.49 | 0.43 | 0.42 |
| 3.55 | 2.90 | 3.03 | 4.33 | 12.51 | 17.88 | 18.85 | 10.50 | n.d. | n.d. | | | 3.34 | 2.53 | 3.63 | 2.37 | 2.56 |
| 0.76 | 0.59 | 0.58 | 0.91 | 2.54 | 3.55 | 4.12 | 1.80 | n.d. | n.d. | | 0.41+/-0.04 | 0.64 | 0.53 | 0.60 | 0.48 | 0.47 |
| 2.11 | 1.61 | 1.71 | 2.67 | 6.89 | 10.51 | 11.23 | 5.68 | n.d. | n.d. | | | 2.09 | 1.28 | 1.58 | 1.34 | 1.33 |
| 1.84 | 1.54 | 1.57 | 2.15 | 6.11 | 9.31 | 9.96 | 5.25 | n.d. | n.d. | | 1.1+/-0.06 | 0.96 | 1.35 | 1.55 | 1.09 | 1.14 |

# Appendix A.III

# Ion probe data

# (2) Plagioclase data

Correction factors for plagioclase analyses used due to the higher ion yeilds obtained from feldspar than clinopyroxene or glass

| Element | divide by |
|---|---|
| Li | 0.921 |
| Be | 1 |
| Mg | 0.881 |
| K | 0.768 |
| Ti | 0.793 |
| V | 0.704 |
| Cr | 0.704 |
| Rb | 0.768 |
| Sr | 0.796 |
| Y | 0.796 |
| Zr | 0.796 |
| Ba | 0.773 |
| La | 0.859 |
| Ce | 0.859 |
| Pr | 0.859 |
| Nd | 0.859 |
| Sm | 0.859 |
| Eu | 0.859 |
| Gd | 0.859 |
| Tb | 0.859 |
| Dy | 0.859 |
| Ho | 0.859 |
| Er | 0.859 |
| Yb | 0.859 |

| Sample | 153-923A-3R1-2 18-22 | 153-923A-3R1-2 18-22 | 153-923A-3R1-2 18-22 | 153-923A-3R2-2 39-45 | 153-923A-3R2-2 39-45 | 153-923A-3R2-2 39-45 | 153-923A-5R1-2A 46-50 | 153-923A-5R1-2A 46-50 | 153-923A-5R1-2A 46-50 | 153-923A-5R1-2A 46-50 | 153-923A-6R1-9 58-61 | 153-923A-6R1-9 58-61 | 153-923A-8R1-9 126-131 | 153-923A-8R1-9 126-131 | 153-923A-8R1-9 126-131 | 153-923A-8R1-9 126-131 | 153-923A-8R1-9 126-131 |
|---|---|---|---|---|---|---|---|---|---|---|---|---|---|---|---|---|---|
| **Analysis** | P3R1155 | P3R1156 | P3R1157 | P3R2047 | P3R2048 | P3R2049 | P5R1012 | P5R1013 | P5R1014 | P5R1015 | P6R1050 | P6R1051 | P8R1041 | P8R1042 | P8R1043 | P8R1059 | P8R1060 |
| **Depth (m)** | 19.38 | 19.38 | 19.38 | 21.08 | 21.08 | 21.08 | 23.46 | 23.46 | 23.46 | 23.46 | 25.28 | 25.28 | 30.26 | 30.26 | 30.26 | 30.26 | 30.26 |
| **Location** | rim | intermed | core | rim | chadaxst core | core | rim | core | chadaxst core | chadaxst rim | rim | core | rim | core | core | rim | core |
| **SiO2** | 58.63 | 57.72 | 58.53 | 57.91 | 57.76 | 57.56 | 54.75 | 55.94 | 54.77 | 55.00 | 54.55 | 54.54 | 52.93 | 49.56 | 48.92 | 52.52 | 50.17 |
| **TiO2** | 0.02 | 0.05 | 0.07 | 0.02 | 0.06 | 0.02 | 0.04 | 0.01 | 0.07 | 0.08 | 0.10 | 0.08 | 0.08 | 0.04 | 0.01 | 0.03 | 0.01 |
| **Al2O3** | 27.09 | 26.94 | 27.02 | 27.64 | 27.85 | 27.50 | 28.54 | 28.19 | 28.62 | 28.87 | 28.28 | 28.37 | 29.67 | 31.90 | 31.56 | 30.35 | 31.32 |
| **Cr2O3** | 0.04 | 0.02 | 0.03 | 0.04 | 0.00 | 0.04 | 0.05 | 0.02 | 0.01 | 0.04 | 0.04 | 0.01 | 0.00 | 0.01 | 0.02 | 0.02 | 0.04 |
| **FeO** | 0.24 | 0.26 | 0.27 | 0.16 | 0.26 | 0.27 | 0.31 | 0.30 | 0.30 | 0.36 | 0.33 | 0.31 | 0.19 | 0.29 | 0.28 | 0.19 | 0.19 |
| **MnO** | 0.03 | 0.04 | 0.03 | 0.03 | 0.03 | 0.02 | 0.03 | 0.00 | 0.02 | 0.03 | 0.03 | 0.04 | 0.03 | 0.02 | 0.03 | 0.00 | 0.05 |
| **MgO** | 0.00 | 0.03 | 0.01 | 0.02 | 0.01 | 0.00 | 0.03 | 0.04 | 0.03 | 0.03 | 0.03 | 0.02 | 0.01 | 0.03 | 0.02 | 0.02 | 0.01 |
| **CaO** | 9.63 | 9.56 | 9.33 | 9.87 | 9.99 | 9.91 | 11.40 | 10.95 | 11.62 | 11.60 | 11.31 | 11.58 | 13.14 | 15.65 | 15.77 | 13.66 | 15.21 |
| **Na2O** | 6.36 | 5.74 | 6.40 | 6.17 | 6.21 | 6.10 | 5.32 | 5.49 | 5.16 | 5.25 | 5.13 | 4.89 | 4.01 | 2.57 | 2.55 | 3.84 | 2.91 |
| **K2O** | 0.09 | 0.10 | 0.10 | 0.10 | 0.08 | 0.09 | 0.06 | 0.06 | 0.04 | 0.05 | 0.06 | 0.05 | 0.05 | 0.05 | 0.05 | 0.03 | 0.03 |
| **Total** | 102.15 | 100.48 | 101.81 | 101.98 | 102.25 | 101.51 | 100.57 | 101.01 | 100.66 | 101.33 | 99.88 | 99.90 | 100.13 | 100.14 | 99.20 | 100.67 | 99.94 |
| **Cations** | | | | | | | | | | | | | | | | | |
| **Si** | 10.31 | 10.30 | 10.32 | 10.20 | 10.16 | 10.20 | 9.85 | 9.99 | 9.84 | 9.82 | 9.87 | 9.87 | 9.59 | 9.05 | 9.03 | 9.48 | 9.17 |
| **Ti** | 0.00 | 0.01 | 0.01 | 0.00 | 0.01 | 0.00 | 0.01 | 0.00 | 0.01 | 0.01 | 0.01 | 0.01 | 0.01 | 0.01 | 0.00 | 0.00 | 0.00 |
| **Al** | 5.61 | 5.67 | 5.62 | 5.74 | 5.78 | 5.74 | 6.05 | 5.94 | 6.06 | 6.08 | 6.03 | 6.05 | 6.34 | 6.87 | 6.87 | 6.46 | 6.75 |
| **Cr** | 0.01 | 0.00 | 0.00 | 0.01 | 0.00 | 0.01 | 0.01 | 0.00 | 0.00 | 0.01 | 0.01 | 0.00 | 0.00 | 0.00 | 0.00 | 0.00 | 0.01 |
| **Fe** | 0.04 | 0.04 | 0.04 | 0.02 | 0.04 | 0.04 | 0.05 | 0.04 | 0.05 | 0.05 | 0.05 | 0.05 | 0.03 | 0.04 | 0.04 | 0.03 | 0.03 |
| **Mn** | 0.00 | 0.01 | 0.00 | 0.00 | 0.00 | 0.00 | 0.00 | 0.00 | 0.00 | 0.00 | 0.00 | 0.01 | 0.00 | 0.00 | 0.00 | 0.00 | 0.01 |
| **Mg** | 0.00 | 0.01 | 0.00 | 0.01 | 0.00 | 0.00 | 0.01 | 0.01 | 0.01 | 0.01 | 0.01 | 0.01 | 0.00 | 0.01 | 0.01 | 0.00 | 0.00 |
| **Ca** | 1.81 | 1.83 | 1.76 | 1.86 | 1.88 | 1.88 | 2.20 | 2.10 | 2.24 | 2.22 | 2.19 | 2.24 | 2.55 | 3.06 | 3.12 | 2.64 | 2.98 |
| **Na** | 2.17 | 1.99 | 2.19 | 2.11 | 2.12 | 2.09 | 1.86 | 1.90 | 1.80 | 1.82 | 1.80 | 1.72 | 1.41 | 0.91 | 0.91 | 1.34 | 1.03 |
| **K** | 0.02 | 0.02 | 0.02 | 0.02 | 0.02 | 0.02 | 0.01 | 0.01 | 0.01 | 0.01 | 0.01 | 0.01 | 0.01 | 0.01 | 0.01 | 0.01 | 0.01 |
| **Total** | 19.97 | 19.87 | 19.97 | 19.98 | 20.01 | 19.99 | 20.05 | 20.00 | 20.02 | 20.04 | 20.00 | 19.96 | 19.94 | 19.97 | 20.00 | 19.97 | 19.97 |
| **An** | 45.3 | 47.6 | 44.4 | 46.7 | 46.9 | 47.1 | 54.0 | 52.3 | 55.3 | 54.8 | 54.7 | 56.5 | 64.2 | 76.9 | 77.1 | 66.2 | 74.2 |

| Sample | 153-923A-3R1-2 18-22 | 153-923A-3R1-2 18-22 | 153-923A-3R1-2 18-22 | 153-923A-3R2-2 39-45 | 153-923A-3R2-2 39-45 | 153-923A-3R2-2 39-45 | 153-923A-5R1-2A 46-50 | 153-923A-5R1-2A 46-50 | 153-923A-5R1-2A 46-50 | 153-923A-5R1-2A 46-50 | 153-923A-6R1-9 58-61 | 153-923A-6R1-9 58-61 | 153-923A-8R1-9 126-131 | 153-923A-8R1-9 126-131 | 153-923A-8R1-9 126-131 | 153-923A-8R1-9 126-131 | 153-923A-8R1-9 126-131 |
|---|---|---|---|---|---|---|---|---|---|---|---|---|---|---|---|---|---|
| **Analysis** | P3R1155 | P3R1156 | P3R1157 | P3R2047 | P3R2048 | P3R2049 | P5R1012 | P5R1013 | P5R1014 | P5R1015 | P6R1050 | P6R1051 | P8R1041 | P8R1042 | P8R1043 | P8R1059 | P8R1060 |
| **Depth (m)** | 19.38 | 19.38 | 19.38 | 21.08 | 21.08 | 21.08 | 23.46 | 23.46 | 23.46 | 23.46 | 25.28 | 25.28 | 30.26 | 30.26 | 30.26 | 30.26 | 30.26 |
| **Location** | rim | intermed | core | rim | chadaxst core | core | rim | core | chadaxst core | chadaxst rim | rim | core | rim | core | core | rim | core |
| **Traces (ppm)** | | | | | | | | | | | | | | | | | |
| **K** | 772 | 735 | 794 | 877 | 729 | 870 | 415 | 463 | 363 | 361 | 411 | 417 | 292 | 159 | 153 | n.d. | n.d. |
| **Ti** | 165 | 315 | 423 | 231 | 675 | 226 | 380 | 445 | 415 | 322 | 445 | 674 | 316 | 196 | 184 | n.d. | 315 |
| **Ba** | 5.37 | 4.83 | 5.19 | 4.28 | 3.88 | 4.75 | 2.30 | 2.24 | 1.99 | 1.96 | 2.33 | 2.42 | 1.39 | 0.84 | 0.92 | 1.36 | 1.04 |
| **Li** | n.d. | 0.00 | 0.10 | 0.03 | 0.04 | 0.05 | 0.03 | 0.05 | 0.02 | 0.03 | 0.03 | 0.04 | 0.04 | 0.04 | 0.08 | 0.70 | 0.04 |
| **Be** | 0.63 | 0.66 | 0.62 | n.d. | n.d. | n.d. | n.d. | n.d. | n.d. | n.d. | n.d. | n.d. | n.d. | n.d. | n.d. | 0.16 | 0.14 |
| **Mg** | n.d. | n.d. | n.d. | 234 | 201 | 239 | 223 | 328 | 200 | 208 | 163 | 236 | 205 | 216 | 178 | 11 | n.d. |
| **V** | n.d. | n.d. | n.d. | 6.95 | 9.88 | 6.93 | 7.32 | 9.22 | 8.55 | 6.66 | 6.38 | 7.77 | 5.98 | 7.19 | 6.88 | n.d. | n.d. |
| **Cr** | n.d. | n.d. | n.d. | 1.07 | 0.82 | 0.95 | 0.68 | 1.36 | 0.80 | 0.85 | 0.73 | 0.83 | 0.72 | 0.51 | 0.45 | n.d. | n.d. |
| **Rb** | 0.30 | 0.31 | 0.28 | 0.24 | 0.33 | 0.32 | 0.31 | 0.35 | 0.28 | 0.22 | 0.20 | 0.20 | 0.25 | 0.28 | 0.29 | 0.34 | 0.14 |
| **Sr** | n.d. | n.d. | n.d. | 256 | 248 | 251 | 229 | 231 | 226 | 230 | 230 | 230 | 185 | 184 | 183 | n.d. | n.d. |
| **Y** | 0.48 | 0.49 | 0.49 | 0.50 | 0.36 | 0.34 | 0.25 | 0.36 | 0.27 | 0.22 | 0.19 | 0.20 | 0.28 | 0.47 | 0.37 | 0.26 | 0.35 |
| **Zr** | 0.02 | 0.02 | 0.04 | 0.01 | 0.05 | 0.04 | 0.03 | 0.03 | 0.08 | 0.01 | 0.03 | 0.03 | 0.04 | 0.09 | 0.08 | 0.03 | 0.03 |
| **La** | 1.33 | 1.14 | 1.01 | 0.99 | 0.42 | 0.88 | 0.52 | 0.43 | 0.25 | 0.49 | 0.44 | 0.55 | 0.41 | 0.15 | 0.15 | 0.40 | 0.44 |
| **Ce** | 2.78 | 2.48 | 2.13 | 2.36 | 1.00 | 2.20 | 1.14 | 1.15 | 0.73 | 1.18 | 0.94 | 1.06 | 1.05 | 0.45 | 0.34 | 1.13 | 1.26 |
| **Pr** | 0.33 | 0.31 | 0.29 | 0.26 | 0.14 | 0.28 | 0.13 | 0.13 | 0.09 | 0.16 | 0.10 | 0.15 | 0.11 | 0.06 | 0.06 | 0.14 | 0.18 |
| **Nd** | 1.39 | 1.40 | 1.20 | 1.45 | 0.57 | 1.29 | 0.69 | 0.59 | 0.53 | 0.55 | 0.51 | 0.79 | 0.77 | 0.25 | 0.29 | 0.73 | 0.71 |
| **Sm** | 0.20 | 0.27 | 0.25 | 0.21 | 0.23 | 0.14 | 0.05 | 0.15 | 0.14 | 0.12 | 0.07 | 0.21 | 0.10 | 0.14 | 0.12 | 0.15 | 0.14 |
| **Eu** | 1.38 | 1.31 | 1.30 | 1.11 | 0.82 | 0.96 | 0.44 | 0.49 | 0.41 | 0.52 | 0.45 | 0.41 | 0.34 | 0.39 | 0.35 | 0.33 | 0.36 |
| **Gd** | 0.11 | 0.10 | 0.09 | 0.12 | 0.07 | 0.21 | 0.00 | 0.00 | 0.00 | 0.00 | 0.16 | 0.14 | 0.11 | 0.07 | 0.09 | 0.11 | 0.12 |
| **Tb** | 0.02 | 0.02 | 0.02 | 0.02 | 0.02 | 0.03 | 0.01 | 0.02 | 0.02 | 0.00 | 0.02 | 0.03 | 0.01 | 0.02 | 0.00 | 0.00 | 0.02 |
| **Dy** | 0.11 | 0.10 | 0.10 | 0.07 | 0.07 | 0.06 | 0.02 | 0.04 | 0.07 | 0.04 | 0.01 | 0.01 | 0.03 | 0.08 | 0.05 | 0.02 | 0.07 |
| **Ho** | 0.02 | 0.02 | 0.02 | n.d. | n.d. | n.d. | n.d. | n.d. | n.d. | n.d. | n.d. | n.d. | n.d. | n.d. | n.d. | n.d. | n.d. |
| **Er** | 0.06 | 0.04 | 0.04 | 0.09 | b.d.l. | b.d.l. | 0.02 | 0.02 | 0.03 | 0.01 | 0.04 | 0.06 | 0.02 | 0.04 | 0.05 | 0.01 | 0.01 |
| **Tm** | n.d. | n.d. | n.d. | b.d.l. | 0.08 | 0.13 | 0.00 | 0.01 | b.d.l. | b.d.l. | 0.00 | 0.01 | 0.00 | b.d.l. | 0.00 | 0.02 | 0.02 |
| **Yb** | 0.02 | 0.04 | 0.03 | 0.02 | b.d.l. | 0.09 | n.d. | n.d. | n.d. | n.d. | 0.03 | 0.05 | 0.02 | 0.04 | 0.02 | 0.01 | 0.02 |

| Sample | 153-923A-8R2-8 81-88 | 153-923A-8R2-8 81-88 | 153-923A-8R2-8 81-88 | 153-923A-8R2-8 81-88 | 153-923A-8R2-8 81-88 | 153-923A-8R2-8 81-88 | 153-923A-8R2-8 81-88 | 153-923A-8R2-8 81-88 | 153-923A-8R2-8 81-88 | 153-923A-8R2-8 81-88 | 153-923A-8R2-8 81-88 | 153-923A-9R2-9A 101-103 | 153-923A-9R2-9A 101-103 | 153-923A-9R2-9A 101-103 | 153-923A-10R2-1A 1-4 | 153-923A-10R2-1A 1-4 |
|---|---|---|---|---|---|---|---|---|---|---|---|---|---|---|---|---|
| **Analysis** | P8R2008 | P8R2009 | P8R2010 | P8R2062 | P8R2111 | P8R2112 | P8R2064 | P8R2113 | P8R263 | P8R2011 | P8R2114 | P9R2044 | P9R2045 | P9R2046 | P10R052 | P10R053 |
| **Depth (m)** | 31.31 | 31.31 | 31.31 | 31.31 | 31.31 | 31.31 | 31.31 | 31.31 | 31.31 | 31.31 | 31.31 | 34.41 | 34.41 | 34.41 | 38.01 | 38.01 |
| **Location** | chadaxst rim | chadaxst core | 0.12 | 0.14 | 0.16 | traverse 0.42 | distance 1.04 | from 1.58 | rim 2.02 | (mm) 2.18 | 2.88 | core | rim | rim | rim | core |
| **SiO2** | 54.62 | 55.56 | 54.39 | 54.39 | 54.15 | 53.72 | 53.45 | 53.90 | 53.90 | 54.66 | 53.64 | 50.72 | 53.30 | 51.23 | 52.20 | 53.29 |
| **TiO2** | 0.05 | 0.02 | 0.03 | 0.03 | 0.02 | 0.03 | 0.06 | 0.02 | 0.02 | 0.03 | 0.06 | 0.02 | 0.07 | 0.02 | 0.02 | 0.08 |
| **Al2O3** | 28.38 | 28.06 | 28.86 | 28.86 | 29.19 | 29.52 | 29.45 | 29.32 | 29.32 | 29.90 | 29.31 | 30.57 | 29.68 | 31.00 | 29.50 | 28.80 |
| **Cr2O3** | 0.02 | 0.00 | 0.03 | 0.03 | 0.02 | 0.04 | 0.01 | 0.04 | 0.04 | 0.02 | 0.02 | 0.00 | 0.02 | 0.02 | 0.05 | 0.01 |
| **FeO** | 0.22 | 0.21 | 0.27 | 0.27 | 0.30 | 0.32 | 0.34 | 0.38 | 0.38 | 0.35 | 0.35 | 0.26 | 0.24 | 0.27 | 0.20 | 0.42 |
| **MnO** | 0.03 | 0.04 | 0.02 | 0.02 | 0.02 | 0.03 | 0.02 | 0.03 | 0.03 | 0.03 | 0.02 | 0.03 | 0.02 | 0.01 | 0.03 | 0.03 |
| **MgO** | 0.01 | 0.03 | 0.04 | 0.04 | 0.02 | 0.00 | 0.05 | 0.02 | 0.02 | 0.05 | 0.00 | 0.05 | 0.03 | 0.03 | 0.04 | 0.03 |
| **CaO** | 11.33 | 11.01 | 11.90 | 11.90 | 12.06 | 12.23 | 12.57 | 12.34 | 12.34 | 12.64 | 12.26 | 14.46 | 12.98 | 14.58 | 12.95 | 12.18 |
| **Na2O** | 4.99 | 5.37 | 4.98 | 4.98 | 4.84 | 4.65 | 4.64 | 4.73 | 4.73 | 4.66 | 4.73 | 3.47 | 4.57 | 3.52 | 4.19 | 4.58 |
| **K2O** | 0.06 | 0.06 | 0.08 | 0.08 | 0.06 | 0.05 | 0.06 | 0.05 | 0.05 | 0.07 | 0.06 | 0.04 | 0.06 | 0.02 | 0.06 | 0.04 |
| **Total** | 99.73 | 100.39 | 100.62 | 100.62 | 100.70 | 100.62 | 100.66 | 100.85 | 100.85 | 102.43 | 100.46 | 99.64 | 100.99 | 100.73 | 99.26 | 99.48 |
| **Cations** | | | | | | | | | | | | | | | | |
| **Si** | 9.89 | 9.98 | 9.79 | 9.79 | 9.74 | 9.67 | 9.64 | 9.69 | 9.69 | 9.68 | 9.68 | 9.29 | 9.59 | 9.28 | 9.55 | 9.71 |
| **Ti** | 0.01 | 0.00 | 0.00 | 0.00 | 0.00 | 0.00 | 0.01 | 0.00 | 0.00 | 0.00 | 0.01 | 0.00 | 0.01 | 0.00 | 0.00 | 0.01 |
| **Al** | 6.06 | 5.94 | 6.12 | 6.12 | 6.19 | 6.27 | 6.26 | 6.22 | 6.22 | 6.24 | 6.24 | 6.60 | 6.30 | 6.62 | 6.36 | 6.19 |
| **Cr** | 0.00 | 0.00 | 0.00 | 0.00 | 0.00 | 0.01 | 0.00 | 0.01 | 0.01 | 0.00 | 0.00 | 0.00 | 0.00 | 0.00 | 0.01 | 0.00 |
| **Fe** | 0.03 | 0.03 | 0.04 | 0.04 | 0.05 | 0.05 | 0.05 | 0.06 | 0.06 | 0.05 | 0.05 | 0.04 | 0.04 | 0.04 | 0.03 | 0.06 |
| **Mn** | 0.00 | 0.01 | 0.00 | 0.00 | 0.00 | 0.00 | 0.00 | 0.00 | 0.00 | 0.00 | 0.00 | 0.00 | 0.00 | 0.00 | 0.00 | 0.00 |
| **Mg** | 0.00 | 0.01 | 0.01 | 0.01 | 0.01 | 0.00 | 0.01 | 0.01 | 0.01 | 0.01 | 0.00 | 0.01 | 0.01 | 0.01 | 0.01 | 0.01 |
| **Ca** | 2.20 | 2.12 | 2.29 | 2.29 | 2.32 | 2.36 | 2.43 | 2.38 | 2.38 | 2.40 | 2.37 | 2.84 | 2.50 | 2.83 | 2.54 | 2.38 |
| **Na** | 1.75 | 1.87 | 1.74 | 1.74 | 1.69 | 1.62 | 1.62 | 1.65 | 1.65 | 1.60 | 1.66 | 1.23 | 1.59 | 1.24 | 1.49 | 1.62 |
| **K** | 0.01 | 0.01 | 0.02 | 0.02 | 0.01 | 0.01 | 0.01 | 0.01 | 0.01 | 0.02 | 0.01 | 0.01 | 0.01 | 0.00 | 0.01 | 0.01 |
| **Total** | 19.96 | 19.98 | 20.02 | 20.02 | 20.01 | 20.00 | 20.04 | 20.02 | 20.02 | 20.01 | 20.03 | 20.03 | 20.06 | 20.03 | 20.01 | 20.00 |
| **An** | 55.5 | 52.9 | 56.6 | 56.6 | 57.7 | 59.1 | 59.7 | 58.9 | 58.9 | 59.7 | 58.7 | 69.6 | 60.9 | 69.5 | 62.9 | 59.4 |

| Sample | 153-923A-8R2-8 81-88 | 153-923A-8R2-8 81-88 | 153-923A-8R2-8 81-88 | 153-923A-8R2-8 81-88 | 153-923A-8R2-8 81-88 | 153-923A-8R2-8 81-88 | 153-923A-8R2-8 81-88 | 153-923A-8R2-8 81-88 | 153-923A-8R2-8 81-88 | 153-923A-8R2-8 81-88 | 153-923A-8R2-8 81-88 | 153-923A-9R2-9A 101-103 | 153-923A-9R2-9A 101-103 | 153-923A-9R2-9A 101-103 | 153-923A-10R2-1A 1-4 | 153-923A-10R2-1A 1-4 |
|---|---|---|---|---|---|---|---|---|---|---|---|---|---|---|---|---|
| **Analysis** | P8R2008 | P8R2009 | P8R2010 | P8R2062 | P8R2111 | P8R2112 | P8R2064 | P8R2113 | P8R263 | P8R2011 | P8R2114 | P9R2044 | P9R2045 | P9R2046 | P10R052 | P10R053 |
| **Depth (m)** | 31.31 | 31.31 | 31.31 | 31.31 | 31.31 | 31.31 | 31.31 | 31.31 | 31.31 | 31.31 | 31.31 | 34.41 | 34.41 | 34.41 | 38.01 | 38.01 |
| **Location** | chadaxst rim | chadaxst core | 0.12 | 0.14 | 0.16 | traverse 0.42 | distance 1.04 | from 1.58 | rim 2.02 | (mm) 2.18 | 2.88 | core | rim | rim | rim | core |
| **Traces (ppm)** | | | | | | | | | | | | | | | | |
| **K** | 399 | 471 | 399 | n.d. | 438 | 356 | n.d. | 398 | n.d. | 404 | 380 | 385 | 391 | 363 | 387 | 440 |
| **Ti** | 180 | 287 | 251 | 345 | 387 | 332 | 377 | 389 | 339 | 357 | 383 | 395 | 327 | 322 | 343 | 387 |
| **Ba** | 2.42 | 3.62 | 2.21 | 2.15 | 2.46 | 1.61 | 1.11 | 0.95 | 0.84 | 0.91 | 0.93 | 1.50 | 1.96 | 1.96 | 1.83 | 2.01 |
| **Li** | 0.03 | 0.07 | 0.03 | 0.05 | 0.06 | 0.10 | 0.11 | 0.05 | 0.14 | 0.17 | 0.03 | 0.02 | 0.02 | 0.03 | 0.02 | 0.22 |
| **Be** | n.d. | n.d. | n.d. | 0.22 | 0.21 | 0.18 | 0.13 | 0.10 | 0.11 | n.d. | 0.11 | n.d. | n.d. | n.d. | n.d. | n.d. |
| **Mg** | 139 | 502 | 167 | n.d. | n.d. | n.d. | n.d. | n.d. | n.d. | 336 | n.d. | 224 | 192 | 161 | 260 | 251 |
| **V** | 6.10 | 7.22 | 6.29 | n.d. | n.d. | n.d. | n.d. | n.d. | n.d. | 9.10 | n.d. | 7.08 | 6.07 | 6.33 | 6.18 | 7.48 |
| **Cr** | 0.75 | 1.19 | 0.68 | n.d. | n.d. | n.d. | n.d. | n.d. | n.d. | 1.05 | n.d. | 0.72 | 0.74 | 0.71 | 0.76 | 0.76 |
| **Rb** | 0.24 | 0.36 | 0.25 | 0.21 | 0.22 | 0.21 | 0.31 | 0.28 | 0.28 | 0.36 | 0.25 | 0.25 | 0.34 | 0.24 | 0.21 | 0.30 |
| **Sr** | 228 | 243 | 226 | n.d. | n.d. | n.d. | n.d. | n.d. | n.d. | 204 | n.d. | 216 | 226 | 232 | 222 | 215 |
| **Y** | 0.21 | 0.22 | 0.23 | 0.28 | 0.31 | 0.35 | 0.34 | 0.27 | 0.23 | 0.26 | 0.28 | 0.25 | 0.22 | 0.23 | 0.30 | 0.29 |
| **Zr** | 0.03 | 0.03 | 0.02 | 0.03 | 0.02 | 0.04 | 0.04 | 0.05 | 0.04 | 0.07 | 0.03 | 0.05 | 0.04 | 0.02 | 0.03 | 0.03 |
| **La** | 0.92 | 0.97 | 0.74 | 0.79 | 0.84 | 0.43 | 0.15 | 0.18 | 0.15 | 0.14 | 0.18 | 0.44 | 0.45 | 0.52 | 0.40 | 0.23 |
| **Ce** | 1.73 | 1.84 | 1.58 | 1.69 | 1.72 | 1.18 | 0.48 | 0.44 | 0.38 | 0.44 | 0.43 | 1.01 | 1.10 | 1.12 | 1.05 | 0.70 |
| **Pr** | 0.19 | 0.22 | 0.15 | 0.19 | 0.19 | 0.14 | 0.08 | 0.06 | 0.07 | 0.06 | 0.06 | 0.13 | 0.13 | 0.16 | 0.14 | 0.07 |
| **Nd** | 0.66 | 0.92 | 0.79 | 0.82 | 0.76 | 0.70 | 0.43 | 0.34 | 0.33 | 0.46 | 0.42 | 0.47 | 0.53 | 0.65 | 1.01 | 0.57 |
| **Sm** | 0.10 | 0.10 | 0.15 | 0.12 | 0.12 | 0.11 | 0.08 | 0.08 | 0.08 | 0.06 | 0.09 | 0.07 | 0.07 | 0.07 | 0.14 | 0.09 |
| **Eu** | 0.59 | 0.55 | 0.53 | 0.49 | 0.46 | 0.46 | 0.33 | 0.33 | 0.31 | 0.37 | 0.31 | 0.41 | 0.49 | 0.53 | 0.44 | 0.41 |
| **Gd** | 0.00 | 0.00 | 0.00 | 0.10 | 0.11 | 0.11 | 0.11 | 0.07 | 0.04 | 0.00 | 0.08 | 0.01 | 0.16 | b.d.l. | b.d.l. | 0.15 |
| **Tb** | 0.01 | 0.01 | 0.01 | 0.01 | 0.01 | 0.01 | 0.02 | 0.01 | 0.01 | 0.01 | 0.01 | 0.02 | 0.02 | 0.01 | 0.01 | 0.02 |
| **Dy** | 0.06 | 0.05 | 0.02 | 0.05 | 0.07 | 0.05 | 0.07 | 0.06 | 0.04 | 0.08 | 0.07 | 0.04 | 0.03 | 0.06 | 0.13 | b.d.l. |
| **Ho** | n.d. | n.d. | n.d. | n.d. | 0.01 | 0.01 | n.d | 0.01 | n.d. | n.d. | 0.01 | n.d. | n.d. | n.d. | n.d. | n.d. |
| **Er** | 0.03 | 0.06 | 0.03 | 0.01 | 0.02 | 0.08 | 0.01 | 0.03 | 0.01 | 0.02 | 0.13 | 0.02 | 0.02 | 0.06 | 0.06 | b.d.l. |
| **Tm** | 0.00 | b.d.l. | b.d.l. | 0.03 | n.d. | n.d. | 0.01 | n.d. | 0.03 | b.d.l. | n.d. | 0.01 | 0.03 | 0.01 | b.d.l. | 0.01 |
| **Yb** | n.d. | n.d. | n.d. | 0.02 | 0.02 | 0.02 | 0.03 | 0.02 | 0.04 | n.d. | 0.03 | 0.02 | 0.00 | 0.04 | 0.12 | 0.03 |

| Sample | 153-923A-11R2-6B 87-91 | 153-923A-11R2-6B 87-91 | 153-923A-11R2-6B 87-91 | 153-923A-12R1-4 30-38 | 153-923A-12R1-4 30-38 | 153-923A-12R1-4 30-38 | 153-923A-12R1-4 30-38 | 153-923A-12R1-4 30-38 | 153-923A-12R1-4 30-38 | 153-923A-12R1-4 30-38 | 153-923A-12R1-4 30-38 | 153-923A-12R1-5 133-139 | 153-923A-12R1-5 133-139 | 153-923A-12R1-5 133-139 | 153-923A-12R1-5 133-139 | 153-923A-12R1-5 133-139 | 153-923A-12R2-5 66-73 |
|---|---|---|---|---|---|---|---|---|---|---|---|---|---|---|---|---|---|
| **Analysis** | P11R001 | P11R002 | P11R003 | P12R021 | P12R022 | P12R023 | P12R025 | P12R026 | P12R027 | P12R076 | P12R077 | P133036 | P133037 | P133038 | P133094 | P133095 | P12R254 |
| **Depth (m)** | 43.57 | 43.57 | 43.57 | 46.30 | 46.30 | 46.30 | 46.30 | 46.30 | 46.30 | 46.30 | 46.30 | 47.33 | 47.33 | 47.33 | 47.33 | 47.33 | 48.66 |
| **Location** | rim | int | core | intermed | core | core | rim | core | rim | core | rim | core | rim | core | rim | core | core |
| **SiO2** | 51.33 | 52.45 | 49.56 | 52.19 | 50.31 | 50.41 | 48.66 | 50.15 | 49.53 | 49.85 | 51.57 | 50.71 | 49.56 | 49.22 | 52.45 | 51.33 | 52.86 |
| **TiO2** | 0.05 | 0.07 | 0.07 | 0.05 | 0.04 | 0.04 | 0.03 | 0.07 | 0.01 | 0.07 | 0.10 | 0.05 | 0.07 | 0.02 | 0.07 | 0.05 | 0.02 |
| **Al2O3** | 30.23 | 29.33 | 31.25 | 30.25 | 31.36 | 31.56 | 32.22 | 31.56 | 32.45 | 30.99 | 29.97 | 30.24 | 31.25 | 31.83 | 29.33 | 30.23 | 29.30 |
| **Cr2O3** | 0.04 | 0.00 | 0.04 | 0.01 | 0.04 | 0.03 | 0.04 | 0.01 | 0.02 | 0.01 | 0.04 | 0.04 | 0.04 | 0.02 | 0.00 | 0.04 | 0.02 |
| **FeO** | 0.32 | 0.25 | 0.25 | 0.22 | 0.20 | 0.16 | 0.17 | 0.17 | 0.19 | 0.25 | 0.59 | 0.31 | 0.25 | 0.30 | 0.25 | 0.32 | 0.21 |
| **MnO** | 0.03 | 0.01 | 0.01 | 0.01 | 0.00 | 0.03 | 0.01 | 0.01 | 0.02 | 0.03 | 0.03 | 0.02 | 0.01 | 0.03 | 0.01 | 0.03 | 0.00 |
| **MgO** | 0.02 | 0.03 | 0.03 | 0.03 | 0.00 | 0.02 | 0.02 | 0.03 | 0.03 | 0.01 | 0.49 | 0.02 | 0.03 | 0.03 | 0.03 | 0.02 | 0.02 |
| **CaO** | 13.61 | 12.76 | 15.14 | 13.22 | 14.43 | 14.65 | 15.76 | 14.82 | 15.73 | 14.99 | 13.57 | 13.90 | 15.14 | 15.74 | 12.76 | 13.61 | 12.25 |
| **Na2O** | 3.80 | 4.23 | 3.06 | 4.12 | 3.34 | 3.29 | 2.70 | 3.35 | 2.97 | 3.01 | 3.58 | 3.62 | 3.06 | 2.75 | 4.23 | 3.80 | 4.70 |
| **K2O** | 0.05 | 0.04 | 0.04 | 0.04 | 0.04 | 0.01 | 0.03 | 0.02 | 0.02 | 0.01 | 0.00 | 0.03 | 0.04 | 0.04 | 0.04 | 0.05 | 0.04 |
| **Total** | 99.48 | 99.19 | 99.45 | 100.17 | 99.78 | 100.21 | 99.66 | 100.21 | 100.99 | 99.24 | 99.98 | 98.96 | 99.45 | 100.00 | 99.19 | 99.48 | 99.46 |
| **Cations** | | | | | | | | | | | | | | | | | |
| **Si** | 9.39 | 9.59 | 9.11 | 9.47 | 9.19 | 9.18 | 8.94 | 9.14 | 8.98 | 9.17 | 9.40 | 9.34 | 9.11 | 9.02 | 9.59 | 9.39 | 9.64 |
| **Ti** | 0.01 | 0.01 | 0.01 | 0.01 | 0.01 | 0.01 | 0.00 | 0.01 | 0.00 | 0.01 | 0.01 | 0.01 | 0.01 | 0.00 | 0.01 | 0.01 | 0.00 |
| **Al** | 6.52 | 6.32 | 6.77 | 6.47 | 6.76 | 6.77 | 6.98 | 6.78 | 6.94 | 6.72 | 6.44 | 6.57 | 6.77 | 6.87 | 6.32 | 6.52 | 6.30 |
| **Cr** | 0.01 | 0.00 | 0.01 | 0.00 | 0.01 | 0.00 | 0.01 | 0.00 | 0.00 | 0.00 | 0.01 | 0.01 | 0.01 | 0.00 | 0.00 | 0.01 | 0.00 |
| **Fe** | 0.05 | 0.04 | 0.04 | 0.03 | 0.03 | 0.02 | 0.03 | 0.03 | 0.03 | 0.04 | 0.09 | 0.05 | 0.04 | 0.05 | 0.04 | 0.05 | 0.03 |
| **Mn** | 0.00 | 0.00 | 0.00 | 0.00 | 0.00 | 0.00 | 0.00 | 0.00 | 0.00 | 0.00 | 0.00 | 0.00 | 0.00 | 0.00 | 0.00 | 0.00 | 0.00 |
| **Mg** | 0.01 | 0.01 | 0.01 | 0.01 | 0.00 | 0.01 | 0.01 | 0.01 | 0.01 | 0.00 | 0.13 | 0.01 | 0.01 | 0.01 | 0.01 | 0.01 | 0.01 |
| **Ca** | 2.67 | 2.50 | 2.98 | 2.57 | 2.83 | 2.86 | 3.10 | 2.89 | 3.06 | 2.96 | 2.65 | 2.74 | 2.98 | 3.09 | 2.50 | 2.67 | 2.39 |
| **Na** | 1.35 | 1.50 | 1.09 | 1.45 | 1.18 | 1.16 | 0.96 | 1.18 | 1.04 | 1.08 | 1.27 | 1.29 | 1.09 | 0.98 | 1.50 | 1.35 | 1.66 |
| **K** | 0.01 | 0.01 | 0.01 | 0.01 | 0.01 | 0.00 | 0.01 | 0.00 | 0.00 | 0.00 | 0.00 | 0.01 | 0.01 | 0.01 | 0.01 | 0.01 | 0.01 |
| **Total** | 20.02 | 19.99 | 20.04 | 20.02 | 20.01 | 20.01 | 20.04 | 20.05 | 20.07 | 19.99 | 20.00 | 20.02 | 20.04 | 20.03 | 19.99 | 20.02 | 20.05 |
| **An** | 66.2 | 62.4 | 73.1 | 63.8 | 70.3 | 71.1 | 76.2 | 70.9 | 74.5 | 73.3 | 67.7 | 67.9 | 73.1 | 75.8 | 62.4 | 66.2 | 58.9 |

| Sample | 153-923A-11R2-6B 87-91 | 153-923A-11R2-6B 87-91 | 153-923A-11R2-6B 87-91 | 153-923A-12R1-4 30-38 | 153-923A-12R1-4 30-38 | 153-923A-12R1-4 30-38 | 153-923A-12R1-4 30-38 | 153-923A-12R1-4 30-38 | 153-923A-12R1-4 30-38 | 153-923A-12R1-4 30-38 | 153-923A-12R1-4 30-38 | 153-923A-12R1-5 133-139 | 153-923A-12R1-5 133-139 | 153-923A-12R1-5 133-139 | 153-923A-12R1-5 133-139 | 153-923A-12R1-5 133-139 | 153-923A-12R2-5 66-73 |
|---|---|---|---|---|---|---|---|---|---|---|---|---|---|---|---|---|---|
| **Analysis** | P11R001 | P11R002 | P11R003 | P12R021 | P12R022 | P12R023 | P12R025 | P12R026 | P12R027 | P12R076 | P12R077 | P133036 | P133037 | P133038 | P133094 | P133095 | P12R254 |
| **Depth (m)** | 43.57 | 43.57 | 43.57 | 46.30 | 46.30 | 46.30 | 46.30 | 46.30 | 46.30 | 46.30 | 46.30 | 47.33 | 47.33 | 47.33 | 47.33 | 47.33 | 48.66 |
| **Location** | rim | int | core | intermed | core | core | rim | core | rim | core | rim | core | rim | core | rim | core | core |
| **Traces (ppm)** | | | | | | | | | | | | | | | | | |
| **K** | 492 | 441 | 392 | 248 | 222 | 154 | 228 | 178 | 164 | n.d. | n.d. | 281 | 228 | 259 | n.d. | n.d. | 271 |
| **Tl** | 392 | 310 | 364 | 518 | 313 | 225 | 538 | 251 | 356 | 266 | 748 | 329 | 226 | 344 | 303 | 386 | 320 |
| **Ba** | 2.30 | 2.15 | 1.90 | 1.62 | 1.19 | 1.10 | 1.39 | 1.25 | 1.23 | 0.81 | 1.27 | 0.71 | 0.86 | 1.11 | 1.51 | 1.09 | 1.51 |
| **Li** | 0.03 | 0.01 | 1.98 | 0.01 | 0.61 | 0.01 | 0.01 | 0.01 | 0.01 | 0.01 | 0.00 | 0.17 | 0.02 | 0.01 | 0.13 | 0.01 | 0.03 |
| **Be** | n.d. | n.d. | n.d. | n.d. | n.d. | n.d. | n.d. | n.d. | n.d. | 0.14 | 0.14 | n.d. | n.d. | n.d. | 0.23 | 0.18 | n.d. |
| **Mg** | 170 | 178 | 207 | 162 | 1578 | 199 | 176 | 249 | 200 | n.d. | n.d. | 369 | 170 | 225 | n.d. | n.d. | 217 |
| **V** | 6.04 | 5.93 | 8.25 | 9.00 | 7.05 | 6.63 | 6.69 | 7.80 | 5.30 | n.d. | n.d. | 10.41 | 5.97 | 7.10 | n.d. | n.d. | 6.32 |
| **Cr** | 0.74 | 0.76 | 0.66 | 0.70 | 2.16 | 0.67 | 0.75 | 0.71 | 0.76 | n.d. | n.d. | 0.73 | 0.44 | 0.58 | n.d. | n.d. | 0.69 |
| **Rb** | 0.33 | 0.35 | 0.41 | 0.19 | 0.21 | 0.25 | 0.22 | 0.21 | 0.22 | 0.17 | 0.16 | 0.32 | 0.20 | 0.21 | 1.01 | 0.25 | 0.17 |
| **Sr** | 222 | 222 | 223 | 189 | 183 | 184 | 176 | 182 | 181 | n.d. | n.d. | 178 | 177 | 179 | n.d. | n.d. | 211 |
| **Y** | 0.31 | 0.26 | 0.40 | 0.50 | 0.46 | 0.49 | 0.27 | 0.52 | 0.27 | 0.60 | 0.34 | 0.91 | 0.55 | 0.81 | 0.35 | 0.57 | 0.17 |
| **Zr** | 0.04 | 0.06 | 0.05 | 0.05 | 0.05 | 0.03 | 0.07 | 0.04 | 0.08 | 0.03 | 0.11 | 0.08 | 0.03 | 0.06 | 0.03 | 0.02 | 0.03 |
| **La** | 0.56 | 0.64 | 0.20 | 0.39 | 0.36 | 0.21 | 0.40 | 0.36 | 0.46 | 0.15 | 0.46 | 0.22 | 0.63 | 0.32 | 0.64 | 0.23 | 0.33 |
| **Ce** | 1.30 | 1.30 | 0.59 | 1.01 | 0.89 | 0.66 | 1.05 | 0.90 | 1.29 | 0.41 | 1.21 | 0.54 | 1.62 | 1.00 | 1.47 | 0.68 | 0.67 |
| **Pr** | 0.15 | 0.18 | 0.07 | 0.16 | 0.14 | 0.07 | 0.16 | 0.13 | 0.14 | 0.07 | 0.15 | 0.08 | 0.24 | 0.16 | 0.18 | 0.11 | 0.10 |
| **Nd** | 0.69 | 0.79 | 0.43 | 0.75 | 0.58 | 0.48 | 0.68 | 0.86 | 0.79 | 0.41 | 0.75 | 0.54 | 1.06 | 0.62 | 0.77 | 0.51 | 0.37 |
| **Sm** | 0.17 | 0.13 | 0.05 | 0.18 | 0.10 | 0.08 | 0.16 | 0.28 | 0.11 | 0.13 | 0.16 | 0.15 | 0.21 | 0.13 | 0.13 | 0.11 | 0.09 |
| **Eu** | 0.50 | 0.46 | 0.56 | 0.36 | 0.31 | 0.35 | 0.35 | 0.38 | 0.37 | 0.29 | 0.38 | 0.30 | 0.34 | 0.43 | 0.39 | 0.40 | 0.26 |
| **Gd** | 0.00 | 0.00 | 0.00 | 0.09 | 0.28 | 0.28 | 0.12 | 0.16 | 0.21 | 0.14 | 0.17 | 0.14 | 0.10 | 0.13 | 0.14 | 0.13 | b.d.l. |
| **Tb** | 0.02 | 0.02 | 0.02 | 0.02 | 0.02 | 0.03 | 0.01 | 0.04 | 0.01 | 0.02 | 0.01 | 0.03 | 0.04 | 0.05 | 0.01 | 0.02 | 0.01 |
| **Dy** | 0.07 | 0.09 | 0.15 | 0.12 | 0.09 | 0.15 | 0.07 | 0.08 | 0.57 | 0.09 | 0.07 | 0.15 | 0.07 | 0.21 | 0.05 | 0.12 | b.d.l. |
| **Ho** | n.d. | n.d. | n.d. | n.d. | n.d. | n.d. | n.d. | n.d. | n.d. | 0.02 | 0.01 | n.d. | n.d. | n.d. | 0.01 | 0.02 | n.d. |
| **Er** | 0.03 | 0.05 | 0.04 | 0.04 | 0.05 | 0.03 | 0.04 | 0.03 | 0.11 | 0.06 | 0.02 | 0.06 | 0.02 | 0.02 | 0.02 | 0.05 | b.d.l. |
| **Tm** | 0.01 | 0.02 | 0.00 | b.d.l. | 0.01 | 0.00 | 0.00 | 0.02 | 0.02 | n.d. | n.d. | 0.01 | 0.00 | 0.01 | n.d. | n.d. | 0.01 |
| **Yb** | 0.07 | 0.02 | n.d. | 0.06 | 0.05 | 0.06 | b.d.l. | 0.02 | 0.00 | 0.03 | 0.01 | 0.08 | 0.09 | 0.06 | 0.01 | 0.03 | 0.05 |

| Sample | 153-923A-12R2-5 66-73 | 153-923A-12R2-5 66-73 | 153-923A-12R2-5 66-73 | 153-923A-13R2-6B 68-75 | 153-923A-13R2-6B 68-75 | 153-923A-13R2-6B 68-75 | 153-923A-13R2-6B 68-75 | 153-923A-13R2-6B 68-75 | 153-923A-13R2-6B 68-75 | 153-923A-13R2-6B 68-75 | 153-923A-13R2-6B 68-75 | 153-923A-14R1-12 100-112 | 153-923A-14R1-12 100-112 | 153-923A-14R1-12 100-112 | 153-923A-14R1-12 100-112 | 153-923A-14R1-12 100-112 | 153-923A-14R1-12 100-112 |
|---|---|---|---|---|---|---|---|---|---|---|---|---|---|---|---|---|---|
| Analysis | P12R255 | P12R256 | P12R257 | P13R017 | P13R018 | P13R019 | P13R020 | P13R069 | P13R070 | P13R71 | P13R072 | P14R028 | P14R029 | P14R030 | P14R031 | P14R065 | P14R066 |
| Depth (m) | 48.66 | 48.66 | 48.66 | 52.98 | 52.98 | 52.98 | 52.98 | 52.98 | 52.98 | 52.98 | 52.98 | 56.58 | 56.58 | 56.58 | 56.58 | 56.58 | 56.58 |
| Location | core | rim | core | core | rim | core | rim | core | rim | rim | core | core | intermed | rim | core | core | rim |
| SiO2 | 52.62 | 53.13 | 53.96 | 50.39 | 50.62 | 49.88 | 54.90 | 50.49 | 52.22 | 53.07 | 50.39 | 51.10 | 49.28 | 51.99 | 50.25 | 49.56 | 51.36 |
| TiO2 | 0.01 | 0.08 | 0.07 | 0.04 | 0.03 | 0.06 | 0.08 | 0.00 | 0.05 | 0.08 | 0.04 | 0.00 | 0.04 | 0.08 | 0.03 | 0.04 | 0.06 |
| Al2O3 | 29.07 | 28.73 | 28.33 | 30.85 | 30.19 | 30.57 | 29.35 | 30.65 | 29.71 | 28.60 | 30.85 | 30.80 | 30.77 | 30.23 | 30.43 | 31.05 | 29.99 |
| Cr2O3 | 0.04 | 0.04 | 0.00 | 0.01 | 0.02 | 0.04 | 0.00 | 0.01 | 0.01 | 0.03 | 0.01 | 0.04 | 0.04 | 0.04 | 0.01 | 0.01 | 0.04 |
| FeO | 0.22 | 0.16 | 0.24 | 0.24 | 0.30 | 0.16 | 0.19 | 0.20 | 0.16 | 0.22 | 0.24 | 0.26 | 0.24 | 0.26 | 0.30 | 0.27 | 0.24 |
| MnO | 0.03 | 0.01 | 0.00 | 0.00 | 0.03 | 0.04 | 0.03 | 0.04 | 0.02 | 0.03 | 0.00 | 0.01 | 0.00 | 0.03 | 0.02 | 0.01 | 0.02 |
| MgO | 0.04 | 0.02 | 0.02 | 0.02 | 0.19 | 0.01 | 0.03 | 0.02 | 0.03 | 0.01 | 0.02 | 0.03 | 0.01 | 0.03 | 0.04 | 0.01 | 0.03 |
| CaO | 12.34 | 11.83 | 11.47 | 14.45 | 13.67 | 14.51 | 11.87 | 14.06 | 12.86 | 11.84 | 14.45 | 14.08 | 14.65 | 13.58 | 14.11 | 14.84 | 13.37 |
| Na2O | 4.66 | 4.82 | 5.09 | 3.42 | 3.73 | 3.46 | 4.87 | 3.58 | 4.35 | 4.90 | 3.42 | 3.73 | 3.25 | 3.99 | 3.60 | 3.17 | 3.91 |
| K2O | 0.04 | 0.05 | 0.04 | 0.02 | 0.09 | 0.02 | 0.04 | 0.03 | 0.04 | 0.03 | 0.02 | 0.05 | 0.03 | 0.06 | 0.02 | 0.03 | 0.04 |
| Total | 99.09 | 98.89 | 99.24 | 99.46 | 98.88 | 98.77 | 101.37 | 99.12 | 99.50 | 98.81 | 99.46 | 100.15 | 98.33 | 100.29 | 98.83 | 99.00 | 99.06 |
| Cations | | | | | | | | | | | | | | | | | |
| Si | 9.64 | 9.73 | 9.83 | 9.24 | 9.33 | 9.22 | 9.79 | 9.28 | 9.53 | 1.82 | 9.24 | 9.30 | 9.16 | 9.43 | 9.28 | 9.15 | 9.43 |
| Ti | 0.00 | 0.01 | 0.01 | 0.01 | 0.00 | 0.01 | 0.01 | 0.00 | 0.01 | 0.00 | 0.01 | 0.00 | 0.01 | 0.01 | 0.00 | 0.01 | 0.01 |
| Al | 6.28 | 6.20 | 6.09 | 6.67 | 6.56 | 6.66 | 6.17 | 6.64 | 6.39 | 1.16 | 6.67 | 6.61 | 6.74 | 6.47 | 6.62 | 6.76 | 6.49 |
| Cr | 0.01 | 0.01 | 0.00 | 0.00 | 0.00 | 0.01 | 0.00 | 0.00 | 0.00 | 0.00 | 0.00 | 0.01 | 0.01 | 0.01 | 0.00 | 0.00 | 0.01 |
| Fe | 0.03 | 0.02 | 0.04 | 0.04 | 0.05 | 0.02 | 0.03 | 0.03 | 0.02 | 0.01 | 0.04 | 0.04 | 0.04 | 0.04 | 0.05 | 0.04 | 0.04 |
| Mn | 0.00 | 0.00 | 0.00 | 0.00 | 0.00 | 0.01 | 0.00 | 0.01 | 0.00 | 0.00 | 0.00 | 0.00 | 0.00 | 0.00 | 0.00 | 0.00 | 0.00 |
| Mg | 0.01 | 0.01 | 0.01 | 0.01 | 0.05 | 0.00 | 0.01 | 0.01 | 0.01 | 0.00 | 0.01 | 0.01 | 0.00 | 0.01 | 0.01 | 0.00 | 0.01 |
| Ca | 2.42 | 2.32 | 2.24 | 2.84 | 2.70 | 2.87 | 2.27 | 2.77 | 2.52 | 0.44 | 2.84 | 2.75 | 2.92 | 2.64 | 2.79 | 2.94 | 2.63 |
| Na | 1.65 | 1.71 | 1.80 | 1.22 | 1.33 | 1.24 | 1.68 | 1.28 | 1.54 | 0.33 | 1.22 | 1.32 | 1.17 | 1.40 | 1.29 | 1.13 | 1.39 |
| K | 0.01 | 0.01 | 0.01 | 0.00 | 0.02 | 0.00 | 0.01 | 0.01 | 0.01 | 0.00 | 0.00 | 0.01 | 0.01 | 0.01 | 0.00 | 0.01 | 0.01 |
| Total | 20.05 | 20.02 | 20.02 | 20.03 | 20.06 | 20.06 | 19.97 | 20.03 | 20.04 | 3.76 | 20.03 | 20.05 | 20.05 | 20.03 | 20.05 | 20.04 | 20.01 |
| An | 59.3 | 57.4 | 55.3 | 69.9 | 66.6 | 69.8 | 57.3 | 68.3 | 61.9 | 57.1 | 69.9 | 67.4 | 71.2 | 65.1 | 68.3 | 72.0 | 65.2 |

| Sample | 153-923A-12R2-5 66-73 | 153-923A-12R2-5 66-73 | 153-923A-12R2-5 66-73 | 153-923A-13R2-6B 68-75 | 153-923A-13R2-6B 68-75 | 153-923A-13R2-6B 68-75 | 153-923A-13R2-6B 68-75 | 153-923A-13R2-6B 68-75 | 153-923A-13R2-6B 68-75 | 153-923A-13R2-6B 68-75 | 153-923A-13R2-6B 68-75 | 153-923A-14R1-12 100-112 | 153-923A-14R1-12 100-112 | 153-923A-14R1-12 100-112 | 153-923A-14R1-12 100-112 | 153-923A-14R1-12 100-112 | 153-923A-14R1-12 100-112 |
|---|---|---|---|---|---|---|---|---|---|---|---|---|---|---|---|---|---|
| **Analysis** | P12R255 | P12R256 | P12R257 | P13R017 | P13R018 | P13R019 | P13R020 | P13R069 | P13R070 | P13R71 | P13R072 | P14R028 | P14R029 | P14R030 | P14R031 | P14R065 | P14R066 |
| **Depth (m)** | 48.66 | 48.66 | 48.66 | 52.98 | 52.98 | 52.98 | 52.98 | 52.98 | 52.98 | 52.98 | 52.98 | 56.58 | 56.58 | 56.58 | 56.58 | 56.58 | 56.58 |
| **Location** | core | rim | core | core | rim | core | rim | core | rim | rim | core | core | intermed | rim | core | core | rim |
| **Traces (ppm)** | | | | | | | | | | | | | | | | | |
| **K** | 256 | 317 | 343 | 226 | 300 | 223 | 381 | n.d. | n.d. | n.d. | n.d. | 371 | 326 | 305 | 234 | n.d. | n.d. |
| **Ti** | 315 | 366 | 590 | 250 | 276 | 232 | 481 | 343 | 358 | 305 | 270 | 226 | 255 | 342 | 267 | 220 | 328 |
| **Ba** | 1.57 | 2.10 | 2.14 | 0.86 | 1.38 | 1.08 | 2.59 | 0.66 | 1.29 | 1.52 | 0.78 | 0.94 | 1.66 | 1.17 | 0.67 | 0.83 | 1.09 |
| **Li** | 0.02 | 0.01 | 0.01 | 0.03 | 0.02 | 0.03 | 0.07 | 0.04 | 0.03 | 0.01 | 0.03 | 0.02 | 0.01 | 0.02 | 0.02 | 0.01 | 0.02 |
| **Be** | n.d. | n.d. | n.d. | n.d. | n.d. | n.d. | n.d. | 0.15 | 0.18 | 0.18 | 0.15 | n.d. | n.d. | n.d. | n.d. | 0.10 | 0.12 |
| **Mg** | 173 | 163 | 206 | 267 | 143 | 146 | 180 | n.d. | n.d. | n.d. | n.d. | 328 | 159 | 269 | 223 | n.d. | n.d. |
| **V** | 6.26 | 5.84 | 6.61 | 8.52 | 5.38 | 7.43 | 7.69 | n.d. | n.d. | n.d. | n.d. | 7.83 | 5.54 | 7.44 | 7.49 | n.d. | n.d. |
| **Cr** | 0.67 | 0.65 | 0.72 | 0.60 | 0.65 | 0.50 | 0.79 | n.d. | n.d. | n.d. | n.d. | 0.75 | 0.54 | 0.92 | 0.76 | n.d. | n.d. |
| **Rb** | 0.20 | 0.22 | 0.19 | 0.40 | 0.21 | 0.19 | 0.30 | 0.20 | 0.17 | 0.13 | 0.18 | 0.28 | 0.15 | 0.24 | 0.21 | 0.22 | 0.21 |
| **Sr** | 214 | 224 | 222 | 193 | 190 | 193 | 214 | n.d. | n.d. | n.d. | n.d. | 196 | 181 | 189 | 182 | n.d. | n.d. |
| **Y** | 0.18 | 0.16 | 0.21 | 0.66 | 0.35 | 0.54 | 0.36 | 0.64 | 0.37 | 0.36 | 0.60 | 0.32 | 0.17 | 0.31 | 0.25 | 0.30 | 0.22 |
| **Zr** | 0.02 | 0.03 | 0.03 | 0.15 | 0.05 | 0.04 | 0.09 | 0.08 | 0.04 | 0.05 | 0.08 | 0.03 | 0.03 | 0.03 | 0.02 | 0.04 | 0.03 |
| **La** | 0.31 | 0.46 | 0.47 | 0.12 | 0.53 | 0.16 | 0.49 | 0.13 | 0.39 | 0.50 | 0.11 | 0.11 | 0.38 | 0.30 | 0.11 | 0.15 | 0.22 |
| **Ce** | 0.67 | 1.13 | 1.02 | 0.34 | 1.27 | 0.56 | 1.12 | 0.35 | 1.12 | 1.27 | 0.38 | 0.28 | 0.75 | 0.70 | 0.38 | 0.39 | 0.61 |
| **Pr** | 0.09 | 0.11 | 0.12 | 0.05 | 0.19 | 0.06 | 0.14 | 0.05 | 0.16 | 0.17 | 0.06 | 0.04 | 0.11 | 0.08 | 0.05 | 0.06 | 0.09 |
| **Nd** | 0.27 | 0.37 | 0.65 | 0.45 | 0.84 | 0.59 | 0.71 | 0.38 | 0.73 | 0.76 | 0.29 | 0.34 | 0.35 | 0.35 | 0.26 | 0.40 | 0.42 |
| **Sm** | 0.07 | 0.02 | 0.10 | 0.08 | 0.12 | 0.11 | 0.06 | 0.09 | 0.15 | 0.16 | 0.10 | 0.08 | 0.05 | 0.07 | 0.15 | 0.07 | 0.10 |
| **Eu** | 0.25 | 0.45 | 0.48 | 0.47 | 0.43 | 0.42 | 0.46 | 0.38 | 0.40 | 0.38 | 0.40 | 0.46 | 0.32 | 0.38 | 0.37 | 0.35 | 0.31 |
| **Gd** | 0.02 | 0.07 | 0.12 | 0.14 | b.d.l. | 0.18 | 0.20 | 0.09 | 0.12 | 0.08 | 0.09 | 0.10 | 0.03 | 0.12 | 0.10 | 0.08 | 0.05 |
| **Tb** | 0.02 | 0.01 | 0.01 | 0.01 | 0.03 | 0.02 | 0.01 | 0.01 | 0.01 | 0.01 | 0.02 | 0.01 | 0.01 | 0.01 | 0.02 | 0.01 | 0.02 |
| **Dy** | 0.07 | 0.06 | 0.04 | 0.05 | 0.04 | 0.20 | 0.12 | 0.09 | 0.06 | 0.07 | 0.11 | 0.04 | 0.07 | 0.04 | 0.06 | 0.07 | 0.05 |
| **Ho** | n.d. | n.d. | n.d. | n.d. | n.d. | n.d. | n.d. | n.d. | n.d. | n.d. | 0.02 | n.d. | n.d. | n.d. | n.d. | n.d. | n.d. |
| **Er** | 0.03 | 0.02 | 0.02 | 0.07 | 0.03 | 0.10 | 0.03 | 0.02 | 0.01 | 0.01 | 0.05 | 0.01 | b.d.l. | 0.07 | 0.05 | 0.01 | 0.00 |
| **Tm** | b.d.l. | 0.15 | 0.00 | 0.01 | 0.00 | 0.00 | b.d.l. | 0.08 | 0.03 | 0.02 | n.d. | b.d.l. | 0.00 | 0.01 | b.d.l. | 0.01 | 0.01 |
| **Yb** | 0.05 | 0.01 | 0.03 | 0.06 | 0.03 | 0.06 | 0.06 | 0.07 | 0.02 | 0.01 | 0.05 | 0.01 | 0.02 | 0.01 | 0.01 | 0.02 | 0.02 |

| Sample | 153-923A-14R1-12 100-112 | 153-923A-14R1-12 100-112 | 153-923A-16R1-2 17-19 | 153-923A-16R1-2 17-19 | 153-923A-16R1-2 17-19 | 153-923A-16R1-2 17-19 | 153-923A-16R1-2 17-19 | 153-923A-16R1-2 17-19 | 153-923A-16R1-2 17-19 | 153-923A-16R1-2 17-19 | 153-923A-16R1-2 17-19 | 153-923A-16R1-2 17-19 | 153-923A-16R1-2 17-19 | 153-923A-16R1-2 17-19 | 153-923A-16R1-2 17-19 | 153-923A-16R1-2 17-19 | 153-923A-16R3-1 3-6 |
|---|---|---|---|---|---|---|---|---|---|---|---|---|---|---|---|---|---|
| Analysis | P14R067 | P14R068 | P16R032 | P16R033 | P16R034 | P16R035 | P16R073 | P16R074 | P16R075 | P16R130 | P16R129 | P16R132 | P16R141 | P16R133 | P16R140 | P16R134 | P17R004 |
| Depth (m) | 56.58 | 56.58 | 64.87 | 64.87 | 64.87 | 64.87 | 64.87 | 64.87 | 64.87 | 64.87 | 64.87 | 64.87 | 64.87 | 64.87 | 64.87 | 64.87 | 67.73 |
| Location | intermed | core | core | rim | rim | core | core | intermed | rim | rim | 0.00 | traverse 0.56 | distance 0.76 | from 1.04 | rim 1.36 | (mm) 1.48 | core |
| SiO2 | 50.70 | 50.44 | 50.09 | 53.46 | 53.46 | 50.09 | 50.07 | 50.13 | 50.78 | 51.58 | 52.36 | 50.02 | 49.10 | 50.76 | 49.81 | 52.90 | 50.72 |
| TiO2 | 0.03 | 0.01 | 0.04 | 0.09 | 0.09 | 0.04 | 0.01 | 0.01 | 0.05 | 0.08 | 0.02 | 0.02 | 0.03 | 0.01 | 0.05 | 0.01 | 0.02 |
| Al2O3 | 29.89 | 30.40 | 31.36 | 30.06 | 30.06 | 31.36 | 30.52 | 30.54 | 30.35 | 30.51 | 30.39 | 31.47 | 31.91 | 30.94 | 31.44 | 30.28 | 30.57 |
| Cr2O3 | 0.01 | 0.01 | 0.04 | 0.01 | 0.01 | 0.04 | 0.02 | 0.01 | 0.03 | 0.02 | 0.02 | 0.04 | 0.00 | 0.04 | 0.02 | 0.01 | 0.00 |
| FeO | 0.22 | 0.25 | 0.21 | 0.18 | 0.18 | 0.21 | 0.23 | 0.27 | 0.23 | 0.23 | 0.14 | 0.22 | 0.14 | 0.21 | 0.16 | 0.14 | 0.26 |
| MnO | 0.03 | 0.03 | 0.01 | 0.00 | 0.00 | 0.01 | 0.03 | 0.02 | 0.01 | 0.02 | 0.06 | 0.02 | 0.00 | 0.03 | 0.03 | 0.03 | 0.03 |
| MgO | 0.03 | 0.02 | 0.02 | 0.02 | 0.02 | 0.02 | 0.04 | 0.02 | 0.03 | 0.04 | 0.02 | 0.03 | 0.01 | 0.02 | 0.02 | 0.02 | 0.05 |
| CaO | 13.61 | 13.93 | 14.78 | 13.06 | 13.06 | 14.78 | 14.65 | 14.66 | 14.35 | 13.78 | 13.50 | 14.96 | 15.48 | 14.32 | 15.09 | 13.21 | 14.46 |
| Na2O | 3.27 | 3.53 | 3.30 | 4.42 | 4.42 | 3.30 | 3.15 | 3.22 | 3.54 | 3.80 | 4.06 | 3.20 | 2.76 | 3.45 | 3.07 | 4.23 | 3.47 |
| K2O | 0.03 | 0.03 | 0.03 | 0.05 | 0.05 | 0.03 | 0.03 | 0.03 | 0.04 | 0.03 | 0.03 | 0.02 | 0.04 | 0.03 | 0.02 | 0.04 | 0.04 |
| Total | 97.84 | 98.67 | 99.90 | 101.37 | 101.37 | 99.90 | 98.74 | 98.91 | 99.42 | 100.10 | 100.62 | 100.03 | 99.49 | 99.84 | 99.73 | 100.89 | 99.64 |
| Cations | | | | | | | | | | | | | | | | | |
| Si | 9.41 | 9.31 | 9.16 | 9.57 | 9.57 | 9.16 | 9.25 | 9.25 | 9.32 | 9.38 | 9.46 | 9.14 | 9.02 | 9.27 | 9.12 | 9.52 | 9.29 |
| Ti | 0.00 | 0.00 | 0.01 | 0.01 | 0.01 | 0.01 | 0.00 | 0.00 | 0.01 | 0.01 | 0.00 | 0.00 | 0.00 | 0.00 | 0.01 | 0.00 | 0.00 |
| Al | 6.54 | 6.62 | 6.76 | 6.34 | 6.34 | 6.76 | 6.65 | 6.64 | 6.56 | 6.54 | 6.47 | 6.78 | 6.91 | 6.66 | 6.79 | 6.42 | 6.60 |
| Cr | 0.00 | 0.00 | 0.01 | 0.00 | 0.00 | 0.01 | 0.00 | 0.00 | 0.00 | 0.00 | 0.00 | 0.01 | 0.00 | 0.01 | 0.00 | 0.00 | 0.00 |
| Fe | 0.03 | 0.04 | 0.03 | 0.03 | 0.03 | 0.03 | 0.03 | 0.04 | 0.04 | 0.03 | 0.02 | 0.03 | 0.02 | 0.03 | 0.02 | 0.02 | 0.04 |
| Mn | 0.00 | 0.00 | 0.00 | 0.00 | 0.00 | 0.00 | 0.00 | 0.00 | 0.00 | 0.00 | 0.01 | 0.00 | 0.00 | 0.00 | 0.00 | 0.00 | 0.00 |
| Mg | 0.01 | 0.01 | 0.01 | 0.01 | 0.01 | 0.01 | 0.01 | 0.00 | 0.01 | 0.01 | 0.01 | 0.01 | 0.00 | 0.01 | 0.01 | 0.01 | 0.01 |
| Ca | 2.71 | 2.76 | 2.90 | 2.51 | 2.51 | 2.90 | 2.90 | 2.90 | 2.82 | 2.68 | 2.61 | 2.93 | 3.05 | 2.80 | 2.96 | 2.55 | 2.84 |
| Na | 1.18 | 1.26 | 1.17 | 1.53 | 1.53 | 1.17 | 1.13 | 1.15 | 1.26 | 1.34 | 1.42 | 1.13 | 0.98 | 1.22 | 1.09 | 1.48 | 1.23 |
| K | 0.01 | 0.01 | 0.01 | 0.01 | 0.01 | 0.01 | 0.01 | 0.01 | 0.01 | 0.01 | 0.01 | 0.00 | 0.01 | 0.01 | 0.00 | 0.01 | 0.01 |
| Total | 19.90 | 20.01 | 20.04 | 20.02 | 20.02 | 20.04 | 19.99 | 20.01 | 20.03 | 20.01 | 20.02 | 20.04 | 20.01 | 20.01 | 20.02 | 20.01 | 20.03 |
| An | 69.6 | 68.4 | 71.1 | 61.8 | 61.8 | 71.1 | 71.9 | 71.4 | 69.0 | 66.6 | 64.6 | 72.0 | 75.4 | 69.5 | 73.0 | 63.2 | 69.6 |

| Sample | 153-923A-14R1-12 100-112 | 153-923A-14R1-12 100-112 | 153-923A-16R1-2 17-19 | 153-923A-16R1-2 17-19 | 153-923A-16R1-2 17-19 | 153-923A-16R1-2 17-19 | 153-923A-16R1-2 17-19 | 153-923A-16R1-2 17-19 | 153-923A-16R1-2 17-19 | 153-923A-16R1-2 17-19 | 153-923A-16R1-2 17-19 | 153-923A-16R1-2 17-19 | 153-923A-16R1-2 17-19 | 153-923A-16R1-2 17-19 | 153-923A-16R1-2 17-19 | 153-923A-16R1-2 17-19 | 153-923A-16R3-1 3-6 |
|---|---|---|---|---|---|---|---|---|---|---|---|---|---|---|---|---|---|
| **Analysis** | P14R067 | P14R068 | P16R032 | P16R033 | P16R034 | P16R035 | P16R073 | P16R074 | P16R075 | P16R130 | P16R129 | P16R132 | P16R141 | P16R133 | P16R140 | P16R134 | P17R004 |
| **Depth (m)** | 56.58 | 56.58 | 64.87 | 64.87 | 64.87 | 64.87 | 64.87 | 64.87 | 64.87 | 64.87 | 64.87 | 64.87 | 64.87 | 64.87 | 64.87 | 64.87 | 67.73 |
| **Location** | intermed | core | core | rim | rim | core | core | intermed | rim | rim | 0.00 | traverse 0.56 | distance 0.76 | from 1.04 | rim 1.36 | (mm) 1.48 | core |
| **Traces (ppm)** | | | | | | | | | | | | | | | | | |
| **K** | n.d. | n.d. | 237 | 276 | 358 | 219 | n.d. | n.d. | n.d. | 201 | n.d. | 226 | 212 | 232 | 225 | 314 | 213 |
| **Ti** | 270 | 216 | 204 | 333 | 503 | 200 | 205 | 221 | 310 | 350 | 174 | 0 | 252 | 257 | 279 | 132 | 288 |
| **Ba** | 1.23 | 0.99 | 0.74 | 1.18 | 2.33 | 0.96 | 0.72 | 0.96 | 1.06 | 1.09 | 1.59 | 1.18 | 1.11 | 0.98 | 1.20 | 1.69 | 1.18 |
| **Li** | 0.01 | 0.02 | 0.22 | 0.21 | 0.01 | 1.55 | 0.34 | 0.09 | 0.01 | 0.01 | n.d. | 0.02 | 0.05 | 0.03 | 0.01 | 0.26 | 0.02 |
| **Be** | 0.13 | 0.13 | n.d. | n.d. | n.d. | n.d. | 0.12 | 0.14 | 0.14 | 0.14 | n.d. | 0.12 | 0.12 | 0.13 | 0.15 | 0.13 | 0.00 |
| **Mg** | n.d. | n.d. | 246 | 241 | 203 | 223 | n.d. | n.d. | n.d. | n.d. | n.d. | n.d. | n.d. | n.d. | n.d. | n.d. | 179 |
| **V** | n.d. | n.d. | 7.11 | 9.07 | 6.32 | 6.98 | n.d. | n.d. | n.d. | n.d. | 3.99 | n.d. | n.d. | n.d. | n.d. | n.d. | 7.58 |
| **Cr** | n.d. | n.d. | 0.66 | 0.78 | 0.68 | 0.66 | n.d. | n.d. | n.d. | n.d. | 0.46 | n.d. | n.d. | n.d. | n.d. | n.d. | 0.55 |
| **Rb** | 0.16 | 0.16 | 0.29 | 0.18 | 0.22 | 0.22 | 0.16 | 0.21 | 0.19 | 0.21 | n.d. | 0.21 | 0.25 | 0.17 | 0.18 | 0.33 | 0.23 |
| **Sr** | n.d. | n.d. | 173 | 181 | 200 | 185 | n.d. | n.d. | n.d. | n.d. | n.d. | n.d. | n.d. | n.d. | n.d. | n.d. | 179 |
| **Y** | 0.24 | 0.27 | 0.32 | 0.33 | 0.27 | 0.32 | 0.29 | 0.36 | 0.44 | 0.28 | 0.12 | 0.23 | 0.31 | 0.28 | 0.20 | 0.09 | 0.75 |
| **Zr** | 0.04 | 0.02 | 0.05 | 0.12 | 0.04 | 0.04 | 0.04 | 0.05 | 0.04 | 0.02 | 0.02 | 0.02 | 0.03 | 0.02 | 0.02 | 0.03 | 0.08 |
| **La** | 0.28 | 0.11 | 0.09 | 0.20 | 0.48 | 0.13 | 0.10 | 0.10 | 0.27 | 0.36 | 0.42 | 0.35 | 0.17 | 0.16 | 0.36 | 0.39 | 0.31 |
| **Ce** | 0.76 | 0.30 | 0.32 | 0.41 | 1.10 | 0.34 | 0.27 | 0.29 | 0.77 | 1.00 | 0.91 | 1.00 | 0.63 | 0.58 | 0.87 | 0.85 | 1.13 |
| **Pr** | 0.11 | 0.05 | 0.05 | 0.07 | 0.14 | 0.06 | 0.04 | 0.04 | 0.11 | 0.14 | 0.11 | 0.13 | 0.09 | 0.08 | 0.09 | 0.09 | 0.15 |
| **Nd** | 0.45 | 0.29 | 0.29 | 0.30 | 0.41 | 0.27 | 0.19 | 0.28 | 0.49 | 0.62 | 0.47 | 0.56 | 0.45 | 0.45 | 0.49 | 0.40 | 0.98 |
| **Sm** | 0.06 | 0.07 | 0.03 | 0.06 | 0.14 | 0.11 | 0.05 | 0.08 | 0.13 | 0.10 | 0.04 | 0.13 | 0.11 | 0.14 | 0.10 | 0.06 | 0.13 |
| **Eu** | 0.39 | 0.34 | 0.32 | 0.35 | 0.38 | 0.39 | 0.32 | 0.32 | 0.35 | 0.38 | 0.37 | 0.36 | 0.33 | 0.34 | 0.32 | 0.35 | 0.41 |
| **Gd** | 0.05 | 0.06 | 0.08 | 0.04 | 0.15 | 0.04 | 0.03 | 0.08 | 0.09 | 0.05 | 0.01 | 0.07 | 0.09 | 0.07 | 0.11 | 0.04 | 0.00 |
| **Tb** | 0.01 | 0.01 | 0.02 | 0.02 | 0.02 | 0.02 | 0.01 | 0.01 | 0.02 | 0.02 | 0.01 | 0.01 | 0.01 | 0.01 | 0.01 | 0.01 | 0.02 |
| **Dy** | 0.03 | 0.06 | 0.06 | 0.02 | 0.08 | 0.07 | 0.06 | 0.06 | 0.05 | 0.06 | 0.01 | 0.07 | 0.07 | 0.05 | 0.05 | 0.03 | 0.26 |
| **Ho** | n.d. | n.d. | n.d. | n.d. | n.d. | n.d. | 0.01 | 0.01 | 0.02 | 0.01 | 0.00 | 0.01 | 0.01 | 0.01 | 0.01 | 0.00 | n.d. |
| **Er** | 0.01 | 0.01 | 0.02 | 0.05 | 0.03 | 0.03 | 0.03 | 0.04 | 0.04 | 0.03 | b.d.l. | 0.02 | 0.02 | 0.02 | 0.01 | 0.01 | 0.08 |
| **Tm** | 0.02 | 0.02 | 0.01 | 0.02 | 0.00 | b.d.l. | n.d. | n.d. | n.d. | n.d. | n.d. | n.d. | n.d. | n.d. | n.d. | n.d. | 0.02 |
| **Yb** | 0.03 | 0.03 | 0.07 | 0.06 | 0.01 | 0.04 | 0.03 | 0.05 | 0.04 | 0.04 | 0.02 | 0.05 | 0.03 | 0.03 | 0.02 | 0.01 | n.d. |

| Sample | 153-923A-16R3-1 3-6 | 153-923A-16R3-1 3-6 | 153-923A-16R3-1 3-6 | Lake county feldspar standard | Accepted values | SHFLP40 | SHFL182 |
|---|---|---|---|---|---|---|---|
| Analysis | P17R005 | P17R006 | P17R007 | | | | |
| Depth (m) | 67.73 | 67.73 | 67.73 | | | | |
| Location | core | rim | rim | | | | |
| SiO2 | 51.23 | 52.20 | 53.30 | | | | |
| TiO2 | 0.02 | 0.02 | 0.07 | | | | |
| Al2O3 | 31.00 | 29.50 | 29.68 | | | | |
| Cr2O3 | 0.02 | 0.05 | 0.02 | | | | |
| FeO | 0.27 | 0.20 | 0.24 | | | | |
| MnO | 0.01 | 0.03 | 0.02 | | | | |
| MgO | 0.03 | 0.04 | 0.03 | | | | |
| CaO | 14.58 | 12.95 | 12.98 | | | | |
| Na2O | 3.52 | 4.19 | 4.57 | | | | |
| K2O | 0.02 | 0.06 | 0.06 | | | | |
| Total | 100.73 | 99.26 | 100.99 | | | | |
| Cations | | | | | | | |
| Si | 9.28 | 9.55 | 9.59 | | | | |
| Ti | 0.00 | 0.00 | 0.01 | | | | |
| Al | 6.62 | 6.36 | 6.30 | | | | |
| Cr | 0.00 | 0.01 | 0.00 | | | | |
| Fe | 0.04 | 0.03 | 0.04 | | | | |
| Mn | 0.00 | 0.00 | 0.00 | | | | |
| Mg | 0.01 | 0.01 | 0.01 | | | | |
| Ca | 2.83 | 2.54 | 2.50 | | | | |
| Na | 1.24 | 1.49 | 1.59 | | | | |
| K | 0.00 | 0.01 | 0.01 | | | | |
| Total | 20.03 | 20.01 | 20.06 | | | | |
| An | 69.5 | 62.9 | 60.9 | | | | |

| Sample | 153-923A-16R3-1 3-6 | 153-923A-16R3-1 3-6 | 153-923A-16R3-1 3-6 | Lake county feldspar standard | Accepted values | SHFLP40 | SHFL182 |
|---|---|---|---|---|---|---|---|
| **Analysis** | P17R005 | P17R006 | P17R007 | | | | |
| **Depth (m)** | 67.73 | 67.73 | 67.73 | | | | |
| **Location** | core | rim | rim | | | | |
| **Traces (ppm)** | | | | | | | |
| **K** | 229 | 331 | 303 | | 32375 | 36795 | 30598 |
| **Ti** | 392 | 434 | 428 | | | 113 | 109 |
| **Ba** | 1.52 | 1.59 | 1.76 | | 170 | 167 | 171 |
| **Li** | 0.01 | 0.02 | 0.01 | | | 0.75 | 0.65 |
| **Be** | n.d. | n.d. | n.d. | | | | |
| **Mg** | 213 | 243 | 217 | | | 11 | |
| **V** | 7.26 | 6.98 | 6.91 | | | 7.73 | 6.18 |
| **Cr** | 0.71 | 0.76 | 0.77 | | | 2.42 | 1.99 |
| **Rb** | 0.28 | 0.30 | 0.32 | | | 5.69 | 5.13 |
| **Sr** | 180 | 180 | 187 | | 2706 | 2306 | 2425 |
| **Y** | 0.82 | 0.64 | 0.52 | | | 0.01 | 0.01 |
| **Zr** | 0.08 | 0.04 | 0.06 | | | 0.05 | 0.04 |
| **La** | 0.74 | 1.08 | 0.96 | | 0.69 | 0.56 | 0.61 |
| **Ce** | 1.96 | 2.63 | 2.27 | | 0.73 | 0.61 | 0.76 |
| **Pr** | 0.27 | 0.35 | 0.30 | | | 0.05 | 0.06 |
| **Nd** | 1.38 | 1.74 | 1.21 | | | 0.18 | 0.13 |
| **Sm** | 0.32 | 0.28 | 0.24 | | 0.01 | 0.03 | 0.02 |
| **Eu** | 0.48 | 0.47 | 0.47 | | 0.62 | 0.97 | 0.33 |
| **Gd** | 0.00 | 0.00 | 0.00 | | | 0.01 | 0.00 |
| **Tb** | 0.11 | 0.01 | 0.02 | | | 0.00 | 0.00 |
| **Dy** | 0.08 | 0.10 | 0.21 | | | 0.14 | 0.11 |
| **Ho** | n.d. | n.d. | n.d. | | | 0.00 | |
| **Er** | b.d.l. | 0.05 | 0.03 | | | 0.00 | 0.01 |
| **Tm** | 0.00 | b.d.l. | 0.02 | | | | 0.03 |
| **Yb** | n.d. | n.d. | n.d. | | | | 0.09 |

# Appendix A.III

# Ion probe data

## (3) Accessory phase data

| Sample | 153-923A-16R3-1 3-6 | 153-923A-16R3-1 3-6 | 153-923A-16R3-1 3-6 | 153-923A-16R3-1 3-6 | 153-923A-16R3-1 3-6 | 153-923A-16R3-1 3-6 | 153-923A-13R2-6B 68-75 |
|---|---|---|---|---|---|---|---|
| **Phase** | **Amphibole** | **Amphibole** | **Ilmenite** | **Ilmenite** | **Ilmenite** | **Ilmenite** | **Olivine** |
| **Analysis** | P17R088 | P17R089 | P17R143 | P17R144 | P17R146 | P17R147 | P13R083 |
| **Description** | interstitial | interstitial | core of large crystal | rim of large crystal | interstitial | interstitial | core of cumulus crystal |
| **Majors** | | | | | | | |
| **SiO2** | 44.44 | 44.75 | | | | | 38.97 |
| **TiO2** | 3.77 | 4.03 | 54.29 | 53.34 | 52.70 | 52.89 | |
| **Al2O3** | 11.39 | 10.87 | | | | | |
| **Cr2O3** | 0.05 | 0.05 | 0.10 | 0.06 | 0.08 | 0.04 | |
| **FeO** | 7.98 | 7.84 | 36.48 | 38.82 | 44.10 | 44.20 | 20.80 |
| **MnO** | 0.11 | 0.13 | 0.48 | 0.92 | 2.11 | 2.08 | 0.29 |
| **MgO** | 15.87 | 16.02 | 8.13 | 6.55 | 0.67 | 0.71 | 40.98 |
| **CaO** | 11.80 | 11.85 | | | | | 0.03 |
| **NaO2** | 2.47 | 2.56 | | | | | |
| **K2O** | 0.18 | 0.19 | | | | | |
| **V2O3** | | | 0.46 | 0.44 | 0.28 | 0.29 | |
| **NiO** | | | | | | | 0.10 |
| **Total** | 98.23 | 98.45 | 100.05 | 100.27 | 99.99 | 100.25 | 101.17 |
| **Cations** | | | | | | | |
| **Si** | 6.65 | 6.68 | | | | | 0.99 |
| **Ti** | 0.42 | 0.45 | | | | | |
| **Al** | 2.01 | 1.91 | | | | | |
| **Cr** | 0.01 | 0.01 | | | | | |
| **Fe** | 1.00 | 0.98 | | | | | 0.44 |
| **Mn** | 0.01 | 0.02 | | | | | 0.01 |
| **Mg** | 3.54 | 3.57 | | | | | 1.56 |
| **Ca** | 1.89 | 1.90 | | | | | 0.00 |
| **Na** | 0.72 | 0.74 | | | | | |
| **K** | 0.03 | 0.04 | | | | | |
| **Ni** | | | | | | | 0.00 |
| **Total** | 16.29 | 16.29 | | | | | 3.00 |
| **Trace elements (ppm)** | | | | | | | |
| **K** | 1249 | 1137 | n.d. | n.d. | n.d. | n.d. | n.d. |
| **Tl** | 23521 | 23495 | n.d. | n.d. | n.d. | n.d. | 62.68 |
| **Sr** | 42.66 | 41.31 | n.d. | n.d. | n.d. | n.d. | n.d. |
| **Y** | 154 | 126 | 0.07 | 0.07 | 0.00 | 0.00 | 0.14 |
| **Zr** | 556 | 553 | 185 | 150 | 45 | 49.19 | 0.18 |
| **Nb** | 8.54 | 8.08 | 34.31 | 32.52 | 37.53 | 40.01 | 0.08 |
| **Ba** | 2.12 | 2.10 | n.d. | n.d. | n.d. | n.d. | n.d. |
| **La** | 1.96 | 1.57 | n.d. | n.d. | n.d. | n.d. | n.d. |
| **Ce** | 13.06 | 11.71 | n.d. | n.d. | n.d. | n.d. | 0.00 |
| **Pr** | 3.46 | 3.02 | n.d. | n.d. | n.d. | n.d. | n.d. |
| **Nd** | 25.47 | 22.30 | n.d. | n.d. | n.d. | n.d. | n.d. |
| **Sm** | 12.14 | 11.30 | n.d. | n.d. | n.d. | n.d. | n.d. |
| **Eu** | 1.39 | 1.31 | n.d. | n.d. | n.d. | n.d. | n.d. |
| **Gd** | 20.34 | 15.08 | n.d. | n.d. | n.d. | n.d. | n.d. |
| **Tb** | 3.69 | 3.05 | n.d. | n.d. | n.d. | n.d. | n.d. |
| **Dy** | 27.12 | 21.11 | n.d. | n.d. | n.d. | n.d. | n.d. |
| **Ho** | 5.23 | 4.26 | n.d. | n.d. | n.d. | n.d. | n.d. |
| **Er** | 15.91 | 12.40 | n.d. | n.d. | n.d. | n.d. | n.d. |
| **Yb** | 12.80 | 11.23 | n.d. | n.d. | n.d. | n.d. | n.d. |
| **Sc** | n.d. | n.d. | 50.66 | 46.88 | 18.53 | 19.28 | 12.96 |
| **Ta** | n.d. | n.d. | 1.43 | 1.42 | 1.91 | 1.97 | n.d. |
| **Hf** | n.d. | n.d. | 3.86 | 3.24 | 1.33 | 1.34 | n.d. |
| **Cr** | n.d. | n.d. | 385 | 357 | 294 | 301 | n.d. |
| **P** | n.d. | n.d. | n.d. | n.d. | n.d. | n.d. | 30.29 |
| **Ni** | n.d. | n.d. | n.d. | n.d. | n.d. | n.d. | 2554 |

# Appendix A.IV

# Representative photomicrographs of thin sections studied

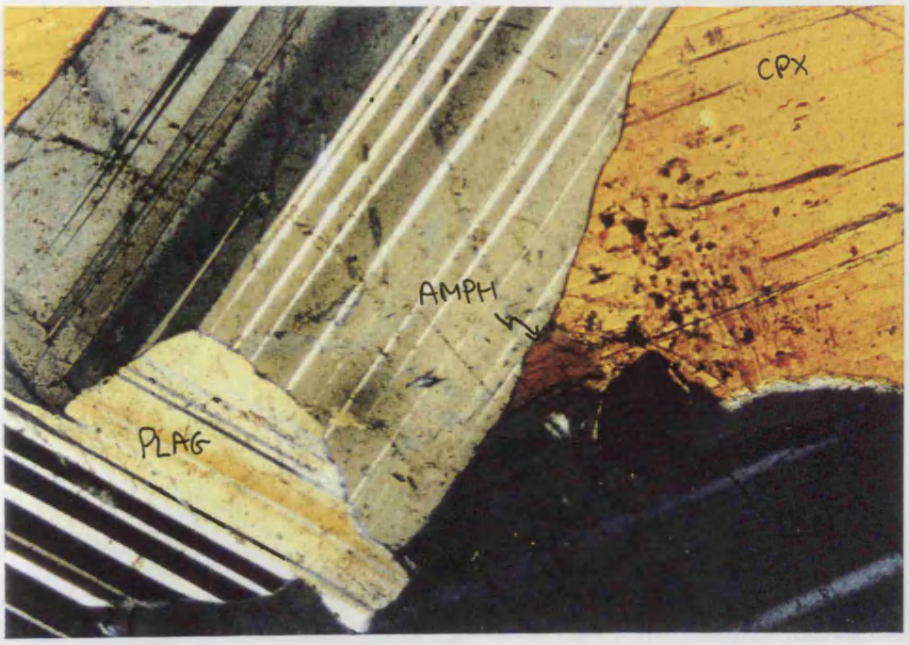


Fig. A.IV.1 XPL view of junction of clinopyroxene oikocryst with two plagioclase chadacrysts within the core of the oikocryst at 67.79 mbsf. Brown amphibole and ilmenite occur at the tip of the clinopyroxene. Field of view 2 mm.


Fig. A.IV.2 XPL view of olivine oikocryst enclosing plagioclase in a troctolite from 30.26 mbsf. Note the plagioclase within the oikocryst are more elongate than those outside it. Field of view 8 mm.


Fig. A.IV.3 XPL close up showing form of plagioclase chadacrysts in an olivine oikocryst in a troctolite from 30.26 mbsf. Note the resorbed form of the plagioclase crystals. Field of view 2 mm.

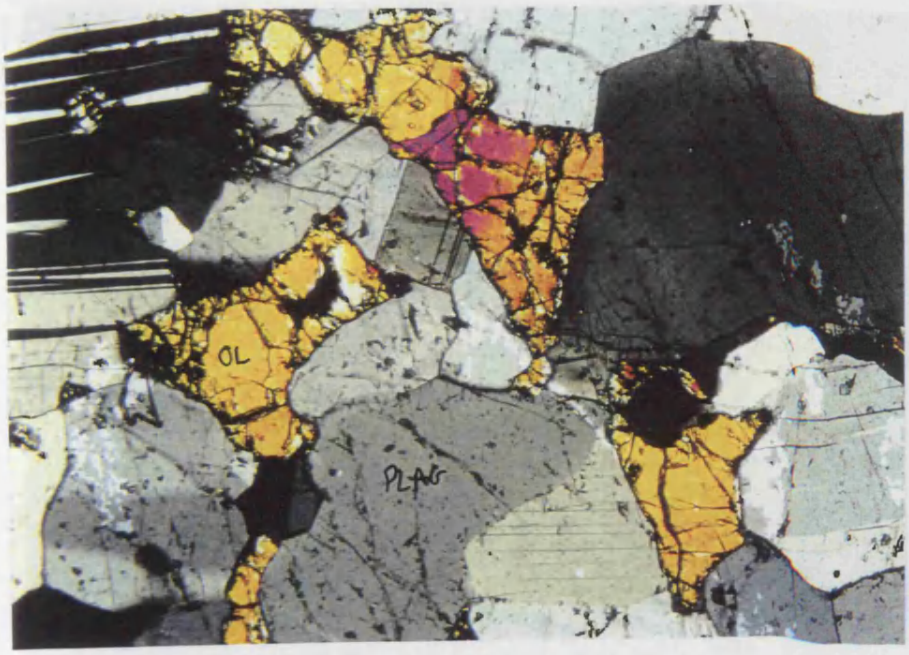


Fig. A.IV.4. XPL close up of edge of olivine oikocryst in a troctolite from 30.26 mbsf. Note relatively equilibrated plagioclase grain boundaries and their 120° triple junctions. Field of view 2 mm.

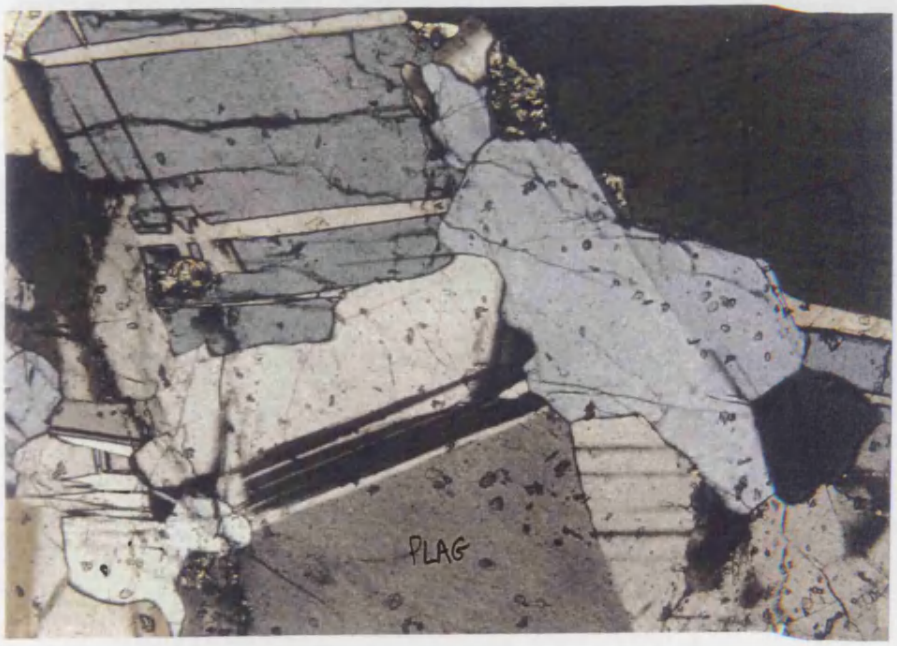


Fig. A.IV.5. XPL view of anorthositic patch between olivine oikocrysts in a troctolite from 52.98 mbsf. Note the ~120° triple junctions and approach to smooth grain boundary curvature. Field of view 2 mm.

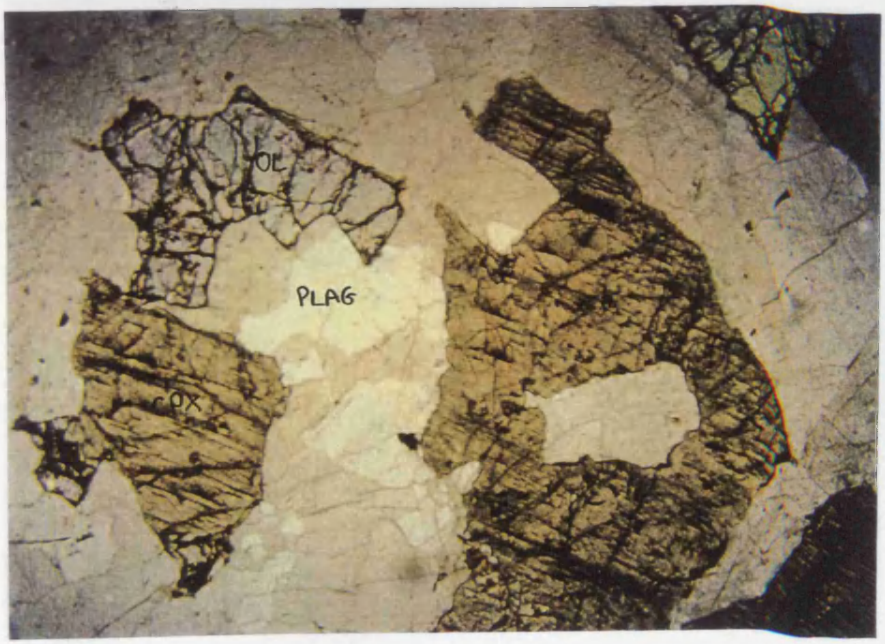


Fig. A.IV.6. PPL view of medium grained brown-pyroxene gabbro from 23.28 mbsf. Note the olivine tips on the clinopyroxene in the bottom left of the photograph. Field of view 8 mm.

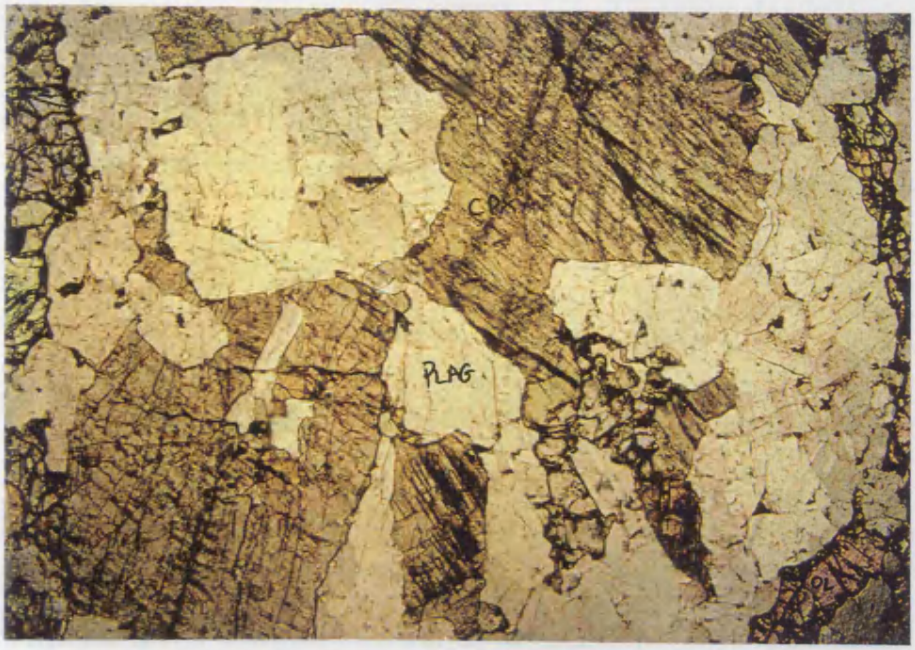


Fig. A.IV.7. PPL view of medium to fine grained brown-pyroxene gabbro from 23.19 mbsf. Field of view 8 mm.

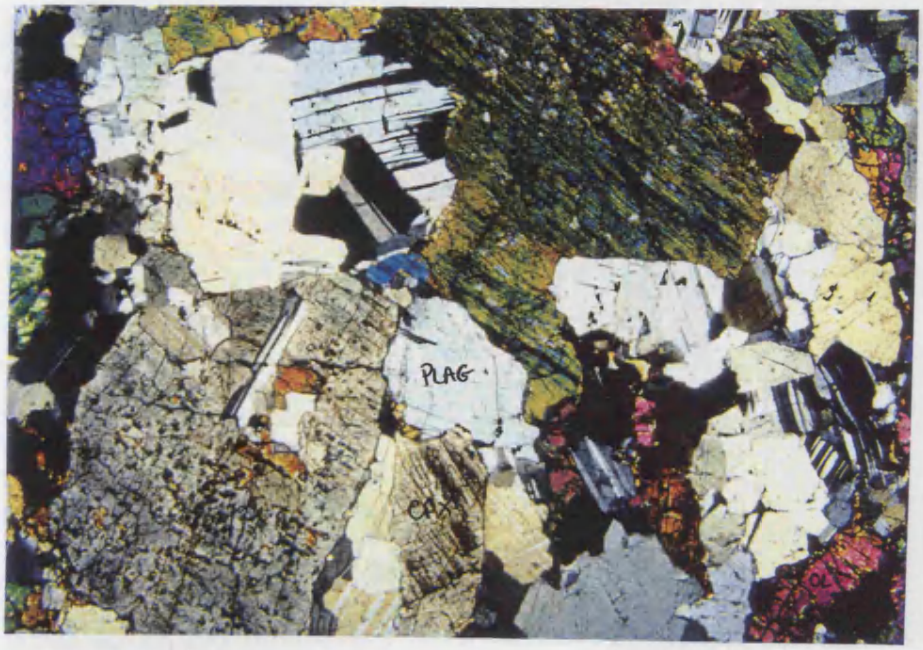


Fig. A.IV.8. XPL view of Fig. A.IV.7. Note the deformation twins in some plagioclase crystals. Field of view 8 mm.

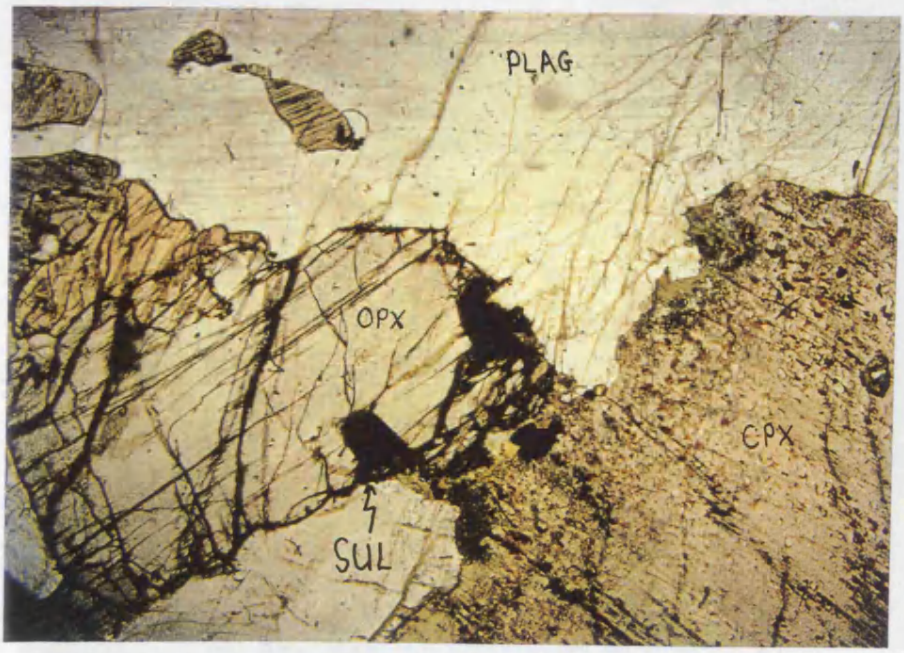


Fig. A.IV.9. PPL view of coarse grained portion of a brown-pyroxene gabbro from 54.53 mbsf. Note the subhedral orthopyroxene with sulphides indenting its margin. Field of view 8 mm.

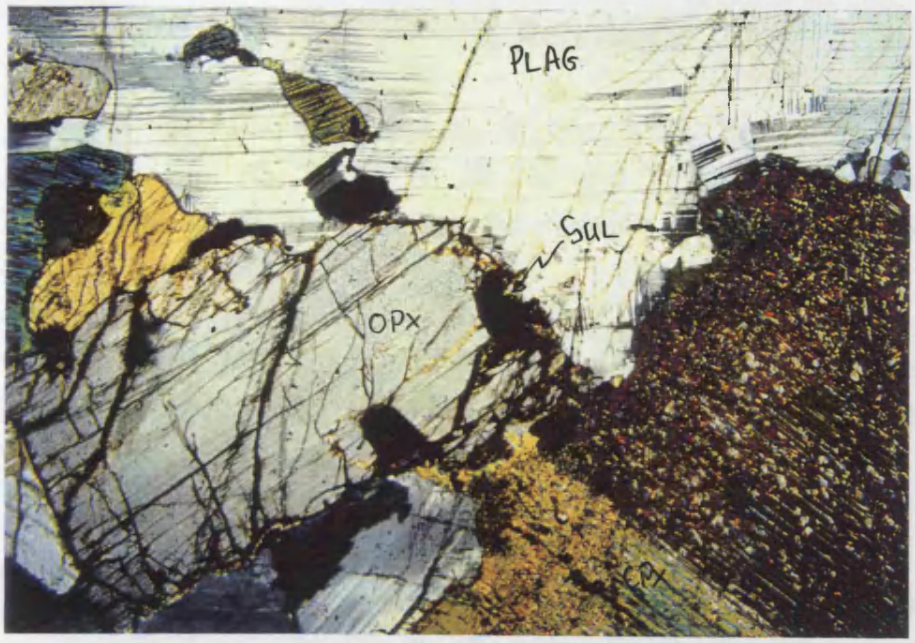


Fig. A.IV.10. XPL view of Fig. A.IV.9. Note the deformation twins in plagioclase and the deformation induced plagioclase neoblasts at the clinopyroxene-plagioclase margin. Field of view 8 mm.


Fig. A.IV.11. PPL view of coarse protion of brown-pyroxene gabbros from 39.16 mbsf. Note the subhedral orthopyroxene and ilmenite at the margin of the clinopyroxene. Field of view 8 mm.

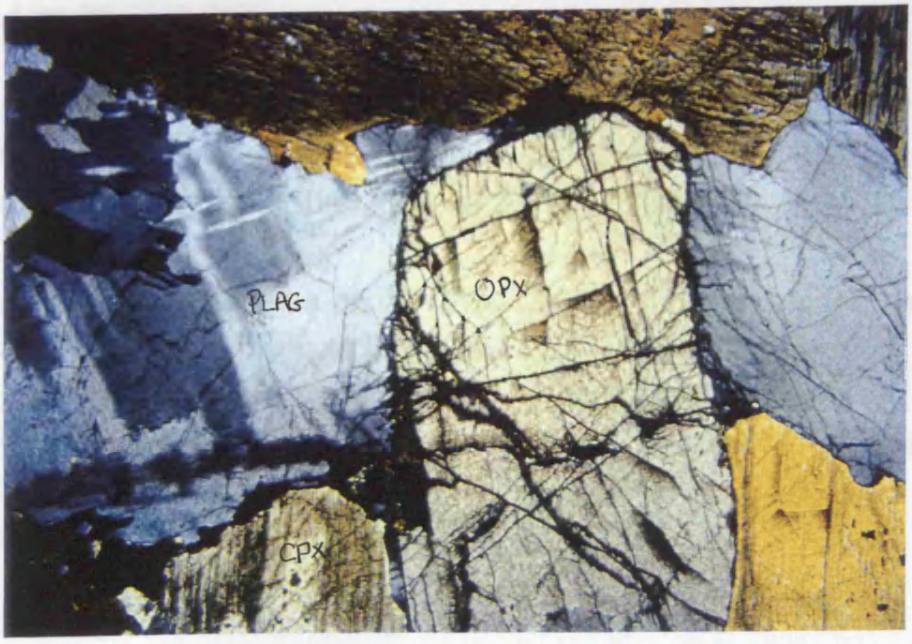


Fig. A.IV.12. XPL view of Fig. A.IV.11. Note the internal deformation in plagioclase and the relatively smoothly curved grain boundaries. Field of view 8 mm.

# References

J. Adam, T. H. Green and S. H. Sie. 1993. Proton microprobe determined partitioning of Rb, Sr, Ba, Y, Zr, Nb and Ta between experimentally produced amphiboles and silicate melts with variable F content. *Chemical Geology*, **109**, 29-49.

S. M. Agar and G. E. Lloyd. 1997. Deformation of Fe-Ti oxides in gabbroic shear zones from the MARK area. *In* J. A. Karson, M. Cannat, D. J. Miller and D. Elthon (eds.), Proc. Sci. Results. **153**, Ocean Drilling Program (College Station, Texas), 123-141.

E. Aharonov, M. Speigelman and P. Kelemen. 1997. Three-dimensional flow and reaction in porous media: Implications for the Earth's mantle and sedimentary basins. *Journal of Geophysical Research*, **102**, 14821-14833.

F. Albarède. 1985. Regime and trace-element evolution of open magma chambers. *Nature*, **318**, 356-358.

E. Anders and N. Grevasse. 1989. Abundances of the elements: Meteoric and solar. *Geochimica et Cosmochimica Acta*, **53**, 197-214.

J. C. Ayers and E. B. Watson. 1993. Apatite/fluid partitioning of rare-earth elements and strontium - experimental results at 1.0 GPa and 1000°C and application to fluid-rock interaction. *Chemical Geology*, **110**, 299-314.

M. B. Baker and E. M. Stolper. 1994. Determining the composition of high-pressure mantle melts using diamond aggregates. *Geochimica et Cosmochimica Acta*, **58**, 2811-2828.

M. B. Baker, M. M. Hirschmann, M. S. Ghiorso and E. M. Stolper. 1995. Composition of near-solidus peridotite melts from experiments and thermodynamic calculations. *Nature*, **375**, 308-311.

J. Barling, J. Hertogen and D. Weis. 1997. Whole-rock geochemistry and Sr-, Nd-, and Pb- isotopic characteristics of undeformed, deformed, and recrystallized gabbros from Sites 921, 922, and 923 in the MARK area. *In* J. A. Karson, M. Cannat, D. J. Miller and D. Elthon (eds.), Proc. Sci. Results. **153**, Ocean Drilling Program (College Station, Texas), 351-362.

S. J. Barnes. 1986. The effect of trapped liquid crystallisation on cumulus mineral compositions in layered intrusions. *Contributions to Mineralogy and Petrology,* **93**, 524-531.

G. A. Barth, M. C. Kleinrock and R. T. Helz. 1994. The magma body at Kileaua Iki lava lake: Potential insights into mid-ocean ridge magma chambers. *Journal of Geophysical Research,* **90**, 7199-7217.

P. Beattie. 1993. The generation of uranium series disequilibria by partial melting of spinel peridotite: constraints from partitioning studies. *Earth and Planetary Science Letters,* **117**, 379-391.

P. Beattie. 1994. Systematics and energetics of trace-element partitioning between olivine and silicate melts: Implications for the nature of mineral/melt partitioning. *Chemical Geology,* **117**, 57-71.

J. F. Bender, C. H. Langmuir and G. N. Hanson. 1984. Petrogenesis of Basalt Glasses from the Tamayo Region, East Pacific Rise. *Journal of Petrology,* **25**, 213-254.

S. H. Bloomer, P. S. Meyer, H. J. B. Dick, K. Ozawa and J. H. Natland. 1991. Textural and mineralogical variations in gabbroic rocks from Hole 735B. *In* P. R. Von Herzen, P. T. Robinson et al., Proc. ODP Sci. Results **118**, Ocean Drilling Program (College Station, Texas), 21-39.

J. Blundy. 1997a. Experimental study of a Kiplapait marginal rock and implications for trace element partitioning in layered intrusions. *Chemical Geology,* **141**, 73-92.

J. D. Blundy, 1997b. Thermodynamics of trace element partitioning: implications for modelling magmatic processes. Abs. *In* Rogers, N, Hawksworth, C and Kelley, S. (eds.). Rates and timescales of magmatic processes. Geological Society of London.

J. D. Blundy and B. J. Wood. 1991. Crystal chemical controls on partitioning of Sr and Ba between plagioclase feldspar, silicate melts, and hydrothermal solutions. *Geochimica et Cosmochimica Acta,* **55**, 193-209.

J. D. Blundy and B. J. Wood. 1994. Prediction of crystal-melt partition coefficients from elastic moduli. *Nature,* **372**, 452-454.

Y. Bottinga and D. F. Weill. 1970. Densities of liquid silicate systems calculated from partial molar volumes of oxide components. *American Journal of Science,* **269**, 169-182.

F. Boudier and A. Nicolas. 1995. Nature of the Moho Transition Zone in the Oman Ophiolite. *Journal of Petrology,* **36**, 777-796.

A. E. Boudreau. 1995. Some geochemical considerations for platinum-group element exploration in layered intrusions. *Exploration and Mining Geology,* **4**, 215-226.

A. E. Boudreau, E. A. Mathez and I. S. McCallum. 1986. Halogen Geochemistry of the Stillwater and Bushveld Complexes: Evidence for transport of the Platinum-Group elements by Cl-rich fluids. *Journal of Petrology,* **27**, 967-986.

A. E. Boudreau and I. S. McCallum. 1990. Low temperature alteration of REE-rich chlorapatite from the Stillwater Complex, Montana. *American Mineralogist,* **75**, 687-693.

A. E. Boudreau and A. R. McBirney. 1997. The Skaergaard Layered Series. Part III. Non-dynamic layering. *Journal of Petrology,* **38**, 1003-1020.

A. E. Boudreau, M. A. Stewart and A. J. Spivack. 1997. Stable Cl isotopes and origin of high-Cl magmas of the Stillwater Complex, Montana. *Geology,* **25**, 791-794.

B. Bourdon, A. Zindler, T. Elliot and C. H. Langmuir. 1996. Constraints on mantle melting at mid-ocean ridges from global 238U-230Th disequilibrium data. *Nature,* **384**, 231-236.

J. B. Brady and R. H. McCallister. 1983. Diffusion data for clinopyroxene from homogenisation and self diffusion experiments. *American Mineralogist,* **68**, 95-105.

J. Brenan. 1994. Kinetics of fluorine, chlorine and hydroxyl exchange in fluorapatite. *Chemical Geology,* **110**, 195-210.

J. M. Brenan, H. F. Shaw, F. J. Ryerson and D. L. Phinney. 1995. Experimental determination of trace-element partitioning between pargasite and a synthetic hydrous andesitic melt. *Earth and Planetary Science Letters,* **35**, 1-11.

J. C. Brice. 1975. Some thermodynamic aspects of the growth of strained crystals. *Journal of Crystal Growth*, **28**, 249-253.

G. C. Brown and A. E. Mussett. 1981. The Inaccessible Earth. George Allen & Unwin (London), 235.

J. R. Brown and J. A. Karson. 1988. Variations in Axial processes on the Mid-Atlantic Ridge - The median valley of the MARK area. *Marine Geophysical Researches*, **10**, 109-138.

W. B. Bryan, G. Thompson and J. N. Ludden. 1981. Compositional variation in Normal MORB from 22°-25°N Mid-Atlantic Ridge and Kane Fracture Zone. *Journal of Geophysical Research*, **86**, 11815-11836.

W. B. Bryan, S. E. Humphris, G. Thompson and J. F. Casey. 1994. Comparative volcanology of small axial eruptive centres in the MARK area. *Journal of Geophysical Research*, **99**, 2973-2984.

P. R. Buseck, G. L. Nord and D. R. Veblen. 1980. Subsolidus phenomena in pyroxenes. *In* C. T. Prewitt, Pyroxenes, Bookmakers 117-212.

A. J. Calvert. 1995. Seismic evidence for a magma chamber beneath the slow-spreading Mid-Atlantic Ridge. *Nature*, **377**, 410-414.

M. Cameron and J. J. Papike. 1980. Crystal chemistry of the silicate pyroxenes. *In* C. T. Prewitt, Pyroxenes, Bookmakers, 5-92.

A. C. Campbell, M. R. Palmer, G. P. Klinkhammer, T. S. Bowers, J. M. Edmond, J. R. Lawrence, J. F. Casey, G. Thompson, S. Humphris, P. Rona and J. A. Karson. 1988. Chemistry of hot springs on the Mid-Atlantic Ridge. *Nature*, **335**, 514-519.

I. H. Campbell. 1978. Some problems with the cumulus theory. *Lithos*, **11**, 311-323.

I. H. Campbell. 1996. Fluid Dynamic Processes in Basaltic Magma Chambers. *In* R. G. Cawthorn (ed.), Layered Intrusions, Elsevier (Amsterdam), 45-76.

I. H. Campbell, P. L. Roeder and J. M. Dixon. 1978. Plagioclase buoyancy in basaltic liquids as determined with a centrifuge furnace. *Contributions to Mineralogy and Petrology*, **67**, 369-377.

I. H. Campbell and J. S. Turner. 1989. Fountains in magma chambers. *Journal of Petrology*, **30**, 885-923.

J. Cann and D. Smith. 1994. Volcanoes of the mid-ocean ridges and the building of new oceanic crust. *Endeavour*, **18**, 61-66.

J. R. Cann, D. K. Blackman, D. K. Smith, E. McAllister, B. Janssen, S. Mello, E. Avgerinos, A. R. Pascoe and J. Escartin. 1997. Corrugated slip surfaces formed at ridge-transform intersections on the Mid-Atlantic Ridge. *Nature*, **385**, 329-332.

M. Cannat. 1993. Emplacement of Mantle Rocks in the Seafloor at Mid-Ocean Ridges. *Journal of Geophysical Research*, **98**, 4163-4172.

M. Cannat. 1996. How thick is the magmatic crust at slow spreading ridges ? *Journal of Geophysical Research*, **101**, 2847-2857.

M. Cannat, J. A. Karson, D. J. Miller *et al.* 1995. Proc. ODP Initial Reports, Leg 153. Ocean Drilling Program (College station, Texas), 798.

M. Cannat, G. Ceuleneer and J. Fletcher. 1997. Localisation of ductile strain and the magmatic evolution of gabbroic rocks drilled at the Mid-Atlantic Ridge (23°N). *In* J. A. Karson, M. Cannat, D. J. Miller and D. Elthon (eds.), Proc. Sci. Results. **153**, Ocean Drilling Program (College Station, Texas), 77-98.

I. S. E. Carmichael and M. S. Ghiorso. 1986. Oxidation-reduction relations in basic magma: a case for homogenous equilibria. *Earth and Planetary Science Letters*, **78**, 200-210.

M. Caroff. 1995. Open system crystallisation and mixing in two layer magma chambers. *Lithos*, **36**, 85-102.

M. Caroff, Y. Lagabreille, P. Spadea and J.-M. Auzende. 1997. Geochemical modelling of non-steady state magma chamber chambers: A case study from an ultra fast spreading ridge, East Pacific Rise, 17-19°S. *Geochimica et Cosmochimica Acta*, **61**, 4367-4374.

J. F. Casey. 1997. Comparison of major and trace-element geochemistry of abyssal peridotites and mafic plutonics with basalts from the MARK region of the Mid-Atlantic Ridge. *In* J. A. Karson, M. Cannat, D. J. Miller and D. Elthon (eds.), Proc. Sci. Results. **153**, Ocean Drilling Program (College Station, Texas), 181-241.

K. V. Cashman and B. D. Marsh. 1988. Crystal size distribution (C.S.D.) in rocks and the Kinetics and dynamics of crystallisation. 2. Makaopuhi lava lake. *Contributions to Mineralogy and Petrology*, **99**, 292-305.

R. G. Cawthorn. 1996a. Models for incompatible trace-element abundances in cumulus minerals and their application to plagioclase and pyroxenes in the Bushveld Complex. *Contributions to Mineralogy and Petrology*, **123**, 109-115.

R. G. Cawthorn. 1996b. Re-evaluation of magma compositions in the uppermost Critical Zone of the Bushveld Complex. *Mineralogical Magazine*, **60**, 131-148.

G. Chazot, M. A. Menzies and B. Harte. 1996. Determination of partition coefficients between apatite, clinopyroxene, amphibole, and melt in natural spinel lherzolites from Yemen: Implications for wet melting of the lithospheric mantle. *Geochimica et Cosmochimica Acta*, **60**, 423-437.

M. Cheadle, 1990. The geometry of texturally equilibrated two phase aggregates. Unpublished PhD, Cambridge.

J. Collier and M. Sinha. 1990. Seismic images of a magma chamber beneath the Lau Basin back arc spreading centre. *Nature*, **346**, 646-648.

M. Constantin, R. Hekinian, D. Bideau and R. Herbet. 1996. Construction of the oceanic lithosphere by magmatic intrusions: Petrological evidence from plutonic rocks formed along the fast-spreading East Pacific Rise. *Geology*, **24**, 731-734.

K. G. Cox. 1988. Numerical modelling of a randomized RTF magma chamber: a comparison with continental flood basalt sequences. *Journal of Petrology*, **29**, 681-697.

W. A. Deer, R. A. Howie and J. Zussman. 1966. An Introduction to the Rock Forming Minerals. Longman (Harlow), 527.

M. J. DeFant and R. L. Nielsen. 1989. Interpretation of open system petrogenetic processes: phase equilibria constraints on magma evolution. *Geochimica et Cosmochimica Acta*, **54**, 87-102.

S. E. DeLong and C. Chatelain. 1990. Trace-element constraints on accessory-phase saturation in evolved MORB magma. *Earth and Planetary Science Letters*, **101**, 206-215.

D. J. DePaolo. 1981. Trace element and isotopic effects of combined wallrock assimilation and fractional crystallisation. *Earth and Planetary Science Letters*, **53**, 189-202.

R. S. Detrick, P. Buhl, E. Vera, J. Mutter, J. Orcutt, J. Madsen and T. Brocher. 1987. Multi-channel seismic imaging of a crustal magma chamber along the East Pacific Rise. *Nature*, **326**, 35-41.

R. S. Detrick, J. C. Mutter, P. Buhl and I. I. Kim. 1990. No evidence from multichannel reflection data for a crustal magma chamber in the MARK area on the Mid-Atlantic ridge. *Nature*, **347**, 61-64.

R. S. Detrick, J. Collins, R. Stephen and S. Swift. 1994. In-Situ evidence for the nature of the seismic layer 2/3 boundary in oceanic crust. *Nature*, **370**, 288-290.

H. J. B. Dick. 1989. Abyssal Peridotites, very slow spreading ridges and ocean ridge magmatism. *In* A. D. Saunders and M. J. Norry (eds.), Magmatism in the Ocean Basins **42**, Blackwell (Oxford), 71-106.

H. J. B. Dick, R. L. Fisher and W. B. Bryan. 1984. Mineralogical variability of the uppermost mantle along mid-ocean ridges. *Earth and Planetary Science Letters*, **69**, 88-106.

H. J. B. Dick, P. S. Meyer, S. H. Bloomer, S. Kirby, D. Stakes and C. Mauwer. 1991. Lithostratigraphic evolution of an *in situ* section of oceanic layer 3. *In* P. R. Von Herzen, P. T. Robinson *et al.*, Proc. ODP Sci. Results **118**, Ocean Drilling Program (College Station, Texas), 439-540.

H. J. B. Dick and J. H. Natland. 1996. Late-stage melt evolution and transport in the shallow mantle beneath the East Pacific Rise. *In* C. Mevel, K. M. Gillis, J. F. Allan and P. S. Meyer, Proc. ODP, Sci. Results **147**, Ocean Drilling Program (College Station, Texas), 103-133.

S. Dixon and M. J. Rutherford. 1979. Plagiogranites as late stage immiscible liquids in ophiolite and mid-ocean ridge suites: an experimental study. *Earth and Planetary Science Letters*, **45**, 45-60.

L. Dosso, H. Bougault and J.-L. Joron. 1993. Geochemical Morphology of the North Mid-Atlantic Ridge, 10°-24°N: Trace element-isotope complementarity. *Earth and Planetary Science Letters*, **120**, 443-462.

M. J. Drake and D. F. Weill. 1975. Partitioning of Sr, Ba, Ca, Y, $Eu^{2+}$, $Eu^{3+}$, and other REE between plagioclase feldspar and magmatic liquid: and experimental study. *Geochimica et Cosmochimica Acta*, **39**, 689-712.

G. T. R. Droop. 1987. A general equation for estimating $Fe^{3+}$ concentrations in ferromagnesian silicates and oxides from microprobe analyses, using stoichiometric criteria. *Mineralogical Magazine*, **51**, 431-435.

M. A. Dungan and J. M. Rhodes. 1978. Residual glasses and melt inclusions in basalts from DSDP Leg 45 and 46: evidence for magma mixing. *Contributions to Mineralogy and Petrology*, **67**, 417-431.

C. Dupuy, J. M. Liotard and J. Dostal. 1992. Zr/Hf fractionation in intraplate basaltic rocks: Carbonate metasomatism in the mantle source. *Geochimica et Cosmochimica Acta*, **56**, 2417-2423.

H. Elderfield and M. J. Greaves. 1982. The rare earth elements in seawater. *Nature*, **296**, 214-219.

A. J. G. Ellison and P. C. Hess. 1989. Solution properties of rare earth elements in silicate melts: Inferences from immiscible liquids. *Geochimica et Cosmochimica Acta*, **53**, 1965-1974.

D. Elthon. 1987. Petrology of Gabbroic Rocks from the Mid-Cayman Rise Spreading Centre. *Journal of Geophysical Research*, **92**, 658-682.

D. Elthon, M. Stewart and D. K. Ross. 1992. Compositional Trends of Minerals in Oceanic cumulates. *Journal of Geophysical Research*, **979**, 15,189-15,199.

A. E. J. Engel, C. G. Engel and R. G. Havens. 1965. Chemical characteristics of oceanic basalts and the upper mantle. *Bulletin of the Geological Society of America*, **76**, 719-734.

L. M. Forsythe, R. L. Nielsen and M. R. Fisk. 1994. High field strength element partitioning between pyroxene and basaltic to dacitic magmas. *Chemical Geology*, **117**, 107-125.

G. A. Gaetani and T. L. Grove. 1995. Partitioning of rare-earth elements between clinopyroxene and silicate melt: Crystal-chemical controls. *Geochimica et Cosmochimica Acta*, **59**, 1951-1962.

L. Gaggero and M. Gazzotti. 1996. Primary and secondary oxides, sulphides and accessory minerals in Mid-Atlantic gabbros: Mineralogy and Petrology. *Ofioliti*, **21**, 105-116.

P. W. Gast. 1965. Terrestrial Ratio of Potassium to Rubidium and the Composition of the Earth's Mantle. *Science*, **147**, 858-860.

P. Gente, R. A. Pockalny, C. Durand, C. Deplus, M. Maia, G. Ceuleneer, C. Mevel, M. Cannat and C. Laverne. 1995. Characteristics and evolution of the segmentation of the Mid-Atlantic Ridge between 20°N and 24°N during the last 10 million years. *Earth and Planetary Science Letters*, **129**, 55-71.

M. S. Ghiorso. 1997. Thermodynamic models of igneous processes. *Annual Review of Earth and Planetary Sciences*, **25**, 2214-2241.

M. S. Ghiorso and P. B. Kelemen. 1987. Evaluating reaction stoichiometry in magmatic systems evolving under generalised thermodynamic constraints: Examples comparing isothermal and isenthalpic assimilation. *In* B. O. Mysen (ed.), Magmatic Processes: Physicochemical principles, The Geochemical Society 319-337.

I. Ghose, M. Cannat and M. Seyler. 1996. Transform Fault Effect on Mantle Melting in the MARK Area (Mid-Atlantic Ridge south of the Kane Transform). *Geology*, **24**, 1139-1142.

B. J. Giletti and J. E. D. Casserly. 1994. Strontium diffusion kinetics in plagioclase feldspars. *Geochimica et Cosmochimica Acta*, **58**, 3785-3793.

J. Gill and M. Condomines. 1992. Short-lived radioactivity and magma genesis. *Science*, **257**, 1368-1376.

K. M. Gillis. 1996. Rare Earth Element constraints on the origin of amphibole in gabbroic rocks from Site 894, Hess Deep. *In* C. Mevel, K. M. Gillis, J. F. Allan and P. S. Meyer, Proc. ODP, Sci. Results **147**, Ocean Drilling Program (College Station, Texas), 59-75.

T. H. Green. 1994. Experimental Studies of trace-element partitioning applicable to igneous petrogenesis - Sedona 16 years later. *Chemical Geology*, **117**, 1-36.

N. R. Grindley, P. J. Fox and K. C. MacDonald. 1991. Second-order ridge axis discontinuities in the south Atlantic - morphology, structure and evolution. *Marine Geophysical Researches*, **13**, 21-49.

T. L. Grove. 1990. Cooling Histories of lavas from Serocki volcano. *In* R. S. Detrick, J. Honnorez, W. B. Bryan, T. Juteau *et al.* (eds.), Proc. Sci. Results **106/9**, Ocean Drilling Program (College Station, Texas), 3-8.

T. L. Grove and W. B. Bryan. 1983. Fractionation of pyroxene-phyric MORB at low pressure : An experimental study. *Contributions to Mineralogy and Petrology*, **84**, 293-309.

T. L. Grove, M. B. Baker and R. J. Kinzler. 1984. Coupled CaAl-NaSi diffusion in plagioclase feldspar: Experiments and applications to cooling rate speedometry. *Geochimica et Cosmochimica Acta*, **48**, 2113-2121.

T. L. Grove, R. J. Kinzler and W. B. Bryan. 1990. Natural and Experimental phase relations of lavas from Serocki volcano. *In* R. Detrick, J. Honnorez, W. B. Bryan, T. Juteau et al. (eds.), Proc. Sci. Results **106/9**, Ocean Drilling Program (College Station, Texas), 9-17.

T. L. Grove, R. J. Kinzler and W. B. Bryan. 1992. Fractionation of Mid-Ocean Ridge Basalt (MORB). *In* J. Phipps-Morgan, D. K. Blackman and J. M. Sinton (eds.), Mantle Flow and Melt Generation at Mid-Ocean Ridges **71**, American Geophysical Union, 281-311.

M. Grutzeck, S. Kridelbaugh and D. Weill. 1974. The distribution of Sr and REE between diopside and silicate liquid. *Geophysical Research Letters*, **1**, 273-275.

S. E. Haggerty. 1976. Oxidation of opaque minerals in basalts. *In* D. Rumble (ed.), Oxide Minerals, Bookcrafters (Chelsea), Hg1-Hg98.

S. R. Hart and T. Dunn. 1993. Experimental cpx/melt partitioning of 24 trace elements. *Contributions to Mineralogy and Petrology*, **113**, 1-8.

R. Hebert, M. Constantin and P. T. Robinson. 1991. Primary mineralogy of Leg 118 gabbroic rocks and their place in the spectrum of oceanic mafic igneous rocks. *In* P. R. Von Herzen, P. T. Robinson et al., Proc. ODP Sci. Results **118**, Ocean Drilling Program (College Station, Texas), 3-20.

R. Hekinian, R. Herbet, R. C. Maury and E. T. Berger. 1985. Orthopyroxene-bearing gabbroic xenoliths in basalts from the East Pacific Rise axis near 12°50'N. *Bulletin of Mineralogy*, **108**, 691-698.

R. T. Helz. 1987. Differentiation behaviour of Kilauea Iki lava lake, Kilauea Volcano, Hawaii: An overview of past and current work. *In* B. O. Mysen (ed.), Magmatic Processes: Physicochemical principles, 241-258.

T. J. Henstock, A. W. Woods and R. S. White. 1993. The Accretion of Oceanic Crust by Episodic Sill Intrusion. *Journal of Geophysical Research*, **98**, 4143-4161.

P. C. Hess. 1992. Phase Equilibria Constraints on the Origin Of Ocean Floor Basalts. *In* J. Phipps-Morgan, D. K. Blackman and J. M. Sinton (eds.), Mantle Flow and Melt Generation at Mid-Ocean Ridges, **71**, American Geophysical Union, 67-102.

M. D. Higgins. 1991. The origin of laminated and massive anorthosite, Sept Iles layered intrusion, Quebec, Canada. *Contributions to Mineralogy and Petrology*, **106**, 340-354.

M. D. Higgins. 1996. Magma dynamics beneath Kameni volcano, Thera, Greece, as revealed by crystal size and shape measurements. *Journal of Volcanology and Geothermal Research*, **70**, 37-48.

R. W. Hinton and B. G. J. Upton. 1991. The crystal chemistry of zircon - variations within and between large crystals from syenite and alkali basalt xenoliths. *Geochimica et Cosmochimica Acta*, **55**, 3287-3302.

M. M. Hirschmann and E. M. Stolper. 1996. A possible role for garnet pyroxenite in the origin of the 'garnet signature' in MORB. *Contributions to Mineralogy and Petrology*, **124**, 185-208.

G. Hirth and D. L. Kohlstedt. 1996. Water in the oceanic upper mantle: implications for rheology, melt extraction and the evolution of the lithosphere. *Earth and Planetary Science Letters*, **144**, 93-108.

F. N. Hodges and J. J. Papike. 1976. DSDP Site 334: Magmatic Cumulates From Oceanic Layer 3. *Journal of Geophysical Research*, **81**, 4135-4150.

E. Humler and H. Whitechurch. 1988. Petrology of basalts from the Central Indian Ridge (lat. 25 23's, long. 70 04'E): estimates of frequencies and fractional volumes

of magma injections in a two layered reservoir. *Earth and Planetary Science Letters*, **88**, 169-181.

R. H. Hunter. 1987. Textural Equilibrium in Layered Igneous Rocks. *In* Parsons (ed.), Origins of Igneous Layering D. Reidel (Dordrecht), 473-503.

R. H. Hunter. 1996. Texture Development in Cumulate Rocks. *In* R. G. Cawthorn (ed.), Layered Intrusions, Elsevier (Amsterdam), 77-101.

R. H. Hunter and P. Kokelaar. 1994. Igneous cumulates in sedimentological perspective. *Geoscientist*, **4**, 15-17.

H. E. Huppert and R. S. J. Sparks. 1980a. Restrictions on the compositions of mid-ocean ridge basalts: a fluid dynamical investigation. *Nature*, **286**, 46-48.

H. E. Huppert and R. S. J. Sparks. 1980b. The fluid dynamics of a basaltic magma chamber replenished by influx of hot, dense ultrabasic magma. *Contributions to Mineralogy and Petrology*, **75**, 279-289.

H. E. Huppert and J. S. Turner. 1981. A laboratory model of a replenished magma chamber. *Earth and Planetary Science Letters*, **54**, 144-152.

T. N. Irvine. 1970. Heat transfer during solidification of layered intrusions. I. Sheets and sills. *Canadian Journal of Earth Sciences*, **7**, 1031-1061.

T. N. Irvine. 1980. Magmatic density currents and cumulus processes. *American Journal of Science*, **280A**, 1-58.

A. Jambon, B. Deruelle, G. Dreibus and F. Pineau. 1995. Chlorine and bromine abundance in MORB: the contrasting behaviour of the Mid-Atlantic Ridge and East Pacific Rise and implications for chlorine geodynamic cycles. *Chemical Geology*, **126**, 101-117.

B. B. Jensen. 1973. Patterns of trace element partitioning. *Geochimica et Cosmochimica Acta*, **37**, 2227-2242.

Z. M. Jin, H. W. Green and Y. Zhou. 1994. Melt Topology in partially molten mantle peridotite during ductile deformation. Nature, **372**, 164-167.

K. T. M. Johnson and H. J. B. Dick. 1992. Open system melting and temporal and spatial variation in peridotite and basalt at the Atlantis II Fracture Zone. *Journal of Geophysical Research*, **97**, 9219-9241.

K. T. M. Johnson, H. J. B. Dick and N. Shimizu. 1990. Melting in the oceanic upper mantle: An ion-microprobe study of diopsides in abyssal peridotites. *Journal of Geophysical Research*, **95**, 2661-2678.

T. Juteau, E. Berger and M. Cannat. 1990. Serpentinised, residual mantle peridotites from the M.A.R. median valley, ODP Hole 670A (21°10'N, 45°02'W Leg 109): Primary mineralogy and geothermometry. *In* R. Detrick, J. Honnorez, W. B. Bryan, T. Juteau et al. (eds.), Proc. Sci. Results **106/9**, Ocean Drilling Program (College Station, Texas), 123-142.

J. A. Karson, G. Thompson, S. E. Humphris, J. M. Edmond, W. B. Bryan, J. R. Brown, A. T. Winters, R. A. Pockalny, J. F. Casey, A. C. Campbell, G. Klinkhammer, M. R. Palmer, R. J. Kinzler and M. M. Sulanowska. 1987. Along-axis variations in the seafloor spreading in the MARK area. *Nature*, **328**, 681-685.

P. B. Kelemen. 1986. Assimilation of ultramafic rocks in subduction-related magmatic rocks. *Journal of Geology*, **94**, 829-843.

P. B. Kelemen, K. T. M. Johnson, R. J. Kinzler and A. J. Irving. 1990. High-field-strength element depletions in arc basalts due to mantle-magma interaction. *Nature*, **345**, 521-23.

P. B. Kelemen, H. J. B. Dick and J. E. Quick. 1992. Formation of harzburgite by pervasive melt/rock reaction in the upper mantle. *Nature*, **358**, 635-641.

P. B. Kelemen, N. Shimizu and T. Dunn. 1993. Relative depletion of niobium in some arc magmas and the continental crust: partitioning of K, Nb, La, and Ce during melt/rock reaction in the upper mantle. *Earth and Planetary Science Letters*, **120**, 111-134.

P. B. Kelemen, N. Shimizu and V. J. M. Salters. 1995. Extraction of mid-ocean-ridge basalt from the upwelling mantle by focused flow of melt in dunite channels. *Nature*, **375**, 747-753.

D. S. Kelley. 1997. Fluid evolution in slow-spreading environments. *In* J. A. Karson, M. Cannat, D. J. Miller and D. Elthon (eds.) , Proc. Sci. Results. **153**, Ocean Drilling Program (College Station, Texas), 399-415.

P. D. Kempton and J. F. Casey. 1997. Petrology and Geochemistry of Cross-cutting Diabase Dikes, Sites 920 and 921, ODP Leg 153. *In* J. A. Karson, M. Cannat, D. J. Miller and D. Elthon (eds.) , Proc. Sci. Results. **153**, Ocean Drilling Program (College Station, Texas), 363-377.

P. D. Kempton and A. G. Hunter. 1997. A Sr-Nd-Pb-O isotope study of plutonic rocks from MARK, ODP Leg 153: Implications for mantle heterogeneity and magma chamber processes. *In* J. A. Karson, M. Cannat, D. J. Miller and D. Elthon (eds.) , Proc. Sci. Results. **153**, Ocean Drilling Program (College Station, Texas), 305-320.

R. C. Kerr and S. R. Tait. 1986. Crystallisation and compositional convection in a porous medium with application to layered igneous intrusions. *Journal of Geophysical Research*, **91**, 3591-3608.

R. J. Kinzler and T. L. Grove. 1992a. Primary Magmas of Mid-Ocean Ridge Basalts 1. Experiments and Methods. *Journal of Geophysical Research*, **97**, 6885-6906.

R. J. Kinzler and T. L. Grove. 1992b. Primary Magmas of Mid-Ocean Ridge Basalts 2. Applications. *Journal of Geophysical Research*, **97**, 6907-6926.

R. J. Kinzler and T. L. Grove. 1992c. Correction and Further Discussion of the Primary Magmas of Mid-Ocean Ridge Basalts, 1 and 2. *Journal of Geophysical Research*, **98**, 22,339-22347.

E. M. Klein and C. H. Langmuir. 1987. Global correlation of ocean ridge basalt chemistry with axial depth and crustal thickness. *Journal of Geophysical Research*, **92**, 8089-8115.

E. M. Klein and C. H. Langmuir. 1989. Local Versus Global Variations in Ocean Ridge Basalt Composition: A reply. *Journal of Geophysical Research*, **99**, 4241-4252.

L. S. L. Kong, R. S. Detrick, P. J. Fox, L. A. Meyer and W. B. F. Ryan. 1988. The morphology and tectonics of the MARK area from sea beam and sea mark-1 observations (Mid-Atlantic ridge 23N). *Marine Geophysical Researches*, **10**, 59-90.

N. J. Kuznir. 1980. Thermal evolution of the oceanic crust; its dependence on spreading rate and effect on crustal structure. *Geophysical Journal of the Royal Astronomical Society*, **61**, 167-181.

C. H. Langmuir. 1989. Geochemical consequences of in situ differentiation. *Nature*, **340**, 199-205.

C. H. Langmuir, J. F. Bender and R. Batiza. 1986. Petrological and tectonic segmentation of the East Pacific Rise, 5°30'-14°30'N. *Nature*, **322**, 422-429.

C. H. Langmuir, E. M. Klein and T. Plank. 1992. Petrological Systematics of Mid-Ocean Ridge Basalts: Constraints on Melt Generation Beneath Ocean Ridges. *In* J. P. Morgan, G. K. Blackman and J. M. Sinton (eds.), Mantle flow and melt generation at Mid-Ocean Ridges **71**, American Geophysical Union, 361.

T. LaTourette, R. L. Hervig and J. R. Holloway. 1995. Trace element partitioning between amphibole, phlogopite, and basinite melt. *Earth and Planetary Science Letters*, **35**, 13-30.

B. E. Leake. 1978. Nomenclature of amphiboles. *American Mineralogist*, **63**, 1023-1052.

C. E. Lesher. 1986. Effects of Silicate liquid composition on mineral-liquid element partitioning from soret diffusion studies. *Journal of Geophysical Research*, **91**, 6123-6141.

C. E. Lesher and D. Walker. 1988. Cumulate Maturation and Melt Migration in a Temperature Gradient. *Journal of Geophysical Research*, **93**, 10,295-10,311.

B. T. R. Lewis. 1983. The East Pacific Rise and the thermal model. *Journal of Geophysical Researches*, **91**, 88.

D. J. Lieftink, T. G. Nijland and C. Maijer. 1994. The behaviour of Rare-earth elements in high-temperature Cl-bearing aqueous fluids: Results from the Odegardens Verk natural laboratory. *The Canadian Mineralogist*, **32**, 149-158.

J. Lin, G. M. Purdy, H. Schouten, J.-C. Sempere and C. Zervas. 1990. Evidence from gravity for focused magmatic accretion along the Mid-Atlantic Ridge. *Nature*, **344**, 627-632.

G. Lofgren. 1980. Experimental studies on the dynamic crystallisation of silicate melts. *In* R. B. Hargraves (ed.), Physics of magmatic processes, Princeton University Press (Princeton, New Jersey), 487-551.

P. Lonsdale, N. Blum and H. Puchelt. 1992. The RRR triple junction at the southern end of the Pacific-Cocos East Pacific Rise. *Earth and Planetary Science Letters*, **109**, 73-85.

C. C. Lundstrom, H. F. Shaw, F. J. Ryerson, D. L. Phinney, J. B. Gill and Q. Williams. 1994. Compositional controls on the partitioning of U, Th, Ba, Pb, Sr and Zr between clinopyroxene and haplobasaltic melts: implications for uranium series disequilibria in basalts. *Earth and Planetary Science Letters*, **128**, 407-423.

N. Machado, J. N. Ludden, C. Brooks and G. Thompson. 1982. Fine-scale isotopic heterogeneity in the sub-Atlantic mantle. *Nature*, **295**, 226-228.

B. D. Marsh. 1981. On the Crystallinity, Probability of Occurrence and Rheology of Lava and Magma. *Contributions to Mineralogy and Petrology*, **78**, 85-98.

B. D. Marsh. 1988a. On convective style and vigour in sheet-like magma chambers. *Journal of Petrology*, **30**, 479-530.

B. D. Marsh. 1988b. Crystal size distribution (CSD) in rocks and the kinetics and dynamics of crystallisation. *Contributions in Mineralogy and Petrology*, **99**, 277-291.

B. D. Marsh. 1996. Solidification fronts and magmatic evolution. *Mineralogical Magazine*, **60**, 5-40.

B. D. Marsh and M. R. Maxey. 1985. On the distribution and separation of crystals in convecting magma. *Journal of Volcanological and geothermal Research*, **24**, 95-150.

B. D. Marsh, B. Gunnarsson, R. Congdon and R. Carmody. 1991. Hawaiian basalt and Icelandic rhyolite: indicators of differentiation and partial melting. *Geologische Rundschau*, **80/2**, 481-510.

D. Martin and R. Nokes. 1988. Crystal settling in a vigorously convecting magma chamber. *Nature*, **332**, 534-536.

E. A. Mathez. 1984. Influence of degassing on oxidation states of basaltic magmas. *Nature*, **310**, 371-375.

E. A. Mathez. 1989. Vapour associated with mafic magma and controls on its composition. *In* J. A. Whitney and A. J. Naldrett (eds.), Ore deposition associated with magmas **4**, Society of Economic Geologists 21-31.

E. A. Mathez. 1995. Magmatic metasomatism and the formation of the Merensky reef, Bushveld complex. *Contributions to Mineralogy and Petrology,* **119**, 277-286.

E. A. Mathez, R. H. Hunter and R. Kinzler. 1997. Petrologic evolution of partially molten cumulate: The Atok section of the Bushveld complex. *Contributions to Mineralogy and Petrology,* **129**, 20-34.

A. R. McBirney. 1987. Constitutional zone refining of layered intrusions. *In* I. Parsons (ed.), Origins of Igneous Layering, D. Reidel (Dordrecht), 437-452.

A. R. McBirney. 1995. Mechanisms of differentiation in the Skaergaard Intrusion. *Journal of the Geological Society of London,* **152**, 421-435.

A. R. McBirney and R. M. Noyes. 1979. Crystallisation and layering of the Skaergaard intrusion. *Journal of Petrology,* **20**, 487-554.

A. R. McBirney and T. Murase. 1984. Rheological properties of magmas. *Annual Review of Earth and Planetary Sciences,* **12**, 337-357.

A. R. McBirney and R. H. Hunter. 1995. The cumulate paradigm reconsidered. *Journal of Geology,* **103**, 114-122.

D. McKenzie. 1984. The generation and compaction of partially molten rock. *Journal of Petrology,* **25**, 713-765.

D. McKenzie. 1985. 230Th-238U disequilibrium and the melting processes beneath ridge axes. *Earth and Planetary Science Letters,* **72**, 149-157.

D. McKenzie. 1987. The compaction of igneous and sedimentary rocks. *Journal of the Geological Society of London,* **144**, 299-307.

D. McKenzie and M. J. Bickle. 1988. The volume and composition of melt generated by extension of the lithosphere. *Journal of Petrology,* **29**, 625-679.

D. McKenzie and R. K. O'Nions. 1991. Partial Melt Distributions from Inversion of Rare Earth Element Concentrations. *Journal of Petrology,* **32**, 1021-1091.

D. McKenzie and R. K. O'Nions. 1995. The source region for ocean island basalts. *Journal of Petrology*, **36**, 133-159.

W. P. Meurer and A. E. Boudreau. 1996. Comparison of Density-Stratified Cumulates: Effect on Trapped-Liquid Distributions. *Journal of Geology*, **104**, 115-120.

P. S. Meyer, H. J. B. Dick and G. Thompson. 1989. Cumulate gabbros from the Southwest Indian Ridge, 54°S-7°16'E: implications for magmatic processes at a slow spreading ridge. *Contributions to Mineralogy and Petrology*, **103**, 44-63.

P. S. Meyer and T. Shibata. 1990. Complex zonation in plagioclase feldspar from ODP site 648. *In* R. Detrick, J. Honnorez, W. B. Bryan, T. Juteau *et al.* (eds.), Proc. Sci. Results **106/9**, Ocean Drilling Program (College Station, Texas), 123-142.

P. J. Michael and E. Bonatti. 1985. Peridotite composition from the North-Atlantic: regional and tectonic variations and implications for partial melting. *Earth and Planetary Science Letters*, **73**, 91-104.

P. J. Michael and J.-G. Schilling. 1989. Chlorine in mid-ocean ridge magmas: Evidence for assimilation of seawater-influenced components. *Geochimica et Cosmochimica Acta*, **53**, 3131-3143.

A. Miyashiro. 1973. The Troodos ophiolite was probably formed in an island arc. *Earth and Planetary Science Letters*, **19**, 218-224.

J. P. Morgan and Y. J. Chen. 1993. The Genesis of oceanic crust - magma injection, hydrothermal cooling, and crustal flow. *Journal of Geophysical Research*, **98**, 6283-6297.

R. Morishita and M. Obata. 1995. A New Statistical Description of the Spatial Distribution of Minerals in Rocks. *Journal of Geology*, **103**, 232-240.

S. A. Morse. 1984. Cation Diffusion in Plagioclase Feldspar. *Science*, **225**, 504-505.

S. A. Morse. 1986. Convection in Aid of Adcumulus Growth. *Journal of Petrology*, **27**, 1183-1214.

M. R. Muller, C. J. Robinson, T. A. Minshall, R. S. White and M. J. Bickle. 1997. Thin crust beneath ocean drilling program borehole 735B at the Southwest Indian Ridge? *Earth and Planetary Science Letters*, **148**, 93-107.

B. O. Mysen. 1990. Relationships between silicate melt structure and petrologic processes. *Earth Science Reviews*, **27**, 281-365.

A. J. Naldrett. 1989. Sulphide melts - Crystallisation temperatures, solubilities in silicate melts, and Fe, Ni and Cu partitioning between basaltic magmas and olivine. *In* J. A. Whitney and A. J. Naldrett (eds.), Ore deposition associated with magmas **4**, Society of Economic Geologists

H. R. Naslund and A. R. McBirney. 1996. Mechanisms of Formation of Igneous Layering. *In* R. G. Cawthorn (ed.), Layered Intrusions, Elsevier (Amsterdam), 1-43.

J. H. Natlund and H. J. B. Dick. 1996. Melt migration through high-level gabbroic cumulates of the east pacific rise at the Hess Deep: The origin of magma lenses and the deep crustal structure of fast-spreading ridges. *In* C. Mevel, K. M. Gillis, J. F. Allan and P. S. Meyer, Proc. ODP, Sci. Results **147**, Ocean Drilling Program (College Station, Texas), 21-58.

J. H. Natland, P. S. Meyer, H. J. B. Dick and S. H. Bloomer. 1991. Magmatic oxides and sulphides in gabbroic rocks from Hole 735B and the later development of the liquid line of descent. *In* P. R. Von Herzen, P. T. Robinson *et al.*, Proc. ODP Sci. Results **118**, Ocean Drilling Program (College Station, Texas), 75-111.

O. Navon and E. Stolper. 1987. Geochemical consequences of melt percolation: The upper mantle as a chromatographic column. *Journal of Geology*, **95**, 285-307.

A. Navrotsky. 1978. Thermodynamics of element partitioning: (1) systematics of transition metals in crystalline and molten silicates and (2) defect chemistry and "the Henry's law problem". *Geochimica et Cosmochimica Acta*, **42**, 887-902.

R. L. Nielsen and S. E. DeLong. 1992. A numerical approach to boundary layer fractionation: application to differentiation in natural systems. *Contributions to Mineralogy and Petrology*, **10**, 355-369.

A. Nicolas. 1989. Structure of Ophiolites and Dynamics of Oceanic Lithosphere. Kluwer Academic Publishers, 367.

A. Nicolas and B. Ildefonse. 1996. Flow mechanism and viscosity in basaltic magma chambers. *Geophysical Research Letters*, **23**, 2013-2016.

K. Niida. 1997. Mineralogy of MARK peridotites: replacement through magma channelling examined from Hole 920D, MARK AREA. *In* J. A. Karson, M. Cannat, D. J. Miller and D. Elthon (eds.) , Proc. Sci. Results. **153**, Ocean Drilling Program (College Station, Texas), 265-275.

Y. Niu. 1997. Mantle melting and melt extraction processes beneath ocean ridges: evidence from abyssal peridotites. *Journal of Petrology*, **38**, 1047-1074.

Y. Niu and R. Batiza. 1991. An empirical Method for Calculating Melt Compositions Produced Beneath Mid-Ocean Ridges: Application for Axis and Off-Axis (Seamount) Melting. *Journal of Geophysical Research*, **96**, 21,753-21,777.

Y. Niu and R. Batiza. 1993. Chemical variation trends at fast and slow spreading mid-ocean ridges. *Journal of Geophysical Research*, **98**, 7887-7902.

Y. Niu and R. Hekinian. 1997a. Basaltic liquids and harzburgitic residues in the Garrett Transform: a case study at fast spreading ridges. *Earth and Planetary Science Letters*, **146**, 243-258.

Y. Niu and R. Hekinian. 1997b. Spreading-rate dependence of the extent of mantle melting beneath ocean ridges. *Nature*, **385**, 326-329.

Y. Niu, C. H. Langmuir and R. J. Kinzler. 1997. The origin of abyssal peridotites: a new perspective. *Earth and Planetary Science Letters*, **152**, 251-265.

M. J. O'Hara. 1968. Are ocean floor basalts primary magma. *Nature*, **220**, 683-685.

M. J. O'Hara. 1977. Geochemical evolution during fractional of a periodically refilled magma chamber. *Nature*, **266**, 503-507.

M. J. O'Hara and R. E. Mathews. 1981. Geochemical evolution in an advancing, periodically replenished, periodically tapped, continuously fractionating magma chamber. *Journal of the Geological Society of London*, **138**, 237-277.

N. Onuma, H. Higuchi, H. Watika and H. Nagasawa. 1968. Trace element partitioning between two pyroxenes and the host lava. *Earth and Planetary Science Letters*, **5**, 47-51.

K. Ozawa, P. S. Meyer and S. H. Bloomer. 1991. Mineralogy and textures of iron-titanium oxide gabbros and associated olivine gabbros from Hole 735B. *In* P. R.

Von Herzen, P. T. Robinson et al., Proc. ODP Sci. Results **118**, Ocean Drilling Program (College Station, Texas), 41-74.

Y. Panjasawatwong, L. V. Danyushevsky, A. J. Crawford and K. L. Harris. 1995. An experimental study of the effects of melt composition on plagioclase - melt equilibria at 5 and 10 kbars: implications for the origin of magmatic high An plagioclase. *Contributions to Mineralogy and Petrology*, **118**, 420-432.

I. Parsons. 1979. The Klokken Gabbro-Syenite Complex, South Greenland: Cryptic Variation and Origin of Inversely Graded Layering. *Journal of Petrology*, **20**, 653-694.

M. R. Perfit and D. J. Fornari. 1983. Geochemical Studies of Abyssal Lavas Recovered by DSRV *Alvin* From Eastern Galapagos Rift, Inca Transform, and Ecuador Rift 2. Phase Chemistry and Crystallisation History. *Journal of Geophysical Research*, **88**, 10,530-10,550.

A. R. Philpotts and C. D. Doyle. 1983. Effect of magma oxidation state on the extent of silicate liquid immiscibility in a tholeiitic basalt. *American Journal of Science*, **283**, 967-986.

T. Plank and C. H. Langmuir. 1992. Effects of the Melting Regime on the composition of the ocean crust. *Journal of Geophysical Research*, **97**, 19,749-19,770.

R. Powell and M. Powell. 1977. Geothermometry and oxygen barometry using co-existing iron-titanium oxides: a reappraisal. *Mineralogical Magazine*, **41**, 257-263.

G. M. Purdy, L. S. L. Kong, G. L. Christeson and S. C. Solomon. 1992. Relationship between spreading rate and the seismic structure of mid-ocean ridges. *Nature*, **355**, 815-817.

J. E. Quick and R. P. Delinger. 1993. Ductile Deformation and the Origin of Layered Gabbro in Ophiolites. *Journal of Geophysical Research*, **98**, 14015-14027.

J. R. Reynolds and C. H. Langmuir. 1997. Petrological systematics of the Mid-Atlantic Ridge south of Kane: Implications for ocean crust formation. *Journal of Geophysical Research*, **102**, 14,915-14,946.

J. M. Rhodes, M. A. Dungan, D. P. Blanchard and P. E. Long. 1979. Magma mixing at mid-ocean ridges: evidence from basalts drilled near 22°N on the Mid-Atlantic Ridge. *Tectonophysics*, **55**, 35-61.

P. T. Robinson, R. Von Herzen *et al.* 1995. Proc. ODP Initial Reports, **118**, Ocean Drilling Program (College station, Texas), 826.

P. L. Roeder and R. F. Emslie. 1970. Olivine-Liquid Equilibria. *Contributions to Mineralogy and Petrology*, **29**, 275-289.

K. Ross and D. Elthon. 1993. Cumulates from strongly depleted mid-ocean-ridge basalt. *Nature*, **365**, 826-828.

K. Ross and D. Elthon. 1997a. Cumulus and postcumulus crystallisation in the oceanic crust: Major and trace-element geochemistry of Leg 153 Gabbroic rocks. *In* J. A. Karson, M. Cannat, D. J. Miller and D. Elthon (eds.) , Proc. Sci. Results. **153**, Ocean Drilling Program (College Station, Texas), 333-353.

K. Ross and D. Elthon. 1997b. Extreme incompatible trace-element depletion in diopside in residual mantle from south of the Kane Fracture Zone. *In* J. A. Karson, M. Cannat, D. J. Miller and D. Elthon (eds.) , Proc. Sci. Results. **153**, Ocean Drilling Program (College Station, Texas), 277-284.

M. P. Ryan. 1993. Neutral Buoyancy and the structure of Mid-Ocean Ridge Magma Reservoirs. *Journal of Geophysical Research*, **98**, 22,321-22338.

F. J. Ryerson and P. C. Hess. 1978. Implications of Liquid-Liquid distribution coefficients to mineral-liquid partitioning. *Geochimica et Cosmochimica Acta*, **42**, 921-932.

V. J. M. Salters and N. Shimizu. 1988. World-wide occurrence of HFSE-depleted mantle. *Geochimica et Cosmochimica Acta*, **52**, 2177-2182.

V. J. M. Salters and S. R. Hart. 1989. The hafnium paradox and the role of garnet in the source of mid-ocean-ridge basalts. *Nature*, **342**, 420-422.

V. J. M. Salters and A. Zindler. 1995. Extreme 176Hf/177Hf in the sub-oceanic mantle. *Earth and Planetary Science letters*, **129**, 13-30.

N. J. Schultz, R. S. Detrick and S. P. Miller. 1988. Two-dimensional and 3-dimensional inversions of magnetic-anomalies in the MARK area (Mid-Atlantic ridge 23N). *Marine Geophysical Researches*, **10**, 41-57.

R. D. Shannon. 1976. Revised effective ionic radii and systematic studies of interatomic distances in halides and chalcogenides. *Acta Cryst.*, **A32**, 751-767.

J. W. Shervais. 1982. Ti-V plots and the petrogenesis of modern and ophiolitic lavas. *Earth and Planetary Science Letters*, **59**, 101-118.

N. Shimizu. 1981. Trace element incorporation into growing augite phenocryst. *Nature*, **289**, 575-577.

D. N. Shirley. 1986. Compaction of Igneous Cumulates. *Journal of Geology*, **94**, 795-809.

D. N. Shirley. 1987. Differentiation and Compaction in the Palisades sill, New Jersey. *Journal of Petrology*, **28**, 835-865.

M. C. Sinha, D. A. Navin, L. M. MacGregor, S. Constable, C. Pierce, A. White, G. Heinson and M. A. Inglis. 1997. Evidence for accumulated melt beneath the slow-spreading Mid-Atlantic Ridge. *Philosophical Transactions of the Royal Society of London. Series A*, **335**, 233-253.

C. W. Sinton, D. M. Christie, V. L. Coombs, R. L. Nielsen and M. R. Fisk. 1993. Near-primary melt inclusions in anorthite phenocrysts from the Galapagos Platform. *Earth and Planetary Science Letters*, **119**, 527-537.

J. M. Sinton and R. S. Detrick. 1992. Mid-Ocean Ridge Magma Chambers. *Journal of Geophysical Research*, **97**, 197-216.

N. H. Sleep. 1975. Formation of oceanic crust: some thermal constraints. *Journal of Geophysical Researches*, **80**, 4037-4042.

D. K. Smith and J. R. Cann. 1992. The role of seamount volcanism in crustal construction at the Mid-Atlantic Ridge (24°-30°N). *Journal of Geophysical Research*, **97**, 1645-1658.

M. Sneeringer, S. R. Hart and N. Shimizu. 1984. Strontium and samarium diffusion in diopside. *Geochimica et Cosmochimica Acta*, **48**, 1589-1608.

A. V. Sobolev. 1996. Melt Inclusions in Minerals as a Source of Principle Petrological Information. *Petrology*, **4**, 209-220.

A. V. Sobolev and N. Shimizu. 1993. Ultra-depleted primary melt inclusions in an olivine from the Mid-Atlantic Ridge. *Nature*, **363**, 151-154.

D. W. Sparks and E. M. Parmentier. 1991. Melt extraction from the mantle beneath spreading centres. *Earth and Planetary Science Letters*, **105**, 368-377.

R. S. J. Sparks and H. E. Huppert. 1984. Density changes during the fractional crystallisation of basaltic magmas: fluid dynamic implications. *Contributions to Mineralogy and Petrology*, **85**, 300-309.

R. S. J. Sparks, P. Meyer and H. Sigurdsson. 1980. Density variations amongst mid-ocean ridge basalts: implications for magma mixing and the scarcity of primitive lavas. *Earth and Planetary Science Letters*, **46**, 419-430.

R. S. J. Sparks, H. E. Huppert, R. C. Kerr, D. P. McKenzie and S. R. Tait. 1985. Postcumulus processes in layered intrusions. *Geological Magazine*, **122**, 555-568.

R. S. J. Sparks, H. E. Huppert, T. Koyaguchi and M. A. Hallworth. 1993. Origins of modal and rhythmic igneous layering by sedimentation in a convecting magma chamber. *Nature*, **361**, 246-249.

M. Spiegelman and D. McKenzie. 1987. Simple 2-D models for melt extraction at mid-ocean ridges and island arcs. *Earth and Planetary Science Letters*, **83**, 137-152.

C. J. Stephens. 1997. Heterogeneity of oceanic peridotite from the western canyon wall at MARK: Results from Site 920. *In* J. A. Karson, M. Cannat, D. J. Miller and D. Elthon (eds.) , Proc. Sci. Results. **153**, Ocean Drilling Program (College Station, Texas), 285-33.

D. J. Stevenson. 1994. Weakening under stress. *Nature*, **372**, 129-130.

J. Stimac and D. Hickmott. 1994. Trace-element partition coefficients for ilmenite, orthopyroxene and pyrhotite in rhyolite determined by micro-PIXE analysis. *Chemical Geology*, **117**, 313-330.

E. Stolper and D. Walker. 1980. Melt density and the average composition of basalt. *Contributions to Mineralogy and Petrology*, **74**, 7-12.

G. E. Sullivan. 1991. Chemical evolution of basalts from 23N along the mid-Atlantic ridge: evidence from melt inclusion. *Contributions to Mineralogy and Petrology*, **106**, 296-308.

C.-O. Sun, R. J. Williams and S.-s. Sun. 1974. Distribution coefficients of Eu and Sr for plagioclase-liquid and clinopyroxene-liquid equilibria in oceanic ridge basalt: an experimental study. *Geochimica et Cosmochimica Acta*, **38**, 1415-1433.

S. -s Sun, and W. F. McDonough. 1989. Chemical and isotopic systematics of oceanic basalts: implications for mantle composition and processes. *In* A. D. Saunders and M. J. Norry (eds.), Magmatism in the ocean basins, Blackwell (Oxford), 313-345.

R. C. Tacker and J. C. Stormer Jr. 1989. A thermodynamic model for apatite solid solutions, applicable to high-temperature geologic problems. *American Mineralogist*, **74**, 877-888.

S. R. Tait, H. E. Huppert and R. S. J. Sparks. 1984. The role of compositional convection in the formation of adcumulate rocks. *Lithos*, **17**, 139-146.

S. Tait and C. Jaupart. 1992. Compositional Convection in a Reactive Crystalline Mush and Melt Differentiation. *Journal of Geophysical Research*, **97**, 6735-6756.

C. Tegner, J. R. Wilson and C. K. Brooks. 1993. Intraplutonic Quench Zones in the Kap Edvard Holm Layered Gabbro Complex, East Greenland. *Journal of Petrology*, **34**, 681-710.

G. Thompson, W. B. Bryan and W. G. Melson. 1979. Geological and geophysical investigation of the Mid-Cayman Rise spreading centre: Geochemical variation and petrogenesis of basalt glasses. *Journal of Geology*, **88**, 41-55.

L. J. Tiezzi and R. B. Scott. 1980. Crystal fractionation in a cumulate gabbro, Mid-Atlantic-Ridge 26°N. *Journal of Geophysical Research*, **85**, 5438-5454.

D. R. Toomey, S. C. Solomon, G. M. Purdy and M. H. Murray. 1985. Microearthquakes beneath the median valley of the Mid-Atlantic ridge near 23N-hypocenters and focal mechanisms. *Journal of Geophysical Researches*, **90**, 5443-5458.

M. J. Toplis, G. Libourel and M. R. Carroll. 1994. The role of phosphorous in crystallisation processes of basalt: An experimental study. *Geochimica et Cosmochimica Acta*, **58**, 797-810.

D. R. Tormey, T. L. Grove and W. B. Bryan. 1987. Experimental petrology of N-MORB near the Kane Fracture Zone: 22-25°N, mid-Atlantic ridge. *Contributions to Mineralogy and Petrology*, **96**, 121-139.

B. E. Tucholke and H. Schouten. 1988. Kane Fracture Zone. *Marine Geophysical Researches*, **10**, 1-39.

J. Tullis. 1983. Deformation of Feldspars. *In* P. H. Ribbe (ed.), Feldspar Mineralogy, Bookcrafters (Chelsea), 297-323.

J. Tullis, R. Yund, and J. Farver, 1993. Interactions of deformation, fluid distribution and bulk transport in feldspar aggregates *EOS*, **74**, 611.

P. Ulmer. 1989. The dependence of the Fe2+ - Mg2+ cation-partitioning between olivine and basaltic liquid on pressure, temperature and composition. An experimental study at 30 kbars. *Contributions to Mineralogy and Petrology*, **101**, 261-273.

E. Valsami-Jones, V. Ragnarsdottir, J. Haas and E. H. Bailey. 1994. Rare earth element transport in crustal fluids. *EOS*, **75**, 718.

L. R. Wager and G. M. Brown. 1968. Layered Igneous Rocks, Oliver and Boyd, 588.

D. Walker and S. E. DeLong. 1982. Soret Separation of Mid-Ocean Ridge Basalt Magma. *Contributions to Mineralogy and Petrology*, **79**, 231-240.

D. Walker, T. Shibata and S. E. DeLong. 1979. Abyssal tholeiites From the Oceanographer Fracture Zone. *Contributions to Mineralogy and Petrology*, **70**, 111-125.

C. Waters and A. E. Boudreau. 1996. A re-evaluation of crystal-size distributions in chromite cumulates. *American Mineralogist*, **81**, 1452-1459.

E. B. Watson. 1976. Two-liquid partition coefficients: Experimental data and geochemical implications. *Contributions to Mineralogy and Petrology*, **56**, 119-134.

E. B. Watson. 1996. Surface enrichment and trace-element uptake during crystal growth. *Geochimica et Cosmochimica Acta*, **60**, 5013-5060.

E. B. Watson and T. H. Green. 1981. Apatite/liquid partition coefficients for the rare earth elements and strontium. *Earth and Planetary Science Letters*, **56**, 405-421.

J. Weaver and C. Langmuir. 1990. Calculations of phase equilibrium in mineral-melt systems. *Computers in Geoscience*, **16**, 1-19.

R. A. Weibe and D. Snyder. 1993. Slow dense replenishments of a basic magma chamber: the layered series of the Newark Island layered intrusion, Nain, Labrador. *Contributions to Mineralogy and Petrology*, **113**, 59-72.

R. S. White, D. McKenzie and R. K. O'Nions. 1992. Oceanic Crustal Thickness From Seismic Measurements and Rare Earth Element Inversions. *Journal of Geophysical Research*, **97**, 19,683-19,715.

B. J. Wood and J. D. Blundy. 1997. A predictive model for rare earth element partitioning between clinopyroxene and anhydrous silicate melt. *Contributions to Mineralogy and Petrology*, **129**, 166-181.

M. G. Worster. 1991. Natural convection in a mushy layer. *Journal of Fluid Mechanics*, **224**, 335-359.

H.-J. Yang, G. Sen and N. Shimizu. 1998. Mid-Ocean Ridge Melting: Constraints from Lithospheric Xenoliths at Oahu, Hawaii. *Journal of Petrology*, **39**, 277-295.

A. J. Zingg. 1996. Recrystallization and the origin of layering in the Bushveld Complex. *Lithos*, **37**, 15-37.